frontiers | Research Topics

Regulation of prokaryotic cell division

Edited by
Joe Lutkenhaus, Shishen Du, Iain G. Duggin, Martin Loose, Cara C. Boutte and Yaodong Chen

Published in
Frontiers in Microbiology

ISSN 1664-8714
ISBN 978-2-83251-483-2
DOI 10.3389/978-2-83251-483-2

About Frontiers

Frontiers is more than just an open access publisher of scholarly articles: it is a pioneering approach to the world of academia, radically improving the way scholarly research is managed. The grand vision of Frontiers is a world where all people have an equal opportunity to seek, share and generate knowledge. Frontiers provides immediate and permanent online open access to all its publications, but this alone is not enough to realize our grand goals.

Frontiers journal series

The Frontiers journal series is a multi-tier and interdisciplinary set of open-access, online journals, promising a paradigm shift from the current review, selection and dissemination processes in academic publishing. All Frontiers journals are driven by researchers for researchers; therefore, they constitute a service to the scholarly community. At the same time, the *Frontiers journal series* operates on a revolutionary invention, the tiered publishing system, initially addressing specific communities of scholars, and gradually climbing up to broader public understanding, thus serving the interests of the lay society, too.

Dedication to quality

Each Frontiers article is a landmark of the highest quality, thanks to genuinely collaborative interactions between authors and review editors, who include some of the world's best academicians. Research must be certified by peers before entering a stream of knowledge that may eventually reach the public - and shape society; therefore, Frontiers only applies the most rigorous and unbiased reviews. Frontiers revolutionizes research publishing by freely delivering the most outstanding research, evaluated with no bias from both the academic and social point of view. By applying the most advanced information technologies, Frontiers is catapulting scholarly publishing into a new generation.

What are Frontiers Research Topics?

Frontiers Research Topics are very popular trademarks of the *Frontiers journals series*: they are collections of at least ten articles, all centered on a particular subject. With their unique mix of varied contributions from Original Research to Review Articles, Frontiers Research Topics unify the most influential researchers, the latest key findings and historical advances in a hot research area.

Find out more on how to host your own Frontiers Research Topic or contribute to one as an author by contacting the Frontiers editorial office: frontiersin.org/about/contact

Regulation of prokaryotic cell division

Topic editors

Joe Lutkenhaus — University of Kansas Medical Center Research Institute, United States
Shishen Du — Wuhan University, China
Iain G. Duggin — University of Technology Sydney, Australia
Martin Loose — Institute of Science and Technology Austria (IST Austria), Austria
Cara C. Boutte — University of Texas at Arlington, United States
Yaodong Chen — Northwest University, China

Citation

Lutkenhaus, J., Du, S., Duggin, I. G., Loose, M., Boutte, C. C., Chen, Y., eds. (2023). *Regulation of prokaryotic cell division*. Lausanne: Frontiers Media SA.
doi: 10.3389/978-2-83251-483-2

Table of contents

frontiers in Microbiology

ORIGINAL RESEARCH
published: 30 March 2021
doi: 10.3389/fmicb.2021.639883

The Assembly Switch Mechanism of FtsZ Filament Revealed by All-Atom Molecular Dynamics Simulations and Coarse-Grained Models

Dashuai Lv[1], Jingyuan Li[2] and Sheng Ye[1,3]**

[1] Life Sciences Institute, Zhejiang University, Hangzhou, China, [2] Zhejiang Province Key Laboratory of Quantum Technology and Device, Department of Physics, Institute of Quantitative Biology, Hangzhou, China, [3] Tianjin Key Laboratory of Function and Application of Biological Macromolecular Structures, School of Life Sciences, Tianjin University, Tianjin, China

Bacterial cytoskeletal protein FtsZ binds and hydrolyzes GTP, and assembles into dynamic filaments that are essential for cell division. Here, we used a multi-scale computational strategy that combined all-atom molecular dynamics (MD) simulations and coarse-grained models to reveal the conformational dynamics of assembled FtsZ. We found that the top end of a filament is highly dynamic and can undergo T-to-R transitions in both GTP- and GDP-bound states. We observed several subcategories of nucleation related dimer species, which leading to a feasible nucleation pathway. In addition, we observed that FtsZ filament exhibits noticeable amounts of twisting, indicating a substantial helicity of the FtsZ filament. These results agree with the previously models and experimental data. Anisotropy network model (ANM) analysis revealed a polymerization enhanced assembly cooperativity, and indicated that the cooperative motions in FtsZ are encoded in the structure. Taken together, our study provides a molecular-level understanding of the diversity of the structural states of FtsZ and the relationships among polymerization, hydrolysis, and cooperative assembly, which should shed new light on the molecular basis of FtsZ's cooperativity.

Keywords: FtsZ, molecular dynamics simulation, assembly, cooperative, conformational transition

OPEN ACCESS

Edited by:
Shishen Du,
Wuhan University, China

Reviewed by:
Harold Erickson,
Duke University, United States
Marisela Velez,
Institute of Catalysis and Petrochemistry (ICP), Spain

****Correspondence:***
Sheng Ye
sye@tju.edu.cn
Jingyuan Li
jingyuanli@zju.edu.cn

Specialty section:
This article was submitted to Microbial Physiology and Metabolism, a section of the journal Frontiers in Microbiology

Received: *10 December 2020*
Accepted: *05 March 2021*
Published: *30 March 2021*

Citation:
Lv D, Li J and Ye S (2021) The Assembly Switch Mechanism of FtsZ Filament Revealed by All-Atom Molecular Dynamics Simulations and Coarse-Grained Models. Front. Microbiol. 12:639883. doi: 10.3389/fmicb.2021.639883

INTRODUCTION

FtsZ, an ancient tubulin-like GTPase, plays pivotal roles in dividing a cell into two daughter cells (Bi and Lutkenhaus, 1991). In the presence of GTP, FtsZ subunits first polymerize into single-stranded protofilaments (Artola et al., 2017), that further coalesce into a ring-shaped pattern called Z ring (Strauss et al., 2012; Yang et al., 2017). FtsZ catalyzes the hydrolysis of GTP to GDP, which is coupled to its polymerization because the GTPase active site is completed at the interface between consecutive subunits (Mukherjee et al., 1993; Leung et al., 2004). Unlike tubulin that exhibits dynamic instability (Mitchison and Kirschner, 1984), FtsZ exhibits treadmilling (Bisson-Filho et al., 2017; Yang et al., 2017), which further directs the septal cell wall synthesis and cell division (Bisson-Filho et al., 2017; Yang et al., 2017). Treadmilling, characterized by polymerization at one end (i.e., plus end) and depolymerization at the other end (i.e., minus end), is coupled to GTPase activity and the GTPase-regulated conformational change of FtsZ subunits (Chen and Erickson, 2011; Li et al., 2013; Wagstaff et al., 2017).

FtsZ subunit adopts in two distinct conformations: an open-cleft conformation (high affinity, T state) and a closed-cleft conformation (low affinity, R state) (Fujita et al., 2017). Although two different conformations have been observed in both free subunit and filaments from different organisms, and with GTP or GDP bound (Oliva et al., 2007; Matsui et al., 2014; Fujita et al., 2017; Wagstaff et al., 2017), considerable controversy remains regarding the effect of nucleotide on the conformational change of FtsZ subunit. These results have led to two different mechanisms for the conformational changes. The "hydrolyze and bend" model proposed that the protofilament is straight with GTP- and curved with GDP-bound (Allard and Cytrynbaum, 2009). This model has been supported by both biochemical and theoretical studies. In the presence of GTP, purified FtsZ adopts either straight or intermediate curved filaments. With the hydrolysis of GTP to GDP, highly curved filaments form (Erickson et al., 1996; Lu et al., 2000; Huecas and Andreu, 2004). Molecular dynamics (MD) simulations have shown different curvatures of FtsZ filaments that are supported by a nucleotide-regulated hinge motion between subunits (Hsin et al., 2012; Ramírez-Aportela et al., 2014). Crystallographic study of the *Mycobacterium tuberculosis* FtsZ (MtbFtsZ) proposed that hydrolysis of GTP triggers a hinge-opening motion of the FtsZ subunits, thereby leading to a straight-to-curved conformational change of FtsZ filaments (Li et al., 2013). By contrast, a structural comparison of *Staphylococcus aureus* FtsZ (SaFtsZ, PDB entries: 3VOA) (Matsui et al., 2012) that adopt an open-cleft conformation in the straight filament with *Bacillus subtilis* FtsZ (BsFtsZ, PDB entry: 2RHL) (Raymond et al., 2009) that adopt an closed-cleft conformation in free subunit implies that the change of subunit conformation is affected by the structure change of FtsZ filament rather than the bound nucleotide (i.e., a polymerization-associated model). Thus, the exact role of the nucleotide in the conformational changes of FtsZ remains controversial.

In addition, the cooperative assembly of FtsZ is a prerequisite for the treadmilling of the single-stranded protofilaments. In a cooperative polymerization, the assembly of a single-stranded protofilament was proposed to have two stages: an unfavorable weak dimer or trimer nucleation followed by a more favorable elongation (Huecas et al., 2008; Miraldi et al., 2008). However, it raises a previously posed question of how a single-stranded protofilament with only one type of bond can assemble in an apparently cooperative manner. A "polymerization-associated" model was recently proposed by Wagstaff et al. to enable such a manner if the assembly switching of the R subunits (corresponding to a free subunit) into the T subunits (corresponding to the polymerized subunit) is coupled to the formation of a tight association interface between consecutive subunits along the filament (Wagstaff et al., 2017). Similarly, Miraldi et al. have proposed some possible nucleation pathways and all of which occurred of two R subunits to form a T-T dimer (Miraldi et al., 2008). Dajkovic et al. proposed a related model in which two R subunits switched to T and then associated to make a T-T dimer (Dajkovic et al., 2008). Recently Corbin and Erickson have presented a much more detailed model and suggested that nucleation occurrs when a T subunit binds an R subunit which then switches to T, resulting in a T-T dimer (Corbin and Erickson, 2020). All of the proposed models seem to work and shed light on several aspects of FtsZ assembly dynamics, but more data, especially those at the molecular-level, are needed to identify the feasible nucleation pathway from the previously proposed ones.

Along with many other studies, Ramirez-Aportela et al. suggested that a dimer or a trimer may be enough to produce the first polymerization nucleus (Chen et al., 2005; Huecas et al., 2008; Lan et al., 2008; Miraldi et al., 2008; Martín-Galiano et al., 2010; Ramírez-Aportela et al., 2014). Moreover, Corbin and Erickson proposed that if the penultimate subunit has a GDP, this interface is considerably weakened to permit the terminal subunit to switch to low affinity conformation and dissociate. As suggested by these studies (Corbin and Erickson, 2020), the middle subunit in a trimer is maintained in the T conformation regardless of GTP or GDP. Only a terminal subunit with GDP can switch to R. In order to better understand the cooperative mechanism of the protofilament assembly, the computational study about the conformation dynamics of FtsZ guided by nucleotide hydrolysis and polymerization is highly warranted.

Molecular dynamics (MD) simulation is suitable to investigate such a process. Due to the limit of computation compacity, it is difficult for MD simulations to address the process with the milliseconds-to-seconds timescales like the formation of functional FtsZ protofilaments (less than 20 subunits *in vivo* and 30–50 *in vitro*) (Romberg et al., 2001; Walker et al., 2020). Simplified coarse-grained models such as gaussian network model (GNM) and the anisotropic network model (ANM) (Bahar et al., 1997a,b; Atilgan et al., 2001; Wang et al., 2019) have been established as valid and efficient means to probe the large-scale collective motions relevant to protein functions and flexibility.

In this work, we investigated the assembly dynamics of a MtbFtsZ trimer in different nucleotide-binding states using both all-atom MD simulations and coarse-grained models. Our study provides a molecular-level understanding of the diversity of the structural states of FtsZ and the relationships among polymerization, hydrolysis, and cooperative assembly. The results allow us to fit the previously published models, and to identify the feasible nucleation pathway.

MATERIALS AND METHODS

Homology Modeling of the FtsZ Trimer

Li et al. (2013) found that a biologically relevant MtbFtsZ protofilament exhibits a curved conformation, adopting the opposite curvature toward the membrane. Such a conformation is at odds with the known membrane-facing geometry of the C terminus of the FtsZ filaments (Osawa et al., 2009). To probe whether MtbFtsZ can also adopt the curvature toward the membrane, we performed MD simulations based on MtbFtsZ. As the high affinity conformation of MtbFtsZ has not been crystallized, we constructed the three-dimensional structure of this state using Swiss-Model (Waterhouse et al., 2018)[1] with the

[1]http://swissmodel.expasy.org/

corresponding wild-type structure of SaFtsZ (Fujita et al., 2017) bound to GDP as a template (2.2 Å resolution, chain A, PDB code: 5H5G), which is an appropriate choice because of the high sequence identity (63.28%) between the target sequence and the template as well as the high structural similarity (i.e., the RMSD of C_α atoms between the low affinity conformations of MtbFtsZ (PDB entry 5ZUE, residues 9-312) (Guan et al., 2018), and SaFtsZ (PDB entry 3WGK, residues 12-315) (Matsui et al., 2014) is less than 0.9 Å). The GTP coordinate was obtained from MtbFtsZ-GTP (PDB entry 5zue) (Guan et al., 2018). The GTP- and GDP-bound trimers were constructed based on crystallographic symmetry from the SaFtsZ structure (PDB code: 5H5G), and the subunit segment residues from Ala^9 to Phe^{312} were used for simulations. The quality of the homology model was assessed by Ramachandran plot generated from PROCHECK program with 99.6% residues in the allowed regions (Laskowski et al., 1993). The stereochemistries of the models were further improved using a typical equilibrated protocol (Phillips et al., 2005) (see details below).

Systems Preparation

Two simulations systems were constructed: GTP- and GDP-bound trimers. Amber force fields ff14SB and Amber parameter database from tLeap of AmberTools 18 were used to describe the interaction of the protein and ligands (GDP and GTP) (Meagher et al., 2003; Case et al., 2005). Each trimer was immersed in cuboid boxes of TIP3P (Jorgensen et al., 1983) water molecules. The boxes were replicated by the periodic boundary conditions. All systems were neutralized by randomly placing a proper number of sodium cations in the simulation boxes.

Molecular Dynamics Simulations

All simulations were performed using the NAMD 2.12 package (Phillips et al., 2005). All systems were simulated in the NPT ensemble conditions. The temperature was maintained at 298 K by the Langevin thermostat, and the pressure was kept at 1.013 bar using the Nosé-Hoover Langevin piston control (Feller et al., 1995). The covalent bonds involving hydrogen atoms were constrained using the SHAKE algorithm (Miyamoto and Kollman, 1992), which allows the usage of a time step of 2 fs. The short-range non-bonded interactions were truncated at 12 Å. Meanwhile, the long-range electrostatic interactions were treated via the particle-mesh Ewald method (Darden et al., 1993) with a grid spacing of 1 Å. The system was equilibrated using the following sequence of steps: First, energy minimization was performed using steepest descent and conjugated gradient algorithm for 20000 steps. Then, the system was slowly heated from 50 K to the target 298 K over 6 ns through increasing the temperature by 50 K every 1 ns with the ligands and protein restrained. Thirdly, equilibration was continued for another 6 ns with only C_α atoms of protein restrained. Two 150 ns independent production runs were performed for the GTP-bound trimer. As for the GDP-bound trimer, three 450 ns independent production MD simulations were performed to obtain reliable results of the conformations of more flexible GDP-bound trimer.

Although larger-sized filaments and longer timescales (several microseconds or more) should better reproduce the macroscopic mechanics of FtsZ filaments. Two reasons lead us to believe that our simulations sampled different representative conformations of the FtsZ filaments. First, two GTP-bound simulations and two of three GDP-bound simulations showed consistent dynamical behavior of the subunit interfaces. The subunits' conformations in the GTP-bound trimer tend to maintain in T state, while those in the GDP-bound trimer tend to switch to R state. Second, our simulation times are similar with previous dimeric and heptameric filament studies (Hsin et al., 2012; Ramírez-Aportela et al., 2014), where they suggested the simulations on FtsZ were quite stable after 200 ns and the GTP state can be much more stable than GDP state. We have test this by extending one GTP-bound simulation to 300 ns, and no differences between the 150 ns and 300 ns simulations were observed in our GTP-bound state (**Supplementary Figure 1**). Two things should be noted. First, in some figures we scaled timescale of these 150 ns and 450 ns simulation to a range of 0 to 1 for easier comparison, and used "reaction coordinate" to represent it, e.g., 0 represent 0 ns and 1 represented 150 ns and 450 ns for GTP and GDP state, respectively. Second, we analyzed the results by averaging all the independent MD simulations to grasp the average behavior of FtsZ filament dynamics. Meanwhile, we further analyzed all independent trajectories to get the detailed order of switching of each subunit in the trimer and fit the results into the previously published models.

SVD Analysis of the MD Trajectories

Singular value decomposition (SVD) analysis of the MD trajectories provides an effective means for separating different conformations (Ren, 2016). SVD of C-alpha atom's distance matrices of FtsZ obtained from MD trajectories was performed in each system using Matlab. Because the first few singular vectors (here refer as principal components, PCs) provide useful description of subpopulations. Thus, we performed FEL analysis (Tripathi et al., 2018) to compare the independent trajectories in one conformation space by calculating joint probability distribution from essential plane made by top two PCs obtained from the SVD analysis of the MD trajectories.

Linear Regression

Linear regressions were calculated by the LinearModel class in Matlab. F-statistic were used for the observed *p*-values of linear regressions, where the null hypothesis is a zero coefficient of regression. The *p*-values were adjusted to represent a sample size corresponding to a 1-ns interval between independent states for the simulation (Ng et al., 2019).

Calculation of Buried Solvent-Accessible Surface Area

The buried SASA between subunits can be expressed as:

$$\text{buried SASA} = (M_1 + M_2 - M_{1+2})/2 \quad (6)$$

where M_1 and M_2 represent the SASA of each subunit, M_{1+2} represent the SASA of the complex of the two subunits.

More details regarding the buried SASA calculations have been described in previous work (Hsin et al., 2012).

Cross Correlations Between Atomic Fluctuations

To remove the border effects that are induced in MD simulations while without the expense of removing the end subunits, we calculated the correlation between residue fluctuations based on ANM method (ANM source codes obtained from Bahar lab)[2], which is exclusively based on inter-residue contacts without the consideration of environment. In the studies, the final simulated GTP- and GDP-bound structures were chosen for ANM studies. A cutoff distance of 15 Å is adopted to include a somewhat broader range of interactions. And the correlations are obtained over 45 modes of motion. The values of pair-wise cross-correlations between residues (C_{ij}) are between –1 and 1. The positive values represent the motions in the same direction, and the negative values illustrate the residues move in the opposite direction (**Figure 11H**). The higher the absolute value is, the more the two residues are correlated. The value $C_{ij} = 0$ means that the motions of residues are completely uncorrelated.

RESULTS

Comparison of the Independent Simulations

Free energy landscape analysis (see Methods) was performed to study both GTP- and GDP-bound states (**Figure 1**). There are two and three energy funnels for GTP- and GDP-bound states, respectively. The energy barriers between the energy funnels in the GTP-bound state are higher, whereas the GDP-bound state has broader local energy minima and can access multiple states for both trimer and subunit (**Figure 1** and **Supplementary Figure 2**). We found that the conformations with lowest energy in the five funnels correspond to the structures obtained from the final five MD trajectories (two and three for GTP- and GDP-bound states, respectively). The final simulated structures were shown around the corresponding funnels. We monitored the association strength between subunits by calculating inter-subunit's buried SASA (**Supplementary Figure 3**), and observed a clear gap between the buried SASAs of the open and closed interfaces. We hereafter denote the closed interface with a value of buried SASA higher than 1100 Å^2, and the open interface with a value lower than 1000 Å^2, respectively. In addition, we monitored the subunit's T to R transition by calculating inter-domain's distances during every MD trajectory (**Supplementary Figure 4**) and also observed a clear gap between the inter-domain distances of the T and R states. We therefore denote the R state with a reduction of the inter-domain distance more than 2.5 Å than that of the T state. We hereafter use R and T to refer the subunit conformational states, and open and closed to refer the interfaces. **Supplementary Videos 1–4** show the time evolutions of the interfaces and the conformations in the GTP- and GDP-bound states by snapshots (time-averaged structures), respectively. **Supplementary Figure 5** shows the comparison of every subunit within structures in **Figure 1** with the initial subunit in T state and the crystallographic structure of MtbFtsZ (PDB ID 4KWE) subunit in R state.

We observed both homogeneous and heterogeneous distributions of conformations for both subunits (T and R conformations) and interfaces (open and closed conformations) in the FtsZ trimers. The structure I and II obtained from the final GTP-bound trajectories share structural features with the top (binding nucleotide) interface open (GTP-interface 2, GTP-IF2) and the bottom one closed (GTP-interface 1, GTP-IF1) (**Figure 1A** and **Supplementary Figure 3**). The subunits in GTP-bound structure I form a homogeneous T-T-T (bottom-middle-top) trimer and the subunits in GTP-bound structure II form a heterogeneous T-T-R (bottom-middle-top) trimer (**Figure 1A** and **Supplementary Figure 4**). On the other hand, structure II and III of the final GDP-bound trajectories share a distinct structural feature with both interfaces open (GDP-interface 2, GDP-IF2), albeit structure I is in a somewhat closed interface (GDP-interface 1, GDP-IF1) (**Figure 1B** and **Supplementary Figure 3**). The subunits in GDP-bound structure I, II and III form R-R-R (bottom-middle-top, homogeneous), R-R-T (bottom-middle-top, heterogeneous) and R-T-R (bottom-middle-top, heterogeneous) trimers, respectively (Figure B and **Supplementary Figure 4**). Overall, the GDP-bound filaments revealed a higher conformational variability, whereas the GTP-bound filaments adopted rigid conformations. Such a nucleotide-regulated conformational variability agrees with previous studies (Hsin et al., 2012; Ramírez-Aportela et al., 2014). Although both GTP- and GDP-bound states can exhibit a heterogeneous distribution of T and R conformations in trimers, we observed that the T conformations tend to be adopted by GTP-bound FtsZ, while the R conformations by GDP-bound FtsZ. Next, to obtain useful information from the simulations, both the average behavior from all parallel trajectories and also the specific behavior in individual trajectory were analyzed in each case. Importantly, we further discuss the heterogeneous distribution of T and R conformations in trimers and fit the results into the previously published models.

Bending Flexibility and Dynamics of a FtsZ Trimer

A FtsZ filament asymmetrically contains two ends. To understand what happens to the top interface in the trimer when there is no subunit above the top, and to the bottom interface with no subunit below, we used the root mean square deviations (RMSDs) of the C_α atoms of dimers to measure the structural changes of the top and bottom dimers during the simulation (**Figure 2**). As shown in **Figure 2**, both RMSDs of the top (binding nucleotide) and bottom dimers of a GDP-bound trimer were ∼11 Å (red solid and dashed lines). By contrast, the RMSDs of the dimers in GTP-bound trimer are asymmetric: the RMSD of the bottom dimer was ∼7 Å (**Figure 2**, blue dashed line), while that of the top one was ∼13 Å (**Figure 2**, blue solid line).

[2]http://anm.csb.pitt.edu/

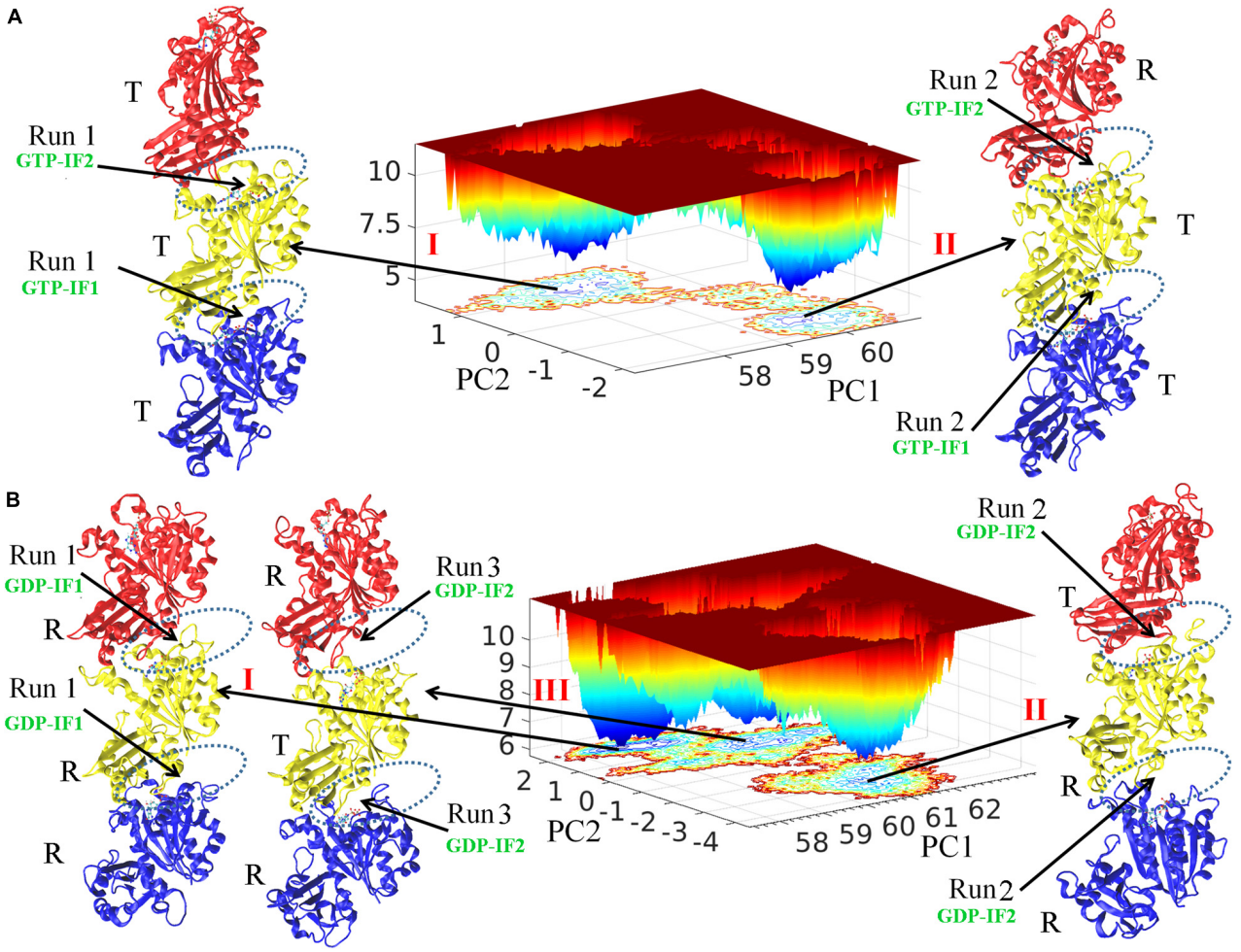

FIGURE 1 | Free energy landscape and the structural analysis. FEL plot of GTP- **(A)** and GDP-bound **(B)** trimers during whole production simulations. The final conformations from independent simulations were named I, II and III. The interfaces are indicated by dashed ellipses. The bottom, middle and top subunit are colored with blue, yellow and red, respectively. PC1 and PC2 are the first and second singular vectors obtained from SVD analysis, respectively. The *z* axis corresponds to free energy (k_BT).

In addition, the buried SASAs of the dimers revealed a similar trend while with more details. The GTP-bound bottom dimer tends to maintain a high buried SASA of ∼1100 Å^2 (**Figure 3**, blue line and **Supplementary Figure 6A**), indicating a stronger inter-subunit interaction and a more compact interface (closed interface). By contrast, the buried SASA for the GTP-bound top interface reduces to ∼900 Å^2 (**Figure 3**, yellow line and **Supplementary Figure 6A**), indicating the tendency to form a weakened inter-subunit interaction (open interface). As for the case of GDP-bound trimer, the top and bottom interfaces reached similar buried SASA values of ∼980 Å^2 and ∼930 Å^2 (**Figure 3**, red and green lines and **Supplementary Figure 6B**), indicating the tendency to form weak inter-subunit interactions. Nevertheless, the buried SASA values of the GDP-bound top interface significantly reduces in the early stage of simulation (**Supplementary Figure 6B**, blue line), while the bottom interface experiences a period of relatively large buried SASA for nearly 100 ns, fluctuating around 1100 Å^2. At ≈ 100 ns, the buried SASA of the GDP-bound bottom interface continuously reduces (**Supplementary Figure 6B**, red line). These results demonstrate that the intrinsic structure dynamic of the top interface without subunit above in the filament is considerable, and thus more prone to disassembly. The dynamic difference between the top and bottom interface leads us to suggest that the top end of FtsZ filament to be the kinetic minus end and the bottom end to be the plus end. This agrees well with the mutagenesis studies (Du et al., 2018).

We further analyzed the averaged rotation angles of the subunit-subunit interfaces (see **Figure 4** for details). Both GTP- and GDP-bound trimers exhibit noticeable bending flexibility (**Supplementary Figures 7A–C**). The probability distributions (**Figures 5A–C**) revealed a higher bending flexibility in the GDP-bound state ($\theta_1 = -24.7°$, $\theta_2 = 13.7°$ and $\theta_3 = 3.8°$) than that in the GTP-bound state ($\theta_1 = -21.2°$, $\theta_2 = 2.8°$ and $\theta_3 = 0.6°$), and the preferred bending modes are along θ_1 and θ_2. Rotation around θ_2 matches previously proposed direction to generate

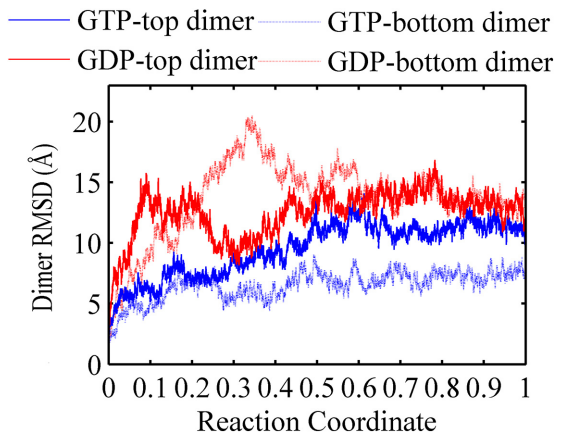

FIGURE 2 | Root mean square deviations of the C_α atoms of dimers from the initial conformation as a function of time. Blue solid line: GTP-bound top dimer. Blue dashed line: GTP-bound bottom dimer. Red solid line: GDP-bound top dimer. Red dashed line: GDP-bound bottom dimer. Reaction coordinate: 0 represent 0 ns and 1 represented 150 ns and 450 ns for GTP and GDP state, respectively. The RMSDs are from a starting zero for initial dimer conformation. In all the cases, the RMSDs are calculated by averaging all of the GTP-bound (two runs) or GDP-bound (three runs) trajectories.

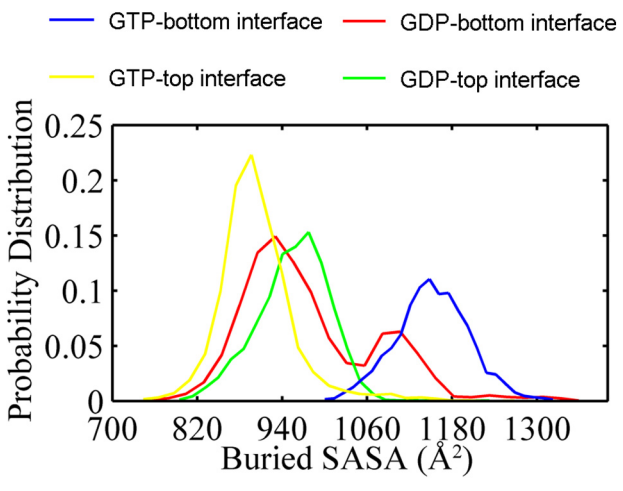

FIGURE 3 | Distribution of buried SASA values for the GTP- (yellow) and the GDP-bound (green) top interfaces, and for the GTP- (blue) and the GDP-bound (red) bottom interfaces. The interfaces start from the same value about 1200 Å^2. In all the cases, the buried SASAs are calculated by averaging all the GTP-bound (two runs) or GDP-bound (three runs) trajectories.

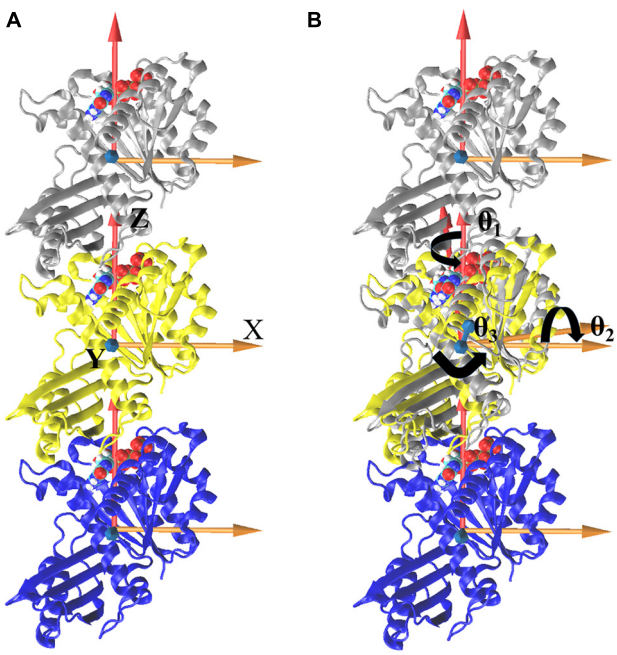

FIGURE 4 | Definitions of bending and twisting angles. Overall, the coordinate system was defined by aligning the *z* axis along the center of mass position of the one subunit to that of another subunit, fixing the *x* axis along a preferred bending direction for the trimer and defining an orthogonal *y* axis **(A)**. To measure the relative motions, trimer was first aligned with respect to the initial straight frame by superposing the middle subunits (yellow). The bending angles, θ_1 (rotations around the *Z* axis), θ_2 (rotations around the *X* axis), and θ_3 (rotations around the *Y* axis), were then tracked by calculating the rotations of the top (silver) subunit to align the initial reference frame of the middle subunit (**B**, align top subunit as an example). The same procedure is performed for bottom subunit, and the right-handed coordinate system is used here.

bending forces on the membrane (Osawa et al., 2009) with the C terminus on the outside. But our simulated bending direction (θ_2) is opposite to the direction in the crystal structure (Li et al., 2013), indicating that MtbFtsZ can bend in two opposite directions. The above twisting angle (θ_1) reflects the mean twisting flexibility in each case. In fact, we observed both homogeneous and heterogeneous interfaces in FtsZ trimers. In **Supplementary Figure 8**, we calculated the distributions of twist angles (θ_1) in four different types of interfaces. The highest probability values of θ_1 were −6.1°, −9.4°, −33.1° and −35.7° for GTP-IF1, GDP-IF1, GDP-IF2 and GTP-IF2, respectively. The ability of the FtsZ filament to access at such a large range of θ_1 in our simulations suggests a substantial plasticity of the FtsZ filament.

Coupled Motions Between Inter-domain and Inter-subunit

We found that the T-to-R conformation transitions are correlated with the dimeric conformations. The average subunit RMSDs revealed that the GDP-bound subunits exhibit larger deviations than that of the GTP-bound state (**Figure 6** and **Supplementary Figure 9**). Further analysis of the distribution of the mean inter-domain distance revealed that the GTP-bound T conformation and the GDP-bound R conformation are well defined and separated by a clear inter-domain distance about 2.5 Å (**Figure 7**). The conformational switch from T-to-R involves an inward rotation of ∼19° (calculated by DynDom (Hayward and Berendsen, 1998)) of the C-terminal domain (**Figure 8B**). In addition, we monitored the T-to-R transitions of all FtsZ subunits, including bottom, middle and top ones, in GTP-bound and GDP-bound trajectories individually (**Supplementary Figure 4**) and parallelly (**Supplementary Figure 10**). Although

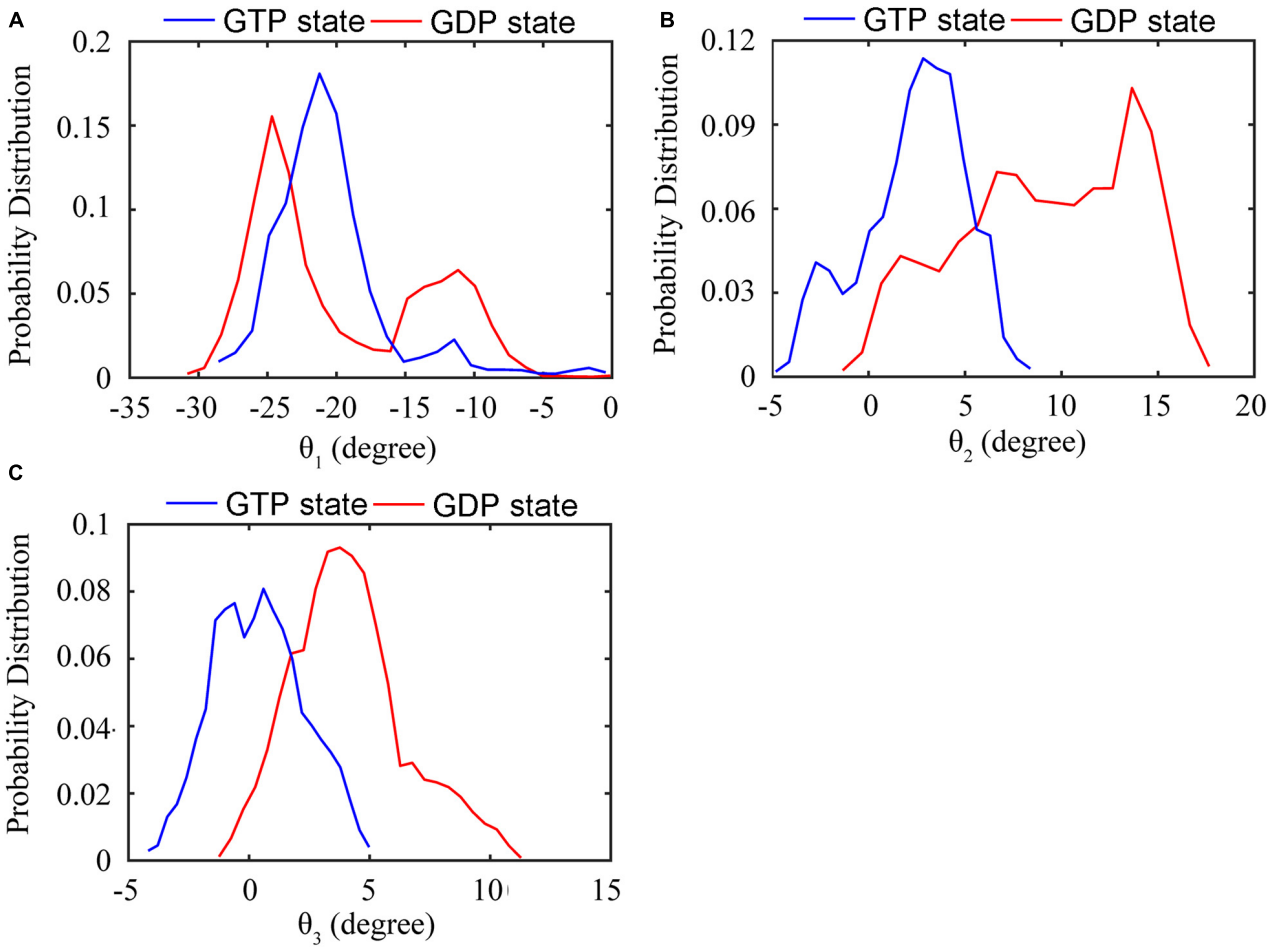

FIGURE 5 | Distribution of the relative rotation angles between subunits in the GTP- (blue) and GDP-bound (red) trimers. **(A)** Twisting motion around θ_1. **(B)** Bending motion around θ_2. **(C)** Bending motion around θ_3. In all the cases, the rotation angles are calculated by averaging both top and bottom interfaces over all GTP-bound (two runs) or GDP-bound (three runs) trajectories.

all the three subunits in GDP-bound state have the tendency to finally transition to R conformations, we found that the middle subunit experiences a period of relatively higher inter-domain distance for nearly 150 ns (**Supplementary Figure 10B**, green line), implying that the internal structural dynamics are non-homogeneously distributed within a filament. The subunits at two ends are more dynamic than the middle one, which is stabilized by subunits above and below. Importantly, we observed that the T-to-R transitions in GDP-bound subunits exhibit considerable correlation with the twisting (θ_1), bending (θ_2) and open-closed motions between subunits (**Figure 9**). This indicated that the T-to-R conformation transitions are correlated with the dimeric conformations.

Nucleotide Regulated Flexibility in FtsZ

The average root mean square fluctuations (RMSFs) of the C_α atoms of FtsZ subunit are shown in **Figure 10** and **Supplementary Figure 11**. GTP hydrolysis markedly changes the subunit flexibility. The GDP-bound state has larger RMSFs in both N- and C-terminal domains than that of the GTP-bound state (**Supplementary Figure 11**). Similar with the previous MD simulations (Hsin et al., 2012), GTP hydrolysis induced the higher flexibilities of the covering residues around the dimerization interface, i.e., the interface between the C-terminal domain of the top subunit and the N-terminal domain of the bottom subunit, especially the residues near the bound nucleotide (**Figure 10**). Surprisingly, there are some residues exhibiting higher flexibility in the regions far from the nucleotide binding site and the interface, including H1 (Q30), T1(L32, G34), H2-S3 loop (S50-A52), S3 (K55), H3 (D81) and H9-S8 loop (L246-S250) (**Figure 10**). This implies a possible long-range allosteric effect of the nucleotides on FtsZ's flexibility and dynamics. The fluctuation in both H2/H2-S3 regions (A44, S50-A52, around the switch I region (Leung et al., 2004)) and T3 loop (R64, G67-A70, in switch II region) increases upon GTP hydrolysis, indicating that nucleotide binding and hydrolysis is coupled to the perturbation of the secondary structural fluctuations. In addition, the dynamic changes at loop regions are in coordination with structural changes of the whole protein (Skliros et al., 2012; Papaleo et al., 2016). Particularly, our results show that the

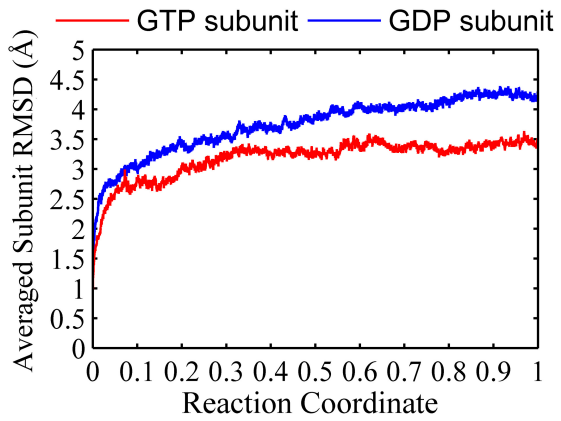

FIGURE 6 | Root mean square deviations of the C_α atoms of subunits from the initial conformation as a function of time. Red line: GTP-bound subunit. Blue line: GDP-bound subunit. Reaction coordinate: 0 represent 0 ns and 1 represented 150 ns and 450 ns for GTP and GDP state, respectively. The RMSDs are from a starting zero for initial subunit conformation. In all the cases, the RMSDs are calculated by averaging all of the three subunits of trimers in GTP-bound (two runs) or GDP-bound (three runs) trajectories.

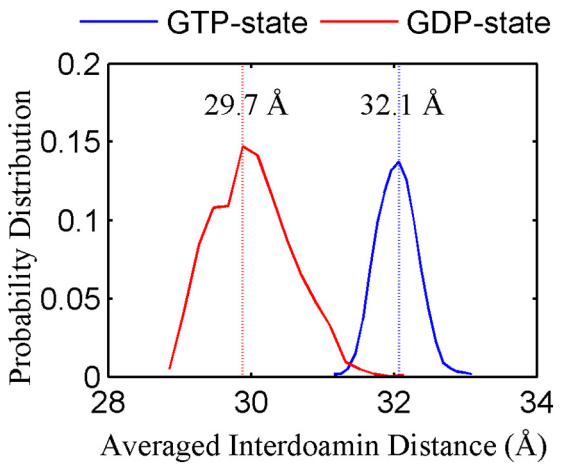

FIGURE 7 | The inter-domain distance distributions for the GTP- (blue) and GDP-bound (red) states. In all the cases, the distances are calculated by averaging all the GTP-bound (two runs) or GDP-bound (three runs) trajectories.

regions with higher flexibility mainly distribute around loops (**Figure 10**). Interestingly, both the bottom region of the top subunit, including S9 sheet (I295), S9-S10 loop (D296-S298) and H10 helix (G268-F270), and the top region of the bottom subunit associated with nucleotide binding and hydrolysis, including T5 loop, H6-H7 loop, H6 and the tip of H7 helices, exhibit higher flexibility. Thus, the flexibility change induced by GTP hydrolysis to GDP in the bottom subunit is presumably transmitted to the top subunit through direct interactions. Such a long-range allosteric effect of nucleotide is captured by our simulation.

Insights Into the Subunit Structural Switch

Detailed information about the rearrangement of the intra-subunit contacts during the structural movement is shown in **Supplementary Table 1** and **Supplementary Figure 11**. The difference of the intra-subunit contacts between GTP- and GDP-bound states reveals subtle intramolecular rearrangements, and indicates that the inter-domain's communication is indeed mediated by the central regions. During the T-to-R transitions, the contacts between H5 helix (R152, E153) and S7 sheet (G219, T220), and between H6 helix (R165, L166) and H9-S8 loop (P245, L246) were missing (**Supplementary Table 1** black and **Supplementary Figure 11B**). The switching of these interactions can play paramount roles in the T-to-R transitions. Significant changes of the inter-domain interactions mediated by the central regions (**Supplementary Figure 11**), including H7 helix (**Supplementary Table 1**, blue), T7 loop (**Supplementary Table 1**, red) and H8 helix (**Supplementary Table 1**, green), suggest a dominant role of the central regions in inter-domain's communication. Especially, key contacts made by the T7 loop (G202-N205) with the S9 sheet (F291-T293, I295) are present in the GTP-bound open-cleft subunit, whereas all of these interactions are lost in the GDP-bound closed-cleft subunit. Some other residue contacts between H7 helix (V186, G190) and the S7 (M223) and S10 sheets (T306) of the C-terminal domain formed during the T-to-R transitions, accompanying with the disruption of contacts between H7 helix (Q192, G193) and the S7 (M223, G224), S10 sheets (V307) of the C-terminal domain. Meanwhile, subtle structural rearrangements were captured in the two simulation (**Supplementary Table 1**, blue and italic), i.e., initially the bottom part of H7 helix (L196, L197) contacts with S10 sheet (T306, I308) in the GTP-bound state, whereas this region eventually forms contacts with S9 sheet (G292, V294) in the GDP-bound state. It should be noted that most of the observed residue contacts among H7 helix, and S7 and S10 sheets are participated in the regulation of PC190723 (an SaFtsZ inhibitor) on the inter-domain motions (Matsui et al., 2012). In addition, two conserved contacts (**Supplementary Table 1**, blue and bold) between H7 helix (D184, V191) and the H1 helix (M27), T1 loop (V35) of the N-terminal domain are observed during the T-to-R transitions which are consistent with previous studies (Martín-Galiano et al., 2010; Fujita et al., 2017; Wagstaff et al., 2017).

Comparison of Our Results With Previously Published Models

As shown in **Supplementary Figure 4**, the top end subunit (blue line) can switch to R conformation in either GTP-bound or GDP-bound state. We have shown that the top interface tends to be easier to open than that of the bottom interface (**Figures 2**, **3** and **Supplementary Figures 3**, **6**), thus the top end subunit tends to switch to R and rapidly dissociates. This agrees with previous experimental and theoretical studies (Du et al., 2018; Corbin and Erickson, 2020). Importantly, the middle subunit and the bottom end subunit can be seen

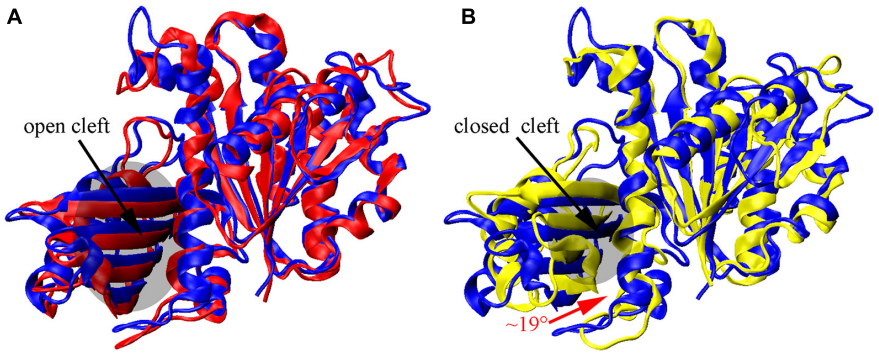

FIGURE 8 | Nucleotide-regulated subunit conformational changes. **(A,B)** superimposition of the N-terminal domain of the initial T structure (blue) on monomeric structures obtained by averaging over all three subunits from the final 10 ns GTP- (red) and GDP-bound (yellow) simulations. The inward rotation of the C-terminal domain is indicated by the red curved arrow in **(B)**.

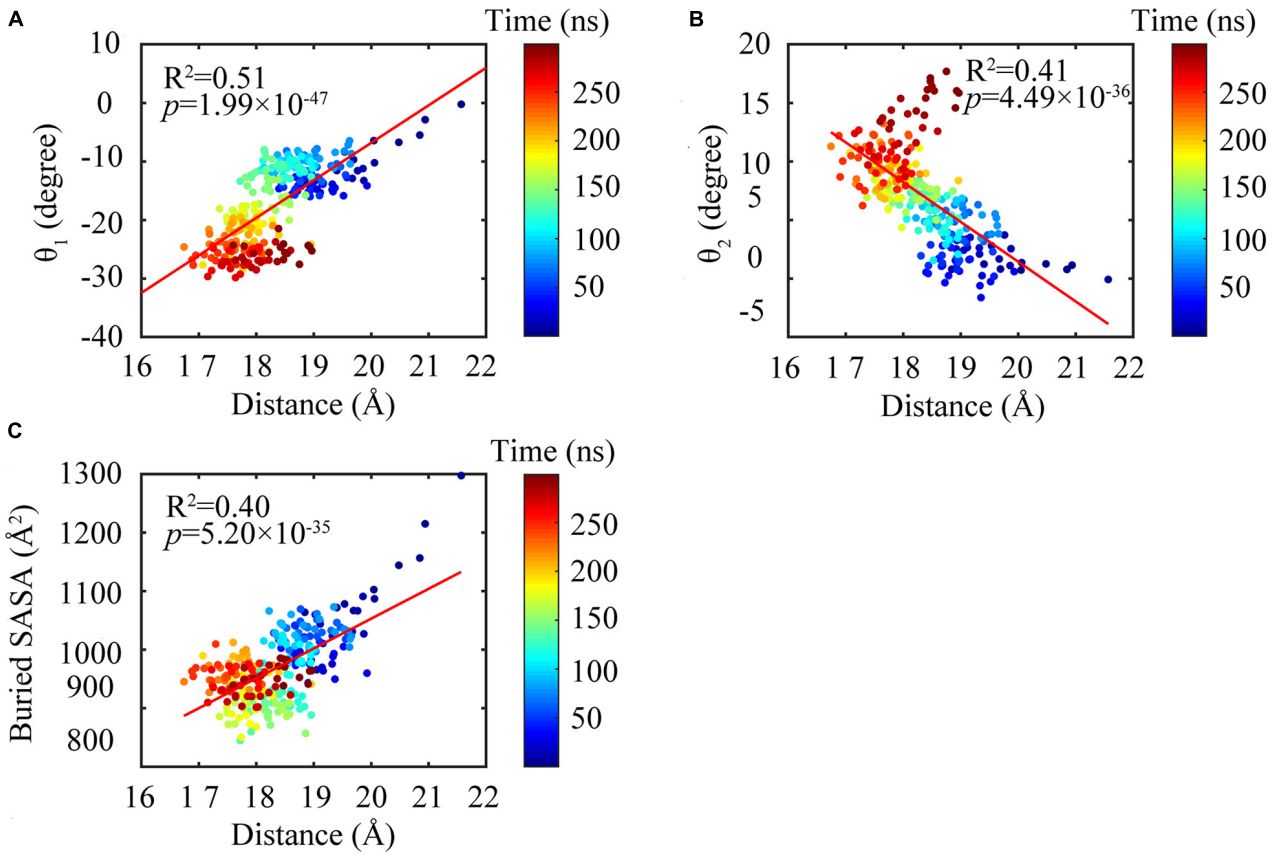

FIGURE 9 | Subunit conformations were highly correlated with the dimeric conformations. Highlighting the changing of the distance between the N- and C-terminal domains were highly correlated with bending angles θ_1 **(A)** and θ_2 **(B)** and buried SASA **(C)**.

as a nucleation related dimer. Interestingly, there are three main subcategories of the dimer species, e.g., T-T (middle-bottom, **Supplementary Figure 4**, ellipse c) dimer in the GTP state, R-R (middle-bottom, **Supplementary Figure 4**, ellipse b) and T-R (middle-bottom, **Supplementary Figure 4**, ellipse d) dimers in the GDP state. A close look at the detailed order of switching of each subunit revealed that the disassembly speed of the T-to-R transition for GDP-bound middle subunit (**Supplementary Figure 4**, green line) is slower than that of the bottom end subunit (**Supplementary Figure 4**, red line). Dajkovic et al. proposed a related model in which two R subunits switch to T and then associate to make a T-T dimer (Dajkovic et al., 2008). This will lead to a subcategory dimer T-T (top-middle) in one GTP-bound simulation while in the disassembly

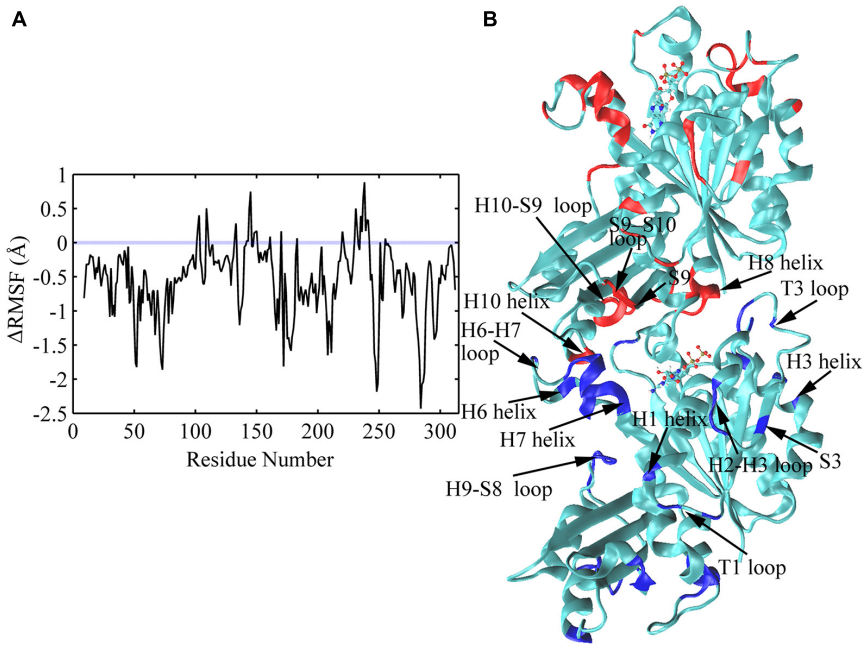

FIGURE 10 | Comparison of subunit RMSFs between GTP- and GDP-bound states. **(A)** Difference in RMSF values of each amino acid between GTP- and GDP-bound states averaged over the full trajectories. Positive values denote higher flexibility in the GTP-bound state, and negative values denote higher flexibility in the GDP-bound state. Amino acids exhibiting the largest nucleotide dependent differences in flexibility (> 1.0 Å) were discussed in the main text, and highlighted with blue and red colors in panel **(B)** in a dimeric snapshot obtained from GDP-bound trajectories.

end (**Supplementary Figure 4**, ellipse a). In agreement with Corbin and Erickson (Corbin and Erickson, 2020), the pathway is equivalent in an equilibrium situation and may represent a rare species. In addition, Miraldi et al. had suggested the existence of two possibilities of unstable intermediate dimer, T-R (top-bottom) or R-T (top-bottom) during the process to forming of a T-T dimer from two R subunits (Miraldi et al., 2008). Fujita et al. suggested that there exists a structural equilibrium between filaments in T and R states (Fujita et al., 2017). This would lead to a subcategory dimer R-R (middle-bottom, **Supplementary Figure 4**, ellipse b) in two GDP-bound simulations. However, Corbin and Erickson suggested that the structural equilibrium does not exist in solution but occurs upon crystallization (Corbin and Erickson, 2020). These seemingly contradictory findings raised an obvious question: which nucleation model is possible? Our simulation results revealed a subcategory dimer T-R (middle-bottom, **Supplementary Figure 4B**, ellipse d) during all GDP-bound simulations (**Supplementary Figure 4A**, red and blue lines) in the assembly end. Recently Corbin and Erickson had suggested that nucleation occurs when a T subunit binds an R subunit which then switches to T, resulting in a T-T dimer (Corbin and Erickson, 2020). This agrees well with our simulations results. They proposed two possible pathways following the initial association of an R subunit at the bottom end: it either switches to T and remains tightly bound, or dissociates before switching. In our results, we found that the bottom end subunit shows a nucleotide-regulated transition: R tends in GDP-bound state and T tends in GTP-bound state. Taken together, we suggested a more feasible nucleation pathway: one R and one T subunits associate to form a T-R (top-bottom) dimer, which then switches to a T-T dimer.

Analysis of Domain Motions

To remove the border effects that are induced in MD simulations, we calculated the correlation between residue fluctuations based on ANM method. As shown in **Figures 11A,B**, the cross-correlation maps based on fluctuation calculations for GTP- and GDP-bound monomeric structures cannot reveal the distinctive regions indicative of correlated motions. By contrast, in the dimeric structures, the residues within the N- and C-terminal subdomains of each subunit have positive correlations within their own regions (**Figures 11C–E**), indicating that the N- and C-terminal subdomains retain their structures during the inter-domain motions. Meanwhile, large negative correlations exist between the two subdomains of each subunit, reflecting that each subunit of dimer can individually undergo a T-R transition. Further comparison of the cross-correlations between GTP- (**Figures 11C,D**) and GDP-bound (**Figure 11E**) states revealed that the relative weak correlations between some residues of different domains in the GTP-bound dimer (**Figures 11C,D**, black circles), become positively stronger in GDP-bound dimer (**Figure 11E**, black circles). These residue pairs mainly distribute between the regions of T1 and T2 loops in the N-terminal subdomains, and the regions of S7/S8/S9 sheets and S7-H9/S8-H10/S9-S10 loops in the C-terminal subdomains. During the T-to-R transitions, more interactions form between the residues in the N-terminal subdomain and those in the C-terminal

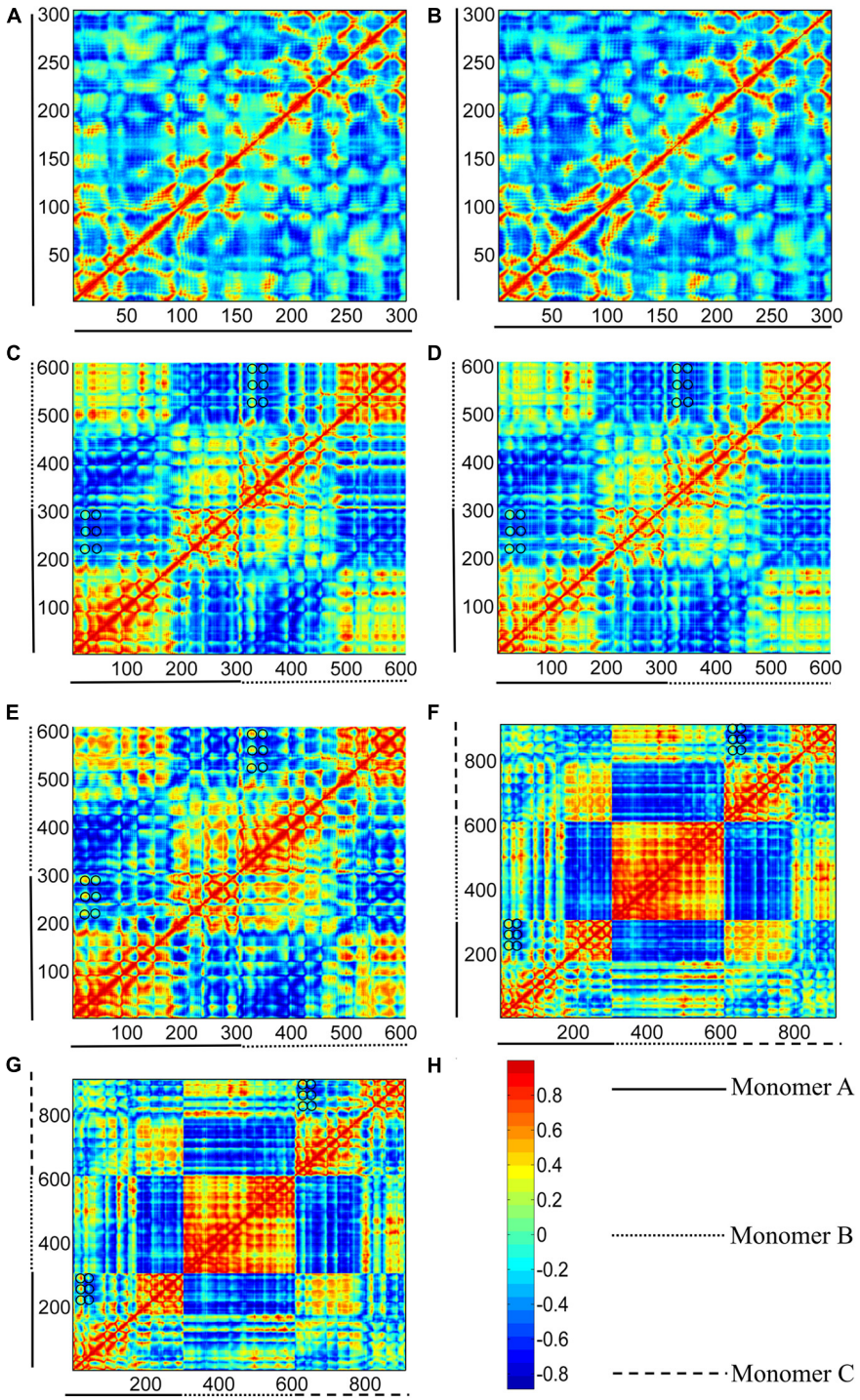

FIGURE 11 | Correlation maps between residue fluctuations calculated from GTP- and GDP-bound structure I (see **Figure 1**). **(A,B)** subunits in GTP- and GDP-bound structure I, respectively. **(C–E)** bottom (middle-bottom) and top (top-middle) dimers in GTP-bound structures I, and dimer in GDP-bound structure I. **(F,G)** trimers for GTP- and GDP-bound structure I. The two axes refer to residue indices. As shown in the color bar **(H)**, blue and red regions correspond to negatively (opposite-direction) and positively (same-direction) correlated motions, respectively. Important residues were highlight with black circles.

subdomain in the front of each subunit. In addition, the relative motions between the N- and C-terminal subdomains of the bottom subunit are negatively correlated with their counterparts in the top subunit. This indicates that each subunit exhibits symmetrical, opposite direction motions with respect to their dimer interface.

Such a T-R transition also exists in the two end subunits of a trimer (**Figures 11F,G**). It is worth noting that the middle subunit of a trimer is positively correlated, indicating that its motion is relatively rigid. This can be attributed to the fact that the middle subunit is stabilized by the adjacent subunits. We further tested such correlated motions in a tetramer and a pentamer (**Supplementary Figure 13**). Interestingly, we observed that the correlated motions in the two end subunits are gradually reduced with more subunits in a filament, (**Supplementary Figure 13**). The results based on ANM analysis suggested that a trimer can access several subcategories of dimer species that have been observed in MD simulations. Thus, strong inter-domain and inter-subunit cooperative motions are observed in the dimer and trimer structures. While in the subunits, residues are only correlated with nearby residues. Local connectivity may be the driving force for subunit motion, whereas long-range effects play a dominant role in the allosteric signal transmission and conformational couplings in polymers (Keskin et al., 2002; Atilgan et al., 2007). The results of ANM calculation suggest that the enhanced assembly cooperativity is encoded in the topological features of FtsZ polymer.

DISCUSSION

In this work, we performed molecular dynamics simulations on the GTP- or GDP-bound MtbFtsZ trimers. Different interface configurations have been observed in previous MD simulations, i.e., multiple intermediate conformations between the closed and open interfaces coexist along the GDP-bound filament rather than that of the GTP-bound ones (Ramírez-Aportela et al., 2014). Similarly, we observed that the GDP-bound trimer exhibits a higher interfacial variability. On the other hand, our simulation showed that the closed (bottom) and open (top) interfaces can also coexist within the GTP-bound trimer, which is different from previous studies. Such a discrepancy indicates that the top end of a filament is highly dynamic, which is prerequisite for treadmilling. Thus, our results suggested that the top and bottom ends of FtsZ filament are the kinetic minus and plus ends, respectively, confirming the previous experimental studies (Osawa and Erickson, 2005; Redick et al., 2005; Du et al., 2018). Notably, one of the five trajectories showed that both top and bottom interfaces are closed (**Supplementary Figure 3**).

The regulation of nucleotide state on the bending flexibility of inter-subunit interfaces were also studied by calculating three rotational angles between subunits (θ_1, θ_2, θ_3, **Figure 5**). The preferred bending directions are on θ_1 and θ_2. The importance of the preferred bending directions around θ_1 and θ_2 on generating filament curvature and force have been highlighted (Hsin et al., 2012; González De Prado Salas et al., 2014; Ramírez-Aportela et al., 2014). The mean values of θ_1 in GTP- and GDP-bound states are $\sim -25°$ and $\sim -20°$, respectively. The decomposition of θ_1 based on the four identified interfaces (GTP-IF1, GDP-IF1, GTP-IF2 and GDP-IF2) shows the ability of the FtsZ filament to access a large range of θ_1 from $\sim 0°$ to $\sim 35°$, indicating a substantial plasticity of the FtsZ filament. The combination of the bending and twisting motions between FtsZ subunits would lead to the assembly of helical FtsZ filaments. Arumugam et al. (Arumugam et al., 2012) observed that *E. coli* FtsZ filament can form helices with a pitch of about 150 nm, leading to a twist of $\sim 4.8°$ per subunit (~ 4 nm). This is compatible with those of GTP-IF1 ($-6.1°$) and GDP-IF1 ($-9.4°$) interfaces. By contrast, the crystal structures obtained by Li et al. (2013) and Guan et al. (2018) showed that the MtbFtsZ filament forms helices with six subunits per turn, a small pitch of 13 nm, leading to a twist of $\sim 30°$ per subunit. Meanwhile, an EM study showed a highly curved PaFtsZ protofilament with a pitch of about 19 nm, leading to a twist of $\sim 34.3°$ per subunit. These are compatible with those of GTP-IF2 ($-35.7°$) and GDP-IF2 ($-33.1°$) interfaces. To clearly show the twisting directions, we calculated the twisting angles (θ_1) in the structures determined in different crystal forms. By comparing our simulation results with the structures determined in different crystal forms (**Supplementary Figure 14**), we had two findings. First, FtsZ can twist in two opposite directions, supporting the earlier experimental evidence (Ramirez-Diaz et al., 2018). An inherent helical character of the filaments with more than one direction of curvature have been observed by both theoretical (González De Prado Salas et al., 2014) and experimental studies (Arumugam et al., 2012; Márquez et al., 2019). Second, the dimers with the smaller twisting angles are in tightly associated conformations, while larger twisting angles result in the loosely associated conformations. Meanwhile, as the pitch size of a helical filament is directly related to the size of the twisting angle, we suggest that GTP-bound FtsZ can form less twisted ($<\sim 6°$) filament with large-sized pitches, while GTP hydrolysis promotes FtsZ to form highly twisted ($>\sim 6°$) filament with small-sized pitches. Several lines of experimental evidence from *in vitro* studies (Arumugam et al., 2012; Mateos-Gil et al., 2019; Márquez et al., 2019) suggest that FtsZ filaments are twisted, which is functionally important, particularly considering the also frequently overlooked fact that filaments are associated to the membrane through a flexible linker. By contrast, Turner et al. (2012) suggested that the FtsZ fibers have no intrinsic global or local curvatures. Thus, exactly how much force exerted by FtsZ on the inner side of the cell membrane during cell division is due to the formation of helical structures remains elusive.

Both experimental (Artola et al., 2017) and structural studies (Wagstaff et al., 2017) proposed that the assembly switch of FtsZ involves inter-domain motions, i.e., opening clefts between subdomains, which are allosterically coupled to the formation of the longitudinal inter-subunit interfaces along the filament. Our results validated such a scenario and indicated that polymerization-associated assembly switch is driven by coupled motions between subdomains as well as the motion between subunits. Moreover, cross-correlation maps revealed that strong inter-domain and inter-subunit coupled motions are observed in both the dimer and trimer, while the correlation within subunit is very limited. These findings are in line with previously proposed views that polymerization enhances the assembly cooperativity (Wagstaff et al., 2017).

By analyzing the independent simulation trajectories, three subcategories of the dimer species, e.g., T-T (middle-bottom) dimer in GTP state, R-R (middle-bottom) and T-R

(middle-bottom) dimers in GDP state, were observed. It should be noted that the MD simulations with trimers may be influenced by border effects. However, both the ANM results (without the border effects) and the convergence between our MD simulations and previous models lead us to believe that the results of our MD simulations sampled different representative conformations of FtsZ, instead of the subject to border effects. Our data lead us to propose a model for FtsZ assembly-disassembly mechanism. In cooperative polymerization, assembly initiates in a nucleation step, followed by an elongation step (Oliva et al., 2004; Chen and Erickson, 2009). During nucleation stage, one GTP-bound R subunit and one GTP-bound T subunit associate to form a T-R (top-bottom) dimer which then forms a GTP-bound T-T dimer. Once the dimer nucleus comes into shape, the additional subunits may use similar pathways as nucleation to elongate from the bottom end. Simultaneously, polymerization-associated nucleotide hydrolysis increases the flexibility of subunits and causes filament depolymerization from the top end.

Taken together, we have four important findings. First, we observed both homogeneous and heterogeneous distributions of T and R conformations in FtsZ dimers of trimers, including T-T, T-R and R-R dimers. Second, the top end subunit of a filament tends to undergo T-to-R transitions in both GTP- and GDP-bound states. Third, FtsZ filament exhibits noticeable amounts of twisting (θ_1), ranging from $\sim$0° to $\sim$35°, in agreement with previous experimental data, indicating a substantial helicity of the FtsZ filament. Fourth, ANM analysis revealed a polymerization enhanced assembly cooperativity. It should be noted that our results do not exclude other possible assembly dynamics, considering FtsZ as 'soft' filaments that can also associate with each other and with other partners.

DATA AVAILABILITY STATEMENT

The raw data supporting the conclusions of this article will be made available by the authors, without undue reservation.

AUTHOR CONTRIBUTIONS

SY, DL, and JL conceived and designed this project. DL performed the simulations and analyzed the data. All authors participated in the data analysis and manuscript.

ACKNOWLEDGMENTS

This work was supported in part by Ministry of Science and Technology (2020YFA0908500 to SY), the National Natural Science Foundation of China (31971127 to SY), and the Fundamental Research Funds for the Central Universities (to SY).

SUPPLEMENTARY MATERIAL

The Supplementary Material for this article can be found online at: https://www.frontiersin.org/articles/10.3389/fmicb.2021.639883/full#supplementary-material

REFERENCES

Allard, J. F., and Cytrynbaum, E. N. (2009). Force generation by a dynamic Z-ring in *Escherichia coli* cell division. *Proc. Natl. Acad. Sci. U.S.A.* 106, 145–150. doi: 10.1073/pnas.0808657106

Artola, M., Ruíz-Avila, L. B., Ramírez-Aportela, E., Martínez, R. F., Araujo-Bazán, L., Vázquez-Villa, H., et al. (2017). The structural assembly switch of cell division protein FtsZ probed with fluorescent allosteric inhibitors. *Chem. Sci.* 8, 1525–1534. doi: 10.1039/c6sc03792e

Arumugam, S., Chwastek, G., Fischer-Friedrich, E., Ehrig, C., Mönch, I., and Schwille, P. (2012). Surface topology engineering of membranes for the mechanical investigation of the tubulin homologue FtsZ. *Angew. Chem. Int. Ed. Engl.* 51, 11858–11862. doi: 10.1002/anie.201204332

Atilgan, A. R., Durell, S. R., Jernigan, R. L., Demirel, M. C., Keskin, O., and Bahar, I. (2001). Anisotropy of fluctuation dynamics of proteins with an elastic network model. *Biophys. J.* 80, 505–515. doi: 10.1016/S0006-3495(01)76033-X

Atilgan, A. R., Turgut, D., and Atilgan, C. (2007). Screened nonbonded interactions in native proteins manipulate optimal paths for robust residue communication. *Biophys. J.* 92, 3052–3062. doi: 10.1529/biophysj.106.099440

Bahar, I., Atilgan, A. R., and Erman, B. (1997a). Direct evaluation of thermal fluctuations in proteins using a single-parameter harmonic potential. *Fold. Des.* 2, 173–181. doi: 10.1016/S1359-0278(97)00024-2

Bahar, I., Erman, B., and Haliloglu, T. (1997b). Gaussian dynamics of folded proteins. *Phys. Rev. Lett.* 79, 3090–3093. doi: 10.1103/PhysRevLett.79.3090

Bi, E., and Lutkenhaus, J. (1991). FtsZ ring structure associated with division in *Escherichia coli*. *Nature* 354, 161–164. doi: 10.1038/354161a0

Bisson-Filho, A. W., Hsu, Y., Squyres, G. R., Kuru, E., Wu, F., Jukes, C., et al. (2017). Treadmilling by FtsZ filaments drives peptidoglycan synthesis and bacterial cell division. *Science* 355, 739–743. doi: 10.1126/science.aak9973

Case, D. A., Cheatham, T. E. R., Darden, T., Gohlke, H., Luo, R., Merz, K. M. J., et al. (2005). The Amber biomolecular simulation programs. *J. Comput. Chem.* 26, 1668–1688. doi: 10.1002/jcc.20290

Chen, Y., Bjornson, K., Redick, S. D., and Erickson, H. P. (2005). A rapid fluorescence assay for FtsZ assembly indicates cooperative assembly with a dimer nucleus. *Biophys. J.* 88, 505–514. doi: 10.1529/biophysj.104.044149

Chen, Y., and Erickson, H. P. (2009). FtsZ filament dynamics at steady state: subunit exchange with and without nucleotide hydrolysis. *Biochemistry* 48, 6664–6673. doi: 10.1021/bi8022653

Chen, Y., and Erickson, H. P. (2011). Conformational changes of FtsZ reported by tryptophan mutants. *Biochemistry* 50, 4675–4684. doi: 10.1021/bi200106d

Corbin, L. C., and Erickson, H. P. (2020). A unified model for treadmilling and nucleation of single-stranded FtsZ protofilaments. *Biophys. J.* 119, 792–805. doi: 10.1016/j.bpj.2020.05.041

Dajkovic, A., Mukherjee, A., and Lutkenhaus, J. (2008). Investigation of regulation of FtsZ assembly by SulA and development of a model for FtsZ polymerization. *J. Bacteriol.* 190:2513. doi: 10.1128/JB.01612-07

Darden, T., York, D., and Pedersen, L. (1993). Particle mesh Ewald: an N·log(N) method for Ewald sums in large systems. *J. Chem. Phys.* 98, 10089–10092. doi: 10.1063/1.464397

Du, S., Pichoff, S., Kruse, K., and Lutkenhaus, J. (2018). FtsZ filaments have the opposite kinetic polarity of microtubules. *Proc. Natl. Acad. Sci. U.S.A.* 115:10768. doi: 10.1073/pnas.1811919115

Erickson, H. P., Taylor, D. W., Taylor, K. A., and Bramhill, D. (1996). Bacterial cell division protein FtsZ assembles into protofilament sheets and minirings, structural homologs of tubulin polymers. *Proc. Natl. Acad. Sci. U.S.A.* 93, 519–523. doi: 10.1073/pnas.93.1.519

Feller, S. E., Zhang, Y., Pastor, R. W., and Brooks, B. R. (1995). Constant pressure molecular dynamics simulation: the Langevin piston method. *J. Chem. Phys.* 103, 4613–4621. doi: 10.1063/1.470648

Fujita, J., Harada, R., Maeda, Y., Saito, Y., Mizohata, E., Inoue, T., et al. (2017). Identification of the key interactions in structural transition pathway of FtsZ from Staphylococcus aureus. *J. Struct. Biol.* 198, 65–73. doi: 10.1016/j.jsb.2017.04.008

González De Prado Salas, P., Hörger, I., Martín-García, F., Mendieta, J., Alonso, Á, Encinar, M., et al. (2014). Torsion and curvature of FtsZ filaments. *Soft Matter* 10, 1977–1986. doi: 10.1039/C3SM52516C

Guan, F., Yu, J., Yu, J., Liu, Y., Li, Y., Feng, X., et al. (2018). Lateral interactions between protofilaments of the bacterial tubulin homolog FtsZ are essential for cell division. *eLife* 7:e35578. doi: 10.7554/eLife.35578

Hayward, S., and Berendsen, H. J. C. (1998). Systematic analysis of domain motions in proteins from conformational change: new results on citrate synthase and T4 lysozyme. *Proteins* 30, 144–154. doi: 10.1002/(SICI)1097-0134(19980201)30:2<144::AID-PROT4<3.0.CO;2-N

Hsin, J., Gopinathan, A., and Huang, K. C. (2012). Nucleotide-dependent conformations of FtsZ dimers and force generation observed through molecular dynamics simulations. *Proc. Natl. Acad. Sci. U.S.A.* 109, 9432–9437. doi: 10.1073/pnas.1120761109

Huecas, S., and Andreu, J. M. (2004). Polymerization of nucleotide-free, GDP- and GTP-bound cell division protein FtsZ: GDP makes the difference. *FEBS Lett.* 569, 43–48. doi: 10.1016/j.febslet.2004.05.048

Huecas, S., Llorca, O., Boskovic, J., Martín-Benito, J., Valpuesta, J. M., and Andreu, J. M. (2008). Energetics and geometry of FtsZ polymers: nucleated self-assembly of single protofilaments. *Biophys. J.* 94, 1796–1806. doi: 10.1529/biophysj.107.115493

Jorgensen, W. L., Chandrasekhar, J., Madura, J. D., Impey, R. W., and Klein, M. L. (1983). Comparison of simple potential functions for simulating liquid water. *J. Chem. Phys.* 79, 926–935. doi: 10.1063/1.445869

Keskin, O., Durell, S. R., Bahar, I., Jernigan, R. L., and Covell, D. G. (2002). Relating molecular flexibility to function: a case study of tubulin. *Biophys. J.* 83, 663–680. doi: 10.1016/S0006-3495(02)75199-0

Lan, G., Dajkovic, A., Wirtz, D., and Sun, S. X. (2008). Polymerization and bundling kinetics of FtsZ filaments. *Biophys. J.* 95, 4045–4056. doi: 10.1529/biophysj.108.132837

Laskowski, R. A., MacArthur, M. W., Moss, D. S., and Thornton, J. M. (1993). PROCHECK: a program to check the stereochemical quality of protein structures. *J. App. Cryst.* 26, 283–291. doi: 10.1107/S0021889892009944

Leung, A. K. W., Lucile White, E., Ross, L. J., Reynolds, R. C., DeVito, J. A., and Borhani, D. W. (2004). Structure of Mycobacterium tuberculosis FtsZ reveals unexpected, G Protein-like conformational switches. *J. Mol. Biol.* 342, 953–970. doi: 10.1016/j.jmb.2004.07.061

Li, Y., Hsin, J., Zhao, L., Cheng, Y., Shang, W., Huang, K. C., et al. (2013). FtsZ protofilaments use a hinge-opening mechanism for constrictive force generation. *Science* 341, 392–395. doi: 10.1126/science.1239248

Lu, C., Reedy, M., and Erickson, H. P. (2000). Straight and curved conformations of FtsZ are regulated by GTP hydrolysis. *J. Bacteriol.* 182, 164–170. doi: 10.1128/jb.182.1.164-170.2000

Márquez, I., Díaz-Haro, G., and Vélez, M. (2019). Surface orientation and binding strength modulate shape of FtsZ on lipid surfaces. *Int. J. Mol. Sci.* 20:2545. doi: 10.3390/ijms20102545

Martín-Galiano, A. J., Buey, R. M., Cabezas, M., and Andreu, J. M. (2010). Mapping flexibility and the assembly switch of cell division protein FtsZ by computational and mutational approaches. *J. Biol. Chem.* 285, 22554–22565. doi: 10.1074/jbc.M110.117127

Mateos-Gil, P., Tarazona, P., and Vélez, M. (2019). Bacterial cell division: modeling FtsZ assembly and force generation from single filament experimental data. *FEMS Microbiol. Rev.* 43, 73–87. doi: 10.1093/femsre/fuy039

Matsui, T., Han, X., Yu, J., Yao, M., and Tanaka, I. (2014). Structural change in FtsZ Induced by intermolecular interactions between bound GTP and the T7 loop. *J. Biol. Chem.* 289, 3501–3509. doi: 10.1074/jbc.M113.514901

Matsui, T., Yamane, J., Mogi, N., Yamaguchi, H., Takemoto, H., Yao, M., et al. (2012). Structural reorganization of the bacterial cell-division protein FtsZ from Staphylococcus aureus. *Acta. Crystallogr. D Biol. Crystallogr.* 68, 1175–1188. doi: 10.1107/S0907444912022640

Meagher, K. L., Redman, L. T., and Carlson, H. A. (2003). Development of polyphosphate parameters for use with the AMBER force field. *J. Comput. Chem.* 24, 1016–1025. doi: 10.1002/jcc.10262

Miraldi, E. R., Thomas, P. J., and Romberg, L. (2008). Allosteric models for cooperative polymerization of linear polymers. *Biophys. J.* 95, 2470–2486. doi: 10.1529/biophysj.107.126219

Mitchison, T., and Kirschner, M. (1984). Dynamic instability of microtubule growth. *Nature* 312, 237–242. doi: 10.1038/312237a0

Miyamoto, S., and Kollman, P. A. (1992). Settle: an analytical version of the SHAKE and RATTLE algorithm for rigid water models. *J. Comput. Chem.* 13, 952–962. doi: 10.1002/jcc.540130805

Mukherjee, A., Dai, K., and Lutkenhaus, J. (1993). *Escherichia coli* cell division protein FtsZ is a guanine nucleotide binding protein. *Proc. Natl. Acad. Sci. U.S.A.* 90, 1053–1057. doi: 10.1073/pnas.90.3.1053

Ng, N., Shi, H., Colavin, A., and Huang, K. C. (2019). Conservation of conformational dynamics across prokaryotic actins. *PLoS Comput. Biol.* 15:e1006683. doi: 10.1371/journal.pcbi.1006683

Oliva, M. A., Cordell, S. C., and Löwe, J. (2004). Structural insights into FtsZ protofilament formation. *Nat. Struct. Mol. Biol.* 11, 1243–1250. doi: 10.1038/nsmb855

Oliva, M. A., Trambaiolo, D., and Löwe, J. (2007). Structural insights into the conformational variability of FtsZ. *J. Mol. Biol.* 373, 1229–1242. doi: 10.1016/j.jmb.2007.08.056

Osawa, M., Anderson, D. E., and Erickson, H. P. (2009). Curved FtsZ protofilaments generate bending forces on liposome membranes. *EMBO J.* 28, 3476–3484. doi: 10.1038/emboj.2009.277

Osawa, M., and Erickson, H. P. (2005). Probing the domain structure of FtsZ by random truncation and insertion of GFP. *Microbiology* 151, 4033–4043. doi: 10.1099/mic.0.28219-0

Papaleo, E., Saladino, G., Lambrughi, M., Lindorff-Larsen, K., Gervasio, F. L., and Nussinov, R. (2016). The role of protein loops and linkers in conformational dynamics and allostery. *Chem. Rev.* 116, 6391–6423. doi: 10.1021/acs.chemrev.5b00623

Phillips, J. C., Braun, R., Wang, W., Gumbart, J., Tajkhorshid, E., Villa, E., et al. (2005). Scalable molecular dynamics with NAMD. *J. Comput. Chem.* 26, 1781–1802. doi: 10.1002/jcc.20289

Ramírez-Aportela, E., López-Blanco, J. R., Andreu, J. M., and Chacón, P. (2014). Understanding nucleotide-regulated FtsZ filament dynamics and the monomer assembly switch with large-scale atomistic simulations. *Biophys. J.* 107, 2164–2176. doi: 10.1016/j.bpj.2014.09.033

Ramirez-Diaz, D. A., García-Soriano, D. A., Raso, A., Mücksch, J., Feingold, M., Rivas, G., et al. (2018). Treadmilling analysis reveals new insights into dynamic FtsZ ring architecture. *PLoS Biol.* 16:e2004845. doi: 10.1371/journal.pbio.2004845

Raymond, A., Lovell, S., Lorimer, D., Walchli, J., Mixon, M., Wallace, E., et al. (2009). Combined protein construct and synthetic gene engineering for heterologous protein expression and crystallization using Gene Composer. *BMC Biotechnol.* 9:37. doi: 10.1186/1472-6750-9-37

Redick, S. D., Stricker, J., Briscoe, G., and Erickson, H. P. (2005). Mutants of FtsZ targeting the protofilament interface: effects on cell division and GTPase activity. *J. Bacteriol.* 187, 2727–2736. doi: 10.1128/JB.187.8.2727-2736.2005

Ren, Z. (2016). Molecular events during translocation and proofreading extracted from 200 static structures of DNA polymerase. *Nucleic Acids Res.* 44, 7457–7474. doi: 10.1093/nar/gkw555

Romberg, L., Simon, M., and Erickson, H. P. (2001). Polymerization of Ftsz, a bacterial homolog of tubulin. Is assembly cooperative? *J. Biol. Chem.* 276, 11743–11753. doi: 10.1074/jbc.M009033200

Skliros, A., Zimmermann, M. T., Chakraborty, D., Saraswathi, S., Katebi, A. R., Leelananda, S. P., et al. (2012). The importance of slow motions for protein functional loops. *Phys. Biol.* 9:014001. doi: 10.1088/1478-3975/9/1/014001

Strauss, M. P., Liew, A. T. F., Turnbull, L., Whitchurch, C. B., Monahan, L. G., and Harry, E. J. (2012). 3D-SIM super resolution microscopy reveals a bead-like arrangement for FtsZ and the division machinery: implications for triggering cytokinesis. *PLoS Biol.* 10:e1001389. doi: 10.1371/journal.pbio.1001389

Tripathi, S., Srivastava, G., Singh, A., Prakasham, A. P., Negi, A. S., and Sharma, A. (2018). Insight into microtubule destabilization mechanism of 3,4,5-trimethoxyphenyl indanone derivatives using molecular dynamics simulation and conformational modes analysis. *J. Comput. Aid. Mol. Des.* 32, 559–572. doi: 10.1007/s10822-018-0109-y

Turner, D. J., Portman, I., Dafforn, T. R., Rodger, A., Roper, D. I., Smith, C. J., et al. (2012). The mechanics of FtsZ fibers. *Biophys. J.* 102, 731–738. doi: 10.1016/j.bpj.2012.01.015

Wagstaff, J. M., Tsim, M., Oliva, M. A., García-Sanchez, A., Kureisaite-Ciziene, D., Andreu, J. M., et al. (2017). A polymerization-associated structural switch in FtsZ that enables treadmilling of model filaments. *mBio* 8, e254–e217. doi: 10.1128/mBio.00254-17

Walker, B. E., Männik, J., and Männik, J. (2020). Transient membrane-linked FtsZ assemblies precede Z-Ring formation in *Escherichia coli*. *Curr. Biol.* 30, 499.e–508.e. doi: 10.1016/j.cub.2019.12.023

Wang, W. B., Zhu, J. Z., Li, X. Y., Li, C. H., Su, J. G., and Li, J. Y. (2019). Enhancement of protein mechanical stability: correlated deformations are handcuffed by ligand binding. *J. Chem. Phys.* 150:155102. doi: 10.1063/1.5054932

Waterhouse, A., Bertoni, M., Bienert, S., Studer, G., Tauriello, G., Gumienny, R., et al. (2018). SWISS-MODEL: homology modelling of protein structures and complexes. *Nucleic Acids Res.* 46, W296–W303. doi: 10.1093/nar/gky427

Yang, X., Lyu, Z., Miguel, A., McQuillen, R., Huang, K. C., and Xiao, J. (2017). GTPase activity-coupled treadmilling of the bacterial tubulin FtsZ organizes septal cell wall synthesis. *Science* 355, 744–747. doi: 10.1126/science.aak9995

Conflict of Interest: The authors declare that the research was conducted in the absence of any commercial or financial relationships that could be construed as a potential conflict of interest.

frontiers in Microbiology

HYPOTHESIS AND THEORY
published: 10 May 2021
doi: 10.3389/fmicb.2021.664704

How Teichoic Acids Could Support a Periplasm in Gram-Positive Bacteria, and Let Cell Division Cheat Turgor Pressure

*Harold P. Erickson**

Department of Cell Biology, Duke University Medical Center, Durham, NC, United States

The cytoplasm of bacteria is maintained at a higher osmolality than the growth medium, which generates a turgor pressure. The cell membrane (CM) cannot support a large turgor, so there are two possibilities for transferring the pressure to the peptidoglycan cell wall (PGW): (1) the CM could be pressed directly against the PGW, or (2) the CM could be separated from the PGW by a periplasmic space that is isoosmotic with the cytoplasm. There is strong evidence for gram-negative bacteria that a periplasm exists and is isoosmotic with the cytoplasm. No comparable studies have been done for gram-positive bacteria. Here I suggest that a periplasmic space is probably essential in order for the periplasmic proteins to function, including especially the PBPs that remodel the peptidoglycan wall. I then present a semi-quantitative analysis of how teichoic acids could support a periplasm that is isoosmotic with the cytoplasm. The fixed anionic charge density of teichoic acids in the periplasm is ~0.5 M, which would bring in ~0.5 M Na^+ neutralizing ions. This approximately balances the excess osmolality of the cytoplasm that would produce a turgor pressure of 19 atm. The 0.5 M fixed charge density is similar to that of proteoglycans in articular cartilage, suggesting a comparability ability to support pressure. An isoosmotic periplasm would be especially important for cell division, since it would allow CM constriction and PGW synthesis to avoid turgor pressure.

Keywords: periplasm, turgor pressure, teichoic acids, cartilage, plasmolysis, cryo-electron microscopy, peptidoglycan, FtsZ

OPEN ACCESS

Edited by:
Martin Loose,
Institute of Science and Technology Austria (IST Austria), Austria

Reviewed by:
Seamus Holden,
Newcastle University, United Kingdom
Sven Van Teeffelen,
Université de Montréal, Canada

***Correspondence:**
Harold P. Erickson
h.erickson@cellbio.duke.edu

Specialty section:
This article was submitted to Microbial Physiology and Metabolism, a section of the journal Frontiers in Microbiology

Received: *05 February 2021*
Accepted: *06 April 2021*
Published: *10 May 2021*

Citation:
Erickson HP (2021) How Teichoic Acids Could Support a Periplasm in Gram-Positive Bacteria, and Let Cell Division Cheat Turgor Pressure Front. Microbiol. 12:664704. doi: 10.3389/fmicb.2021.664704

INTRODUCTION

Bacterial cytoplasm has a high concentration of proteins and nucleic acids, plus their neutralizing counterions and various small molecule osmolytes. The higher osmolality of the cytoplasm relative to the outside growth medium causes it to generate a turgor pressure on the cell envelope. An important question is whether constriction of the cell envelope at cell division needs to overcome the turgor pressure. I have previously argued that it does not, based on compelling evidence from gram-negative bacteria (Erickson, 2017). Here I extend this argument with an emphasis on gram-positive bacteria.

The envelope of gram-negative bacteria comprises an inner cytoplasmic membrane (CM), a peptidoglycan wall (PGW) and an outer membrane (OM). The OM is closely attached to the

PGW by multiple covalent crosslinks, so the OM and PGW operate as a functional unit [see diagrams in Erickson (2017)]. The envelope of gram-positive bacteria has a CM and PGW and is lacking an OM. We will define the periplasm as the space between the outer face of the CM and the inner face of the PGW. Some authors have defined the periplasm as the space between the inner and outer membranes for gram-negative bacteria, but our definition provides consistency for gram-positive bacteria.

There are two possibilities for the state of the periplasm. In case 1 the CM is pressed against the PGW by cytoplasmic turgor pressure, and there is essentially no periplasmic space. In Case 2 the CM is separated from the PGW by a periplasmic space. I will first present a general argument that a periplasmic space is necessary for periplasmic proteins, in particular PGW remodeling enzymes, to function. I will review the abundant evidence that gram-negative bacteria do have a periplasm, and that the periplasm is isoosmotic with the cytoplasm. Evidence for a periplasm in gram-positive bacteria is more limited, but I will argue that a periplasm exists here also. Qualitative and quantitative analyses will suggest how teichoic acids could support and maintain this periplasmic space in gram-positive bacteria. I will conclude that the periplasm of both gram-negative and gram-positive bacteria are likely isoosmotic with the cytoplasm, which means that cytokinesis does not need to generate a force to overcome turgor pressure.

A Periplasmic Space Is Needed for the Peptidoglycan Synthesis Machinery

Matias and Beveridge (2005) briefly proposed a general argument for why a periplasm is needed: "It is probable that PBPs require a certain amount of free space within the periplasm to catalyze the development of new wall fabric." This argument needs reemphasis and elaboration.

The *Escherichia coli* PBP1b is an elongated molecule 11.5 nm long, with its transglycosylase domain near its transmembrane attachment and its transpeptidase domain at the other end (**Figure 1A**; Sung et al., 2009). The perpendicular arrangement to the membrane was supported by the arrangement of the transmembrane helix, which was present in this crystal structure. PBP1b would thus span the 11 nm periplasmic space of *E. coli* and have its transpeptidase activity near the PGW. A structure of *Staphylococcus aureus* PBP2 showed a similar arrangement of the transglycosylase domain at the membrane and the transpeptidase domain about 10 nm distal (**Figure 1B**) (Lovering et al., 2007). These authors drew the molecule tilted with respect to the membrane, but this would still require a substantial periplasmic space. Even in the most extreme case, if the PBP were flattened against the CM, its thickness of 4–5 nm would necessitate a periplasm at least that thick.

We can estimate the force that a 20 atm turgor pressure would generate on a protein molecule. 20 atm is 2×10^6 N/m^2 = 2 pN/nm^2. The tip of a PBP is about 2 × 2 nm, giving a total force of 8 pN pressing on the PBP. This is the same magnitude as the ∼5 pN force that stalls a kinesin or myosin motor molecule. If the PBP had to support a 20 atm turgor it would have to operate against the maximum force that can be generated by motor molecules.

An equally important consideration is the stereochemistry. In the extreme case where the PBP is squashed against the PGW, the transpeptidase domain would have to arrange the entrance of the peptides from two adjacent glycan strands, then form the peptide crosslink and release the product under this pressure. The transglycosidase would face similar difficulties. No structural study has addressed how a PBP might be able to function if it were flattened and squashed between the PGW and CM.

A final important point is that the diffusion of transmembrane proteins is similar in gram-negative and gram-positive bacteria. In *E. coli* the diffusion coefficient, D, ranged from 0.1 to 0.2 $\mu m^2 s^{-1}$ for proteins with a transmembrane radius up to 2.5 nm (Oswald et al., 2016). In *Bacillus subtilis* D ranged from 0.2 to 0.5 $\mu m^2 s^{-1}$ for proteins with 2–12 transmembrane segments (Lucena et al., 2018). Particularly relevant to cell division, the transpeptidases PBP3 (FtsI) in *E. coli,* and PBP2b in *B. subtilis* had virtually identical diffusion coefficients of 0.041 and 0.038 $\mu m^2\ s^{-1}$ (McCausland et al., 2021). These values are lower than ranges quoted above, perhaps because the tall PBPs are interacting with the PGW. If the gram-positive CM were pressed against the PGW by turgor, one would expect the diffusion of transmembrane proteins, especially those with a bulky periplasmic domain, to be slowed almost to zero. The approximately equal diffusion coefficients measured in gram-negative and gram-positive bacteria argues for an equivalent periplasm in both.

Evidence That the Periplasm of Gram-Negative Bacteria Is Isoosmotic With the Cytoplasm

Two studies have used radiotracers to measure the volume of the periplasm and cytoplasm in gram-negative bacteria, and how these volumes responded to osmotic shock. They provided compelling evidence that a periplasm exists and is isoosmotic with the cytoplasm. CryoEM has provided images of the periplasm consistent with these volume measurements.

The first study was from Stock et al. (1977). They labeled bacterial cell cultures with three molecules to differentiate the spaces in a bacterial pellet. $^3H\ H_2O$, which permeates all spaces including the cytoplasm, was coupled with either ^{14}C inulin, which is excluded by the OM and labels only the extracellular space, or ^{14}C sucrose, which permeates extracellular space and the periplasm but not the cytoplasm. They found that the "periplasmic volume" (which here would include the space from the IM to the OM) of *E. coli* and *Salmonella typhimurium* was 20–40% of the total cell volume when growing under static osmolal conditions. When bacteria were exposed to an osmotic shock of sucrose, which crosses the OM but not the CM, the periplasm increased in volume as the cytoplasm leaked water and contracted. They concluded that the "cytoplasmic membrane is flexible and unable to support a pressure gradient. . .Under all conditions the periplasm and cytoplasm remained isoosmotic" (Stock et al., 1977).

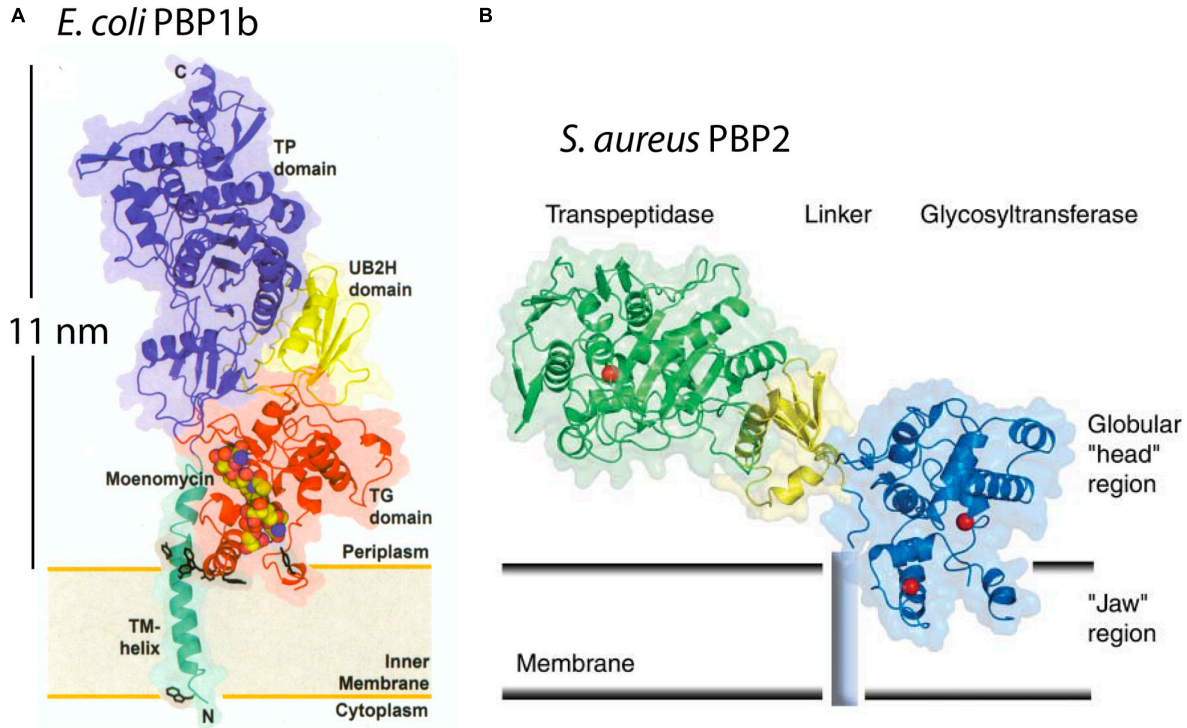

FIGURE 1 | The x-ray structures are shown for *E. coli* PBP1b **(A)** and *S. aureus* PBP2 **(B)**. They project 11 nm or 6 nm above the CM in the interpretation of the authors (Lovering et al., 2007; Sung et al., 2009). This would require a periplasmic space of at least this width. Reprinted with permission from the referenced publications.

Cayley et al. (2000) expanded the study to measure effects of osmotic shock on cells initially in low to high osmolal medium. For *E. coli* cells in low osmolal medium, the "periplasm" (here also from IM to OM) was 13% of the total cell volume. Upon osmotic shock of 1 M NaCl, which like sucrose crosses the OM but not the CM, the periplasm increased to 50% of the total cell volume. They concluded that "the periplasm and cytoplasm are isoosmotic, and that *E. coli* maintains turgor pressure across the cell wall and not across the cytoplasmic membrane" (Cayley et al., 2000). Cayley et al. (2000) is now the definitive study of osmolality of the periplasm in *E. coli* and gram-negative bacteria in general.

The osmolality of the gram-negative periplasm is thought to be generated by membrane-derived oligosaccharides, which were recently renamed osmoregulated periplasmic glucans (OPGs) (Bontemps-Gallo et al., 2017). OPGs are anionic glucose oligomers with an average charge of –5 and a size of ∼2,300 Da, which is too large to pass through the small pores of the OM-PGW layer (Kennedy, 1982; Miller et al., 1986; Cayley et al., 2000). The OPGs and their neutralizing cations generate an osmolality that matches that of the cytoplasm. Upon osmotic shock the periplasm expands, and this expansion persists for 30 min or more. However, if cells are maintained in a high osmolal medium they down-regulate synthesis of OPGs (Kennedy, 1982; Miller et al., 1986; Cayley et al., 2000). The periplasm then shrinks and the cytoplasm expands. Recent work suggests that there may be additional osmoregulatory mechanisms, since mutants defective in OPGs can survive; see (Bontemps-Gallo et al., 2017) for a comprehensive review.

Well before the study of Stock et al. (1977), the response of gram-negative bacteria to osmotic shock had been observed by phase contrast light microscopy. The response was termed "plasmolysis" and it involved the formation of one or two phase-light bubbles, usually located at the poles of the bacterium (**Figure 2A**). These "plasmolysis spaces" were understood to be expansions of the periplasm. Plasmolysis spaces in *E. coli* have been imaged more precisely in two recent studies. Sochacki et al. (2011) used periplasmic GFP to directly image the periplasm and its expansion upon osmotic shock. An elegant study of Pilizota and Shaevitz (2013) used super-resolution light microscopy to image the outer membrane and the cytoplasmic volume of *E. coli*, and thereby reconstruct the periplasm. Both studies found plasmolysis spaces at the poles of *E. coli* in response to osmotic shock of 0.3 M sucrose. We will discuss below that *B. subtilis* required much higher osmotic shock to produce visible plasmolysis (**Figure 2B**).

Turgor Pressure of *E. coli* Is Highly Dependent on External Osmolality

Cayley et al. (2000) are widely referenced for determining the turgor pressure of *E. coli* to be ∼3 atm. A later study by Deng et al. (2011) reported a turgor pressure of only 0.3 atm, and this is sometimes referenced as questioning the 3 atm of

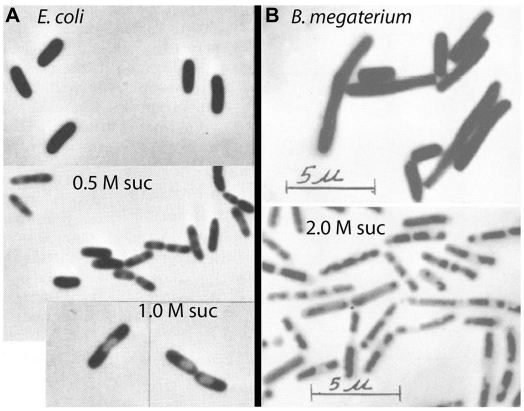

FIGURE 2 | Phase contrast images of phase-light plasmolysis spaces induced by sucrose shock. **(A)** *E. coli* undergoes plasmolysis at 0.5 – 1.0 M sucrose (Scheie and Rehberg, 1972). **(B)** Gram-positive bacteria require much higher osmotic shock to produce visible plasmolysis (Weibull, 1965). Reprinted from the indicated references with permission.

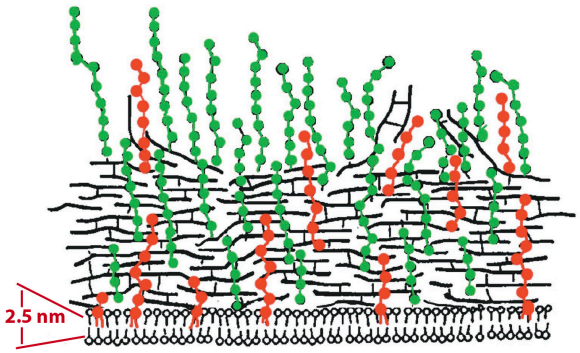

FIGURE 3 | An illustration of the gram-positive cell envelope showing a modern view of the periplasm. Neuhaus and Baddiley (2003) drew the CM pressed against the PGW, leaving essentially no periplasmic space. Horizontal black lines represent PG; Teichoic acids are green (WTA) and red (LTA). An earlier illustration of Umeda et al. (1992), which was modified to generate this figure, showed a small periplasmic space separating the CM and PGW. Reprinted from Neuhaus and Baddiley (2003) with permission.

Cayley et al. (2000). However, the 3 atm turgor in the Cayley et al. (2000) study applied only to growth in media of very low osmolality. They actually explored a full range of growth media (**Table 1**) and found that at higher osmolality the turgor dropped to the range later reported by Deng et al. (2011). It should be emphasized that normal growth media are in this higher osmolal range, where turgor pressure of *E. coli* is so small that it can hardly be measured.

Existence of a Periplasm in Gram-Positive Bacteria Is Controversial

As detailed above, volume measurements using radiotracers have provided compelling evidence for a periplasmic space in *E. coli.* Remarkably, comparable measurements for gram-positive bacteria are almost completely lacking. There is currently a widespread belief that gram-positive bacteria don't have a periplasm. This is illustrated in a figure from a modern review, where the CM is drawn pressed against the PGW (**Figure 3**) (Neuhaus and Baddiley, 2003). A much earlier diagram, which was revised to produce **Figure 3**, showed a small but distinct periplasmic space, based on early EM images (Umeda et al., 1992). In their more recent adaptation Neuhaus and Baddiley eliminated the periplasm, in keeping with the widespread belief. There is no room here for a PBP - even a bent-over PBP (**Figure 1B**) would project half-way through the indicated PGW.

TABLE 1 | Turgor pressure of *E. coli* as a function of osmolality of growth medium.

Osm of growth medium	ΔΠ atm	References
0.03	3.1 ± 0.4	Cayley et al., 2000
0.10	1.5 ± 0.3	Cayley et al., 2000
0.28	0.7 ± 1.1	Cayley et al., 2000
0.8	<0.5	Cayley et al., 2000
0.44	0.3	Deng et al., 2011

Plasmolysis is the term used for the expansion of the periplasm in response to osmotic shock. As discussed above, this was easily visualized by phase contrast microscopy as formation of plasmolysis spaces in *E. coli*. In contrast, it has long been thought that gram-positive bacteria cannot be plasmolyzed. Weibull commented in 1955 "*B. megaterium* is not plasmolysable according to Fisher, as has been confirmed by the author" (Weibull, 1955). Ten years later he amended this and suggested "that most bacteria can be plasmolyzed, but that media of a very high osmotic pressure are required to effect plasmolysis in gram-positive organisms" (Weibull, 1965). By "high osmotic pressure" he meant greater than 1 M sucrose. His image of plasmolyzed *B. megaterium* is shown in **Figure 2B**.

One early study of plasmolysis of *B. megaterium*, a gram-positive bacterium, used a radiotracer technique similar to that of Stock et al. (1977) and Cayley et al. (2000). This study by Marquis (1967) actually preceded the Stock study by 10 years. Marquis used high molecular weight dextran, which cannot penetrate the PGW, to measure the total volume of the cells in a bacterial pellet, and radio-labeled sucrose, which can penetrate the PGW but not the CM, to measure the volume of cytoplasm. The cytoplasmic volume was 66% of the total cell volume for control cells and remained at this level for sucrose shocks of 0.1 to 0.5 Osm (**Figure 4A**). Cytoplasmic volume dropped to 57% at 1 Osm, and to ∼35% at very high osmolality. Interestingly, the data of Marquis showed no change in cytoplasmic volume for shocks of 0.1 to 0.5 Osm, and only a small drop at 1 Osm. Substantial shrinkage of the cytoplasm was only seen above 1 M sucrose, consistent with the light microscopy observations of Weibull (1965) (**Figure 2B**).

Whatmore and Reed (1990) reported a similar curve for sucrose shock of *B. subtilis* (**Figure 4B**). Their article is mostly referenced for determining the turgor pressure of *B. subtilis* to be 19 atm. Their data are also relevant to the question of plasmolysis. They used a "C1000 channelizer" to measure cell volume. This assay was suggested to report cell volume, but it

may be reporting primarily cytoplasmic volume. They showed no change in cytoplasmic volume for sucrose shocks of 0.2 to 0.5 Osm, and decreasing volume for 1 Osm and above.

Whatmore and Reed (1990) analyzed the data in **Figure 4B** as a Boyle-van't Hoff plot, and calculated a turgor pressure of 19 atm for growth of *B. subtilis* in media of 0.27 Osm. This is almost two orders of magnitude higher than *E. coli* growing at 0.3 Osm, so it is important to know if this extends to other gram-positive bacteria. The Poolman lab has recently done a similar analysis of cell volume vs osmotic shock for two species. *Lactococcus lactis* had a turgor of 19 atm (Mika et al., 2014) and *Listeria monocytogenes* a turgor of 14 atm (Tran et al., 2021) in chemically defined media of 0.23 Osm. This suggests that high turgor is a general feature of gram-positive bacteria. The primary focus of both studies was to measure diffusion of cytoplasmically expressed GFP, which should be reduced by osmotic shock as cytoplasmic volume is reduced. They found large reductions in D_L even for small osmotic shocks. This contradicts the lack of response for shocks less than 1 Osm reported in the earlier studies (**Figure 4**). This unexplained plateau for low osmolal shocks may not be a general feature of gram-positive bacteria, and should be reinvestigated.

Cryosectioning EM Shows a Periplasm in Gram-Positive Bacteria; Tomographic cryoEM Does Not

Some of the best evidence for a periplasm in bacteria is the cryoEM of Matias and Beveridge. This group initially imaged *E. coli,* where they could resolve the IM, the OM and a thin PGW. There was a clear periplasmic space of 11 nm separating the IM and PGW (**Figure 5A**; Matias et al., 2003). The space between the IM and OM corresponds to 13% of the cell volume, consistent with that measured by Cayley et al. (2000). The Beveridge group subsequently used the same cryosectioning technology to image a periplasmic space of 22 nm In *B. subtilis* (**Figure 5B**) and 16 nm in *S. aureus* (Matias and Beveridge, 2005, 2006). Another laboratory using the same cryosectioning technology obtained similar images of a periplasm in *B. subtilis* (**Figure 5C**) and other gram-positive bacteria (Zuber et al., 2006).

These results were contradicted by Beeby et al. (2013), who reported that most gram-positive species showed no periplasmic space. In their cryoEM images the CM was pressed against the PGW. However, these contradictory studies used different cryoEM techniques. The Beveridge group, which showed a periplasm in both gram-negative and gram-positive bacteria, used high pressure freezing followed by cryosectioning to image thin frozen sections. Beeby, Jensen and colleagues, who reported no periplasm for gram-positive bacteria, used plunge freezing, and they imaged whole bacteria through a series of tilts. They then used tomographic reconstruction to calculate the image of a thin section at the midplane of the cell. The different results might be due to the different technologies. Curiously, however, the Jensen group (Chang et al., 2016) obtained images of the *E. coli* periplasm that are almost identical to those of the Beveridge group.

A recent cryoEM study of *B. subtilis* also showed no periplasm (Khanna et al., 2020). Because *B. subtilis* is too large for direct imaging, this group used ion beam milling to etch the cells to a ∼200 nm section of the cell center. The tomographic

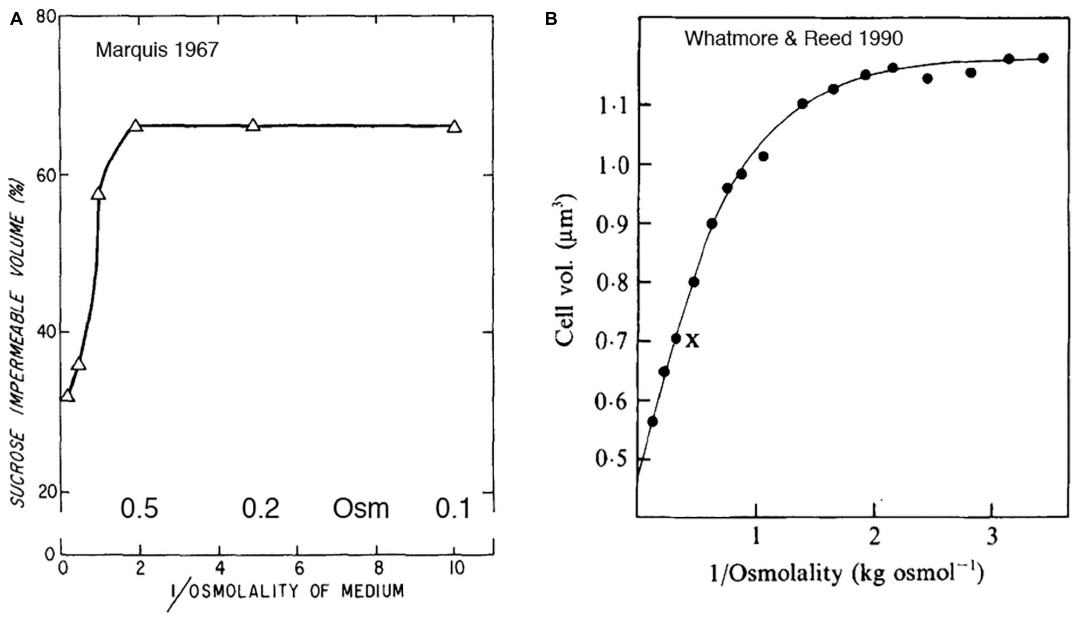

FIGURE 4 | (A) An early study of Marquis (1967) showed shrinkage of gram-positive cytoplasm in response to osmotic shock, but only above 1 M sucrose. **(B)** Whatmore and Reed (1990) measured the response of cell volume to sucrose shock. The cell volume they report may be primarily the cytoplasmic volume. As in 4A, cytoplasmic volume decreased only above 1 M. Note that both graphs plot reciprocal osmolality on the x axis. Reprinted from the referenced works with permission.

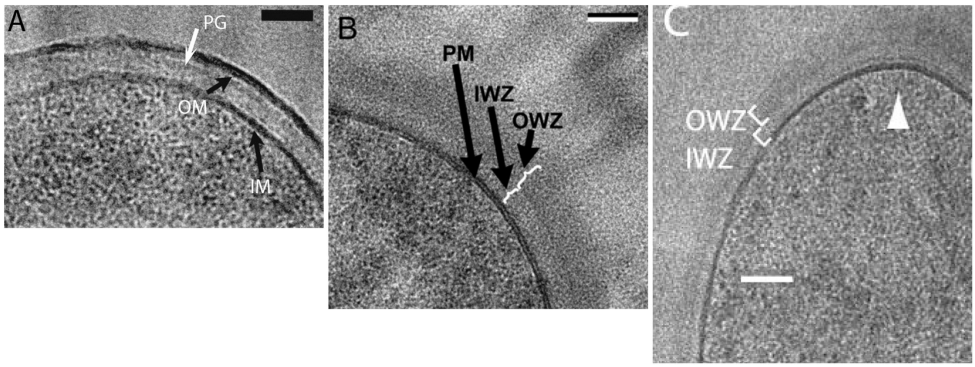

FIGURE 5 | CryoEM using high pressure freezing and cryosectioning shows a periplasmic space in *E. coli* [**A**: (Matias et al., 2003)] and *B. subtilis* [**B**: (Matias and Beveridge, 2005) and **C**: (Zuber et al., 2006)]. PGW is indicated by PG in **(A)** and OWZ (outer wall zone) in **(B,C)**. The periplasm is indicated by IWZ (inner wall zone) in **(B,C)**. Reprinted from the referenced works with permission.

reconstructions of these sections were of sufficient quality to image FtsA and FtsZ filaments beneath the cell membrane. Although not explicitly discussed the article, the images showed the ∼25 nm PG layer abutting directly the CM, with no periplasmic space.

This major discrepancy for cryoEM, where some studies see a periplasm in gram-positive bacteria, while others do not, remains unresolved.

How Teichoic Acids Can Maintain the Osmolality of the Periplasm

As discussed above *E. coli* maintains the osmolality of the periplasm by OPGs, which are anionic glucose oligomers, ∼2,300 Da with an average –5 charge. Their neutralizing cations and associated Donnan equilibrium maintain an osmolality that matches that of the cytoplasm (Kennedy, 1982; Miller et al., 1986; Cayley et al., 2000). OPGs are retained in the periplasm because they are too large to pass through the small porins of the OM-PGW layer. OPGs would not work in gram-positive bacteria because they would easily pass through the more porous PGW. Note that I had earlier concluded that the PGW of gram-positive bacteria might have a limited porosity, blocking molecules larger than ∼1,200 Da (Erickson, 2017). However, my colleague Masaki Osawa later convinced me that the PGW is probably porous to globular molecules of 20,000 Da or more (Osawa and Erickson, 2018). In that case OPGs, and even longer glycan chains, would slide through the pores of the PGW and escape.

There is, however, an alternative polyanion in gram-positive bacteria that is an excellent candidate for maintaining periplasmic osmolality – teichoic acids. Teichoic acids (TAs) are chains of ∼25 glycerol phosphates or ribitol phosphates, where the phosphates give them a polyanionic character. They exist in two forms. Lipoteichoic acid (LTA) has a terminal lipid that inserts into the periplasmic side of the CM. Wall teichoic acids (WTA) are covalently attached to the peptidoglycan. Although the TAs would easily pass through the PGW if they were free chains, the anchors to the CM or PGW prevent their escape and trap them in the periplasmic space (**Figure 6**).

Oku et al. (2009) have previously suggested that TAs may be functioning to maintain the osmolality of the gram-positive periplasm, similar to the role of OPG in gram-negative bacteria. They knocked out the *ltaS* gene in *S. aureus,* which completely eliminated LTA, but left WTA. The cells lacking LTA were viable but had a growth defect – they could grow at 30° but not 37°. If, however, the NaCl in the growth media was raised from 0.17 M to 1.3 M, or if sucrose was added to 1.1 M, cells lacking LTA could grow at 37°. Moreover, if the NaCl was decreased to 0.08 M, cells could not even grow at the permissive 30°. Thus cells lacking LTA are viable, but only in a high osmolal growth medium. Similarly in *B. subtilis,* Schirner et al. (2009) showed that knockout of LTA produced viable cells, but with defects in cell division and separation. They did not explore changing the osmolality of the growth media.

Previous studies showed that knockout of WTA produced mild growth defects in *S. aureus* (Weidenmaier et al., 2004), but caused severe cell rounding and clumping in *B. subtilis* (D'Elia et al., 2006). The double knockout was lethal in both *S. aureus* and *B. subtilis* (Oku et al., 2009; Schirner et al., 2009). Here we follow up the suggestion of Oku et al. (2009), that TAs may function to maintain the osmolality of the periplasm.

LTA and WTA May Force the Existence of a Periplasmic Space

Figure 6 shows a schematic diagram for how the LTA and WTA chains could be arranged in the periplasm. The LTA chains are spaced about 2 nm apart, which is much closer than their 22 nm length (see the next section). This fits the classic description of a polymer brush. If an LTA chain were isolated in solution it would tend to collapse into a spherical blob. When grafted onto the CM at high density, the flexible chains are forced to extend into the brush. Several physical-chemical forces contribute to this extension: (1) excluded volume, where the chains cannot occupy the same space; (2) electrostatic repulsion within and between chains; (3) reduced entropy of the chains as they are confined to a narrow cylinder; (4) reduced entropy of the counterions as they are concentrated near the anionic charges. These forces not only cause the TA chains to extend into the brush, but they

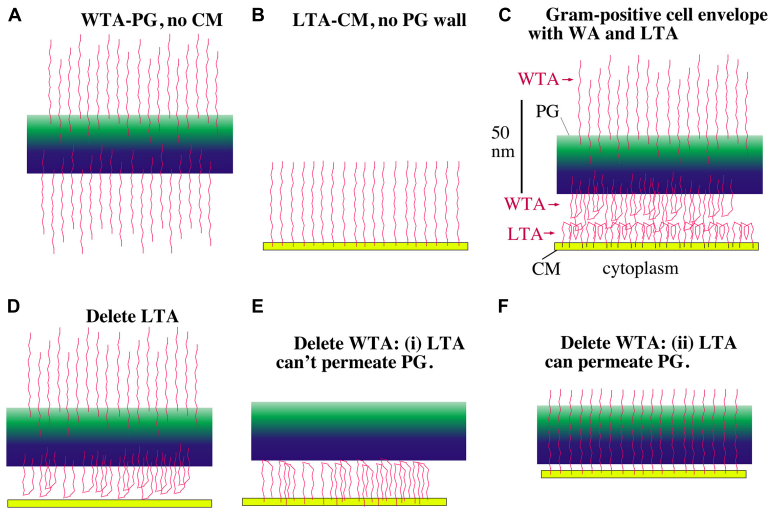

FIGURE 6 | Models showing how LTA and WTA can maintain a periplasm. The PGW is green, the CM is yellow and the TAs are red. WTAs are thought to be longer than LTAs but are shown here the same length for drawing convenience. **(A)** Without a CM, the WTA would project straight out on both sides of the PG wall. **(B)** Without a PG wall, LTA would project from the CM. **(C)** In the gram-positive cell envelope the LTA and WTA in the periplasm will meet and compress each other until their electrostatic repulsion matches the turgor pressure of the cytoplasm. **(D)** If LTA is deleted, the WTA facing the CM can still support a periplasm, although the periplasmic width should be compressed. **(E,F)** If WTA is deleted there are two possibilities. If the LTA is blocked from penetrating the PG wall, it can still maintain a periplasm **(E)**. If the LTA can freely permeate the PG, however, it should not be able to maintain a periplasm **(F)**. Recent images of the periplasmic face of the PGW show a tight mesh of glycan strands that the LTA should not penetrate (Pasquina-Lemonche et al., 2020), relieving the concern of **(F)**.

will generate a pressure when the brushes are pushed toward a surface or toward each other. These physical chemical forces can be used to calculate this pressure, as described by Pincus (1991) and by Zhulina and Rubinstein (2012). A detailed application of polyelectrolyte brush theory to TAs should be possible, but is beyond the scope of the present article.

Here I will develop two arguments to explain qualititatively how the TAs could generate a periplasmic space that balances turgor pressure. I will first present a pictorial description based on electrostatic repulsion of TAs. This is similar to the simple explanation of cartilage mechanics in histology texts. I will then develop a calculation of the fixed charge density of the TAs, which bring a concentration of neutralizing counterions approximately equal to the osmolality of the cytoplasm.

In the pictorial description, consider first the WTA chains. **Figure 6A** shows these negatively charged chains repelling each other and extending from both sides of their attachment to the PGW. **Figure 6B** shows LTAs, which are tethered to the periplasmic side of the CM, extending into the periplasmic space. The important diagram is **Figure 6C**, which shows how the WTA and LTA should interact in the full bacterial envelop. Since both WTAs and LTAs are long enough to extend the full 22 nm [according to Matias and Beveridge (2005)] width of the periplasm, and they are both negatively charged, they will repel each other. If there were no turgor pressure they would generate a periplasmic space equal to the sum of their lengths. If the CM is under turgor it should push the LTAs and WTAs toward each other, forcing them to interdigitate charges or fold back upon themselves (**Figure 6C**). The CM will be pushed by turgor toward the PGW until the electrostatic repulsive force of the WTA-LTA balances the turgor pressure.

Gene knockout studies in both *S. aureus* and *B. subtilis* have shown that one can eliminate either LTA or WTA but not both (Oku et al., 2009; Schirner et al., 2009). Let us explore how these knockouts would affect the periplasm in our model. If LTA is eliminated the WTA would project equally inward and outward. Those WTA chains projecting inward can't penetrate the CM, so they would push against it, establishing a periplasm (**Figure 6D**). (Although we have ignored it for the model, WTA are up to twice as long as LTA (Neuhaus and Baddiley, 2003; Brown et al., 2013), so they would have to fold back even without repulsion by LTA.) The CM would press against the WTA compressing them until the electrostatic repulsion balanced the turgor pressure. The periplasm should be thinner than with both WTA and LTA because the density of negative charges is lower, but it should still exist.

Eliminating WTA seemed at first more problematic for the simple model. There would be no problem if the LTA were blocked from penetrating the PGW (**Figure 6E**), because the negative charges of the LTA would then be confined to the periplasmic space. However, if the PGW is porous (Osawa and Erickson, 2018), the LTA chains may be able to extend through the PGW, and would not establish a periplasm (**Figure 6F**). This concern now seems to be relieved by a recent study imaging the PGW by high resolution atomic force microscopy (Pasquina-Lemonche et al., 2020). The periplasmic surface of the PGW appeared to be a dense mesh of glycan strands, with pores noted up to a maximum diameter of 6.4 nm, although most pores were smaller. The authors did not analyze this inner surface in detail, but I counted roughly 30 pores over a 60 nm square in their **Figure 2F**. Using the value of 5.4 nm^2 per LTA calculated below, there would be 667 LTA in this same 60 nm square. Thus, there

is only one pore for twenty LTAs. Inserting a single LTA into a pore would be inhibited by its loss of entropy; trying to fit two LTAs into a single pore would encounter additional electrostatic repulsion. Overall, the inner surface of the PGW would seem to be impenetrable by LTAs, negating the concern of **Figure 6F**.

The Counterions That Neutralize LTA and WTA Could Approximately Counter the Cytoplasmic Osmotic Pressure

We now turn from the pictorial description of polyanionic TA chains repelling each other, to a more quantitative description based on fixed charge density. This is similar to the quantitative description of cartilage mechanics (Lu and Mow, 2008). LTAs are very abundant, being 1/9 (Percy and Grundling, 2014) or 1/5 to 1/10 (Oku et al., 2009) of the outer leaflet lipids. The area per lipid in a bilayer is generally given as 0.6 nm^2. If 1/9 of lipids are LTA, the area per LTA is 5.4 nm^2. A typical LTA is a chain of 25 GroP (Percy and Grundling, 2014), which should be fully extended because the negative charges will repel each other. At 0.9 nm per GroP, the extended LTA chains would be 22 nm long, which is equal to the width of the periplasm measured by cryoEM (Matias and Beveridge, 2005).

The phosphate groups in TAs are in a diester linkage and carry a single minus charge. We can calculate the effective concentration of the P^- as follows. The volume per LTA is 5.4 $nm^2 \times 22$ nm = 119 nm^3. The 25 P^- in 119 nm^3, gives 0.21 nm^3 per P^-, which converts to a concentration of 0.35 M.

WTAs are comparable in number and density to LTAs (Neuhaus and Baddiley, 2003); 1 out of 9 MurNac in the PGW has an attached WTA (Brown et al., 2013). WTAs are twice as long as LTAs (Neuhaus and Baddiley, 2003), but only half are projecting into the periplasm (**Figure 6**), so we can assume the WTA contribute a concentration of P^- approximately equal to the 0.35 M of the LTA, for a total of 0.7 M. It is important to note, however, that 20–70% of the glycerol phosphate groups have an attached D-alanyl group (Neuhaus and Baddiley, 2003; Percy and Grundling, 2014). Each D-alanyl creates a positive charge, which effectively neutralizes one P^-. The D-alanyl groups are dynamically removed and re-added (Neuhaus and Baddiley, 2003), providing a mechanism to modify and fine tune the anionic concentration of the periplasm. Perego et al. (1995) measured the percent D-alanylation for *B. subtilis* growing in a defined medium of ∼0.3 Osm. 44% of the glycerophosphate groups in LTA and 9% in WTA were D-alanylated, for an average 27%. The net concentration of anionic P^- in the periplasm will then be ∼0.5 M. This will bring into the periplasm a concentration of 0.5 M Na^+ counterions.

A 19 atm turgor pressure means that the cytoplasm has an excess osmolality of 0.75 Osm relative to the growth medium. An isoosmolar periplasm should therefore be 0.75 Osm above the growth medium. The P^- groups themselves will contribute little to the osmolality of the periplasm because 25 of them are connected into a single TA chain. The osmolality will be generated primarily by the 0.5 M Na^+ cations that neutralize the P^-. The Donnan equilibrium will increase periplasmic osmolality only slightly in normal growth medium. Using the formulation of Tsujii (2002) the Donnan equilibrium will add 0.024 M to the periplasmic osmolality for growth medium containing 0.1 M NaCl (e.g., LB with 0.5% NaCl). The Donnan contribution will rise to 0.25 M in 0.4 M NaCl, a very high-salt medium. The anionic surfaces of membrane proteins should contribute additional neutralizing Na^+. The 0.5 M Na^+ was a very approximate calculation. Overall, the cations neutralizing the anionic TAs and proteins should approximately match the excess osmolality of the cytoplasm, leaving the periplasm and cytoplasm isoosmotic.

We should recognize that the simple calculation of counterion concentration is only one contribution to pressure in the brush theory. The situation is especially complicated when the NaCl in the growth media approaches or exceeds the fixed charge density of the TAs. However, normal growth media contain 0.5% or 1% NaCl (0.08 M or 0.17 M) well below the 0.5 M concentration of TA anions. This corresponds to Regime I of Zhulina and Rubinstein (2012), where the osmotic pressure is determined primarily by the concentration of counterions. Thus, in normal growth media the concentration of counterions is a good approximation to the osmolality of the periplasm.

Comparing the Periplasm to Articular Cartilage

The description above of TAs acting through electronegative repulsion was inspired by the treatment of articular cartilage presented in many textbooks. Articular cartilage is a rigid tissue covering the surfaces of bones where they meet in a joint. Articular cartilage is a compressible cushion that can support very high compressive forces, many times body weight, up to 20 atm at the hip (Lu and Mow, 2008). The chemical basis for this rigidity to compression is a gel of polyanionic glycosaminoglycans, which are chains of sugars with negatively charged COO^- and SO_3^- groups attached. The glycosaminoglycans are attached to other molecules to make proteoglycan aggregates, which reach a length of ∼40 μm. The glycosaminoglycan chains are highly concentrated, and electrostatic repulsion would drive them to escape. They are held in the concentrated state by a series of strong chemical bonds within the proteoglycan aggregate. The proteoglycan aggregates themselves are retained in the cartilage matrix by physical entrapment as they snake through a network of collagen fibrils (Lu and Mow, 2008). The rigidity to compression can be attributed pictorially to the repulsion of the concentrated, polyanionic glycosaminoglycan strands.

A more quantitative analysis of cartilage mechanics is based on the fixed charge density, which has been reported to be 0.28 M (Lesperance et al., 1992) or 0.4 M (Ehrlich et al., 1998). This is somewhat less than the 0.5 M fixed charge density estimated above for the combined LTA and WTA in the gram-positive periplasm. This analogy suggests that the periplasm may be considered a gel with a rigidity similar to that of articular cartilage. This rigid gel is pressed against the PGW on the outside, and the CM presses against it on the inside. The TA gel thus supports the turgor pressure of the CM. Note that in spite of its mechanical rigidity, articular cartilage permits diffusion of ions and protein molecules. The same would be true of a

periplasm with highly compressed TAs. These should permit the functioning of PGW remodeling enzymes and diffusion of their substrates.

CONCLUSION

I have presented arguments that a periplasmic space is needed for the PGW synthesis proteins to function, and I developed a quantitative estimate that TAs could generate a concentration of counterions that approximately balances the osmolality of the cytoplasm. This would leave the CM floating between the turgor pressure of the cytoplasm and the brush pressure of the TAs in the periplasm, and subject to no net force from turgor. As noted above, a full treatment by brush theory is needed to complete this argument, especially for growth in high salt media. There are also major experimental gaps that need to be filled. The failure of cryoEM tomography to image a periplasm is a concern that needs to be resolved by electron microscopists. Most important would be to repeat for gram-positive bacteria the isotopic labeling experiments of Stock et al. {1977 #10230} and Cayley et al. {2000 #10236} to establish the existence and osmolality of the gram-positive periplasm. Alternatively, the periplasm could be imaged by super-resolution light microscopy to quantitate its response to osmotic shock, as has been done for *E. coli* (Pilizota and Shaevitz, 2013).

Although septation may not need to overcome turgor pressure, force is needed to bend the membrane and perhaps to invaginate into the restricted volume of the cytoplasm. There are currently three favored mechanisms for generating this force. First is FtsZ pulling on the CM from the inside. This mechanism is supported by *in vitro* experiments showing that FtsZ alone can constrict liposomes (Osawa et al., 2008; Osawa and Erickson, 2013); also FtsZ is apparently needed to initiate constriction *in vivo* (Monteiro et al., 2018; Whitley et al., 2021). The second potential force mechanism is PGW synthesis pushing the CM from the outside. Supporting this is the observation that mutations in FtsI reduced the rate of constriction (Coltharp et al., 2016); however, this would also occur if PGW synthesis was simply limiting constriction, rather than generating the force. The third force mechanism is excess membrane production (Osawa and Erickson, 2018). Once a constriction furrow has been initiated, excess membrane production would preferentially add to this constriction as opposed to initiating a new invagination. In support of this, experiments with L forms have shown that excess membrane production is crucial to their division (Mercier et al., 2013).

In *Streptoccous pneumoni*ae and *B. subtilis*, when FtsZ treadmilling was blocked by the drug PC190723, Z rings that had already initiated constriction could continue constricting to complete division (Monteiro et al., 2018; Whitley et al., 2021). This suggests that, after constriction is initiated by FtsZ, the primary forces are the second and/or third mechanisms. It is difficult to separate the roles of these two mechanisms since they are likely physically linked. A simple scenario would have FtsZ bending the membrane to initiate constriction, with excess membrane production forcing the continued invagination, and PGW synthesis limiting the rate of constriction and perhaps contributing to the force.

An Analogy for Cell Division Needing to Fight Turgor or Not

Imagine a space station capsule where the outer wall is a strong, airtight fabric, forming an elongated cylinder that contains the 1 atm pressure. Suppose the Russians and Americans had a serious dispute and decided to split the capsule in two. One engineer proposed constructing a large belt that could wrap around the cylinder at mid-length, and using a large winch to gradually tighten the belt to squeeze the cylinder in two. Another engineer suggested that this winch and belt might not be able to achieve the necessary force with the energy reserves available. She proposed that they use their store of excess fabric to build two closely parallel walls, each securely glued to the outside cylinder. When the walls were complete she proposed a space walk to cut the cylinder between them. Since the astronauts are in zero gravity, only negligible force would be needed for any step.

DATA AVAILABILITY STATEMENT

The original contributions presented in the study are included in the article/supplementary material, further inquiries can be directed to the corresponding author.

AUTHOR CONTRIBUTIONS

HPE did the analysis and wrote the manuscript.

ACKNOWLEDGMENTS

The author thanks Masaki Osawa for insightful and challenging discussions.

REFERENCES

Beeby, M., Gumbart, J. C., Roux, B., and Jensen, G. J. (2013). Architecture and assembly of the Gram-positive cell wall. *Mol. Microbiol.* 88, 664–672. doi: 10.1111/mmi.12203

Bontemps-Gallo, S., Bohin, J. P., and Lacroix, J. M. (2017). Osmoregulated periplasmic glucans. *EcoSal Plus* 7, doi: 10.1128/ecosalplus.ESP-0001-2017

Brown, S., Santa Maria, J. P. Jr., and Walker, S. (2013). Wall teichoic acids of gram-positive bacteria. *Annu. Rev. Microbiol.* 67, 313–336. doi: 10.1146/annurev-micro-092412-155620

Cayley, D. S., Guttman, H. J., and Record, M. T. Jr. (2000). Biophysical characterization of changes in amounts and activity of *Escherichia coli* cell and compartment water and turgor pressure in response to osmotic stress. *Biophys. J.* 78, 1748–1764.

Chang, Y. W., Rettberg, L. A., Treuner-Lange, A., Iwasa, J., Sogaard-Andersen, L., and Jensen, G. J. (2016). Architecture of the type IVa pilus machine. *Science* 351:aad2001. doi: 10.1126/science.aad2001

Coltharp, C., Buss, J., Plumer, T. M., and Xiao, J. (2016). Defining the rate-limiting processes of bacterial cytokinesis. *Proc. Natl. Acad. Sci. U.S.A.* 113, E1044–E1053. doi: 10.1073/pnas.1514296113

D'Elia, M. A., Millar, K. E., Beveridge, T. J., and Brown, E. D. (2006). Wall teichoic acid polymers are dispensable for cell viability in Bacillus subtilis. *J. Bacteriol.* 188, 8313–8316. doi: 10.1128/JB.01336-06

Deng, Y., Sun, M., and Shaevitz, J. W. (2011). Direct measurement of cell wall stress stiffening and turgor pressure in live bacterial cells. *Phys. Rev. Lett.* 107:158101. doi: 10.1103/PhysRevLett.107.158101

Ehrlich, S., Wolff, N., Schneiderman, R., Maroudas, A., Parker, K. H., and Winlove, C. P. (1998). The osmotic pressure of chondroitin sulphate solutions: experimental measurements and theoretical analysis. *Biorheology* 35, 383–397. doi: 10.1016/s0006-355x(99)80018-3

Erickson, H. P. (2017). How bacterial cell division might cheat turgor pressure - a unified mechanism of septal division in Gram-positive and Gram-negative bacteria. *Bioessays* 39:1700045. doi: 10.1002/bies.201700045

Kennedy, E. P. (1982). Osmotic regulation and the biosynthesis of membrane-derived oligosaccharides in *Escherichia coli*. *Proc. Natl. Acad. Sci. U.S.A.* 79, 1092–1095.

Khanna, K., Lopez-Garrido, J., Sugle, J., Pogliano, K., and Villa, E. (2020). Asymmetric localization of the cell division machinery during Bacillus subtilis sporulation. *BioRxiv [preprint]* doi: 10.1101/2020.07.22.216184

Lesperance, L. M., Gray, M. L., and Burstein, D. (1992). Determination of fixed charge density in cartilage using nuclear magnetic resonance. *J. Orthop. Res.* 10, 1–13. doi: 10.1002/jor.1100100102

Lovering, A. L., de Castro, L. H., Lim, D., and Strynadka, N. C. (2007). Structural insight into the transglycosylation step of bacterial cell-wall biosynthesis. *Science* 315, 1402–1405. doi: 10.1126/science.1136611

Lu, X. L., and Mow, V. C. (2008). Biomechanics of articular cartilage and determination of material properties. *Med. Sci. Sports Exercise* 40, 193–199. doi: 10.1249/mss.0b013e31815cb1fc

Lucena, D., Mauri, M., Schmidt, F., Eckhardt, B., and Graumann, P. L. (2018). Microdomain formation is a general property of bacterial membrane proteins and induces heterogeneity of diffusion patterns. *BMC Biol.* 16:97. doi: 10.1186/s12915-018-0561-0

Marquis, R. E. (1967). Osmotic sensitivity of bacterial protoplasts and the response of their limiting membrane to stretching. *Arch. Biochem. Biophys.* 118, 323–331. doi: 10.1016/0003-9861(67)90356-6

Matias, V. R., Al-Amoudi, A., Dubochet, J., and Beveridge, T. J. (2003). Cryo-transmission electron microscopy of frozen-hydrated sections of *Escherichia coli* and *Pseudomonas aeruginosa*. *J. Bacteriol.* 185, 6112–6118.

Matias, V. R., and Beveridge, T. J. (2005). Cryo-electron microscopy reveals native polymeric cell wall structure in Bacillus subtilis 168 and the existence of a periplasmic space. *Mol. Microbiol.* 56, 240–251. doi: 10.1111/j.1365-2958.2005.04535.x

Matias, V. R., and Beveridge, T. J. (2006). Native cell wall organization shown by cryo-electron microscopy confirms the existence of a periplasmic space in Staphylococcus aureus. *J. Bacteriol.* 188, 1011–1021. doi: 10.1128/JB.188.3.1011-1021.2006

McCausland, J. W., Yang, X., Squyres, G. R., Lyu, Z., Bruce, K. E., Lamanna, M. M., et al. (2021). Treadmilling FtsZ polymers drive the directional movement of sPG-synthesis enzymes via a Brownian ratchet mechanism. *Nat. Commun.* 12:609. doi: 10.1038/s41467-020-20873-y

Mercier, R., Kawai, Y., and Errington, J. (2013). Excess membrane synthesis drives a primitive mode of cell proliferation. *Cell* 152, 997–1007. doi: 10.1016/j.cell.2013.01.043

Mika, J. T., Schavemaker, P. E., Krasnikov, V., and Poolman, B. (2014). Impact of osmotic stress on protein diffusion in Lactococcus lactis. *Mol. Microbiol.* 94, 857–870. doi: 10.1111/mmi.12800

Miller, K. J., Kennedy, E. P., and Reinhold, V. N. (1986). Osmotic adaptation by gram-negative bacteria: possible role for periplasmic oligosaccharides. *Science* 231, 48–51.

Monteiro, J. M., Pereira, A. R., Reichmann, N. T., Saraiva, B. M., Fernandes, P. B., Veiga, H., et al. (2018). Peptidoglycan synthesis drives an FtsZ-treadmilling-independent step of cytokinesis. *Nature* 554, 528–532. doi: 10.1038/nature25506

Neuhaus, F. C., and Baddiley, J. (2003). A continuum of anionic charge: structures and functions of D-alanyl-teichoic acids in gram-positive bacteria. *Microbiol. Mol. Biol. Rev.* 67, 686–723. doi: 10.1128/mmbr.67.4.686-723.2003

Oku, Y., Kurokawa, K., Matsuo, M., Yamada, S., Lee, B. L., and Sekimizu, K. (2009). Pleiotropic roles of polyglycerolphosphate synthase of lipoteichoic acid in growth of Staphylococcus aureus cells. *J. Bacteriol.* 191, 141–151. doi: 10.1128/JB.01221-08

Osawa, M., Anderson, D. E., and Erickson, H. P. (2008). Reconstitution of contractile FtsZ rings in liposomes. *Science* 320, 792–794. doi: 10.1126/science.1154520

Osawa, M., and Erickson, H. P. (2013). Liposome division by a simple bacterial division machinery. *Proc. Natl. Acad. Sci. U.S.A.* 110, 11000–11004. doi: 10.1073/pnas.1222254110

Osawa, M., and Erickson, H. P. (2018). Turgor pressure and possible constriction mechanisms in bacterial division. *Front. Microbiol.* 9:111. doi: 10.3389/fmicb.2018.00111

Oswald, F., Varadarajan, A., Lill, H., Peterman, E. J., and Bollen, Y. J. (2016). MreB-Dependent organization of the E. coli cytoplasmic membrane controls membrane protein diffusion. *Biophys. J.* 110, 1139–1149. doi: 10.1016/j.bpj.2016.01.010

Pasquina-Lemonche, L., Burns, J., Turner, R. D., Kumar, S., Tank, R., Mullin, N., et al. (2020). The architecture of the Gram-positive bacterial cell wall. *Nature* 582, 294–297. doi: 10.1038/s41586-020-2236-6

Percy, M. G., and Grundling, A. (2014). Lipoteichoic acid synthesis and function in gram-positive bacteria. *Annu. Rev. Microbiol.* 68, 81–100. doi: 10.1146/annurev-micro-091213-112949

Perego, M., Glaser, P., Minutello, A., Strauch, M. A., Leopold, K., and Fischer, W. (1995). Incorporation of D-alanine into lipoteichoic acid and wall teichoic acid in Bacillus subtilis. Identification of genes and regulation. *J. Biol. Chem.* 270, 15598–15606. doi: 10.1074/jbc.270.26.15598

Pilizota, T., and Shaevitz, J. W. (2013). Plasmolysis and cell shape depend on solute outer-membrane permeability during hyperosmotic shock in E. coli. *Biophys. J.* 104, 2733–2742. doi: 10.1016/j.bpj.2013.05.011

Pincus, P. (1991). Colloid stabilization with grafted polyelectrolytes. *Macromolecules* 24, 2912–2919.

Scheie, P. O., and Rehberg, R. (1972). Response of *Escherichia coli* B-r to high concentrations of sucrose in a nutrient medium. *J. Bacteriol.* 109, 229–235. doi: 10.1128/JB.109.1.229-235.1972

Schirner, K., Marles-Wright, J., Lewis, R. J., and Errington, J. (2009). Distinct and essential morphogenic functions for wall- and lipo-teichoic acids in Bacillus subtilis. *EMBO J.* 28, 830–842. doi: 10.1038/emboj.2009.25

Sochacki, K. A., Shkel, I. A., Record, M. T., and Weisshaar, J. C. (2011). Protein diffusion in the periplasm of E. coli under osmotic stress. *Biophys. J.* 100, 22–31. doi: 10.1016/j.bpj.2010.11.044

Stock, J. B., Rauch, B., and Roseman, S. (1977). Periplasmic space in *Salmonella* typhimurium and *Escherichia coli*. *J. Biol. Chem.* 252, 7850–7861.

Sung, M. T., Lai, Y. T., Huang, C. Y., Chou, L. Y., Shih, H. W., Cheng, W. C., et al. (2009). Crystal structure of the membrane-bound bifunctional transglycosylase PBP1b from *Escherichia coli*. *Proc. Natl. Acad. Sci. U.S.A.* 106, 8824–8829. doi: 10.1073/pnas.0904030106

Tran, B. M., Prabha, H., Iyer, A., O'Byrne, C., Abee, T., and Poolman, B. (2021). Measurement of protein mobility in listeria monocytogenes reveals a unique tolerance to osmotic stress and temperature dependence of diffusion. *Front. Microbiol.* 12:640149. doi: 10.3389/fmicb.2021.640149

Tsujii, K. (2002). Donnan equilibria in microbial cell walls: a pH-homeostatic mechanism in alkaliphiles. *Colloids Surf B Biointerfaces* 24, 247–251.

Umeda, A., Yokoyama, S., Arizono, T., and Amako, K. (1992). Location of peptidoglycan and teichoic acid on the cell wall surface of Staphylococcus aureus as determined by immunoelectron microscopy. *J. Electron Microsc. (Tokyo)* 41, 46–52.

Weibull, C. (1955). Osmotic properties of protoplasts of Bacillus megaterium. *Exp. Cell Res.* 9, 294–304. doi: 10.1016/0014-4827(55)90102-6

Weibull, C. (1965). Plasmolysis in Bacillus megaterium. *J. Bacteriol.* 89, 1151–1154.

Weidenmaier, C., Kokai-Kun, J. F., Kristian, S. A., Chanturiya, T., Kalbacher, H., Gross, M., et al. (2004). Role of teichoic acids in Staphylococcus aureus nasal colonization, a major risk factor in nosocomial infections. *Nat. Med.* 10, 243–245. doi: 10.1038/nm991

Whatmore, A. M., and Reed, R. H. (1990). Determination of turgor pressure in Bacillus subtilis: a possible role for K+ in turgor regulation. *J. Gen. Microbiol.* 136, 2521–2526. doi: 10.1099/00221287-136-12-2521

Whitley, K. D., Jukes, C., Tregidgo, N., Karinou, E., Almada, P., Henriques, R., et al. (2021). FtsZ treadmilling is essential for Z-ring condensation and septal

constriction initiation in 1 Bacillus subtilis cell division. *BioRxiv [preprint]* doi: 10.1101/2020.07.01.182006

Zhulina, E. B., and Rubinstein, M. (2012). Ionic strength dependence of polyelectrolyte brush thickness. *Soft Matter* 8, 9376–9383. doi: 10.1039/C2SM25863C

Zuber, B., Haenni, M., Ribeiro, T., Minnig, K., Lopes, F., Moreillon, P., et al. (2006). Granular layer in the periplasmic space of gram-positive bacteria and fine structures of Enterococcus gallinarum and Streptococcus gordonii septa revealed by cryo-electron microscopy of vitreous sections. *J. Bacteriol.* 188, 6652–6660. doi: 10.1128/JB.00391-06

Conflict of Interest: The author declares that the research was conducted in the absence of any commercial or financial relationships that could be construed as a potential conflict of interest.

frontiers in Microbiology

REVIEW
published: 16 June 2021
doi: 10.3389/fmicb.2021.685687

Mechanisms for Chromosome Segregation in Bacteria

*Christos Gogou†, Aleksandre Japaridze† and Cees Dekker**

Department of Bionanoscience, Kavli Institute of Nanoscience Delft, Delft University of Technology, Delft, Netherlands

The process of DNA segregation, the redistribution of newly replicated genomic material to daughter cells, is a crucial step in the life cycle of all living systems. Here, we review DNA segregation in bacteria which evolved a variety of mechanisms for partitioning newly replicated DNA. Bacterial species such as *Caulobacter crescentus* and *Bacillus subtilis* contain pushing and pulling mechanisms that exert forces and directionality to mediate the moving of newly synthesized chromosomes to the bacterial poles. Other bacteria such as *Escherichia coli* lack such active segregation systems, yet exhibit a spontaneous de-mixing of chromosomes due to entropic forces as DNA is being replicated under the confinement of the cell wall. Furthermore, we present a synopsis of the main players that contribute to prokaryotic genome segregation. We finish with emphasizing the importance of bottom-up approaches for the investigation of the various factors that contribute to genome segregation.

Keywords: bacterial chromosome, chromosome segregation, entropic segregation, structural maintenance of chromosome, ParABS system, prokaryotic segregation mechanisms

OPEN ACCESS

Edited by:
Shishen Du,
Wuhan University, China

Reviewed by:
Alan Leonard,
Florida Institute of Technology, United States
Gregory Marczynski,
McGill University, Canada

***Correspondence:**
Cees Dekker
c.dekker@tudelft.nl

†These authors share first authorship

Specialty section:
This article was submitted to Microbial Physiology and Metabolism, a section of the journal Frontiers in Microbiology

Received: *25 March 2021*
Accepted: *19 May 2021*
Published: *16 June 2021*

Citation:
Gogou C, Japaridze A and Dekker C (2021) Mechanisms for Chromosome Segregation in Bacteria. Front. Microbiol. 12:685687. doi: 10.3389/fmicb.2021.685687

INTRODUCTION

In all domains of life, proliferation of organisms essentially includes a faithful replication of the genetic material to pass it on to their offspring. The separation of newly copied DNA material into individual physical chromosomes that are spatially relocalized toward the daughter cells is generally called DNA segregation.

Notably, the ∼1–10 megabase pair (Mbp) (Blattner et al., 1997; Kunst et al., 1997; Schoolnik and Yildiz, 2000; Nierman et al., 2001) sized genomes of bacteria need to be highly condensed in order to fit inside the volume of a bacterial cell. Bacteria realize such a strong condensation through DNA supercoiling (Travers and Muskhelishvili, 2005; Dorman and Dorman, 2016), DNA-binding Nucleoid Associated Proteins (NAPs) (Anuchin et al., 2011; Ohniwa et al., 2011; Wang et al., 2011), and other DNA-compacting proteins like the DNA-loop-extruding Structural Maintenance of the Chromosome (SMC) complexes (Lindow et al., 2002; Postow et al., 2004). Replication of the circular prokaryotic chromosome initiates at a dedicated origin of replication (ori) locus and terminates near the terminus of replication (ter) on the opposite side of the chromosome (Nielsen et al., 2006; David et al., 2014; Wang et al., 2014a; Youngren et al., 2014; Cass et al., 2016), while segregation occurs simultaneously with the replication process (**Figure 1**). In the replication process, the replication machinery (the replisomes) acts bi-directionally: one traversing along each chromosome arm to duplicate the DNA (Japaridze et al., 2020). Throughout the 20–200 min of a typical bacterial cell cycle, the sequential positioning of chromosomal regions is tightly regulated.

Obviously, segregation requires temporal coordination with the cell division (Mierzejewska and Jagura-Burdzy, 2012; den Blaauwen, 2013; Adams et al., 2014; Dewachter et al., 2018; Marczynski et al., 2019; Reyes-Lamothe and Sherratt, 2019; Pióro and Jakimowicz, 2020). Divisome constriction needs to be postponed until the segregation is finalized, as failure in doing so will result in "guillotining" of the nucleoid, anucleate cells, or the complete inhibition of the cell division (Mulder and Woldringh, 1989; Woldringh et al., 1990; Åkerlund et al., 2002; Wu and Errington, 2004; Lee and Grossman, 2006; Mierzejewska and Jagura-Burdzy, 2012; den Blaauwen, 2013; Adams et al., 2014; Dewachter et al., 2018).

What are the mechanisms that orchestrate chromosome segregation in prokaryotes that ensure that each daughter cell faithfully acquires its own chromosome copy? In this review, we discuss the various underlying mechanisms for segregation in the best studied model bacterial species *Caulobacter crescentus*, *Bacillus subtilis*, and *Escherichia coli*. Firstly, we address early models that explain segregation as a consequence of being coupled to other cellular growth processes. Secondly, we discuss recent studies of SMCs that organize and compact DNA, and their alleged role in mediating global segregation, as well as the role of topoisomerases that catalyze disentanglement by resolving knots. Thirdly, two well-studied segregation apparatuses are outlined that are known to actively exert pushing or pulling forces on specific sequences of plasmids or chromosomes. Finally, we review the emerging understanding of contributions by entropic de-mixing of DNA polymers as drivers of spontaneous segregation.

Although many of these processes have been studied and reported separately, they do not act independently but jointly co-operate in ensuring reliable DNA segregation. Understanding the coupling between these multiple factors is important to uncover the mysteries of genetic proliferation. The principles of the combinatorial segregation mechanisms are likely not limited to bacteria but also form the basis of similar process in the more complex archaea and eukaryotes.

EARLY MODELS

The symmetric distribution of copied genomes into opposite cell halves was the subject of different models that coupled segregation to other processes such as cell growth and replication. Very early on, Jacob et al. (1963) postulated segregation as being governed by the attachment of DNA to the bi-directionally elongating cell wall. Based on this cell wall anchoring, Kleppe et al. (1979) proposed the so-called transertion model which was further developed in parallel by Norris (1995) and Woldringh et al. (1995); Woldringh (2002)). According to this model, the bacterial nucleoid is organized into supercoiled segments, and this nucleoid is separated from the cytoplasm through volume exclusion resulting from crowding interactions. The model emphasizes the translation of membrane proteins that is occurring co−transcriptionally, i.e., translation of the protein occurs simultaneously with the transcription of genes (Woldringh et al., 1995). Genes coding for membrane proteins will therefore become transiently bound to the membrane (**Figure 2A**). As the result, nearby genes expressed on the same chromosome also get localized to that spot near the membrane. Upon DNA replication, genes on the two daughter chromosomes will compete with each other for membrane binding which is self-enhanced upon expression of new genes (Roggiani and Goulian, 2015), leading to the formation of separate transertion areas per chromosome. Although anchoring of plasmids (Lynch and Wang, 1993) and chromosome regions to the membrane has been observed in some bacterial species (Leibowitz and Schaechter, 1975), there is, however, no clear evidence that the transertion plays a major role in the chromosome segregation.

Chromosome replication and segregation occur simultaneously in bacteria. Another early segregation mechanism involved the coupling of both these processes, where fluorescence microscopy data by Lemon and Grossman (1998) appeared to indicate a fixed replisome near the cell center in *B. Subtilis*. A central anchoring of the replisome

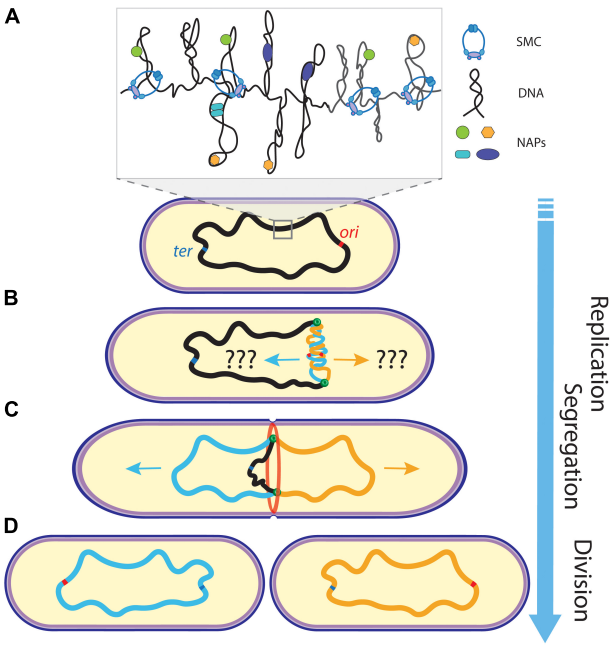

FIGURE 1 | Schematics of chromosome replication and segregation in bacteria. **(A)** A mother chromosome (black) with an origin (ori) and terminus (ter) of replication site resides in the cell. Inset shows the compacted organization of the chromosome into supercoiled domains organized by NAPs and SMCs. **(B)** Upon replication initiation at ori, sister chromosomes (blue and orange) are being synthesized by the replisomes (green dots). **(C)** While the replisomes move bi-directionally along the chromosome arms to further replicate the DNA, the sister chromosomes segregate into opposite cell halves and the cell starts to divide (through the divisome ring shown in red). **(D)** Ultimately, two daughter cells are formed after cell division, with each containing one copy of the chromosome. Arrow of time runs from top to bottom.

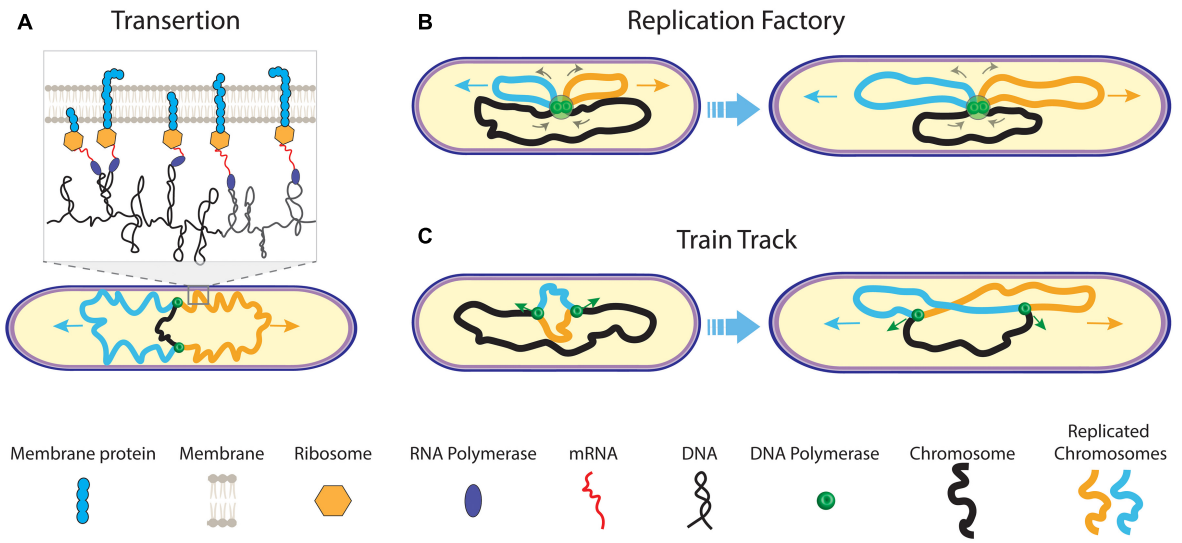

FIGURE 2 | Early models of prokaryotic DNA segregation. **(A)** The transertion model. During replication of the mother chromosome (black) by the replisomes (green dots), co-translational transcription of membrane protein mRNA leads to tethering of the sister chromosomes (orange and blue) to the cell membrane. As genes on one chromosome are biased in their position relative to genes on the other chromosome, a transertion area forms on the cell membrane for each sister (inset). Both transertion areas move in opposite direction on the elongating cell membrane. **(B)** The replication factory model. During replication, centrally fixed replisomes extrude replicated sister chromosomes (orange and blue) toward the cell pole, concomitantly pulling the yet un-replicated mother chromosome (black) inward. **(C)** The train track replication model. The two replisomes independently act on and move along the separate chromosome arms during replication. Their position in the cell is determined by the localization of the to-be copied genetic material.

could allow the cell to push the newly synthesized chromosome sisters bi-directionally outward (**Figure 2B**). This is known as the "replication factory model". Fluorescently tagged genomic foci were moving toward the replisome at mid cell before duplication, suggesting that the DNA is actively pulled inward by the replisome before being extruded outward in the opposite directions again (Lemon and Grossman, 2000). While similar observations were reported for *E. coli* (Mangiameli et al., 2017), conflicting findings were also reported for both *B. subtilis* (Migocki et al., 2004) and *E. coli* (Reyes-Lamothe et al., 2008), where the replisomes were not fixed relative to mid cell in live cells but rather moved along the chromosome in accordance with a "train track model" (**Figure 2C**). Fluorescence time-lapse imaging data revealed that the replisome foci for both organisms would split into two–one focus for each replisome that replicates a separate chromosome arm (Japaridze et al., 2020). In widened cells, we similarly visualized that replisomes assembled near ori before splitting to move separately over opposing chromosome arms. For *C. crescentus* (Jensen et al., 2001), movement of the replication machinery was also observed throughout replication. The replisome movement in *C. crescentus*, *E. coli*, and *B. subtilis*, as well as the splitting of replisome foci in the latter two organisms strongly argue against the factory model. The causation between replication and segregation may even be inverted: A central replisome position may be a consequence of the newly synthesized sister chromosome moving outward while the mother chromosome moves inward. Another early model by Kleckner et al. (2014) suggested that segregating forces result from the build-up of the mechanical stress by the chromosome replication, where segregation would result from stress relaxation upon the loss of sister cohesion (Bates and Kleckner, 2005; Javer et al., 2014; Lim et al., 2014).

SMCS COMPACT SISTER CHROMOSOMES INTO INDIVIDUAL ENTITIES

Structural Maintenance of the Chromosome are an important class of proteins that organize genomes in all domains of life (Cobbe and Heck, 2004). Indeed, all bacteria have such SMCs (Hirano, 2016) that are loaded onto the genome, for example near the ori regions in *B. subtilis* (Wang et al., 2014b) and *C. crescentus* (Tran et al., 2017). These complexes densely compact the chromosome by locally looping DNA. Although not demonstrated yet for bacterial SMCs, *in vitro* visualization of the structurally similar eukaryotic condensin SMC showed that these SMCs are capable of tethering to the DNA and utilizing ATP hydrolysis to extrude DNA loops (Ganji et al., 2018) (**Figure 3A**). Similarly, AFM imaging captured DNA loops of varying size with a single SMC complex of budding yeast at the base of the loop (**Figure 3B**). These SMCs exhibited two predominant conformations, (Ryu et al., 2020) indicating that the SMCs undergo very sizable conformational changes to progressively extrude DNA. Here, we describe the compacting functions of SMCs as well as emergent insights in the role they play in organizing replicated DNA into individual sister chromosomes in anticipation of their subsequent segregation.

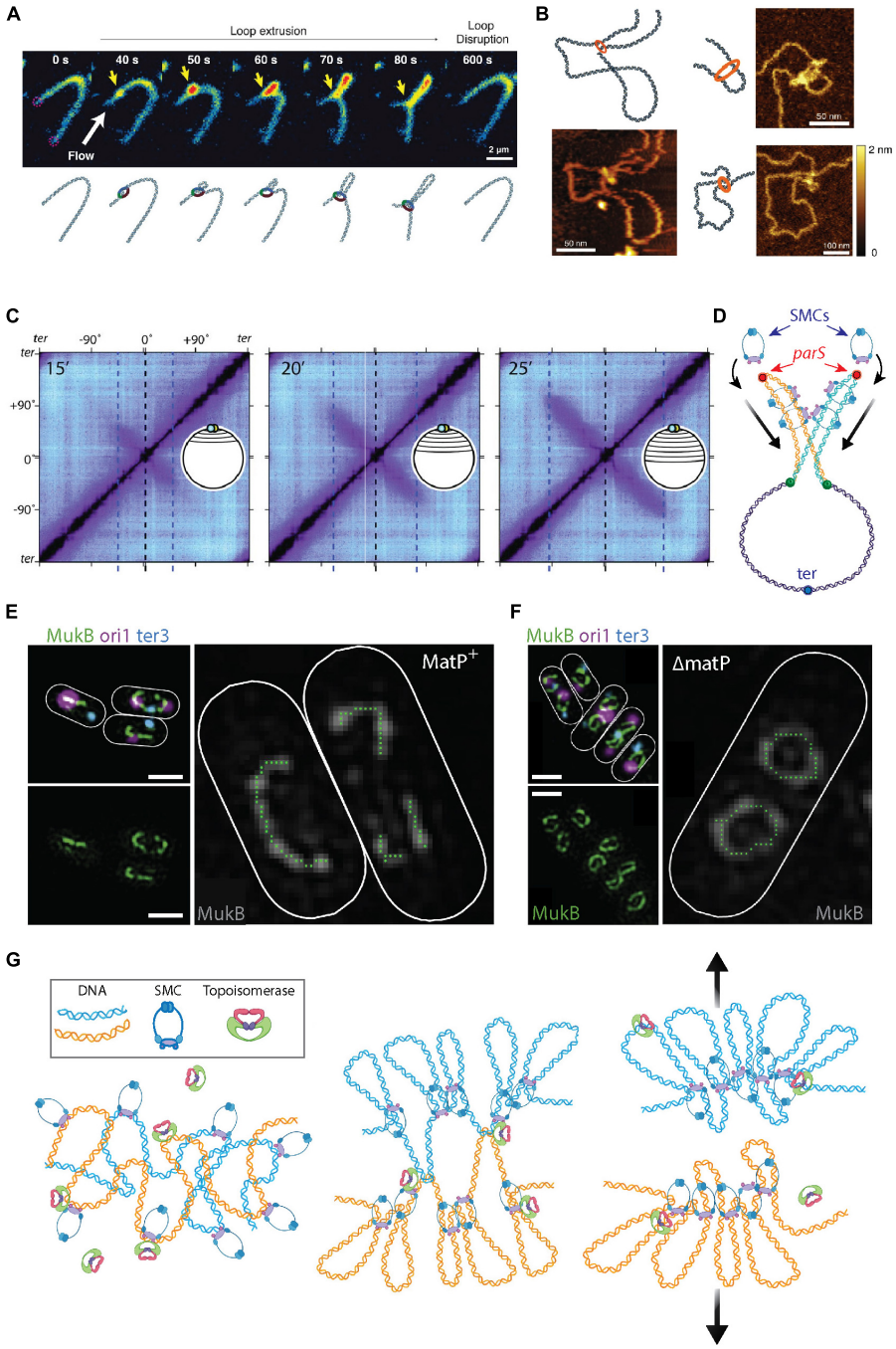

FIGURE 3 | The roles of SMCs in organizing and segregating the bacterial chromosomes. **(A)** Time-lapse images of a single SMC complex (yellow arrow) that extrudes a DNA loop *in vitro*. From Ganji et al. (2018). **(B)** Atomic force microscopy images of a single SMC complex bound to the stem of a DNA loop of varying sizes. From Ryu et al. (2020). **(C)** Hi-C contact maps show the progressive juxtaposition of chromosome arms as the downward-oriented diagonal lines that increase in size over time. From Wang et al. (2017). **(D)** Schematic representation of SMC molecules loading onto the *parS* sites (red dots) at newly replicated sister DNA (orange and blue strands) from the mother (purple strand). Upon loading, the SMC complexes slide over the DNA toward the terminus of replication (blue focus), juxtaposing the chromosome arms of the two sister chromosomes. **(E)** Fluorescent microscopy images of the MukB SMC (green) structures in *Escherichia coli* cells. The smaller images on the left show an overlay of MukB with the origin (magenta) and terminus-of-replication (blue) sites. The large image shows a trace of the MukB signal, which visualizes the horse-shoe-shaped half ring, that is discontinued at ter by the presence of MatP. Scale bars 1 μm. From Mäkelä and Sherratt (2020). **(F)** Same as panel **(E)** but for cells where MatP was deleted. Here, the horse-shoe shapes are closed into a fully circular structure. From Mäkelä and Sherratt (2020). **(G)** *Left* Sketch of two entangled sister chromosomes directly after replication. *Middle* Chromosome compaction by the action of SMCs. DNA loop extrusion by SMCs leads to a bottle brush chromosome structure, but full segregation between sister chromosomes is impeded by topological links between the sister chromosomes. *Right* Concatenations between the chromosome sister are resolved by topoisomerase action and entropic repulsion completes the segregation.

The major SMC in *B. subtilis* is called the BsSMC condensin and it is associated with compaction of the chromosome (Kleine Borgmann et al., 2013). Recruitment of condensin is mediated through interactions with ParB (Gruber and Errington, 2009) proteins that bind to ori-proximal *parS* sequences. Endogenous expression of a chemically degradable version of the SMC protein elucidated that ParB-dependent SMC recruitment is essential in fast growing bacteria (Wang et al., 2014b). Using high-throughput chromosome conformation capture (Hi-C) techniques, Rudner et al. showed how different genetic loci spatiotemporally relate to each other (Wang et al., 2017, 2018). The Hi-C method characterizes chromosome folding by measuring the rate of interactions between genomic loci that are nearby in space but may be separated by a large distance genomically (for reviews, see de Wit and de Laat, 2012; Denker and De Laat, 2016; McCord et al., 2020). Population-based Hi-C at different stages of segregation provided evidence that, following ParB-mediated loading onto DNA, SMCs "zip" along a single chromosome from the origin to the terminus of replication, while holding on to both chromosome arms and thus sequentially aligning regions on the opposing arms (Wang et al., 2017, 2018). This is indicated by an appearance, increasing in size over time, of a second diagonal that is perpendicular to the main one (**Figure 3C**). Using fluorescent microscopy, it was observed that GFP-tagged SMCs nucleate at *parS* before spreading out over more distal regions. The data indicate that multiple copies of SMCs consecutively bind at, and slide away from, *parS* during the observed juxtaposition of chromosome arms. Similar SMC behavior was recently observed in *C. crescentus* (Tran et al., 2017) cells. Furthermore, Karaboja et al. (2021) recently showed that in *B. subtilis* these processive SMCs ultimately unload near the ter macrodomain. It was demonstrated that BsSMC is also capable of entrapping DNA within its structure (Wilhelm et al., 2015). The entrapment and sliding suggest a mechanism for chromosome segregation where BsSMCs are loaded onto each replicating sister chromosome whereupon they impose individualization as the complexes slide over the DNA. This individualization self-organizes a segregation of the daughter nucleoids, see **Figure 3D**.

In *E. coli*, the major SMC is the tripartite MukBEF complex that comprises two copies each of MukB, MukE, and MukF (Valentin et al., 2014). Hi-C data revealed a loss of long-ranged (scales > 280 kb) intra-chromosomal contacts *in vivo* upon MukBEF deletion (Lioy et al., 2018), suggesting that MukBEF is organizing chromosomal loops of hundreds of kb in size in the *E. coli* nucleoid. MatP protein, a protein that specifically binds *matS* sites in the ter region (Mercier et al., 2008), was found to prevent MukBEF-induced long-range contacts in the ter macrodomain (Lioy et al., 2018). Recent *in vivo* 3D SIM imaging revealed that, upon sixfold upregulation of MukBEF, the proteins formed a horse-shoe-like backbone structure, that co-aligned with the chromosome structure, from which DNA loops were inferred to emanate (Mäkelä and Sherratt, 2020) (**Figure 3E**). Such a MukBEF backbone of the chromosome did not form at the ter region in the presence of the MatP protein, consistent with the antagonistic action of MatP on MukBEF (Nolivos et al., 2016). Deletion of MatP led to the closing of the MukBEF ring through ter (**Figure 3F**), resulting in global re-orientation and re-positioning.

A prominent difference between the DNA-binding mechanisms of SMCs in *B. subtilis* and *C. crescentus*, versus those in *E. coli*, is that the latter lacks *parS* sites on its genome for the loading of SMCs near ori (Livny et al., 2007). A recent simulation study, however, showed that some form of preferential loading is nevertheless needed to account for the experimental observations of ori and MukBEF dynamics (Sherratt et al., 2019). Although no mechanism was so far identified for the loading of MukBEF onto the *E. coli* chromosome, a role might be ascribed to the MatP protein which drives MukBEF away from the ter region (Nolivos et al., 2016) which leads to a gradient of MukBEF along the chromosome. Simulations showed that, due to compaction and looping of DNA by MukBEF, preferential loading of MukBEF near ori would cause the formation of a MukBEF focus with ori at the cell centre (Murray and Sourjik, 2017; Sherratt et al., 2019). Cell elongation resulted in splitting of these MukBEF foci to the cell quarter positions, and subsequently a segregation of duplicated oris toward these MukBEF foci. Another player in regulating the distribution of the SMCs along the genome is the XerCD/dif system, where XerC and XerD proteins bind at the dif site in the terminus domain and catalyze the resolution of chromosome dimers that arise as a result of replication (Blakely et al., 1993; Cornet et al., 1997; Sciochetti et al., 1999, 2001; Lesterlin et al., 2004; Midonet and Barre, 2015). It was recently shown that XerD functions as a site-specific unloader of SMC complexes in *B. subtillis* (Karaboja et al., 2021), although such mechanism has not been shown yet in *E. coli*.

Structural maintenance of the chromosome play a regulatory role in coordinating chromosome segregation and cell division. Deletion of the *E. coli* MukB or deletion of the *B. subtilis* SMC, results in guillotining of the nucleoid as well as anucleation of the cells (Niki et al., 1991; Moriya et al., 1998). In *E. coli*, the MatP protein, which binds to the ter region of the chromosome and prevents MukB from binding it, directly connects to the ZapB and ZapA proteins in the divisome. These three proteins interact to form a complex that anchors the ter region to the Z-ring (Espéli et al., 2012; Männik et al., 2016), thus orchestrating divisome positioning with chromosome segregation. A similar coupling of the terminus and the divisome was recently also found in *C. crescentus* (Ozaki et al., 2020, 2021). ZapA and ZauP, the functional counterparts of ZapA and ZapB in *E. coli*, interact with ZapT (the MatP counterpart). Deletion of the ZapT protein resulted in delayed cell division and altered divisome localization, indicating that this mechanism of chromosome anchoring to the divisome could be a general mechanism of coupling chromosome segregation and division.

Structural maintenance of the chromosomes also interact with another important player in chromosome organization and segregation–the bacterial topoisomerases (TopoIV) that can resolve knots and supercoiling. For both *B. subtilis* and *E. coli*, the mutual interaction between their respective SMC and TopoIV has been well described, especially for the latter (Lindow et al., 2002; Tadesse and Graumann, 2006; Nicolas et al., 2014; Wang et al., 2014b; Kumar et al., 2017). MukBEF recruits TopoIV to the chromosome and thus stimulates the

relaxation of negative supercoils (Hayama and Marians, 2010; Li et al., 2010; Hayama et al., 2013; Vos et al., 2013; Nicolas et al., 2014). TopoIV is capable of relieving supercoiling stress through the sequential breaking, passing, and re-ligation of the double-stranded DNA, thereby reducing the linking number of the chromosome (Wang, 1998; Crisona et al., 2000; Seol et al., 2013; Ashley et al., 2017). This strand-passage activity is crucial for the detachment of topologically catenated sister chromosomes after termination of replication (Zechiedrich and Cozzarelli, 1995; Zechiedrich et al., 1997; Seol et al., 2013). Orlandini et al. (2019) simulated how condensins could slide over an entangled ring polymer to sequester the knots. Building on this process, these authors (Orlandini et al., 2019) and others (Goloborodko et al., 2016; Brahmachari and Marko, 2019) showed how the inter- and intra-chromosomal linkage of the polymers substrates was resolved through strand-passage activity of topoisomerases (TopoII) bound to these loop-extruding SMCs.

In eukaryotes, simulations similarly demonstrated that loop extrusion combined with such topoisomerase action resulted in the formation of compacted chromosomes (Goloborodko et al., 2016) consisting of an axial superstructure of condensins with DNA loops that are peripherally protruding, resembling a "bottle brush" structure (Goloborodko et al., 2016; Brahmachari and Marko, 2019). This sufficed to spontaneously segregate two highly entangled and interconnected DNA polymers into separate compacted structures–both for eukaryotic and prokaryotic chromosomes (Brahmachari and Marko, 2019) (**Figure 3G**).

PULLING AND PUSHING PLASMIDS AND CHROMOSOMES

Multiple protein apparatuses have been identified that actively push or pull plasmids or sister chromosomes apart. Plasmids are typically much smaller than chromosomes found in bacteria (Shintani et al., 2015), with sizes of ∼1–1,000 kbp versus ∼1–10 Mbp (Shintani et al., 2015), respectively. We first discuss the simpler and more thoroughly studied segregation mechanisms in plasmids. High-copy-number plasmids typically segregate to daughter cells by random Brownian motion and thus do not require elaborate segregation mechanisms (Summers, 1998). By contrast, for low-copy-number plasmids, two types of active partitioning mechanisms have been described in multiple bacterial species whereby plasmids are symmetrically segregated to the opposing cell halves. These are the actin-like *parABS* and *parMRC* systems, that each are comprised of three components: *parS* and *parC* ori-proximal DNA sequences on the plasmid, ParA and ParM motor proteins that provide kinetic energy under hydrolysis of ATP, and ParB and ParR proteins that bind the *parS/C* DNA sequences and connect them to the motor proteins in the systems (Garner et al., 2007; Havey et al., 2012). Due to the relevance for prokaryotic chromosome segregation, this review focusses on these two well-studied partitioning systems rather than on other plasmid segregation mechanisms such as plasmid accumulation at cell poles and plasmid clustering (Million-Weaver and Camps, 2014).

The tripartite *parABS* system (Type I) actively partitions plasmids by a so-called Walker A-type mechanism (**Figure 4A**). Here, p*arS* sequences are bound by ParB which drags the attached DNA over a carpet of ParA that covers the nucleoid. Fluorescence imaging showed that ParA occupies the nucleoid between ParB-*parS* foci on plasmids and the cell poles (Ringgaard et al., 2009). Upon movement of the ParB-*parS* nucleoproteins over this carpet, the ParA signal depletes. Such observations led to a search for an active filament-based pulling system toward the cell poles. Despite evidence of polymerizing capabilities of ParA *in vitro* (Leonard et al., 2005; Ebersbach et al., 2006), no such filaments were found *in vivo*. Instead, ParA was shown to non-specifically bind chromosomal DNA, which appears to be a necessary step in rendering its interaction with ParB (Volante and Alonso, 2015). Recent studies revealed that ParB binds and hydrolyses CTP in a parS-dependent manner, which in turn is essential for the ParB-ParA interaction (Osorio-Valeriano et al., 2019; Soh et al., 2019; Jalal et al., 2020). *In vitro* reconstitution of the three components showed that ParB locally depletes ParA and then moves up the locally induced gradient, continually depleting proximal ParA (Vecchiarelli et al., 2014) (**Figure 4B**). This "surfing" of ParB over a ParA gradient leaves a wake of unoccupied DNA without ParA behind it. Computer simulations of this Brownian ratchet model (Hu et al., 2017) could re-capture the biased-random walk plasmid trajectories observed in experiments. This mechanism is capable of successfully segregating plasmids by practically dragging them over a carpet of nucleoid-bound ParA.

The ParMRC segregation system (Type II) partitions the plasmids by forming filaments in-between them that are pushing them apart toward the two poles (**Figure 4C**). Fluorescence time-lapse imaging in *E. coli* cells showed that pairs of F-plasmids get partitioned to opposing cell halves by an accumulation of ParM signal in between (Campbell and Mullins, 2007). ParR dimers stably bind to tandem-repeated *parC* sequences (Schumacher et al., 2007), forming a nucleoprotein complex that connects to growing ParM filaments that apply a force on the plasmids due to the their growth (Garner et al., 2007). ATP-bound ParM monomers polymerize to form these filaments, and after pushing the plasmids to opposite cell poles, the monomer-bound ATP is hydrolyzed upon which the filaments disassemble (Gayathri et al., 2012). *In vitro* reconstitution of purified ParMRC from *E. coli's* R1 plasmid (**Figure 4D**) with ATP showed that these filaments could push pairs of beads over distances as large as 120 μm (Garner et al., 2007).

The *parABS* systems have historically been best studied for their role in plasmid partitioning. Interestingly, evidence has also been presented that the *parABS* plays an important role in the organization and segregation of chromosomes. A genome-wide study showed that almost 70% of 400 investigated prokaryotic species possess chromosomal *parS* sites (Livny et al., 2007). About 75% of those species harbor these loci within 5% of the genomic distance from ori, hinting toward the relevance of *parABS* system for ori segregation in the cell cycle. These species include *C. crescentus*, *Vibrio cholerae*, and *B. subtilis*, while *E. coli* lacks chromosomal *parS* sites despite the role of *parABS* in its plasmid segregation. For *C. crescentus* and *V. cholerae*, *parABS* is indispensable for proper chromosome segregation, as deletion of

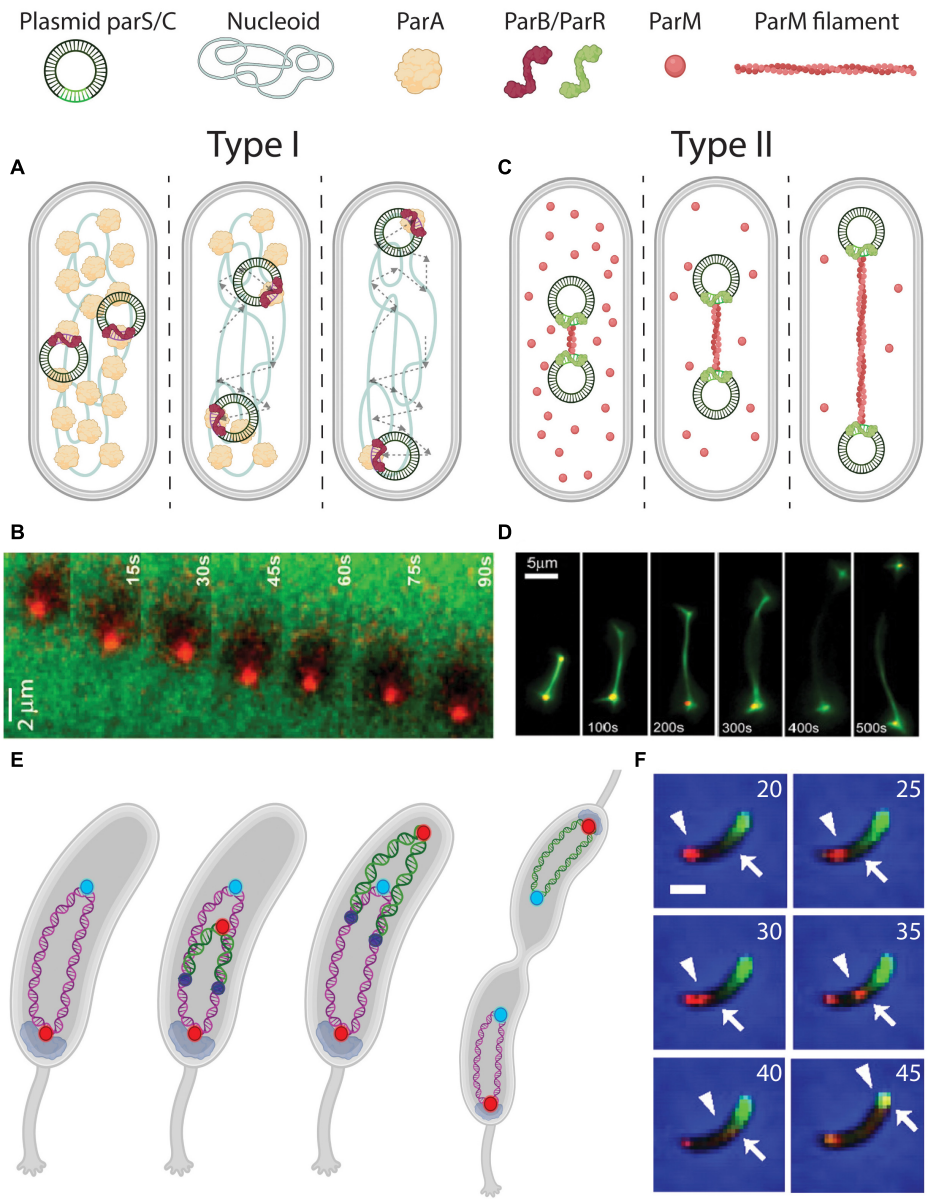

FIGURE 4 | DNA segregation by pushing and pulling. **(A)** Pulling mechanism for plasmid segregation by parABS (Type I). *parS* sequences on the plasmids are bound by ParB (red signal and arrowhead). The ParB-*parS* nucleoprotein then moves outward, with its attached plasmid, through interactions with ParA (green signal and arrow) that is localized between ParB-*parS* and the poles. Dashed arrows indicate the traversed path of the plasmids. **(B)** Fluorescence time-lapse imaging of ParB (red) moving over a ParA carpet (green). From Vecchiarelli et al. (2014). **(C)** Pushing mechanism for plasmid segregation by ParMRC (Type II). *parC* sequences on the plasmids are bound by ParR (green). In between the ParR-*parC* nucleoprotein of a pair of plasmids, a ParM (red) filament polymerizes from soluble monomers, to push the plasmids apart toward the poles. **(D)** Fluorescence time-lapse imaging revealing the *in vitro* growing ParM filament between a pair of plasmids. From Garner et al. (2007). **(E)** Chromosome segregation in *Caulobacter crescentus* bacteria. Before replication, ori (red) is anchored at the old pole by PopZ (gray). After replication initiation (replisomes shown as dark blue circles), one sister ori is pulled over the chromosome toward the new pole. **(F)** Fluorescence time-lapse imaging of parABS-mediated chromosome segregation in *C. crescentus* coexpressing mCherry-ParB (red) and GFP-ParA (green). The ori-proximal ParB that is initially localized at the old pole (indicated by an arrowhead) is duplicated and moves over the ParA gradient (edge indicated by an arrow), depleting it in the process. Scale bar 1µm. Time is indicated in minutes. From Shebelut et al. (2010).

any of the constituents leads to severe chromosome organization and segregation defects (Mohl and Gober, 1997; Mohl et al., 2001; Yamaichi et al., 2007; Toro et al., 2008; Kadoya et al., 2011).

Caulobacter crescentus has its origin of replication and proximal *parS* site held in place at one of its cell poles, known as the old pole (Shebelut et al., 2010) (**Figure 4E**). Consequently, the rest of the chromosome resides along the long axis of the cell (Viollier et al., 2004). Genomic relocation of *parS* from its native ori-proximal site led to a global reorientation of the entire chromosome (Umbarger et al., 2011). This indicates

that forces acting on *parS* are capable of reorienting the entire chromosome. A similar phenotype with a genomic translocation of the primary chromosome *parS* site was observed in *V. cholera* (David et al., 2014).

Upon the initial duplication of ori during replication in *C. crescentus*, the spatial fate of each ori daughter appears determined: One remains stationary at the old pole [anchored by pole organizing protein PopZ (Bowman et al., 2010)], while the other is pulled to the new pole by the *parABS* system (**Figure 4F**). It was shown that other chromosomal loci follow the trajectory of the latter ori, and consequently the chronological order in which they do so matches their respective genomic distance from ori (Viollier et al., 2004). As for the mechanism for the motion of the newly synthesized ori, akin to the process with plasmids, *parS*-bound ParB processively surfs over a readily present ParA carpet, depleting ParA along its trajectory (Shebelut et al., 2010; Lim et al., 2014). High-resolution fluorescence imaging of GFP-tagged ParB-*parS* complexes showed this motion to be not random (Lim et al., 2014), but of a directed diffusive type. At a later point during the replication cycle, the pulled sister chromosome "flips over" along its longitudinal axis, making the entire segregation resemble the "peeling of a banana skin" (**Figure 4E**).

Bacillus subtilis possesses very closely related versions of ParA (Soj), ParB (SpoOJ), and *parS* on the chromosome (Mysliwiec et al., 1991; Ireton et al., 1994; Funnell, 2016). SIM microscopy revealed an ATP-bound ParA gradient in 3D, where ParA was biased toward co-localizing with high-density regions of DNA throughout the cell cycle (Le Gall et al., 2016). However, the *parABS* system seemed not be vital for proper chromosome segregation for *B. subtilis*, since deletions of ParA or ParB in *B. subtilis* showed that the cells remained capable of partitioning the chromosome, albeit with an untimely ori segregation and an increased rate of replication initiation (Lee and Grossman, 2006).

In *C. crescentus*, ParABS has an additional role of regulating the progression of cell division during segregation (Mierzejewska and Jagura-Burdzy, 2012; den Blaauwen, 2013; Marczynski et al., 2019; Pióro and Jakimowicz, 2020). As ParB-*parS* traverses the cell, the slightly higher ParA concentrations at the new pole stimulate PopZ polymerization into a liquid phase-condensate (Bowman et al., 2008; Ebersbach et al., 2008; Laloux and Jacobs-wagner, 2013) to which ParB-*parS* anchors (Bowman et al., 2008, 2010; Ebersbach et al., 2008; Ptacin et al., 2010), while PopZ reciprocally also promotes ParA's ATP binding to further increase ParA levels at the poles. As such, PopZ provides a ParA gradient for ParABS segregating action as well as stable ParB-*parS* polar anchoring, therefore positioning sister chromosomes away from the cell center and thus prevents potential nucleoid occlusion during cell division (Mulder and Woldringh, 1989; Woldringh et al., 1990; den Blaauwen, 2013; Adams et al., 2014). Thanbichler and Shapiro (2006) additionally revealed complex formation between ParB and a newly identified protein, MipZ, (Mera et al., 2014) that was shown to directly interfere with the polymerization of FtsZ that is indispensable in forming the Z ring. Through MipZ, the ParB patterns therefore indirectly prevent Z ring constriction as they traverse the cell during segregation, while allowing divisome assembly when being anchored at the cell poles by PopZ. Other proteins, Noc in *B. subtlis* (Wu and Errington, 2004; Adams et al., 2014) and SlmA in *E. coli* (Bernhardt and De Boer, 2005), also interfere with divisome formation by binding DNA anti-correlated with the ter domains, thus further ensuring that constriction takes place when the ter regions are localized at mid cell, i.e., at the end of the segregation stage in dividing cells (Bernhardt and De Boer, 2005; Adams et al., 2014; Misra et al., 2018; Wang et al., 2020).

ENTROPY AS A SEGREGATING FORCE

Above we discussed various active biological protein systems such as SMCs and Par systems that globally organize and drive sister chromosomes apart. In recent years, a purely physics-based mechanism has emerged that has won some popularity in explaining chromosomal segregation (Jun and Mulder, 2006; Jun and Wrigth, 2010; Kleckner et al., 2014). This concerns the spontaneous segregation of two intermingled DNA polymers from a mixture. While such a spontaneous de-mixing of two polymers may be counterintuitive, a homogenous mixing of two polymers was found to be entropically unfavorable when confined to a cylindrical cell volume (Jun and Mulder, 2006). Directly after active replication, a mixed state of the DNA sister polymers will limit the number of possible adoptable configurations for each of the two polymers. As a result, the two sister DNAs will spontaneously segregate to maximize entropy. This is predicted to occur under specific conditions such as high initial polymer densities and certain geometries, e.g., a cylindrical confinement as opposed to a spherical confinement.

Various computational efforts have been made to probe how such an entropic repulsion of DNA polymers may facilitate segregation of different chromosomes within the cellular confinement (Jun and Mulder, 2006; Jung et al., 2012). Jun and Mulder seminally showed how distinct sister chromosomes, or separate chromosome arms, spontaneously de-mix under strong confinement by the cell wall. The de-mixing resulted in the movement of the sister chromosomes to the freely available outer volumes, i.e., toward the cell poles (Jun and Mulder, 2006) (**Figure 5A**). Consequently, the mother chromosome–still in the process of replication–was kept near the cell center. This phenomenologically captures the sequential segregation of many bacterial genomes. Jun and Wrigth (2010) formulated entropic segregation as dependent on the total polymer length relative to the confinement radius. Plasmids, for example, simply diffuse through a cell since their size is orders of magnitude smaller in size compared to the chromosome. Chromosomes, however, would spontaneously segregate in the typical cylindrical geometries of bacteria.

A recent computational study visualized how successful entropic segregation depends on the relative sizes of the sister chromosomes and the diameter of the cylindrical cell (Polson and Zhu, 2021). Multiple computational efforts on the effect of SMCs in chromosomes also included entropic forces between DNA polymers of sister chromosomes as contributing factors

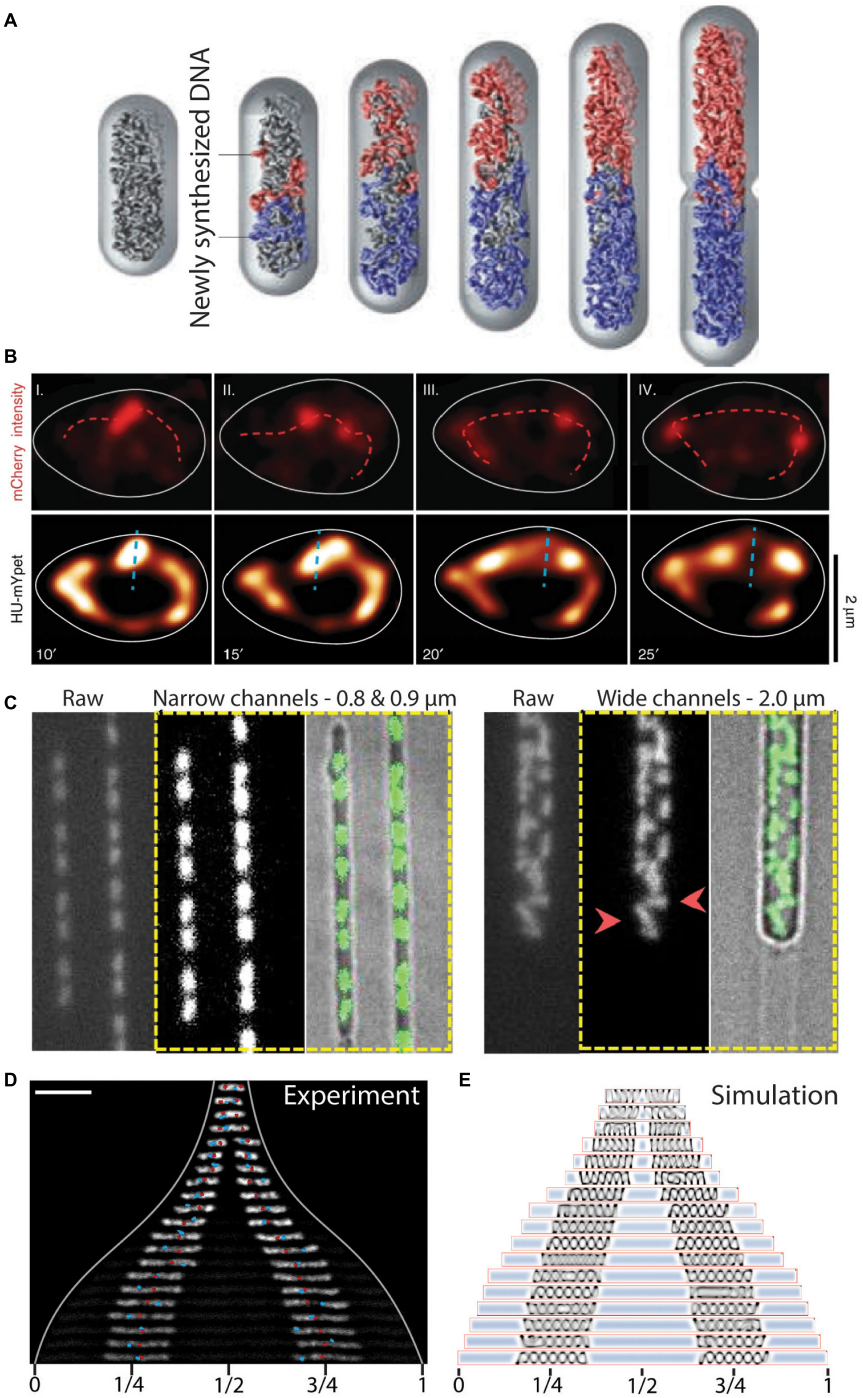

FIGURE 5 | The role of entropy in segregation of chromosomes. **(A)** Simulation of chromosome segregation during replication. Newly synthesized sister chromosomes (blue and red) spontaneously move toward the poles due to entropic forces between the polymers under the confinement of the cell wall. From Jun and Wrigth (2010). **(B)** Independently moving replisomes (labeled in red with mCherry, top row) in widened *E. coli* cells. Initial segregation of the chromosome (labeled in yellow with HU-mYpet, bottom row) is along the short axis of the cell (dashed blue line), indicating a disturbed early ori segregation due to the loss of cell wall confinement on the replicating chromosomes. Time is indicated in minutes. From Japaridze et al. (2020). **(C)** L-form *B. subtilis* cells in microfluidic channels of varying width. Polar segregation of replicating chromosomes is maintained in narrow channels (0.8–0.9 μm), whereas replicated chromosomes are more randomly distributed in the cells in wider channels (2.0 μm). Red arrowheads point at examples of orthogonally and perpendicularly oriented nucleoids relative to the cellular long axis. From Wu et al. (2020). **(D)** Re-distribution of two chromosomes in an elongated *E. coli cell*. The chromosomes increase in size and spontaneously localize at 1/4 and 3/4 positions along the cell length. Ori and ter sites are visualized as red and blue foci, respectively. Scale bar 5 μm. From Wu et al. (2019b). **(E)** Molecular dynamics simulations capture the size and positioning of two chromosomes over the cellular space as a consequence of cytosolic molecular crowding and the entropic spring-like nature of the nucleoids. From Wu et al. (2019b).

to segregation. For example, Brahmachari and Marko (2019) simulated the repulsion between DNA polymers that emanate from their separate SMC cores as a contributor to chromosome segregation. Sherratt et al. (2019) demonstrated that short-ranged repulsive forces between newly replicated ori regions can lead sister foci to spontaneously end up at opposite cell quarter positions in simulations of *E. coli* segregation. Similarly, El Najjar et al. (2020) modeled the linear movement of ori-proximal loci in *B. subtilis* as consequence from entropic repulsion between newly replicated polymers.

Some experimental evidence for entropy as a driver of chromosome segregation has been obtained, although most evidence concerns indirect indications. The cylindrical confinement of bacteria appears to be of importance since increasing the width of *E. coli* cells in microfluidic channels led to a decreased division rate (Liang et al., 2020). Similarly, loss of cell wall confinement after drug-induced expansion in *E. coli* cells led to a decreased success of timely segregation (Japaridze et al., 2020). Furthermore, the initial segregation of ori in these expanded cells (Japaridze et al., 2020) oriented randomly until the replication of chromosomal mass recovered a level of confinement needed to direct the oris toward the cell poles (**Figure 5B**). Other studies showed that cell-wall-less cells (so-called L-form cells) exhibited typical segregation defects, such as more randomly oriented nucleoids that physically separated from one another only rarely, while successful segregation could be recovered by confining these cells into synthetic channels of cell-sized dimensions (Wu et al., 2019b, 2020) (**Figure 5C**). The mere restoration of confinement similar to that imposed by the cell wall thus was able to determine success in segregation, which clearly shows that physics effects are at play, since the biological content of the cells was the same in both shapes.

The entropic spring-like characteristics of nucleoids was experimentally demonstrated *in vivo* and *in vitro* (Pelletier et al., 2012; Wu et al., 2019a,b). Pelletier et al. (2012) revealed that isolated *E. coli* chromosomes would accordingly compress and expand through manipulation with a microchannel-sized piston. The contribution of the entropic forces was tested in *E. coli* cells that contained 1 or 2 chromosomes and had a cell length that was artificially elongated to reach much larger sizes. The cell elongation resulted in the expansion of the chromosomes up to a much longer but finite size (Wu et al., 2019b), indicating that under normal physiological conditions the chromosome acts as a compressed spring. Moreover, two nucleoids distributed to 1/4 and 3/4 positions along the length of the elongated cell (Wu et al., 2019b) (**Figure 5D**). The cellular positioning was recapitulated in a molecular dynamics simulation as a pressure balance between the nucleoid's entropic spring compression and the cytosolic molecular crowding (**Figure 5E**). Widening the *E. coli* cells in all dimensions led to the unfolding of the circular chromosome into a toroidal-shaped chromosome (Wu et al., 2019a). From both studies it appears that relieving cell wall confinement led to occupation of newly vacated cellular space by the nucleoid. All these findings are in accordance with the theoretical framework of the entropic-spring nature of chromosomes under confinement and the accompanying tendency to spontaneously de-mix into two spatially separated polymers.

DISCUSSION AND OUTLOOK

In this review, we described various mechanisms and physical principles that underlie chromosomal segregation in bacteria. Generally, multiple of these mechanisms are simultaneously active within the same organisms to assure a symmetric distribution of replicated genetic material over the daughter cells.

Mixed chromosomes, by their mere physical nature as long circular polymers, will avoid each other and spontaneously move apart to maximize their conformational entropy and minimize the free energy. This entropic de-mixing could very well provide a common primordial driver of segregation throughout taxa. Spontaneous segregation of sisters, with the concomitant inward movement of the yet un-replicated mother chromosome (Jun and Mulder, 2006), elegantly explains the central positioning of the replisome (Lemon and Grossman, 1998, 2000; Mangiameli et al., 2017) and inward movement of loci (Mangiameli et al., 2017) before their replication (Japaridze et al., 2020). Currently, evidence for the contribution of such entropic forces to global segregation of genome-sized DNA polymers has mainly been obtained from simulation studies. Experimental work thus far merely provided indirect evidence of emergent features of such physical models, like the entropic spring-like nature of the nucleoid.

Cells feature a myriad of protein systems that additionally come into play in regulating segregation. For example, SMCs load onto the nucleoid, apparently rather uniformly in *E. coli* (Mäkelä and Sherratt, 2020) or at specific *parS* sequences in *B. subtilis* (Wang et al., 2017) and *C. crescentus* (Tran et al., 2017), to slide along the genome and locally loop it into a bottle brush structure (Petrushenko et al., 2010; Wang et al., 2014a; Lioy et al., 2018). SMCs thus compact the genome as well as interact with topoisomerases that allow them to resolve inter- and intra-chromosomal links. Progressive lengthwise DNA compaction by SMCs may lead to formation of clusters and the amounting mass of replicating DNA may build up stress in the process, which is released by the action of topoisomerase strand-passage activity (**Figure 3G**). This phenomenon may underlie what was reported as waves of clustered chromosomes and consequent segregation described by Fisher et al. (2013). As an ultimate result of the continued DNA condensation, SMC axial cores (Mäkelä and Sherratt, 2020) form on the individualized chromosomes. Repulsion between the emanating loops also drives apart the untangled sisters under cylindrical confinement (Brahmachari and Marko, 2019). This exemplifies how spontaneous de-mixing of genome-sized polymers can synergistically be catalyzed by the local action of proteins to segregate replicated chromosomes during their individual global organization.

Proteinaceous mechanisms also contribute to global chromosome segregation. In *B. subtilis* and *C. crescentus*, ori-proximal *parS* functions as a handle on sister chromosomes for being pulled apart by the *parABS* system. These combined actions–sister-selective compaction by SMCs and the pulling mechanism by *parABS*–could instantiate repulsion between sisters upon individualization directly after replication initiation.

These multiple contributors to segregation are at play in most bacteria and appear to be well conserved. An exception

is the *parABS* system, which is beneficial for segregation, but not essential, as it is lacking in *E. coli*, but clearly contributes to chromosome segregation and loading of SMCs onto chromosomes in *B. subtilis* and *C. crescentus*. Multi-component mechanism such as *parABS*, SMCs, or combinations of both, may have evolved to ensure segregation in increasingly large and more complex organisms with increasing genome sizes. The presence and conservation of SMC structure and function throughout all kingdoms of life (Cobbe and Heck, 2004) strongly suggest that it emerged very early in evolution. Analogously, the absence of *parABS* in *E. coli* and the versatile functions of the system's homologs in bacterial species (Jalal and Le, 2020) indicate that its role in segregation has developed later in some prokaryotes. It is tempting to hypothesize that spontaneous de-mixing was evolutionarily the earliest form of DNA segregation, as it is the simplest physical mechanism.

New model organisms, beyond the well-studied trio of *E. coli*, *C. crescentus*, *or B. subtilis*, may provide new insights as well. One can for example study the effects of cell shape by looking at non-rod-shape bacteria such as *Staphylococcus* which are spherical, yet provide reliable segregation. In search of a model organisms for primordial segregation, cell-wall-less bacteria such as *Mycoplasma pneumonia* are also of interest because of its very small genome (Himmelreich et al., 1996; Hutchison et al., 2016).

Thus far, it has remained difficult to disentangle the relative importance of various individual mechanisms in segregating genome-sized substrates in cells. To investigate this in an alternative way, a recently proposed bottom-up approach named "genome-in-a-box" may provide an interesting starting-point (Birnie and Dekker, 2020). Here, a Mbp-long genome, stripped of all proteins is confined within a microfluidic device, and single components such as SMCs, *parABS*, or other genome-structuring proteins can be added to monitor their individual effects, irrespective of the additional mechanisms that are normally simultaneously at play in cells. Microfluidics-based droplet (oil in water) or liposome techniques allow, in a very controllable way, to generate vesicles of various size and composition (Wu and Dekker, 2016; Deshpande and Dekker, 2019). These can encapsulate bacterial chromosomes and thus provide a model test object to study the dynamics of genome-sized polymers under confinement. By mixing two such minimal genomes, one may be able to investigate how confinement and the contributions of different proteins prime and influence the segregation process. While various technical challenges arise in trying to establish this genome-in-a-box methodology, a bottom-up technology such as this has great potential for providing essential insights in the mechanisms underlying DNA segregation.

Segregation and its coordination with replication and division undeniably belongs to the fundamental processes that sustain all life forms. Understanding how replicated chromosomes in the simpler organisms are driven to disentangle and partition into daughter cells lays the groundwork for understanding the mechanism of chromosome segregation in more complex organisms like eukaryotes. Unraveling the basic principles and contributions of different mechanisms may furthermore lead to applications in ultimately creating the first synthetic cell (Schwille et al., 2018; Spoelstra et al., 2018; Deshpande and Dekker, 2019; Gaut and Adamala, 2021).

AUTHOR CONTRIBUTIONS

CG and AJ contributed equally to writing the review. All authors wrote the manuscript and CD supervised the project.

FUNDING

The work was supported by the ERC Advanced Grant LoopingDNA (No. 883684) and the Netherlands Organization for Scientific Research (NWO/OCW), as part of the NanoFront and BaSyC programs. AJ acknowledges support by the Swiss National Science Foundation (Grant No. P300P2_177768).

ACKNOWLEDGMENTS

The authors would like to thank Miloš Tišma for discussions. Schematics in **Figures 3D,G**, **4A,C,E** were created with Biorender.com.

REFERENCES

Adams, D. W., Wu, L. J., and Errington, J. (2014). Cell cycle regulation by the bacterial nucleoid. *Curr. Opin. Microbiol.* 22, 94–101. doi: 10.1016/j.mib.2014.09.020

Åkerlund, T., Gullbrand, B., and Nordström, K. (2002). Effects of the Min system on nucleoid segregation in *Escherichia coli*. *Microbiology* 148, 3213–3222. doi: 10.1099/00221287-148-10-3213

Anuchin, A. M., Goncharenko, A. V., Demidenok, O. I., and Kaprelyants, A. S. (2011). Histone-like proteins of bacteria. *Appl. Biochem. Microbiol.* 47, 580–585. doi: 10.1134/S0003683811060020

Ashley, R. E., Dittmore, A., McPherson, S. A., Turnbough, C. L., Neuman, K. C., and Osheroff, N. (2017). Activities of gyrase and topoisomerase IV on positively supercoiled DNA. *Nucleic Acids Res.* 45, 9611–9624. doi: 10.1093/nar/gkx649

Bates, D., and Kleckner, N. (2005). Chromosome and replisome dynamics in E. coli: Loss of sister cohesion triggers global chromosome movement and mediates chromosome segregation. *Cell* 121, 899–911. doi: 10.1016/j.cell.2005.04.013

Bernhardt, T. G., and De Boer, P. A. J. (2005). SlmA, a nucleoid-associated, FtsZ binding protein required for blocking septal ring assembly over chromosomes in E. coli. *Mol. Cell.* 18, 555–564. doi: 10.1016/j.molcel.2005.04.012

Birnie, A., and Dekker, C. (2020). Genome-in-a-box: building a chromosome from the bottom up. *ACS Nano*. 21:397. doi: 10.1021/acsnano.0c07397

Blakely, G., May, G., McCulloch, R., Arciszewska, L. K., Burke, M., Lovett, S. T., et al. (1993). Two related recombinases are required for site-specific recombination at *dif* and *cer* in *E. coli* K12. *Cell* 75, 351–361. doi: 10.1016/0092-8674(93)80076-q

Blattner, F. R., Plunkett, G., Bloch, C. A., Perna, N. T., Burland, V., Riley, M., et al. (1997). The complete genome sequence of *Escherichia coli* K-12. *Science* 277, 1453–1462. doi: 10.1126/science.277.5331.1453

Bowman, G. R., Comolli, L. R., Gaietta, G. M., Fero, M., Hong, S. H., Jones, Y., et al. (2010). *Caulobacter* PopZ forms a polar subdomain dictating sequential changes in pole composition and function. *Mol. Microbiol.* 76, 173–189. doi: 10.1111/j.1365-2958.2010.07088.x

Bowman, G. R., Comolli, L. R., Zhu, J., Eckart, M., Koenig, M., Downing, K. H., et al. (2008). A Polymeric Protein Anchors the Chromosomal Origin / ParB

Complex at a Bacterial Cell Pole. *Cell* 134, 945–955. doi: 10.1016/j.cell.2008.07.015

Brahmachari, S., and Marko, J. F. (2019). Chromosome disentanglement driven via optimal compaction of loop-extruded brush structures. *Proc. Natl. Acad. Sci. U. S. A*. 116, 24956–24965. doi: 10.1073/pnas.1906355116

Campbell, C. S., and Mullins, R. D. (2007). In vivo visualization of type II plasmid segregation: Bacterial actin filaments pushing plasmids. *J. Cell Biol*. 179, 1059–1066. doi: 10.1083/jcb.200708206

Cass, J. A., Kuwada, N. J., Traxler, B., and Wiggins, P. A. (2016). *Escherichia coli* chromosomal loci segregate from midcell with universal dynamics. *Biophys. J*. 110, 2597–2609. doi: 10.1016/j.bpj.2016.04.046

Cobbe, N., and Heck, M. M. S. (2004). The evolution of SMC proteins: Phylogenetic analysis and structural implications. *Mol. Biol. Evol*. 21, 332–347. doi: 10.1093/molbev/msh023

Cornet, F., Hallet, B., and Sherratt, D. J. (1997). Xer recombination in *Escherichia coli*: Site-specific DNA topoisomerase activity of the XerC and XerD recombinases. *J. Biol. Chem*. 272, 21927–21931. doi: 10.1074/jbc.272.35.21927

Crisona, N. J., Strick, T. R., Bensimon, D., Croquette, V., and Cozzarelli, N. R. (2000). Preferential relaxation of positively supercoiled DNA by E. coli topoisomerase IV in single-molecule and ensemble measurements. *Genes Dev*. 14, 2881–2892. doi: 10.1101/gad.838900

David, A., Demarre, G., Muresan, L., Paly, E., Barre, F. X., and Possoz, C. (2014). The two cis-acting sites, parS1 and oriC1, contribute to the longitudinal organisation of *Vibrio cholerae* chromosome I. *PLoS Genet*. 10:e4448. doi: 10.1371/journal.pgen.1004448

de Wit, E., and de Laat, W. A. (2012). decade of 3C technologies: Insights into nuclear organization. *Genes Dev*. 26, 11–24. doi: 10.1101/gad.179804.111

den Blaauwen, T. (2013). Prokaryotic cell division: Flexible and diverse. *Curr. Opin. Microbiol*. 16, 738–744. doi: 10.1016/j.mib.2013.09.002

Denker, A., and De Laat, W. (2016). The second decade of 3C technologies: Detailed insights into nuclear organization. *Genes Dev*. 30, 1357–1382. doi: 10.1101/gad.281964.116

Deshpande, S., and Dekker, C. (2019). Synthetic life on a chip. *Emerg Top Life Sci*. 3, 559–566. doi: 10.1042/ETLS20190097

Dewachter, L., Verstraeten, N., Fauvart, M., and Michiels, J. (2018). An integrative view of cell cycle control in *Escherichia coli*. *FEMS Microbiol. Rev*. 42, 116–136. doi: 10.1093/femsre/fuy005

Dorman, C. J., and Dorman, M. J. D. N. A. (2016). supercoiling is a fundamental regulatory principle in the control of bacterial gene expression. *Biophys. Rev*. 8, 89–100. doi: 10.1007/s12551-016-0238-2

Ebersbach, G., Briegel, A., Jensen, G. J., and Jacobs-wagner, C. A. (2008). Self-Associating Protein Critical for Chromosome Attachment, Division, and Polar Organization in Caulobacter. *Cell* 134, 956–968. doi: 10.1016/j.cell.2008.07.016

Ebersbach, G., Ringgaard, S., Møller-Jensen, J., Wang, Q., Sherratt, D. J., and Gerdes, K. (2006). Regular cellular distribution of plasmids by oscillating and filament-forming para ATPase of plasmid pB171. *Mol. Microbiol*. 61, 1428–1442. doi: 10.1111/j.1365-2958.2006.05322.x

El Najjar, N., Geisel, D., and Schmidt, F. (2020). Chromosome segregation in Bacillus subtilis follows an overall pattern of linear movement and is highly robust against cell cycle perturbations. *mSphere* 5:255. doi: 10.1128/msphere.00255-20

Espéli, O., Borne, R., Dupaigne, P., Thiel, A., Gigant, E., Mercier, R., et al. (2012). A MatP-divisome interaction coordinates chromosome segregation with cell division in E. coli. *EMBO J*. 31, 3198–3211. doi: 10.1038/emboj.2012.128

Fisher, J. K., Bourniquel, A., Witz, G., Weiner, B., Prentiss, M., and Kleckner, N. (2013). Four-dimensional imaging of E. coli nucleoid organization and dynamics in living cells. *Cell* 153, 882–895. doi: 10.1016/j.cell.2013.04.006

Funnell, B. E. (2016). ParB partition proteins: Complex formation and spreading at bacterial and plasmid centromeres. *Front. Mol. Biosci*. 3, 1–6. doi: 10.3389/fmolb.2016.00044

Ganji, M., Shaltiel, I. A., Bisht, S., Kim, E., Kalichava, A., Haering, C. H., et al. (2018). Real-time imaging of DNA loop extrusion by condensin. *Science* 105, 102–105. doi: 10.1126/science.aar7831

Garner, E. C., Campbell, C. S., Weibel, D. B., and Dyche, R. (2007). Reconstitution of DNA segregation driven by assembly of a prokaryotic actin homolog. *Science* 315, 1270–1274. doi: 10.1126/science.1138527

Gaut, N. J., and Adamala, K. P. (2021). Reconstituting natural cell elements in synthetic cells. *Adv. Biol*. 5, 1–20. doi: 10.1002/adbi.202000188

Gayathri, P., Fujii, T., Møller-Jensen, J., Ent, F., van den Namba, K., and Löwe, J. (2012). A bipolar spindle of antiparallel ParM filaments drives bacterial plasmid segregation. *Sci. Exp*. 10, 1–7. doi: 10.1002/jcc.20084

Goloborodko, A., Imakaev, M. V., Marko, J. F., and Mirny, L. (2016). Compaction and segregation of sister chromatids via active loop extrusion. *Elife* 5, 1–16. doi: 10.7554/eLife.14864

Gruber, S., and Errington, J. (2009). Recruitment of condensin to replication origin regions by ParB/SpoOJ promotes chromosome segregation in B. subtilis. *Cell* 137, 685–696. doi: 10.1016/j.cell.2009.02.035

Havey, J. C., Vecchiarelli, A. G., and Funnell, B. E. (2012). ATP-regulated interactions between P1 ParA, ParB and non-specific DNA that are stabilized by the plasmid partition site, parS. *Nucleic Acids Res*. 40, 801–812. doi: 10.1093/nar/gkr747

Hayama, R., and Marians, K. J. (2010). Physical and functional interaction between the condensin MukB and the decatenase topoisomerase IV in *Escherichia coli*. *Proc. Natl. Acad. Sci. U. S. A*. 107, 18826–18831. doi: 10.1073/pnas.1008140107

Hayama, R., Bahng, S., Karasu, M. E., and Marians, K. J. (2013). The MukB-ParC interaction affects the intramolecular, not intermolecular, activities of topoisomerase IV. *J. Biol. Chem*. 288, 7653–7661. doi: 10.1074/jbc.M112.418087

Himmelreich, R., Hubert, H., Plagens, H., Pirkl, E., Li, B. C., and Herrmann, R. (1996). Complete sequence analysis of the genome of the bacterium Mycoplasma pneumoniae. *Nucleic Acids Res*. 24, 4420–4449. doi: 10.1093/nar/24.22.4420

Hirano, T. (2016). Condensin-based chromosome organization from bacteria to vertebrates. *Cell* 164, 847–857. doi: 10.1016/j.cell.2016.01.033

Hu, L., Vecchiarelli, A. G., Mizuuchi, K., Neuman, K. C., and Liu, J. (2017). Brownian ratchet mechanism for faithful segregation of low-copy-number plasmids. *Biophys. J*. 112, 1489–1502. doi: 10.1016/j.bpj.2017.02.039

Hutchison, C. A., Chuang, R. Y., and Noskov, V. N. (2016). Design and synthesis of a minimal bacterial genome. *Science* 351:6280. doi: 10.1126/science.aad6253

Ireton, K., Gunther, I. V. N. W., and Grossman, A. D. (1994). spo0J is required for normal chromosome segregation as well as the initiation of sporulation in Bacillus subtilis. *J. Bacteriol*. 176, 5320–5329. doi: 10.1128/jb.176.17.5320-5329.1994

Jacob, F., Brenner, S., and Cuzin, F. (1963). On the regulation of DNA replication in bacteria. *Cold Spring Harb. Symp. Quant. Biol*. 28, 329–348. doi: 10.1101/SQB.1963.028.01.048

Jalal, A. S. B., and Le, T. B. K. (2020). Bacterial chromosome segregation by the ParABS system. *Open Biol*. 10:97.doi: 10.1098/rsob.200097rsob200097

Jalal, A. S., Tran, N. T., and Le, T. B. (2020). ParB spreading on dna requires cytidine triphosphate in vitro. *eLife*. 9, 1–24. doi: 10.7554/eLife.53515

Japaridze, A., Gogou, C., Kerssemakers, J. W. J., Nguyen, H. M., and Dekker, C. (2020). Direct observation of independently moving replisomes in *Escherichia coli*. *Nat. Commun*. 11:46. doi: 10.1038/s41467-020-16946-7

Javer, A., Kuwada, N. J., Long, Z., Benza, V. G., Dorfman, K. D., Wiggins, P. A., et al. (2014). Persistent super-diffusive motion of *Escherichia coli* chromosomal loci. *Nat. Commun*. 5:854. doi: 10.1038/ncomms4854

Jensen, R. B., Wang, S. C., and Shapiro, L. A. (2001). moving DNA replication factory in Caulobacter crescentus. *EMBO J*. 20, 4952–4963. doi: 10.1093/emboj/20.17.4952

Jun, S., and Mulder, B. (2006). Entropy-driven spatial organization of highly confined polymers: Lessons for the bacterial chromosome. *Proc. Natl. Acad. Sci. U. S*. A. 103, 12388–12393.

Jun, S., and Wrigth, A. (2010). Entropy as the driver of chromosome segregation. *Nat. Rev. Microbiol*. 8, 600–607. doi: 10.1038/nrmicro2391

Jung, Y., Jeon, C., Kim, J., Jeong, H., Jun, S., and Ha, B. Y. (2012). Ring polymers as model bacterial chromosomes: Confinement, chain topology, single chain statistics, and how they interact. *Soft Matter*. 8, 2095–2102. doi: 10.1039/c1sm05706e

Kadoya, R., Baek, J. H., Sarker, A., and Chattoraj, D. K. (2011). Participation of chromosome segregation protein ParAI of *Vibrio cholerae* in chromosome replication. *J. Bacteriol*. 193, 1504–1514. doi: 10.1128/JB.01067-10

Karaboja, X., Ren, Z., Paul, P., Rudner, D. Z., and Wang, X. (2021). XerD unloads bacterial SMC complexes at the replication terminus. *Mol. Cell*. 81, 1–11. doi: 10.1016/j.molcel.2020.12.027

Kleckner, N., Fisher, J. K., Stouf, M., White, M. A., Bates, D., and Witz, G. (2014). The bacterial nucleoid: Nature, dynamics and sister segregation. *Curr. Opin. Microbiol.* 22, 127–137. doi: 10.1016/j.mib.2014.10.001

Kleine Borgmann, L. A. K., Hummel, H., Ulbrich, M. H., and Graumanna, P. L. S. M. C. (2013). condensation centers in bacillus subtilis are dynamic structures. *J. Bacteriol.* 195, 2136–2145. doi: 10.1128/JB.02097-12

Kleppe, K., Övrebö, S., and Lossius, I. (1979). The bacterial nucleoid. *J. Gen. Microbiol.* 112, 1–13. doi: 10.1099/00221287-112-1-1

Kumar, R., Nurse, P., Bahng, S., Lee, C. M., and Marians, K. J. (2017). The MukB–topoisomerase IV interaction is required for proper chromosome compaction. *J. Biol. Chem.* 292, 16921–16932. doi: 10.1074/jbc.M117.803346

Kunst, F., Ogasawara, N., Moszer, I., Albertini, A. M., Alloni, G., Azevedo, V., et al. (1997). The complete genome sequence of the Gram-positive bacterium Bacillus subtilis. *Nature* 390, 249–256. doi: 10.1038/36786

Laloux, G., and Jacobs-wagner, C. (2013). Spatiotemporal control of PopZ localization through cell cycle–coupled multimerization. *J. Cell Biol.* 201, 827–841. doi: 10.1083/jcb.201303036

Le Gall, A., Cattoni, D. I., Guilhas, B., Mathieu-Demazière, C., Oudjedi, L., Fiche, J. B., et al. (2016). Bacterial partition complexes segregate within the volume of the nucleoid. *Nat. Commun.* 7, 1–10. doi: 10.1038/ncomms12107

Lee, P. S., and Grossman, A. D. (2006). The chromosome partitioning proteins Soj (ParA) and Spo0J (ParB) contribute to accurate chromosome partitioning, separation of replicated sister origins, and regulation of replication initiation in Bacillus subtilis. *Mol. Microbiol.* 60, 853–869. doi: 10.1111/j.1365-2958.2006.05140.x

Leibowitz, P. J., and Schaechter, M. (1975). The attachment of the bacterial chromosome to the cell membrane. *Int. Rev. Cytol.* 41, 1–28. doi: 10.1016/s0074-7696(08)60964-x

Lemon, K. P., and Grossman, A. D. (1998). Localization of bacterial DNA polymerase: Evidence for a factory model of replication. *Science* 282, 1516–1519. doi: 10.1126/science.282.5393.1516

Lemon, K. P., and Grossman, A. D. (2000). Movement of replicating DNA through a stationary replisome. *Mol. Cell.* 6, 1321–1330. doi: 10.1016/S1097-2765(00)00130-1

Leonard, T. A., Butler, P. J., and Löwe, J. (2005). Bacterial chromosome segregation: Structure and DNA binding of the Soj dimer - A conserved biological switch. *EMBO J.* 24, 270–282. doi: 10.1038/sj.emboj.7600530

Lesterlin, C., Barre, F. X., and Cornet, F. (2004). Genetic recombination and the cell cycle: What we have learned from chromosome dimers. *Mol. Microbiol.* 54, 1151–1160. doi: 10.1111/j.1365-2958.2004.04356.x

Li, Y., Stewart, N. K., and Berger, A. J. (2010). *Escherichia coli* condensin MukB stimulates topoisomerase IV activity by a direct physical interaction. *Proc. Natl. Acad. Sci. U. S. A.* 107, 18832–18837. doi: 10.1073/pnas.1008678107

Liang, B., Quan, B., and Li, J. (2020). Artificial modulation of cell width significantly affects the division time of *Escherichia coli*. *Sci. Rep.* 10, 1–9. doi: 10.1038/s41598-020-74778-3

Lim, H. C., Surovtsev, I. V., Beltran, B. G., Huang, F., Bewersdorf, J., and Jacobs-Wagner, C. (2014). Evidence for a DNA-relay mechanism in ParABS-mediated chromosome segregation. *Elife* 2014, 1–32. doi: 10.7554/eLife.02758

Lindow, J. C., Britton, R. A., and Grossman, A. D. (2002). Structural maintenance of chromosomes protein of Bacillus subtilis affects supercoiling in vivo. *J. Bacteriol.* 184, 5317–5322. doi: 10.1128/JB.184.19.5317-5322.2002

Lioy, V. S., Cournac, A., and Marbouty, M. (2018). Multiscale structuring of the E. coli chromosome by nucleoid-associated and condensin proteins. *Cell* 172, 771–783.e5. doi: 10.1016/j.cell.2017.12.027

Livny, J., Yamaichi, Y., and Waldor, M. K. (2007). Distribution of centromere-like parS sites in bacteria: Insights from comparative genomics. *J. Bacteriol.* 189, 8693–8703. doi: 10.1128/JB.01239-07

Lynch, A. S., and Wang, J. C. (1993). Anchoring of DNA to the bacterial cytoplasmic membrane through cotranscriptional synthesis of polypeptides encoding membrane proteins or proteins for export: A mechanism of plasmid hypernegative supercoiling in mutants deficient in DNA topoisomerase I. *J. Bacteriol.* 175, 1645–1655. doi: 10.1128/jb.175.6.1645-1655.1993

Mäkelä, J., and Sherratt, D. J. (2020). Organization of the *Escherichia coli* chromosome by a MukBEF axial Core. *Mol. Cell.* 78, 1–11. doi: 10.1016/j.molcel.2020.02.003

Mangiameli, S. M., Veit, B. T., Merrikh, H., and Wiggins, P. A. (2017). The replisomes remain spatially proximal throughout the cell cycle in bacteria. *PLoS Genet.* 13:e6582. doi: 10.1371/journal.pgen.1006582

Männik, J., Castillo, D. E., Yang, D., Siopsis, G., and Männik, J. (2016). The role of MatP, ZapA and ZapB in chromosomal organization and dynamics in *Escherichia coli*. *Nucleic Acids Res.* 44, 1216–1226. doi: 10.1093/nar/gkv1484

Marczynski, G. T., Petit, K., and Patel, P. (2019). Crosstalk regulation between bacterial chromosome replication and chromosome partitioning. *Front. Microbiol.* 10, 1–12. doi: 10.3389/fmicb.2019.00279

McCord, R. P., Kaplan, N., and Giorgetti, L. (2020). Chromosome Conformation Capture and Beyond: Toward an Integrative View of Chromosome Structure and Function. *Mol. Cell.* 77, 688–708. doi: 10.1016/j.molcel.2019.12.021

Mera, P. E., Kalogeraki, V. S., and Shapiro, L. (2014). Replication initiator DnaA binds at the caulobacter centromere and enables chromosome segregation. *Proc. Natl. Acad. Sci. U. S. A.* 111, 16100–16105. doi: 10.1073/pnas.1418989111

Mercier, R., Petit, M. A., Schbath, S., Robin, S., El Karoui, M., Boccard, F., et al. (2008). The MatP/matS site-specific system organizes the terminus region of the E. coli chromosome into a macrodomain. *Cell* 135, 475–485. doi: 10.1016/j.cell.2008.08.031

Midonet, C., and Barre, F. X. (2015). Xer site-specific recombination: Promoting vertical and horizontal transmission of genetic information. *Microbiol. Spectr.* 2, 163–182. doi: 10.1128/microbiolspec.MDNA3-0056-2014

Mierzejewska, J., and Jagura-Burdzy, G. (2012). Prokaryotic ParA-ParB-parS system links bacterial chromosome segregation with the cell cycle. *Plasmid* 67, 1–14. doi: 10.1016/j.plasmid.2011.08.003

Migocki, M. D., Lewis, P. J., Wake, R. G., and Harry, E. J. (2004). The midcell replication factory in Bacillus subtilis is highly mobile: Implications for coordinating chromosome replication with other cell cycle events. *Mol. Microbiol.* 54, 452–463. doi: 10.1111/j.1365-2958.2004.04267.x

Million-Weaver, S., and Camps, M. (2014). Mechanisms of plasmid segregation: have multicopy plasmids been overlooked? *Plasmid* 0, 27–36. doi: 10.1016/j.plasmid.2014.07.002

Misra, H. S., Maurya, G. K., Chaudhary, R., and Misra, C. S. (2018). Interdependence of bacterial cell division and genome segregation and its potential in drug development. *Microbiol. Res.* 208, 12–24. doi: 10.1016/j.micres.2017.12.013

Mohl, D. A., and Gober, J. W. (1997). Cell cycle–dependent polar localization of chromosome partitioning proteins in Caulobacter crescentus. *Cell* 88, 675–684. doi: 10.1016/s0092-8674(00)81910-8

Mohl, D. A., Easter, J., and Gober, J. W. (2001). The chromosome partitioning protein, ParB, is required for cytokinesis in Caulobacter crescentus. *Mol. Microbiol.* 42, 741–755. doi: 10.1046/j.1365-2958.2001.02643.x

Moriya, S., Tsujikawa, E., Hassan, A. K. M., Asai, K., Kodama, T., and Ogasawara, N. A. (1998). Bacillus subtilis gene-encoding protein homologous to eukaryotic SMC motor protein is necessary for chromosome partition. *Mol. Microbiol.* 29, 179–187. doi: 10.1046/j.1365-2958.1998.00919.x

Mulder, E., and Woldringh, C. L. (1989). Actively replicating nucleoids influence positioning of division sites in *Escherichia coli* filaments forming cells lacking DNA. *J. Bacteriol.* 171, 4303–4314. doi: 10.1128/jb.171.8.4303-4314.1989

Murray, S. M., and Sourjik, V. (2017). Self-organization and positioning of bacterial protein clusters. *Nat. Phys.* 13, 1006–1013. doi: 10.1038/nphys4155

Mysliwiec, T. H., Errington, J., Vaidya, A. B., and Bramucci, M. G. (1991). The Bacillus subtilis spo0J gene: Evidence for involvement in catabolite repression of sporulation. *J. Bacteriol.* 173, 1911–1919. doi: 10.1128/jb.173.6.1911-1919.1991

Nicolas, E., Upton, A. L., Uphoff, S., Henry, O., Badrinarayanan, A., and Sherratt, D. (2014). The SMC complex MukBEF recruits topoisomerase IV to the origin of replication region in live *Escherichia coli*. *MBio* 5, 1–10. doi: 10.1128/mBio.01001-13

Nielsen, H. J., Li, Y., Youngren, B., Hansen, F. G., and Austin, S. (2006). Progressive segregation of the *Escherichia coli* chromosome. *Mol. Microbiol.* 61, 383–393. doi: 10.1111/j.1365-2958.2006.05245.x

Nierman, W. C., Feldblyum, T. V., Laub, M. T., Paulsen, I. T., Nelson, K. E., Eisen, J. A., et al. (2001). Complete genome sequence of Caulobacter crescentus. *Proc. Natl. Acad. Sci. U. S. A.* 98, 4136–4141. doi: 10.1073/pnas.061029298

Niki, H., Jaffe, A., Imamura, R., Ogura, T., and Hiraga, S. (1991). The new gene mukB codes for a 177 kd protein with coiled-coil domains involved in

chromosome partitioning of E. coli. *EMBO J*. 10, 183–193. doi: 10.1002/j.1460-2075.1991.tb07935.x

Nolivos, S., Upton, A. L., Badrinarayanan, A., Müller, J., Zawadzka, K., Wiktor, J., et al. (2016). MatP regulates the coordinated action of topoisomerase IV and MukBEF in chromosome segregation. *Nat. Commun*. 7, 1–12. doi: 10.1038/ncomms10466

Norris, V. (1995). Hypothesis: chromosome separation in *Escherichia coli* involves autocatalytic gene expression, transertion and membrane—domain formation. *Mol. Microbiol*. 16, 1051–1057. doi: 10.1111/j.1365-2958.1995.tb02330.x

Ohniwa, R. L., Ushijima, Y., Saito, S., and Morikawa, K. (2011). Proteomic analyses of nucleoid-associated proteins in *escherichia coli*, *pseudomonas aeruginosa*, bacillus subtilis, and staphylococcus aureus. *PLoS One*. 6:e9172. doi: 10.1371/journal.pone.0019172

Orlandini, E., Marenduzzo, D., and Michieletto, D. (2019). Synergy of topoisomerase and structural-maintenance-of-chromosomes proteins creates a universal pathway to simplify genome topology. *Proc. Natl. Acad. Sci. U. S. A*. 116, 8149–8154. doi: 10.1073/pnas.1815394116

Osorio-Valeriano, M., Altegoer, F., Steinchen, W., Urban, S., Liu, Y., Bange, G., et al. (2019). ParB-Type DNA segregation proteins are CTP-dependent molecular switches. *Cell* 179, 1512–1524. doi: 10.1016/j.cell.2019.11.015

Ozaki, S., Jenal, U., and Katayama, T. (2020). Novel divisome-associated protein spatially coupling the z-ring with the chromosomal replication terminus in caulobacter crescentus. *MBio* 11, 1–19. doi: 10.1128/mBio.00487-20

Ozaki, S., Wakasugi, Y., and Katayama, T. Z. - (2021). ring-associated proteins regulate clustering of the replication terminus-binding protein zapt in caulobacter crescentus. *MBio* 12, 1–17. doi: 10.1128/mBio.02196-20

Pelletier, J., Halvorsen, K., and Ha, B. Y. (2012). Physical manipulation of the *Escherichia coli* chromosome reveals its soft nature. *Proc. Natl. Acad. Sci. U. S. A*. 89:109. doi: 10.1073/pnas.1208689109

Petrushenko, Z. M., Cui, Y., She, W., and Rybenkov, V. V. (2010). Mechanics of DNA bridging by bacterial condensin MukBEF in vitro and in singulo. *EMBO J*. 29, 1126–1135. doi: 10.1038/emboj.2009.414

Pióro, M., and Jakimowicz, D. (2020). Chromosome Segregation Proteins as Coordinators of Cell Cycle in Response to Environmental Conditions. *Front. Microbiol*. 11, 1–15. doi: 10.3389/fmicb.2020.00588

Polson, J. M., and Zhu, Q. (2021). Free energy and segregation dynamics of two channel-confined polymers of different lengths. *Phys. Rev*. E103, 1–15. doi: 10.1103/PhysRevE.103.012501

Postow, L., Hardy, C. D., Arsuaga, J., and Cozzarelli, N. R. (2004). Topological domain structure of the *Escherichia coli* chromosome. *Genes Dev*. 18, 1766–1779. doi: 10.1101/gad.1207504

Ptacin, J. L., Lee, S. F., and Garner, E. C. A. (2010). spindle-like apparatus guides bacterial chromosome segregation. *Nat. Cell Biol*. 12, 791–798. doi: 10.1038/ncb2083

Reyes-Lamothe, R., and Sherratt, D. J. (2019). The bacterial cell cycle, chromosome inheritance and cell growth. *Nat. Rev. Microbiol*. 17, 467–478. doi: 10.1038/s41579-019-0212-7

Reyes-Lamothe, R., Possoz, C., Danilova, O., and Sherratt, D. J. (2008). Independent positioning and action of *Escherichia coli* replisomes in live cells. *Cell* 133, 90–102. doi: 10.1016/j.cell.2008.01.044

Ringgaard, S., Van Zon, J., Howard, M., and Gerdes, K. (2009). Movement and equipositioning of plasmids by ParA filament disassembly. *Proc. Natl. Acad. Sci. U. S. A*. 106, 19369–19374. doi: 10.1073/pnas.0908347106

Roggiani, M., and Goulian, M. (2015). Chromosome-membrane interactions in bacteria. *Annu. Rev. Genet*. 49, 115–129. doi: 10.1146/annurev-genet-112414-054958

Ryu, J. K., Katan, A. J., van der Sluis, E. O., Wisse, T., de Groot, R., Haering, C. H., et al. (2020). The condensin holocomplex cycles dynamically between open and collapsed states. *Nat. Struct. Mol. Biol*. 27, 1134–1141. doi: 10.1038/s41594-020-0508-3

Schoolnik, G. K., and Yildiz, F. H. (2000). The complete genome sequence of *Vibrio cholerae*: a tale of two chromosomes and of two lifestyles. *Genome Biol*. 1, 1–3. doi: 10.1186/gb-2000-1-3-reviews1016

Schumacher, M. A., Glover, T. C., and Brzoska, A. J. (2007). Segrosome structure revealed by a complex of ParR with centromere DNA. *Nature* 450, 1268–1271. doi: 10.1038/nature06392

Schwille, P., Spatz, J., and Landfester, K. (2018). MaxSynBio: Avenues towards creating cells from the bottom up. *Angew Chem. Int.* 57, 13382–13392. doi: 10.1002/anie.201802288

Sciochetti, S. A., Piggot, P. J., and Blakely, G. W. (2001). Identification and characterization of the dif site from Bacillus subtilis. *J. Bacteriol*. 183, 1058–1068. doi: 10.1128/JB.183.3.1058-1068.2001

Sciochetti, S. A., Piggot, P. J., Sherratt, D. J., and Blakely, G. (1999). The ripX locus of Bacillus subtilis encodes a site-specific recombinase involved in proper chromosome partitioning. *J. Bacteriol*. 181, 6053–6062. doi: 10.1128/jb.181.19.6053-6062.1999

Seol, Y., Hardin, A. H., Strub, M. P., Charvin, G., and Neuman, K. C. (2013). Comparison of DNA decatenation by *Escherichia coli* topoisomerase IV and topoisomerase III: Implications for non-equilibrium topology simplification. *Nucleic Acids Res*. 41, 4640–4649. doi: 10.1093/nar/gkt136

Shebelut, C. W., Guberman, J. M., Van Teeffelen, S., Yakhnina, A. A., and Gitai, Z. (2010). Caulobacter chromosome segregation is an ordered multistep process. *Proc. Natl. Acad. Sci. U. S. A*. 107, 14194–14198. doi: 10.1073/pnas.1005274107

Sherratt, D. J., Heermann, D., Hofmann, A., and Ma, J. (2019). Self-organised segregation of bacterial chromosomal origins. *Elife* 8, 1–26. doi: 10.7554/eLife.46564

Shintani, M., Sanchez, Z. K., and Kimbara, K. (2015). Genomics of microbial plasmids: Classification and identification based on replication and transfer systems and host taxonomy. *Front. Microbiol*. 6, 1–16. doi: 10.3389/fmicb.2015.00242

Soh, Y.-M.., Davidson, I. F., Zamuner, S., Basquin, J., Bock, F. P., Taschner, M. T., et al. (2019). Self-organization of *ParS* centromeres by the ParB CTP hydrolase. *Science* 366, 1129–1133. doi: 10.1126/science.aay3965

Spoelstra, W. K., Deshpande, S., and Dekker, C. (2018). Tailoring the appearance: what will synthetic cells look like? *Curr. Opin. Biotechnol*. 51, 47–56. doi: 10.1016/j.copbio.2017.11.005

Summers, D. (1998). Timing, self—control and a sense of direction are the secrets of multicopy plasmid stability. *Mol. Microbiol*. 29, 1137–1145. doi: 10.1046/j.1365-2958.1998.01012.x

Tadesse, S., and Graumann, P. L. (2006). Differential and dynamic localization of topoisomerases in Bacillus subtilis. *J. Bacteriol*. 188, 3002–3011. doi: 10.1128/JB.188.8.3002-3011.2006

Thanbichler, M., and Shapiro, L. (2006). MipZ, a Spatial Regulator Coordinating Chromosome Segregation with Cell Division in Caulobacter. *Cell* 126, 147–162. doi: 10.1016/j.cell.2006.05.038

Toro, E., Hong, S. H., McAdams, H. H., and Shapiro, L. (2008). Caulobacter requires a dedicated mechanism to initiate chromosome segregation. *Proc. Natl. Acad. Sci. U. S. A*. 105, 15435–15440. doi: 10.1073/pnas.0807448105

Tran, N. T., Laub, M. T., and Le, T. B. (2017). progressively aligns chromosomal arms in Caulobacter crescentus but is antagonized by convergent transcription. *Cell Rep*. 20, 2057–2071. doi: 10.1016/j.celrep.2017.08.026

Travers, A., and Muskhelishvili, G. D. N. A. (2005). supercoiling - A global transcriptional regulator for enterobacterial growth? *Nat. Rev. Microbiol*. 3, 157–169. doi: 10.1038/nrmicro1088

Umbarger, M. A., Toro, E., and Wright, M. A. (2011). The three-dimensional architecture of a bacterial genome. *Mol. Cell*. 44:90. doi: 10.1016/j.molcel.2011.09.010.The

Valentin, V., Rybenkov, V. H., Petrushenko, Z. M., and Zhao, H. (2014). MukBEF, a chromosomal organizer. *J. Mol. Microbiol. Biotechnol*. 24, 371–383. doi: 10.1016/j.physbeh.2017.03.040

Vecchiarelli, A. G., Neuman, K. C., and Mizuuchi, K. A. (2014). propagating ATPase gradient drives transport of surface-confined cellular cargo. *Proc. Natl. Acad. Sci. U. S. A*. 111, 4880–4885. doi: 10.1073/pnas.1401025111

Viollier, P. H., Thanbichler, M., McGrath, P. T., West, L., Meewan, M., McAdams, H. H., et al. (2004). Rapid and sequential movement of individual chromosomal loci to specific subcellular locations during bacterial DNA replication. *Proc. Natl. Acad. Sci. U. S. A*. 101, 9257–9262. doi: 10.1073/pnas.0402606101

Volante, A., and Alonso, J. C. (2015). Molecular anatomy of ParA-ParA and ParA-ParB interactions during plasmid partitioning. *J. Biol. Chem*. 290, 18782–18795. doi: 10.1074/jbc.M115.649632

Vos, S. M., Stewart, N. K., Oakley, M. G., and Berger, J. M. (2013). Structural basis for the MukB-topoisomerase IV interaction and its functional implications in vivo. *EMBO J*. 32, 2950–2962. doi: 10.1038/emboj.2013.218

Wang, C. (1998). Moving one DNA double helix through another by a type II DNA topoisomerase: the story of a simple molecular machine. *Q. Rev. Biophys*. 31, 107–144. doi: 10.1017/s0033583598003424

Wang, M., Fang, C., Ma, B., Luo, X., and Hou, Z. (2020). Regulation of cytokinesis: FtsZ and its accessory proteins. *Curr. Genet*. 66, 43–49. doi: 10.1007/s00294-019-01005-6

Wang, W., Li, G.-W., Chen, C., Xie, S. X., and Zhuang, X. (2011). Chromosome organization by a nucleoid-associated protein in live bacteria. *Science* 333, 1445–1449. doi: 10.1126/science.1204697

Wang, X., Brandão, H. B., Le, T. B. K., Laub, M. T., and Rudner, D. Z. (2017). Bacillus subtilis SMC complexes juxtapose chromosome arms as they travel from origin to terminus. *Science* 527, 524–527. doi: 10.1126/science.aai8982

Wang, X., Hughes, A. C., Brandão, H. B., Walker, B., Lierz, C., Cochran, J. C., et al. (2018). In vivo evidence for ATPase-dependent DNA translocation by the Bacillus subtilis SMC condensin complex. *Mol. Cell*. 71, 841–847.e5. doi: 10.1016/j.molcel.2018.07.006

Wang, X., Llopis, P. M., and Rudner, D. Z. (2014a). Bacillus subtilis chromosome organization oscillates between two distinct patterns. *Proc. Natl. Acad. Sci. U. S. A*. 111, 12877–12882. doi: 10.1073/pnas.1407461111

Wang, X., Tang, O. W., Riley, E. P., and Rudner, D. Z. (2014b). The SMC condensin complex is required for origin segregation in Bacillus subtilis. *Curr. Biol*. 24, 1–6. doi: 10.1016/j.cub.2013.11.050

Wilhelm, L., Bürmann, F., Minnen, A., Shin, H. C., Toseland, C. P., Oh, B. H., et al. (2015). SMC condensin entraps chromosomal DNA by an ATP hydrolysis dependent loading mechanism in Bacillus subtilis. *Elife* 4, 1–18. doi: 10.7554/eLife.06659

Woldringh, C. L. (2002). The role of co-transcriptional translation and protein translocation (transertion) in bacterial chromosome segregation. *Mol. Microbiol*. 45, 17–29. doi: 10.1046/j.1365-2958.2002.02993.x

Woldringh, C. L., Jensen, P. R., and Westerhoff, H. V. (1995). Structure and partitioning of bacterial DNA: determined by a balance of compaction and expansion forces? *FEMS Microbiol. Lett*. 131, 235–242. doi: 10.1016/0378-1097(95)00243-X

Woldringh, C. L., Mulder, E., Valkenburg, J. A. C., Wientjes, F. B., Zaritsky, A., and Nanninga, N. (1990). Role of the nucleoid in the toporegulation of division. *Res. Microbiol*. 141, 39–49. doi: 10.1016/0923-2508(90)90096-9

Wu, F., and Dekker, C. (2016). Nanofabricated structures and microfluidic devices for bacteria: From techniques to biology. *Chem. Soc. Rev*. 45, 268–280. doi: 10.1039/c5cs00514k

Wu, F., Japaridze, A., Zheng, X., Wiktor, J., Kerssemakers, J. W. J., and Dekker, C. (2019a). Direct imaging of the circular chromosome in a live bacterium. *Nat. Commun*. 10, 1–9. doi: 10.1038/s41467-019-10221-0

Wu, F., Swain, P., and Kuijpers, L. (2019b). Cell boundary confinement sets the size and position of the E. coli chromosome. *Curr. Biol*. 29, 2131–2144.e12. doi: 10.1016/j.cub.2019.05.015

Wu, L. J., and Errington, J. (2004). Coordination of cell division and chromosome segregation by a nucleoid occlusion protein in Bacillus subtilis. *Cell* 117, 915–925. doi: 10.1016/j.cell.2004.06.002

Wu, L. J., Lee, S., and Park, S. (2020). Geometric principles underlying the proliferation of a model cell system. *Nat. Commun*. 11, 1–13. doi: 10.1038/s41467-020-17988-7

Yamaichi, Y., Fogel, M. A., McLeod, S. M., Hui, M. P., and Waldor, M. K. (2007). Distinct centromere-like parS sites on the two chromosomes of Vibrio spp. *J. Bacteriol*. 189, 5314–5324. doi: 10.1128/JB.00416-07

Youngren, B., Nielsen, H. J., Jun, S., and Austin, S. (2014). The multifork *Escherichia coli* chromosome is a self-duplicating and self-segregating thermodynamic ring polymer. *Genes Dev*. 28, 71–84. doi: 10.1101/gad.231050.113

Zechiedrich, E. L., and Cozzarelli, N. R. (1995). Roles of topoisomerase IV and during replication in Eschericia coli. *Genes Dev*. 9, 2859–2869. doi: 10.1101/gad.9.22.2859

Zechiedrich, E. L., Khodursky, A. B., and Cozzarelli, N. R. (1997). Topoisomerase IV, not gyrase, decatenates products of site-specific recombination in *Escherichia coli*. *Genes Dev*. 11, 2580–2592. doi: 10.1101/gad.11.19.2580

Conflict of Interest: The authors declare that the research was conducted in the absence of any commercial or financial relationships that could be construed as a potential conflict of interest.

frontiers in Microbiology

MINI REVIEW
published: 25 June 2021
doi: 10.3389/fmicb.2021.697930

Metabolic Control of Cell Elongation and Cell Division in *Bacillus subtilis*

Anne Galinier, Elodie Foulquier and Frédérique Pompeo*

Laboratoire de Chimie Bactérienne, UMR 7283, CNRS/Aix-Marseille Université, Institut de Microbiologie de la Méditerranée, Marseille, France

To survive and adapt to changing nutritional conditions, bacteria must rapidly modulate cell cycle processes, such as doubling time or cell size. Recent data have revealed that cellular metabolism is a central regulator of bacterial cell cycle. Indeed, proteins that can sense precursors or metabolites or enzymes, in addition to their enzymatic activities involved in metabolism, were shown to directly control cell cycle processes in response to changes in nutrient levels. Here we focus on cell elongation and cell division in the Gram-positive rod-shaped bacterium *Bacillus subtilis* and we report evidences linking these two cellular processes to environmental nutritional availability and thus metabolic cellular status.

Keywords: *Bacillus subtilis*, metabolism, cell elongation, MreB, cell division, FtsZ

OPEN ACCESS

Edited by:
Martin Loose,
Institute of Science and Technology Austria (IST Austria), Austria

Reviewed by:
Dirk-Jan Scheffers,
University of Groningen, Netherlands
Imrich Barak,
Institute of Molecular Biology (SAS), Slovakia
Petra Levin,
Washington University in St. Louis, United States

****Correspondence:***
Anne Galinier
galinier@imm.cnrs.fr

Specialty section:
This article was submitted to Microbial Physiology and Metabolism, a section of the journal Frontiers in Microbiology

Received: *20 April 2021*
Accepted: *31 May 2021*
Published: *25 June 2021*

Citation:
Galinier A, Foulquier E and Pompeo F (2021) Metabolic Control of Cell Elongation and Cell Division in Bacillus subtilis. Front. Microbiol. 12:697930. doi: 10.3389/fmicb.2021.697930

INTRODUCTION

To survive in their environment, bacteria have to rapidly adapt to nutrient availability. For example, in rich nutritional conditions, bacterial size can be increased and doubling time can be notably reduced in comparison to poor growth conditions (Schaechter et al., 1958; Sargent, 1975). This observation suggests that cell cycle processes like cell length doubling, duplication then separation of DNA, and finally cell division are highly linked to central metabolism to ensure a viable progeny (Sperber and Herman, 2017).

Bacillus subtilis is the best-characterized Gram-positive endospore-forming bacteria. This aerobic rod-shaped bacterium belongs to the Firmicute phylum. It grows by elongation along its long axis until cell length has doubled and then divides at midcell to give two identical daughter cells.

To grow, *B. subtilis* must synthetize the cell wall (CW) and the membrane. The main component of CW is the peptidoglycan (PG) in almost all bacteria (Egan et al., 2020). PG is a three-dimensional polymer that surrounds the surface of the cell and that is continuously remodeled during growth. It is composed of glycan chains crosslinked by short peptides and covers all the cytoplasmic or inner membrane. PG precursors like uridine diphosphate N-acetylglucosamine (UDP-GlcNAc) and lipid II are synthesized in the cytoplasm (Mengin-Lecreulx et al., 1982; van Heijenoort, 2007). Then, lipid II, a disaccharide pentapeptide coupled to bactoprenol, is exported to be integrated into existing CW sacculus (Mengin-Lecreulx et al., 1982; van Heijenoort, 2007). More precisely, lipid II is flipped outside the cell and assembled into the existing sacculus by penicillin-binding proteins (PBPs),

Abbreviations: Fru6P, fructose 6-phosphate; Glc, glucose; GlcN6P, glucosamine-6-phosphate; GlN, glutamine; LTA, lipoteichoic acids; Man6P, D-mannose 6-phosphate; PG, peptidoglycan; TA, teichoic acid; UDP-GlcNAc, uridine diphosphate N-acetylglucosamine; WTA, wall teichoic acids.

enzymes that possess transglycosylases (TG) and transpeptidase (TP) activities. These enzymes are required to extend the glycan strands and construct peptide cross bridges (Errington and Wu, 2017; Egan et al., 2020). These PBPs are well characterized and are the targets of several antibiotics (Hugonnet et al., 2016; Sharifzadeh et al., 2020). They act in collaboration with RodA and FtsW, SEDS-family TG, to enable, respectively, elongation and division of the bacterial cell (Meeske et al., 2016; Emami et al., 2017; Sjodt et al., 2020). Extracellular enzymes with autolytic activities are also necessary to permit the expansion of the PG by breaking bonds in pre-existing material. All these enzymatic activities should be regulated to allow controlled elongation of the CW during growth (Sassine et al., 2020). Being just outside the cytoplasmic membrane, PG serves as a protective layer that protects the membrane against the turgor pressure due to the high osmolarity of the cytoplasm. The PG, with the help of the cytoskeletal proteins of the MreB family that guide PG synthesis and hydrolysis, contributes to the shape of the cell (Jones et al., 2001; den Blaauwen et al., 2008). MreB proteins are related to eukaryotic actins from a structural and biochemical point of view; they reversibly polymerize depending on the binding and hydrolysis of ATP (van den Ent et al., 2001b; Esue et al., 2005). *B. subtilis* possesses three actin-like proteins, MreB, Mbl, and MreBH, that possess some functional redundancies (Kawai et al., 2009). Deletions of *mreB* genes abolish rod-cell shape but overproduction of an MreB-like protein can compensate the absence of another (Kawai et al., 2009). Concerning the molecular role of MreB, it was proposed that this protein polymerizes as dynamic patches and orchestrates the elongasome (Domínguez-Escobar et al., 2011; Garner et al., 2011). In addition, it was recently shown that MreBH is essential for the activation of the major autolysin LytE and for its localization to the sites where the new PG is inserted (Carballido-López et al., 2006; Patel et al., 2020). The elongasome seems to be present only in rod-shaped bacteria, even if this point of view is debated, and directs lateral insertion of PG along the long axis of the cell to allow cylindrical growth (Szwedziak and Löwe, 2013). It is composed of a variety of enzymes (**Figure 1**), including MreB, MreC, MreD, RodA, RodZ, PBP2a, and PBPH (Errington, 2015; Errington and Wu, 2017; Egan et al., 2020; Patel et al., 2020).

The second major class of polymers that constitutes the bacillus CW are the teichoic acids (TAs) (Auer and Weibel, 2017; Wu et al., 2020). In many Gram-positive bacteria, there are two main forms, the wall TAs (WTA) covalently linked to the PG and lipoteichoic acids (LTA) connected to a lipid carrier. In *B. subtilis*, these two TAs have the same global composition and are mainly constituted of poly-[glycerol-phosphate].

Bacillus subtilis grows by cylindrical elongation and divides at the middle of the cell. This process necessitates a reorientation of CW synthesis. This process is orchestrated by a tubulin-like protein, FtsZ. This cytoskeletal protein is present in almost all bacteria. It is structurally and biochemically related to eukaryotic tubulin and its reversible polymerization is regulated by binding and hydrolysis of GTP (van den Ent et al., 2001a); it governs cell division (Aldea et al., 1990). Actually, FtsZ polymerizes to form a circumferential ring (also called Z-ring) that defines the site of cell division (or septum) (de Boer et al., 1992; RayChaudhuri and Park, 1992). In addition, FtsZ also recruits several proteins (more than a dozen of proteins identified in *B. subtilis*) involved in the division machine, also called the divisome (Gamba et al., 2009; Errington and Wu, 2017). The presence of a divisome is almost ubiquitous but its composition varies depending on bacteria; it is responsible of the constriction of inner and outer membranes and the PG synthesis at the division site (Szwedziak and Löwe, 2013). In *B. subtilis*, it was observed that the assembly of divisome occurs in two steps (Gamba et al., 2009). In the first step, Z-ring assembles early and concomitantly with FtsA, ZapA, and EzrA. Then, a second set of division proteins, including GpsB, FtsL, DivIB, FtsW, PBP2b, and DivIVA, are recruited to the middle of the cell. Several regulators of the divisome function have been identified; they are mostly inhibitors of FtsZ (Errington and Wu, 2017).

The aim of this mini review is to focus on how the cellular metabolism regulates cell cycle. Indeed, to spatially and temporally regulate their cell cycle according to nutritional availability, bacteria possess proteins that bind metabolites or precursors or metabolic enzymes that, in addition to their dedicated enzymatic functions, participate in cell cycle regulation. In this review, we describe metabolic proteins that regulate cell elongation (and cell shape) and cell division depending on growth conditions in the Gram-positive rod-shaped bacterium *B. subtilis*.

METABOLISM AND REGULATION OF CELL ELONGATION AND CELL SHAPE

Stimulation of PG Synthesis by GlmR During Growth on Non-glycolytic Carbon Sources

The GlmR protein (YvcK) is a good illustration of a link between carbon metabolism and cell elongation. This protein is present in many bacteria, but it has been mostly studied in *B. subtilis*. Although *glmR* is dispensable during growth on glucose or glycolytic carbon sources, cells with a *glmR* deletion have abnormal shape and lyse under non-glycolytic growth conditions, like growth in the presence of Krebs cycle intermediates and substrates of pentose phosphate pathway (Görke et al., 2005). GlmR overproduction was shown to compensate the absence of MreB and its localization was similar to that of MreB suggesting a putative role in CW synthesis or in cell elongation (Foulquier et al., 2011). It was demonstrated that GlmR binds to UDP-GlcNAc, a cytoplasmic precursor of PG synthesis (Foulquier and Galinier, 2017). However, mutations in GlmR affecting its binding to UDP-GlcNAc do not perturb bacterial growth on non-glycolytic carbon sources. In a genetic study, it was proposed that GlmR stimulates the activity of GlmS (**Figure 1**) and the binding of UDP-GlcNAc to GlmR could prevent this stimulation (Patel et al., 2018). GlmS is an enzyme involved in the synthesis of UDP-GlcNAc; it converts fructose 6-phosphate (Fru6P) and glutamine (GlN) into glucosamine-6-phosphate (GlcN6P) and glutamate (Badet et al., 1987). By measuring the production of GlcN6P with purified proteins, it was indeed

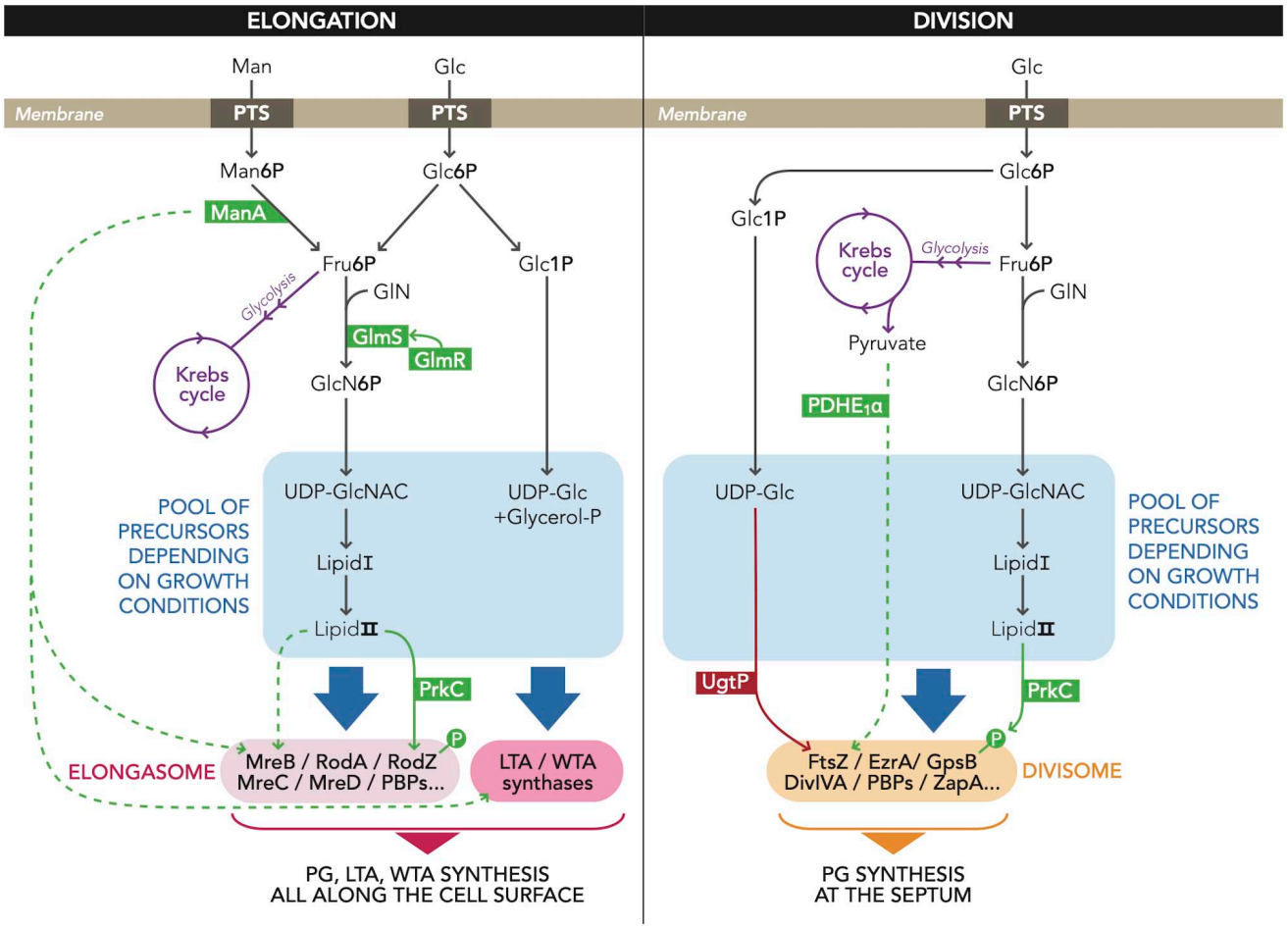

FIGURE 1 | Schematic summary of metabolic regulations of CW elongation and cell division in *B. subtilis* described in the review. The two panels represent regulations of bacterial CW elongation (left) and cell division (right) by proteins whose activity or function is modulated by metabolic intermediates. Metabolic changes adjust the pool of precursors, visualized in blue boxes, in order to regulate LTA, WTA, or PG synthesis. Metabolic reactions are drawn with black arrows and the enzymes involved in the regulations are represented in green or red boxes. The several levels of regulation are mapped by dotted arrows, green for activations and red for inhibitions. When direct interaction exists between proteins and metabolites, dashed arrows are converted to solid lines. The available precursors are then used by LTA synthases and proteins from the elongasome or the divisome for CW synthesis all along the cell surface or at the septum, respectively. Abbreviations: Man, mannose; Man6P, D-mannose 6-phosphate; Glc, glucose; Glc6P, D-glucose 6-phosphate; Glc1P, D-glucose 1-phosphate; Fru6P, fructose 6-phosphate; GlN, glutamine; GlcN6P; glucosamine-6-phosphate; UDP-GlcNAc, uridine diphosphate N-acetylglucosamine; UDP-Glc, uridine diphosphate glucose; AcylACP, acyl-acyl carrier protein; lipid I, undecaprenyl-phosphate UDP-MurNAc-pentapeptide; lipid II, undecaprenyl-phosphate UDP-GlcNAc UDP-MurNAc-pentapeptide; PG, peptidoglycan; WTA, wall teichoic acids; LTA, lipoteichoic acids; PBP, penicillin-binding protein.

shown that GlmR directly stimulates GlmS activity and this positive effect is inhibited by UDP-GlcNAc (Foulquier et al., 2020). Combining these genetic and biochemical studies, the role of GlmR was elucidated (Foulquier and Galinier, 2017; Patel et al., 2018; Foulquier et al., 2020). When growth conditions are poor (non-glycolytic carbon sources), GlmR is essential because the intracellular concentration of UDP-GlcNAc is low. GlmR needs to interact with GlmS to stimulate GlmS activity and thus permit a normal PG synthesis and an efficient CW elongation. Indeed, during gluconeogenesis since Fru6P, the substrate of GlmS is present at low levels. The GlmR-stimulatory effect is probably essential under these conditions. In rich growth conditions, the intracellular concentration of UDP-GlcNAc is high and GlmR binds to this UDP-sugar. GlmR does not interact with GlmS and thus does not stimulate its activity. A *glmR* deletion has thus no effect in such conditions (Patel et al., 2018; Foulquier et al., 2020).

ManA: A Protein That Links Metabolism and Cell Shape

Phosphomannose isomerase (ManA) is another protein in *B. subtilis* that links metabolism and cell shape. ManA is a mannose phosphate isomerase that converts D-mannose 6-phosphate (Man6P) to D-Fru6P when bacteria are grown on mannose as carbon source (Sun and Altenbuchner, 2010). However, the role of this enzyme is not limited to mannose utilization. Indeed, ManA is also necessary for normal rod shape when bacteria are grown in LB medium that does not contain

mannose. In such growth conditions, the presence of ManA avoids chromosome polyploidy and abnormal morphologies (Elbaz and Ben-Yehuda, 2010). This observation was completely unexpected and mysterious. It is noticeable that the deletion of *pmi*, the gene encoding a second mannose phosphate isomerase, had no observable phenotype when bacteria were grown in LB medium, indicating a specific role of ManA. The authors observed that the CW of the *manA* mutant composition has a significant decrease in the amounts of four carbohydrates that are also typical components of WTA. In contrast, the concentration of GlcNAc, the major PG carbohydrate, was similar in wild-type and Δ*manA* cells. Thus, the authors proposed that ManA is required for proper formation of WTA (**Figure 1**) and thus to maintain an equilibrium between PG and WTA; this proper balance is crucial for a correct CW formation. As a result, the deletion of *manA* causes an abnormal CW synthesis that induces a deregulation and an asynchrony between cell elongation, division, and nucleoid segregation (Elbaz and Ben-Yehuda, 2010). Up to now, the molecular mechanism in which ManA is implied is uncharacterized.

Regulation of MreB Dynamics by the Richness of the Growth Medium

Other connections were observed between MreB and richness of growth conditions. Indeed, during fast growth in rich medium, bacteria need a faster synthesis of PG in comparison to slow growth in poor medium. For example, to adapt to nutrient shifts, while *Escherichia coli* potentially regulates the amount of PG inserted by MreB patches, *B. subtilis* regulates the dynamics of MreB patches (Billaudeau et al., 2017). Indeed, it was shown that the speed of MreB patches is correlated to the growth rate in *B. subtilis* and the richness of the growth medium, with a cell elongation per patch that is constant. More the medium is rich in nutrients, more the dynamics of MreB patches is high. Another recent study demonstrates that the membrane fluidity and thus MreB dynamics depend on growth conditions (Zielińska et al., 2020). This regulation is mediated by membrane proteins that form microdomains, the flotillins. These proteins may recruit specific lipids more or less rigid and whose synthesis could be dependent on the nutrient content of the growth medium. The authors observed that the addition of fluidizer is able to restore MreB dynamics and a normal cell shape to fast growing *B. subtilis* mutant cells that lack flotillins. They propose that, in rich medium when the bacteria are growing fast, the control of the membrane fluidity by flotillins, and thus the dynamics of MreB patches, is essential and sufficient for an efficient PG synthesis (Zielińska et al., 2020).

Regulation of MreB by Lipid II

Other studies demonstrate an additional level of regulation of MreB via the PG precursor lipid II (**Figure 1**) (Schirner et al., 2015). Indeed, MreB membrane association was shown to be actively regulated and to depend on the presence of cytoplasmic lipid-linked PG precursors in *B. subtilis*. When these PG precursors are depleted (like in poor nutrient medium), MreB patches disassemble and PG synthesis becomes anarchic. In addition, dynamics of MreB patches are still observed in mutant cells that lack WTA but synthesize PG. However, these patches alone cannot maintain a cellular rod shape. The authors proposed that the cell regulates the interaction of the MreB patches with the membrane and this level of regulation allows a rapid and reversible inactivation of CW enzyme complexes in response to the inhibition of CW synthesis (Schirner et al., 2015). This also suggests that the availability of precursors, and in particular lipid II, at specific sites in the cell envelope likely acts upstream of MreB, in the spatial and temporal control of CW growth (Sperber and Herman, 2017). In complement to these data, a new study has very recently revealed another action of lipid II in the regulation of MreB via the serine/threonine kinase PrkC and the morphogenic protein RodZ (Sun and Garner, 2020). Indeed, comparing the single-cell growth rate to the density of moving MreB patches under different conditions, it was observed that the density of MreB patches is related to the growth rate. This effect requires the *mur* genes involved in biosynthesis of lipid II. In stationary phase, during germination and probably in poor growth conditions, the Ser/Thr kinase PrkC interacts with the lipid II or PG fragments via its extracellular domain (Shah et al., 2008; Squeglia et al., 2011; Pompeo et al., 2018). This interaction induces the oligomerization of PrkC that is evenly distributed in the CW and stimulates its kinase activity (Pompeo et al., 2018). During exponential growth in nutrient-rich conditions, PrkC has a septal localization. In such conditions, its activity is not regulated via its extracellular domain and interaction with PG fragments or lipid II but it requires the division protein GpsB (Pompeo et al., 2015, 2018). PrkC has several substrates and probably connects CW state to cellular processes. In particular, it phosphorylates GlmR to regulate its activity (Foulquier et al., 2014) and also the morphogenic protein RodZ (Ravikumar et al., 2014) (**Figure 1**). Phosphorylated RodZ increases the density of MreB patches (Sun and Garner, 2020). As a result, the cell elongation is stimulated and the growth rate increases. In addition, an overproduction of PrkC results in cells that elongate faster than wild type in nutrient-poor conditions. The authors propose that PrkC may act as a cellular rheostat, adapting cellular processes in response to lipid II (and also probably to PG fragments), allowing cells to adjust their growth under various nutrient conditions.

METABOLISM AND CELL DIVISION

Regulation of Z-Ring Formation by UDP-Glucose and UgtP

A link between richness of growth medium and cell division was highlighted showing a direct regulation of FtsZ polymerization by a metabolic enzyme, UgtP, in *B. subtilis* (Weart et al., 2007). This protein acts a key metabolic regulator of cell division and is involved in glucolipids synthesis; it transfers Glc from UDP-Glc to diacylglycerol-containing sugar acceptors. Deletion of the *ugtP* gene induces smaller cells than wild-type cells. In fact, UgtP binds to FtsZ (**Figure 1**) and inhibits its polymerization in a UDP-Glc-dependent manner both *in vivo* and *in vitro* (Weart et al., 2007; Chien et al., 2012). In addition, it was shown that UDP-Glc,

and consequently nutrient availability, modulates UgtP levels and localization. In summary, under rich-nutrient conditions, when UDP-Glc and UgtP intracellular concentrations are high, UgtP is localized to the septum where it binds to FtsZ to inhibit Z-ring formation. Cell division is thus delayed until the cell reaches their critical mass. Once critical mass is attained, it was proposed that a second unknown nutrient-dependent sensor alleviates this inhibition of cell division and permits progression through the remainder of the division cycle (Weart et al., 2007). In such conditions, cells are long. In poor-nutrient medium, when UDP-Glc level is low, UgtP intracellular concentration is reduced and the protein is sequestered in randomly positioned foci. In such conditions, UgtP does not inhibit FtsZ polymerization and cell division occurs. Thus, the changes in UgtP levels, that depend on nutrients and are coupled with a substrate-dependent localization, link cell division with growth rate in *B. subtilis* (Weart et al., 2007).

Regulation of Cell Division by Pyruvate and Glycolysis

Another level of regulation of cell division by carbon metabolism was also emphasized in *B. subtilis*; this regulation involves glycolysis enzymes and production of pyruvate (Monahan et al., 2014). Indeed, *B. subtilis* strain deleted for *pyk*, the gene encoding the pyruvate kinase, an enzyme that produces pyruvate from phosphoenolpyruvate (PEP) in the final reaction of glycolysis, exhibits aberrant division events at the cell poles. The mutant cells have defects in FtsZ assembly with mislocalized Z rings. Addition of exogenous pyruvate reestablishes a normal cell division in these mutants. This observation supports the idea that pyruvate is a metabolite that plays an essential role in the coordination of bacterial cell cycle with cellular metabolic status. It was proposed that the pyruvate level is correlated to Z-ring polymerization via the E1α subunit of pyruvate dehydrogenase (PDH E1α), an enzyme that metabolizes pyruvate (**Figure 1**). Importantly, this enzyme localizes in a pyruvate-dependent manner over the nucleoid (Monahan et al., 2014). In this model, PDH E1α may be involved in the stimulation of Z ring formation at midcell when bacteria are cultivated in nutrient-rich conditions. In such conditions, cells divide more often due to a shorter mass doubling time. The quantity of PDH E1α localized within this central region increases with the augmentation of nutrient levels; this could deliver a positive signal for Z ring formation that becomes stronger under rich conditions. However, up to now, it is not known how PDH E1α regulates FtsZ (directly or indirectly), how it affects cell division, and how it colocalizes with the nucleoid.

CONCLUSION

In this mini review, we focused on the well-studied Gram-positive bacterium *B. subtilis* and showed some examples of how this bacterium adapts its cell division and elongation in response to its metabolism (**Figure 1**). The understanding of this adaptation is central in microbiology. Recent findings showed that metabolic enzymes play an essential role in this process. Indeed, in addition to their catalytic functions, these proteins, able to bind metabolites or precursors like UDP-Glc, UDP-GlcNAc, or Lipid II, sense the metabolic status of the bacterial cell. Then they transmit this information directly to the cell-cycle machineries, interacting with the elongasome, in particular with MreB, and/or with the divisome, in particular with FtsZ but not only. The discovery and the study of all those regulatory interactions that must occur to coordinate cell growth and division are a major focus in the future.

AUTHOR CONTRIBUTIONS

AG wrote the original draft. FP conceived **Figure 1**. AG, EF, and FP edited the manuscript. All authors contributed to the article and approved the submitted version.

FUNDING

This work was supported by the CNRS, Aix-Marseille University, and an ANR Grant (ANR-19-CE15-0011).

ACKNOWLEDGMENTS

We thank J. R. Fantino for his help in the realization of **Figure 1**. We also thank the reviewers for their constructive comments to improve the manuscript.

REFERENCES

Aldea, M., Garrido, T., Pla, J., and Vicente, M. (1990). Division genes in *Escherichia coli* are expressed coordinately to cell septum requirements by gearbox promoters. *EMBO J.* 9, 3787–3794. doi: 10.1002/j.1460-2075.1990.tb07592.x

Auer, G. K., and Weibel, D. B. (2017). Bacterial cell mechanics. *Biochemistry* 56, 3710–3724. doi: 10.1021/acs.biochem.7b00346

Badet, B., Vermoote, P., Haumont, P. Y., Lederer, F., and LeGoffic, F. (1987). Glucosamine synthetase from *Escherichia coli*: purification, properties, and glutamine-utilizing site location. *Biochemistry* 26, 1940–1948. doi: 10.1021/bi00381a023

Billaudeau, C., Chastanet, A., Yao, Z., Cornilleau, C., Mirouze, N., Fromion, V., et al. (2017). Contrasting mechanisms of growth in two model rod-shaped bacteria. *Nat. Commun.* 8:15370. doi: 10.1038/ncomms15370

Carballido-López, R., Formstone, A., Li, Y., Ehrlich, S. D., Noirot, P., and Errington, J. (2006). Actin homolog MreBH governs cell morphogenesis by localization of the cell wall hydrolase LytE. *Dev. Cell.* 11, 399–409. doi: 10.1016/j.devcel.2006.07.017

Chien, A. C., Zareh, S. K., Wang, Y. M., and Levin, P. A. (2012). Changes in the oligomerization potential of the division inhibitor UgtP co-ordinate *Bacillus subtilis* cell size with nutrient availability. *Mol. Microbiol.* 86, 594–610. doi: 10.1111/mmi.12007

de Boer, P., Crossley, R., and Rothfield, L. (1992). The essential bacterial cell-division protein FtsZ is a GTPase. *Nature* 359, 254–256. doi: 10.1038/359254a0

den Blaauwen, T., de Pedro, M. A., Nguyen-Distèche, M., and Ayala, J. A. (2008). Morphogenesis of rod-shaped sacculi. *FEMS Microbiol. Rev.* 32, 321–344. doi: 10.1111/j.1574-6976.2007.00090.x

Domínguez-Escobar, J., Chastanet, A., Crevenna, A. H., Fromion, V., Wedlich-Söldner, R., and Carballido-López, R. (2011). Processive movement of

MreB-associated cell wall biosynthetic complexes in bacteria. *Science* 333, 225–228. doi: 10.1126/science.1203466

Egan, A. J. F., Errington, J., and Vollmer, W. (2020). Regulation of peptidoglycan synthesis and remodelling. *Nat. Rev. Microbiol.* 18, 446–460.

Elbaz, M., and Ben-Yehuda, S. (2010). The metabolic enzyme ManA reveals a link between cell wall integrity and chromosome morphology. *PLoS Genet* 6:e1001119. doi: 10.1371/journal.pgen.1001119

Emami, K., Guyet, A., Kawai, Y., Devi, J., Wu, L. J., Allenby, N., et al. (2017). Rod a as the missing glycosyltransferase in *Bacillus subtilis* and antibiotic discovery for the peptidoglycan polymerase pathway. *Nat. Microbiol.* 2:16253. doi: 10.1038/nmicrobiol.2016.253

Errington, J. (2015). Bacterial morphogenesis and the enigmatic MreB helix. *Nat. Rev. Microbiol.* 13, 241–248. doi: 10.1038/nrmicro3398

Errington, J., and Wu, L. J. (2017). Cell cycle machinery in *Bacillus subtilis*. *Subcell. Biochem.* 84, 67–101. doi: 10.1007/978-3-319-53047-5_3

Esue, O., Cordero, M., Wirtz, D., and Tseng, Y. (2005). The assembly of MreB, a prokaryotic homolog of actin. *J. Biol. Chem.* 280, 2628–2635. doi: 10.1074/jbc.M410298200

Foulquier, E., and Galinier, A. (2017). YvcK, a protein required for cell wall integrity and optimal carbon source utilization, binds uridine diphosphate-sugars. *Sci. Rep.* 7:4139. doi: 10.1038/s41598-017-04064-2

Foulquier, E., Pompeo, F., Bernadac, A., Espinosa, L., and Galinier, A. (2011). The YvcK protein is required for morphogenesis via localization of PBP1 under gluconeogenic growth conditions in *Bacillus subtilis*. *Mol. Microbiol.* 80, 309–318. doi: 10.1111/j.1365-2958.2011.07587.x

Foulquier, E., Pompeo, F., Byrne, D., Fierobe, H. P., and Galinier, A. (2020). Uridine diphosphate N-acetylglucosamine orchestrates the interaction of GlmR with either YvcJ or GlmS in Bacillus subtilis. *Sci. Rep.* 10:15938. doi: 10.1038/s41598-020-72854-2

Foulquier, E., Pompeo, F., Freton, C., Cordier, B., Grangeasse, C., and Galinier, A. (2014). PrkC-mediated phosphorylation of overexpressed YvcK protein regulates PBP1 protein localization in *Bacillus subtilis* mreB mutant cells. *J. Biol. Chem.* 289, 23662–23669. doi: 10.1074/jbc.M114.562496

Gamba, P., Veening, J. W., Saunders, N. J., Hamoen, L. W., and Daniel, R. A. (2009). Two-step assembly dynamics of the *Bacillus subtilis* divisome. *J. Bacteriol.* 191, 4186–4194. doi: 10.1128/JB.01758-08

Garner, E. C., Bernard, R., Wang, W., Zhuang, X., Rudner, D. Z., and Mitchison, T. (2011). Coupled, circumferential motions of the cell wall synthesis machinery and MreB filaments in B. subtilis. *Science* 333, 222–225. doi: 10.1126/science.1203285

Görke, B., Foulquier, E., and Galinier, A. (2005). YvcK of *Bacillus subtilis* is required for a normal cell shape and for growth on Krebs cycle intermediates and substrates of the pentose phosphate pathway. *Microbiology* 151(Pt. 11), 3777–3791. doi: 10.1099/mic.0.28172-0

Hugonnet, J. E., Mengin-Lecreulx, D., Monton, A., den Blaauwen, T., Carbonnelle, E., Veckerlé, C., et al. (2016). Factors essential for L, D-transpeptidase-mediated peptidoglycan cross-linking and β-lactam resistance in *Escherichia coli*. *Elife* 5:e19469. doi: 10.7554/eLife.19469

Jones, L. J., Carballido-López, R., and Errington, J. (2001). Control of cell shape in bacteria: helical, actin-like filaments in *Bacillus subtilis*. *Cell* 104, 913–922.

Kawai, Y., Asai, K., and Errington, J. (2009). Partial functional redundancy of MreB isoforms, MreB, Mbl and MreBH, in cell morphogenesis of *Bacillus subtilis*. *Mol. Microbiol.* 73, 719–731. doi: 10.1111/j.1365-2958.2009.06805.x

Meeske, A. J., Riley, E. P., Robins, W. P., Uehara, T., Mekalanos, J. J., Kahne, D., et al. (2016). SEDS proteins are a widespread family of bacterial cell wall polymerases. *Nature* 537, 634–638. doi: 10.1038/nature19331

Mengin-Lecreulx, D., Flouret, B., and van Heijenoort, J. (1982). Cytoplasmic steps of peptidoglycan synthesis in *Escherichia coli*. *J. Bacteriol.* 151, 1109–1117. doi: 10.1128/jb.151.3.1109-1117.1982

Monahan, L. G., Hajduk, I. V., Blaber, S. P., Charles, I. G., and Harry, E. J. (2014). Coordinating bacterial cell division with nutrient availability: a role for glycolysis. *mBio* 5:e00935-14. doi: 10.1128/mBio.00935-14

Patel, V., Wu, Q., Chandrangsu, P., and Helmann, J. D. (2018). A metabolic checkpoint protein GlmR is important for diverting carbon into peptidoglycan biosynthesis in *Bacillus subtilis*. *PLoS Genet* 14:e1007689. doi: 10.1371/journal.pgen.1007689

Patel, Y., Zhao, H., and Helmann, J. D. (2020). A regulatory pathway that selectively up-regulates elongasome function in the absence of class A PBPs. *Elife* 9:e57902. doi: 10.7554/eLife.57902

Pompeo, F., Byrne, D., Mengin-Lecreulx, D., and Galinier, A. (2018). Dual regulation of activity and intracellular localization of the PASTA kinase PrkC during *Bacillus subtilis* growth. *Sci. Rep.* 8:1660. doi: 10.1038/s41598-018-20145-2

Pompeo, F., Foulquier, E., Serrano, B., Grangeasse, C., and Galinier, A. (2015). Phosphorylation of the cell division protein GpsB regulates PrkC kinase activity through a negative feedback loop in Bacillus subtilis. *Mol. Microbiol.* 97, 139–150. doi: 10.1111/mmi.13015

Ravikumar, V., Shi, L., Krug, K., Derouiche, A., Jers, C., Cousin, C., et al. (2014). Quantitative phosphoproteome analysis of *Bacillus subtilis* reveals novel substrates of the kinase PrkC and phosphatase PrpC. *Mol. Cell. Proteomics* 13, 1965–1978. doi: 10.1074/mcp.M113.035949

RayChaudhuri, D., and Park, J. T. (1992). *Escherichia coli* cell-division gene ftsZ encodes a novel GTP-binding protein. *Nature* 359, 251–254. doi: 10.1038/359251a0

Sargent, M. G. (1975). Control of cell length in *Bacillus subtilis*. *J. Bacteriol.* 123, 7–19. doi: 10.1128/jb.123.1.7-19.1975

Sassine, J., Sousa, J., Lalk, M., Daniel, R. A., and Vollmer, W. (2020). Cell morphology maintenance in *Bacillus subtilis* through balanced peptidoglycan synthesis and hydrolysis. *Sci. Rep.* 10:17910. doi: 10.1038/s41598-020-74609-5

Schaechter, M., Maaloe, O., and Kjeldgaard, N. O. (1958). Dependency on medium and temperature of cell size and chemical composition during balanced grown of *Salmonella* typhimurium. *J. Gen. Microbiol.* 19, 592–606. doi: 10.1099/00221287-19-3-592

Schirner, K., Eun, Y. J., Dion, M., Luo, Y., Helmann, J. D., Garner, E. C., et al. (2015). Lipid-linked cell wall precursors regulate membrane association of bacterial actin MreB. *Nat. Chem. Biol.* 11, 38–45. doi: 10.1038/nchembio.1689

Shah, I. M., Laaberki, M. H., Popham, D. L., and Dworkin, J. (2008). A eukaryotic-like Ser/Thr kinase signals bacteria to exit dormancy in response to peptidoglycan fragments. *Cell* 135, 486–496. doi: 10.1016/j.cell.2008.08.039

Sharifzadeh, S., Dempwolff, F., Kearns, D. B., and Carlson, E. E. (2020). Harnessing β-lactam antibiotics for illumination of the activity of penicillin-binding proteins. *ACS Chem. Biol.* 15, 1242–1251. doi: 10.1021/acschembio.9b00977

Sjodt, M., Rohs, P. D. A., Gilman, M. S. A., Erlandson, S. C., Zheng, S., Green, A. G., et al. (2020). Structural coordination of polymerization and crosslinking by a SEDS-bPBP peptidoglycan synthase complex. *Nat. Microbiol.* 5, 813–820. doi: 10.1038/s41564-020-0687-z

Sperber, A. M., and Herman, J. K. (2017). Metabolism shapes the cell. *J. Bacteriol.* 199:e00039-17. doi: 10.1128/JB.00039-17

Squeglia, F., Marchetti, R., Ruggiero, A., Lanzetta, R., Marasco, D., Dworkin, J., et al. (2011). Chemical basis of peptidoglycan discrimination by PrkC, a key kinase involved in bacterial resuscitation from dormancy. *J. Am. Chem. Soc.* 133, 20676–20679. doi: 10.1021/ja208080r

Sun, T., and Altenbuchner, J. (2010). Characterization of a mannose utilization system in *Bacillus subtilis*. *J. Bacteriol.* 192, 2128–2139. doi: 10.1128/JB.01673-09

Sun, Y., and GarnerProkaryotic origin of the actin , E. (2020). PrkC modulates MreB filament density and cellular growth rate by monitoring cell wall precursors. *bioRxiv* [preprint] doi: 10.1101/2020.08.28.272336

Szwedziak, P., and Löwe, J. (2013). Do the divisome and elongasome share a common evolutionary past? *Curr. Opin. Microbiol.* 16, 745–751. doi: 10.1016/j.mib.2013.09.003

van den Ent, F., Amos, L. A., and Löwe, J. (2001b). Prokaryotic origin of the actin cytoskeleton. *Nature* 413, 39–44. doi: 10.1038/35092500

van den Ent, F., Amos, L., and Löwe, J. (2001a). Bacterial ancestry of actin and tubulin. *Curr. Opin. Microbiol.* 4, 634–638. doi: 10.1016/s1369-5274(01)00262-4

van Heijenoort, J. (2007). Lipid intermediates in the biosynthesis of bacterial peptidoglycan. *Microbiol. Mol. Biol. Rev.* 71, 620–635. doi: 10.1128/MMBR.00016-07

Weart, R. B., Lee, A. H., Chien, A. C., Haeusser, D. P., Hill, N. S., and Levin, P. A. (2007). A metabolic sensor governing cell size in bacteria. *Cell* 130, 335–347. doi: 10.1016/j.cell.2007.05.043

Wu, X., Han, J., Gong, G., Koffas, M. A. G., and Zha, J. (2020). Wall teichoic acids: physiology and applications. *FEMS Microbiol. Rev.* doi: 10.1093/femsre/fuaa064 [Epub ahead of print].

Zielińska, A., Savietto, A., de Sousa Borges, A., Martinez, D., Berbon, M., Roelofsen, J. R., et al. (2020). Flotillin-mediated membrane fluidity controls peptidoglycan synthesis and MreB movement. *Elife* 9:e57179. doi: 10.7554/eLife.57179

Conflict of Interest: The authors declare that the research was conducted in the absence of any commercial or financial relationships that could be construed as a potential conflict of interest.

frontiers in Microbiology

ORIGINAL RESEARCH
published: 04 August 2021
doi: 10.3389/fmicb.2021.717013

A Novel Z-Ring Associated Protein ZapA-Like Protein (PA5407) From *Pseudomonas aeruginosa* Promotes FtsZ to Form Double Filaments

*Xiaoyu Wang†, Xueqin Ma†, Zhe Li†, Mingyue Niu, Meiting Zhai and Yaodong Chen**

Key Laboratory of Resources Biology and Biotechnology in Western China, Ministry of Education, College of Life Sciences, Northwest University, Xi'an, China

OPEN ACCESS

Edited by:
Zhaomin Yang, Virginia Tech, United States

Reviewed by:
Tanneke Den Blaauwen, University of Amsterdam, Netherlands
William T. Doerrler, Louisiana State University, United States

***Correspondence:**
Yaodong Chen
ydchen@nwu.edu.cn

†These authors have contributed equally to this work and share first authorship

Specialty section:
This article was submitted to Microbial Physiology and Metabolism, a section of the journal Frontiers in Microbiology

Received: *30 May 2021*
Accepted: *13 July 2021*
Published: *04 August 2021*

Citation:
Wang X, Ma X, Li Z, Niu M, Zhai M and Chen Y (2021) A Novel Z-Ring Associated Protein ZapA-Like Protein (PA5407) From Pseudomonas aeruginosa Promotes FtsZ to Form Double Filaments. Front. Microbiol. 12:717013. doi: 10.3389/fmicb.2021.717013

Bacterial cell division is initiated by the assembly of the contraction ring (Z-ring), which consists of the self-assembled FtsZ protofilaments and dozens of other associate proteins. ZapA, a regulatory protein found in almost all bacteria, stabilizes FtsZ protofilaments to form bundles and enhances the Z-ring condensation. Here, we reported that another small protein from *Pseudomonas aeruginosa*, ZapA-Like protein (ZapAL; PA5407), is a new FtsZ associated protein. ZapAL exists in many *Pseudomonas* species and shares only 20% sequence identity to ZapA. ZapAL interacts with FtsZ and induces FtsZ to form long straight double filaments; in comparison, ZapA promotes long bundles with multiple FtsZ filaments. ZapAL has only a mild effect on GTPase activity of FtsZ, which is reduced by around 26% when 10 μM ZapAL is added in the solution. However, to study their assembly dynamics using light-scattering assay, we found that FtsZ-ZapAL double filament is stable and no depolymerization process is observed, which is different from ZapA. Further research found that ZapA and ZapL are likely to form heterodimers. The bundles formed by the mixture of FtsZ-ZapA-ZapAL will depolymerize after GTP is hydrolyzed. Consistent with ZapAL interaction with FtsZ *in vitro*, the expression of ZapAL-GFP was observed as a narrow band or spots in the middle of the cells, suggesting that it is a component of bacterial division machinery. Similar to ZapA, ZapAL is also not essential for bacterial cell division. Little changes were observed when *zapAL* gene was deleted, or overexpressed under normal conditions; however, overexpression of ZapAL caused *zapA*-deficient cells to grow approximately two times longer, showing a mild bacterial division defect. Although we still do not know the exact physiological roles of ZapAL, our results suggest that ZapAL is a novel Z-ring associate protein, which may work together with ZapA to stabilize the FtsZ protofilament and Z-ring structure.

Keywords: bacterial cell division, FtsZ, ZapA, Z-ring, FtsZ assembly, ZapA-like protein

INTRODUCTION

Bacterial tubulin homolog FtsZ spontaneously polymerizes to dynamic protofilaments as a scaffold and combines with dozens of accessory proteins to form a highly dynamic Z-ring – a large protein complex, also known as the bacterial divisome. Z-ring is precisely and effectively activated and regulated by a variety of proteins, including scaffolders, stabilizers, regulators, and many downstream proteins and enzymes (Haeusser and Margolin, 2016; Erickson and Osawa, 2017; McQuillen and Xiao, 2020; Ur Rahman et al., 2020; Barrows and Goley, 2021). In *Escherichia coli*, FtsZ with two other proteins, FtsZ interacting protein A (ZipA) and FtsA, are the earliest proteins to assemble the proto-ring (Hale and de Boer, 1997; Pichoff and Lutkenhaus, 2002; Vicente and Rico, 2006). FtsA and ZipA are two membrane proteins that have the function of anchoring FtsZ on the inner membrane. FtsA is also a key protein for recruiting other downstream proteins. Although not essential for bacterial division, the FtsZ associated protein, ZapA, is considered as a stabilizer of the proto-ring (Huang et al., 2013). In *Bacillus subitilis*, it is reported that FtsA, SepF, ZapA, and EzrA directly interact with FtsZ and participate in the early proto-ring assembly (Gamba et al., 2009). Then, the proto-ring provides a scaffold for the binding of dozens of other associated proteins and downstream proteins.

FtsZ is the crucial protein for bacterial cell division. *In vitro*, fast-growing bacterial FtsZ usually self-assembles into mostly single, dynamic protofilaments (Chen et al., 2005; Chen and Erickson, 2005), but through lateral contact, FtsZ rearranges into bundles or sheets in the solution of calcium, high concentration magnesium, or in some crowding environments (Yu and Margolin, 1997; Mukherjee and Lutkenhaus, 1999; Chen and Erickson, 2009). Some slow-growing bacterial and chloroplast FtsZ could assemble into bundles, and circles directly (White et al., 2000; Chen et al., 2007, 2017b; Wang et al., 2019; Porter et al., 2021). FtsZ filaments are also regulated by some associated proteins. Positive regulators, so-called stabilizers, could enhance FtsZ polymerization and form bundles by increasing the lateral interaction of the FtsZ protofilaments (Huang et al., 2013; Barrows and Goley, 2021). Recent studies using super-resolution fluorescence microscopy revealed that FtsZ filaments, as well as Z-ring *in vivo*, are very dynamic, traveling with a treadmilling pattern, selectively adding FtsZ subunits to one end and releasing from another end (Bisson-Filho et al., 2017; Yang et al., 2017; Ramirez-Diaz et al., 2018; McCausland et al., 2021).

In *E. coli*, FtsZ stabilizers include ZipA and Zap family proteins (FtsZ associated protein), such as ZapA, ZapC, and ZapD (Huang et al., 2013). ZipA exists only in γ–proteobacteria. It is a transmembrane protein that can attach FtsZ filaments onto the inner membrane (Hale and de Boer, 1997). ZipA was previously considered a Z-ring stabilizer since it could promote FtsZ into bundles (Raychaudhuri, 1999; Hale et al., 2000). However, several *in vitro* studies showed that ZipA only induces FtsZ bundling when pH is below 7 (Mateos-Gil et al., 2012), and when the pH is larger than 7, ZipA has the function of enhancing and stabilizing the FtsZ curved conformation, not bundling (Chen et al., 2017a; Rahman et al., 2020). ZapA, ZapC, and ZapD are all FtsZ stabilizers, which are located at midcell and promote FtsZ to form bundles, but they do not share any primary sequence identity (Gueiros-Filho and Losick, 2002; Hale et al., 2011; Durand-Heredia et al., 2012; Huang et al., 2013). Both ZapC and ZapD mainly exist in γ–proteobacteria, and ZapA is broadly conserved in almost all bacteria. ZapA is a small cytoplasmic protein; previous results reported that ZapA dimers or tetramers cross-link adjacent FtsZ protofilaments to associate into long straight loose bundles and/or sheets *in vitro* and thus increase the stability of the Z-ring *in vivo* (Gueiros-Filho and Losick, 2002; Low et al., 2004; Mohammadi et al., 2009; Pacheco-Gomez et al., 2013; Roseboom et al., 2018; Rahman et al., 2020). Even though ZapA is functionally redundant under normal conditions, and ZapA knockout strains show minor morphological changes, previous results suggested that *zapA* deletion strain in *B. subitilis* had serious defects in bacterial division function if it is knocked out together with the *ezrA* gene, or the level of FtsZ is reduced (Gueiros-Filho and Losick, 2002). Different from FtsZ tight bundling induced by divalent cations, which significantly inhibit FtsZ GTPase activity and dynamic (Yu and Margolin, 1997; Mukherjee and Lutkenhaus, 1999; Chen and Erickson, 2009), the loose bundles or sheets promoted by ZapA has only mild reduction of FtsZ GTPase activity (Gueiros-Filho and Losick, 2002; Mohammadi et al., 2009; Rahman et al., 2020). Further studies by super-resolution fluorescence microscopy revealed that ZapA did not alter FtsZ treadmilling rates *in vivo* (Walker et al., 2020; Squyres et al., 2021) and *in vitro* (Caldas et al., 2019).

FtsZ bundling may be an important process for bacterial division. Recent research suggested that the FtsZ stabilizers increase the Z-ring condensation, beneficial for recruiting downstream proteins to the division site (Squyres et al., 2021). Several different FtsZ stabilizers were also identified in different bacterial species, including GpsB in *Staphylococcus aureus* (Eswara et al., 2018), SepH in actinobacteria (Ramos-Leon et al., 2021), WhmD in *Mycobacterium smegmatis* (Bhattacharya et al., 2017), and MsmK in *Streptococcus suis* (Tan et al., 2021).

Here, we reported a new FtsZ stabilizer: a small regulatory protein, ZapA-Like protein (ZapAL; PA5407), from *Pseudomonas aeruginosa*. ZapAL contains 96 amino acids. Although ZapAL has only about 20% sequence identity with ZapA (PA5227), it is also labeled as ZapA in some sequencing data. To solve the puzzle, we studied the properties of this protein and found that it is a novel Z-ring associated protein that can stabilize FtsZ protofilaments to form double straight filaments.

MATERIALS AND METHODS

Bacterial Strains, Plasmids, and Growth Conditions

Bacterial strains were grown in LB or on LB agar at 37°C supplemented with the following antibiotics when necessary: 100 μg/ml Carbenicillin and 50 μg/ml Tetracycline. Liquid cultures were grown under aeration at 37°C at 250 rpm.

Plasmids and oligonucleotides used to generate or to verify strains and plasmids are listed in **Tables 1** and **2**, respectively.

Protein Expression and Purification

Expression vectors for FtsZ, ZapAL, and ZapA from *P. aeruginosa* were constructed in the plasmid pET15b at the NdeI/BamHI sites. After the plasmid transformed into an *E. coli* strain BL21(DE3), protein expression was induced at 16°C overnight by the addition of 0.5 mM isopropyl β-D-1-thiogalactopyranoside (IPTG). Following sonication and centrifugation, the soluble His6-tag proteins were purified by affinity chromatography on a Talon column (Clontech Lab, Inc.). Proteins were firstly washed with 0–30 mM imidazole, and then eluted with the elution buffer containing 50 mM Tris pH 7.7, 300 mM KCl, and 300 mM imidazole. After dialysis with HMK buffer (50 mM HEPES, pH 7.5, 5 mM MgAc, and 100 mM KAc), ZapAL and ZapA proteins with His6 tag were stored at −80°C.

Since FtsZ with His-tag may affect its activity, the purified His6-PaFtsZ was incubated with 2 units/ml of thrombin for 2 h at room temperature to remove the His6-tag. A further purification followed by chromatography on a source Q 10/10 column (GE healthcare) with a linear gradient of 50–500 mM KCl in 50 mM Tris, pH 7.9, 1 mM EDTA, and 10% glycerol. The purified proteins were dialyzed into HMK buffer and stored at −80°C.

TABLE 1 | List of strains and plasmids used in this study.

Strain or plasmid	Phenotype	Source or reference
Escherichia coli		
DH5α	*F⁻ φ80lacZ ΔM15 Δ(lacZYA-argF)U169 recA1 endA1 hsdR17(rk⁻, mk⁺) phoA supE44 thi-1 gyrA96 relA1 tonA*	Lab stock
BL21(DE3)	*F⁻ ompT gal dcm lon hsdSB*(rB- mB-) λ(DE3)	Lab stock
Plasmid		
Pet15b	His6-tag expression vector, Amp^r	Lab stock
Pet15b-*ftsz*	Pet15b containing the entire *ftsZ* gene	Chen et al., 2012
Pet15b-*zapAL*	Pet15b containing the entire *zapAL* gene	This study
Pet15b-*zapA*	Pet15b containing the entire *zapA* gene	Rahman et al., 2020
Pseudomonas aeruginosa		
PAO1	Wild type	
Δ*zapAL*	*zapAL* knock out mutant of PAO1	This study
Δ*zapA*	*zapA* knock out mutant of PAO1	This study
Δ*zapAL*Δ*zapA*	*zapAL/zapA* knock out mutant of PAO1	This study
Plasmid		
pEX18AMP	*oriT*$^+$*sacB*$^+$ gene replacement vector with multiple-cloning site from pUC18, Amp^r	Hoang et al., 1998
pME6032-*zapAL*	pME6032 containing the entire *zapAL* gene	This study
PME6032-*zapAL-gfp*	pME6032 containing the entire *zapAL* gene fused with GFP tag at C-terminal; Tc^r	This study
pME6032-*zapA*	pME6032 containing the entire *zapA* gene	This study

Construction of *P. aeruginosa* Deletion Mutants

A SacB-based strategy was applied to generate the *P. aeruginosa* gene knockout mutants, modified as previously described (Hoang et al., 1998; Peng et al., 2020). Briefly, upstream and downstream fragments of the genes were amplified by PCR using the corresponding primers (**Table 1**). Each fragment contained about 2,000 bp. After digested with appropriate restriction enzymes, both upstream and downstream fragments were ligated and inserted into pEX18Amp plasmid. To avoid errors introduced by PCR, the DNA inserts were verified by DNA sequencing. The resultant plasmids were electroporated into PAO1 and subjected to selection for carbenicillin-resistance. Colonies were then selected on *Pseudomonas* isolation agar plates with 10% sucrose, which indicates a double-crossover event and therefore gene replacement occurring. The resultant mutants were verified by PCR on the region containing the target gene.

Kinetics Measurement

The assembly kinetics of FtsZ filaments and bundles with or without ZapA and ZapAL were measured by the light scattering method at room temperature. After FtsZ and the ZapAL or ZapA mixture is quickly mixed with GTP, the changes of the light scattering signal are tracked to obtain their assembly kinetics. Both excitation and emission were set to 340 nm with a Shimadzu RF-5301 PC spectrofluorometer. Each measurement was repeated two or three times.

Negative Stain Electron Microscopy

Negative stain electron microscopy (EM) was used to visualize FtsZ filaments, as described previously (Rahman et al., 2020). Briefly, samples were incubated with GTP to polymerize for 1–3 min at room temperature. Then, 10 μl samples were added to a carbon-coated copper grid. After standing for about 5 s, the solution was quickly absorbed with filter papers. Grids were immediately stained with 3–5 drops of 2% uranyl acetate, and the excess droplets were dried with filter papers. Images were obtained on a Philips EM420 equipped with a CCD camera.

Sedimentation Assay

To determine the composition of the FtsZ-ZapAL polymers, a sedimentation assay was applied, modified as previously described (Huang et al., 2018). The mixture of 15 μM FtsZ and 15 or 30 μM ZapAL were incubated with 1 mM GTP or without GTP at room temperature for 10 min and centrifuged at 80,000 rpm for 30 min at 25°C in a Beckman TLA100 rotor. The supernatant was carefully removed, and the pellet was resuspended in the same volume of buffer. The protein in the pellet and supernatant was assayed by SDS-PAGE. The ratio of supernatant and pellet was analyzed using ImageJ software (Schneider et al., 2012),

and the protein concentrations of FtsZ or ZapAL in the pellet were calculated from the percentage of total protein concentration. The measurement was repeated three times.

GTPase Activity Measurement

GTPase activity was determined by a continuous assay coupled with a GTP regeneration system, as described previously (Rahman et al., 2020). The solution included 1 mM Phosphoenolpyruvic acid monopotassium, 0.9 mM NADH, 10 units/ml pyruvate kinase and lactate dehydrogenase (Sigma-Aldrich), and 0.5 mM GTP, in HMK buffer (50 mM HEPES, pH 7.5, 5 mM MgAc, and 100 mM KAc), and a 3 mm path cuvette was used for measurement. In this assay, when a molecule of GTP is hydrolyzed to GDP, a molecule of NADH in the solution will be consumed in the subsequent reaction, and at the same time, GDP is regenerated to GTP. The GTP concentration in the solution remains constant, and it can avoid the effect of GDP accumulation on the GTPase activity in the solution. The GTP hydrolysis rate is equal to the NADH consumption rate, which is measured at room temperature using the extinction coefficient 0.00567 μM^{-1} cm^{-1} at 350 nm with an L5 UV-vis spectrophotometer (INESA analytical Instrument Co.). The hydrolysis rate was plotted as a function of FtsZ concentration, and the slope of the line above the critical concentration (Cc) represents the GTPase activity per unit FtsZ concentration. Each measurement was repeated two or three times.

Microscopy and Image Acquisition

Pseudomonas aeruginosa PAO1 carrying pME6032-*zapAL* and pME6032-*zapAL-gfp* were cultured in LB with 50 μg/ml Tetracycline until OD600 value reached ~0.4, and 0.5 mM IPTG was added and induced at 37°C for 1.5 h. PAO1 and the deletion mutants were cultured in LB for 4 h at 37°C until OD600 reached ~0.5.

The cells in the agarose pad were visualized with phase contrast and fluorescence microscopy using a Leica DMI3000B fluorescence microscopy. PAO1 cell lengths were measured for each mutant, and the results were reported as the mean ± SD.

RESULTS

ZapAL Interacts With FtsZ and Promotes FtsZ to Form Double Straight Protofilaments

ZapA is a broadly conserved Z-ring associate protein in most bacteria (Gueiros-Filho and Losick, 2002). When we searched for the ZapA protein sequences in the database (Winsor et al., 2016), we found there were two small proteins from *P. aeruginosa*, PA5227 and PA5407; both were marked as ZapA in some sequencing data. We used Clustal Omega (Sievers et al., 2011) to align these two proteins and found that they share only 20% sequence identity and around 40% similarity (**Figure 1**).

TABLE 2 | Primers used in this study.

Primer	Sequence (5′ → 3″)	Restriction site
pME-*gfp*-S	AAA GGTACC ATGAG TAAAG GAGAA GAACT	*Kpn*I
pME-*gfp*-A	AAA AGATCT TTATT TGTAT AGTTC ATCCA	*Bgl*II
pME-*zapAL-gfp*-S	AAAAGAATTCATGAGCCGCGACGGCGTCCA	*EcoR*I
pME-*zapAL-gfp*-A	AAAA GGTACC GCCGGA TGCCCC GGCGAT	*Kpn*I
pME-*zapA-gfp*-S	AAA GAATTC ATGAG CCAGT CGAAT ACCCT	*EcoR*I
pME-*zapA-gfp*-A	AAAA GGTACC GCCGGA TGCCCC GGCGAT	*Kpn*I
pME-*zapAL*-S	AAAA GGTACC ATGAG CCGCG ACGGC GTCCA	*Kpn*I
pME-*zapAL*-A	AAAA AGATCT CTAGCC GGATGC CCCGGC GAT	*Bgl*II
pEX-*zapAL*-upstream-S	ATAGGTACCAACGAACTCGTTCGGCGGCT	*Kpn*I
pEX-*zapAL*-upstream-A	GGTTCTAGATGGCTCATGTGTCCTGCTCC	*Xba*I
pEX-*zapAL*-downstream-S	AAATCTAGAGATGCCGGCGAAGCCTGACC	*Xba*I
pEX-*zapAL*-downstream-A	AGTAAGCTTTAGGGGCTGGCGGGATCCAG	*Hind*III
pEX-*zapA*-upstream-S	ATA GAATTC GTGCGCCAGATCACAAGTTA	*EcoR*I
pEX-*zapA*-upstream-A	AGG TCTAGA TGTTCTCCAGCATGATCTCG	*Xba*I
pEX-*zapA*-downstream-S	AAC TCTAGA CCTGGAAGCGCTGGTCGAGC	*Xba*I
pEX-*zapA*-downstream-A	ATA AAGCTT CTACGAGCTGGATGGCCGCC	*Hind*III

Restriction enzyme sites are underlined.

```
ZapA    MSQSNTLTVQILDKEYCINCPDDERANLESAARYLDGKMREIRSSGKVIGADRVAVMAAL   60
ZapAL   MSRDGVQVLSILGRDYSIRVPAGEERALADAAALLQAEVDANKRKFPYVTSNELVVLSAL   60
        **:... .:.**.::*.*. * .*.  * .**  *:.::   : .   : ::.:.*::**

ZapA    NITHDLLHRKERLDQESSSTRERVRELLDRVDRALANPADAGEA        104
ZapAL   NLCARQLGANDGESPRLRAVEQRLEALVERIAGASG--------        96
        *:    *  ::  . .  :..:*:. *::*:  * .
```

FIGURE 1 | Sequence comparison of ZapA and ZapA-Like protein (ZapAL) from *P. aeruginosa* using Clustal Omega. These two proteins share only 20% sequence identity and around 40% similarity.

PA5227 contains 104 amino acids, which is ZapA. Another protein PA5407 contains 96 amino acids and is mainly found in *Pseudomonas* species. We name this protein ZapAL.

To characterize ZapAL, we first investigated whether or not ZapAL interacts with FtsZ and affects FtsZ assembly. Using negative-stain EM, we found that ZapAL induced FtsZ to form long, straight double filaments (**Figure 2**). FtsZ from *P. aeruginosa* alone assembles into mostly the mixture of single straight and arc-shaped filaments in the presence of GTP (**Figure 2A**). After ZapAL was added, FtsZ-ZapAL mostly assembles into long, double straight filaments in the presence of GTP (**Figures 2B,C**). It is different from ZapA which promotes FtsZ to form large bundles/sheets composed of multiple FtsZ filaments (**Figure 2D**, also previous publication; Rahman et al., 2020). From EM images of FtsZ-ZapAL, we could observe the striations across the FtsZ-ZapAL double filaments, indicating ZapAL cross-links (**Figures 2B,C**, arrows). The distance between ZapAL molecules is around 3.7 ± 0.4 nm, which suggests that ZapAL binds to each FtsZ molecule. Similar to FtsZ-ZapA, the FtsZ-ZapAL double filaments are also loose structures. The average distance from the outer edge of one FtsZ protofilament to another is about 9.2 ± 1.1 nm. Considering the thickness of FtsZ filaments in our measurement is around 3 nm, the interval distance between filaments is approximately 3.2 nm.

We next used sedimentation and SDS-PAGE to analyze the stoichiometry of the FtsZ-ZapAL copolymers (**Figure 2E**). Following centrifugation at 80,000 rpm, most copolymers were in pellets. Without GTP, little protein could be seen in the

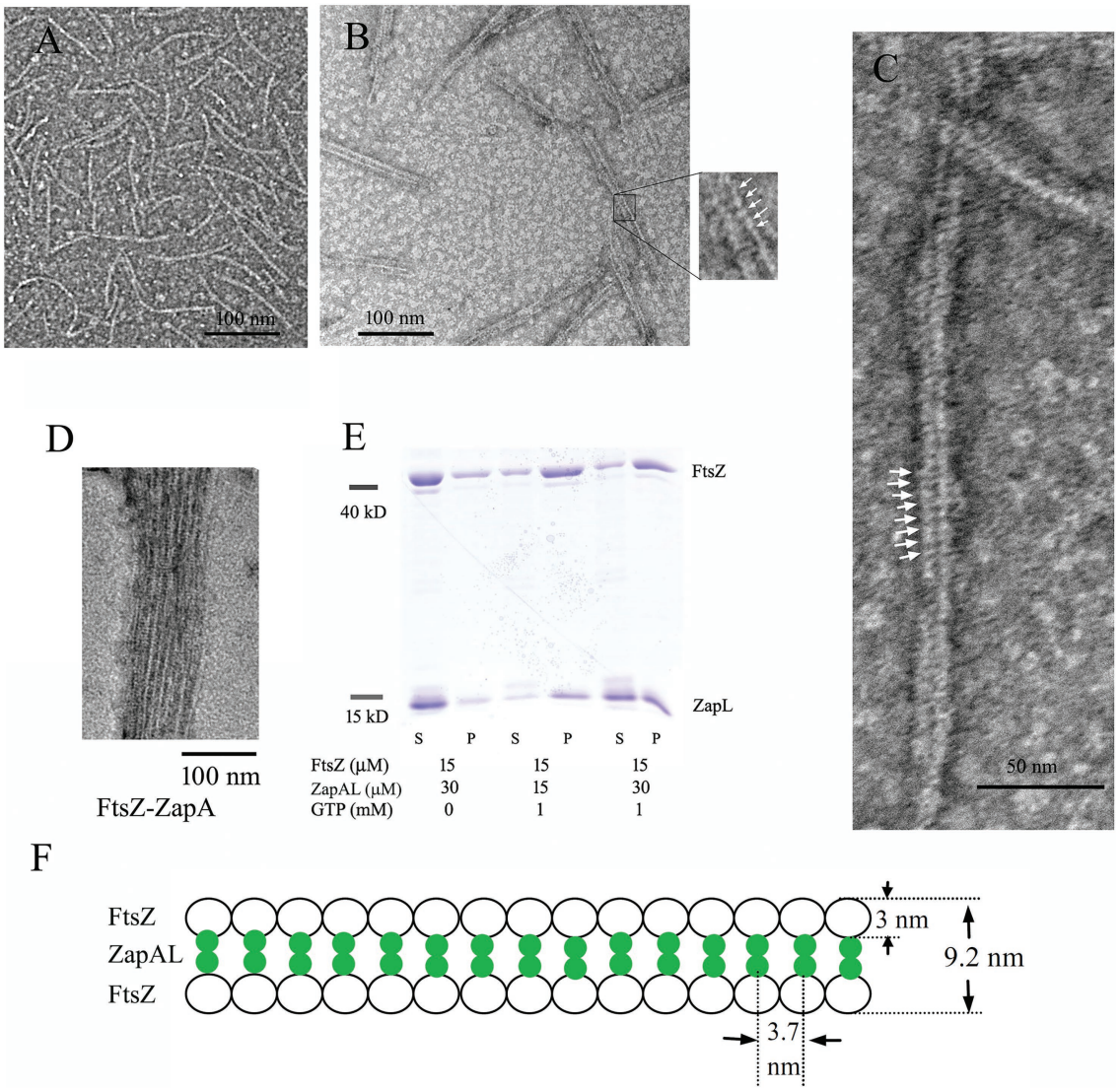

FIGURE 2 | (A–D) show negative stain electron microscopy (EM) of 5 μM FtsZ **(A)**, 5 μM FtsZ and 10 μM ZapAL **(B,C)**, and 5 μM FtsZ and 10 μM ZapA **(D)** in the presence of 1 mM GTP. The arrows in **(B,C)** show periodic striations that could be due to ZapAL crosslinks. **(E)** shows the SDS-PAGE analysis of sedimentation in different ratios of FtsZ and ZapAL (S, supernatant; P, pellet). The concentrations of FtsZ and ZapAL in the pellet were calculated through SDS-PAGE analysis. **(F)** shows the model of FtsZ-ZapAL double filaments.

pellet. In the presence of GTP, FtsZ and ZapAL were pre-mixed at the ratio of 1:1 or 1:2, and the stoichiometry of the copolymer in the pellet was estimated by SDS-PAGE analysis from the percentage of total protein amounts. In the mixture of 15 μM FtsZ and 15 μM ZapAL, FtsZ concentration is around 11.5 ± 1.2 μM, and ZapAL is around 10.7 ± 1.8 μM in the pellet. In the mixture of 15 μM FtsZ and 30 μM ZapAL, FtsZ concentration is around 10.4 ± 1.5 μM, and ZapAL is around 12.6 ± 1.0 μM in the pellet. The molar ratio of FtsZ and ZapAL in the polymer is almost 1:1. We proposed a model to show the FtsZ-ZapAL double filaments (**Figure 2F**). Acting as a bridge, ZapAL connects two FtsZ protofilaments to form long straight double filaments.

Characterization of the Assembly of FtsZ-ZapAL Filaments

Since FtsZ-ZapAL assembles into large, straight double filaments, a light-scattering assay will be a useful tool to measure its assembly dynamics. In our experiments, we used the light-scattering assay to study how ZapAL affects the FtsZ assembly kinetics. **Figure 3** shows the comparison of FtsZ assembly kinetics with ZapAL and ZapA. FtsZ alone assembles into single filaments and its light-scattering signal is very weak. ZapAL induced FtsZ to form long double filaments, corresponding to a strong light-scattering signal. **Figure 3A** shows the assembly of a 1:1 mixture of 5 and 10 μM FtsZ-ZapAL in the presence of 1 mM GTP. After a short fast rising, the light-scattering signal increased slowly and reached a plateau at around 300 s. However, the light-scattering signal of FtsZ-ZapAL was completely stable, and no decrease was observed in our measurements, up to 1,200 s. We repeated the measurement of 10 μM FtsZ-ZapAL with 1 mM GTP and 0.1 mM GTP, and almost similar results were obtained (**Figure 3B**). It is different from the assembly of FtsZ-ZapA (**Figure 3C**). The assembly of FtsZ-ZapA is faster; it took around 100 s to reach the plateau. Comparing the polymerization kinetics of 10 μM FtsZ-ZapA at different concentrations of GTP, we observed that the light scattering signal with 0.1 mM GTP began to decrease rapidly at about 100 s, and then decreased to near the baseline at about 250 s (**Figure 3C**). This shows that when GTP is used up, FtsZ-ZapA will completely depolymerize, consistent with the decrease of light scattering signal. However, it seems that the FtsZ-ZapAL copolymers are stable, and no depolymerization could be observed even with 0.1 mM GTP in our measurements (**Figure 3B**). The similarity between ZapAL and ZapA makes it possible to form heterodimers between them. The **Figure 3D** compares the effects of ZapA, ZapAL, and a mixture of ZapA and ZapAL in a ratio of 1:1 on the FtsZ polymerization kinetics in the presence of 0.1 mM GTP. We found that the light scattering intensity of the mixture of FtsZ and ZapAL-ZapA was weaker and faster, reaching the maximum in less than 20 s. Then, it began to decline, showing that it would depolymerize after GTP was hydrolyzed, similar to FtsZ-ZapA. This result implies that ZapA and ZapAL are very likely to form a heterodimer and promote FtsZ to form a small bundle, which maintain the dynamic characteristics of the FtsZ filaments.

To obtain more information, we next investigated how ZapAL affects the GTPase activity of FtsZ. **Figure 3E** shows the GTPase activity of FtsZ at different concentrations with or without ZapAL at room temperature. The GTPase activity of FtsZ is around 4.57 ± 0.34 GTP/FtsZ/min, and it drops to 4.14 ± 0.33 GTP/FtsZ/min with 5 μM ZapAL and to 3.39 ± 0.12 GTP/FtsZ/min with 10 μM ZapAL, only a 26% reduction. We concluded that ZapAL has a mild effect on the GTPase

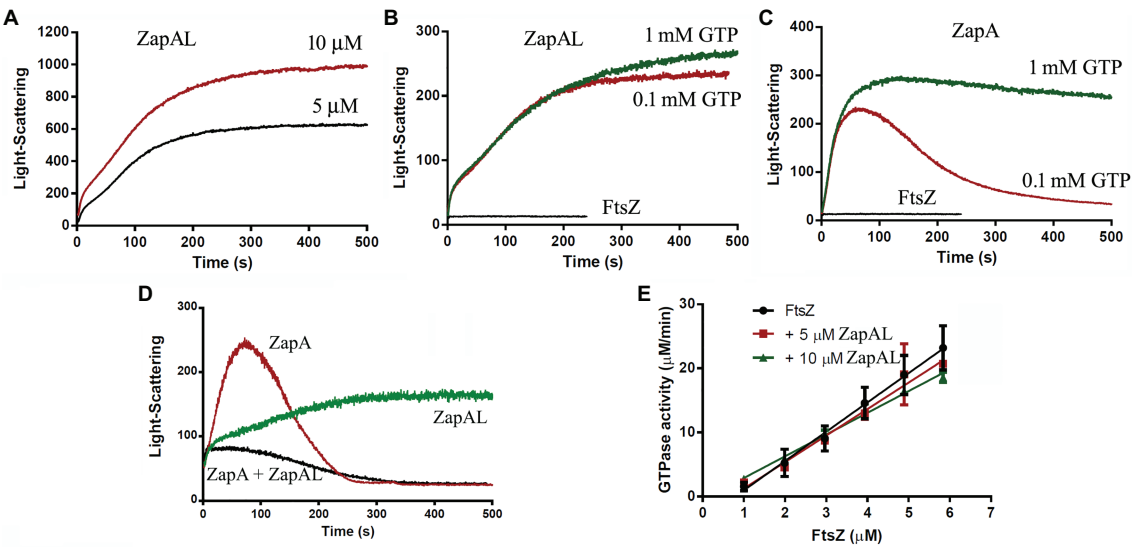

FIGURE 3 | Kinetics of FtsZ assembly in the presence of or in the absence of ZapAL or ZapA followed by light scattering. **(A)** shows the bundles formation of 5 μM FtsZ-ZapAL and 10 μM FtsZ-ZapAL in HMK buffer measured by light scattering assay. **(B,C)** show the comparison of the assembly kinetics of 10 μM FtsZ-ZapAL **(B)** or 10 μM FtsZ-ZapA **(C)** in the presence of 1 mM and 0.1 mM GTP. **(D)** shows the comparison of the assembly kinetics of 10 μM FtsZ with 10 μM ZapAL, 10 μM ZapA, and the mixture of 5 μM ZapAL and 5 μM ZapA in the presence of 0.1 mM GTP. **(E)** shows the comparison of the GTPase activity of FtsZ, FtsZ with 5 μM ZapAL and FtsZ with 10 μM ZapAL at room temperature. Error bars show the SD of three replicates.

activity of FtsZ, similar to ZapA. If there is only 0.1 mM GTP in the solution, 10 μM FtsZ-ZapAL mixtures will hydrolyze all GTP in about 3 min; however, no depolymerization of FtsZ-ZapAL copolymers was observed in our measurements of light-scattering signals (**Figure 3B**), meanwhile, the filaments formed by FtsZ-ZapA and FtsZ-ZapA-ZapAL can be depolymerized after GTP is hydrolyzed.

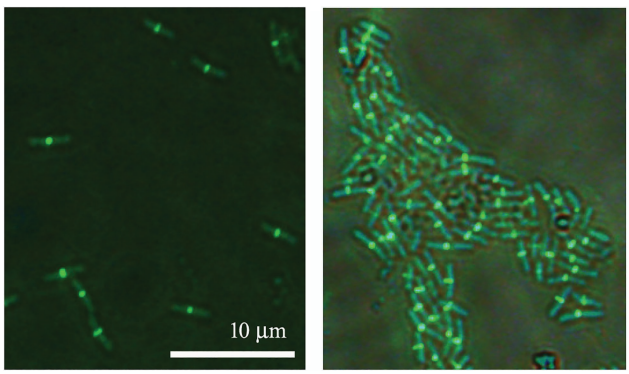

FIGURE 4 | Subcellular localization of ZapAL-GFP. Fluorescence images of PAO1 cells expressing *pME6032-zapAL-gfp* are examined after 1.5 h at 37°C with 0.5 mM isopropyl β-D-1-thiogalactopyranoside (IPTG). They are two representative images from different areas of same batch of samples.

ZapAL Is Located in the Middle of the Cell, but It Is Not Essential for Cell Division

Since ZapAL interacts with FtsZ *in vitro*, we wanted to know its localization and its possible physiological function *in vivo*. Fused with GFP at C-terminus, we expressed ZapAL-GFP in wildtype PAO1 strain. Fluorescence microscopy of a GFP-ZapAL producing strain revealed narrow bands or spots in the middle of cells (**Figure 4**), a localization pattern characteristic of division proteins, similar to ZapA. It suggests that ZapAL is also one of the components of the division machinery.

To investigate the physiological function of ZapAL, we knocked out the *ZapAL* gene from *P. aeruginosa* PAO1 strain. However, we found that knockout *ZapAL* exhibited no recognizable defects in bacterial cell division and growth. Similar results were obtained after we knocked out the *zapA* gene. Since both protein ZapAL and ZapA show a function to stabilize FtsZ protofilaments, we knocked out both of the *zapA* and *ZapAL* genes, and there were still no obvious effects on bacterial morphology (**Figure 5A**). These results suggest that both ZapAL and ZapA are not essential for cell division under normal laboratory conditions.

In an attempt to uncover a role for ZapAL in bacterial division and growth, we also investigated the effects of the overexpressed ZapAL protein on bacterial cell division. Induced by 0.5 mM IPTG, the ZapAL protein was expressed in

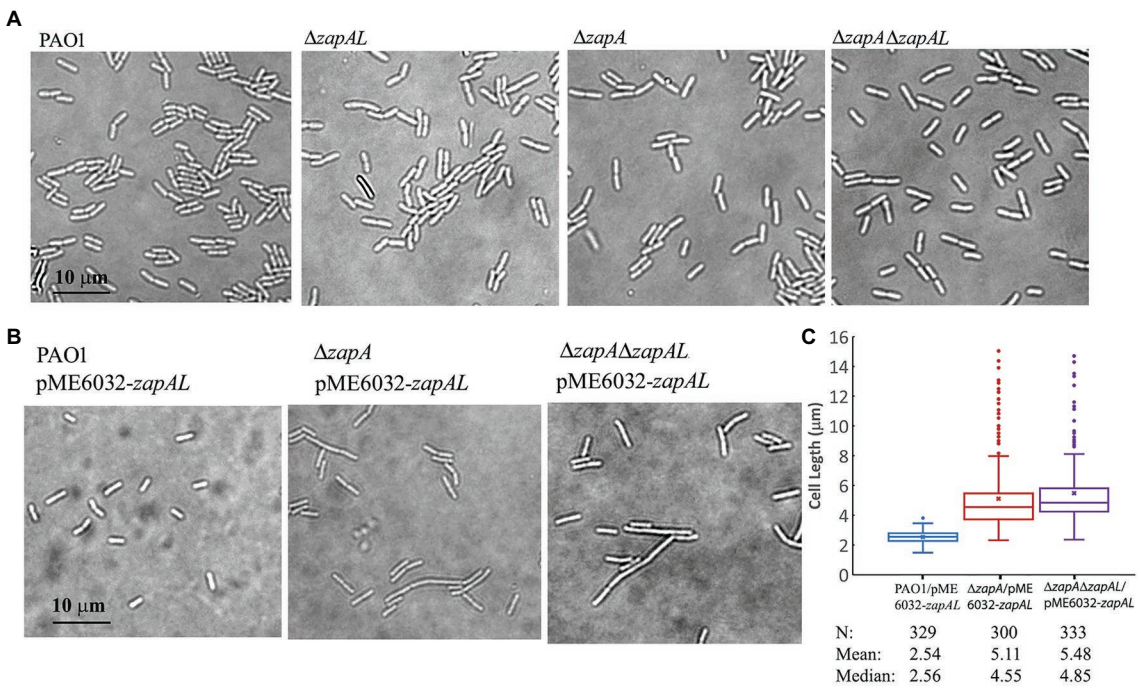

FIGURE 5 | Morphology of strains of *zapAL* deletion or overexpression. **(A)** Representative images of strains of wildtype (PAO1), Δ*zapAL*, Δ*zapA*, and Δ*zapA*Δ*zapAL* show little change of cell morphology, indicating that both *zapAL* and *zapA* are not essential genes. **(B)** Overexpression of ZapAL has little effect on the morphology of wildtype PAO1, while it causes slight cell elongation in the strains of Δ*zapA* and Δ*zapA*Δ*zapAL*. **(C)** Box plot illustrating the comparison of bacterial lengths when ZapAL is overexpressed in the strains of PAO1, Δ*zapA* and Δ*zapAL*Δ*zapA*. The boxes in the box plot show the median and the first and third quartiles. The length of the upper whisker is the largest value that is no greater than the third quartile plus 1.5 times the interquartile range. The number of bacterial cells, mean and median values of bacterial length (μm) are presented at the bottom of the graph. The average length of *zapA*-deleted cells is approximately twice that of wildtype cells after overexpression of ZapAL and part of them exceed 10 μm.

P. aeruginosa PAO1 containing *pME6032-zapAL* plasmid. However, few changes were observed when ZapAL was overexpressed (**Figure 5B**). But when ZapAL was overexpressed in the *zapA* knockout strain, we observed an obvious increase in bacterial length (**Figure 5B**). After overexpression of ZapAL, the bacterial length is around 2.5 ± 0.4 μm (n = 329) in wildtype PAO1 strain, 5.1 ± 2.2 μm (n = 300) in *zapA* deletion strain, and 5.5 ± 2.1 μm (n = 333) in both *zapA* and *zapAL* deletion strain (**Figure 5C**). It suggests that overexpression of ZapAL would mildly impair bacterial cell division without ZapA. Meanwhile, overexpression of ZapA in PAO1 strain and *zapAL* deletion has no obvious effect on bacterial division and growth under normal conditions (data not shown).

DISCUSSION

In this study, we reported a novel FtsZ/Z-ring associated protein ZapAL (PA5407) from *P. aeruginosa*. ZapAL is a small ZapA-like protein that contains 96 amino acids and shares around 20% identity (~ 40% similarity) with ZapA (PA5207, 104 amino acids). Similar to ZapA, ZapAL cross-links adjacent FtsZ protofilament subunits and stabilizes FtsZ polymers. However, unlike ZapA, which promotes FtsZ to form loose bundles or sheets of multiple straight filaments, ZapAL induces FtsZ to form loose, double straight filaments. *In vivo*, ZapAL-GFP is located at midcell, and it suggests that ZapAL is a Z-ring associated protein to stabilize the Z-ring. Our research revealed that ZapAL has only a mild effect on the GTPase activity of FtsZ. Approximately, 75% of GTPase activity of FtsZ can still be maintained after adding 10 μM ZapAL in solution. However, from our light-scattering experiments, we found that the FtsZ-ZapAL double filament is stable. Although GTP is required for their polymerization, the double filaments do not depolymerize after GTP is used up. Furthermore, ZapAL and ZapA are likely to form heterodimers. The mixture of ZapAL and ZapA can promote FtsZ to form a smaller bundle, which corresponds to their weaker light scattering signal. Meanwhile, like ZapA, ZapA-ZapAL heterodimer can also maintain the dynamic characteristics of FtsZ protofilaments, and the bundles they form can be depolymerized after GTP hydrolysis. This implies that ZapAL and ZapA together play a physiological function of stabilizing the Z-ring *in vivo*.

From our studies on the biochemical properties of ZapAL, an interesting finding is a contradiction between its mild reduction in FtsZ GTPase activity and the formation of the stable FtsZ-ZapAL double filaments. This contradiction was also found in previous studies of ZapA, and we suggested that it is due to the loose bundles or sheets formed by FtsZ-ZapA. Bundle formation usually reduces their dynamics, as well as their GTPase activity. However, the assembly of FtsZ-ZapA bundles only mildly reduced the GTP hydrolysis activity of FtsZ by less than 20%, suggesting that this loose bundle has a slight effect on the FtsZ GTPase activity, although it still affects its subunits exchange rate. FtsZ-ZapA bundle is dynamic and depolymerizes after GTP is hydrolyzed. The subunits exchange rate of the FtsZ-ZapA bundles was about four times slower than that of FtsZ protofilaments (Rahman et al., 2020). It is different from the tight bundles caused by divalent ions, which will greatly reduce the activity of FtsZ GTPase and slow down their dynamics (Yu and Margolin, 1997; Mukherjee and Lutkenhaus, 1999; Chen and Erickson, 2009). Recent research discovered that ZapA does not affect the FtsZ treadmilling rate *in vivo* and *in vitro* and suggested the dynamics of FtsZ polymers *in vivo* may be intrinsic to the polymer itself (Caldas et al., 2019; Walker et al., 2020; Squyres et al., 2021). The double filament formed by FtsZ-ZapAL also has a loose structure; the gap between two FtsZ filaments is about 3 nm. Similar to ZapA, ZapAL has only a mild reduction in the GTP hydrolysis activity of FtsZ, by about 26%. However, the FtsZ-ZapAL double filament is stable, and no depolymerization process was observed after GTP hydrolysis in our light-scattering experiments, implying that the GTP/GDP exchanges should occur within FtsZ filaments, and no depolymerization of the FtsZ filaments is required. Bridging by FtsZ associated proteins, adjacent FtsZ filaments form straight loose bundles with large gaps, which may be sufficient to allow the efficient exchange of nucleotides between the FtsZ filaments.

Pseudomonas aeruginosa contains two similar proteins, ZapA and ZapAL, as FtsZ stabilizers to enhance its lateral contact, suggesting that the FtsZ stabilizers *in vivo* may be important for bacterial cell division. In cells, there may be multiple FtsZ bundling proteins with overlapping functions, so knocking out a single stabilizer might lack an obvious effect on cell division under normal conditions. In *B. subtilis*, previous studies showed that FtsZ binding proteins contain ZapA, SepF, and EzrA, and knockout of *zapA* or *sepF* gene alone did not alter cell morphology, but when *ezrA* is knocked out together, the cell displays severe division impairment (Gueiros-Filho and Losick, 2002). Squyres et al. (2021) suggested that FtsZ binding proteins bundle FtsZ filaments into a condensed Z-ring, which is important to recruit downstream proteins, including cell wall synthesis enzymes to the division site. Without FtsZ-binding proteins, ZapA and EzrA, Z-ring condensation disappears. Furthermore, FtsZ suppressor mutant K86E that enhances its lateral interactions partially restores Z-ring condensation (Squyres et al., 2021). A variety of specific FtsZ bundling proteins were recently reported in different bacterial species (Bhattacharya et al., 2017; Eswara et al., 2018; Ramos-Leon et al., 2021; Tan et al., 2021), these also indicate the importance of FtsZ stabilizers for bacterial division.

Different from ZapA, our studies found that FtsZ-ZapAL double straight filaments are stable, so we initially hypothesized that ZapAL might inhibit the dynamics of FtsZ filaments and Z-ring. But, when we overexpressed ZapAL *in vivo*, we did not observe any inhibition of bacterial division under normal conditions. Interestingly, when we overexpressed ZapAL in the *zapA* deficient strains *in vivo*, we observed a mild inhibition, and the size of bacteria was twice as long as normal bacteria. It shows that ZapA may be able to competitively regulate the effects of ZapAL. This also suggests that ZapAL and ZapA may play a physiological function together, or/and ZapAL regulates the function of ZapA to maintain the stability and dynamics of the Z-ring. Further research is needed to solve this question.

DATA AVAILABILITY STATEMENT

The original contributions presented in the study are included in the article/supplementary material, further inquiries can be directed to the corresponding author.

AUTHOR CONTRIBUTIONS

YC conceived and designed the experiments. XW, XM, ZL, and YC did most of the experiments. MN and MZ contributed to experimental work and interpretation. YC wrote the manuscript with contributions from all authors. All authors contributed to the article and approved the submitted version.

FUNDING

This research was funded by the National Natural Science Foundation of China (Grant No. 31970050) to YC and the Opening Foundation of Key Laboratory of Resource Biology and Biotechnology in Western China (Northwest University), Ministry of Education (ZSK2019004) to YC.

ACKNOWLEDGMENTS

We thank Harold Erickson (Duke University) for providing laboratory and EM resources for some of this work and helpful comments on the manuscript.

REFERENCES

Barrows, J. M., and Goley, E. D. (2021). FtsZ dynamics in bacterial division: what, how, and why? *Curr. Opin. Cell Biol.* 68, 163–172. doi: 10.1016/j.ceb.2020.10.013

Bhattacharya, D., Kumar, A., and Panda, D. (2017). WhmD promotes the assembly of *Mycobacterium smegmatis* FtsZ: a possible role of WhmD in bacterial cell division. *Int. J. Biol. Macromol.* 95, 582–591. doi: 10.1016/j.ijbiomac.2016.11.056

Bisson-Filho, A. W., Hsu, Y. P., Squyres, G. R., Kuru, E., Wu, F., Jukes, C., et al. (2017). Treadmilling by FtsZ filaments drives peptidoglycan synthesis and bacterial cell division. *Science* 355, 739–743. doi: 10.1126/science.aak9973

Caldas, P., Lopez-Pelegrin, M., Pearce, D. J. G., Budanur, N. B., Brugues, J., and Loose, M. (2019). Cooperative ordering of treadmilling filaments in cytoskeletal networks of FtsZ and its crosslinker ZapA. *Nat. Commun.* 10:5744. doi: 10.1038/s41467-019-13702-4

Chen, Y., Anderson, D. E., Rajagopalan, M., and Erickson, H. P. (2007). Assembly dynamics of *Mycobacterium tuberculosis* FtsZ. *J. Biol. Chem.* 282, 27736–27743. doi: 10.1074/jbc.M703788200

Chen, Y., Bjornson, K., Redick, S. D., and Erickson, H. P. (2005). A rapid fluorescence assay for FtsZ assembly indicates cooperative assembly with a dimer nucleus. *Biophys. J.* 88, 505–514. doi: 10.1529/biophysj.104.044149

Chen, Y., and Erickson, H. P. (2005). Rapid in vitro assembly dynamics and subunit turnover of FtsZ demonstrated by fluorescence resonance energy transfer. *J. Biol. Chem.* 280, 22549–22554. doi: 10.1074/jbc.M500895200

Chen, Y., and Erickson, H. P. (2009). FtsZ filament dynamics at steady state: subunit exchange with and without nucleotide hydrolysis. *Biochemistry* 48, 6664–6673. doi: 10.1021/bi8022653

Chen, Y., Huang, H., Osawa, M., and Erickson, H. P. (2017a). ZipA and FtsA* stabilize FtsZ-GDP miniring structures. *Sci. Rep.* 7:3650. doi: 10.1038/s41598-017-03983-4

Chen, Y., Milam, S. L., and Erickson, H. P. (2012). SulA inhibits assembly of FtsZ by a simple sequestration mechanism. *Biochemistry* 51, 3100–3109. doi: 10.1021/bi201669d

Chen, Y., Porter, K., Osawa, M., Augustus, A. M., Milam, S. L., Joshi, C., et al. (2017b). The chloroplast tubulin homologs FtsZA and FtsZB from the red alga Galdieria sulphuraria co-assemble into dynamic filaments. *J. Biol. Chem.* 292, 5207–5215. doi: 10.1074/jbc.M116.767715

Durand-Heredia, J., Rivkin, E., Fan, G., Morales, J., and Janakiraman, A. (2012). Identification of ZapD as a cell division factor that promotes the assembly of FtsZ in *Escherichia coli*. *J. Bacteriol.* 194, 3189–3198. doi: 10.1128/JB.00176-12

Erickson, H. P., and Osawa, M. (2017). FtsZ constriction force—curved protofilaments bending membranes. *Subcell. Biochem.* 84, 139–160. doi: 10.1007/978-3-319-53047-5_5

Eswara, P. J., Brzozowski, R. S., Viola, M. G., Graham, G., Spanoudis, C., Trebino, C., et al. (2018). An essential *Staphylococcus aureus* cell division protein directly regulates FtsZ dynamics. *Elife* 7:e38856. doi: 10.7554/eLife.38856

Gamba, P., Veening, J. W., Saunders, N. J., Hamoen, L. W., and Daniel, R. A. (2009). Two-step assembly dynamics of the Bacillus subtilis divisome. *J. Bacteriol.* 191, 4186–4194. doi: 10.1128/JB.01758-08

Gueiros-Filho, F. J., and Losick, R. (2002). A widely conserved bacterial cell division protein that promotes assembly of the tubulin-like protein FtsZ. *Genes Dev.* 16, 2544–2556. doi: 10.1101/gad.1014102

Haeusser, D. P., and Margolin, W. (2016). Splitsville: structural and functional insights into the dynamic bacterial Z ring. *Nat. Rev. Microbiol.* 14, 305–319. doi: 10.1038/nrmicro.2016.26

Hale, C. A., and De Boer, P. A. (1997). Direct binding of FtsZ to ZipA, an essential component of the septal ring structure that mediates cell division in *E. coli*. *Cell* 88, 175–185. doi: 10.1016/S0092-8674(00)81838-3

Hale, C. A., Rhee, A. C., and De Boer, P. A. (2000). ZipA-induced bundling of FtsZ polymers mediated by an interaction between C-terminal domains. *J. Bacteriol.* 182, 5153–5166. doi: 10.1128/JB.182.18.5153-5166.2000

Hale, C. A., Shiomi, D., Liu, B., Bernhardt, T. G., Margolin, W., Niki, H., et al. (2011). Identification of *Escherichia coli* ZapC (YcbW) as a component of the division apparatus that binds and bundles FtsZ polymers. *J. Bacteriol.* 193, 1393–1404. doi: 10.1128/JB.01245-10

Hoang, T. T., Karkhoff-Schweizer, R. R., Kutchma, A. J., and Schweizer, H. P. (1998). A broad-host-range Flp-FRT recombination system for site-specific excision of chromosomally-located DNA sequences: application for isolation of unmarked *Pseudomonas aeruginosa* mutants. *Gene* 212, 77–86. doi: 10.1016/S0378-1119(98)00130-9

Huang, K. H., Durand-Heredia, J., and Janakiraman, A. (2013). FtsZ ring stability: of bundles, tubules, crosslinks, and curves. *J. Bacteriol.* 195, 1859–1868. doi: 10.1128/JB.02157-12

Huang, H., Wang, P., Bian, L., Osawa, M., Erickson, H. P., and Chen, Y. (2018). The cell division protein MinD from *Pseudomonas aeruginosa* dominates the assembly of the MinC-MinD copolymers. *J. Biol. Chem.* 293, 7786–7795. doi: 10.1074/jbc.RA117.001513

Low, H. H., Moncrieffe, M. C., and Lowe, J. (2004). The crystal structure of ZapA and its modulation of FtsZ polymerisation. *J. Mol. Biol.* 341, 839–852. doi: 10.1016/j.jmb.2004.05.031

Mateos-Gil, P., Marquez, I., Lopez-Navajas, P., Jimenez, M., Vicente, M., Mingorance, J., et al. (2012). FtsZ polymers bound to lipid bilayers through ZipA form dynamic two dimensional networks. *Biochim. Biophys. Acta* 1818, 806–813. doi: 10.1016/j.bbamem.2011.12.012

McCausland, J. W., Yang, X., Squyres, G. R., Lyu, Z., Bruce, K. E., Lamanna, M. M., et al. (2021). Treadmilling FtsZ polymers drive the directional movement of sPG-synthesis enzymes via a Brownian ratchet mechanism. *Nat. Commun.* 12:609. doi: 10.1038/s41467-020-20873-y

McQuillen, R., and Xiao, J. (2020). Insights into the structure, function, and dynamics of the bacterial cytokinetic FtsZ-ring. *Annu. Rev. Biophys.* 49, 309–341. doi: 10.1146/annurev-biophys-121219-081703

Mohammadi, T., Ploeger, G. E., Verheul, J., Comvalius, A. D., Martos, A., Alfonso, C., et al. (2009). The GTPase activity of *Escherichia coli* FtsZ determines the magnitude of the FtsZ polymer bundling by ZapA in vitro. *Biochemistry* 48, 11056–11066. doi: 10.1021/bi901461p

Mukherjee, A., and Lutkenhaus, J. (1999). Analysis of FtsZ assembly by light scattering and determination of the role of divalent metal cations. *J. Bacteriol.* 181, 823–832. doi: 10.1128/JB.181.3.823-832.1999

Pacheco-Gomez, R., Cheng, X., Hicks, M. R., Smith, C. J., Roper, D. I., Addinall, S., et al. (2013). Tetramerization of ZapA is required for FtsZ bundling. *Biochem. J.* 449, 795–802. doi: 10.1042/BJ20120140

Peng, J., Chen, G., Xu, X., Wang, T., and Liang, H. (2020). Iron facilitates the RetS-Gac-Rsm cascade to inversely regulate protease IV (piv) expression via the sigma factor PvdS in *Pseudomonas aeruginosa*. *Environ. Microbiol.* 22, 5402–5413. doi: 10.1111/1462-2920.15270

Pichoff, S., and Lutkenhaus, J. (2002). Unique and overlapping roles for ZipA and FtsA in septal ring assembly in *Escherichia coli*. *EMBO J.* 21, 685–693. doi: 10.1093/emboj/21.4.685

Porter, K. J., Cao, L., Chen, Y., Terbush, A. D., Chen, C., Erickson, H. P., et al. (2021). The *Arabidopsis thaliana* chloroplast division protein FtsZ1 counterbalances FtsZ2 filament stability in vitro. *J. Biol. Chem.* 296:100627. doi: 10.1016/j.jbc.2021.100627

Rahman, M. U., Li, Z., Zhang, T., Du, S., Ma, X., Wang, P., et al. (2020). Assembly properties of bacterial tubulin homolog FtsZ regulated by the positive regulator protein ZipA and ZapA from *Pseudomonas aeruginosa*. *Sci. Rep.* 10:21369. doi: 10.1038/s41598-020-78431-x

Ramirez-Diaz, D. A., Garcia-Soriano, D. A., Raso, A., Mucksch, J., Feingold, M., Rivas, G., et al. (2018). Treadmilling analysis reveals new insights into dynamic FtsZ ring architecture. *PLoS Biol.* 16:e2004845. doi: 10.1371/journal.pbio.2004845

Ramos-Leon, F., Bush, M. J., Sallmen, J. W., Chandra, G., Richardson, J., Findlay, K. C., et al. (2021). A conserved cell division protein directly regulates FtsZ dynamics in filamentous and unicellular actinobacteria. *Elife* 10:e63387. doi: 10.7554/eLife.63387

Raychaudhuri, D. (1999). ZipA is a MAP-tau homolog and is essential for structural integrity of the cytokinetic FtsZ ring during bacterial cell division. *EMBO J.* 18, 2372–2383. doi: 10.1093/emboj/18.9.2372

Roseboom, W., Nazir, M. G., Meiresonne, N. Y., Mohammadi, T., Verheul, J., Buncherd, H., et al. (2018). Mapping the contact sites of the *Escherichia coli* division-initiating proteins FtsZ and ZapA by BAMG cross-linking and site-directed mutagenesis. *Int. J. Mol. Sci.* 19:2928. doi: 10.3390/ijms19102928

Schneider, C. A., Rasband, W. S., and Eliceiri, K. W. (2012). NIH image to ImageJ: 25 years of image analysis. *Nat. Methods* 9, 671–675. doi: 10.1038/nmeth.2089

Sievers, F., Wilm, A., Dineen, D., Gibson, T. J., Karplus, K., Li, W., et al. (2011). Fast, scalable generation of high-quality protein multiple sequence alignments using Clustal omega. *Mol. Syst. Biol.* 7:539. doi: 10.1038/msb.2011.75

Squyres, G. R., Holmes, M. J., Barger, S. R., Pennycook, B. R., Ryan, J., Yan, V. T., et al. (2021). Single-molecule imaging reveals that Z-ring condensation is essential for cell division in *Bacillus subtilis*. *Nat. Microbiol.* 6, 553–562. doi: 10.1038/s41564-021-00878-z

Tan, M. F., Hu, Q., Hu, Z., Zhang, C. Y., Liu, W. Q., Gao, T., et al. (2021). *Streptococcus suis* MsmK: novel cell division protein interacting with FtsZ and maintaining cell shape. *mSphere* 6, e00119–e00121. doi: 10.1128/mSphere.00119-21

Ur Rahman, M., Wang, P., Wang, N., and Chen, Y. (2020). A key bacterial cytoskeletal cell division protein FtsZ as a novel therapeutic antibacterial drug target. *Bosn. J. Basic Med. Sci.* 20, 310–318. doi: 10.17305/bjbms.2020.4597

Vicente, M., and Rico, A. I. (2006). The order of the ring: assembly of *Escherichia coli* cell division components. *Mol. Microbiol.* 61, 5–8. doi: 10.1111/j.1365-2958.2006.05233.x

Walker, B. E., Mannik, J., and Mannik, J. (2020). Transient membrane-linked FtsZ assemblies precede Z-ring formation in *Escherichia coli*. *Curr. Biol.* 30, 499–508.e6. doi: 10.1016/j.cub.2019.12.023

Wang, N., Bian, L., Ma, X., Meng, Y., Chen, C. S., Rahman, M. U., et al. (2019). Assembly properties of the bacterial tubulin homolog FtsZ from the cyanobacterium Synechocystis sp. PCC 6803. *J. Biol. Chem.* 294, 16309–16319. doi: 10.1074/jbc.RA119.009621

White, E. L., Ross, L. J., Reynolds, R. C., Seitz, L. E., Moore, G. D., and Borhani, D. W. (2000). Slow polymerization of *Mycobacterium tuberculosis* FtsZ. *J. Bacteriol.* 182, 4028–4034. doi: 10.1128/JB.182.14.4028-4034.2000

Winsor, G. L., Griffiths, E. J., Lo, R., Dhillon, B. K., Shay, J. A., and Brinkman, F. S. (2016). Enhanced annotations and features for comparing thousands of *Pseudomonas* genomes in the *Pseudomonas* genome database. *Nucleic Acids Res.* 44, D646–D653. doi: 10.1093/nar/gkv1227

Yang, X., Lyu, Z., Miguel, A., McQuillen, R., Huang, K. C., and Xiao, J. (2017). GTPase activity-coupled treadmilling of the bacterial tubulin FtsZ organizes septal cell wall synthesis. *Science* 355, 744–747. doi: 10.1126/science.aak9995

Yu, X. C., and Margolin, W. (1997). Ca^{2+}-mediated GTP-dependent dynamic assembly of bacterial cell division protein FtsZ into asters and polymer networks in vitro. *EMBO J.* 16, 5455–5463. doi: 10.1093/emboj/16.17.5455

Conflict of Interest: The authors declare that the research was conducted in the absence of any commercial or financial relationships that could be construed as a potential conflict of interest.

Publisher's Note: All claims expressed in this article are solely those of the authors and do not necessarily represent those of their affiliated organizations, or those of the publisher, the editors and the reviewers. Any product that may be evaluated in this article, or claim that may be made by its manufacturer, is not guaranteed or endorsed by the publisher.

frontiers in Microbiology

ORIGINAL RESEARCH
published: 13 August 2021
doi: 10.3389/fmicb.2021.718600

Hyperosmotic Shock Transiently Accelerates Constriction Rate in *Escherichia coli*

Jiawei Sun[1], *Handuo Shi*[1,2] *and Kerwyn Casey Huang*[1,2,3]*

[1] Department of Bioengineering, Stanford University, Stanford, CA, United States, [2] Department of Microbiology and Immunology, Stanford University School of Medicine, Stanford, CA, United States, [3] Chan Zuckerberg Biohub, San Francisco, CA, United States

Bacterial cells in their natural environments encounter rapid and large changes in external osmolality. For instance, enteric bacteria such as *Escherichia coli* experience a rapid decrease when they exit from host intestines. Changes in osmolality alter the mechanical load on the cell envelope, and previous studies have shown that large osmotic shocks can slow down bacterial growth and impact cytoplasmic diffusion. However, it remains unclear how cells maintain envelope integrity and regulate envelope synthesis in response to osmotic shocks. In this study, we developed an agarose pad-based protocol to assay envelope stiffness by measuring population-averaged cell length before and after a hyperosmotic shock. Pad-based measurements exhibited an apparently larger length change compared with single-cell dynamics in a microfluidic device, which we found was quantitatively explained by a transient increase in division rate after the shock. Inhibiting cell division led to consistent measurements between agarose pad-based and microfluidic measurements. Directly after hyperosmotic shock, FtsZ concentration and Z-ring intensity increased, and the rate of septum constriction increased. These findings establish an agarose pad-based protocol for quantifying cell envelope stiffness, and demonstrate that mechanical perturbations can have profound effects on bacterial physiology.

Keywords: FtsZ, divisome, cytokinesis, sucrose, osmolarity, microfluidics

OPEN ACCESS

Edited by:
Martin Loose, Institute of Science and Technology Austria (IST Austria), Austria

Reviewed by:
Jaan Männik, The University of Tennessee, Knoxville, United States
Ramanujam Srinivasan, National Institute of Science Education and Research (NISER), India

***Correspondence:**
Kerwyn Casey Huang
kchuang@stanford.edu

Specialty section:
This article was submitted to Microbial Physiology and Metabolism, a section of the journal Frontiers in Microbiology

Received: *01 June 2021*
Accepted: *26 July 2021*
Published: *13 August 2021*

Citation:
Sun J, Shi H and Huang KC (2021) Hyperosmotic Shock Transiently Accelerates Constriction Rate in Escherichia coli. Front. Microbiol. 12:718600. doi: 10.3389/fmicb.2021.718600

INTRODUCTION

The bacterial cytoplasm contains a dense combination of nucleic acids, proteins, and numerous metabolites that together generate a high internal osmotic pressure relative to the extracellular environment. These turgor pressures of ∼1–10 atm (Cayley et al., 2000; Deng et al., 2011) must be balanced to maintain cellular integrity. To counter this mechanical load, virtually all bacteria have a rigid, highly cross-linked peptidoglycan cell wall (Holtje, 1998) that can bear substantial stress (Yao et al., 1999). Bacterial cells typically encounter a wide range of environmental osmolalities, for example enteric bacteria rapidly transition between high and low osmolalities inside and outside the host, respectively (Gauthier, 2000). Rapid increases in external osmolality

cause plasmolysis in which water exits the cytoplasm, leading to reduced stress on the cell envelope [membrane(s) and cell wall] and cytoplasm shrinkage (Cota-Robles, 1963; Pilizota and Shaevitz, 2013). During relatively small hyperosmotic shocks (≤100 mM of osmolyte), cell-wall insertion and elongation continue unaffected (Rojas et al., 2014), while larger hyperosmotic shocks inhibit growth (Walter, 1924; Christian and Scott, 1953; Scott, 1953; Christian, 1955) as well as intracellular diffusion and molecular mobility (van den Bogaart et al., 2007; Boersma et al., 2015). In general, whether intracellular processes are affected by osmolality changes has not been fully investigated, particularly how changes to mechanical load shape cellular structure and physiology.

Microfluidic devices are powerful tools for monitoring growth and division dynamics at single-cell resolution (Taniguchi et al., 2010; Wang et al., 2010; Campos et al., 2014; Taheri-Araghi et al., 2015; Camsund et al., 2020), particularly during acute environmental changes such as osmotic shocks (Pilizota and Shaevitz, 2012; Rojas et al., 2014, 2017; Zhou et al., 2015; Buda et al., 2016; Rojas and Huang, 2018; Yang et al., 2020). A salient example of the utility of microfluidics in bacterial cell biology is the recent discovery that the Gram-negative outer membrane (OM) can bear substantial mechanical stress (Rojas et al., 2018). In a flow cell, *Escherichia coli* cells were exposed to a large hyperosmotic shock, followed by detergent treatment that induced lysis. The large contraction upon lysis indicated that the stiffness of the OM is comparable to that of the cell wall (Rojas et al., 2018).

Although microfluidic devices can provide dynamical single-cell information and can be used to screen libraries using elaborate designs (Taniguchi et al., 2010; Camsund et al., 2020), cost and throughput is often limiting, with only one strain or species typically tested at a time. Moreover, microfluidic devices limit the movement of cells via rigid physical constraints and hence allow only cells within a particular size range to enter, which imposes additional mechanical stress and makes a single device incompatible with species across a wide range of shapes and sizes. The unintended selection of particular sizes in microfluidic devices also potentially introduces biases (Oliveira et al., 2020). The traditional alternative to microfluidic devices for single-cell imaging is agarose pads, which are versatile platforms that are easy to prepare and applicable for morphologically diverse species. Several recent studies have introduced high-throughput methods for rapidly imaging collections of strains on large-format agarose pads (Kuwada et al., 2015; Shi et al., 2017b), enabling screening of genome-scale libraries. However, it is difficult to track the effects of acute environmental transitions on single cells using agarose pads; instead one must rely on population averages measured pre- and post-transition. Moreover, in the time period required for pad preparation, physiological changes may have taken place that are not captured by snapshots. Thus, it remains unclear whether osmotic shock-related phenomena can be robustly probed in high-throughput on agarose pads.

As a critical part of the bacterial cell cycle, cell division is highly regulated. In bacteria, a ring of the conserved tubulin homolog FtsZ (the "Z-ring") (Bi and Lutkenhaus, 1991; Dai and Lutkenhaus, 1991) assembles at mid-cell and initiates assembly of the divisome machinery (Goley et al., 2011; Barrows and Goley, 2021). After the Z-ring forms and recruits other division proteins, it progressively constricts the membrane (Osawa and Erickson, 2013) and directs synthesis of the septal cell envelope (Bisson-Filho et al., 2017; Yang et al., 2017) at a constant rate (Reshes et al., 2008b), resulting in growth of new hemispherical endcaps. FtsZ concentration has been linked to the proportion of dividing cells, which changes across nutrient conditions (Ward and Lutkenhaus, 1985; Weart and Levin, 2003; Weart et al., 2007; Hill et al., 2012). Regulation of FtsZ expression affects cell size homeostasis (Si et al., 2019) and FtsZ synthesis and degradation predict the timing of the first division in starved cells supplied with nutrient pulses (Sekar et al., 2018). While it remains unclear whether constriction of the bacterial inner membrane must fight against turgor pressure (Erickson, 2009, 2017), in fission yeast reduction of turgor pressure accelerates cell division (Basu et al., 2014; Chang, 2017). Taken together, bacterial cell division is a natural candidate for processes affected by environmental osmolality.

Here, we developed an agarose pad-based protocol for Gram-negative envelope stiffness measurements, and sought to establish that pad measurements could recapitulate previous findings regarding the stiffness of the OM. To our surprise, the population-averaged length of cells after hyperosmotic shock as observed on agarose pads was significantly smaller than expected based on microfluidic measurements. By tracking single-cell dynamics during an osmotic shock in a microfluidic flow cell, we discovered that the rate of cell division transiently increased after the shock, and the fraction of dividing cells was quantitatively consistent with the apparent decrease in cell length. Treatment with the division inhibitor aztreonam was sufficient to recover the same level of contraction as observed by tracking single cells, thereby enabling quantification of the effects of hyperosmotic shock and detergent treatment in high-throughput on agarose pads. Using a strain expressing a functional msfGFP-tagged FtsZ, we show that FtsZ concentration and Z-ring intensity increased rapidly upon osmotic shock, and that constriction dynamics were significantly accelerated relative to steady-state growth, supporting the hypothesis that the divisome can provide constrictive force that acts against turgor pressure.

RESULTS

Apparent Length Contraction Due to Hyperosmotic Shock Is Much Larger on Agarose Pads Than in a Microfluidic Flow Cell

In a previous study (Rojas et al., 2018), we exposed *E. coli* cells as well as other Gram-negative bacteria to a large hyperosmotic shock in a microfluidic flow cell to remove turgor pressure (**Figure 1A**). The plasmolyzed, shrunken cells were then exposed to either EDTA (to remove lipopolysaccharides from the OM) or detergent (to remove the OM altogether); both treatments caused the length of the cell wall to decrease

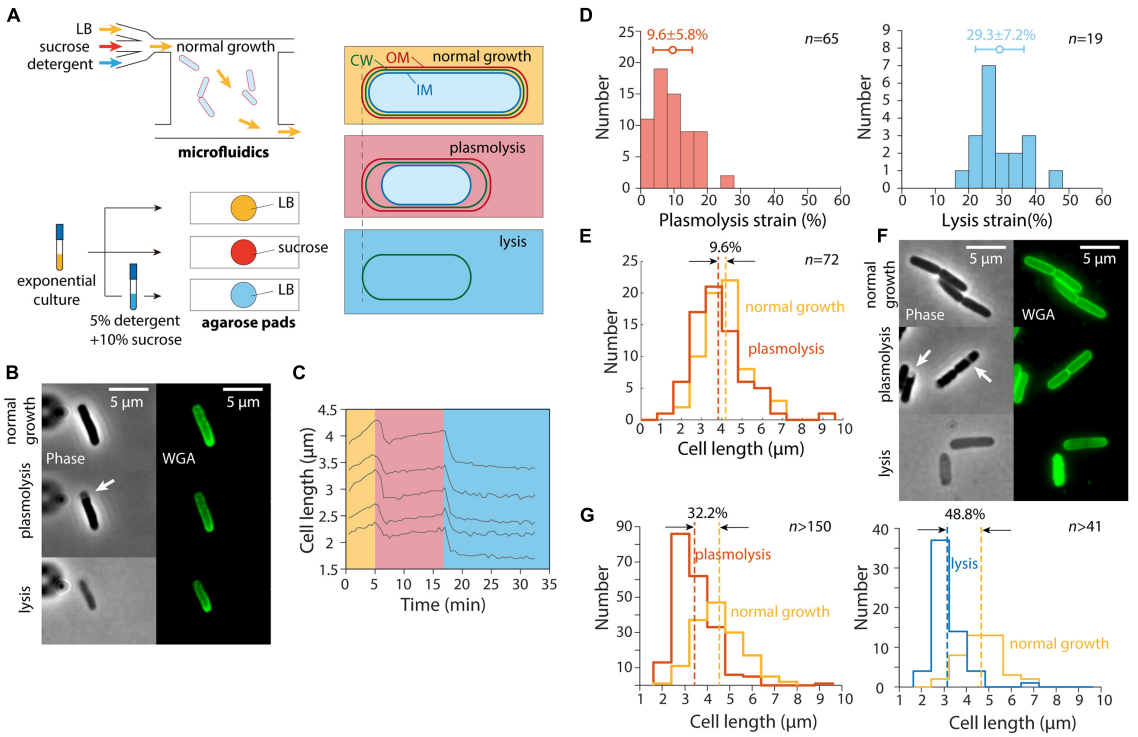

FIGURE 1 | Population-averaged relative length change after hyperosmotic shock is greater on agarose pads than from single-cell tracking in microfluidic devices. **(A)** Schematic of microfluidic (top) and agarose pad-based (bottom) measurements of length changes (right) due to hyperosmotic shock (plasmolysis) and detergent-mediated lysis. **(B)** Relative to normal growth (top), cells exposed to a hyperosmotic shock in a microfluidic flow cell (middle) decreased in length and exhibited plasmolysis (white arrow). Subsequent lysis due to detergent treatment (bottom) resulted in further shrinkage. Shown are phase contrast images (left) and fluorescence from the wall label WGA-AF488 (right). **(C)** Quantification of cell length dynamics for 5 representative cells for the experiment in panel **B**. Cell elongation was inhibited after the shock. **(D)** Quantification of the mechanical strain (extension relative to the smaller state) in cell wall length due to hyperosmotic shock (left) and detergent treatment (right). The additional strain revealed by detergent treatment shows that the stiffness of the outer membrane is comparable to that of the cell wall (Rojas et al., 2018). **(E)** Population-averaged cell wall length of the same set of cells in a microfluidic device before and after hyperosmotic shock yielded a similar estimate of plasmolysis strain as in panel **D**. **(F)** Cells imaged during normal growth in a test tube (top), on agarose pads with 20% sucrose to cause a hyperosmotic shock (middle, white arrows indicate plasmolysis bays), and after detergent treatment to cause lysis (bottom). **(G)** The relative change in length of cells on an agarose pad before and after a hyperosmotic shock (left) was substantially greater than the relative length change in a microfluidic device shown in panel **D**, as was the relative length change after lysis (right).

even further (Rojas et al., 2018), indicating that the OM was exerting substantial stretching forces on the cell wall in the plasmolyzed state. We carried out similar experiments and observed similar cell wall mechanical strains (normalized length changes relative to the unextended state) using the wall dye wheat germ agglutinin conjugated to AlexaFluor 488 (WGA-AF488) (Ursell et al., 2014) upon hyperosmotic shock and detergent treatment (**Figures 1B,C**); unshocked cell walls were extended by 9.6% relative to shocked cells, with a larger contraction upon lysis (**Figure 1D**).

While tracking of cells within the microfluidic device allowed us to measure the relative length change of each cell throughout the hyperosmotic shock and subsequent OM destabilization, we found that the plasmolysis strain could be accurately quantified based on the population-averaged length before and after each treatment (**Figure 1E**). Moreover, cell growth was inhibited for at least 5 min after the hyperosmotic shock, with most non-dividing cells maintaining a stable length (**Figure 1C**). Thus, we hypothesized that we could take advantage of traditional agarose pad-based imaging to quantify OM stiffness in high throughput (**Figure 1A**).

To test whether agarose pad measurements would recapitulate our microfluidics-based measurements of length changes due to hyperosmotic shock, we exposed an exponentially growing *E. coli* culture in LB to the same hyperosmotic shock as in our microfluidics experiments. To perform the shock as quickly as possible, we directly spotted cells onto agarose pads containing LB+20% sucrose to induce a large (∼0.5 M) osmotic shock, and imaged the cells as quickly as possible (**Figures 1A,F**). To our surprise, the mean length strain was 32.2% (**Figure 1G**), far larger than for cells in the microfluidic device (**Figures 1D,E**).

Next, we diluted exponentially growing cells into a concentrated solution of detergent and sucrose (see section "Materials and Methods") to induce cell lysis. The lysed cells were spotted onto agarose pads with LB for imaging after 20 min of detergent treatment. The decrease in cell length after lysis (**Figure 1G**) was also much larger than expected based on our microfluidic measurements (**Figure 1D**). Thus, we conclude that

despite the seemingly simple nature of our length measurements, there was an unidentified factor that was affecting cell length differentially in the microfluidic device and on agarose pads.

Osmotic Shock Transiently Increases the Rate of Cell Division

Despite the slowing of elongation after the hyperosmotic shock (**Figure 1C**), we noted that some cells continued to divide (**Figure 2A**). Thus, we hypothesized that one cause of the discrepancy between our microfluidic and agarose pad measurements was the subset of cells that completed constriction in the time interval between the shock and the time of image acquisition, resulting in a decrease in the population-averaged length post-shock. For a population of cells with average length L during exponential growth that is extended by a factor ε relative to its shocked length L_0, $L = L_0(1+\varepsilon)$. If the fraction of cells that divide between the time of the shock and agarose pad imaging is f, the total number of cells increases by the factor $(1+f)$. Therefore, the mean length of shocked cells decreases by $(1+f)$, yielding an apparent extension during exponential growth relative to shocked cells of $(1+\varepsilon)(1+f) - 1 = \varepsilon+f+\varepsilon f$ (**Figure 2B**). Thus, we hypothesized that the fraction of cells that were dividing after the shock was approximately 20%, based on the difference in the apparent extension on pads and in the microfluidic device.

To test this hypothesis, we manually identified cells that divided in a 3-min time interval before and after the hyperosmotic shock using microfluidics. Because it is difficult to pinpoint the time of division initiation due to the diffraction limit of light microscopy, we used WGA-AF488 to label the cell wall and identified cells that formed a clear septum during the 3-min interval (see section "Materials and Methods"). The fraction of dividing cells pre-shock was 11.6% per 3 min (**Figure 2C**), consistent with our measured doubling time of ~23 min (**Supplementary Figure 1**). In the 3 min after the shock, the dividing fraction increased to 17.3% (**Figure 2B**), in reasonable agreement with our prediction. Division halted completely 10 min after the shock, likely due to the lack of growth (**Figure 2C**). Thus, we conclude that cell division was a major factor in the discrepancy between contraction estimates.

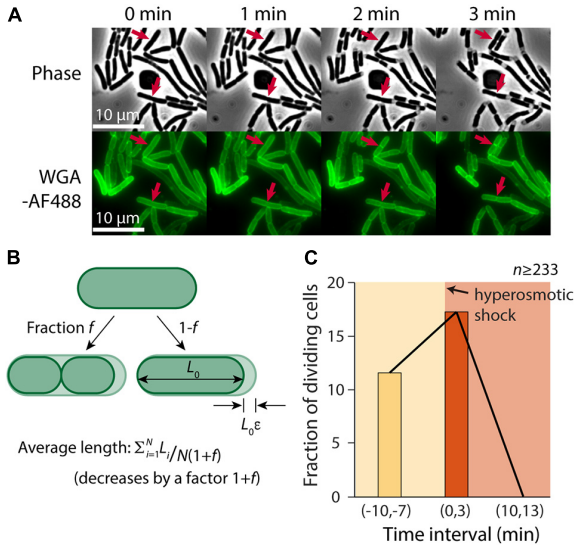

FIGURE 2 | A transient burst of cell division follows hyperosmotic shock. **(A)** In the 3 min after exposure to a hyperosmotic shock, a fraction of cells continued to divide (red arrows indicate a few examples) despite growth largely halting (Figure 1C). Shown is a time-lapse in phase contrast (top) and fluorescence of the wall label WGA-AF488 (bottom). **(B)** If a fraction f of cells divide during the interval between the hyperosmotic shock and imaging on an agarose pad, the average length of cells post-shock will decrease by a factor $(1+f)$, leading to a predicted increase in the plasmolysis strain by $(1+f)$. **(C)** The fraction of dividing cells (see section "Materials and Methods") increased from 11.6% pre-shock to 17.3% in the 3 min following the shock. By 10 min after the shock, division had halted completely.

Inhibition of Cell Division Restores the Same Length Contraction After Hyperosmotic Shock as in Microfluidics

To determine whether cell division was the sole factor distinguishing our microfluidic and agarose pad measurements, we treated cells with the beta-lactam aztreonam, which inhibits the division-specific transpeptidase PBP3 (Spratt, 1975). We exposed cells to 50 μg/mL aztreonam in a microfluidic flow cell to determine the time scale of complete division inhibition, and found that division completely halted within 20 min (**Figure 3A**). We then exposed cells in a test tube to aztreonam for varying amounts of time before hyperosmotic shock (**Figure 3B**), and as expected mean length increased monotonically with the duration of treatment (**Figure 3C**). Moreover, the degree of contraction after hyperosmotic shock relative to initial length decreased with the duration of treatment, plateauing after 20 min (**Figure 3C**), consistent with the time scale of complete division inhibition (**Figure 3A**).

We then exposed cells treated for 20 min with aztreonam to a solution of sucrose and detergent. The vast majority of cells lysed (>90%), and the mean length decreased such that unshocked cells were extended by 37.2% relative to the lysed cell wall length (**Figure 3D**). This value is reasonably consistent with the distribution of extensions of single cells in a microfluidic device (**Figure 1D**). We also treated cells with detergent in the absence of a hyperosmotic shock, surmising that the removal of the OM should remove both the membranes and turgor pressure, and thereby allow the cell wall to relax to its unstretched state. To our surprise, most cells (>95%) failed to lyse, suggesting that cells are more susceptible to detergent while plasmolyzed.

Thus, we conclude that the transient burst of cell division after hyperosmotic shock is responsible for the large decrease in population-averaged cell length, and that division inhibition is sufficient to enable pad-based measurements of cell envelope mechanical properties.

Septum Formation Time Is Largely Constant Across Mutants With Variable Cell Width

In a previous study, we showed that the concentration of FtsZ is largely constant across a set of MreB mutants with various cell

widths and volumes (Shi et al., 2017a). However, the Z-ring in wider mutants was both broader and more intense (Shi et al., 2017a), suggesting that Z-ring assembly is width-dependent, which may lead to different dynamics during septum formation. To further probe the connection between cell width and septum formation, we selected a set of MreB mutants with different cell widths but similar growth rates in exponential phase (Shi et al., 2017a), and performed time-lapse imaging to determine the duration of septum formation in each strain (see section "Materials and Methods"). In these strains, mean cell width varied from 1 μm to 1.6 μm, corresponding to a ∼2.5-fold difference in septum areas. Nonetheless, all strains completed septum formation in ∼19 min, regardless of their width (**Figure 4A**; $r = -0.13$, $p = 0.68$, two-sided Student's t-test). Thus, the broader and more intense Z-rings in wider cells potentially boost the rate of septum formation and allow cells to synthesize a larger septum within the same duration.

FtsZ Concentrates at Midcell After Hyperosmotic Shock

To probe the mechanism underlying the transient increase in division after hyperosmotic shock, we performed time-lapse imaging in a microfluidic flow cell using an *E. coli* MG1655 strain expressing *ftsZ* fused to *msfGFP* as the sole copy of *ftsZ* (**Figure 4B**). This strain exhibits approximately normal growth (Moore et al., 2017) although the fusion does affect cell length by altering FtsZ GTPase activity (Yang et al., 2017). We first quantified the total amount and concentration of FtsZ within each cell (see section "Materials and Methods"). FtsZ concentration (total amount normalized by cell volume) increased directly after hyperosmotic shock (**Figure 4C**), as expected based on cytoplasmic shrinkage. A similar concentration increase was observed for another divisome protein, ZapA (Buss et al., 2013), in a strain expressing GFP-ZapA (**Supplementary Figure 2**), as well as in a control strain expressing cytoplasmic GFP (**Figure 4C**). In all cases, the increase was larger than the normalized length decrease of the cell wall, due to plasmolysis collapsing the cytoplasm away from the cell wall (**Figure 4B**). In addition to FtsZ and ZapA, other divisome proteins likely increase rapidly in concentration given the short time scale of cytoplasmic contraction.

To address whether the increase in FtsZ concentration is associated with accelerated constriction, we quantified the intensity and width of the Z-ring (Shi et al., 2017a). Strikingly, Z-ring intensity increased almost immediately after the shock (**Figure 4D**). Moreover, Z-ring constriction proceeded at a much faster pace in shocked compared with non-shocked cells (**Figures 4E,F**), despite the lack of overall volume expansion (**Figure 1C**). This accelerated Z-ring constriction largely explains the increase in the fraction of cells that complete constriction shortly after osmotic shock (**Figure 2C**). It is unclear whether the rate of division initiation also increased; regardless, initiation rate is unlikely to be the only cause of increased cell division after shock since septum formation typically requires ∼10–15 min during normal growth. Together, these results support the hypothesis that the enhanced rate of cell division post-hyperosmotic shock is due at least in part to the higher intensity of the Z-ring and faster rate of constriction.

DISCUSSION

In this study, we developed an agarose pad-based measurement protocol to quantify the stiffness of the OM from cell length measurements after hyperosmotic shock and lysis. Our measurements of length strain after plasmolysis were inconsistent between agarose pads and microfluidic devices (**Figure 1**), which was quantitatively explained by the increase in cell division directly after hyperosmotic shock (**Figures 2–4**). Treatment with the division inhibitor aztreonam restored the expected degree of length strain (**Figure 3C**), and thus enables characterization of osmotic shock-induced morphological changes and OM stiffness on agarose pads (**Figure 3D**). This strategy provides a simpler and more versatile methodology than microfluidics, especially for screening a diverse set of species or mutants. Using single-cell tracking, we discovered that FtsZ (**Figure 4C**) and ZapA (**Supplementary Figure 2**) concentration and Z-ring intensity (**Figure 4D**) increased and Z-ring constriction accelerated (**Figures 4E,F**) directly after a hyperosmotic shock, providing mechanistic hypotheses for the increased rate of division during plasmolysis. Division may also be affected by the likely increase in the concentration of cell-envelope precursors after the shock.

Our findings suggest that progression of bacterial cell division is coupled to environmental osmolality. The observation that the Z-ring constricts more quickly in the absence of turgor suggests that the divisome exerts constrictive forces on the envelope. During a hyperosmotic shock, both the decrease in turgor and increase in FtsZ concentration may contribute to the acceleration of constriction; it is difficult to decouple the two factors, since the cytoplasmic shrinkage that accompanies the reduced stress on the cell envelope inevitably concentrates FtsZ and presumably all other divisome components. Given the immediate response of cells to osmotic shock, the association between division and osmolarity points to possible ecological implications wherein transitions to a high osmotic environment that limits growth will result in proliferation into a larger population of cells that increases survival odds, reminiscent of the reductive divisions that take place when cells enter stationary phase (Sutterlin et al., 2016). Perhaps turgor decreases along with stationary-phase entry to facilitate division, or in other environmental transitions in which an increase in cell number would be beneficial. In our experiments, division halted almost completely after the initial boost induced by the shock despite the higher concentration of FtsZ relative to normal growth (**Figure 2C**), potentially due to other limiting factors that prevented growth (**Figure 1C**). It remains unclear how the activities of FtsZ and other divisome components are generally affected by osmolarity or intracellular crowding.

Our finding that cell division is affected by osmolarity suggests that environmental perturbations such as osmotic shocks may generally induce widespread cellular responses. Indeed, *E. coli* cells were found to respond in a coupled manner to heat and

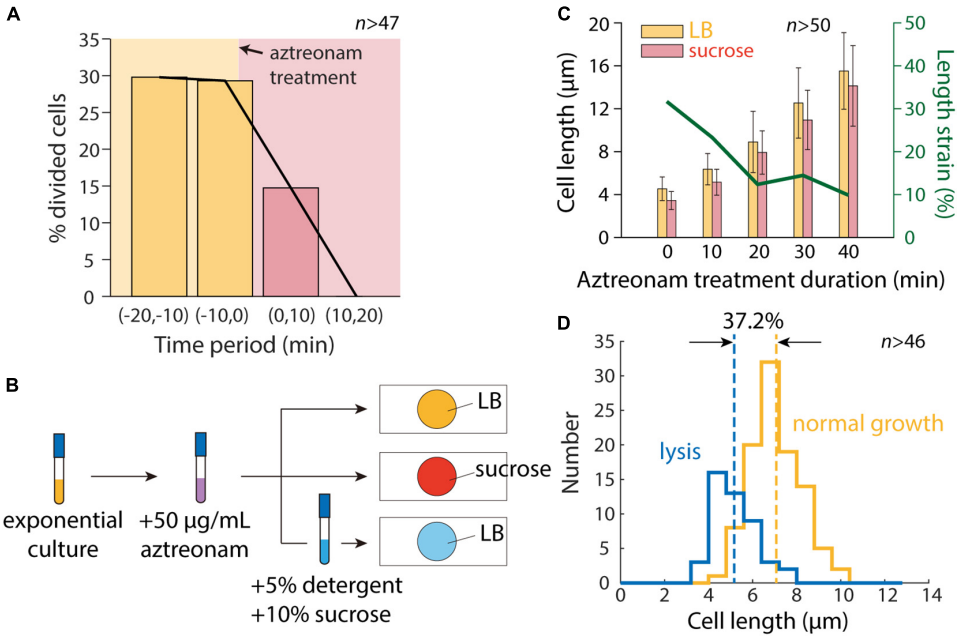

FIGURE 3 | Inhibition of cell division allows for accurate measurement of length contraction after hyperosmotic shock. **(A)** During time-lapse imaging of *E. coli* cells treated with 50 μg/mL aztreonam, cell division was fully inhibited within 20 min. **(B)** Schematic of modified protocol for agarose pad-based measurements of cell envelope stiffness, in which cells are treated with 50 μg/mL aztreonam for various amounts of time before imaging on agarose pads. **(C)** Mean length of cells grown in a test tube with 50 μg/mL aztreonam increased with the duration of treatment, due to the inhibition of cell division. After a hyperosmotic shock on an agarose pad with LB+20% sucrose, the measured length strain gradually decreased with the duration of treatment and plateaued at ∼10%, consistent with microfluidic device measurements (**Figure 1D**). **(D)** After detergent treatment, the population-averaged length of aztreonam-treated cells was lower by an amount corresponding to a strain of 37.2%, consistent with microfluidic device measurements (**Figure 1D**).

oxygen shock (Tagkopoulos et al., 2008), likely reflecting the correlation between high temperature and anoxia in human hosts. Certain antibiotics also induce acid stress (Mitosch et al., 2017) or heat-shock response pathways concurrently (Evans et al., 2019). In addition to the divisome, osmolality may affect other cellular structures such as the cytoskeletal filament MreB (Szatmári et al., 2020) and the nucleoid (Finan and Guilak, 2010; Cagliero and Jin, 2013; Wu et al., 2019; Yang et al., 2020), both of which could have widespread downstream physiological consequences. Our findings confirm that agarose pads can be used as a high-throughput platform for bacterial cell mechanics measurements, although microfluidics provides a critical ground truth in which the fate of single cells can be tracked. Thus, rapid screening of large libraries of mutants (Baba et al., 2006; Peters et al., 2016) or species should be straightforward as long as cell division can be inhibited, which should help to uncover the molecular basis of envelope stiffness and understand the role of physical forces in shaping cellular structures and bacterial physiology.

MATERIALS AND METHODS

Strain Culturing

Escherichia coli cells were grown overnight in LB at 37°C and used to inoculate a test tube with fresh LB. Strains used in this study are listed in **Supplementary Table 1**.

WGA Staining of the Cell Wall

Cell wall was labeled with wheat germ agglutinin (WGA) conjugated to AlexaFluor-488 (AF488, Invitrogen W11261). WGA-AF488 was added to exponential phase cells at a final concentration of 25 μg/mL and incubated in dark conditions with shaking at 37°C for at least 2.5 h prior to imaging.

Hyperosmotic Shock Application on Agarose Pads

To apply a hyperosmotic shock on an agarose pad, cells were first cultured in liquid LB into steady-state exponential growth using the following serial dilution protocol: starting with a 1:200 dilution from an overnight saturated culture, 1:10 dilutions were performed after 60 and 150 min. After the second dilution, ∼1 μL of liquid culture was spotted onto a 1% agarose pad with LB+20% sucrose, leading to a hyperosmotic shock.

Detergent Treatment for Agarose-Pad Measurements

Exponentially growing cells were exposed to a lysis solution of N-lauroylsarcosine sodium salt (detergent) and sucrose dissolved in 1X PBS. By directly diluting cultures into the lysis solution at a 1:1 ratio, the final concentration of detergent and sucrose was 5% and 10%, respectively. Sucrose was added to promote lysis, recapitulating the perturbation in a microfluidic device in which

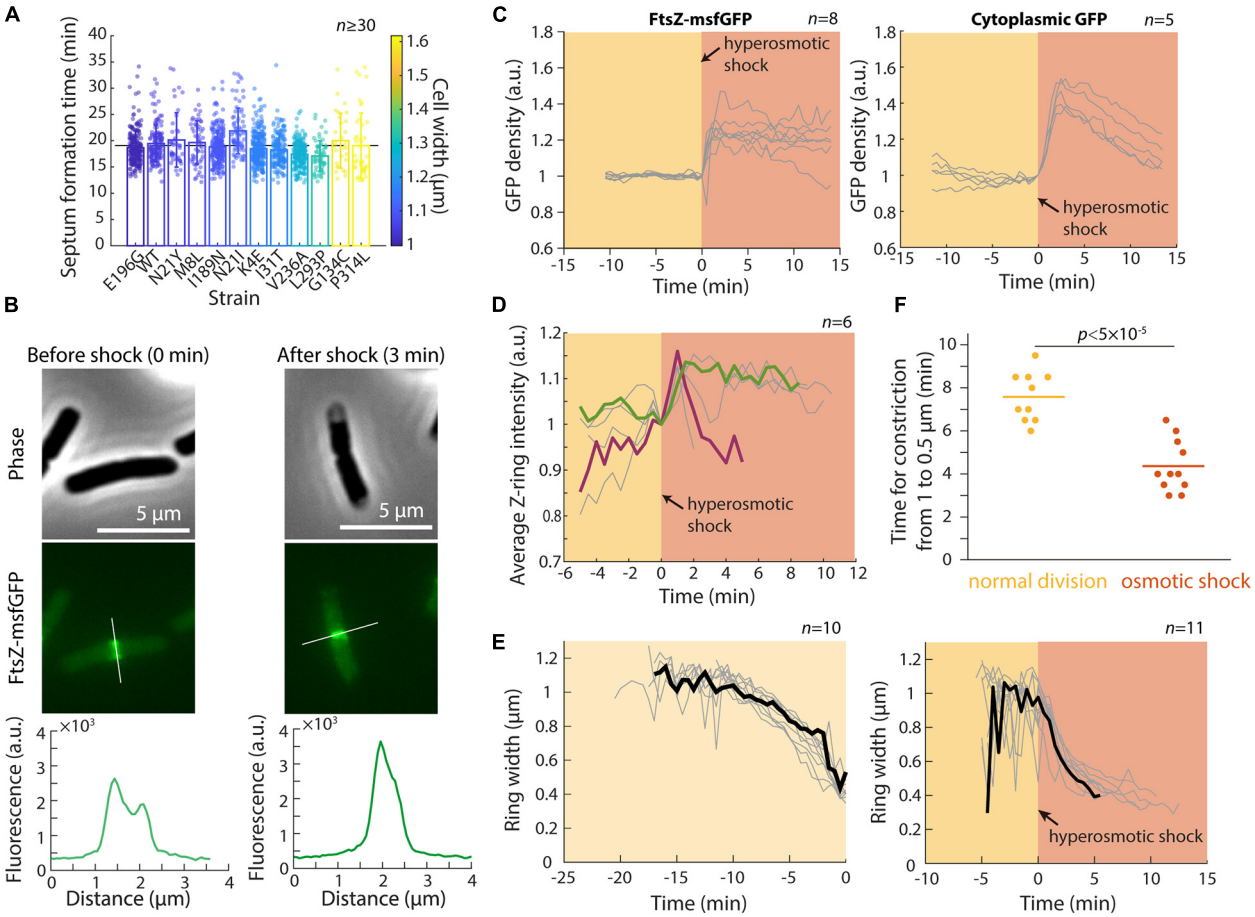

FIGURE 4 | Hyperomostic shock leads to increased FtsZ concentration and ring intensity and faster constriction. **(A)** Septum formation time (see section "Materials and Methods") for *mreB* mutants of various cell widths was approximately constant as a function of mean cell width. **(B)** Phase-constrast (top) and epifluorescence (middle) images of *E. coli* cells expressing FtsZ-msfGFP, before (left) and 3 min after (right) a hyperosmotic shock. Fluorescence profiles along the cell contour show that Z-ring intensity increased immediately after the shock (bottom). **(C)** The concentration of FtsZ-msfGFP (left) and cytoplasmic GFP (right) increased directly after the hyperosmotic shock, consistent with the decrease in cell volume (**Figure 1B**). **(D)** Z-ring intensity increased after the shock. Shown are 6 representative cells; the cell colored in green maintained high Z-ring intensity for 10 min after the shock, while Z-ring intensity in the maroon cell increased and then decreased for the ensuing 4 min leading up to the completion of cell division. **(E)** Z-rings constricted more rapidly after hyperosmotic shock (right) than during normal growth (left). The black curves are representative cells in each category. **(F)** The time required for Z-ring constriction was substantially shorter after hyperosmotic shock.

cells were plasmolyzed by a hyperosmotic shock before being exposed to detergent.

Single-Cell Imaging

One microliter of cells was spotted onto a 1% agarose pad with the appropriate medium, and imaged on a Nikon Eclipse Ti-E inverted fluorescence microscope with a 100X (NA 1.40) oil-immersion objective (Nikon Instruments). For microfluidic experiments, cells were loaded into B04A (CellASIC) microfluidic plates following previous protocols (Rojas et al., 2018). Phase-contrast and epifluorescence images were collected on a DU885 electron-multiplying CCD camera (Andor Technology) or a Neo sCMOS camera (Andor Technology) using μManager v. 1.4 (Edelstein et al., 2010). Cells were maintained at 37°C during imaging with an active-control environmental chamber (Haison Technology).

Identifying Cell Division Events From WGA Signal

In a microfluidic flow cell, cell division events were identified based on the clear formation of a septum in the WGA-AF488 signal. Although septum formation does not represent the end of cell division, the septum can be easily identified visually or from a peak in the fluorescence profile along the long axis of the cell. The fraction of dividing cells was computed based on a combination of visual inspection and fluorescence profile examination, with constriction dynamics in the phase channel serving as further confirmation.

Image Analysis

The MATLAB (MathWorks, Natick, MA, United States) image processing code *Morphometrics* (Ursell et al., 2017) was used to segment cells and to identify cell outlines from phase-contrast

and epifluorescence microscopy images. A local coordinate system was generated for each cell outline using a method adapted from *MicrobeTracker* (Sliusarenko et al., 2011). Cell length was calculated as the length of the midline from pole to pole. See figure legends for the number of cells analyzed (n) and error bar definitions.

Quantification of FtsZ Fluorescence

Total FtsZ fluorescence was calculated by integrating fluorescence values within the cell contour after background subtraction, and FtsZ concentration was computed as the total fluorescence divided by cross-sectional area. The fluorescence profile along the cell contour had low values at the cell poles and high values at mid-cell, corresponding to the Z-ring. Z-ring intensity was calculated by averaging the fluorescence intensity within the Z-ring (Shi et al., 2017a).

Tracking the Dynamics of Septum Formation

Assuming cells incorporate new septum area at a constant rate k and the shape of the cell poles is hemispherical, the septum area $A(t)$ changes as a function of time according to $\frac{dA(t)}{dt} = k$, and $A(t) = 4\pi {w_0}^2\sqrt{1-(w(t)/w_0)^2}$, where, w_0 is initial septum width (i.e., cell width) and $w(t)$ is the current septum width (Reshes et al., 2008a). Integration yields

$$t = \frac{4\pi {w_0}^2}{k}\sqrt{1-(w(t)/w_0)^2},$$

where $t = 0$ corresponds to division onset. Through linear fitting of experimental measurements of $\sqrt{1-(w(t)/w_0)^2}$ as a function of t, we obtained the time required for septum formation, $T = \frac{4\pi {w_0}^2}{k}$. To reduce the error in estimating septum width, only time points with $0.5w_0 \leq w(t) \leq 0.9w_0$ were used for the fit.

DATA AVAILABILITY STATEMENT

The original contributions presented in the study are included in the article/**Supplementary Material**, further inquiries can be directed to the corresponding author.

AUTHOR CONTRIBUTIONS

JS, HS, and KCH designed the research, wrote the manuscript, and analyzed the data. JS and HS performed the research. All authors contributed to the article and approved the submitted version.

FUNDING

We acknowledge funding from a James S. McDonnell Postdoctoral Fellowship (to HS) and NIH grant RM1 GM135102 (to KCH). KCH is a Chan Zuckerberg Biohub Investigator.

ACKNOWLEDGMENTS

We thank members of the Huang lab for helpful discussions.

SUPPLEMENTARY MATERIAL

The Supplementary Material for this article can be found online at: https://www.frontiersin.org/articles/10.3389/fmicb.2021.718600/full#supplementary-material

Supplementary Figure 1 | The distribution of steady-state growth rates is similar in microfluidic devices and on agarose pads.

Supplementary Figure 2 | GFP-ZapA concentration increases directly after a hyperosmotic shock. This increase was consistent with the decrease in cytoplasmic volume (**Figure 1B**) and the increases in FtsZ-msfGFP and cytoplasmic GFP (**Figure 4C**).

Supplementary Table 1 | Strains used in this study.

REFERENCES

Baba, T., Ara, T., Hasegawa, M., Takai, Y., Okumura, Y., Baba, M., et al. (2006). Construction of *Escherichia coli* K-12 in-frame, single-gene knockout mutants: the Keio collection. *Mol. Syst. Biol.* 2:2006.0008.

Barrows, J. M., and Goley, E. D. (2021). FtsZ dynamics in bacterial division: what, how, and why? *Curr. Opin. Cell Biol* 68, 163–172. doi: 10.1016/j.ceb.2020.10.013

Basu, R., Munteanu, E. L., and Chang, F. (2014). Role of turgor pressure in endocytosis in fission yeast. *Mol. Biol. Cell* 25, 679–687. doi: 10.1091/mbc.e13-10-0618

Bi, E. F., and Lutkenhaus, J. (1991). FtsZ ring structure associated with division in *Escherichia coli*. *Nature* 354, 161–164. doi: 10.1038/354161a0

Bisson-Filho, A. W., Hsu, Y. P., Squyres, G. R., Kuru, E., Wu, F., Jukes, C., et al. (2017). Treadmilling by FtsZ filaments drives peptidoglycan synthesis and bacterial cell division. *Science* 355, 739–743. doi: 10.1126/science.aak9973

Boersma, A. J., Zuhorn, I. S., and Poolman, B. (2015). A sensor for quantification of macromolecular crowding in living cells. *Nat. Methods* 12, 227–229. doi: 10.1038/nmeth.3257

Buda, R., Liu, Y., Yang, J., Hegde, S., Stevenson, K., Bai, F., et al. (2016). Dynamics of *Escherichia coli*'s passive response to a sudden decrease in external osmolarity. *Proc. Natl. Acad. Sci. U.S.A.* 113, E5838–E5846.

Buss, J., Coltharp, C., Huang, T., Pohlmeyer, C., Wang, S. C., Hatem, C., et al. (2013). *In vivo* organization of the FtsZ-ring by ZapA and ZapB revealed by quantitative super-resolution microscopy. *Mol. Microbiol.* 89, 1099–1120. doi: 10.1111/mmi.12331

Cagliero, C., and Jin, D. J. (2013). Dissociation and re-association of RNA polymerase with DNA during osmotic stress response in *Escherichia coli*. *Nucleic Acids Res.* 41, 315–326. doi: 10.1093/nar/gks988

Campos, M., Surovtsev, I. V., Kato, S., Paintdakhi, A., Beltran, B., Ebmeier, S. E., et al. (2014). A constant size extension drives bacterial cell size homeostasis. *Cell* 159, 1433–1446. doi: 10.1016/j.cell.2014.11.022

Camsund, D., Lawson, M. J., Larsson, J., Jones, D., Zikrin, S., Fange, D., et al. (2020). Time-resolved imaging-based CRISPRi screening. *Nat. Methods* 17, 86–92. doi: 10.1038/s41592-019-0629-y

Cayley, D. S., Guttman, H. J., and Record, M. T. Jr. (2000). Biophysical characterization of changes in amounts and activity of *Escherichia coli* cell and

compartment water and turgor pressure in response to osmotic stress. *Biophys. J.* 78, 1748–1764. doi: 10.1016/s0006-3495(00)76726-9

Chang, F. (2017). Forces that shape fission yeast cells. *Mol. Biol. Cell* 28, 1819–1824. doi: 10.1091/mbc.e16-09-0671

Christian, J. (1955). The influence of nutrition on the water relations of *Salmonella oranienburg*. *Aust. J. Biol. Sci.* 8, 75–82. doi: 10.1071/bi9550075

Christian, J., and Scott, W. (1953). Water relations of *Salmonellae* at 30 C. *Aust. J. Biol. Sci.* 6, 565–573.

Cota-Robles, E. H. (1963). Electron Microscopy of Plasmolysis in *Escherichia Coli*. *J. Bacteriol.* 85, 499–503. doi: 10.1128/jb.85.3.499-503.1963

Dai, K., and Lutkenhaus, J. (1991). *ftsZ* is an essential cell division gene in *Escherichia coli*. *J. Bacteriol.* 173, 3500–3506. doi: 10.1128/jb.173.11.3500-3506.1991

Deng, Y., Sun, M., and Shaevitz, J. W. (2011). Direct measurement of cell wall stress stiffening and turgor pressure in live bacterial cells. *Phys. Rev. Lett.* 107:158101.

Edelstein, A., Amodaj, N., Hoover, K., Vale, R., and Stuurman, N. (2010). Computer control of microscopes using microManager. *Curr. Protoc. Mol. Biol.* 92, 14.20.1–14.20.17.

Erickson, H. P. (2009). Modeling the physics of FtsZ assembly and force generation. *Proc. Natl. Acad. Sci. U.S.A.* 106, 9238–9243. doi: 10.1073/pnas.0902258106

Erickson, H. P. (2017). How bacterial cell division might cheat turgor pressure–a unified mechanism of septal division in Gram-positive and Gram-negative bacteria. *Bioessays* 39:1700045. doi: 10.1002/bies.201700045

Evans, C. R., Fan, Y., and Ling, J. (2019). Increased mistranslation protects *E. coli* from protein misfolding stress due to activation of a RpoS-dependent heat shock response. *FEBS Lett.* 593, 3220–3227. doi: 10.1002/1873-3468.13578

Finan, J. D., and Guilak, F. (2010). The effects of osmotic stress on the structure and function of the cell nucleus. *J. Cell. Biochem.* 109, 460–467.

Gauthier, M. J. (2000). "Environmental parameters associated with the viable but nonculturable state," in *Nonculturable Microorganisms in the Environment*, eds R. R. Colwell and D. J. Grimes (Boston, MA: Springer), 87–112. doi: 10.1007/978-1-4757-0271-2_7

Goley, E. D., Yeh, Y. C., Hong, S. H., Fero, M. J., Abeliuk, E., Mcadams, H. H., et al. (2011). Assembly of the *Caulobacter* cell division machine. *Mol. Microbiol.* 80, 1680–1698. doi: 10.1111/j.1365-2958.2011.07677.x

Hill, N. S., Kadoya, R., Chattoraj, D. K., and Levin, P. A. (2012). Cell size and the initiation of DNA replication in bacteria. *PLoS Genet.* 8:e1002549. doi: 10.1371/journal.pgen.1002549

Holtje, J. V. (1998). Growth of the stress-bearing and shape-maintaining murein sacculus of *Escherichia coli*. *Microbiol. Mol. Biol. Rev.* 62, 181–203. doi: 10.1128/mmbr.62.1.181-203.1998

Kuwada, N. J., Traxler, B., and Wiggins, P. A. (2015). Genome-scale quantitative characterization of bacterial protein localization dynamics throughout the cell cycle. *Mol. Microbiol.* 95, 64–79. doi: 10.1111/mmi.12841

Mitosch, K., Rieckh, G., and Bollenbach, T. (2017). Noisy response to antibiotic stress predicts subsequent single-cell survival in an acidic environment. *Cell Syst.* 4:e395.

Moore, D. A., Whatley, Z. N., Joshi, C. P., Osawa, M., and Erickson, H. P. (2017). Probing for binding regions of the FtsZ protein surface through site-directed insertions: discovery of fully functional FtsZ-fluorescent proteins. *J. Bacteriol.* 199:e553–16.

Oliveira, R. A., Ng, K. M., Correia, M. B., Cabral, V., Shi, H., Sonnenburg, J. L., et al. (2020). *Klebsiella michiganensis* transmission enhances resistance to Enterobacteriaceae gut invasion by nutrition competition. *Nat. Microbiol.* 5, 630–641. doi: 10.1038/s41564-019-0658-4

Osawa, M., and Erickson, H. P. (2013). Liposome division by a simple bacterial division machinery. *Proc. Natl. Acad. Sci. U.S.A.* 110, 11000–11004. doi: 10.1073/pnas.1222254110

Peters, J. M., Colavin, A., Shi, H., Czarny, T. L., Larson, M. H., Wong, S., et al. (2016). A comprehensize, CRISPR-based approach to functional analysis of essential genes in bacteria. *Cell* 165, 1493–1506. doi: 10.1016/j.cell.2016.05.003

Pilizota, T., and Shaevitz, J. W. (2012). Fast, multiphase volume adaptation to hyperosmotic shock by *Escherichia coli*. *PLoS One* 7:e35205. doi: 10.1371/journal.pone.0035205

Pilizota, T., and Shaevitz, J. W. (2013). Plasmolysis and cell shape depend on solute outer-membrane permeability during hyperosmotic shock in *E. coli*. *Biophys. J.* 104, 2733–2742. doi: 10.1016/j.bpj.2013.05.011

Reshes, G., Vanounou, S., Fishov, I., and Feingold, M. (2008a). Cell shape dynamics in *Escherichia coli*. *Biophys. J.* 94, 251–264. doi: 10.1529/biophysj.107.104398

Reshes, G., Vanounou, S., Fishov, I., and Feingold, M. (2008b). Timing the start of division in *E. coli*: a single-cell study. *Phys. Biol.* 5:046001. doi: 10.1088/1478-3975/5/4/046001

Rojas, E., Theriot, J. A., and Huang, K. C. (2014). Response of *Escherichia coli* growth rate to osmotic shock. *Proc. Natl. Acad. Sci. U.S.A.* 111, 7807–7812. doi: 10.1073/pnas.1402591111

Rojas, E. R., Billings, G., Odermatt, P. D., Auer, G. K., Zhu, L., Miguel, A., et al. (2018). The outer membrane is an essential load-bearing element in Gram-negative bacteria. *Nature* 559, 617–621. doi: 10.1038/s41586-018-0344-3

Rojas, E. R., and Huang, K. C. (2018). Regulation of microbial growth by turgor pressure. *Curr. Opin. Microbiol.* 42, 62–70. doi: 10.1016/j.mib.2017.10.015

Rojas, E. R., Huang, K. C., and Theriot, J. A. (2017). Homeostatic cell growth is accomplished mechanically through membrane tension inhibition of cell-wall synthesis. *Cell. Syst.* 5:e576.

Scott, W. (1953). Water relations of *Staphylococcus aureus* at 30 C. *Aust. J. Biol. Sci.* 6, 549–564. doi: 10.1071/bi9530549

Sekar, K., Rusconi, R., Sauls, J. T., Fuhrer, T., Noor, E., Nguyen, J., et al. (2018). Synthesis and degradation of FtsZ quantitatively predict the first cell division in starved bacteria. *Mol. Syst. Biol.* 14:e8623.

Shi, H., Colavin, A., Bigos, M., Tropini, C., Monds, R. D., and Huang, K. C. (2017a). Deep phenotypic mapping of bacterial cytoskeletal mutants reveals physiological robustness to cell size. *Curr. Biol.* 27, 3419–3429. doi: 10.1016/j.cub.2017.09.065

Shi, H., Colavin, A., Lee, T. K., and Huang, K. C. (2017b). Strain Library Imaging Protocol: high-throughput, automated single-cell microscopy for large bacterial collections arrayed on multiwell plates. *Nat. Protoc.* 12, 429–438. doi: 10.1038/nprot.2016.181

Si, F., Le Treut, G., Sauls, J. T., Vadia, S., Levin, P. A., and Jun, S. (2019). Mechanistic origin of cell-size control and homeostasis in bacteria. *Curr. Biol.* 29, 1760.–1770.

Sliusarenko, O., Heinritz, J., Emonet, T., and Jacobs-Wagner, C. (2011). High-throughput, subpixel precision analysis of bacterial morphogenesis and intracellular spatio-temporal dynamics. *Mol. Microbiol.* 80, 612–627. doi: 10.1111/j.1365-2958.2011.07579.x

Spratt, B. G. (1975). Distinct penicillin binding proteins involved in the division, elongation, and shape of *Escherichia coli* K12. *Proc. Natl. Acad. Sci. U.S.A.* 72, 2999–3003. doi: 10.1073/pnas.72.8.2999

Sutterlin, H. A., Shi, H., May, K. L., Miguel, A., Khare, S., Huang, K. C., et al. (2016). Disruption of lipid homeostasis in the Gram-negative cell envelope activates a novel cell death pathway. *Proc. Natl. Acad. Sci. U.S.A.* 113, E1565–E1574.

Szatmári, D., Sárkány, P., Kocsis, B., Nagy, T., Miseta, A., Barkó, S., et al. (2020). Intracellular ion concentrations and cation-dependent remodelling of bacterial MreB assemblies. *Sci. Rep.* 10:12002.

Tagkopoulos, I., Liu, Y. C., and Tavazoie, S. (2008). Predictive behavior within microbial genetic networks. *Science* 320, 1313–1317. doi: 10.1126/science.1154456

Taheri-Araghi, S., Bradde, S., Sauls, J. T., Hill, N. S., Levin, P. A., Paulsson, J., et al. (2015). Cell-size control and homeostasis in bacteria. *Curr. Biol.* 25, 385–391. doi: 10.1016/j.cub.2014.12.009

Taniguchi, Y., Choi, P. J., Li, G. W., Chen, H., Babu, M., Hearn, J., et al. (2010). Quantifying *E. coli* proteome and transcriptome with single-molecule sensitivity in single cells. *Science* 329, 533–538. doi: 10.1126/science.1188308

Ursell, T., Lee, T. K., Shiomi, D., Shi, H., Tropini, C., Monds, R. D., et al. (2017). Rapid, precise quantification of bacterial cellular dimensions across a genomic-scale knockout library. *BMC Biol.* 15:17. doi: 10.1186/s12915-017-0348-8

Ursell, T. S., Nguyen, J., Monds, R. D., Colavin, A., Billings, G., Ouzounov, N., et al. (2014). Rod-like bacterial shape is maintained by feedback between cell curvature and cytoskeletal localization. *Proc. Natl. Acad. Sci. U.S.A.* 111, E1025–E1034.

van den Bogaart, G., Hermans, N., Krasnikov, V., and Poolman, B. (2007). Protein mobility and diffusive barriers in *Escherichia coli*: consequences of osmotic stress. *Mol. Microbiol.* 64, 858–871. doi: 10.1111/j.1365-2958.2007.05705.x

Walter, H. (1924). Plasmaquellung und wachstum. *Z. Bot.* 16:1931.

Wang, P., Robert, L., Pelletier, J., Dang, W. L., Taddei, F., Wright, A., et al. (2010). Robust growth of *Escherichia coli*. *Curr. Biol.* 20, 1099–1103.

Ward, J. E. Jr., and Lutkenhaus, J. (1985). Overproduction of FtsZ induces minicell formation in *E. coli*. *Cell* 42, 941–949. doi: 10.1016/0092-8674(85)90290-9

Weart, R. B., Lee, A. H., Chien, A. C., Haeusser, D. P., Hill, N. S., and Levin, P. A. (2007). A metabolic sensor governing cell size in bacteria. *Cell* 130, 335–347. doi: 10.1016/j.cell.2007.05.043

Weart, R. B., and Levin, P. A. (2003). Growth rate-dependent regulation of medial FtsZ ring formation. *J. Bacteriol.* 185, 2826–2834. doi: 10.1128/jb.185.9.2826-2834.2003

Wu, F., Swain, P., Kuijpers, L., Zheng, X., Felter, K., Guurink, M., et al. (2019). Cell boundary confinement sets the size and position of the *E. coli* chromosome. *Curr. Biol.* 29, 2131–2144.e4.

Yang, D., Männik, J., Retterer, S. T., and Männik, J. (2020). The effects of polydisperse crowders on the compaction of the *Escherichia coli* nucleoid. *Mol. Microbiol.* 113, 1022–1037. doi: 10.1111/mmi.14467

Yang, X., Lyu, Z., Miguel, A., Mcquillen, R., Huang, K. C., and Xiao, J. (2017). GTPase activity-coupled treadmilling of the bacterial tubulin FtsZ organizes septal cell wall synthesis. *Science* 355, 744–747. doi: 10.1126/science.aak9995

Yao, X., Jericho, M., Pink, D., and Beveridge, T. (1999). Thickness and elasticity of Gram-negative murein sacculi measured by atomic force microscopy. *J. Bacteriol.* 181, 6865–6875. doi: 10.1128/jb.181.22.6865-6875.1999

Zhou, X., Halladin, D. K., Rojas, E. R., Koslover, E. F., Lee, T. K., Huang, K. C., et al. (2015). Bacterial division. Mechanical crack propagation drives millisecond daughter cell separation in *Staphylococcus aureus*. *Science* 348, 574–578. doi: 10.1126/science.aaa1511

Conflict of Interest: The authors declare that the research was conducted in the absence of any commercial or financial relationships that could be construed as a potential conflict of interest.

frontiers in Microbiology

ORIGINAL RESEARCH
published: 18 August 2021
doi: 10.3389/fmicb.2021.729307

Diversification of LytM Protein Functions in Polar Elongation and Cell Division of *Agrobacterium tumefaciens*

Wanda M. Figueroa-Cuilan[1†‡], Amelia M. Randich[2†], Caroline M. Dunn[1‡], Gustavo Santiago-Collazo[1,3], Andrew Yowell[1‡] and Pamela J. B. Brown[1]*

[1] Division of Biological Sciences, University of Missouri, Columbia, MO, United States, [2] Department of Biology, University of Scranton, Scranton, PA, United States, [3] Molecular Pathogenesis and Therapeutics Graduate Program, University of Missouri, Columbia, MO, United States

OPEN ACCESS

Edited by:
Cara C. Boutte,
University of Texas at Arlington,
United States

Reviewed by:
Tsuyoshi Uehara,
Venatorx Pharmaceuticals, Inc.,
United States
Joseph Boll,
University of Texas at Arlington,
United States
Tobias Dörr,
Cornell University, United States

***Correspondence:**
Pamela J. B. Brown
brownpb@missouri.edu

[†] These authors have contributed equally to this work and share first authorship

[‡] Present address:
Wanda M. Figueroa-Cuilan,
Department of Biological Chemistry, Johns Hopkins University School of Medicine, Baltimore, MD, United States
Caroline M. Dunn,
Department of Biology, Indiana University, Bloomington, IN, United States
Andrew Yowell,
College of Dentistry and Dental Clinics, University of Iowa, Iowa City, IA, United States

Specialty section:
This article was submitted to Microbial Physiology and Metabolism, a section of the journal Frontiers in Microbiology

Received: 22 June 2021
Accepted: 26 July 2021
Published: 18 August 2021

Citation:
Figueroa-Cuilan WM, Randich AM, Dunn CM, Santiago-Collazo G, Yowell A and Brown PJB (2021) Diversification of LytM Protein Functions in Polar Elongation and Cell Division of Agrobacterium tumefaciens. Front. Microbiol. 12:729307. doi: 10.3389/fmicb.2021.729307

LytM-domain containing proteins are LAS peptidases (lysostaphin-type enzymes, D-Ala-D-Ala metallopeptidases, and sonic hedgehog) and are known to play diverse roles throughout the bacterial cell cycle through direct or indirect hydrolysis of the bacterial cell wall. A subset of the LytM factors are catalytically inactive but regulate the activity of other cell wall hydrolases and are classically described as cell separation factors NlpD and EnvC. Here, we explore the function of four LytM factors in the alphaproteobacterial plant pathogen *Agrobacterium tumefaciens*. An LmdC ortholog (Atu1832) and a MepM ortholog (Atu4178) are predicted to be catalytically active. While Atu1832 does not have an obvious function in cell growth or division, Atu4178 is essential for polar growth and likely functions as a space-making endopeptidase that cleaves amide bonds in the peptidoglycan cell wall during elongation. The remaining LytM factors are degenerate EnvC and NlpD orthologs. Absence of these proteins results in striking phenotypes indicative of misregulation of cell division and growth pole establishment. The deletion of an amidase, AmiC, closely phenocopies the deletion of *envC* suggesting that EnvC might regulate AmiC activity. The NlpD ortholog DipM is unprecedently essential for viability and depletion results in the misregulation of early stages of cell division, contrasting with the canonical view of DipM as a cell separation factor. Finally, we make the surprising observation that absence of AmiC relieves the toxicity induced by *dipM* overexpression. Together, these results suggest EnvC and DipM may function as regulatory hubs with multiple partners to promote proper cell division and establishment of polarity.

Keywords: LytM, bacterial division, divisome, polar growth, DD-endopeptidase, amidase, bacterial polarity, Alphaproteobacteria

INTRODUCTION

In bacteria, the peptidoglycan (PG) cell wall plays an essential role in maintaining cell shape, protecting bacteria from environmental stressors, and preventing cell lysis (Scheffers and Pinho, 2005; Vollmer et al., 2008; Cava et al., 2013; Cameron et al., 2015; Ruiz, 2016). The PG cell wall is a net-like structure that consists of glycan strands containing alternating β-1,4-linked *N*-acetylglucosamine (NAG) and *N*-acetylmuramic acid (NAM) sugars crosslinked together

through peptide stems (Höltje, 1998). While the bacterial PG cell wall is necessary and sufficient to determine bacterial cell shape, expansion, and separation of the cell wall requires enzymatic action (Uehara and Bernhardt, 2011). In order to expand the existing cell wall, coordination between PG cell wall synthesis and hydrolysis is necessary to allow insertion of new cell wall material at very specific locations within the cell (Vollmer, 2012; Egan et al., 2020).

Bacterial PG hydrolases and autolysins are a highly diverse group of enzymes that contribute to many important processes in the cell, including PG biosynthesis (Singh et al., 2012; Vollmer, 2012; Do et al., 2020), separation of bacterial cells (Heidrich et al., 2001; Uehara et al., 2009, 2010; Goley et al., 2010; Möll et al., 2010, 2014; Yakhnina et al., 2015), peptidoglycan recycling (Jacobs et al., 1995; Langaee et al., 2000; Heidrich et al., 2002; Das et al., 2013; Lamers et al., 2015), and insertion of structures that span the entire cell envelope, including flagella and secretion systems (Scheurwater et al., 2008). During cell division of rod-shaped bacteria, septal PG (sPG) is deposited near mid-cell to build new cell poles prior to cell separation. The final steps of cell division require the coordinated activity of cell wall amidases, endopeptidases, carboxypeptidases, lytic transglycosylases, and regulators of these hydrolyzes called LytM factors to enable cell separation (Heidrich et al., 2001; Peters et al., 2011; Vermassen et al., 2019; Do et al., 2020). In members of the Gammaproteobacteria, including *Escherichia coli*, *Pseudomonas aeruginosa*, and *Vibrio cholerae*, inactivation of amidases prevents cleavage of sPG, leading to cell chaining (Uehara et al., 2010; Möll et al., 2014). Overexpression of amidases results in lysis, suggesting that a tight regulation of PG hydrolases is required to avoid cell lysis. Indeed in *E. coli* and *V. cholerae*, endopeptidases that have lost enzymatic activity are termed "degenerate" LytM (dLytM) factors and function as regulators of amidase activity.

Degenerate LytM factors were first characterized in *E. coli*, where they were reported to have redundant function as late divisome components that assist in the final steps of cell separation (Uehara et al., 2009, 2010). While the single mutants had mild or non-existent phenotypes, the double Δ*envC*Δ*nlpD* mutant exhibited significant defects in cell separation: the mutant formed long chains of regularly spaced cytoplasmic compartments separated by layers of PG and surrounded by a single outer membrane layer (Uehara et al., 2009). Since this early characterization, $EnvC_{Ec}$ and $NlpD_{Ec}$ have been shown to have no endopeptidase activity on their own but instead activate cognate amidases: $EnvC_{Ec}$ specifically activated amidases AmiA and AmiB while $NlpD_{Ec}$ activated AmiC in *in vitro* PG hydrolysis assays (Uehara et al., 2010). In addition, the third *E. coli* dLytM factor, an NlpD paralog ("YgeR" or "ActS"), has been shown to be capable of activating all three amidases with a preference for AmiC (Gurnani Serrano et al., 2021). Structural and mutagenic investigations of EnvC–AmiB interactions have revealed that EnvC uses its deactivated LytM catalytic cleft to bind the autoinhibition helix of AmiB (Peters et al., 2013). The same interface is bound by an autoinhibition alpha helix of EnvC in cocrystals of EnvC and its recruiting partner and regulator FtsX (Yang et al., 2011; Cook et al., 2020). Thus, the dLytM interface of EnvC plays a central role in late divisome regulation. The mechanism of EnvC regulation of amidases is used to explain how other dLytMs regulate amidases, although autoinhibition interactions have not yet been reported for NlpD or YgeR. Recent work in $NlpD_{Ec}$ has indicated that it has additional interactions with the Tol–Pal complex that coordinate peptidoglycan remodeling and outer membrane constriction at the division plane (Tsang et al., 2017). Together, the studies on the *E. coli* dLytM factors suggest that EnvC and NlpD have partially redundant, late division roles in activating cognate amidases to complete the last steps of cell separation as well as unique interactions with other protein networks.

In general, studies of dLytM factors in other proteobacteria have largely supported the evidence from *E. coli* with some striking variation. Although most species have fewer amidases than *E. coli*, at least one amidase has been associated with chaining or cell separation defects: AmiA in *Helicobacter* (Chaput et al., 2016); AmiB in *Vibrio* (Möll et al., 2014) and *Pseudomonas* (Yakhnina et al., 2015); AmiC in *Neisseria* (Garcia and Dillard, 2006; Stohl et al., 2016), *Caulobacter* (Meier et al., 2017; Zielińska et al., 2017; Dubey and Priyadarshini, 2018), and *Hyphomonas* (Cserti et al., 2017); and AmiC1 in *Xanthomonas* (Yang et al., 2018). In most cases, EnvC, NlpD, or both, were implicated in the amidase pathway. For gammaproteobacterium *Xanthomonas campestris* and betaproteobacterium *Neisseria gonorrhoeae*, NlpD has been shown to directly activate AmiC *in vitro* (Stohl et al., 2016; Yang et al., 2018). Both EnvC and NlpD have been suggested to activate AmiB in gammaproteobacteria *V. cholerae* (Möll et al., 2014) and *P. aeruginosa* (Yakhnina et al., 2015) by inference from genetic experiments. In most cases, EnvC and NlpD orthologs were non-essential and resulted in late cell separation defects resulting in a failure to separate after cytokinesis of the inner membrane.

The *E. coli* model for the function of amidases and dLytM factors does not have universal agreement among all proteobacteria, however. Interesting outliers are *Pseudomonas*, which exhibited earlier cell constriction defects for AmiB mutants (Yakhnina et al., 2015) and the pathogens *H. influenzae* (Ercoli et al., 2015) and *N. gonorrhoeae* (Stohl et al., 2016), in which Δ*envC* elicited no morphological or division defects. While EnvC and NlpD have generally been seen as redundant in gamma- and betaproteobacteria, this does not appear to be the case in alphaproteobacteria, where dLytM factors are not strictly conserved, and when they are, their loss has given rise to unique late cell separation phenotypes. Deleting the *envC* ortholog "*lpdF*" in *Caulobacter crescentus* resulted in cells that were mildly chained and electron cryotomography images showed that the cells fail to finish separating PG and OM layers (Zielińska et al., 2017). Loss of the *nlpD* ortholog, "*dipM*," in *C. crescentus* resulted in a distinct cell separation phenotype that featured completion of inner membrane cytokinesis with deformation and blebbing of the outer membrane at the division plane (Goley et al., 2010; Möll et al., 2010; Poggio et al., 2010). This outer membrane blebbing was similar to Tol–Pal mutants in *Caulobacter* (Yeh et al., 2010) and indicated a relationship between NlpD and the Tol–Pal system much earlier than later determined for *E. coli* (Tsang et al., 2017).

The studies in alphaproteobacteria have presented an additional puzzle. In both *Caulobacter* and *Hyphomonas*, loss of EnvC or AmiC orthologs appeared to produce similar separation phenotypes: mild chaining in *C. crescentus* (Meier et al., 2017; Zielińska et al., 2017) and elongated stalks terminated by chains of bud cells in *Hyphomonas neptunium* (Cserti et al., 2017). These results suggest some sort of regulatory relationship between EnvC and AmiC rather than NlpD and AmiC. While the story is less clear in *H. neptunium*, which only conserves EnvC and not NlpD, various experiments suggest that the two dLyM factors act in at least two, if not three, distinct pathways to drive the final steps of cell separation in *Caulobacter* (Meier et al., 2017; Zielińska et al., 2017). It is possible that this is also true in other proteobacteria but the genetic associations are occluded by redundancy or epistasis, such as in the case of NlpD and the Tol–Pal system in gammaproteobacteria. Accumulating data in various genera supports the assertion that these two dLytM factors are components of molecularly distinct but overlapping protein-interaction networks with different recruitment and activation partners that intersect late in division.

The different phenotypes among proteobacteria are due to divergent genetic backgrounds in which the role of the ortholog, its binding partners, or other intersecting pathways have shifted evolutionarily. In this way, comparative genetic studies across genera can reveal either species-specific functions or conserved roles that are harder to detect in genera with higher levels of redundancy. Here, we sought to expand our understanding of bacterial cell division within the Alphaproteobacteria by exploring the functions of LytM factors and amidases in the bacterial plant pathogen, *Agrobacterium tumefaciens*, an emerging model for the study of cell division in a polar-growing bacterium (Figueroa-Cuilan and Brown, 2018). We find that the LytM factors play multiple roles throughout the *A. tumefaciens* cell cycle. While the catalytically active LytM factors did not make obvious contributions to cell division, the dLytM factors both exhibited strong localization at mid-cell and played distinct, yet potentially overlapping, roles during cell division. Deletion or depletion of dLytM factors resulted in phenotypes that were vastly different from similar mutants in other proteobacteria, where cells fail to separate. In this work, we begin to dissect the functions of these proteins and find that the dLytM factors still likely contribute to the regulation of PG hydrolases but have additional derived functions related to the establishment of growth poles following cell division.

MATERIALS AND METHODS

Bioinformatics and Phylogenetics

Sequences of the LytM genes in **Supplementary Table 1** were retrieved by pBLAST searches on the Integrated Microbial Genomes and Microbiomes (IMG/M) database (Chen et al., 2017). Multiple alignments were achieved with MUSCLE (Edgar, 2004) and manually adjusted and visualized with Jalview (Waterhouse et al., 2009). Before performing phylogenetic reconstruction, the sequences were truncated to only the conserved LytM domain. The LytM domain from *S. aureus* (GenBank ID: MBH4889575.1) was used in alignments to determine the boundaries of the conserved domain.

Phylogenetic reconstruction was performed using MEGA11 (Kumar et al., 2018; Stecher et al., 2020) to estimate consensus phylogenies and carry out bootstrapping analysis. The LytM gene tree was inferred by using the Maximum Likelihood method and Le Gascuel 2008 model (Le and Gascuel, 2008). A discrete Gamma distribution was used to model evolutionary rate differences among sites [four categories (+*G*, parameter = 1.6678)]. The rate variation model allowed for some sites to be evolutionary invariable [(+*I*), 0.00% sites]. This analysis involved 178 amino acid sequences (**Supplementary Table 1**). The tree was visualized and formatted using iTol (Letunic and Bork, 2016). Presence and absence of LytM clade members was determined from the tree and tabulated in **Supplementary Table 2**.

Full length genes were screened for N-terminal secretory signal sequences using the SignalP-5.0 Server (Almagro Armenteros et al., 2019) and for transmembrane segments using TMHMM (Krogh et al., 2001). Additionally, TREND was used to quickly identify conserved protein domains (Gumerov and Zhulin, 2020) and DeepCoil was used to identify coiled-coil domains (Ludwiczak et al., 2019). The results of this analysis are summarized in **Supplementary Table 1**.

WebLogo 3 (Crooks et al., 2004) was used to plot the amino acid distribution at each position of the LysM domain. To create the alignments for logo generation, LytM sequences from the defined five clades (and the additional subgroup of active NlpD genes) in the tree were simultaneously aligned to the LytM domain from *S. aureus* (GenBank ID: MBH4889575.1) and any insertions causing gaps in the $LytM_{Sa}$ sequence were removed for uniform comparison. This analysis included the 38 MepM, 36 EnvC, 31 LmdC, 27 NlpD, 6 NlpD (with conserved active site HXXXD, HXH), and 21 LpdB LytM domains from the genes listed in **Supplementary Table 1**.

Bacterial Strains and Growth Conditions

Agrobacterium tumefaciens C58 and derived strains were grown in LB rich medium or ATGN (0.5% glucose) minimal medium (Morton and Fuqua, 2012) at 28°C with shaking. When appropriate, antibiotics were used at the following working concentrations: kanamycin 300 μg/ml and gentamycin 200 μg/ml. When indicated, IPTG was used as an inducer at a concentration of 1 mM. In some cases, cumate was used as an inducer at a concentration of 0.1 mM. *E. coli* DH5α and S17-1 were routinely cultivated on LB agar or liquid LB medium at 37°C with shaking. When needed antibiotics were used at the following concentrations: kanamycin 50 μg/ml and gentamycin 20 μg/ml. All strains used in this study are listed in **Supplementary Table 3**. Unless otherwise specified, the experiments were conducted in LB.

Construction of Strains and Plasmids

All strains and plasmids used are listed in **Supplementary Table 3** and primers are listed in **Supplementary Table 4**. To construct expression vectors containing *lmdC-sfgp*, *rgsM-sfgfp*, *dipM-sfgfp*, and *envC-sfgfp*, the corresponding coding sequence

was amplified from purified *A. tumefaciens* C58 genomic DNA without a stop codon. The amplicons and plasmids pSRKKM-Plac-*sfgfp*, pSRKKM-Cym-*sfgfp*, pSRKKM-T7-*sfgfp*, pSRKKM-PenvC-*sfgfp*, were digested overnight and ligated overnight at 4°C using NEB T4 DNA ligase. Ligations were transformed into *E. coli* DH5α and purified plasmids were sequenced to verify expected translational fusions. *Atu1832* was amplified from genomic DNA and inserted into pSRKKM-Cym-*sfgfp* linearized with *Nde*I and *Bam*HI using Gibson cloning (NEB) according to manufacturer's protocols.

For complementation of Δ*envC*, the EnvC native promoter was cloned into the pSRKKM plasmid. Complementation of Δ*amiC* and Δ*amiD* was achieved by constitutively expressing *amiC* and *amiD* under the T7 medium promoter. The T7 medium promoter was introduced into *Eco*RI and *Nde*I sites of pSRKKM using the oligo annealing/ligation method and the T7forwardEcoRINdeI and T7revEcoRINdeI primers. Lastly, *dipM* with a stop codon was ligated into pSRKKM-Ptac-*sfgfp* to allow conditional overexpression of *dipM* from the Ptac promoter in the presence of IPTG.

Construction of Deletion/Depletion Plasmids and Strains

Vectors for gene deletions by allelic exchange were constructed using recommended methods for *A. tumefaciens* (Morton and Fuqua, 2012). Gene deletions were achieved by allelic exchange and vectors were constructed as previously described (Howell et al., 2019). Briefly, 500 bp fragments upstream and downstream of the gene of interest (*envC*, *amiC*, *ampD*) were amplified using primer pairs P1/P2 and P3/P4. Overlapping PCR was used to the amplicons generated by P1/P2 and P3/P4, using primer pair P1/P4. The amplicon was digested and ligated into pNTPS139. Ligations were transformed into *E. coli* DH5α and purified plasmids were sequenced to verify expected inserts. The deletion plasmids were introduced into *A. tumefaciens* by mating using an *E. coli* S17 conjugation strain to create kanamycin resistant, sucrose sensitive primary exconjugants. Primary exconjugants were grown overnight in media with no selection. Secondary recombinants were screened by patching for sucrose resistance and kanamycin sensitivity. Colony PCR with primers P5/P6 for the respective gene target was used to confirm deletion. PCR products from P5/P6 primer sets were sequenced to further confirm deletions.

For the insertional knock-out of *Atu1832*, nucleotides 1172–1771 of Atu1832 were amplified from genomic DNA and cloned into pMCS-2 (Thanbichler et al., 2007) linearized with EcoR1 using Gibson cloning. Integrants were isolated by antibiotic selection and checked for correct insertion of the plasmid using primers upstream of this sequence and inside the plasmid.

To construct the DipM and RgsM depletion strains, the target gene was amplified, digested and ligated into the pUC18-mini-Tn*7*T-GM-Ptac and pUC18-mini-Tn*7*T-GM-Plac, respectively. The mini-Tn7 vector, along with the pTNS3 helper plasmid, were introduced into C58Δ*tetRA*:a-*att*Tn*7* as described previously (Figueroa-Cuilan et al., 2016). Transformants were selected for gentamycin resistance and insertion of the target gene into the a-*att* site was verified by colony PCR using the tet forward and Tn7R109 primers. PCR products were sequenced to confirm insertion of the correct gene. Next, the target genes were deleted from the native locus as described above in the presence of 1 mM IPTG to drive expression of the target gene from the engineered site. Additional deletions were introduced into the DipM depletion strain following the protocol described above with IPTG present during all steps.

Fluorescence, Phase Contrast, and DIC Microscopy

Exponentially growing cells (OD600 ∼ 0.6) were immobilized on 1.25% LB or ATGN agarose pads as described previously (Howell et al., 2017). Phase contrast, differential interference (DIC) and epifluorescence microscopy was performed with an inverted Nikon Eclipse TiE equipped with a QImaging Rolera Em-C2 1K EMCCD camera and Nikon Elements Imaging Software. For time-lapse imaging, cells were imaged every 5 or 10 min for the duration of the experiment. Time-lapse microscopy is conducted at room temperature (∼23°C).

To construct demographs of LmdC-GFP, RgsM-GFP, EnvC-GFP, or DipM-GFP localization (**Figure 2**), cells (∼100 to 500) were imaged for each strain. A GFP channel profile was taken along the medial axis for each imaged cell. These medial axis profiles were then aligned by cell length using MicrobeJ software (Ducret et al., 2016).

Quantitative Image Analysis of Cell Growth and Morphology

Exponentially growing cells were imaged using phase microscopy as described above. Bacterial cell length was detected by MicrobeJ software whereas principal component analysis (PCA) to identify shape variations was performed using CellTool (Pincus and Theriot, 2007). Phase contrast images were converted and edited to binary masks in FIJI (Schindelin et al., 2012) before using CellTool.

Cell Viability Assays

For cell viability spot assays, cultures were grown overnight and diluted to an OD600 = 0.05 and serially diluted in LB or ATGN agar plates. Four microliters of each dilution was spotted and plates were incubated at 28°C for 36 h (LB) or 48 h (ATGN) before imaging. When appropriate plates contained 300 μg/ml kanamycin and/or IPTG at 1 mM as indicated in figure legends. For the RgsM, DipM, or DipM-derived depletion strains, cells were grown in liquid media in the presence of 1 mM IPTG to an OD600 = 0.6. The cells were washed three times by centrifugation in media to remove the inducer and resuspended to an OD600 = 0.05 in media. Serial dilutions were performed, and 4 μl of each dilution was spotted onto and plates were incubated at 28°C for 36 or 48 h before imaging. Each condition was tested in duplicate during three independent experiments ($n = 3$).

Outer Membrane Integrity Assay

For the SDS susceptibility assay, exponentially growing cells were diluted to an OD600 = 0.5. A total of 0.25 ml of each culture was aliquoted into 1.5 ml tubes and centrifuged at 4.5 × *g* for 5 min. Cells were resuspended in 0.25 ml of various concentrations (0.625, 1.25, 2.5, and 5%) of SDS solubilized in HEPES buffer at a pH 7.4, and incubated for 5 min. Untreated controls were resuspended in 0.25 ml of HEPES buffer only. Four microliter of each dilution was spotted onto LB and stored at 28°C for 24 h before imaging. When treating depletion strains with SDS, cells were pre-depleted as indicated, treated with SDS for 5 min and spotted on plates containing IPTG and no SDS. To determine the strain sensitivity to high salt, cell viability assays were conducted as described above on LB plates containing 2% NaCl.

Whole Cell TEM, SEM, and Thin Section TEM

Wildtype and Δ*envC* strains were grown in LB or ATGN for ∼16 h to early stationary or late exponential, respectively, before being spun down and resuspended in fixative (2% paraformaldehyde, 2% glutaraldehyde in 100 mM sodium cacodylate buffer pH = 7.35). DipM depletion strains were grown as described and depleted for the indicated time before being collected, spun down, and resuspended in fixative. Unless otherwise stated, all reagents were purchased from Electron Microscopy Sciences and all specimen preparation was performed at the Electron Microscopy Core Facility, University of Missouri.

For whole cell TEM, fixed whole cells were rinsed by pelleting at 2,500 g and resuspending in water. Samples were placed on negatively charged carbon coated copper grids. A negative charge was applied to the grid using a PELCO easiGlow Glow Discharge Cleaning System. Cells were allowed to settle on prepared grids for 2 min before removing the water solution and replacing it with 1% aqueous uranyl acetate for 2 min before drying and imaging. Images were acquired with a JEOL JEM 1400 Transmission Electron Microscope (JEOL, Peabody, MA, United States) at 80 kV on a Gatan Ultrascan 1000 CCD (Gatan, Inc., Pleasanton, CA, United States).

For SEM, fixed whole cells were plated overnight on cell culture treated coverslips to ensure adhesion and rinsed with 100 mM sodium cacodylate buffer, pH 7.35 containing 130 mM sucrose. Secondary fixation was performed using 1% osmium tetroxide (Ted Pella, Inc., Redding, CA, United States) in cacodylate buffer using a PELCO BioWave (Ted Pella, Inc., Redding, CA, United States) operated at 100 W for 1 min. Specimens were next incubated at 4°C for 1 h, then rinsed with cacodylate buffer and further with distilled water. Using the PELCO BioWave, a graded dehydration series (per exchange, 100 W for 40 s) was performed using ethanol. Samples were dried using the Tousimis Autosamdri 815 (Tousimis, Rockville, MD, United States) and samples were sputter coated with 5 nm of platinum using the EMS 150T-ES Sputter Coater. Images were acquired with a FEI Quanta 600F scanning electron microscope (FEI, Hillsboro, OR, United States) at 2 kV, Spot 7, with the Everhart–Thornley secondary electron detector.

For thin sectioning, each sample was centrifuged at 2,500 × *g* and the resulting pellet was resuspended in HistoGel (Thermo Scientific, Kalamazoo, MI, United States). Next, fixed pellets were rinsed with 100 mM sodium cacodylate buffer, pH 7.35 (Sigma Aldrich, St. Louis, MO, United States), and 130 mM sucrose. Secondary fixation was performed using 1% osmium tetroxide (Ted Pella, Inc., Redding, CA, United States) in 2-ME buffer using a PELCO BioWave (Ted Pella, Inc., Redding, California) operated at 100 W for 1 min. Specimens were next incubated at 4°C for 1 h, then rinsed with cacodylate buffer and further with distilled water. En bloc staining was performed using 1% aqueous uranyl acetate and incubated at 4°C overnight, then rinsed with distilled water. Using the PELCO BioWave, a graded dehydration series (per exchange, 100 W for 40 s) was performed using ethanol, transitioned into acetone, and dehydrated specimens were then infiltrated with EPON resin (250 W for 3 min) and polymerized at 60°C overnight. Sections were cut to a thickness of 75 nm using an ultramicrotome (Ultracut UCT, Leica Microsystems, Germany) and a diamond knife (Diatome, Hatfield, PA, United States). Images were acquired with a JEOL JEM 1400 Transmission Electron Microscope (JEOL, Peabody, MA, United States) at 80 kV on a Gatan Ultrascan 1000 CCD (Gatan, Inc., Pleasanton, CA, United States).

Western Blotting

For monitoring DipM expression in LB and ATGN, 20 ml cultures were grown to an OD600 = 0.6 in the presence of IPTG. A 2-ml aliquot of the culture was removed from each culture, and the pellets were stored to serve as time zero (DipM-replete). The remaining 18 ml of cultures were washed three times with LB or ATGN *via* centrifugation to remove the IPTG. The washed pellets were resuspended and normalized to an OD600 of 0.4 and kept in exponential phase throughout the experiment. Aliquots were collected after 2, 4, 8, 16, and 24 h to monitor the levels of DipM production during the depletion. The cell pellets were stored at -80°C until further analysis. The cell pellets were incubated with 100 μl of a master mix containing 1 ml of BugBuster protein extraction reagent (Novagen) and supplemented with 1 (EDTA-free protease inhibitor cocktail (Sigma), 10 μl of lysonase (Novagen), 2,500 U/ml DNase I (Thermo Scientific), and 1 mM dithiothreitol (DTT) (Thermo Scientific) for 30 min with shaking at room temperature to lyse the cell pellets. The whole-cell lysates were clarified by centrifugation at 17,136 × *g* for 15 min. The BCA protein concentration kit (Thermo Scientific Pierce) was used to measure the total protein concentration of each sample. A final concentration of 1 × Laemmli buffer (BioRad) was added to the cleared cell lysates. Samples were boiled at ∼100°C for 5 min prior to loading equivalent amounts in each well of an SDS-10% PAGE gel. The separated proteins were electroblotted onto polyvinylidene difluoride (PVDF) membranes (Bio-Rad) and blocked for 1 hour in 5% non-fat dry milk powder solubilized in 1% TBST (1 × Tris-buffered saline, 1% Tween 20). The blocked PVDF membranes were probed primary antibody (*Caulobacter crescentus* α-DipM diluted 1:2,000) for 1.5 h in 2.5% milk-TBST, followed by incubation with secondary antibody (horseradish peroxidase-conjugated goat anti-rabbit at a dilution of 1:10,000)

for 1 h in 2.5% milk-TBST. The secondary antibody was detected using the ECL Plus-HRP substrate (Thermo Scientific Pierce).

Quantification of Cell Cycle and Polarity Phenotypes

For **Figure 3G**, DIC time-lapse microscopy of cells growing on agarose pads (as described above) was used to monitor cell cycle progression. Typical cell cycle maintenance indicates that an individual cell elongates, constricts at mid-cell, and divides with growth resuming at new poles generated by cell division. Cell growth inhibition indicates that the cell stops growing; cell division inhibition indicates that cells do not properly constrict or divide; and polarity defect indicates that growth appears to occur from an old pole. The % of cells displaying each cell cycle phenotype was calculated by counting the number of cells displaying the indicated phenotypes and dividing it by the total number of cells analyzed for each strain. For **Figure 4E**, DIC time-lapse microscopy was employed to track growth poles for 1–3 generations. In WT cells, elongation occurs at the new poles generated by cell division in both mother cells and daughter cells. Mother cells are defined as the cells which inherit the oldest (non-growth) pole when a cell divides whereas daughter cells inherit the former growth pole. Cells resuming growth at the newly formed cell poles were categorized as growing through the new pole. Cells resuming growth at the pole opposite to the new pole generated by cell division were categorized as resuming growth at the old pole.

RESULTS

The Four LytM Factors of *A. tumefaciens* Exhibit Distinct Localization Patterns and Functions With No Redundancy

The *A. tumefaciens* genome encodes four open reading frames that contain LytM (M23) enzymatic domains. Because of the wide diversity of genes containing LytM domains among Proteobacteria, it can be difficult to infer whether a given factor should have an ancestral or species-specific role. We took a phylogenetic approach to place the four LytM factors within a greater functional and evolutionary context: we collected all detectable LytM factors from representatives of all the proteobacterial classes, including some deep-branching proteobacterial classes, and constructed a maximum likelihood gene tree using only the LytM domains (**Figure 1A**). In this gene tree, five clades emerged that were distinguished by the conservation of N-terminal protein domains outside of the LytM domain in the full length genes (see also **Supplementary Figures 1**, **2**). All of these clades have characterized members, and we named the clades using the most characterized member. In general, almost all surveyed bacterial representatives encoded orthologs of EnvC, LmdC, and MepM whereas Csd and NlpD orthologs were constrained to or have been lost in certain bacterial classes (**Figure 1B**). Divisome components NlpD and EnvC were further distinguished from other LytM factors and each other by dLytM domains with distinct inactivation patterns of the catalytic site (**Figure 1A** and **Supplementary Figure 3**). LytM endopeptidases belong to the large family of lysostaphin-type metalloenzymes that conserve a zinc chelating active site that catalyzes the cleavage of peptide bonds (Firczuk and Bochtler, 2007). This catalytic site is defined by the conserved signature sequence HXXXD, HXH (Bochtler et al., 2004; Firczuk et al., 2005; Grabowska et al., 2015). Crystal structures of LytM domains with substitutions at these positions do not contain the Zn^{2+} cofactor (Peters et al., 2013; An et al., 2016; Cook et al., 2020). The inactivation of the catalytic site has been well-documented among various studies of dLytM factors in the Proteobacteria and it has been shown in various members that these factors activate cognate amidases rather than directly hydrolyzing peptide bonds themselves (Uehara et al., 2009; Stohl et al., 2016; Yang et al., 2018; Gurnani Serrano et al., 2021).

The *A. tumefaciens* genome encodes four of the five major LytM factor classes detected in our approach. The genome encodes two enzymatically active LytM endopeptidases and two dLytM factors. It does not encode a member of the LpdB clade, which is particularly conserved in the Delta- and Epsilonproteobacteria and Spirochaetia (**Figures 1A,B**). This clade features no distinguishing domains by sequence analysis and we were unable to determine if any orthologs of members of this clade have been well-characterized. Currently this clade is named for the *C. crescentus* ortholog that exhibited no phenotype when deleted (Zielińska et al., 2017).

Agrobacterium tumefaciens encodes one LmdC ortholog (Atu1832). The LmdC clade features an N-terminal transmembrane (TM) segment, one to two coiled coil domains, and an active LytM domain (**Figure 1A**). The LmdC clade has representatives from most classes but is particularly conserved in the Alpha- and Deltaproteobacteria and deep-branching proteobacteria (**Figure 1B**). This clade has few characterized representatives but is essential in *H. neptunium* where it could contribute to growth and division of daughter cells that bud from the reproductive prostheca (Cserti et al., 2017). It has also been implicated in prostheca (stalk) biogenesis in *C. crescentus* (Billini et al., 2019). Our phylogenetic analysis indicated that in all alphaproteobacterial orders, with the exception of Rhizobiales, the coiled-coil domain is preceded by a DUF5930 domain (**Figure 1A**). Overall, our analysis supports the idea that this gene is broadly conserved with specialized roles in the Alphaproteobacteria that has undergone further derivation in the Rhizobiales. To visualize the localization of this ortholog in *A. tumefaciens*, we constructed an cumate-inducible plasmid expressing $LmdC_{Atu}$ with monomeric superfolder GFP fused to its C-terminus. After inducing overnight, the cells showed low, diffuse fluorescence (**Figure 2A**). Attempts at fusing msfGFP at the native locus resulted in even lower levels of diffuse fluorescence (data not shown). An insertional knock-out of this gene exhibited no effect on cell viability or any morphological phenotype when grown in LB or ATGN (**Figures 2E–G**).

Agrobacterium tumefaciens encodes one MepM ortholog (Atu4178). This broadly conserved active LytM clade of DD-endopeptidases is generally distinguished by an N-terminal Csd3 inactivation domain (**Figures 1A,B**), which has been shown to obstruct the substrate binding site of the *Helicobacter pylori*

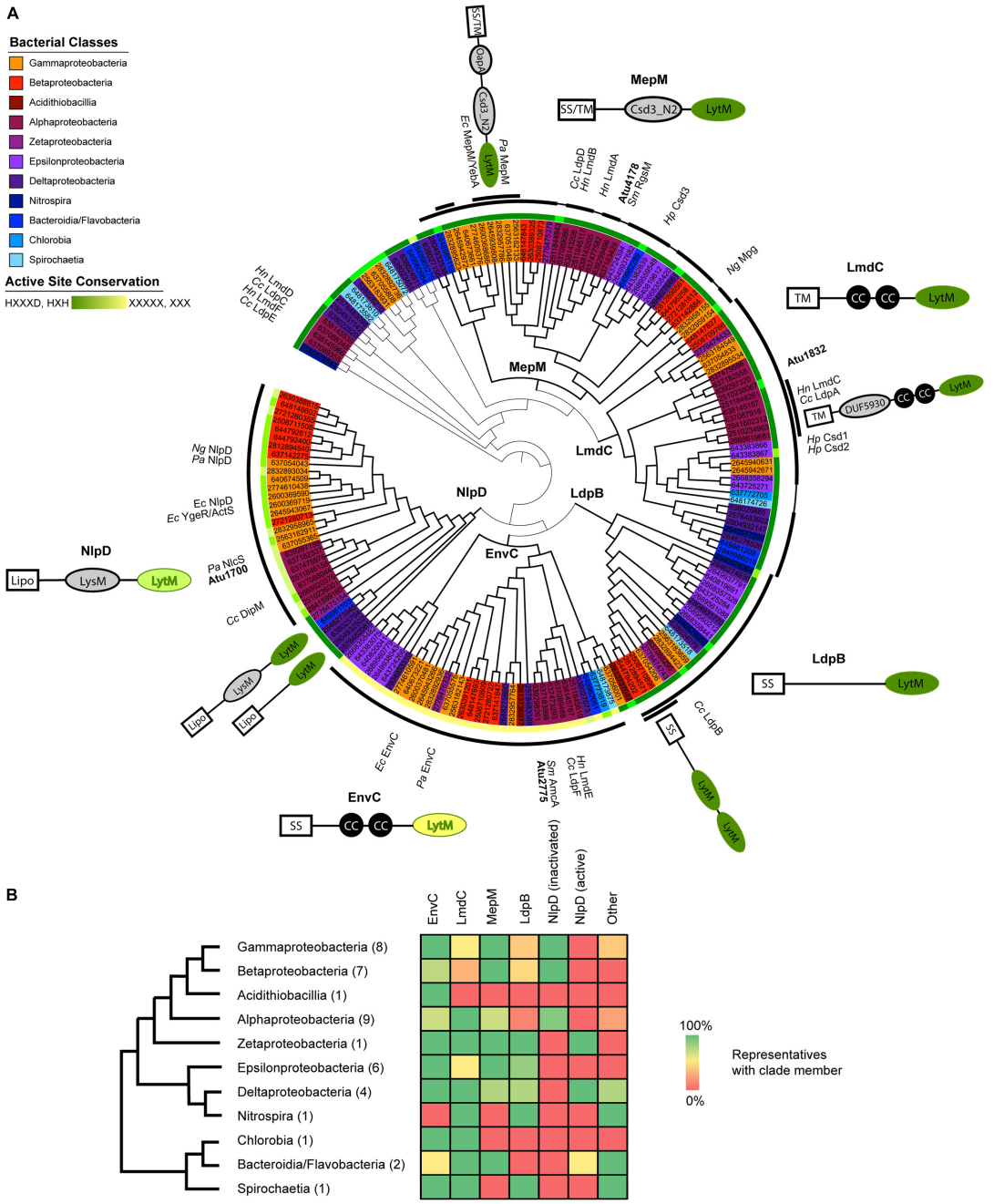

FIGURE 1 | Proteobacterial LytM domain-containing proteins segregate phylogenetically into five major classes with identifiable features outside of the LytM domain. **(A)** Maximum likelihood gene tree of LytM factors constructed with aligned LytM domains from 41 representative species from the Proteobacteria and deep-branching Proteobacteria. The five clades are labeled at their branch point and emphasized by thicker branch weights. This tree has been arbitrarily rooted to clarify the structure of the five clades (see also **Supplementary Figure 1**). The taxa are colored according to bacterial class (see legend) and shown as JGI ID numbers, which are associated with genetic loci and genomes in **Supplementary Table 1**. Taxa that have been studied and named are labeled in the outermost ring (*Cc*, *Caulobacter crescentus*; *Ec*, *Escherichia coli*; *Hn*, *Hyphomonas neptunium*; *Hp*, *Helicobacter pylori*; *Ng*, *Neisseria gonorrhoeae*; *Pa*, *Pseudomonas aeruginosa*; *Sm*, *Sinorhizobium meliloti*). The first ring outside of the taxa indicates the degree to which the active site motif (HXXXD, HXH) is conserved, with dark green indicating full conservation and yellow indicating loss of all conservation. See also **Supplementary Figure 3** for LytM consensus sequences for each clade. The thick black arcs identify which members of the clade include the schematized N-terminal domains and help distinguish where clades begin and end. Some MepM and LmdC members did not have clade-associated domains, which is indicated by a thinner connecting line within the arc. Some groups of LytM factors shared additional features and these are indicated by a second arc layer. Schematics of characteristic clade architectures appear horizontally next to the clades. LytM domains are colored according to active site conservation. N-terminal domains are colored in gray: LysM, PG-binding domain; CC, coiled-coil motif; DUF5930; Csd3_N2, autoinhibition domain identified in Csd3 of *H. pylori*; OapA, PG-binding domain identified in OapA of *H. influenzae*. Subclade architectures appear at an angle close to the arc of the sequences they represent. Some genes have more copies than the indicated number of N-terminal domains; for signal sequences or

(Continued)

FIGURE 1 | Continued
domains identified for each LytM factor gene, see **Supplementary Table 1**. For branch lengths and bootstrap values, see **Supplementary Figure 2**.
(B) Presence/absence of LytM clade members in each bacterial class. Bacterial classes are arranged in a cladogram drawn using phylogenies constructed from concatenated gene trees (Wu et al., 2009; Kysela et al., 2016). The number of representatives of each class is shown in parentheses. Presence/absence is indicated in the heat map using a gradient of green (100%) to yellow (50%) to red (0%). Only the genes in the tree in **(A)** are included. See **Supplementary Table 2** for presence/absence data for each species.

MepM ortholog Csd3 in its crystal structure (An et al., 2015). MepM has been genetically associated with the elongasome in *E. coli* (Park et al., 2020) whereas the ortholog in the alphaproteobacterium *Sinorhizobium meliloti* (named "RgsM") is a component of the polar elongasome (Krol et al., 2020). In agreement with *S. meliloti* and *A. tumefaciens* being close relatives and having polar elongation machinery in common, Atu4178 ($RgsM_{Atu}$) had similar properties as $RgsM_{Sm}$: $RgsM_{Atu}$-msfGFP was mostly diffuse with some observable foci at mid-cell and at one pole (**Figure 2B**). After several attempts to delete $RgsM_{Atu}$, we concluded it was essential, in agreement with its identification as an essential gene from high throughput transposon mutagenesis sequencing (Curtis and Brun, 2014). Thus, we constructed an RgsM depletion strain. In comparison to WT cells (**Supplementary Video 1**), depletion of RgsM inhibited polar elongation resulting in shortening of cells by 20 h (**Figure 2E** and **Supplementary Video 2**). Analysis of cell length indicated a significant decrease in cell length after depletion in comparison to WT or RgsM replete (+RgsM) cells (**Figure 2F**). Depletion of RgsM (−RgsM) results in a 5-log loss of viability confirming its essentiality (**Figure 2G**). The depletion of RgsM phenocopies the depletion of PBP1a, the major cell wall synthase driving polar elongation (Williams et al., 2021). These observations are consistent with characterization of $RgsM_{Sm}$ (Krol et al., 2020) suggesting that RgsM orthologs may function as a space-making DD-endopeptidases involved in the polar growth of Rhizobiales.

Agrobacterium tumefaciens conserves both divisome associated dLytM clades, EnvC (Atu2775) and NlpD (Atu1700). The EnvC protein architecture is characterized by a cleavable signal sequence, two or more coiled-coil domains, and an inactivated LytM domain (**Figure 1A**). The wide conservation of this gene suggests a common role in the proteobacterial divisome, where it activates cognate amidases, such as AmiAB in *E. coli* (Uehara et al., 2010) and AmiB in *V. cholerae* (Möll et al., 2014). $EnvC_{Atu}$-msfGFP expressed from a plasmid under native promoter control localized to mid-cell during cell division, suggesting that this role is also conserved in *Agrobacterium* (**Figure 2C**). However, deleting $envC_{Atu}$ resulted in shorter, hypercurved cells with a viability defect (**Figures 2E–G** and **Supplementary Video 3**). This phenotype differs from what has been reported for Δ*envC* strains in most other proteobacteria, where the deletion phenotype has been associated with cell separation defects, chaining, and often little to no viability loss (Hara et al., 2002; Uehara et al., 2009; Cserti et al., 2017; Zielińska et al., 2017).

Members of the NlpD clade contain a lipidation signal sequence for outer membrane anchoring, one or more PG-binding LysM domains that have been shown to help localize various NlpD orthologs (Goley et al., 2010; Möll et al., 2010; Poggio et al., 2010; Tsang et al., 2017), and a dLytM domain with a different inactivation pattern (two of the four chelating residues are generally conserved) (**Figure 1A**). In contrast to EnvC, this clade, as defined by its dLytM domain, appears to be constrained to the Alpha-, Beta-, and Gammaproteobacteria, while a few deep-branching proteobacteria have genes with a similar genetic architecture but active LytM domains (**Figures 1A,B**). NlpD has been extensively studied in *E. coli* where it activates AmiC and plays a role in outer membrane invagination during division (Uehara et al., 2009, 2010; Tsang et al., 2017). In *C. crescentus*, the NlpD ortholog "DipM" has been linked to cell separation and outer membrane invagination albeit with different morphological phenotypes than those typified by *E. coli* (Collier, 2010; Goley et al., 2010; Möll et al., 2010; Poggio et al., 2010; Zielińska et al., 2017). Expression of $dipM_{Atu}$-msfGFP from a constitutive promoter on a pSRK plasmid indicated that localization was cell cycle dependent, localizing to mid-cell in pre-divisional and dividing cells and to the new pole in non-dividing cells (**Figure 2D**). This is a typical localization pattern for divisome factors in *A. tumefaciens*, such as FtsZ and FtsA (Howell et al., 2019), supporting $DipM_{Atu}$'s role as a divisome component. However, we determined that *dipM* was essential, unlike NlpD orthologs in other proteobacteria. After multiple attempts to delete *dipM*, we constructed a depletion strain for DipM. Depletion of DipM resulted in filamented single cells with mid-cell bulges and loss of viability (**Figures 2E–G** and **Supplementary Video 4**). Similar to our observations for Δ*envC*, this phenotype was unexpectedly different from other proteobacteria, where NlpD is non-essential and the single mutant phenotype is either silent such as in *E. coli* (Uehara et al., 2009, 2010) and *V. cholerae* (Möll et al., 2014), or associated with cell separation defects such as in *N. gonorrhoeae* (Stohl et al., 2016), *H. influenzae* (Ercoli et al., 2015), or *C. crescentus* (Collier, 2010; Goley et al., 2010; Möll et al., 2010; Poggio et al., 2010; Zielińska et al., 2017). Given the uncharacteristic phenotypes of the divisome-associated LytM orthologs in *A. tumefaciens*, we focused on how these factors may function differently in this polar-growing Alphaproteobacterium.

EnvC and AmiC Are Required for Maintenance of Rod Shape and Proper Polar Patterning

Instead of a cell separation defect, which is expected for an ortholog of an amidase activator that functions in the final steps of division, Δ*envC* cells exhibited hypercurvature that was readily detectable in both phase contrast (**Figure 2E**) and DIC (**Figure 3A** and **Supplementary Video 3**) in LB. Cells appeared curled and at times smaller than WT cells

with no signs of cell separation defects. Similar, but less severe effects were seen in ATGN, a defined glucose-based medium (**Supplementary Figures 4A,B**). Although we were able to isolate Δ*envC* mutants on ATGN, the Δ*envC* strain exhibited very low viability in LB (**Figures 2G, 3B**) and suppressors arose fairly easily (data not shown), suggesting that EnvC plays a critical role in cell physiology. The morphological defects of Δ*envC* were complemented with a plasmid containing *envC* under native promoter control (**Figures 3A,B**). Although the cells did not exhibit observable cell separation defects, we tested other properties that have been associated with dLytM and amidase deletion strains in other proteobacteria, such as heightened susceptibility to detergents and salt concentrations (Möll et al., 2014; Zielińska et al., 2017). Δ*envC* was more sensitive to SDS and changes to salt concentrations (**Figure 3C**), suggesting that the defect may also include altered outer membrane stability and/or induce envelope stress. In addition, overproduction of EnvC resulted in a loss of viability (**Figure 3D**), suggesting it may activate cell wall hydrolases.

Given the data that EnvC localized to mid-cell during division and that Δ*envC* exhibited altered outer membrane stability, we used TEM to investigate the subcellular effects of the mutant. Whole cell TEM of Δ*envC* cells grown overnight indicated that the cells were hypercurved, bent, or kinked (**Figure 3E**). At low frequency in LB, some cells exhibited even more pleomorphic traits (**Supplementary Figure 4C**). The kinked or bent morphotypes were more frequently observed in Δ*envC* cells growing in ATGN as cells are generally longer and generate a more uniform rod morphology in this medium (**Supplementary Figure 4D**). In these cells, rather than being gradually curved along the entire cell length, the long axis appeared to be disrupted at one point that skewed the direction/alignment of elongation. This morphological defect may indicate that during the cell cycle, polar growth has become askew or misdirected from its normal polar trajectory that creates reliably straight rods. Thin section TEM indicated that cells did not exhibit any separation or outer membrane defects (**Figure 3F**), even in the most severe cases (see also **Supplementary Figures 4E,F**). Although dividing cells were rarely captured in our preparations of whole cells or thin sections, the few cases we did observe did not display any abnormalities in envelope structure (**Supplementary Figure 4F**). These data confirmed that loss of EnvC did not result in any typical cell separation defects, such as chaining or incomplete constriction of the PG and outer membrane layers, which is in marked contrast to what has been shown for other proteobacteria.

To observe how the Δ*envC* mutant grew and divided in real time, we performed time-lapse microscopy on cells growing on agar pads made with LB. The highly curved cell morphology made determination of division events difficult and hard to characterize (**Supplementary Video 3**). We were able to observe that the mutant displayed several defects in addition to hypercurvature that were generally associated with daughter cells (**Figure 3G**): a small percentage (about 10%) of cells elongated but did not appear to divide during the course of the experiment, indicating that division might be inhibited in a minority of cases. About 14% of the cells on the pad failed to elongate during the full course of the time-lapse experiment or after a division event, suggesting that despite division being possible, a portion of the population was unable to complete another cell cycle. Finally, about 25% of the cells exhibited a polarity defect: we were surprised to observe that after division, some daughter cells were seen to initiate elongation at the opposite pole than expected (**Figure 3H**). In WT cells, both the mother cell and daughter cell initiate growth at the pole produced by the division event, but in a subset of Δ$envC_{Atu}$ cells, the daughter cells instead grew from the other pole (**Figure 3G**). Together, these data suggest that, unlike other proteobacteria, loss of EnvC in *A. tumefaciens* has clear morphological defects that are not due to defects in cell separation but may instead be due to disruption of early polar growth patterning.

Disruption of polar growth patterning has been linked to loss of the AmiC and EnvC orthologs in *S. meliloti* (Krol et al., 2021), leading us to wonder if this relationship was conserved in *A. tumefaciens*. Indeed, Δ*amiC* cells exhibited a similar hypercurved phenotype, decreased viability on LB, and increased sensitivity to SDS and salt (**Figures 4A–C** and **Supplementary Video 5**). The Δ*amiC* phenotype was complemented with a plasmid carrying *amiC* under T7-medium constitutive promoter control (**Figures 4A,B**). Time-lapse microscopy indicated that Δ*amiC* cells displayed the same distinct growth behavior on agarose pads as Δ$envC_{Atu}$ (**Figure 4D**). The double mutant Δ*envC*Δ*amiC* exhibited a slightly more severe viability defect than Δ*amiC* but otherwise appeared to phenocopy the single mutants (**Figures 3B, 4B,D** and **Supplementary Video 6**). Together, this data suggested that, like in *S. meliloti*, EnvC and AmiC function in the same pathway.

We used CellTool (Pincus and Theriot, 2007) to run PCA on the mutant phenotypes to better compare them to WT and to each other (**Supplementary Figure 5A**). The largest deviation between the mutants and WT was attributed to cell curvature (shape mode 2, **Figure 4E**). Between mutants, the majority of the variance between Δ*envC* and Δ*amiC* was explained by cell length (shape mode 1, **Supplementary Figure 5B**). Both Δ*envC* and the double mutant were significantly shorter than WT and Δ*amiC*. Cell width (shape mode 3) contributed to a small amount of the morphological variance due to additive effects in the double mutant (**Supplementary Figure 5C**). While both single mutant strains were wider than WT, the double mutant strain was significantly wider than both. Overall, these differences support the idea that while EnvC and AmiC likely function in the same pathway (possibly by activation of AmiC by EnvC), EnvC appears to have additional roles in the cell and perhaps other regulatory partners.

All three mutants exhibited a similar polarity defect, in which the daughter cell that inherits the former growth pole initiates growth from either the new or old pole (**Figures 4F,G**). These observations are in agreement with data previously reported for *S. meliloti* (Krol et al., 2021). Like all alphaproteobacteria, *Agrobacterium* undergoes a dimorphic cell cycle with a non-motile mother cell that gives rise to a flagellated daughter cell. The cell cycle requires strict asymmetrical cellular patterning with unique poles. As a member of the polar-elongating Rhizobiales, during the cell cycle, the *Agrobacterium* mother cell grows polarly

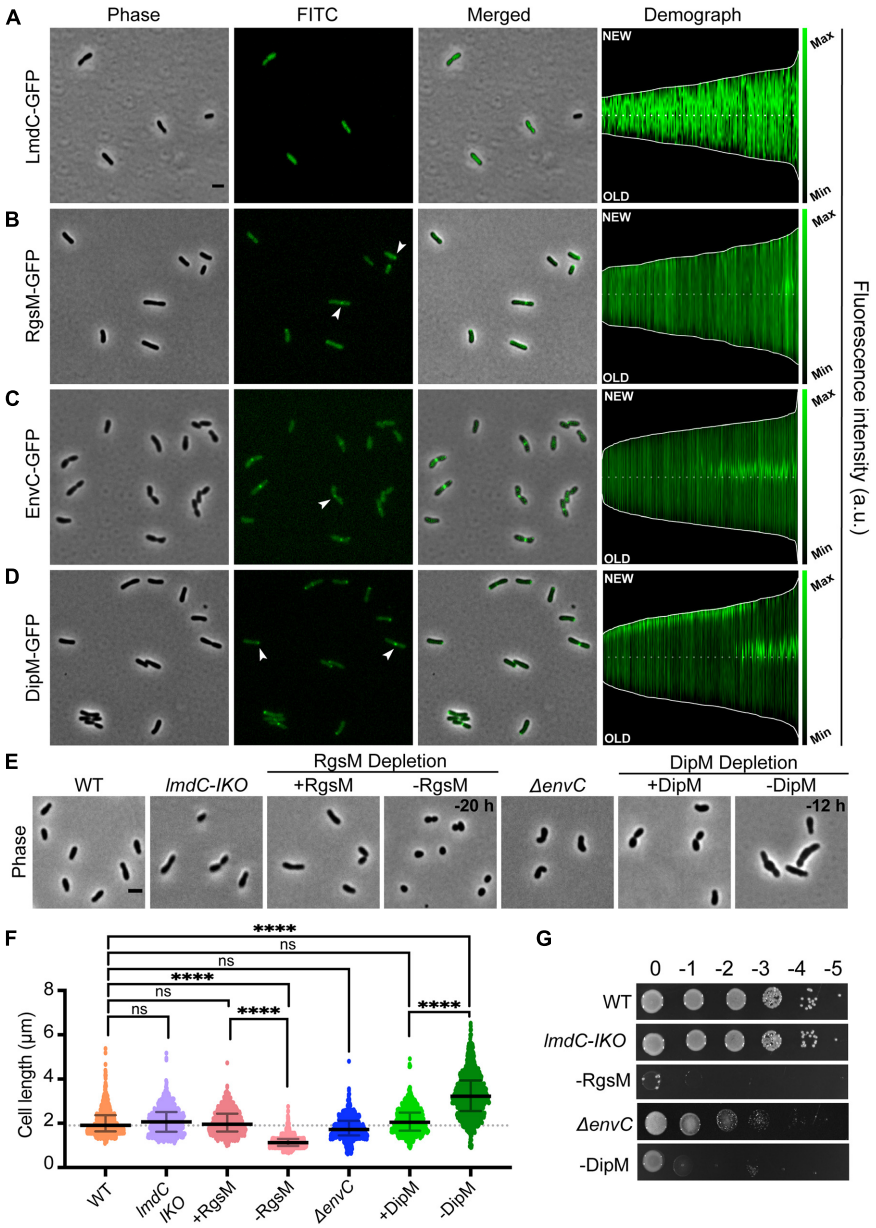

FIGURE 2 | *Agrobacterium tumefaciens* encodes four of the major LytM classes, each with distinct localization patterns and functional roles. (**A–D**, left) Subcellular localization patterns for each LytM-domain containing factor in wildtype (WT) cells. Cells expressing either LmdC-GFP (Pcym-LmdC), RgsM-GFP (Pcym-RgsM), EnvC–GFP (PenvC-EnvC), or DipM-GFP (PT7-DipM) were grown to exponential phase (OD600 ∼ 0.6) and imaged by phase and fluorescence microscopy. Scale bar = 2 μm. (**A–D**, right) Demographs depict the localization of each LytM-domain containing factor at the population level. Median profiles of GFP channel of ∼100 to 500 cells per strain were stacked and ordered by cell length. "New" = active growth pole, "Old" = inert pole. **(E)** Phase contrast microscopy of representative strains. **(F)** Cell length distribution of indicated strains grown in liquid media. The cell length distribution is shown in scattered dot plots. The middle dash line represents the WT median cell length, the error bars represent the interquartile range of the population. ****$P < 0.0001$, ns, not significantly different. **(G)** Cell viability for each strain is shown by spotting serial dilutions. IKO indicates an insertional knockout strain. All data collected for this figure was obtained from cells grown in LB.

at the new pole, the machinery relocates to mid-cell to drive division, and the division event produces two new poles that are primed to be elongation poles (**Figure 4G**). In all three mutants, about half of the daughter cells do not elongate from the newly created pole after completing division, but rather from the opposite (old) pole.

Together, these strong converging phenotypes suggest that the EnvC ortholog may activate AmiC in *A. tumefaciens*, and, moreover, that *A. tumefaciens* can complete division without an amidase. AmpD (Atu2113) is the only other canonical amidase in the *A. tumefaciens* genome and has been previously shown to function in the PG recycling

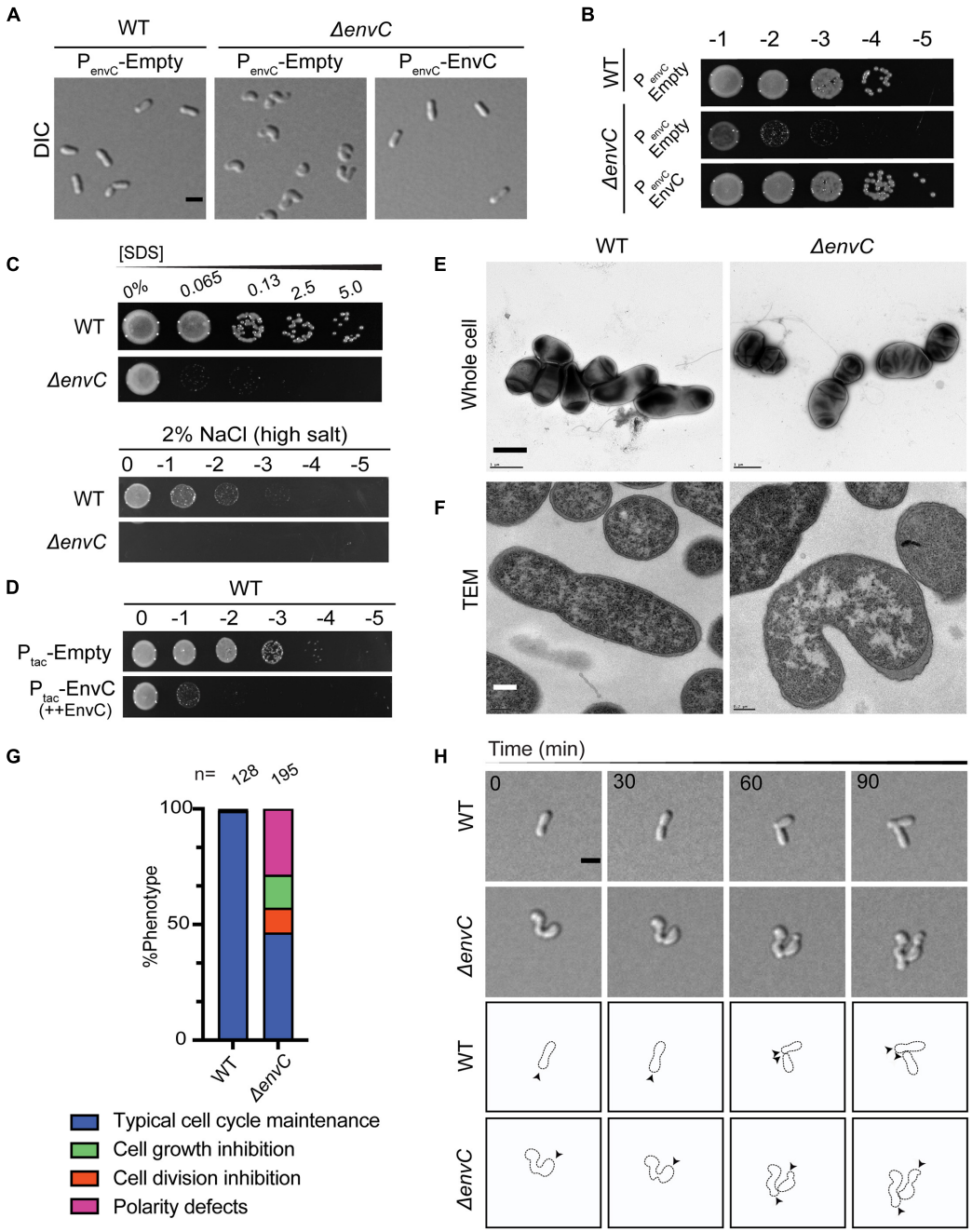

FIGURE 3 | Loss of *envC* results in cell curvature, decreased viability, and OM destabilization in *A. tumefaciens*. **(A)** DIC images of exponentially growing WT cells containing empty plasmid (PenvC-Empty), Δ*envC* containing empty plasmid (PenvC-Empty), or Δ*envC* expressing *envC via* its native promoter [PenvC-EnvC (complementing plasmid)]. **(B)** Cell viability of WT cells expressing empty plasmid (PenvC-Empty), Δ*envC* containing empty plasmid (PenvC-Empty), or Δ*envC* expressing *envC via* its native promoter [PenvC-EnvC (complementing plasmid)] is shown by spotting serial dilutions. **(C)** SDS and salt sensitivity of WT and Δ*envC*. Briefly, for the SDS assay, exponentially growing cells were treated with various concentrations of SDS for 5 min and spotted on LB plates and analyzed 24 h post incubation. To assess salt sensitivity, exponentially growing WT and Δ*envC* were serially diluted and spotted on LB solid medium containing 2% NaCl (high salt) and analyzed ∼36 h post incubation. **(D)** Cell viability of WT strain after overexpression of empty plasmid (Ptac-Empty) or *envC* under the control of the tac promoter (Ptac–EnvC). **(E)** TEM of whole cells of WT (left) *A. tumefaciens* or the Δ*envC* mutant (right). Cells were grown ∼16 h in LB to early stationary phase, fixed, and stained with 2% uranyl acetate. Scale bar = 1 μm. **(F)** Thin section TEM of WT (left) *A. tumefaciens* or the Δ*envC* mutant (right). Cells from **(E)** were embedded in resin and prepared as described in the methods. Scale bar = 0.2 μm. **(G)** Quantitative analysis of the phenotypes of the WT and Δ*envC* strains. % Phenotype was calculated by counting the number of cells in a WT and Δ*envC* time-lapses displaying one of the phenotypes indicated and dividing it by the total number of cells per strain. (**H**, top) Time-lapse microscopy of WT and Δ*envC* over the course of 90 min. Scale bar = 2 μm. (**H**, bottom) Schematic of WT and Δ*envC* time-lapses. Arrows indicate active growth. All data collected for this figure was obtained from cells grown in LB.

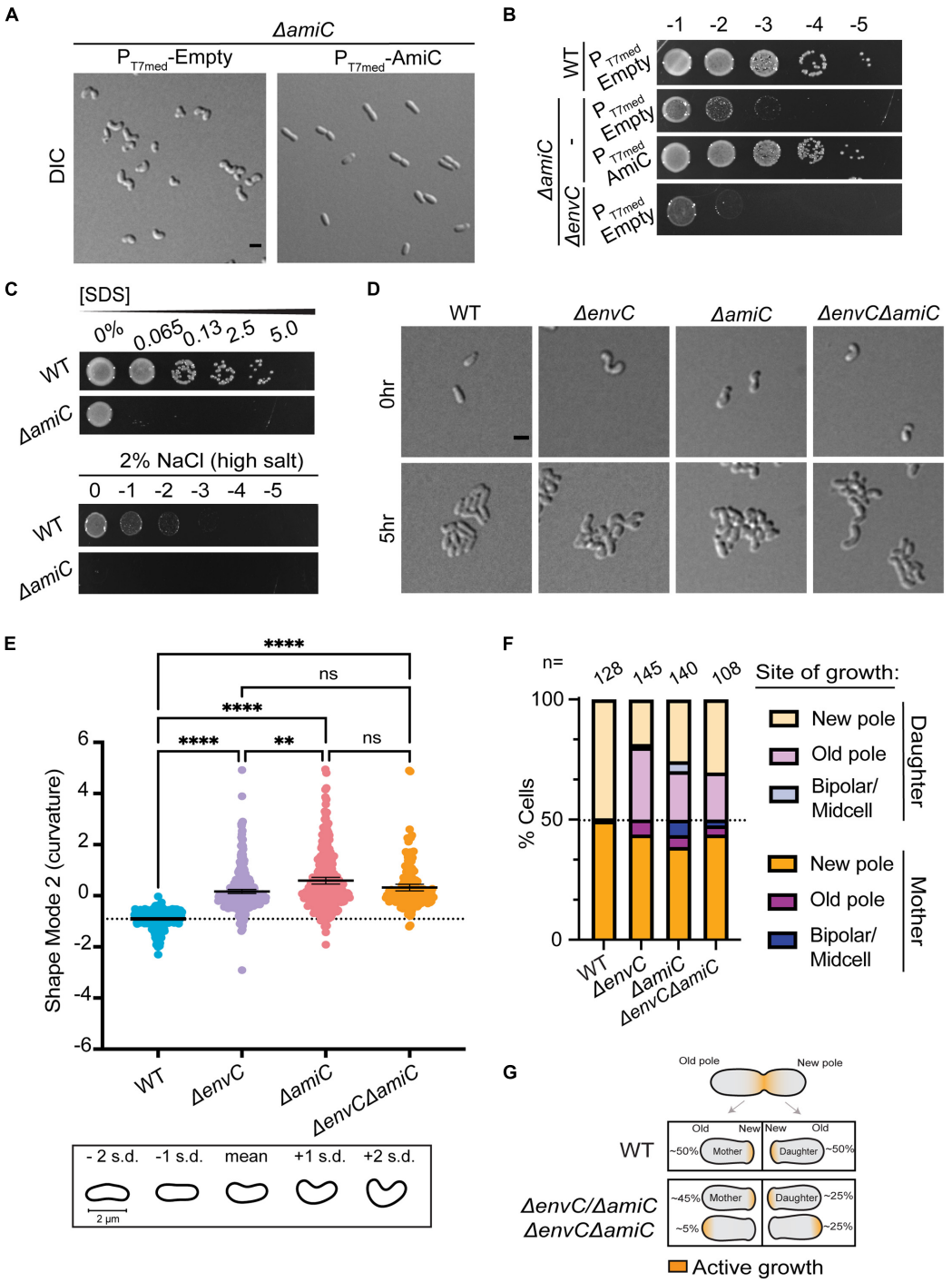

FIGURE 4 | EnvC likely functions in the same pathway as AmiC to help dictate proper polar patterning in *A. tumefaciens*. **(A)** DIC images of exponentially growing WT cells containing empty plasmid (PT7med-Empty), Δ*amiC* containing empty plasmid (PT7med-Empty), or Δ*amiC* constitutively expressing *amiC via* the T7 medium promoter [PT7med-AmiC (complementing plasmid)]. Scale bar = 2 μm. **(B)** Cell viability of WT cells containing empty plasmid (PT7med-Empty), Δ*amiC* containing empty plasmid (PT7med-Empty), or Δ*amiC* constitutively expressing *amiC via* the T7 medium promoter [PT7med-AmiC (complementing plasmid)] is shown by spotting serial dilutions. **(C)** SDS and salt sensitivity of WT and Δ*amiC* as described in **Figure 3**. **(D)** Cell morphology and microcolony formation are shown for WT, Δ*envC*, Δ*amiC*, and Δ*envC*Δ*amiC* at 0 and 5 h. Scale bar = 2 μm. **(E)** Scatter plot depicting shape mode 2 (curvature) from PCA of cell shape for WT, Δ*envC*, Δ*amiC*, and Δ*envC*Δ*amiC*. **(F)** Quantification of sites of growth initiation following cell division events captured during time-lapse imaging in WT, Δ*envC*, Δ*amiC*, and Δ*envC*Δ*amiC*. Daughter cells are defined as cells that inherit the former growth pole. **(G)** Schematic representation of cell growth polarity inheritance. In WT cells, most mother and daughter cells resume polar elongation at the new pole after completing cell division. However, in the absence of *envC*, *amiC*, or both, about 50% of the daughter cells initiate polar growth at the old pole. All data collected for this figure was obtained from cells grown in LB. $^{**}P < 0.01$; $^{****}P < 0.0001$; ns, not signficant.

pathway (Figueroa-Cuilan et al., 2020). Moreover, Δ*ampD* had no morphological defects and the Δ*ampD*Δ*amiC* double mutant morphologically phenocopied Δ*amiC* (**Supplementary Figures 6A–C**). We hypothesize that EnvC may activate AmiC; however, we find that the absence of AmiC does not bypass the toxicity induced by EnvC overexpression (**Supplementary Figure 6D**), consistent with an additional role for EnvC beyond the putative regulation of AmiC. Remarkably, AmiC no longer appears to be necessary for cell separation in Rhizobiales genera and instead it predominantly functions to help establish growth pole patterning in the daughter cell.

dLytM DipM Functions Early During Cell Division and Likely Intersects With the EnvC–AmiC Pathway

Like all NlpD orthologs studied so far, $DipM_{Atu}$-sfGFP localized to mid-cell during division (**Figure 2A**); unlike most NlpD orthologs studied so far, $DipM_{Atu}$ was essential. Depletion of DipM led to highly pleomorphic defects and lysis in most cells after 16 h of growth in LB and a strong cell viability defect (**Figures 5A,B** and **Supplementary Video 4**). DIC imaging of DipM-depleted cells showed that cells exhibited different combinations of mid-cell bulging, branching, overall loss of width control, and lysis by 16 h. The onset of these morphological effects is delayed in ATGN due to increased time for sufficient depletion of DipM; nevertheless DipM-depleted cells showed severe loss of viability on ATGN media in spot assays. Western blot analysis confirmed that the depletion of DipM was more rapid in LB than ATGN medium (**Supplementary Figure 7A**), presumably due to the faster growth rate.

To compare DipM to known properties of NlpD orthologs in other proteobacteria, we determined its overexpression phenotype and sensitivity to detergent. We overexpressed *dipM* by driving *dipM* expression from a plasmid under the pTAC promoter in WT cells. Overproduction of DipM severely reduced cell viability (**Figure 5C**), in agreement with the idea that it may activate hydrolytic factors such as shown in *Caulobacter* (Goley et al., 2010; Möll et al., 2010). While both depletion and overproduction of DipM resulted in loss of viability and lysis, these strains manifested lysis differently in that the overexpression strain did not exhibit the extreme pleomorphic traits of the depletion strain (**Supplementary Figures 6C,E**). Both the depletion strain and the overexpression strains were sensitive to SDS (**Figure 5D**), suggesting that both hypo- and hyperactivity of DipM regulation networks impact outer membrane stability or permeability. All of these observations are in line with what has been demonstrated in other proteobacterial genera (Goley et al., 2010; Möll et al., 2010, 2014; Tsang et al., 2017).

Because the depletion of DipM resulted in pleomorphic defects, we tracked the onset of changes in cell morphology and division over time using multiple approaches. Phase-contrast images of cells undergoing DipM depletion in liquid culture indicated morphological changes accumulate over time (**Figure 5E**): early on, cells elongated and often formed mid-cell bulges, and at later time points most cells appeared to be inhibited in division and had undergone both mid-cell bulging and various kinds of branching. Overall, these observations suggested that cells experienced loss of regulation of PG synthesis at mid-cell at low DipM levels and that in the absence of DipM, division was completely inhibited and the initiation of elongation was no longer strictly at the new pole. Next, we used time-lapse DIC microscopy to observe cells undergoing DipM depletion on agarose pads. In these experiments, we pre-depleted DipM for 6 h in liquid to avoid cell crowding caused by division events prior to sufficient DipM depletion (**Figure 5F** and **Supplementary Video 4**). It is likely that tracking the depletion in time-lapse allowed us to see many events and certain morphological trajectories that were more vulnerable to lysis and lost in sample handling for liquid culture time points. We found that each cell had its own unique trajectory that made it hard to generalize this phenotype and have included one example in **Figure 5F** to outline some major themes (see also **Supplementary Video 4**, for other examples). Of note, the cell in **Figure 5F** never terminated polar growth before division events, leading to tip-splitting and bipolar growth (see daughter cell behavior at 10, 15 h), formed ectopic poles at mid-cell bulges (see mother cell behavior at 10, 15h), and underwent erratic and atypical division events. The different types of branching (tip splitting or ectopic pole formation) observed during DipM depletion have been observed previously: tip splitting with FtsZ depletions and branching from mid-cell with FtsA and FtsW depletions (Howell et al., 2019). Moreover, bulging at mid-cell occurs in the absence of FtsW or both PBP3a and PBP3b and has been interpreted as an indicator of inhibition or misregulation of sPG synthesis (Howell et al., 2019; Williams et al., 2021). The combination of these defects in the depletion of DipM suggests a central role for DipM in the redirection of PG synthesis to mid-cell and subsequent cell division.

We used various forms of electron microscopy to determine the effect of the DipM depletion at the subcellular level. TEM and SEM of whole cells indicated a similar pattern to that seen in phase-contrast and DIC images of cells undergoing DipM depletion (**Figure 5G** and see also **Supplementary Figures 7B,C**). At 8 h, we observed particularly long cells that exhibited multiple bulges, suggesting that if these bulges are mid-cell bulges, these cells might have scaffolded more than one division plane (mid-cell region) over the course of their cell cycles but failed to divide (**Supplementary Figure 7B**). SEM of cells depleted for 9 h indicated rounds of failed constriction as well as multiple mid-cell bulges (**Figure 5G** and **Supplementary Figure 7D**). The accumulation of phenomena associated with the division plane suggests that DipM may play an indirect role in early division, such as stabilizing the divisome, and that depleting DipM may indirectly destabilize nascent, constricting Z-rings.

It seemed possible that some of the branched cellular filaments created by depleting DipM could consist of chained cells, or that areas with constrictions might have completed cytokinesis of the inner membrane but were still linked by PG and the outer membrane. However, thin section TEM of cells at various time points indicated that even cells with massive morphological

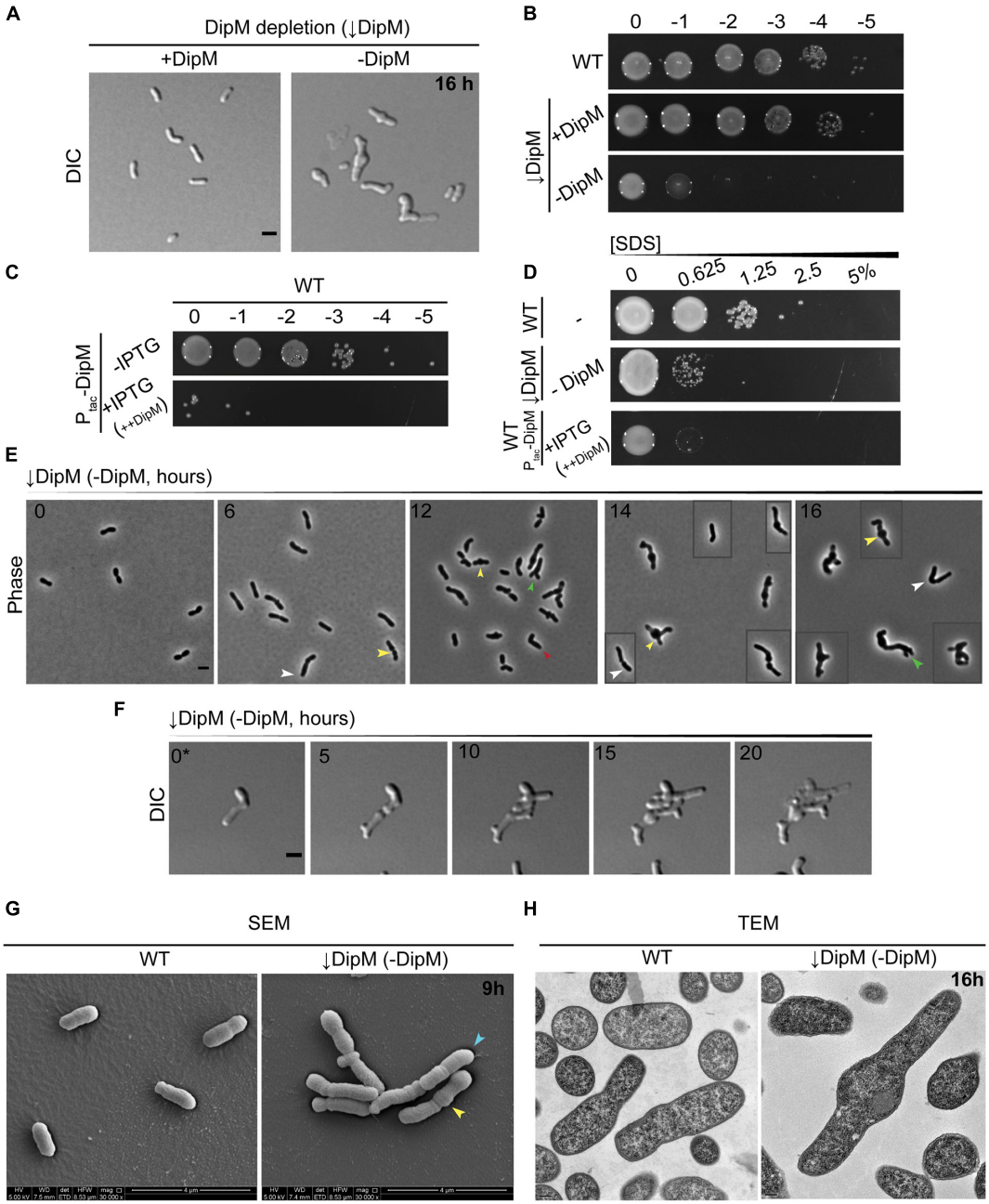

FIGURE 5 | *dipM* is essential in *A. tumefaciens* and depletion results in mid-cell bulging, inhibition of division, and ectopic pole formation. **(A)** DIC imaging of DipM replete (↓DipM, +DipM; grown in the presence of IPTG) and depleted cells (↓DipM, –DipM) for 16 h. Depletion of DipM (↓DipM, –DipM) was achieved by washing the cells three times in LB and resuspending the culture (OD600 ∼ 0.1) in LB –IPTG. DipM depletion in LB results in mid-cell bulges and cell lysis. Scale bar = 2 μm. **(B)** Spot viability assays of WT, DipM replete (↓DipM, +DipM) and DipM depleted ((DipM, −DipM). Depletion of DipM (↓DipM, –DipM) was achieved by washing the cells three times in LB before spotting on LB plates. **(C)** Spot viability assays of WT cells containing a plasmid encoded DipM under the control of the Ptac promoter in the absence (–IPTG, uninduced) and presence [+IPTG, induced (++DipM)] of inducer driving expression from the plasmid. ++DipM indicates that DipM is being overproduced. **(D)** Outer membrane integrity was assessed during SDS sensitivity. WT cells are more resistant than the DipM depletion (↓DipM, –DipM) or DipM overproduction (+IPTG, ++DipM) strains. DipM was overexpressed (+IPTG, ++DipM) for 4 h before the SDS treatment and plated on LB plates. **(E)** Phase contrast images of DipM depleted cells (–DipM) for 0, 6, 12, 14, and 16 h in liquid LB. Arrowheads indicate main DipM depletion phenotypes: yellow arrowheads, mid-cell bulges; green arrowheads, tip-splitting events; white arrowheads, increased cell length; red arrowheads, bent/kinked cells. Boxed cells are additional examples of the field. Scale bar = 2 μm. **(F)** Time-lapse microscopy of DipM depleted cells on LB-agarose pads for 20 h. 0* = DipM cells were pre-depleted for 6 h before starting the time-lapse to avoid overcrowding. Boxed cells are spliced from elsewhere in the field to provide additional examples of diverse morphotypes. Time in hours is indicated on the image. Scale bar = 2 μm. **(G)** Scanning electron microscopy of WT and DipM depleted cells for 9 h (scale bar = 4 μm). Arrowheads indicate main DipM depletion phenotypes: yellow arrowheads, mid-cell bulges; blue arrowheads, cell filamentation. **(H)** Thin section transmission electron microscopy of WT and DipM-depleted cells for 16 h. Scale bar = 0.2 μm. All data collected for this figure was obtained from cells grown in LB.

defects did not exhibit any abnormalities in their envelope layers along the cell length or at division sites (**Figure 5H** and see also **Supplementary Figure 7C**). Slices containing cells sectioned parallel to their long axis did not reveal any internal compartments separated by IM layers, verifying that cell chaining did not underlie the filamenting phenotype. These data indicate that the predominant effect of DipM depletion in *A. tumefaciens* was inhibition of division during early steps of constriction and not the final steps of septation, as shown for other proteobacteria.

Because the defects from depleting DipM could be associated with misregulation of septal hydrolases and because AmiC is directly regulated by the NlpD ortholog in *E. coli* (Uehara et al., 2010), we sought to determine any possible connection between these two genes in *A. tumefaciens*. We first wanted to determine if loss of AmiC would alleviate any of the manifold morphological defects of the DipM depletion. Depleting DipM in the Δ*amiC* background resulted in bloated, curved cells that appeared to exhibit a mixture of the two phenotypes with no improved outcomes in filamentation or viability (**Figures 6A,C,E** and **Supplementary Video 7**). In both time points of liquid culture and in time-lapse observations, it seemed possible that the mid-cell bulges were non-existent or reduced; however, the cumulative effects on cell width made this possible effect hard to determine. We also depleted DipM in the Δ*envC* background to determine if there were any EnvC-specific effects on the DipM depletion phenotype. The outcome was similar to, if not worse than, depleting DipM in the Δ*amiC* background, with additive effects on loss of width control (**Figures 6B,D,E** and **Supplementary Video 8**). In both cases, the double mutants appeared to exhibit a combination of the predominant features of Δ*amiC*/Δ*envC* and the DipM depletion.

The absence of EnvC or AmiC pathways exacerbated the DipM depletion phenotype suggesting that DipM functions in a pathway distinct from EnvC–AmiC or other EnvC pathways. We were therefore surprised to find that loss of AmiC completely alleviated the toxicity of *dipM* overexpression (**Figure 6F** and **Supplementary Figure 6D**). The absence of AmpD was not sufficient to relieve the toxicity of *dipM* overexpression (**Supplementary Figures 6C,D**). These results suggest that the toxic effects of *dipM* overexpression stem predominantly from crosstalk with the EnvC–AmiC pathway and is unrelated to its roles in regulating division or termination of elongation. Therefore, there is some overlap between the DipM and EnvC–AmiC pathways, but DipM's other roles in division and regulation of termination of elongation obscure this relationship during DipM depletion.

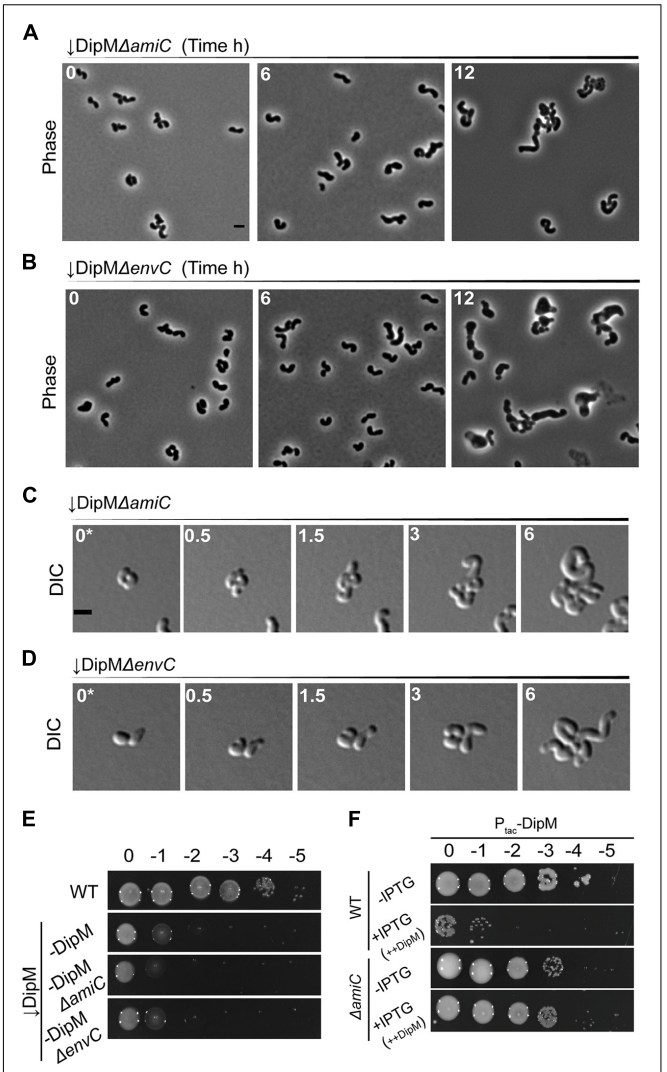

FIGURE 6 | DipM likely functions in pathways that are distinct from, but overlap with, the EnvC–AmiC pathway. Phase-contrast microscopy of **(A)** ↓DipMΔ*amiC* or **(B)** ↓DipMΔ*envC* depleted for exactly 0, 6, and 12 h. **(C)** DIC time-lapse of ↓DipMΔ*amiC* or **(D)** ↓DipMΔ*envC* pre-depleted for 6 h in liquid to avoid overcrowding caused by division events prior to sufficient DipM depletion. **(E)** Spot viability assays of WT, DipM depleted (–DipM), –DipMΔ*amiC*, and –DipMΔ*envC* cells. **(F)** Cell viability of WT and Δ*amiC* cells containing empty plasmid (Ptac-Empty) or overproducing DipM (+IPTG, ++DipM). ++DipM indicates that DipM is being overproduced. To better define the *dipM* overexpression phenotype in WT and Δ*amiC*, spotting assays were conducted in ATGN (minimal medium). All data collected for this figure was obtained from cells grown in LB.

DISCUSSION

LytM domain-containing proteins are widespread in the bacterial domain and have evolved to occupy many roles, most of which are still unknown. Of particular interest in this enzyme family is the frequency at which the catalytic site of this domain has been reconfigured and co-opted for non-enzymatic, regulatory purposes. Using bioinformatics, we determined that *A. tumefaciens* putatively encodes two enzymatically active LytM factors and two inactive (dLytM) factors. By constructing a gene tree of LytM factors from the Proteobacteria and their deep-branching relatives, we showed that these four LytM factors fall into four of five major clades that have orthologs and paralogs in other proteobacterial genera. Although the LmdC ortholog exhibited no clear localization pattern or null

phenotype, the MepM ortholog exhibited weak polar and mid-cell localization and was an essential polar elongation factor (**Figures 2**, **7**). This finding is in agreement with what has been shown for the MepM ortholog "RgsM" in *S. meliloti* (Krol et al., 2020), a close, polar-growing relative of *A. tumefaciens*. Both dLytM factors, $EnvC_{Atu}$ and $DipM_{Atu}$, localized to mid-cell during cell division, in agreement with most studies in proteobacteria that have shown that these factors are divisome components. However, neither dLytM depletion or deletion gave rise to expected cell separation defects in *Agrobacterium* despite consensus of cell separation defects reported in the literature for alphaproteobacterial genera (Cserti et al., 2017; Meier et al., 2017; Zielińska et al., 2017). Cell separation defects due to interrupting the Tol–Pal system have been observed in Rhizobiales member *S. meliloti*, where depletion of TolQ resulted in OM blebbing and envelope defects at the division plane (Krol et al., 2020). Neither Δ*envC* nor the DipM depletion in *A. tumefaciens* manifested as cell separation phenotypes.

Interpretation of phenotypes resulting from deletion/depletion of dLytMs in alphaproteobacterial members is challenging because divisome components potentially impact distinctly different cell cycles and growth modes in these genera. Given that *A. tumefaciens* is a polar-growing alphaproteobacterium, we expect division mutants to have distinct morphological phenotypes from other proteobacteria even if they maintain canonical function. For example, *A. tumefaciens* conserves many essential divisome components such as FtsZ, FtsA, and FtsW. Instead of forming long, smooth filaments typical of laterally elongating proteobacteria, the depletion of these factors results in a division defect unique to polar-growing bacteria. Depletion of FtsZ results in branched cells that accumulate growth poles, suggesting that FtsZ is required for redirection of growth machinery to mid-cell (Howell et al., 2019). In contrast, absence of FtsA or FtsW leads to continuous redirection of growth to mid-cell during each subsequent cell cycle. Since division has not occurred, ectopic growth poles form resulting in an asterisk-shaped cell that ultimately lyses (Howell et al., 2019). Given this framework, it is important to carefully interpret the dLytM mutants we observed in this study. We must determine whether the atypical phenotypes we observed are due to (1) the polar elongation context alone, (2) derived roles for these factors in polar growth in the Rhizobiales, or even (3) ancient and shared roles of these factors that are more evident in this genetic background than other proteobacteria. Although this task will ultimately require many more studies, there are some hypotheses we can make with our current observations.

Because the DipM depletion resulted in a clear division defect, we will consider it first. DipM was unexpectedly essential, and inspection of DipM-depleted cells explained why: depletion of DipM resulted in cells with inefficient termination of polar growth and critical deficiencies in the regulation of sPG synthesis resulting in multiple rounds of attempted cell division. These observations suggest that DipM plays multiple roles in *A. tumefaciens* (**Figure 7**). Some roles may be the same as already demonstrated in other proteobacteria, where NlpD orthologs have been shown or suggested to regulate the activity of hydrolases besides amidases (Uehara et al., 2009; Möll et al., 2014; Zielińska et al., 2017). Misregulation of hydrolases and/or autolysins at mid-cell could explain the mid-cell bulging phenotype. We can also attribute some roles to derived functions for Rhizobiales, as the loss of termination of elongation during the cell cycle was pronounced in many of the cells we observed in time-lapse. Because the types of branching (tip-splitting vs. formation of ectopic poles at mid-cell) were varied, it is possible that this is an indirect effect *via* interactions with the divisome or elongasome. Indeed, this brings us to the final point, that the clear marks of initiated but failed rounds of constriction in the DipM-depleted cells suggests that DipM may indirectly help stabilize the nascently constricting divisome. This final role may be shared by other proteobacteria as Δ*dipM* was shown to perturb FtsZ behavior in *Caulobacter* (Poggio et al., 2010) and *Pseudomonas* Δ*nlpD* cells exhibited early inhibition of constriction in cell filaments (Yakhnina et al., 2015). We conclude that the NlpD ortholog of *A. tumefaciens* functions in conserved, derived, and potentially undetected ancestral roles.

While *envC* was not essential in *A. tumefaciens*, its loss greatly reduced cell viability. Δ*envC* cells were hypercurved and somewhat smaller than WT cells. Time-lapse microscopy revealed that a subset of the Δ*envC* population aberrantly initiated elongation at the old pole. Quantification of these defects suggested that they occur primarily in the daughter cells, perhaps suggesting that the loss of viability in this mutant is due to the production of a significant number of non-viable daughter cells. Therefore, the primary function of EnvC in *A. tumefaciens* appears to lie in its role in polar growth patterning (**Figure 7**). We found that AmiC also appears to function in this pathway, as its deletion strain and double mutant with EnvC generally phenocopy Δ*envC*. Krol et al. (2021) have demonstrated similar phenomena in *S. meliloti*, and have further shown that the EnvC–AmiC pathway facilitates the accumulation of the FtsN-like protein RgsS at mid-cell, presumably by binding amidase-processed PG at the septum. Overall, these observations suggest a derived function for EnvC in the Rhizobiales in which the AmiC pathway has at least been partially co-opted for polar growth patterning. Like DipM, however, EnvC appeared to function in multiple pathways, suggesting that while it has been co-opted, it may also still maintain some ancestral functions that are masked by the dominant polarity defects. The connection between EnvC and AmiC has been suggested in genetic studies of other Alphaproteobacteria. However, in *C. crescentus*, *in vitro* assays showed that the dLytM domain of $NlpD_{Cc}$ ("DipM") mildly stimulated $AmiC_{Cc}$ rather than that of $EnvC_{Cc}$ ("LdpF") (Meier et al., 2017), as expected from similar experiments for *E. coli* orthologs. Therefore the molecular details of this putative EnvC–AmiC pathway might not resemble the EnvC–AmiAB regulatory mechanism demonstrated in *E. coli* (Uehara et al., 2010) and needs further study in *A. tumefaciens*.

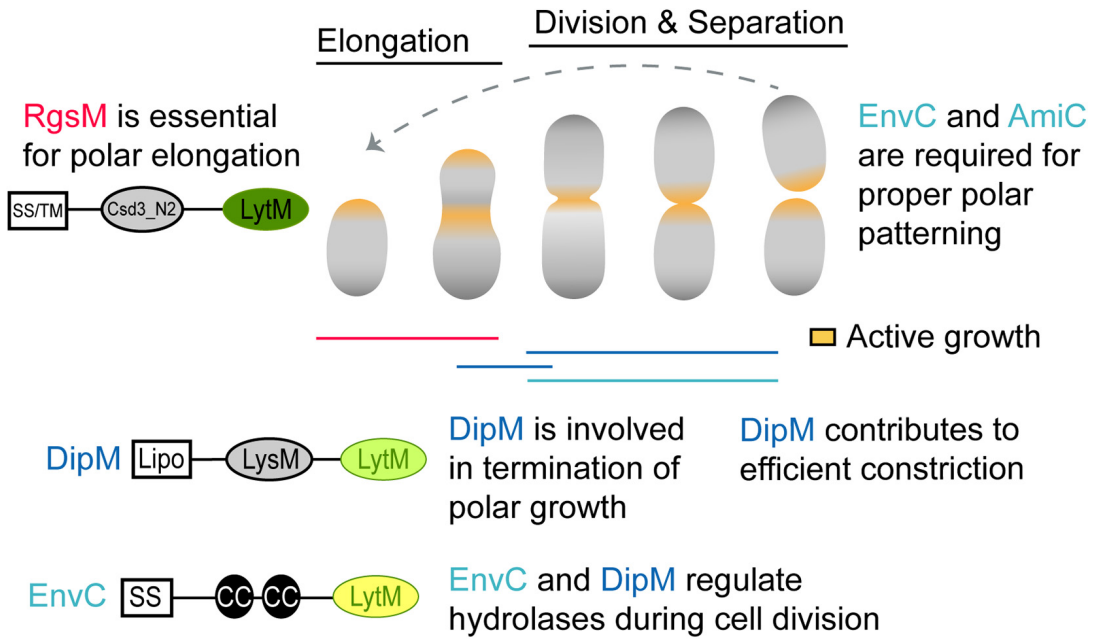

FIGURE 7 | Schematic of proposed LytM factor functions in *A. tumefaciens*. During polar elongation, the essential RgsM likely functions at the new pole, where it likely modifies the cell wall to allow the addition of new PG material. DipM also localizes to the new pole during polar elongation and polar elongation often fails to terminate in absence of DipM, suggesting that DipM may interact with the elongasome and cell wall hydrolases to help regulate unipolar growth. In the absence of DipM the redirection of growth to mid-cell occurs but frequently leads to mid-cell bulges rather than cell division suggesting that DipM likely regulates PG hydrolases involved in early stages of cell division. Finally, EnvC regulates the activity of AmiC at mid-cell during cell division. While this is a canonical function for a dLytM factor, EnvC and AmiC are not required for cell separation but rather for proper establishment of growth poles following cell division. Protein schematics are shown as described in **Figure 1**.

Our phylogenetic approach allowed us a large, if coarse-grained, view of LytM domain evolution. By collecting LytM domain-containing proteins from various proteobacterial and deep-branching proteobacterial relatives, we were able to distinguish five different LytM clades. The short length of the LytM domain (110–120 amino acids) does not give enough signal for confidence in the branching order and therefore the evolutionary relationships of these clades (**Supplementary Figure 2**). Within this study, we can only reliably infer which orthologs a bacterium encodes. It is also important to note that our current study only captured a subset of LytM families and it is likely that with enough sampling of deep-branching proteobacteria, many of the unclassified LytM proteins (thin branches in **Figure 1A** and classified as "other" in **Figure 1B**) would form distinct clades. It is clear that the LytM domain, in both its enzymatic and inactivated forms, has evolved to participate in many different pathways in different classes or genera. Although our analysis has categorized these genes into five major clades, this classification in no way suggests a shared functional role, only a shared ancestral past. For example, the Csd LytM factors that play a role in the helical morphology of *H. pylori* have arisen from both the MepM (Csd3) and LmdC (Csd1 and Csd2) clades (An et al., 2015, 2016; Yang et al., 2019). The MepM ortholog of *N. gonorrhoeae*, Mpg, has been shown to be a virulence factor required for pilus biogenesis and natural competence (Stohl et al., 2012, 2013).

Even clades that we suppose are more constrained by critical roles in division, namely the dLytM clades, have members that have been shown to exhibit derived (class or species-specific) functions, such as influencing protein secretion in *H. influenzae* (Ercoli et al., 2015), T3S apparatus assembly in *X. campestris* (Yang et al., 2018), and stalk biogenesis in *C. crescentus* (Billini et al., 2019). While we cannot determine a branching order for the EnvC and NlpD classes with great confidence using our current approach, using the LytM domain tree in combination with the conserved N-terminal domains makes it possible to infer that EnvC and NlpD were likely inactivated independently from each other. The inactivated enzymatic site itself has been shown to participate in autoinhibitory regulation of both EnvC and AmiB (Peters et al., 2013; Cook et al., 2020), making it an interesting motif to track in both NlpD and EnvC lineages. In general, NlpD orthologs conserve two of the signature residues and have at least one conserved substitution [**N**XXXD (**K**/X)XH] whereas EnvC orthologs conserve none of the signature residues and also exhibit distinct substitution patterns among bacterial classes [(**W**/X)XXX, XX**Y**] (**Supplementary Figure 2**). The conserved yet distinct substitutions in both of these clades reflects their divergence, potentially driven by coevolution with amidases or other potential regulatory partners. In support of this argument, the tryptophan (W) and tyrosine (Y) substitutions in the catalytic site of EnvC have been shown to be required for the activation of cognate amidase AmiB in *E. coli*

(Peters et al., 2013). Conservation of these clade-specific substitutions suggests overall maintenance of regulatory partners among various proteobacteria.

Nevertheless, the data from different proteobacterial species seem to suggest that the relationship between dLytMs and their cognate amidases could be plastic: in some cases, a dLytM has been shown to activate more than one amidase, such as ActS in *E. coli* (Gurnani Serrano et al., 2021); in others multiple dLytM factors are thought to activate one amidase, such as in *V. cholerae* (Möll et al., 2014) or *P. aeruginosa* (Yakhnina et al., 2015); and in still others, dLytM factors could activate a different amidase than in *E. coli*, such as could be the case in *H. neptunium* (Cserti et al., 2017), *S. meliloti* (Krol et al., 2021), and *A. tumefaciens*. Our limited analysis of 178 LytM domains does not indicate for any of these aforementioned species that their dLytM domain sequences contain substitutions that would suggest shifts in protein partners or function. For example, if Rhizobiales dLytM genes had evolved entirely different roles from other proteobacteria, we expect them to form distinct clusters away from the other alphaproteobacteria on the tree, such as how the EnvC orthologs in the Epsilonproteobacteria form a cluster distinct from the rest of all of the EnvC orthologs, or the Rhodobacterales NlpD orthologs form a distinct cluster from the other alphaproteobacterial NlpD orthologs (**Figure 1A**). While the dLytM domains themselves do not indicate strong evidence of positive selection for new partners or function, it is much more likely that the N-terminal domains in the full length LytM genes may be the areas where diversification and subfunctionalization would take place. In fact, in *V. cholerae*, where both dLytM factors appear to regulate $AmiB_{Vc}$, the LytM domain of $NlpD_{Vc}$ does not appear to be necessary for this activation (Möll et al., 2014). This may indicate that amidases could be activated by LytM domains in ways that are much more diverse than currently appreciated.

In summary, we have taken the first steps to characterize the LytM factors of *A. tumefaciens*. The dLytM factors were particularly interesting in that their loss gave rise to unexpected phenotypes that suggest they both operate as regulatory hubs with potentially many partners to influence distinct and overlapping processes during the cell cycle (**Figure 7**). Although the essentiality of DipM made it difficult to assess the potential intersection of these pathways, our preliminary observations that the mid-cell bulging during DipM depletion and the toxicity of *dipM* overexpression were alleviated in the Δ*amiC* strain support this idea. The implication of both of these factors in polar processes might suggest that their dominant functions are derived for polar growth regulation in Rhizobiales, however, that might not necessarily be true. Deletion of DipM in *C. crescentus* resulted in mislocalization of polarity factor PopZ to both poles (Möll et al., 2010). Deletion of FtsE, the recruiter of EnvC, in *C. crescentus* resulted in thin cellular connections between mother and daughter cells that accumulated stalk biogenesis factors and stalk features (Meier et al., 2017). Together, these could suggest that dLytM factors play roles in influencing polarity in alphaproteobacteria in general. Finally, although polarity is not generally studied in bacteria that divide symmetrically, such as the Gamma- and Betaproteobacteria, studies have indicated that molecular polarity in *E. coli* manifests in aging effects (Lindner et al., 2008) and polar cytoplasmic features, such as chemosensory arrays (Rajendran et al., 2014; Santos et al., 2014; Oh et al., 2018). It is our hope that our work in a more recognizably polar bacterium inspires others to look for polarity and factors that may influence it in their own systems.

DATA AVAILABILITY STATEMENT

The original contributions presented in the study are included in the article/**Supplementary Material**, further inquiries can be directed to the corresponding author.

AUTHOR CONTRIBUTIONS

WF-C and AR were responsible for conceptualization, formal analysis, investigation, methodology, validation, visualization, writing the original draft, and reviewing and editing. CD, GS-C, and AY contributed to the investigation. AR and PB acquired funding to support this research. PB contributed to conceptualization, project administration, resources, supervision, and editing and revising. All authors contributed to the article and approved the submitted version.

FUNDING

Research on cell growth and division in the Brown lab is supported by the National Science Foundation (IOS1557806). WF-C and GS-C were funded by a training grant from the National Institute of Health (NIGMS R25 GM 056901). WF-C was also supported by a Gus T. Ridgel Fellowship from the Graduate School at the University of Missouri and the Initiative for Maximizing Student Development (IMSD) Program (T32). This work was supported by the Excellence in Electron Microscopy Award provided by the University of Missouri Electron Microscopy Core and the Office of Research to AR and PB.

ACKNOWLEDGMENTS

We thank Michelle A. Williams for assistance in characterization of the RgsM depletion strain, Jeremy Daniel for construction of the pSRKKM-PT7 and pSRKKM-PcymR vectors, Erin Goley for providing the *Caulobacter* anti-DipM antibody and providing feedback on this data and manuscript, and David Kysela for consultation on the phylogenetic tree construction. We also thank the University of Missouri Electron Microscopy Core (EMC), the Office of Research, as well as the Excellence in Electron Microscopy Grant for training and supervision in electron microscopy. In particular, we recognize EMC members DeAna G. Grant for thin section preparation and supervision in TEM data collection and David Stalla for SEM data collection. We appreciate the Cherng

Summer Scholar Program and the Office of Undergraduate Research at the University of Missouri for their support of undergraduate students AY and CD, respectively. Lastly, we thank members of the Brown lab for critical reading of this manuscript.

SUPPLEMENTARY MATERIAL

The Supplementary Material for this article can be found online at: https://www.frontiersin.org/articles/10.3389/fmicb.2021.729307/full#supplementary-material

REFERENCES

Almagro Armenteros, J. J., Tsirigos, K. D., Sønderby, C. K., Petersen, T. N., Winther, O., Brunak, S., et al. (2019). SignalP 5.0 improves signal peptide predictions using deep neural networks. *Nat. Biotechnol.* 37, 420–423. doi: 10.1038/s41587-019-0036-z

An, D. R., Im, H. N., Jang, J. Y., Kim, H. S., Kim, J., Yoon, H. J., et al. (2016). Structural basis of the Heterodimer formation between cell shape-determining proteins Csd1 and Csd2 from *Helicobacter pylori*. *PLoS One* 11:e0164243. doi: 10.1371/journal.pone.0164243

An, D. R., Kim, H. S., Kim, J., Im, H. N., Yoon, H. J., Yoon, J. Y., et al. (2015). Structure of Csd3 from *Helicobacter pylori*, a cell shape-determining metallopeptidase. *Acta Crystallogr. D Biol. Crystallogr.* 71, 675–686. doi: 10.1107/S1399004715000152

Billini, M., Biboy, J., Kühn, J., Vollmer, W., and Thanbichler, M. (2019). A specialized MreB-dependent cell wall biosynthetic complex mediates the formation of stalk-specific peptidoglycan in *Caulobacter crescentus*. *PLoS Genet.* 15:e1007897. doi: 10.1371/journal.pgen.1007897

Bochtler, M., Odintsov, S. G., Marcyjaniak, M., and Sabala, I. (2004). Similar active sites in lysostaphins and D-Ala-D-Ala metallopeptidases. *Protein Sci. Publ. Protein Soc.* 13, 854–861. doi: 10.1110/ps.03515704

Cameron, T. A., Zupan, J. R., and Zambryski, P. C. (2015). The essential features and modes of bacterial polar growth. *Trends Microbiol.* 23, 347–353. doi: 10.1016/j.tim.2015.01.003

Cava, F., Kuru, E., Brun, Y. V., and de Pedro, M. A. (2013). Modes of cell wall growth differentiation in rod-shaped bacteria. *Curr. Opin. Microbiol.* 16, 731–737. doi: 10.1016/j.mib.2013.09.004

Chaput, C., Ecobichon, C., Pouradier, N., Rousselle, J.-C., Namane, A., and Boneca, I. G. (2016). Role of the N-Acetylmuramoyl-l-Alanyl Amidase, AmiA, of *Helicobacter pylori* in Peptidoglycan metabolism, daughter cell separation, and virulence. *Microb. Drug Resist.* 22, 477–486. doi: 10.1089/mdr.2016.0070

Chen, I.-M. A., Markowitz, V. M., Chu, K., Palaniappan, K., Szeto, E., Pillay, M., et al. (2017). IMG/M: integrated genome and metagenome comparative data analysis system. *Nucleic Acids Res.* 45, D507–D516. doi: 10.1093/nar/gkw929

Collier, J. (2010). A new factor stimulating peptidoglycan hydrolysis to separate daughter cells in *Caulobacter crescentus*. *Mol. Microbiol.* 77, 11–14. doi: 10.1111/j.1365-2958.2010.07225.x

Cook, J., Baverstock, T. C., McAndrew, M. B. L., Stansfeld, P. J., Roper, D. I., and Crow, A. (2020). Insights into bacterial cell division from a structure of EnvC bound to the FtsX periplasmic domain. *Proc. Natl. Acad. Sci. U.S.A.* 117, 28355–28365. doi: 10.1073/pnas.2017134117

Crooks, G. E., Hon, G., Chandonia, J.-M., and Brenner, S. E. (2004). WebLogo: a sequence logo generator. *Genome Res.* 14, 1188–1190. doi: 10.1101/gr.849004

Cserti, E., Rosskopf, S., Chang, Y.-W., Eisheuer, S., Selter, L., Shi, J., et al. (2017). Dynamics of the peptidoglycan biosynthetic machinery in the stalked budding bacterium *Hyphomonas neptunium*. *Mol. Microbiol.* 103, 875–895. doi: 10.1111/mmi.13593

Curtis, P. D., and Brun, Y. V. (2014). Identification of essential alphaproteobacterial genes reveals operational variability in conserved developmental and cell cycle systems. *Mol. Microbiol.* 93, 713–735. doi: 10.1111/mmi.12686

Das, D., Hervé, M., Elsliger, M.-A., Kadam, R. U., Grant, J. C., Chiu, H.-J., et al. (2013). Structure and function of a novel ld-Carboxypeptidase A Involved in Peptidoglycan Recycling. *J. Bacteriol.* 195, 5555–5566. doi: 10.1128/JB.00900-13

Do, T., Page, J. E., and Walker, S. (2020). Uncovering the activities, biological roles, and regulation of bacterial cell wall hydrolases and tailoring enzymes. *J. Biol. Chem.* 295, 3347–3361. doi: 10.1074/jbc.REV119.010155

Dubey, A., and Priyadarshini, R. (2018). Amidase activity is essential for medial localization of AmiC in *Caulobacter crescentus*. *Curr. Genet.* 64, 661–675. doi: 10.1007/s00294-017-0781-9

Ducret, A., Quardokus, E. M., and Brun, Y. V. (2016). MicrobeJ, a tool for high throughput bacterial cell detection and quantitative analysis. *Nat. Microbiol.* 1:16077. doi: 10.1038/nmicrobiol.2016.77

Edgar, R. C. (2004). MUSCLE: multiple sequence alignment with high accuracy and high throughput. *Nucleic Acids Res.* 32, 1792–1797. doi: 10.1093/nar/gkh340

Egan, A. J. F., Errington, J., and Vollmer, W. (2020). Regulation of peptidoglycan synthesis and remodelling. *Nat. Rev. Microbiol.* 18, 446–460. doi: 10.1038/s41579-020-0366-3

Ercoli, G., Tani, C., Pezzicoli, A., Vacca, I., Martinelli, M., Pecetta, S., et al. (2015). LytM proteins play a crucial role in cell separation, outer membrane composition, and pathogenesis in Nontypeable *Haemophilus influenzae*. *mBio* 6:e02575-14. doi: 10.1128/mBio.02575-14

Figueroa-Cuilan, W., Daniel, J. J., Howell, M., Sulaiman, A., and Brown, P. J. B. (2016). Mini-Tn7 insertion in an artificial attTn7 Site enables depletion of the essential master regulator CtrA in the Phytopathogen *Agrobacterium tumefaciens*. *Appl. Environ. Microbiol.* 82, 5015–5025. doi: 10.1128/AEM.01392-16

Figueroa-Cuilan, W. M., and Brown, P. J. B. (2018). Cell wall biogenesis during elongation and division in the plant pathogen *Agrobacterium tumefaciens*. *Curr. Top. Microbiol. Immunol.* 418, 87–110. doi: 10.1007/82_2018_92

Figueroa-Cuilan, W. M., Howell, M., Richards, C., Randich, A., Yadav, A. K., Cava, F., et al. (2020). Induction of AmpC-mediated β-lactam resistance requires a single lytic transglycosylase in *Agrobacterium tumefaciens*. *bioRxiv* [Preprint]. doi: 10.1101/2020.09.10.292490

Firczuk, M., and Bochtler, M. (2007). Folds and activities of peptidoglycan amidases. *FEMS Microbiol. Rev.* 31, 676–691. doi: 10.1111/j.1574-6976.2007.00084.x

Firczuk, M., Mucha, A., and Bochtler, M. (2005). Crystal Structures of Active LytM. *J. Mol. Biol.* 354, 578–590. doi: 10.1016/j.jmb.2005.09.082

Garcia, D. L., and Dillard, J. P. (2006). AmiC Functions as an N-Acetylmuramyl-l-Alanine Amidase Necessaryfor Cell Separation and Can Promote Autolysis in *Neisseria gonorrhoeae*. *J. Bacteriol.* 188, 7211–7221. doi: 10.1128/JB.00724-06

Goley, E. D., Comolli, L. R., Fero, K. E., Downing, K. H., and Shapiro, L. (2010). DipM links peptidoglycan remodeling to outer membrane organization in *Caulobacter*. *Mol. Microbiol.* 77, 56–73. doi: 10.1111/j.1365-2958.2010.07222.x

Grabowska, M., Jagielska, E., Czapinska, H., Bochtler, M., and Sabala, I. (2015). High resolution structure of an M23 peptidase with a substrate analogue. *Sci. Rep.* 5:14833. doi: 10.1038/srep14833

Gumerov, V. M., and Zhulin, I. B. (2020). TREND: a platform for exploring protein function in prokaryotes based on phylogenetic, domain architecture and gene neighborhood analyses. *Nucleic Acids Res.* 48, W72–W76. doi: 10.1093/nar/gkaa243

Gurnani Serrano, C. K., Winkle, M., Martorana, A. M., Biboy, J., Morè, N., Moynihan, P., et al. (2021). ActS activates peptidoglycan amidases during outer membrane stress in *Escherichia coli*. *Mol. Microbiol.* doi: 10.1111/mmi.14712 [Epub ahead of print].

Hara, H., Narita, S., Karibian, D., Park, J. T., Yamamoto, Y., and Nishimura, Y. (2002). Identification and characterization of the *Escherichia coli* envC gene encoding a periplasmic coiled-coil protein with putative peptidase activity. *FEMS Microbiol. Lett.* 212, 229–236. doi: 10.1111/j.1574-6968.2002.tb11271.x

Heidrich, C., Templin, M. F., Ursinus, A., Merdanovic, M., Berger, J., Schwarz, H., et al. (2001). Involvement of N-acetylmuramyl-l-alanine amidases in cell separation and antibiotic-induced autolysis of *Escherichia coli*. *Mol. Microbiol.* 41, 167–178. doi: 10.1046/j.1365-2958.2001.02499.x

Heidrich, C., Ursinus, A., Berger, J., Schwarz, H., and Höltje, J.-V. (2002). Effects of multiple deletions of Murein Hydrolases on viability, septum cleavage, and sensitivity to large toxic molecules in *Escherichia coli*. *J. Bacteriol.* 184, 6093–6099. doi: 10.1128/JB.184.22.6093-6099.2002

Höltje, J. V. (1998). Growth of the stress-bearing and shape-maintaining murein sacculus of *Escherichia coli*. *Microbiol. Mol. Biol. Rev.* 62, 181–203. doi: 10.1128/MMBR.62.1.181-203.1998

Howell, M., Aliashkevich, A., Sundararajan, K., Daniel, J. J., Lariviere, P. J., Goley, E. D., et al. (2019). *Agrobacterium tumefaciens* divisome proteins regulate the transition from polar growth to cell division. *Mol. Microbiol.* 111, 1074–1092. doi: 10.1111/mmi.14212

Howell, M., Daniel, J. J., and Brown, P. J. B. (2017). Live cell fluorescence microscopy to observe essential processes during microbial cell growth. *J. Vis. Exp.* 129:e56497. doi: 10.3791/56497

Jacobs, C., Joris, B., Jamin, M., Klarsov, K., van Beeumen, J., Mengin-Lecreulx, D., et al. (1995). AmpD, essential for both β-lactamase regulation and cell wall recycling, is a novel cytosolic N-acetylmuramyl-L-alanine amidase. *Mol. Microbiol.* 15, 553–559. doi: 10.1111/j.1365-2958.1995.tb02268.x

Krogh, A., Larsson, B., von Heijne, G., and Sonnhammer, E. L. (2001). Predicting transmembrane protein topology with a hidden Markov model: application to complete genomes. *J. Mol. Biol.* 305, 567–580. doi: 10.1006/jmbi.2000.4315

Krol, E., Stuckenschneider, L., Kästle Silva, J. M., Graumann, P. L., and Becker, A. (2021). Stable inheritance of *Sinorhizobium meliloti* cell growth polarity requires an FtsN-like protein and an amidase. *Nat. Commun.* 12:545. doi: 10.1038/s41467-020-20739-3

Krol, E., Yau, H. C. L., Lechner, M., Schäper, S., Bange, G., Vollmer, W., et al. (2020). Tol-Pal system and Rgs proteins interact to promote unipolar growth and cell division in *Sinorhizobium meliloti*. *mBio* 11:e00306-20. doi: 10.1128/mBio.00306-20

Kumar, S., Stecher, G., Li, M., Knyaz, C., and Tamura, K. (2018). MEGA X: molecular evolutionary genetics analysis across computing platforms. *Mol. Biol. Evol.* 35, 1547–1549. doi: 10.1093/molbev/msy096

Kysela, D. T., Randich, A. M., Caccamo, P. D., and Brun, Y. V. (2016). Diversity takes shape: understanding the mechanistic and adaptive basis of bacterial morphology. *PLoS Biol.* 14:e1002565. doi: 10.1371/journal.pbio.1002565

Lamers, R. P., Nguyen, U. T., Nguyen, Y., Buensuceso, R. N. C., and Burrows, L. L. (2015). Loss of membrane-bound lytic transglycosylases increases outer membrane permeability and β-lactam sensitivity in *Pseudomonas aeruginosa*. *MicrobiologyOpen* 4, 879–895. doi: 10.1002/mbo3.286

Langaee, T. Y., Gagnon, L., and Huletsky, A. (2000). Inactivation of the ampD Gene in *Pseudomonas aeruginosa* Leads to Moderate-Basal-Level and Hyperinducible AmpC β-Lactamase Expression. *Antimicrob. Agents Chemother.* 44, 583–589. doi: 10.1128/aac.44.3.583-589.2000

Le, S. Q., and Gascuel, O. (2008). An improved general amino acid replacement matrix. *Mol. Biol. Evol.* 25, 1307–1320. doi: 10.1093/molbev/msn067

Letunic, I., and Bork, P. (2016). Interactive tree of life (iTOL) v3: an online tool for the display and annotation of phylogenetic and other trees. *Nucleic Acids Res.* 44, W242–W245. doi: 10.1093/nar/gkw290

Lindner, A. B., Madden, R., Demarez, A., Stewart, E. J., and Taddei, F. (2008). Asymmetric segregation of protein aggregates is associated with cellular aging and rejuvenation. *Proc. Natl. Acad. Sci. U.S.A.* 105, 3076–3081. doi: 10.1073/pnas.0708931105

Ludwiczak, J., Winski, A., Szczepaniak, K., Alva, V., and Dunin-Horkawicz, S. (2019). DeepCoil-a fast and accurate prediction of coiled-coil domains in protein sequences. *Bioinformatics* 35, 2790–2795. doi: 10.1093/bioinformatics/bty1062

Meier, E. L., Daitch, A. K., Yao, Q., Bhargava, A., Jensen, G. J., and Goley, E. D. (2017). FtsEX-mediated regulation of the final stages of cell division reveals morphogenetic plasticity in *Caulobacter crescentus*. *PLoS Genet.* 13:e1006999. doi: 10.1371/journal.pgen.1006999

Möll, A., Dörr, T., Alvarez, L., Chao, M. C., Davis, B. M., Cava, F., et al. (2014). Cell Separation in *Vibrio cholerae* is mediated by a single amidase whose action is modulated by two nonredundant activators. *J. Bacteriol.* 196, 3937–3948. doi: 10.1128/JB.02094-14

Möll, A., Schlimpert, S., Briegel, A., Jensen, G. J., and Thanbichler, M. (2010). DipM, a new factor required for peptidoglycan remodeling during cell division in *Caulobacter crescentus*. *Mol. Microbiol.* 77, 90–107. doi: 10.1111/j.1365-2958.2010.07224.x

Morton, E. R., and Fuqua, C. (2012). Genetic manipulation of *Agrobacterium*. *Curr. Protoc. Microbiol.* Chapter 3:Unit3D.2. doi: 10.1002/9780471729259.mc03d02s25

Oh, D., Yu, Y., Lee, H., Jeon, J.-H., Wanner, B. L., and Ritchie, K. (2018). Asymmetric polar localization dynamics of the serine chemoreceptor protein Tsr in *Escherichia coli*. *PLoS One* 13:e0195887. doi: 10.1371/journal.pone.0195887

Park, S. H., Kim, Y. J., Lee, H. B., Seok, Y.-J., and Lee, C.-R. (2020). Genetic evidence for distinct functions of peptidoglycan endopeptidases in *Escherichia coli*. *Front. Microbiol.* 11:565767. doi: 10.3389/fmicb.2020.565767

Peters, N. T., Dinh, T., and Bernhardt, T. G. (2011). A fail-safe mechanism in the septal ring assembly pathway generated by the sequential recruitment of cell separation amidases and their activators. *J. Bacteriol.* 193, 4973–4983. doi: 10.1128/JB.00316-11

Peters, N. T., Morlot, C., Yang, D. C., Uehara, T., Vernet, T., and Bernhardt, T. G. (2013). Structure–function analysis of the LytM domain of EnvC, an activator of cell wall remodelling at the *Escherichia coli* division site. *Mol. Microbiol.* 89, 690–701. doi: 10.1111/mmi.12304

Pincus, Z., and Theriot, J. A. (2007). Comparison of quantitative methods for cell-shape analysis. *J. Microsc.* 227, 140–156. doi: 10.1111/j.1365-2818.2007.01799.x

Poggio, S., Takacs, C. N., Vollmer, W., and Jacobs-Wagner, C. (2010). A protein critical for cell constriction in the Gram-negative bacterium *Caulobacter crescentus* localizes at the division site through its peptidoglycan-binding LysM domains. *Mol. Microbiol.* 77, 74–89. doi: 10.1111/j.1365-2958.2010.07223.x

Rajendran, M., Santos, T., and Weibel, D. (2014). The *Escherichia coli* Tol-Pal complex is essential for the positioning of proteins at the cell poles (948.3). *FASEB J.* 28, 948.3. doi: 10.1096/fasebj.28.1_supplement.948.3

Ruiz, N. (2016). Filling holes in peptidoglycan biogenesis of *Escherichia coli*. *Curr. Opin. Microbiol.* 34, 1–6. doi: 10.1016/j.mib.2016.07.010

Santos, T. M. A., Lin, T.-Y., Rajendran, M., Anderson, S. M., and Weibel, D. B. (2014). Polar localization of *Escherichia coli* chemoreceptors requires an intact Tol–Pal complex. *Mol. Microbiol.* 92, 985–1004. doi: 10.1111/mmi.12609

Scheffers, D.-J., and Pinho, M. G. (2005). Bacterial cell wall synthesis: new insights from localization studies. *Microbiol. Mol. Biol. Rev.* 69, 585–607. doi: 10.1128/MMBR.69.4.585-607.2005

Scheurwater, E., Reid, C. W., and Clarke, A. J. (2008). Lytic transglycosylases: bacterial space-making autolysins. *Int. J. Biochem. Cell Biol.* 40, 586–591. doi: 10.1016/j.biocel.2007.03.018

Schindelin, J., Arganda-Carreras, I., Frise, E., Kaynig, V., Longair, M., Pietzsch, T., et al. (2012). Fiji: an open-source platform for biological-image analysis. *Nat. Methods* 9, 676–682. doi: 10.1038/nmeth.2019

Singh, S. K., SaiSree, L., Amrutha, R. N., and Reddy, M. (2012). Three redundant murein endopeptidases catalyse an essential cleavage step in peptidoglycan synthesis of *Escherichia coli* K12. *Mol. Microbiol.* 86, 1036–1051. doi: 10.1111/mmi.12058

Stecher, G., Tamura, K., and Kumar, S. (2020). Molecular Evolutionary Genetics Analysis (MEGA) for macOS. *Mol. Biol. Evol.* 37, 1237–1239. doi: 10.1093/molbev/msz312

Stohl, E. A., Chan, Y. A., Hackett, K. T., Kohler, P. L., Dillard, J. P., and Seifert, H. S. (2012). *Neisseria gonorrhoeae* Virulence Factor NG1686 Is a Bifunctional M23B family metallopeptidase that influences resistance to hydrogen peroxide and colony morphology *. *J. Biol. Chem.* 287, 11222–11233. doi: 10.1074/jbc.M111.338830

Stohl, E. A., Dale, E. M., Criss, A. K., and Seifert, H. S. (2013). *Neisseria gonorrhoeae* metalloprotease NGO1686 is required for full piliation, and piliation is required for resistance to H2O2- and neutrophil-mediated killing. *mBio* 4:e00399-13. doi: 10.1128/mBio.00399-13

Stohl, E. A., Lenz, J. D., Dillard, J. P., and Seifert, H. S. (2016). The Gonococcal NlpD protein facilitates cell separation by activating peptidoglycan cleavage by AmiC. *J. Bacteriol.* 198, 615–622. doi: 10.1128/JB.00540-15

Thanbichler, M., Iniesta, A. A., and Shapiro, L. (2007). A comprehensive set of plasmids for vanillate- and xylose-inducible gene expression in *Caulobacter crescentus*. *Nucleic Acids Res.* 35:e137. doi: 10.1093/nar/gkm818

Tsang, M.-J., Yakhnina, A. A., and Bernhardt, T. G. (2017). NlpD links cell wall remodeling and outer membrane invagination during cytokinesis in *Escherichia coli*. *PLoS Genet.* 13:e1006888. doi: 10.1371/journal.pgen.1006888

Uehara, T., and Bernhardt, T. G. (2011). More than just lysins: peptidoglycan hydrolases tailor the cell wall. *Curr. Opin. Microbiol.* 14, 698–703. doi: 10.1016/j.mib.2011.10.003

Uehara, T., Dinh, T., and Bernhardt, T. G. (2009). LytM-Domain factors are required for daughter cell separation and rapid Ampicillin-Induced Lysis in *Escherichia coli*. *J. Bacteriol.* 191, 5094–5107. doi: 10.1128/JB.00505-09

Uehara, T., Parzych, K. R., Dinh, T., and Bernhardt, T. G. (2010). Daughter cell separation is controlled by cytokinetic ring-activated cell wall hydrolysis. *EMBO J.* 29, 1412–1422. doi: 10.1038/emboj.2010.36

Vermassen, A., Leroy, S., Talon, R., Provot, C., Popowska, M., and Desvaux, M. (2019). Cell Wall Hydrolases in bacteria\nsight on the diversity of cell wall Amidases, Glycosidases and Peptidases Toward Peptidoglycan. *Front. Microbiol.* 10:331. doi: 10.3389/fmicb.2019.00331

Vollmer, W. (2012). Bacterial growth does require peptidoglycan hydrolases. *Mol. Microbiol.* 86, 1031–1035. doi: 10.1111/mmi.12059

Vollmer, W., Blanot, D., and De Pedro, M. A. (2008). Peptidoglycan structure and architecture. *FEMS Microbiol. Rev.* 32, 149–167. doi: 10.1111/j.1574-6976.2007.00094.x

Waterhouse, A. M., Procter, J. B., Martin, D. M. A., Clamp, M., and Barton, G. J. (2009). Jalview Version 2—a multiple sequence alignment editor and analysis workbench. *Bioinformatics* 25, 1189–1191. doi: 10.1093/bioinformatics/btp033

Williams, M. A., Aliashkevich, A., Krol, E., Kuru, E., Bouchier, J. M., Rittichier, J., et al. (2021). Unipolar peptidoglycan synthesis in the Rhizobiales requires an essential class A penicillin-binding protein. *bioRxiv* [Preprint]. doi: 10.1101/2021.03.31.437934

Wu, D., Hugenholtz, P., Mavromatis, K., Pukall, R., Dalin, E., Ivanova, N. N., et al. (2009). A phylogeny-driven genomic encyclopaedia of Bacteria and Archaea. *Nature* 462, 1056–1060. doi: 10.1038/nature08656

Yakhnina, A. A., McManus, H. R., and Bernhardt, T. G. (2015). The cell wall amidase AmiB is essential for *Pseudomonas aeruginosa* cell division, drug resistance, and viability. *Mol. Microbiol.* 97, 957–973. doi: 10.1111/mmi.13077

Yang, D. C., Blair, K. M., Taylor, J. A., Petersen, T. W., Sessler, T., Tull, C. M., et al. (2019). A Genome-Wide *Helicobacter pylori* morphology screen uncovers a membrane-spanning helical cell shape complex. *J. Bacteriol.* 201:e00724-18. doi: 10.1128/JB.00724-18

Yang, D. C., Peters, N. T., Parzych, K. R., Uehara, T., Markovski, M., and Bernhardt, T. G. (2011). An ATP-binding cassette transporter-like complex governs cell-wall hydrolysis at the bacterial cytokinetic ring. *Proc. Natl. Acad. Sci. U.S.A.* 108, E1052–E1060. doi: 10.1073/pnas.1107780108

Yang, L.-C., Gan, Y.-L., Yang, L.-Y., Jiang, B.-L., and Tang, J.-L. (2018). Peptidoglycan hydrolysis mediated by the amidase AmiC and its LytM activator NlpD is critical for cell separation and virulence in the phytopathogen *Xanthomonas campestris*. *Mol. Plant Pathol.* 19, 1705–1718. doi: 10.1111/mpp.12653

Yeh, Y.-C., Comolli, L. R., Downing, K. H., Shapiro, L., and McAdams, H. H. (2010). The Caulobacter Tol-Pal complex is essential for outer membrane integrity and the positioning of a polar localization factor. *J. Bacteriol.* 192, 4847–4858. doi: 10.1128/JB.00607-10

Zielińska, A., Billini, M., Möll, A., Kremer, K., Briegel, A., Martinez, A. I., et al. (2017). LytM factors affect the recruitment of autolysins to the cell division site in *Caulobacter crescentus*. *Mol. Microbiol.* 106, 419–438. doi: 10.1111/mmi.13775

Conflict of Interest: The authors declare that the research was conducted in the absence of any commercial or financial relationships that could be construed as a potential conflict of interest.

Publisher's Note: All claims expressed in this article are solely those of the authors and do not necessarily represent those of their affiliated organizations, or those of the publisher, the editors and the reviewers. Any product that may be evaluated in this article, or claim that may be made by its manufacturer, is not guaranteed or endorsed by the publisher.

frontiers in Microbiology

ORIGINAL RESEARCH
published: 27 August 2021
doi: 10.3389/fmicb.2021.732031

Elongation at Midcell in Preparation of Cell Division Requires FtsZ, but Not MreB nor PBP2 in *Caulobacter crescentus*

Muriel C. F. van Teeseling[1,2]*

[1] Junior Research Group Prokaryotic Cell Biology, Department Microbial Interactions, Institute of Microbiology, Friedrich-Schiller-Universität, Jena, Germany, [2] Department of Biology, University of Marburg, Marburg, Germany

Controlled growth of the cell wall is a key prerequisite for bacterial cell division. The existing view of the canonical rod-shaped bacterial cell dictates that newborn cells first elongate throughout their side walls using the elongasome protein complex, and subsequently use the divisome to coordinate constriction of the dividing daughter cells. Interestingly, another growth phase has been observed in between elongasome-mediated elongation and constriction, during which the cell elongates from the midcell outward. This growth phase, that has been observed in *Escherichia coli* and *Caulobacter crescentus*, remains severely understudied and its mechanisms remain elusive. One pressing open question is which role the elongasome key-component MreB plays in this respect. This study quantitatively investigates this growth phase in *C. crescentus* and focuses on the role of both divisome and elongasome components. This growth phase is found to initiate well after MreB localizes at midcell, although it does not require its presence at this subcellular location nor the action of key elongasome components. Instead, the divisome component FtsZ seems to be required for elongation at midcell. This study thus shines more light on this growth phase in an important model organism and paves the road to more in-depth studies.

Keywords: medial elongation, PBP3-independent peptidoglycan synthesis (PIPS), preseptal peptidoglycan synthesis, cell wall, peptidoglycan, elongasome, divisome

OPEN ACCESS

Edited by:
Cara C. Boutte, University of Texas at Arlington, United States

Reviewed by:
Saswat S. Mohapatra, Khallikote University, India
Michael J. Trimble, Simon Fraser University, Canada

***Correspondence:**
Muriel C. F. van Teeseling
muriel.van.teeseling@uni-jena.de

Specialty section:
This article was submitted to Microbial Physiology and Metabolism, a section of the journal Frontiers in Microbiology

Received: *28 June 2021*
Accepted: *09 August 2021*
Published: *27 August 2021*

Citation:
van Teeseling MCF (2021) Elongation at Midcell in Preparation of Cell Division Requires FtsZ, but Not MreB nor PBP2 in Caulobacter crescentus. Front. Microbiol. 12:732031. doi: 10.3389/fmicb.2021.732031

INTRODUCTION

Almost all bacterial cells rely on the cell-spanning macromolecule peptidoglycan (PG) to provide integrity and shape their cells (de Pedro and Cava, 2015; van Teeseling et al., 2017). It is therefore of key importance for bacteria to tightly control growth and remodeling of its PG sacculus throughout their cell cycle (Typas et al., 2012; Egan et al., 2020). The cell cycle of most bacterial cells involves multiple growth modes, and generally involves that the cells first elongate before they start the process of constriction that effectuates cell division (Randich and Brun, 2015; Kysela et al., 2016). Although some bacteria elongate from one or both poles [e.g., some *Alphaproteobacteria* (Brown et al., 2012) and *Actinobacteria* (Umeda and Amako, 1983; Flärdh, 2010)], most bacteria grow longer by adding new cell wall dispersed throughout their side walls (Kysela et al., 2016). This dispersed elongation mechanism has been studied in great detail, which unveiled an underlying multi-protein complex called the elongasome. The elongasome harbors the scaffolding protein MreB, proteins involved in PG synthesis (e.g., RodA and PBP2), as well as proteins that break

existing PG bonds to make space for insertion of new material (Egan et al., 2020). It is clear that MreB is a crucial part of the elongasome, but its exact role remains puzzling (Ducret and Grangeasse, 2021). Instead of a scaffold that actively directs the movement of all other elongasome proteins, MreB seems to have a subtler coordinating role (Dion et al., 2019; Dersch et al., 2020), in which its movement in part seems to depend on PG synthases that take the lead (Dominguez-Escobar et al., 2011; Garner et al., 2011; van Teeffelen et al., 2011; Özbaykal et al., 2020).

The other important growth phase taking place in bacteria is the constricting process, which incorporates cell wall material at midcell, thereby decreasing the diameter of the cell while generating the new poles. In parallel to the elongasome, this growth phase is supported by a dedicated multiprotein complex, called the divisome. In addition to specific PG synthase (e.g., FtsW and PBP3) and hydrolase enzymes, this complex features the scaffolding protein FtsZ (Egan et al., 2020). Very recent studies point toward two divisome subcomplexes, one consisting of the treadmilling FtsZ (Bisson Filho et al., 2017; Yang et al., 2017) with its anchors (Squyres et al., 2021) that seems to act as a resting stage for the second subcomplex. This second subcomplex consists of PG synthases and seems to be active when it moves around the circumference of the cell as a separate subcomplex (Yang et al., 2021). Interestingly, it seems that after constriction has passed a certain threshold with the help of FtsZ, constriction is finished by the synthase subcomplex (Monteiro et al., 2018; Silber et al., 2021).

Apart from these two thoroughly studied growth phases, some model organisms display an additional growth phase that takes place after elongasome-guided elongation and before divisome-guided constriction. During this process, that has been first described in *E*scherichia *coli* (Wientjes and Nanninga, 1989), the cells elongate exclusively from the midcell outward. Interestingly, this process has been scarcely studied. One observation that might start to explain what happens in the transition from elongasome to divisome-guided growth, is that, at least in *E. coli*, FtsZ arrives at midcell and is then flanked by rings of divisome components, including MreB (Vats and Rothfield, 2007; Vats et al., 2009). This led to the hypothesis that either MreB itself guides growth at midcell or it transfers other elongasome components to FtsZ that then steers elongation at midcell (Potluri et al., 2012). Interestingly, however, all of the tested divisome and elongasome proteins, except for FtsZ and its anchor ZipA were found dispensable for this growth mode in *E. coli* (de Pedro et al., 1997; Varma and Young, 2009; Potluri et al., 2012). Most notably, *E. coli* was shown to still grow *via* medial elongation when the divisome-specific essential PG synthase PBP3, and MreB and its cognate synthase PBP2 were absent or non-functional. More in-depth studies in *E. coli* suggest that a very early divisome consisting of FtsZ anchored by ZipA and FtsA recruits the PG synthases PBP1A and 1B to midcell to drive this preseptal elongation [which has also been described as PBP3-independent peptidoglycan synthesis (PIPS)] (Pazos et al., 2018). It remains puzzling, however, if there is any role for MreB, which after all forms rings next to, and even directly interacts with, FtsZ (Fenton and Gerdes, 2013), shortly before preseptal PG synthesis commences.

Although it remains unclear how widespread this growth phase is, a similar growth phase has been observed in another Gram-negative model organism: *Caulobacter crescentus* (Aaron et al., 2007). Interestingly, in this species a relatively large part of the elongation takes place by the medial elongation growth phase (as it is called in *C. crescentus*). As in *E. coli*, medial elongation in *C. crescentus* requires FtsZ. It furthermore seems that PG synthesis at midcell starts shortly after the arrival of FtsZ at midcell. Also in *C. crescentus*, MreB was seen to form a band at midcell, dependent on FtsZs localization at this site (Figge et al., 2004; Gitai et al., 2004). Indirect evidence suggested that MreBs arrival at midcell is followed quickly by the onset of medial elongation (Aaron et al., 2007). A more in-depth study is needed to further elucidate the role of MreB in medial elongation in *C. crescentus*, as it is believed to play a role in this process by some (Randich and Brun, 2015), but non-quantitative indications by others (Aaron et al., 2007) show it might not be necessary for medial elongation. Furthermore, it remains unclear which PG synthases are involved. All in all, the mechanisms of this growth phase remain puzzling and it is an open question if the growth phases in *E. coli* and *C. crescentus* are mechanistically the same process. In order to build a base toward better understanding of the importance and mechanisms of this growth phase, these questions should be addressed.

This study thus focuses on medial elongation in *C. crescentus* and attempts to build a quantitative base of information about the growth phase in this model organism. Specifically, the timing of events surrounding MreBs arrival at midcell and the onset of medial elongation are elucidated. Furthermore, the importance of MreB for this growth phase is studied and quantified using multiple approaches. Additionally, it is shown that the elongasome-specific PBP2 is not required for this mode of growth, whereas the presence of FtsZ is crucial. It thus seems that preseptal PG synthesis in *E. coli* and medial elongation in *C. crescentus* are governed by the same or very similar molecular mechanisms.

MATERIALS AND METHODS

Bacterial Strains and Growth Conditions

All strains that are analyzed in this study are derivatives of the synchronizable *C. crescentus* wild-type CB15N (Evinger and Agabian, 1977; Marks et al., 2010). Strain MT309 carries a chromosomally integrated *venus-mreB* under the control of the *xylX* promoter (Billini et al., 2019). Strain JAT790 contains the *mreB* variant G165A at the native *mreB* locus and a fluorescently labeled copy of the same mreB variant *venus-*$_{G165A}$*mreB* under the control of the *xylX* promoter (Dye et al., 2011). Another mreB variant, $mreB_{Q26P}$, is present at the native locus instead of the normal MreB in strain CJW1715 (Aaron et al., 2007). In the FtsZ depletion strain YB1585, the sole full copy of *ftsZ* is chromosomally integrated under the control of the *xylX* promotor, whereas a non-functional truncated version (consisting of the first 163 codons) is present at the native locus of *ftsZ* (Wang et al., 2001). Strain information is detailed in **Table 1**.

TABLE 1 | Description of all strains used in this study.

Strain	Genotype	Source
CB15N	*C. crescentus* wild-type	Evinger and Agabian, 1977; Marks et al., 2010
CJW1715	CB15N P_{mreB}:$mreB_{Q26P}$	Aaron et al., 2007
JAT790	CB15N P_{mreB}:$mreB_{G165A}$ P_{xyl}:*venus-*$mreB_{G165A}$	Dye et al., 2011
MT309	CB15N P_{xyl}:*venus-mreB*	Billini et al., 2019
YB1585	CB15N P_{ftsZ}:P_{xyl}-*ftsZ*	Wang et al., 2001

All strains were cultivated in peptone-yeast extract (PYE) medium (Pointdexter, 1964) at 28°C, while shaking at 210 rpm. Gene expression from the xylose-inducible *xylX* promoter (Meisenzahl et al., 1997) was induced for 75 min with 0.03% xylose. The following inhibitors were used: A22 (10 μg/ml) and mecillinam (150 μg/ml).

Synchronization of *C. crescentus* was achieved by density gradient centrifugation, using Percoll (Tsai and Alley, 2001). After synchronization, cells were released in PYE medium (with 0.03% xylose and/or inhibitors, when applicable) and allowed to grow at 28°C, while shaking at 210 rpm.

Peptidoglycan Labeling

To indicate areas of active PG insertion and remodeling, cells were stained with the fluorescent dye hydroxycoumarin-carbonyl-amino-D-alanine (HADA) (Kuru et al., 2012). For this, cells at multiple time points after synchronization were incubated with 500 μM HADA in PYE (including 0.03% xylose, where applicable) while shaking at 300 rpm for 2 min at 28°C. Cells were then washed once in PYE medium without HADA and immediately prepared for imaging.

Microscopy and Image Analysis

After synchronization and PG labeling, cells were immobilized on pads consisting of 1% agar in water (to prevent further growth) and immediately imaged with an Axio Observer Z1 microscope (Zeiss, Germany). Samples were excited with the use of an X-Cite 120PC metal halide light source (EXFO, Canada) and ET-YFP and/or ET-DAPI filter cubes (Chroma, United States) were used for fluorescence detection. Images were obtained through a Zeiss Plan-Apochromat 100×/1.4 oil immersion Ph3 objective and recorded with a pco.edge sCMOS camera (PCO, Germany) using VisiView (Visitron Systems, Germany) software. Dimensions of the cells (length and width) and their fluorescent properties were analyzed with the image analysis software tool BacStalk (Hartmann et al., 2020) using standard settings for stalked cells. All cells were manually inspected to remove wrongly detected cells. The remaining cell outlines generated by BacStalk, as well as the underlying phase contrast images, were inspected by eye to determine if cells were constricting. For each replicate, a number of cells was analyzed until 100 non-constricting cells were present in the analysis, next to a varying number of constricting cells (between 0 and 80, dependent on the conditions). Each cell was then inspected to determine if HADA and/or fluorescently labeled MreB had accumulated at midcell (the midcell region was determined by eye) in respect to the background. The maxima of the different fluorescent channels per cell were extracted using BacStalk. In order to compare the percentage of cells undergoing medial elongation in the different conditions, the fraction of non-constricting cells (n = 100 per replicate) that shows HADA at midcell (either in the presence or absence) was evaluated, as well as the information if a fluorescently tagged MreB (in the relevant strains) was present at midcell in the same cell. Measurements were exported to Excel 2016 (Microsoft, United States), where average and standard deviations were calculated. Images were processed using Fiji (Schindelin et al., 2012) and Adobe Illustrator CS5 (Adobe Systems, United States). Graphs representing cellular dimensions were created using SuperPlotsOfData (Goedhart, 2021) and show constricting, as well as non-constricting cells.

RESULTS

Onset of Medial Elongation Takes Place After MreB Accumulation at Midcell

One of the biggest outstanding questions concerning medial elongation is if it depends on the presence of the elongasome component MreB at midcell. As a first step in addressing this question, the relative timing of arrival of MreB at midcell versus the onset of medial elongation was analyzed. For this, *C. crescentus* cells expressing a fluorescent fusion to MreB were synchronized and stained with a short pulse of the fluorescent PG precursor HADA to visualize both the intracellular location of MreB and PG insertion in the same cells. This analysis showed that in almost all cells, MreB arrives at midcell before medial elongation commences (**Figure 1** and **Supplementary Figure 1**). MreB starts to accumulate at midcell already quite early in the cell cycle, as 9 and 28% of cells respectively 0 and 15 min after synchronization show MreB at midcell (**Figures 1B,C**). Elongation at midcell starts later, as 3 and 24% of the cells show a HADA enrichment at midcell respectively 15 min and 30 min after synchronization. With time and as cells get longer, the fraction of (non-constricting) cells showing HADA incorporation at midcell, as well as the maximum intensity of the HADA signal increases (**Supplementary Figure 1A**), indicating that medial elongation takes over as a growth phase (**Figures 1C,D**). The sequence of events therefore seems to be that cells first recruit MreB to midcell, and as they become longer PG insertion then starts at midcell, where MreB is still present, as most cells that show HADA signal also have MreB at midcell, at least in the early stages. As HADA signal at midcell is very scarcely seen without MreB being at midcell at early stages, it remains unclear if the presence of elongasome components at midcell is a prerequisite for medial elongation or if medial elongation takes place independently.

Medial Elongation Can Start but Proceeds Slower (at the Population Level) When MreB's Arrival to Midcell Is Delayed

To answer the question if medial elongation can only take place when elongasome components, specifically MreB, are

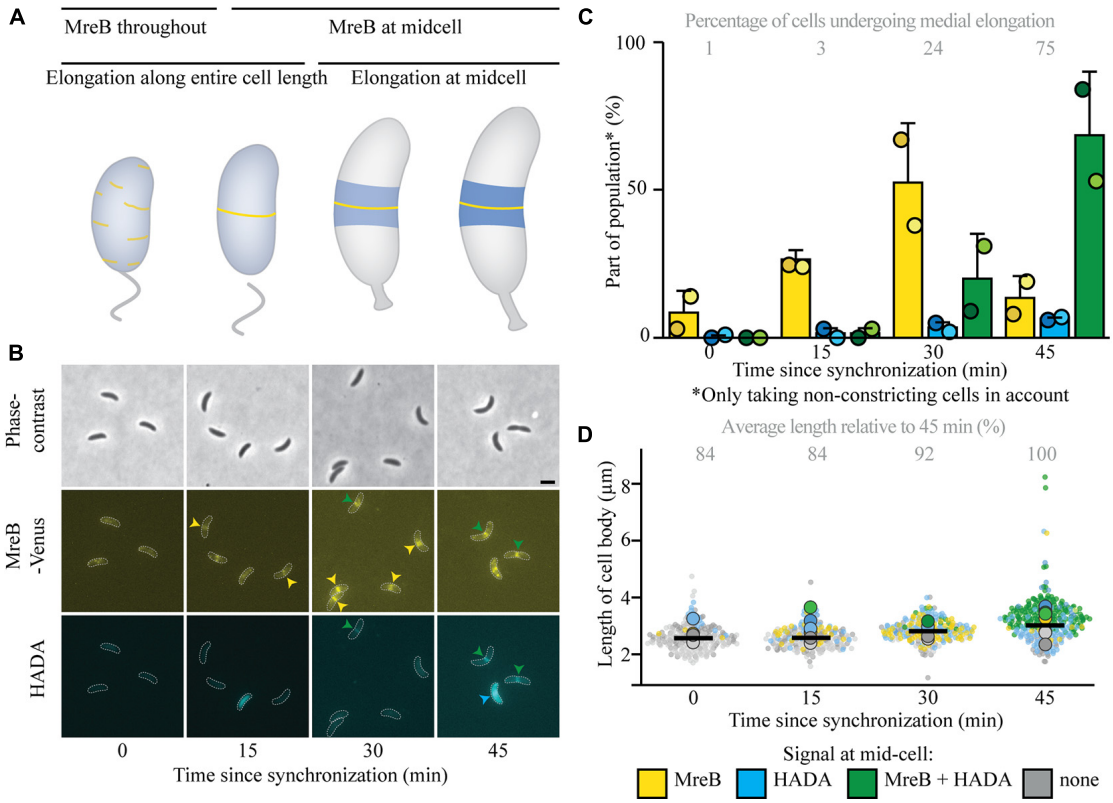

FIGURE 1 | MreB accumulates at midcell clearly before elongation at midcell commences. Intracellular localization of MreB (yellow) and peptidoglycan insertion and remodeling (blue) summarized in a cartoon **(A)**, based on the experiments shown in **(B–D)**. Light microscopy images **(B)** and respective quantification **(C)** of strain MT309 (P_{xyl}-*venus-mreB*) grown for the indicated duration after synchronization, stained with a short pulse of HADA show that with time MreB accumulates at midcell and cell wall remodeling at midcell commences with a delay. Cells in the representative images **(B)** are outlined and midcell localization is indicated by arrowheads: colocalizing MreB and HADA are indicated in green, only MreB in yellow, and only HADA in blue. Quantification of fluorescence signals **(C)** at midcell (using the color scheme outlined above) was performed on 100 non-constricting cells per replicate for two replicates per timepoint (value for each replicate is indicated by circles, replicate 1 is shown in a darker shade and replicate 2 in a light shade). Bars indicate the average of two replicates and error bars indicate standard deviation. In addition, the average percentage of non-constricting cells showing HADA (either in presence or absence of MreB) is given for each timepoint. Analysis of the length of cell bodies (of both constricting and non-constricting cells, in total at least 100 cells per replicate) shows that cells become longer with time and cells that are incorporating HADA are relatively longer **(D)**. Cell lengths are shown in superplots, where each small dot indicates the value for a single cell. The color of each dot follows the color scheme outlined above, in order to identify differences in cell length for the different subpopulations, and shows different shades to differentiate between the replicates. The large dots show the average cell length for each localization subpopulation per replicate. The horizontal black bar indicates the average length over all cells and the numbers above the graph express this average length as a percentage of the average length of the cells after 45 min.

present at midcell, additional experiments were performed. As a first step, a strain expressing the MreB variant $MreB^{G165A}$ instead of the native MreB (and an inducible $MreB^{G165A}$ fused to a fluorescent protein) was investigated (**Figure 2** and **Supplementary Figure 2**), as this strain was previously shown to have a delayed recruitment of MreB to midcell and a longer cell cycle (Dye et al., 2011). Indeed, it could be confirmed that MreB arrived later at midcell by approximately 15 min, as respectively 11 and 17% of cells showed MreB localization at 15 and 30 min (**Figures 2A,B**). Interestingly, the onset of medial elongation was comparable to a strain with native MreB, with respectively 5 and 12% of cells showing HADA at midcell 15 and 30 min after synchronization (**Figure 2B**). Like in the strain with the native MreB variant, with time and increasing cell length (**Figure 2C**), more and more (non-constricting) elongating cells show a HADA accumulation, with a higher maximum intensity, at midcell. However, the fraction of cells that undergoes medial elongation and the maximum HADA intensity increase slower in the strain with the delayed MreB variant than in the wild-type MreB (compare **Figure 1C** with **Figure 2B** and **Supplementary Figure 1A** with **Supplementary Figure 2A**). This population-wide delay of medial elongation becomes very clear when comparing the timepoint at which 75% of non-constricting cells shows a HADA signal at midcell: for cells expressing $MreB_{wt}$ this takes place 45 min after synchronization and for cells with $MreB^{G165A}$ this percentage is reached only slightly before 105 min after synchronization, at which point the cells had more time to elongate and were on average longer than their counterparts expressing $MreB_{wt}$. Taken together, the observations that (a) HADA accumulation at midcell can take place before MreB reaches the same location and (b) a considerable fraction

of cells shows HADA signal at midcell in the absence of MreB (**Figure 2B**) suggests that medial elongation does not require the presence of MreB at midcell, although a timely presence of MreB does speed up medial elongation at the population level.

Medial Elongation Takes Place in the Absence of MreB and PBP2 at Midcell

To further look into the role of MreB and other elongasome components for the onset of medial elongation, multiple parallel routes were taken. First, a strain carrying a MreB variant ($MreB_{Q26P}$) that does not get recruited to midcell at all (Aaron et al., 2007) was followed. This experiment confirmed that medial elongation can take place without MreB being present at midcell, as the majority of cells showed a HADA signal at midcell 45 min after synchronization (**Figures 3A,B**). As compared to cells expressing $MreB_{wt}$ the cell length of this strain was slightly longer, again showing that MreB localization at midcell is not needed for cellular elongation (**Figure 3C**). The fraction of cells that shows medial elongation [and the maximum intensity of the HADA signal (**Supplementary Figure 3A**)] is lower than in strain MT309 at the same timepoint, this might be caused by a delay in the cell cycle, indicated by a lower percentage of constricting cells (**Supplementary Figure 3C**). In parallel, the localization of $MreB_{wt}$ and HADA where studied upon treatment of strain MT309 (P_{xyl}-*venus-mreB*) with the MreB inhibitor A22 (**Figures 3A,D,E** and **Supplementary Figures 3B,D,E**). As expected, only a low fraction of cells showed MreB localization after treatment with A22 (**Figure 3D**) and cells became slightly wider (**Supplementary Figure 3E**) as is typical for cells treated with A22 (Tropini et al., 2014). In line with the previous results on MreB variants, also upon A22 treatment cells showed medial elongation (as shown by the accumulation of HADA, either in the absence or presence of MreB, at midcell), almost up to the same extent as cells untreated with A22 (**Figure 3D**).

The elongasome does not only consist of the actin-homolog MreB, but includes multiple proteins involved in PG synthesis and remodeling, such as the elongasome-specific synthase PBP2. PBP2 was shown to colocalize with FtsZ and MreB at midcell in *C. crescentus* cells that have undergone an osmotic challenge (Hocking et al., 2012). This localization was shown to be dependent on FtsZ, but independent on MreB, which urges the question if PBP2 might be involved in medial elongation. To investigate this question, PG incorporation and $MreB_{wt}$ localization were followed in the presence of the PBP2 inhibitor mecillinam (**Figures 3A,D,E** and **Supplementary Figures 3B,D,E**). Upon treatment with mecillinam, the cell width increased as compared to untreated cells, as has been reported before for mecillinam treatment (Tropini et al., 2014). The results were similar to these for MreB: medial elongation still took place upon inhibition of PBP2, suggesting that medial elongation does not depend on this PBP. The fraction of cells that showed medial elongation was lower as compared to samples without mecillinam, but this might well be caused by a short delay in the cell cycle [also exemplified by a drop in the percentage of constricting cells as compared to the untreated strain (**Supplementary Figure 3D**)] as mecillinam inhibits PBP2 that normally aids in dispersed elongation. All in all, it becomes clear that medial elongation does not depend on both tested elongasome components.

Medial Elongation Requires FtsZ

After showing that medial elongation can take place in the absence of selected elongasome components, the focus was moved toward divisome components. Research in *E. coli* (de Pedro et al., 1997; Varma and Young, 2009; Potluri et al., 2012) and non-quantitative experiments in *C. crescentus* (Aaron et al., 2007) have implicated FtsZ in medial elongation. To investigate the requirement of FtsZ for medial elongation in more detail, cells of the FtsZ depletion strain YB1585 were cultivated and synchronized. After synchronization, cells were either grown in inducing (PYE with xylose) or depleting (PYE without xylose) conditions and PG incorporation was investigated *via* short pulse labeling with HADA 45 min after synchronization (**Figure 4** and **Supplementary Figure 4**). As compared to a strain with wild-type amounts of FtsZ (MT309, grown in PYE without xylose), cells of YB1585 grown in both inducing and depleting conditions were slightly longer (**Figure 4C**) and were less likely to constrict (especially in the absence of FtsZ) (**Supplementary Figure 4B**), but showed less medial elongation (**Figure 4B**). The drop in fraction of cells undergoing medial elongation was especially clear for cells depleted of FtsZ, which contributed to only 6% of the population as opposed to 75% in cells with wild-type levels of FtsZ (MT309), demonstrating that FtsZ is required for medial elongation (**Figures 4A,B**).

DISCUSSION

The results obtained in this study suggest that medial elongation in *C. crescentus* requires FtsZ but not MreB at midcell, similar to PIPS in *E. coli* (de Pedro et al., 1997; Varma and Young, 2009; Potluri et al., 2012). Multiple experiments showed that medial elongation can take place upon MreB inhibition or its inability to get recruited to midcell. In this light, the finding that delayed recruitment of MreB to midcell results in a slower increase in the fraction of cells undergoing medial elongation is puzzling and needs further investigation. Possibly, this specific mutation in MreB has altered interaction properties with its binding partners, thereby affecting the process of medial elongation. The previous observation that the strain carrying this MreB variant has a longer cell cycle (Dye et al., 2011), might suggest all cells need to spend a certain time in the medial elongation phase before they can proceed to constriction.

The question which PG synthase(s) are involved in medial elongation in *C. crescentus* remains unanswered. The experiments presented here suggest PBP2 is not required and the same was suggested for PBP3 (Aaron et al., 2007), which again fits to what is described for PIPS in *E. coli*. PIPS in *E. coli* was reported to depend on two of its three bifunctional PBPs (bPBPs): PBP1A and PBP1B, that can take over each other's role (Potluri et al., 2012; Pazos et al., 2018). *C. crescentus* has

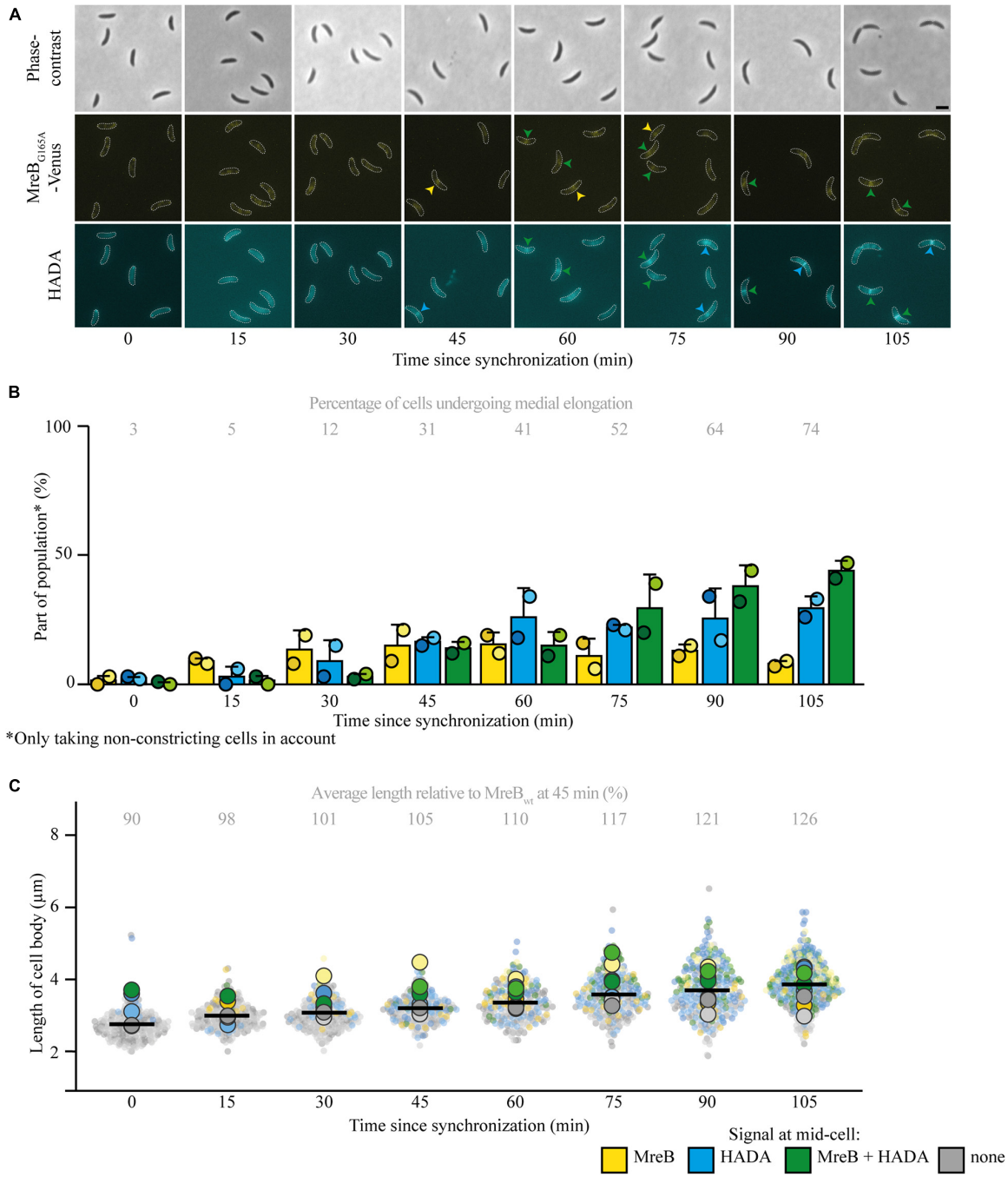

FIGURE 2 | Medial elongation can precede MreB accumulation at midcell in a strain with delayed MreB recruitment. Light microscopy images **(A)** and respective quantification **(B)** of strain JAT790 ($P_{mreB\text{-}G165A}$*mreB* P_{xyl}-*venus*-$_{G165A}$*mreB*) grown for the indicated duration after synchronization, stained with a short pulse of HADA show that medial elongation commences in the absence of MreB at midcell in part of the population. Cells in the representative images **(A)** are outlined and midcell localization is indicated by arrowheads: colocalizing MreB and HADA are indicated in green, only MreB in yellow, and only HADA in blue. Quantification of fluorescence signals **(B)** at midcell (using the color scheme outlined above) was performed on 100 non-constricting cells per replicate for two replicates per timepoint (value for each replicate is indicated by circles, replicate 1 is shown in a darker shade and replicate 2 in a light shade). Bars indicate the average of two replicates and error bars indicate standard deviation. In addition, the average percentage of non-constricting cells showing HADA (either in presence or absence of MreB) is given for each timepoint. Analysis of the length of cell bodies (of both constricting and non-constricting cells, in total at least 100 cells per replicate) shows that cells become longer with time and cells that are incorporating HADA are relatively longer **(C)**. Cell lengths are shown in superplots, where each small dot indicates the value for a single cell. The color of each dot follows the color scheme outlined above, in order to identify differences in cell length for the different subpopulations, and shows different shades to differentiate between the replicates. The large dots show the average cell length for each localization subpopulation per replicate. The horizontal black bar indicates the average length over all cells and the numbers above the graph express this average length as a percentage of the average length of the cells carrying MreB$_{wt}$ after 45 min (strain MT309, indicated in **Figure 1**).

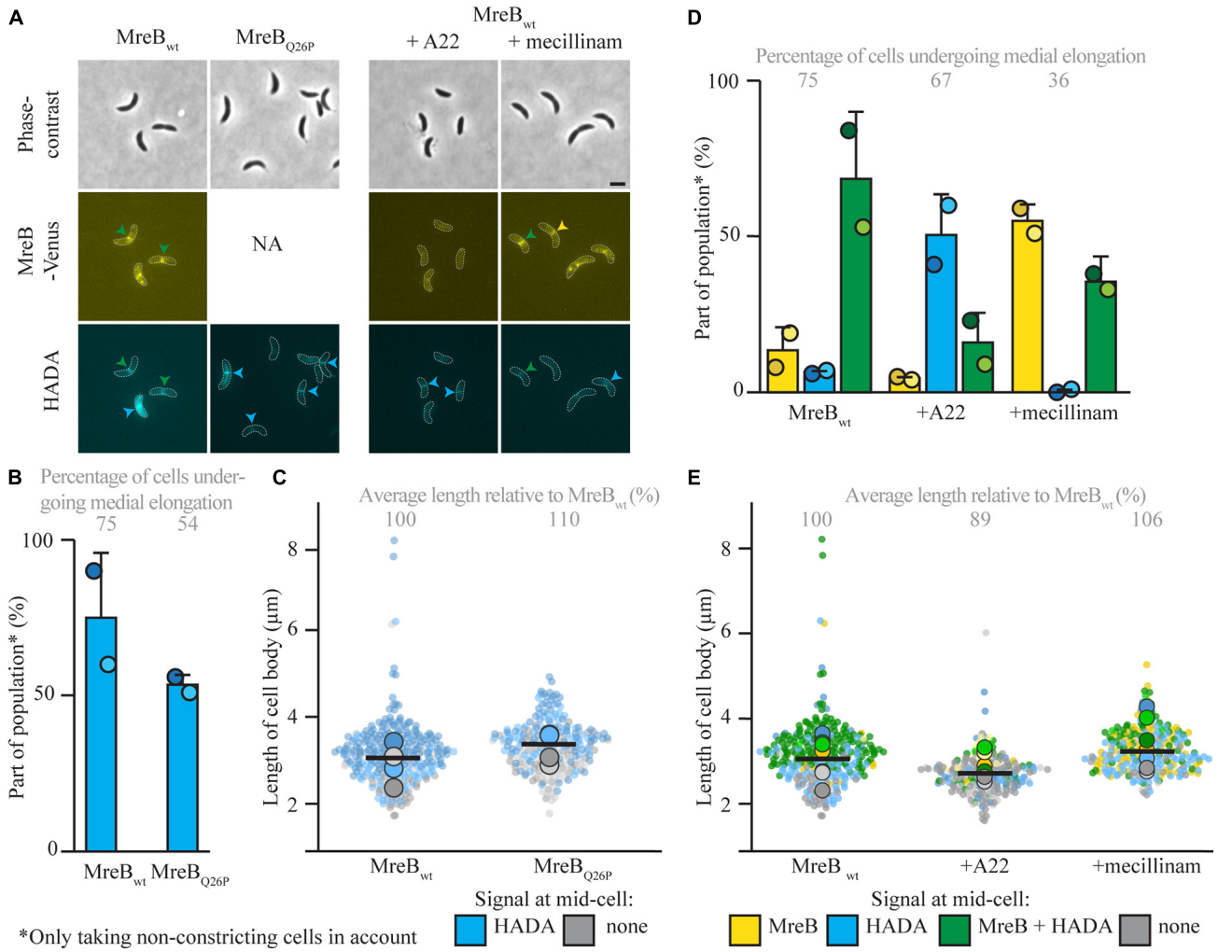

FIGURE 3 | Medial elongation can take place in the absence of elongasome components at midcell. Light microscopy images **(A)** and respective quantification of strains CJW1715 ($P_{mreB^{-}Q26P}$*mreB*) **(B)** and MT309 (P_{xyl}-*venus-mreB*), synchronized and subsequently grown in the absence of additives and (for MT309) in the presence of the MreB inhibitor A22 (10 µg/ml) or the PBP2 inhibitor mecillinam (150 µg/ml) **(D)**. Cells were harvested 45 min after synchronization and subjected to a short pulse HADA staining. Cells in the representative images **(A)** are outlined and midcell localization is indicated by arrowheads: colocalizing MreB and HADA are indicated in green, only MreB in yellow and only HADA in blue. Quantification of fluorescence signals **(B,D)** at midcell (using the color scheme outlined above, with the exception that in the case of strain CJW1715 MreB was not fluorescently labeled, and therefore only blue can be used) was performed on 100 non-constricting cells per replicate for two replicates per timepoint (value for each replicate is indicated by circles, replicate 1 is shown in a darker shade and replicate 2 in a light shade). Bars indicate the average of two replicates and error bars indicate standard deviation. In addition, the average percentage of non-constricting cells showing HADA (either in presence or absence of MreB) is given for each timepoint. Data shown for $MreB_{wt}$ in both cases are from the same two replicates of strain MT309 (also shown in **Figure 1**). Analysis of the length of the cell bodies (of both constricting and non-constricting cells, in total at least 100 cells per replicate) shows that cells expressing $MreB_{Q26P}$ are slightly longer than cells expressing $MreB_{wt}$ **(C)**. Analysis of the length of the cell bodies (of both constricting and non-constricting cells, in total at least 100 cells per replicate) for cells of strain MT309 incubated without additives, shows that with A22 cells are a bit shorter and with mecillinam cells are slightly longer **(E)**. Cell lengths are shown in superplots, where each small dot indicates the value for a single cell. The color of each dot follows the color scheme outlined above, in order to identify differences in cell length for the different subpopulations, and shows different shades to differentiate between the replicates. The large dots show the average cell length for each localization subpopulation per replicate. The horizontal black bar indicates the average length over all cells and the numbers above the graph express this average length as a percentage of the average length of the cells carrying $MreB_{wt}$ after 45 min (strain MT309, indicated in **Figure 1**).

a higher redundancy of bPBPs with five copies in total: in addition to one PBP1C homolog (PbpZ), it interestingly has four PBP1A homologs (PBP1A, PbpC, PbpX, and PbpY), but lacks PBP1B homologs (Yakhnina and Gitai, 2013; Strobel et al., 2014). The observation that strains missing all bPBPs except for PbpX or PbpY or PbpC or to a lesser extent PPB1A are viable (Strobel et al., 2014), suggests that in *C. crescentus* PbpX, PbpY, PbpC, and potentially also Pbp1A might all be able to take up the role as bPBP involved in medial elongation.

Another open question when comparing medial elongation in *C. crescentus* to PIPS in *E. coli* is if any (and if so which) of the proteins anchoring FtsZ is involved in medial elongation.

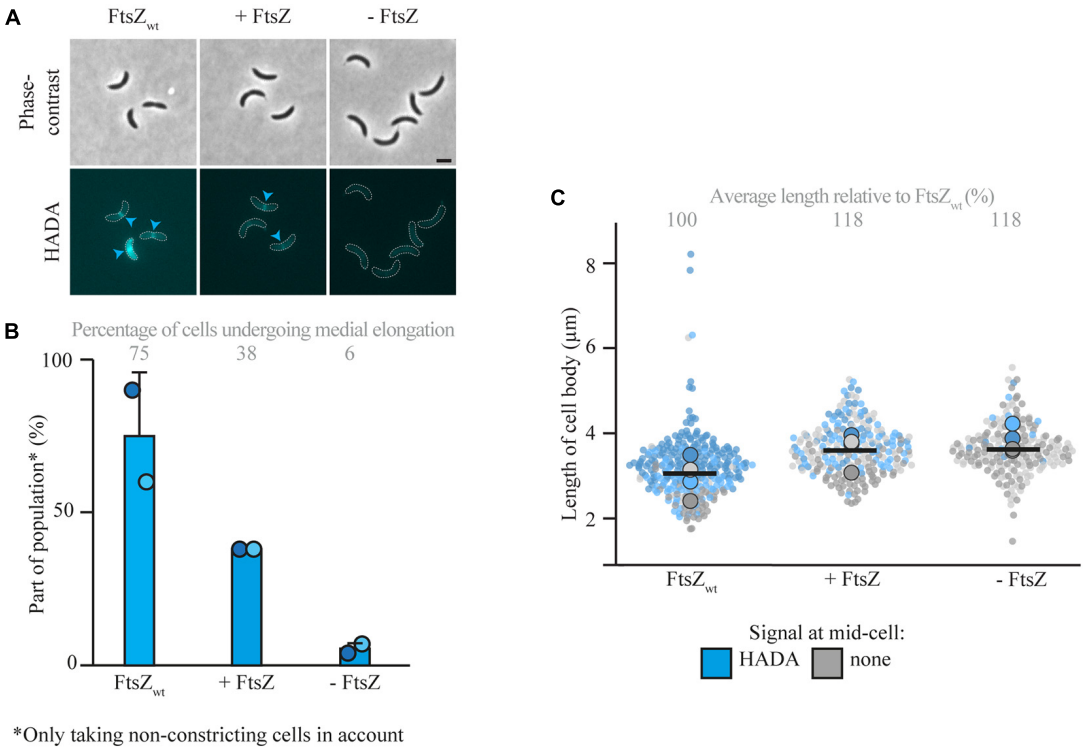

FIGURE 4 | Medial elongation is affected by the absence of FtsZ. Light microscopy images **(A)** and respective quantification **(B)** of FtsZ depletion strain YB1585 (grown under depleting and inducing conditions) and MT309 (P_{xyl}-*venus-mreB*), synchronized and subsequently grown for 45 min and subsequently subjected to a short pulse HADA staining. Cells in the representative images **(A)** are outlined and HADA midcell localization is indicated by blue arrowheads. Quantification of fluorescence signals **(B)** at midcell (using the color scheme outlined above) was performed on 100 non-constricting cells per replicate for two replicates per timepoint (value for each replicate is indicated by circles, replicate 1 is shown in a darker shade and replicate 2 in a light shade). Bars indicate the average of two replicates and error bars indicate standard deviation. In addition, the average percentage of non-constricting cells showing HADA is given for each timepoint. Data shown for $FtsZ_{wt}$ in both cases are from the same replicates of strain MT309 as shown in **Figure 1**. Analysis of the cell length **(C)** of cells of strain YB1585 shows that they are slightly elongated as compared to cells harboring $FtsZ_{wt}$. Cell lengths are shown in superplots, where each small dot indicates the value for a single cell. The color of each dot follows the color scheme outlined above, in order to identify differences in cell length for the different subpopulations, and shows different shades to differentiate between the replicates. The large dots show the average cell length for each localization subpopulation per replicate. The horizontal black bar indicates the average length over all cells and the numbers above the graph express this average length as a percentage of the average length of the cells carrying $MreB_{wt}$ after 45 min (strain MT309, indicated in **Figure 1**).

In *E. coli*, the early divisome protein ZipA works together with FtsA to anchor FtsZ to the membrane and stabilize FtsZ polymers into protofilaments (Pichoff and Lutkenhaus, 2002; Krupka et al., 2018). Both of these proteins are involved in PIPS, for which ZipA is essential unless a hyperactive FtsA allele is present (Potluri et al., 2012; Pazos et al., 2018). *C. crescentus*, however, lacks a ZipA homolog and FtsA is recruited only later to the divisome (Goley et al., 2011). Instead, the FtsZ-binding proteins ZapA, ZauP, FzlC, FtsE, and FzlA are recruited early to the divisome (Goley et al., 2011; Woldemeskel et al., 2017). If any of these proteins is required for medial elongation remains unknown at the moment. It might be that there is more redundancy in FtsZ anchoring proteins that are required for medial elongation compared to *E. coli*, as strains lacking ZapA, ZauP (and a combination of these two), FzlC, and FtsE are viable (Goley et al., 2010; Meier et al., 2017; Woldemeskel et al., 2017), suggesting that each of these alone does not take over the essential role of ZipA in medial elongation. Alternatively, the essential FzlA takes over the role of ZipA, although it is implicated in constriction and described to regulate the curvature of FtsZ filaments (Lariviere et al., 2018), which seems to occur at a later stage than the role ZipA takes in PIPS. All in all, further studies need to be performed in order to understand which other proteins are involved in medial elongation. Until these proteins and the underlying mechanisms they use to make *C. crescentus* cells elongate from midcell are known, it will be impossible to answer if this growth phase is mechanistically the same as PIPS in *E. coli*. For now, however, all results seem consistent. Hopefully research in the future will succeed in elucidating mechanisms behind this elusive growth phase and answer the question how widespread it is in bacteria.

DATA AVAILABILITY STATEMENT

The raw data supporting the conclusions of this article will be made available by the authors, without undue reservation.

AUTHOR CONTRIBUTIONS

MvT conceived and designed this project, performed the analyses, and wrote the manuscript.

ACKNOWLEDGMENTS

Julia Rosum and Adrian Kietz are acknowledged for excellent technical assistance. The author thanks Martin Thanbichler for scientific discussions and support. Julie Theriot is acknowledged for sharing strain JAT790 and Martin Thanbichler and Christine Jacobs-Wagner for CJW1715.

SUPPLEMENTARY MATERIAL

The Supplementary Material for this article can be found online at: https://www.frontiersin.org/articles/10.3389/fmicb.2021.732031/full#supplementary-material

REFERENCES

Aaron, M., Charbon, G., Lam, H., Schwarz, H., Vollmer, W., and Jacobs-Wagner, C. (2007). The tubulin homologue FtsZ contributes to cell elongation by guiding cell wall precursor synthesis in *Caulobacter crescentus*. *Mol. Microbiol.* 64, 938–952. doi: 10.1111/j.1365-2958.2007.05720.x

Billini, M., Biboy, J., Kühn, J., Vollmer, W., and Thanbichler, M. (2019). A specialized MreB-dependent cell wall biosynthetic complex mediates the formation of stalk-specific peptidoglycan in *Caulobacter crescentus*. *PLoS Genet.* 15:e1007897. doi: 10.1371/journal.pgen.1007897

Bisson Filho, A. W., Hsu, Y.-P., Squyres, G. R., Kuru, E., Wu, F., Jukes, C., et al. (2017). Treadmilling by FtsZ filaments drives peptidoglycan synthesis and bacterial cell division. *Science* 355, 739–743. doi: 10.1126/science.aak9973

Brown, P. J. B., de Pedro, M. A., Kysela, D. T., Van der Henst, C., Kim, J., De Bolle, X., et al. (2012). Polar growth in the Alphaproteobacterial order *Rhizobiales*. *Proc. Natl. Acad. Sci. U. S. A.* 109, 1697–1701. doi: 10.1073/pnas.1114476109

de Pedro, M. A., and Cava, F. (2015). Structural constraints and dynamics of bacterial cell wall architecture. *Front. Microbiol.* 6:449. doi: 10.3389/fmicb.2015.00449

de Pedro, M. A., Quintela, J. C., Höltje, J. V., and Schwarz, H. (1997). Murein segregation in *Escherichia coli*. *J. Bacteriol.* 179, 2823–2834. doi: 10.1128/jb.179.9.2823-2834.1997

Dersch, S., Mehl, J., Stuckenschneider, L., Mayer, B., Roth, J., Rohrbach, A., et al. (2020). Super-resolution microscopy and single-molecule tracking reveal distinct adaptive dynamics of MreB and of cell wall-synthesis enzymes. *Front. Microbiol.* 11:1946. doi: 10.3389/fmicb.2020.01946

Dion, M. F., Kapoor, M., Sun, Y., Wilson, S., Ryan, J., Vigouroux, A., et al. (2019). *Bacillus subtilis* cell diameter is determined by the opposing actions of two distinct cell wall synthetic systems. *Nat. Microbiol.* 4, 1294–1305. doi: 10.1038/s41564-019-0439-0

Dominguez-Escobar, J., Chastanet, A., Crevenna, A. H., Fromion, V., Wedlich-Söldner, R., and Carballido-Lopez, R. (2011). MreB-associated cell wall biosynthetic complexes in bacteria. *Science* 333, 225–228. doi: 10.1126/science.1203466

Ducret, A., and Grangeasse, C. (2021). Recent progress in our understanding of peptidoglycan assembly in Firmicutes. *Curr. Opin. Microbiol.* 60, 44–50. doi: 10.1016/j.mib.2021.01.011

Dye, N. A., Pincus, Z., Fisher, I. C., Shapiro, L., and Theriot, J. A. (2011). Mutations in the nucleotide binding pocket of MreB acan alter cell curvature and polar morphology in *Caulobacter*. *Mol. Microbiol.* 81, 368–394. doi: 10.1111/j.1365-2958.2011.07698.x

Egan, A. J. F., Errington, J., and Vollmer, W. (2020). Regulation of peptidoglycan synthesis and remodelling. *Nat. Rev. Microbiol.* 18, 446–460. doi: 10.1038/s41579-020-0366-3

Evinger, M., and Agabian, N. (1977). Envelope-associated nucleoid from *Caulobacter crescentus* stalked and swarmer cells. *J. Bacteriol.* 132, 294–301. doi: 10.1128/jb.132.1.294-301.1977

Fenton, A. K., and Gerdes, K. (2013). Direct interaction of FtsZ and MreB is required for septum synthesis and cell division in *Escherichia coli*. *EMBO J.* 32, 1953–1965. doi: 10.1038/emboj.2013.129

Figge, R. M., Divakaruni, A. V., and Gober, J. W. (2004). MreB, the cell shape-determining bacterial actin homologue, co-ordinates cell wall morphogenesis in *Caulobacter crescentus*. *Mol. Microbiol.* 51, 1321–1332. doi: 10.1111/j.1365-2958.2003.03936.x

Flärdh, K. (2010). Cell polarity and the control of apical growth in Streptomyces. *Curr. Opin. Microbiol.* 13, 758–765. doi: 10.1016/j.mib.2010.10.002

Garner, E. C., Bernard, R., Wang, W., Zhuang, X., Rudner, D. Z., and Mitchinson, T. (2011). Coupled, circumferential motions of the cell wall synthesis machinery and MreB filaments in *B. subtilis*. *Science* 333, 222–225. doi: 10.1126/science.1203285

Gitai, Z., Dye, N. A., and Shapiro, L. (2004). An actin-like gene can determine cell polarity in bacteria. *Proc. Natl. Acad. Sci. U. S. A.* 101, 8643–8648. doi: 10.1073/pnas.0402638101

Goedhart, J. (2021). SuperPlotsOfData- a web app for the transparent display and quantitative comparison of continuous data from different conditions. *Mol. Biol. Cell* 32, 461–505.

Goley, E. D., Dye, N. A., Werner, J. N., Gitai, Z., and Shapiro, L. (2010). Imaging-based identification of a critical regulator of FtsZ protofilament curvature in *Caulobacter*. *Mol. Cell.* 39, 975–987. doi: 10.1016/j.molcel.2010.08.027

Goley, E. D., Yeh, Y.-C., Hong, S.-H., Fero, M. J., Abeliuk, E., McAdams, H. H., et al. (2011). Assembly of the *Caulobacter* cell division machine. *Mol. Microbiol.* 80, 1680–1698. doi: 10.1111/j.1365-2958.2011.07677.x

Hartmann, R., van Teeseling, M. C. F., Thanbichler, M., and Drescher, K. (2020). BacStalk: a comprehensive and interactive image analysis software tool for bacterial cell biology. *Mol. Microbiol.* 220, 140–150. doi: 10.1111/mmi.14501

Hocking, J., Priyadarshini, R., Takacs, C. N., Costa, T., Dye, N. A., and Shapiro, L. (2012). Osmolality-dependent relocation of penicillin-binding protein PBP2 to the division site in *Caulobacter crescentus*. *J. Bacteriol.* 194, 3116–3127. doi: 10.1128/jb.00260-12

Krupka, M., Sobrinos-Sanguino, M., Jiménez, M., Rivas, G., and Margolin, W. (2018). *Escherichia coli* ZipA organizes FtsZ polymers into dynamic ring-like protofilament structures. *mBio* 9:e01008-18.

Kuru, E., Hughes, H. V., Brown, P. J., Hall, E., Tekkam, S., Cava, F., et al. (2012). In situ probing of newly synthesized peptidoglycan in live bacteria with fluorescent D-amino acids. *Angew. Chem. Int. Ed. Engl.* 51, 12519–12523. doi: 10.1002/anie.201206749

Kysela, D. T., Randich, A. M., Caccamo, P. D., and Brun, Y. V. (2016). Diversity takes shape: understanding the mechanistic and adaptive basis of bacterial morphology. *PLoS Biol.* 14:e1002565. doi: 10.1371/journal.pbio.1002565

Lariviere, P. J., Szwedziak, P., Mahone, C. R., Löwe, J., and Goley, E. D. (2018). FzlA, an essential regulator of FtsZ filament curvature, controls constriction rate during *Caulobacter* division. *Mol. Microbiol.* 107, 180–197. doi: 10.1111/mmi.13876

Marks, M. E., Castro Rojas, C. M., Teiling, C., Du, L., Kapatral, V., Walunas, T. L., et al. (2010). The genetic basis of laboratory adaptation in *Caulobacter crescentus*. *J. Bacteriol.* 192, 3678–3688. doi: 10.1128/jb.00255-10

Meier, E. L., Daitch, A. K., Yao, Q., Bhargava, A., Jensen, G. J., and Goley, E. D. (2017). FtsEX-mediated regulation of the final stages of cell division reveals morphogenetic plasticity in *Caulobacter crescentus*. *PLoS Genet.* 13:e1006999. doi: 10.1371/journal.pgen.1006999

Meisenzahl, A. C., Shapiro, L., and Jenal, U. (1997). Isolation and characterization of a xylose-dependent promoter from *Caulobacter crescentus*. *J. Bacteriol.* 179, 592–600. doi: 10.1128/jb.179.3.592-600.1997

Monteiro, J. M., Pereira, A. R., Reichmann, N. T., Saraiva, B. M., Fernandes, P. B., Veiga, H., et al. (2018). Peptidoglycan synthesis drives an FtsZ-treadmilling-independent step of cytokinesis. *Nature* 554, 528–532. doi: 10.1038/nature25506

Özbaykal, G., Wollrab, E., Simon, F., Vigouroux, A., Cordier, B., Aristov, A., et al. (2020). The transpeptidase PBP2 governs initial localization and activity of the major cell-wall synthesis machinery in *E. coli*. *eLife* 9:e50629.

Pazos, M., Peters, K., Casanova, M., Palacios, P., VanNieuwenhze, M., Breukink, E., et al. (2018). Z-ring membrane anchors associate with cell wall synthases to initiate bacterial cell division. *Nat. Commun.* 9:5090.

Pichoff, S., and Lutkenhaus, J. (2002). Unique and overlapping roles for ZipA and FtsA in septal ring assembly in *Escherichia coli*. *EMBO J.* 21, 685–693. doi: 10.1093/emboj/21.4.685

Pointdexter, J. S. (1964). Biological properties and classification of the *Caulobacter* group. *Bacteriol. Rev.* 28, 231–295. doi: 10.1128/br.28.3.231-295.1964

Potluri, L.-P., Kannan, S., and Young, K. D. (2012). ZipA is required for FtsZ-dependent preseptal peptidoglycan synthesis prior to invagination during cell division. *J. Bacteriol.* 194, 5334–5342. doi: 10.1128/jb.00859-12

Randich, A. M., and Brun, Y. V. (2015). Molecular mechanisms for the evolution of bacterial morphologies and growth modes. *Front. Microbiol.* 6:580. doi: 10.3389/fmicb.2015.00580

Schindelin, J., Arganda-Carreras, I., Frise, E., Kaynig, V., Longair, M., Pietzsch, T., et al. (2012). Fihi: an open-source platform for biological-image analysis. *Nat. Methods* 9, 676–682.

Silber, N., Mayer, C., Matos de Opitz, C. L., and Sass, P. (2021). Progression of the late-stage divisome is unaffected by the depletion of the cytoplasmic FtsZ pool. *Commun. Biol.* 4:270.

Squyres, G. R., Holmes, M. J., Barger, S. R., Pennycook, B. R., Ryan, J., Yan, V. T., et al. (2021). Single-molecule imaging reveals that Z-ring condensation is essential for cell division in *Bacillus subtilis*. *Nat. Microbiol.* 6, 553–562. doi: 10.1038/s41564-021-00878-z

Strobel, W., Möll, A., Kiekebusch, D., Klein, K. E., and Thanbichler, M. (2014). Function and localization dynamics of bifunctional penicillin-binding proteins in *Caulobacter crescentus*. *J. Bacteriol.* 196, 1627–1639. doi: 10.1128/jb.01194-13

Tropini, C., Lee, T. K., Hsin, J., Desmarais, S. M., Ursell, T., Monds, R. D., et al. (2014). Principles of bacterial cell-size determination revealed by cell-wall synthesis perturbations. *Cell Rep.* 9, 1520–1527. doi: 10.1016/j.celrep.2014.10.027

Tsai, J. W., and Alley, M. R. (2001). Proteolysis of the *Caulobacter* McpA chemoreceptor is cell cycle regulated by a ClpX-dependent pathway. *J Bacteriol.* 183, 5001–5007. doi: 10.1128/jb.183.17.5001-5007.2001

Typas, A., Banzhaf, M., Gross, C. A., and Vollmer, W. (2012). From the regulation of peptidoglycan synthesis to bacterial growth and morphology. *Nat. Rev. Microbiol.* 10, 123–136. doi: 10.1038/nrmicro2677

Umeda, A., and Amako, K. (1983). Growth of the surface of *Corynebacterium diphtheriae*. *Microbiol. Immunol.* 27, 663–671.

van Teeffelen, S., Wang, S., Furchtgott, L., Huang, K. C., Wingreen, N. S., Shaevitz, J. W., et al. (2011). The bacterial actin MreB rotates, and rotation depends on cell-wall assembly. *Proc. Natl. Acad. Sci. U. S. A.* 108, 15822–15827. doi: 10.1073/pnas.1108999108

van Teeseling, M. C. F., de Pedro, M. A., and Cava, F. (2017). Determinants of bacterial morphology: from fundamentals to possibilities for antimicrobial targeting. *Front. Microbiol.* 8:1264. doi: 10.3389/fmicb.2017.01264

Varma, A., and Young, K. D. (2009). In *Escherichia coli*, MreB and FtsZ direct the synthesis of lateral cell wall via independent pathways that require PBP2. *J. Bacteriol.* 191, 3526–3533. doi: 10.1128/jb.01812-08

Vats, P., and Rothfield, L. (2007). Duplication and segregation of the actin (MreB) cytoskeleton during the prokaryotic cell cycle. *Proc. Natl. Acad. Sci. U. S. A.* 104, 17795–17800. doi: 10.1073/pnas.0708739104

Vats, P., Shih, Y.-L., and Rothfield, L. (2009). Assembly of the MreB-associated cytoskeletal ring of *Escherichia coli*. *Mol. Microbiol.* 72, 170–182. doi: 10.1111/j.1365-2958.2009.06632.x

Wang, Y., Jones, B. D., and Brun, Y. V. (2001). A set of *ftsz* mutants blocked at different stages of cell division in *Caulobacter*. *Mol. Microbiol.* 40, 347–360. doi: 10.1046/j.1365-2958.2001.02395.x

Wientjes, F. B., and Nanninga, N. (1989). Rate and topography of peptidoglycan synthesis during cell division in *Escherichia coli*: concept of a leading edge. *J. Bacteriol.* 171, 3412–3419. doi: 10.1128/jb.171.6.3412-3419.1989

Woldemeskel, S. A., McQuillen, R., Hessel, A. M., Xiao, J., and Goley, E. D. (2017). A conserved coiled-coil protein pair focuses the cytokinetic Z-ring in *Caulobacter crescentus*. *Mol. Microbiol.* 105, 721–740. doi: 10.1111/mmi.13731

Yakhnina, A. A., and Gitai, Z. (2013). Diverse functions for six glaycosyltransferases in *Caulobacter crescentus* cell wall assembly. *J. Bacteriol.* 195, 4527–4535. doi: 10.1128/jb.00600-13

Yang, X., Lyu, Z., Miguel, A., McQuillen, R., Huang, K. C., and Xiao, J. (2017). GTPase activity-coupled treadmilling of the bacterial tubulin FtsZ organizes septal cell wall synthesis. *Science* 355, 744–747. doi: 10.1126/science.aak9995

Yang, X., McQuillen, R., Lyu, Z., Phillips-Mason, P., De La Cruz, A., McCausland, J. W., et al. (2021). A two-track model for the spatiotemporal coordination of bacterial septal cell wall synthesis revealed by single-molecule imaging of FtsW. *Nat. Microbiol.* 6, 584–593. doi: 10.1038/s41564-020-00853-0

Conflict of Interest: The author declares that the research was conducted in the absence of any commercial or financial relationships that could be construed as a potential conflict of interest.

Publisher's Note: All claims expressed in this article are solely those of the authors and do not necessarily represent those of their affiliated organizations, or those of the publisher, the editors and the reviewers. Any product that may be evaluated in this article, or claim that may be made by its manufacturer, is not guaranteed or endorsed by the publisher.

frontiers in Microbiology

REVIEW
published: 08 September 2021
doi: 10.3389/fmicb.2021.732796

Targeting the Achilles Heel of FtsZ: The Interdomain Cleft

Pinkilata Pradhan[1,2], William Margolin[3] and Tushar Kant Beuria[1]**

[1] Institute of Life Sciences, Nalco Square, Bhubaneswar, India, [2] Regional Centre for Biotechnology, Faridabad, India, [3] Department of Microbiology and Molecular Genetics, McGovern Medical School, Houston, TX, United States

Widespread antimicrobial resistance among bacterial pathogens is a serious threat to public health. Thus, identification of new targets and development of new antibacterial agents are urgently needed. Although cell division is a major driver of bacterial colonization and pathogenesis, its targeting with antibacterial compounds is still in its infancy. FtsZ, a bacterial cytoskeletal homolog of eukaryotic tubulin, plays a highly conserved and foundational role in cell division and has been the primary focus of research on small molecule cell division inhibitors. FtsZ contains two drug-binding pockets: the GTP binding site situated at the interface between polymeric subunits, and the inter-domain cleft (IDC), located between the N-terminal and C-terminal segments of the core globular domain of FtsZ. The majority of anti-FtsZ molecules bind to the IDC. Compounds that bind instead to the GTP binding site are much less useful as potential antimicrobial therapeutics because they are often cytotoxic to mammalian cells, due to the high sequence similarity between the GTP binding sites of FtsZ and tubulin. Fortunately, the IDC has much less sequence and structural similarity with tubulin, making it a better potential target for drugs that are less toxic to humans. Over the last decade, a large number of natural and synthetic IDC inhibitors have been identified. Here we outline the molecular structure of IDC in detail and discuss how it has become a crucial target for broad spectrum and species-specific antibacterial agents. We also outline the drugs that bind to the IDC and their modes of action.

Keywords: protein structure, tubulin, bacterial cell division, small molecule inhibitor, antibacterial, ftsZ

OPEN ACCESS

Edited by:
Iain G. Duggin, University of Technology Sydney, Australia

Reviewed by:
Elizabeth Harry, University of Technology Sydney, Australia
Maria A. Oliva, Consejo Superior de Investigaciones Científicas (CSIC), Spain
Leendert Hamoen, University of Amsterdam, Netherlands

****Correspondence:***
William Margolin
William.Margolin@uth.tmc.edu
Tushar Kant Beuria
tkbeuria@ils.res.in

Specialty section:
This article was submitted to Microbial Physiology and Metabolism, a section of the journal Frontiers in Microbiology

Received: *29 June 2021*
Accepted: *16 August 2021*
Published: *08 September 2021*

Citation:
Pradhan P, Margolin W and Beuria TK (2021) Targeting the Achilles Heel of FtsZ: The Interdomain Cleft. Front. Microbiol. 12:732796. doi: 10.3389/fmicb.2021.732796

INTRODUCTION

The battle against infectious diseases has been a persistent challenge for humans. The development and use of antibiotics helped to prevent and control bacterial infections, but at the same time its misuse led to the development of antibacterial resistance (Ma and Ma, 2012). An increase in antibacterial resistance is now of significant concern worldwide, resulting in higher infection and mortality rates. As more bacteria become resistant to currently available antibiotics, discovery of new antibiotics and identification of new targets is more urgent than ever.

Although division of bacterial cells is key for their colonization and pathogenesis, the cell division machinery has not been fully explored for the development of antibacterial agents despite many breakthroughs in the mechanisms and regulation of this fundamental process. Cell division is initiated by the formation of a discontinuous and dynamic circumferential assembly at the

site of division called the Z ring, which is located at the cell midpoint in bacteria that divide by binary fission.

Several proteins are involved in determining the proper assembly and correct placement of the Z-ring (Hale and de Boer, 1997; Pichoff and Lutkenhaus, 2002; Bramkamp et al., 2008; Rowlett and Margolin, 2015). However, the key organizing protein is FtsZ (**F**ilamenting **t**emperature **s**ensitive mutant **Z**), which assembles into treadmilling polymers to form a dynamic skeleton for the Z-ring, ultimately recruiting other cell division proteins to the Z-ring in a sequential manner (Bi and Lutkenhaus, 1991; Wang et al., 2020). FtsZ is present in nearly all bacteria, plant plastids, and many archaea, and is a homolog of eukaryotic tubulin (Mukherjee and Lutkenhaus, 1994; Erickson, 1995; de Pereda et al., 1996; Nogales et al., 1998a,b; Kaur et al., 2010). In search for new antibiotic targets, FtsZ has become the leading candidate, as it is essential for cell division in most bacteria and is absent in eukaryotes (Beall and Lutkenhaus, 1991; Dai and Lutkenhaus, 1991; Pinho and Errington, 2003; Li and Ma, 2015). Although FtsZ is homologous to eukaryotic tubulin, it shares little sequence identity (10–18%) with tubulin, reducing the likelihood that drugs targeting FtsZ will be toxic to eukaryotic cells (de Pereda et al., 1996).

Over the past few decades, researchers have characterized several natural as well as synthetic FtsZ inhibitors. However, the interaction sites/ binding pockets in FtsZ for many inhibitors are not yet fully characterized. To define the functional groups in a small molecule that can efficiently affect the functions of a target, it is critical to understand its binding site in the target. A detailed molecular understanding of the binding site will help to design and develop specific drugs against the target, which will further help to identify more specific and potent FtsZ inhibitors.

FtsZ contains two prominent drug binding sites, the GTP binding site, which we will refer to as the nucleotide binding domain (NBD), and the inter-domain cleft (IDC) (Casiraghi et al., 2020). The NBD is similar to that of tubulin and shares the glycine-rich signature motif GGGTG(T/S)G of tubulin (de Pereda et al., 1996; Löwe, 1998). Consequently, there is a higher chance that drugs that target the FtsZ GTP binding site may also interact with tubulin and cause toxicity in the mammalian cells. In contrast, the IDC of FtsZ exhibits less similarity to tubulin, reducing the odds of toxicity to mammalian cells (Casiraghi et al., 2020). Fortunately, most of the reported FtsZ inhibitors interact with the IDC. This review highlights different drugs that target the IDC, summarizes the residues within the IDC that are important for drug binding, and outlines what is known about the mechanism of action. We also describe why the FtsZ IDC has attracted more attention as a drug target for the development of novel antibacterial compounds.

FTSZ AND THE Z-RING

Bacterial cell division is a complex process that involves replication and segregation of its genetic material, elongation of the lateral cell wall, and formation of a division septum at midcell followed by separation of the two daughter cells. Using immune electron microscopy on *Escherichia coli* cells undergoing binary fission, Bi and Lutkenhaus provided initial proof 30 years ago that FtsZ localizes at the center of the cell and forms a ring like structure (Bi and Lutkenhaus, 1991). The correct localization of the Z-ring at midcell in many rod-shaped bacteria is controlled by diverse spatial regulatory systems. In *E. coli*, the nucleoid occlusion system prevents potentially DNA-damaging formation of the Z-ring over the unsegregated nucleoid, while the Min system oscillates between both cell poles and inhibits the formation of Z-rings at the poles (Rowlett and Margolin, 2015; Taviti and Beuria, 2017). The invagination of the cell envelope behind the Z-ring at midcell is initiated by forces generated by the Z-ring. Several independent studies showed that a ∼8 – 80 pN force generated during the constriction of the Z-ring may be sufficient to initiate this invagination (Lan et al., 2007; Hsin et al., 2012; Yao et al., 2017; Nguyen et al., 2019; Ramirez-Diaz et al., 2021).

Assembly of the Z-ring is regulated by a number of endogenous activator and inhibitor proteins, maintaining a balance between instability and stability (Hale and de Boer, 1997; Trusca et al., 1998; Pichoff and Lutkenhaus, 2002; Haeusser et al., 2004). Overproduction of FtsZ inhibitors such as SulA or MinCD, or inactivation of FtsZ stabilizing proteins such as FtsA, ZipA, or Zap proteins in *E. coli* lead to long, filamentous cells without Z-rings or with multiple stalled Z-rings (Addinall et al., 1996), ultimately preventing viability. Similarly, small molecules that inhibit Z ring formation or hyperstabilize the Z-ring also lead to a block in cell division. As FtsZ is the most important component of the Z-ring, development of FtsZ inhibitors requires a molecular understanding of FtsZ structure, drug-binding sites on FtsZ and the inhibitory effects of drugs on FtsZ functions.

OVERALL FTSZ STRUCTURE AND FUNCTION

Domains of FtsZ

FtsZ consists of a conserved globular core (residues 10–316) comprising an N-terminal domain (H1–H6, S1–S6), a core helix (H7), a spacer loop (T7 loop) and a C-terminal domain (H8–H10, S7–S10), which in turn is connected to a conserved peptide at the extreme C terminus (residues 369–383) by a flexible unstructured linker (317–368) (de Boer et al., 1992; Löwe and Amos, 1998; Nogales et al., 1998b) (**Figure 1**). In some species, such as the archaeon *Methanocaldococcus jannaschii,* FtsZ contains an additional helix (H0) in its N-terminal subdomain (Löwe, 1998).

In *E. coli* FtsZ, the N-terminal domain spans residues 1–177. It contains an unstructured and poorly conserved extreme N terminus and a highly conserved NBD (Löwe and Amos, 1998; Vaughan et al., 2004; Gardner et al., 2013). Although the N-terminal domain contains the NDB, it is not sufficient for hydrolyzing GTP (Jindal and Panda, 2013). In *E. coli,* H7 extends from residues 178 to 201, connects the N-terminal and C-terminal domains of the core, and acts like a sliding door for the opening and closing of the IDC. Some residues of H7 are crucial for FtsZ assembly. For example, a single mutation in *Bacillus subtilis* FtsZ (BsFtsZ) R191 can impede FtsZ assembly (Dhaked et al., 2016).

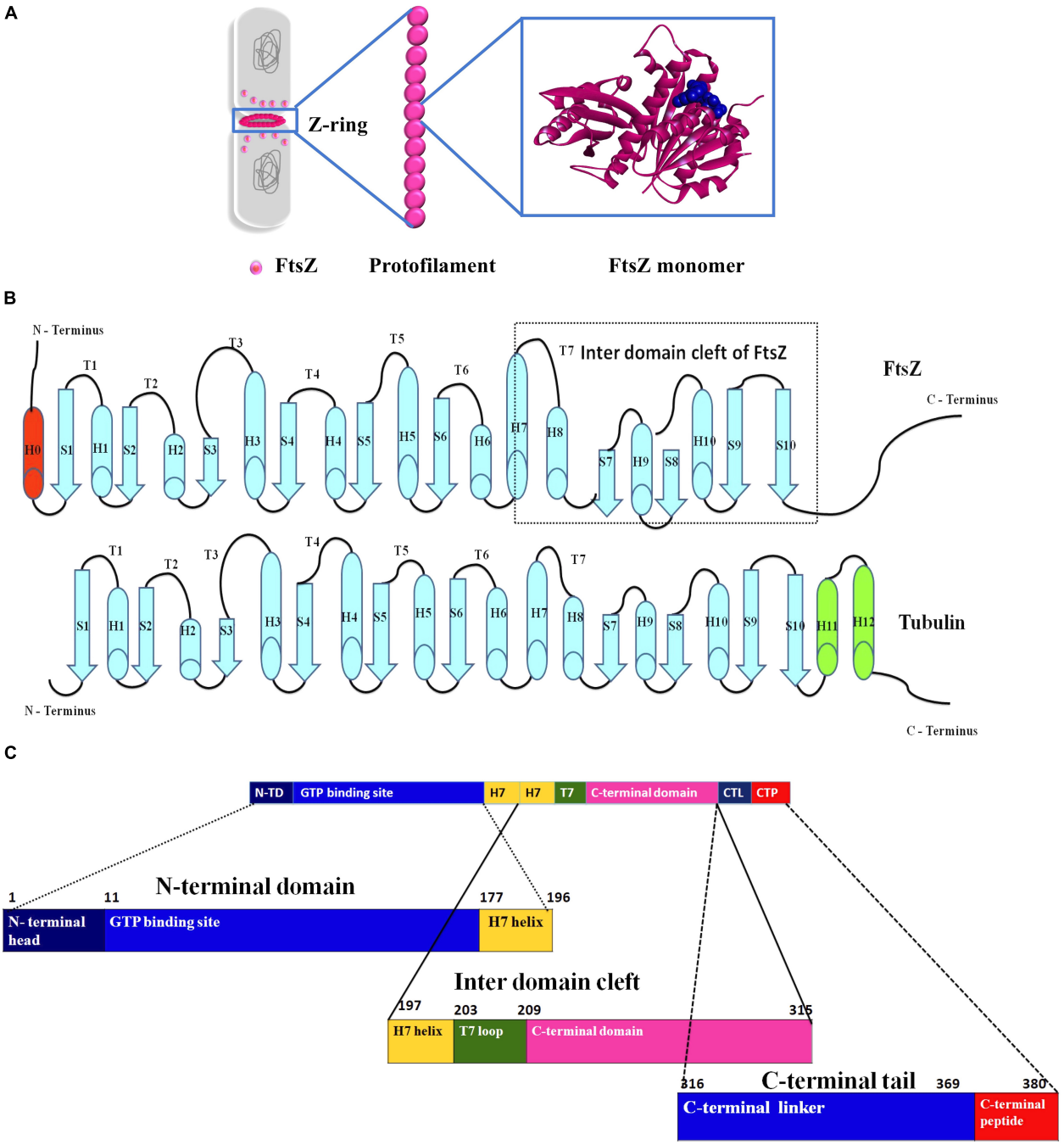

FIGURE 1 | Insight into the structure of FtsZ. **(A)** During bacterial cell division the nucleoids (gray) are segregated and a Z-ring (magenta) is formed at midcell by the coalescence and assembly of FtsZ monomers from the cytoplasm into polymers. Monomers are continuously exchanged with treadmilling FtsZ polymers. **(B)** Secondary structures of both FtsZ and tubulin. **(C)** An outline of the domains of FtsZ.

The highly conserved T7 loop in *E. coli* FtsZ (residues 202 – 209) connects H7 to H8 of the C-terminal subdomain and contains a conserved GXXNXD sequence that is important for GTP hydrolysis. Upon FtsZ assembly, the T7 loop of one FtsZ monomer inserts into the GTP binding pocket of the adjacent FtsZ monomer and initiates GTP hydrolysis (Löwe and Amos, 1999; Scheffers et al., 2002). Drug molecules that bind to this site affect GTPase activity of FtsZ.

The C-terminal domain of the globular core of FtsZ (residues 210 to 316) is highly conserved both in sequence and structure. It consists of helices H8–H10 and beta sheets S7–S10. H10 is notably rich in acidic residues and interacts with Min proteins

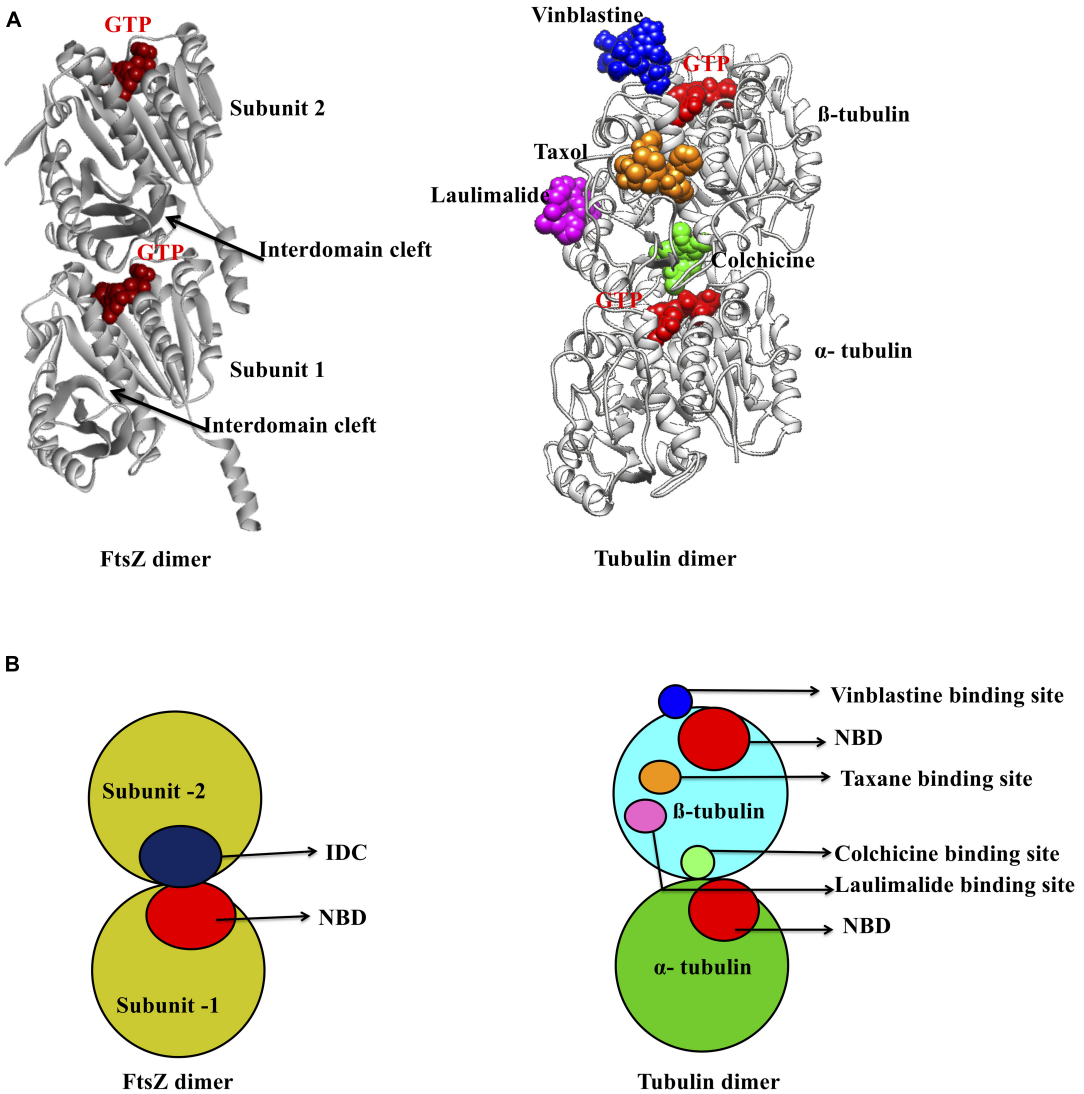

FIGURE 2 | Major inhibitor binding sites in FtsZ and tubulin: **(A)** Structure of FtsZ and tubulin dimers with major drug binding sites. **(B)** Shown is a cartoon representation of the same.

(Taviti and Beuria, 2017). This domain is followed by an unstructured C-terminal linker (CTL) that is highly variable both in composition and length (Taviti and Beuria, 2017). In *E. coli*, the CTL is ∼ 52 residues (317 – 369). In most FtsZs, the CTL connects the globular core domain of FtsZ with a highly conserved 10–20 residue peptide at the extreme end of the C-terminus called the C-terminal peptide (CTP) (Cohan et al., 2020). Although this peptide (residues 369–379 in *E. coli)* is not required for FtsZ assembly, it is crucial for interactions with other membrane-associated cell division proteins like ZipA and FtsA (Ma and Margolin, 1999; Ortiz et al., 2016). Residues D373, I374, F377 and L378 of *E. coli* FtsZ are specifically involved in these protein-protein interactions (Buske and Levin, 2012). As a result, deletion of the CTP blocks FtsZ functions and bacterial division (Din et al., 1998).

FtsZ Assembly and GTPase Activity

FtsZ, in the presence of GTP, polymerizes into head-to-tail protofilaments (Bramhill and Thompson, 1994; Mukherjee and Lutkenhaus, 1994), which then coalesce to form the Z-ring (Haeusser and Margolin, 2016). The Z–ring is anchored to the membrane with the help of other essential cell division proteins, such as FtsA and ZipA of *E. coli* (Pichoff and Lutkenhaus, 2002). In Gram positive bacteria as well as FtsZ-containing archaea, SepF is the key membrane anchor for FtsZ (Duman et al., 2013; Nussbaum et al., 2021; White and Eswara, 2021).

In vitro studies suggest that FtsZ assembles into short protofilaments made up of ∼30 subunits that combine laterally to form the Z-ring (Erickson et al., 2010). These lateral interactions between FtsZ protofilaments help to drive division septum formation (Krupka and Margolin, 2018; Squyres et al., 2021;

TABLE 1 | Reported FtsZ inhibitors, binding sites, and mechanisms of action.

Sl No. of core struct-ure[1]	Sl No. of drugs	Core structure	Drug	Binding site on FtsZ	Effects on assembly or GTPase activity[2]	IC_{50} in μ M (tubulin/ microtubule/ eukaryotic cells)/HC_{50}	MIC in μ M	IC_{50} MIC ratio	References
A.	1.	Benzamide ring 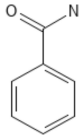	3-MBA and PC190723	IDC	E	> 180	2.81	> 64	Haydon et al., 2008
A.	2.		TXA707,TXA709 and TXA6101	IDC	E	> 233.25	3.9	> 60	Kaul et al., 2015; Fujita et al., 2017; Carro, 2019
A.	3.		3-substituted 2,6-difluorobenzamide derivatives **(I1)**	IDC	-	-	0.88–28.04	-	Bi et al., 2017
A.	4.		Isoxazole benzamide derivatives **(I2)**	IDC	E	> 331	0.04–10.4	> 32	Bi et al., 2018
A.	5.		1, 3, 4 -oxadiazol-2-one-benzamide derivatives **(I3)**	IDC	E	> 150	0.29–2.35	> 64	Bi et al., 2019
A.	6.		3-aminobenzamide derivatives **(I4)**	IDC	I	> 100	3.1	> 32	Lui et al., 2019
A.	7.		BOFP	IDC		-	1.32	-	Ferrer-Gonzalez et al., 2019
B.	8.	Quinoline and quinazoline ring 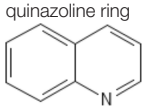	Berberine	NBD	I, G	18	95–380	0.047	Yu et al., 2005; Domadia et al., 2008; Raghav et al., 2017

(Continued)

TABLE 1 | Continued

Sl No. of core struct-ure[1]	Sl No. of drugs	Core structure	Drug	Binding site on FtsZ	Effects on assembly or GTPase activity[2]	IC_{50} in μ M (tubulin/ microtubule/ eukaryotic cells)/HC_{50}	MIC in μ M	IC_{50} MIC ratio	References
A.	9.		Benzofuroquinolinium Derivatives **(I5)**	NBD	I, G	95.5	0.48–15.3	6.2	Zheng et al., 2018
A.	10.		9-phenoxy Berberine derivatives	IDC	I, G	-	4–65	-	Sun et al., 2014
A.	11.		Thiazole Orange Derivatives **(I6)**	IDC	E, G	96.5	1.36–5.45	17.7	Sun et al., 2017b
A.	12.		Indolyl-quinolinium derivatives **(I7)**	IDC	E	-	2.02–32	-	Cai et al., 2019; Carro, 2019
A.	13.		3-methylbenzo[d]thiazol-methylquinolinium **(I8)**	IDC	E, G	78.25	1.81–5.43	14.4	Sun et al., 2018
A.	14.		N-Methylbenzofuro[3,2-b] quinoline and Methylbenzoindole[3,2-b] quinoline derivatives, **(I9)**	IDC	I, G	-	4.16–12.5	-	Sun et al., 2017a
A.	15.		Thiazole-quinolinium derivatives **(I10)**	IDC	E	28.4	2.25	12.6	Li et al., 2015
C.	16.	Benzopyrone ring 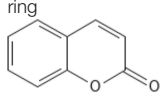	Coumarin and its derivatives	IDC	I, G	> 500	3420	> 0.14	Finn et al., 2001; de Souza et al., 2005; Duggirala et al., 2014
A.	17.		Polyketides compounds **(I11)**	IDC	G	-	5–40	-	Matsui et al., 2017
A.	18.		Quercetin dehydrate	IDC	I	> 100	378.5	> 0.26	Mathew et al., 2016
D.	19.	Phenylpropanoid 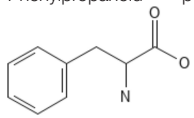	p-coumaric acid	IDC	I, G	215	122	1.7	Hemaiswarya et al., 2011; Lou et al., 2012; Chang and Shen, 2014

(Continued)

TABLE 1 | Continued

Sl No. of core struct-ure[1]	Sl No. of drugs	Core structure	Drug	Binding site on FtsZ	Effects on assembly or GTPase activity[2]	IC_{50} in μ M (tubulin/ microtubule/ eukaryotic cells)/HC_{50}	MIC in μ M	IC_{50} MIC ratio	References
A.	20.		Cinnamic acid	IDC		2400	9000	0.27	Rastogi et al., 2008; Hemaiswarya et al., 2011; Niero and Machado-Santelli, 2013
A.	21.		Cinnamaldehyde	IDC		9.76	7560	0.0013	Domadia et al., 2007; Ng and Wu, 2011
A.	22.		Caffeic acid	IDC		> 100	1800	> 0.055	Rastogi et al., 2008; Hemaiswarya et al., 2011; Sanderson et al., 2013
A.	23.		Ferulic acid	IDC		500	> 515	< 1	Borges et al., 2013; Eroglu et al., 2015
E.	24.	Pyrimidine ring 	pyrimidine-quinuclidine derivatives	NBD	I	> 500	49.2	> 10	Chan et al., 2013; Haranahalli et al., 2016
A.	25.		2,4-disubstituted-6-thiophenyl-pyrimidine derivatives **(I12)**	NBD	I, G	> 128	4	>32	Fang et al., 2019

(Continued)

TABLE 1 | Continued

Sl No. of core struct-ure[1]	Sl No. of drugs	Core structure	Drug	Binding site on FtsZ	Effects on assembly or GTPase activity[2]	IC_{50} in μ M (tubulin/ microtubule/ eukaryotic cells)/HC_{50}	MIC in μ M	IC_{50} MIC ratio	References
F.	26.	Complex ring structure 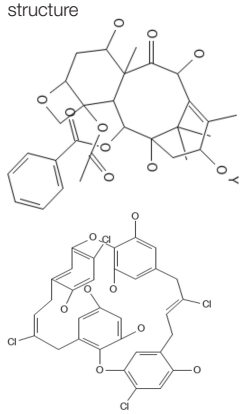	SB-RA-2001	IDC	E, G	45	5	9	Huang et al., 2006; Singh et al., 2014
	27.		Doxorubicin	IDC	I, G	8.3	40	0.20	Panda et al., 2015; Oncul and Ercan, 2017
	28.		Colchicine	IDC		6.5	160	0.04	Mathew et al., 2016
	29.		CCR11	IDC		18	3	6	Singh et al., 2012
	30.		Sulindac analog **(I13)**	IDC		> 100	19.5	> 5.1	Mathew et al., 2016
	31.		Bt-benzo-29	IDC		17	8	2.12	Ray et al., 2015
	32.		Tiplaxtinin	IDC	E	2.7	4.5	0.6	Elokdah et al., 2004; Sun et al., 2017c
	33.		Chrysophaentin A	NBD	I,G	> 150	4.6–9.26	> 32	Plaza et al., 2010; Keffer et al., 2013
	34.		UCM44	NBD	E	44	37.1	1.18	Ruiz-Avila et al., 2013
	35.		Biphenyl derivative **(I14)**	NBD	I	> 100	7	>14.28	Artola et al., 2015

(Continued)

TABLE 1 | Continued

Sl No. of core struct-ure[1]	Sl No. of drugs	Core structure	Drug	Binding site on FtsZ	Effects on assembly or GTPase activity[2]	IC_{50} in μ M (tubulin/ microtubule/ eukaryotic cells)/HC_{50}	MIC in μ M	IC_{50} MIC ratio	References
G.	36.	Simple ring structure 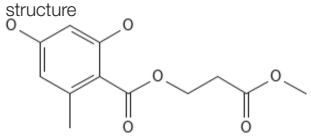	Curcumin	NBD	I	18	100	0.18	Rai et al., 2008; Chakraborti et al., 2011
	37.		Plumbagin	IDC	I,G	14.6	29	0.5	Acharya et al., 2008; Bhattacharya et al., 2013
	38.		*P. cataractum* SYPF 7131 bioactive compound **(I15)**	IDC	G	-	192.5–293	-	Wu et al., 2018
H.	39.	Peptide inhibitor	CRAMP	IDC	I	300	20	15	Ray et al., 2014
	40.		MciZ	Near IDC	I	-	-	-	Bisson-Filho et al., 2015

[1] *Non-peptide FtsZ inhibitors are classified into 7 groups based on their core ring structure (A–G).*

[2] *E, enhances assembly; I, inhibits assembly; G, inhibits GTPase activity; blank if unknown.*

I1*: 3-((2-ethylhexyl)oxy)-2,6-difluorobenzamide,* ***I2****: 3-((5-(4-(Tert-butyl)phenyl)isoxazol-3-yl)methoxy)-2,6-difluorobenzami,* ***I3:*** *2,6-Difluoro-3-((4-(4-bromophenyl)-5-oxo-1,3,4-oxadiazol-2- yl)methoxy)benzamide,* ***I4:*** *2,6-Difluoro-3-(nonylamino)benzamide,* ***I5:*** *5-Methyl-11-((3-(3-dipropylamine)-propylbenzo[d]thiazol-2(3H)-ylidene)methyl)benzofuro[3,2-b]quinolin-5-ium iodide,* ***I6:*** *2-((E)-4- Hydroxystyryl)-1-methyl-4-((Z)-(3-methylbenzo[d]thiazol-2(3H)-ylidene)methyl)quinolin-1-ium iodide,* ***I7:*** *(E)-2-(2-(1H-indol-2-yl)vinyl)-1-methyl-4-(piperidin-1-yl)quinolin1-ium iodide,* ***I8:*** *2-((E)-4-fluorostyryl)-1-methyl-4-((E)-(3-methylbenzo[d]thiazol-2(3H)-ylidene)methyl) quinolin-1-ium iodide,* ***I9:*** *5-Methyl-11-(4-methoxyphenylamino)benzoindolo[3,2-b] quinolin-5-ium iodide****,*** ***I10:*** *Z)-1,2-Dimethyl-4-((3-(3-(4-methylpiperidin-1-yl)propyl)benzo[d]thiazol-2(3H)-ylidene)methyl)quinolin-1-ium iodide,* ***I11:*** *Gancaonin,* ***I12:*** *[1-(4-isopropylbenzyl)-4-(2-(2-(pyridin-4-yl)-6-(thiophen-2-yl)pyrimidin-4-yl)ethyl)-1,4-diazepane (Bb2)],* ***I13:*** *(Z)-N-(2-(dimethylamino)ethyl)-2-(5-fluoro-2-methyl-1-(4-(methylthio)benzylidene)-1H-inden-3-yl)acetamide,* ***I14:*** *[Biphenyl-3,5-diyl bis(3-hydroxybenzoate)],* ***I15:*** *Penicimenolidyu B.*

Whitley et al., 2021). A single FtsZ protofilament is ∼5 nm thick with slightly curved morphology, which becomes highly curved upon GTP hydrolysis (Lu et al., 2000; Romberg et al., 2001). One model proposed that GTP hydrolysis provides the required force for Z-ring constriction and septation (Allard and Cytrynbaum, 2009). As GTP hydrolysis is induced upon FtsZ assembly into polymers, FtsZ subunits within the Z ring are highly dynamic, with a half time of FtsZ subunit turnover as low as 8–9 s in *E. coli* and *B. subtilis* (Anderson et al., 2004). This turnover results from treadmilling, which allows FtsZ polymers to travel circumferentially around the site of septum formation by loss of subunits at one polymer end and gain of subunits at the other (Bisson-Filho et al., 2017; Yang et al., 2017). Surprisingly, only about ∼30% of the FtsZ in *E. coli* cells is actually in the Z-ring at any one time, while the remaining FtsZ circulates in a cytoplasmic pool that is continuously exchanged with treadmilling FtsZ polymers that comprise the Z ring (Stricker et al., 2002). Despite the rapid turnover observed in cells, purified FtsZ in solution hydrolyzes its bound GTP at a rate of only ∼2 GTP per FtsZ molecule per minute (Lu et al., 1998), suggesting that cellular factors may enhance FtsZ GTPase activity. Molecular dynamics simulations of FtsZ dimers predict the forces generated by GTP hydrolysis to be ∼30 pN per FtsZ monomer, which is within the range of force required (8 – 80 pN) to drive cytokinesis as mentioned above (Lan et al., 2007; Hsin et al., 2012). Nonetheless, inward growth of the cell division septum likely contributes significantly to the constriction of the Z ring.

SIMILARITIES AND DIFFERENCES BETWEEN TUBULIN AND FTSZ

Although FtsZ has minimal sequence similarity with tubulin, there are several regions that are highly similar in both proteins. Tubulin and FtsZ share only ∼10–18% sequence identity, yet both exhibit structural homology (de Pereda et al., 1996; Kusuma et al., 2019), suggesting convergent evolution (van den Ent et al., 2001; Battaje and Panda, 2017). Sequence alignment of FtsZ, α-tubulin and β-tubulin demonstrated that the T1 loop (common glycine), T4 loop (with the tubulin signature motif), T5 loop (common prolines), T6 loop (common asparagine), and T7 loop (common asparagine and aspartate) show high sequence identity. No significant sequence similarity was observed between tubulin and FtsZ after the T7 loop (Löwe, 1998; Löwe and Amos, 1998; Nogales et al., 1998a).

The secondary structure of both proteins contains a similar sequence of helices – strands – loops and follows similar nomenclature. FtsZ contains ten helices and ten strands. Although the secondary structures of both tubulin and FtsZ are quite similar, the two extra helices at the C-terminus and the C-terminal tail of tubulin are not long like those in FtsZ (**Figure 1B**) (Nogales et al., 1998a). In terms of tertiary structure, a structural prediction study by Pereda et al. involving 200 tubulin sequences and 12 FtsZ sequences from various organisms showed that FtsZ and tubulin have a nearly identical percentage of folds, helices and sheets (de Pereda et al., 1996).

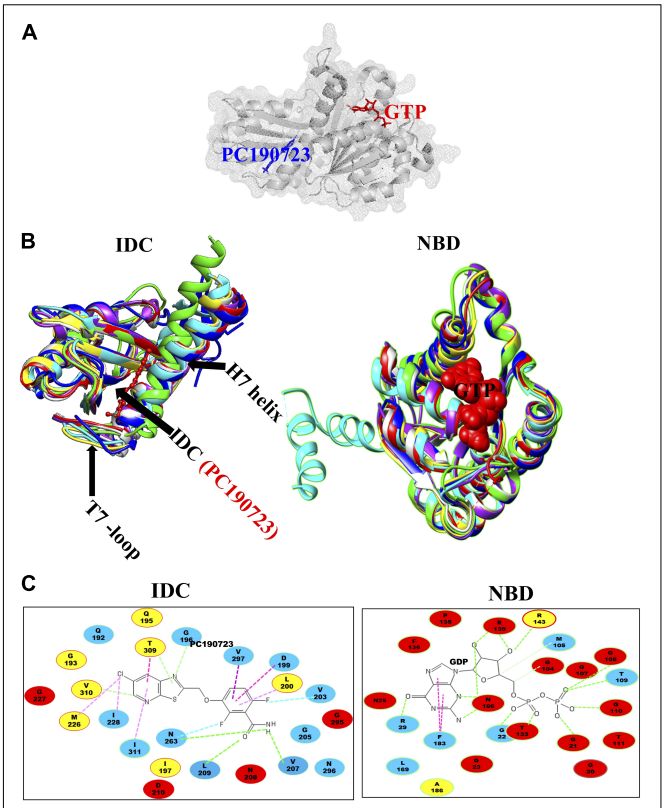

FIGURE 3 | Structural alignment of GTP binding site and IDC in FtsZ. **(A)** IDC and NBD in FtsZ are denoted by mesh structures**. (B)** A structural level comparison of GTP binding sites and the IDC among FtsZs from *E. coli* (red), *B. subtilis (yellow), S. aureus (green), A. aeolicus (blue), P. aeruginosa (violet), M. jannaschii (cyan)*, and *M. tuberculosis (light gray)*. **(C)** Major residues around the GTP binding site and the IDC and their conservation in Gram positive species only (yellow), Gram negative species only (green) or in both Gram positive and Gram negative bacteria (red); non conserved residues are in blue.

However, an *in silico* study that superimposed structures of different FtsZ proteins with tubulin showed that structural differences between FtsZ and tubulin are quite high, with an RMSD value of 8–10 Å (Kusuma et al., 2019). The NBDs of both proteins exhibit a Rossman fold topology (Löwe and Amos, 1998). Both FtsZ and tubulin belong to a distinct GTPase family, which bind to GTP and self-activate GTPase concomitant with polymerization (Nogales et al., 1998a). As suggested by the lack of sequence similarities, there is no structural homology in the C-terminal domains of both proteins. Superimposition of the structures confirmed that the IDC of FtsZ is also absent in tubulin (Battaje and Panda, 2017; Kusuma et al., 2019).

Despite sharing some structural similarities, FtsZ and tubulin diverge in how they form polymers. FtsZ protofilaments are formed by FtsZ monomers, whereas tubulin protofilaments consist of both α and β- tubulin monomers and require a gamma tubulin for nucleation and initiation of tubulin assembly. Another difference is that even if α and β- tubulins show similar degree of similarities with FtsZ, only the β- tubulin can

TABLE 2 | Roles of different IDC residues in binding ligands.

	IDC residues										
*Ec*FtsZ	G191	G195	E198	L199	M206	N207	V208	N263	S297	R307	T309
*Sa*FtsZ	Q192	G196	D199	L200	V207	N208	L209	N263	V297	V307	T309
*Bs*FtsZ	Q192	G196	D199	L200	I207	N208	L209	N263	V297	V307	T309
Thiazole ring	+	+	+	+	+	+	+	+	–	–	+
Quinoline ring	–	–	+	+	–	–	–	–	+	+	+
Benzopyrone	–	–	–	–	–	+	+	–	–	–	–
Phenylpropanoid	–	–	–	–	–	–	+	+	+	–	–
Naphthalene	+	+	+	–	–	–	–	+	–	+	+
Complex ring	+	–	+	+	–	–	+	–	+	–	–
Simple ring	–	–	–	+	–	–	+	+	–	–	+
Peptide	–	–	–	–	–	+	+	–	–	–	–

(+) indicates bonding interaction; (–) indicates non-bonding residues (no interaction).

exchange its GTP, whereas all FtsZ monomers can exchange their GTP and undergo GTP-dependent assembly. Furthermore, the C terminus of FtsZ ends with a β-sheet, whereas a helix is present at the C terminus of tubulin that is responsible for interaction with motor proteins (**Figure 1B**) (Erickson, 1998; Battaje and Panda, 2017). But the key structural difference between FtsZ and tubulin at the monomer level is the presence of the IDC only in FtsZ. This has been a boon for the discovery of compounds unique to FtsZ with minimal cytotoxicity toward eukaryotic cells.

THE TWO DISTINCT DRUG BINDING POCKETS OF FTSZ

The NBD

As mentioned above, there are two main binding pockets for drug binding to FtsZ, the NBD and IDC (**Figure 2**). The NBD, at the interface between FtsZ monomers, includes helices H1–H6, sheets S1–S6 and the T1–T6 loop. It also includes the N-terminal part of H7 (Löwe, 1998; Panda et al., 2016). Seven distinct regions in FtsZ interact with GTP. The T1 loop interacts with the phosphate and the guanine base, whereas the T2 & T3 loops interact with the β- and γ-phosphates (Nogales et al., 1998a; Panda et al., 2016). The T4 loop contains the tubulin signature motif, which interacts with the α and β- phosphates (Mukherjee et al., 1993; de Pereda et al., 1996). The T5-loop interacts with the ribose sugar. The T6 loop possesses an asparagine residue (N165 in *E. coli*), which interacts with the guanine base via a hydrogen bond and is conserved in both FtsZ and tubulin (Panda et al., 2016). The guanine base is mainly recognized by amino acid residues present within the H7 helix. There are several small molecules that are known to interact with the FtsZ NBD (**Table 1**). Most of these could either interact with microtubules or were screened from a library of microtubule-interacting molecules. As the NBD is highly conserved in both FtsZ and tubulin, any molecules that bind to it may be toxic to mammalian cells. Indeed, curcumin, which binds the NBD of both FtsZ and tubulin, has an MIC of 100 μM in *B. subtilis* and an IC_{50} of 18 μM for HeLa cells (Rai et al., 2008; Chakraborti et al., 2011). Some other examples of this cross-toxicity are summarized in **Table 1** (IC_{50}/MIC).

The IDC

The second major binding site in FtsZ that interacts with small molecules is the IDC, formed by the C-terminal half of the H7 helix, the T7 loop and the beta sheets in the C-terminal domain (**Figure 1C**) (Sun et al., 2014). The size of the cleft, the number of amino acid residues, their conservation and types vary among different bacterial species (**Figure 3** and **Table 2**). For example, the IDC is less conserved in Gram negative bacteria (fewer than nine conserved residues) than Gram positive bacteria (more than nine conserved residues). The size of the IDC also varies among bacterial species, depending on the curvature of the H7 helix. For example, in the GTP bound state of *Staphylococcus aureus* FtsZ the curvature of the H7 helix decreases, which in turn increases the size of the cleft opening. The T7 loop of FtsZ also influences the cleft opening size. In bacteria such as *S. aureus* and *B. subtilis,* the T7 loop in the GTP bound state shifts downward, resulting in a larger cleft opening compared to the GDP bound state (Kusuma et al., 2019). As the T7 loop of one FtsZ subunit is inserted into the nucleotide-binding pocket of the adjacent FtsZ subunit to trigger GTPase activity (Panda et al., 2016), this loop is crucial for modulating FtsZ treadmilling dynamics.

In most bacterial species, many archaea, some chloroplasts and a few primitive mitochondria, the globular domains of FtsZ share 40–50% structural and functional similarity (Erickson, 1998; Tripathy and Sahu, 2019). Compared to the NBD, which exhibits 48–67% sequence identity among FtsZs from *E. coli, Pseudomonas aeruginosa*, *B. subtilis, S. aureus, Mycobacterium tuberculosis*, *Aquifex aeolicus*, and the archaeon *M. jannaschii*, the IDC shows less sequence conservation (34–59% identity) (Casiraghi et al., 2020). The three-dimensional structure of the NBD is quite similar among FtsZs from different bacterial species, whereas it is slightly different among various IDCs

TABLE 3 | Comparison of drug binding sites between FtsZ and tubulin.

Protein	Binding site	Secondary structures involved	References
FtsZ	NBD	H1–H7 helix, S1–S6 strands, and T1–T6 loops	Löwe, 1998
	IDC	H7 helix, S7–S10 strands, and T7 loop	Sun et al., 2014
Tubulin	NBD	H1–H7 helix, S1–S6 strands, and T1–T6 loops	Nogales et al., 1998a
	Colchicine	H7,H8 helix, S8,S9 strands, T7-loop : ß- tubulinT5-loop : α- tubulin	Ravelli et al., 2004; Steinmetz and Prota, 2018
	Taxane	H7 helix, S7 strand, H6–H7 loop, S7–H9 (M-loop) and S9–S10 loop : ß- tubulin	Kellogg et al., 2017
	Laulimalide	H9–H10 helix, H9–H9' and H10–S9 loop : ß- tubulin	Prota et al., 2014
	Vinblastine	H6 helix, T5-loop and H6–H7 loop : ß- tubulinH10 helix, S9 strand, and T7-loop : α- tubulin	Steinmetz and Prota, 2018

TABLE 4 | *Ec*FtsZ residues within the IDC and the corresponding *Bs*FtsZ and *Sa*FtsZ residues.

***Ec*FtsZ**	D187	V188	K190	G191	A192	Q194	G195	I196	E198	L199	R202	P203	G204	L205	M206
***Bs*FtsZ**	N188	V189	R191	Q192	G193	Q195	G196	I197	D199	L200	T203	P204	G205	L206	I207
***Sa*FtsZ**	N188	V189	R191	Q192	G193	Q195	G196	I197	D199	L200	V203	S204	G205	E206	V207
***Ec*FtsZ**	N207	V208	V213	M225	G226	S227	V229	L261	V262	N263	T265	A266	L270	R271	L272
***Bs*FtsZ**	N208	L209	V214	M226	G227	I228	I230	L261	M262	N263	T265	G266	L270	S271	L272
***Sa*FtsZ**	N208	L209	V214	M226	G227	I228	V230	L261	M262	N263	T265	G266	L270	S271	L272
***Ec*FtsZ**	F275	G295	T296	S297	L298	D299	P300	D301	M302	N303	E305	R307	T309	V310	V311
***Bs*FtsZ**	V275	G295	S296	V297	I298	N299	E300	N301	L302	K303	E305	V307	T309	V310	I311
***Sa*FtsZ**	A275	G295	T296	V297	I298	N299	P300	E301	L302	Q303	E305	V307	T309	V310	I311

because of how the C-terminal beta sheets are organized (Kusuma et al., 2019).

The sequence level as well as structural level variability of IDCs among different FtsZs should facilitate the design of species-specific antibiotics (Casiraghi et al., 2020). For example, PC190723, an IDC inhibitor that will be described in greater detail below, is most effective against organisms that have a valine at the equivalent position of 307 in *E. coli* FtsZ, such as *S. aureus* and *B. subtilis*. In contrast, PC190723 is ineffective toward *E. coli* (Haydon et al., 2008), although inactivating the AcrAB efflux pump of *E. coli* significantly enhances susceptibility to the PC190723 prodrug TXY436, suggesting that resistance of Gram negative species to this compound is in part due its rapid clearance from the cytoplasm (Kaul et al., 2014).

Although the sequence and structure of the IDC as a whole is not highly conserved, components of the IDC, like the T7 loop, are highly conserved (de Pereda et al., 1996). Kusuma et al. compared the tertiary structure of staphylococcal and non-staphylococcal FtsZ proteins and showed that their structures differ mainly because of variations in the curvature of the H7-helix and organization of the C-terminal β-sheet (Kusuma et al., 2019). Superimposition of staphylococcal and non-staphylococcal FtsZs revealed that staphylococcal FtsZs were similar to each other, with an RMSD value of 0.3 Å, and non-staphylococcal FtsZs were more structurally variable among themselves (RMSD ∼1.3 Å). Conversely, *S. aureus* FtsZ (hereafter referred to as *Sa*FtsZ) showed much higher variation (RMSD ∼3 Å) when superimposed onto non-staphylococcal FtsZ. This difference was mainly due to the diversity in the arrangement of C-terminal β-sheets. Similarly, when compared the drug binding sites, both staphylococcal and non-staphylococcal FtsZ showed no significant structural differences in their GTP binding sites and T7 loops, whereas their IDCs were quite divergent. As the cleft opening size of the IDC and the curvature of helix H7 vary significantly between staphylococcal and non-staphylococcal FtsZs, compounds that bind to a staphylococcal FtsZ may not bind to non-staphylococcal FtsZ with similar affinity. Likewise, a compound targeting a non-staphylococcal FtsZ may not bind to other non-staphylococcal FtsZs with the same affinity (Kusuma et al., 2019).

Comparing the IDCs of FtsZ With Tubulin

Microtubules, formed by polymerization of α-β- tubulin, are eukaryotic cytoskeletal proteins that play important roles in several cellular processes such as cell division, cell motility, intracellular transport and maintaining cell shape. Along with the GTP binding pocket, microtubules contain at least four major drug binding sites, including those for vinblastine, colchicine, laulimalide, and taxane (**Figure 2A**) (Lu et al., 2012). Vinblastine binds at the interface of the α-β- tubulin heterodimer (**Figure 2B**), which comprises the T7- loop, H10 and S9 strand of α tubulin and H6, the T5 loop and H6–H7 loop of β- tubulin (Steinmetz and Prota, 2018). The colchicine binding site includes the T7-loop, helices H7 and H8, and strands S8 and S9 of β-tubulin plus the T5 loop of α tubulin (Ravelli et al., 2004). The laulimalide binding site comprises helices H9 and H10 and the

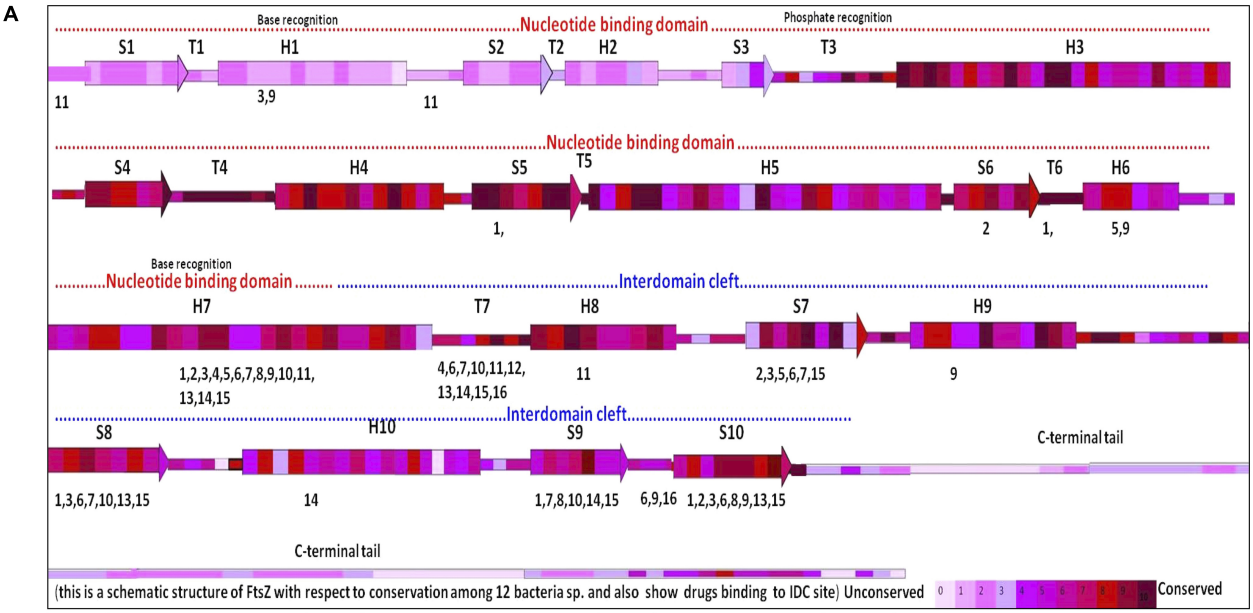

SL NO.	FtsZ Inhibitors	SL NO.	FtsZ Inhibitors	SL NO.	FtsZ Inhibitors	SL NO.	FtsZ Inhibitors
1.	Plumbagin	5.	Benzamides and its derivatives (PC190723)	9.	Doxorubicin	13.	P. cataractum SYPF 7131 bioactive compound
2.	Berberine derivatives	6.	Thiazole Orange derivatives (Compound-1)	10.	Cinnamaldehyde	14.	Benzamidazole derivatives (BT-benzo-29)
3.	Taxane derivatives (SB-RA-2001)	7.	Quinoline (1-methylquinolinium derivatives (c1-c15)	11.	Phenyl propanoid	15.	Polyketides compounds
4.	Tiplaxtinin	8.	N-methylbenzofuro[3,2-b]quinolone derivatives	12.	Coumarin & its derivatives	16.	CRAMP

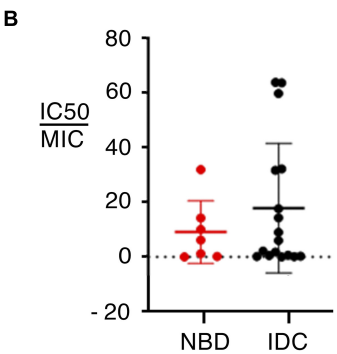

FIGURE 4 | Interaction site for IDC inhibitors and their toxicity. **(A)** Schematic representation of FtsZ with respect to its conservation among 12 bacterial species and the interaction site of IDC inhibitors. **(B)** Comparison of IC_{50}/MIC of both NBD and IDC inhibitors.

H10-S9 loop of β- tubulin, whereas taxol, one of three taxane derivatives commonly used as an anticancer drug, binds to the β-tubulin H7, S7, H6–H7 loop, S7–H9 (M-loop) and S9–S10 loop (Prota et al., 2014; Kellogg et al., 2017).

In contrast to this diversity of binding sites in microtubules, only the NBD and IDC of FtsZ have been identified as drug binding targets. The IDC of FtsZ consists mainly of the H7 helix, S7–S10 strands and T7 loop that structurally map to the taxol and colchicine binding sites in tubulin (**Table 3** and **Figure 2**). Because the IDC has a lower level of sequence and structural similarity with tubulin compared with the NBD, colchicine and taxane can interact with FtsZ, but the interacting residues as well

as binding affinity do not match with tubulin (White et al., 2002; Haydon et al., 2008). For example, although colchicine can bind to the IDC in FtsZ, the colchicine binding pocket of tubulin has no sequence similarity with the colchicine binding site in FtsZ from *M. tuberculosis* (White et al., 2002; Mathew et al., 2016). In another example, PC190723 (an IDC-specific inhibitor) binds to the taxol site on tubulin, but was >64-times more inhibitory to FtsZ than to tubulin (Haydon et al., 2008). Similarly, SB-RA-2001, a taxane derivative, binds to the IDC of *Bs*FtsZ, but when the binding site was superimposed onto the taxol site of tubulin, no identical residues were found; it also binds only very weakly to tubulin (Singh et al., 2014). Consequently, the drugs that bind to the IDC in FtsZ do not interact with tubulin with similar affinity and thus are less likely to be toxic to mammalian cells.

Molecular Insights Into the IDC

The N-terminal domains of FtsZ share high sequence identity in both Gram-positive bacteria (56–89%) and Gram-negative bacteria (43–84%), whereas lower sequence identities (30–70%) are shared within the C-terminal domains and IDCs. Inter-domain clefts of diverse FtsZs are composed of mostly hydrophobic residues along with a few polar and charged amino acids. Available crystallographic structures for protein-ligand interactions indicate that most small molecules prefer to bind to the hydrophobic pockets of their protein targets (Guo et al., 2015). Thus, the hydrophobic residues in the FtsZ IDC likely enhance the binding of organic molecules in aqueous environments, making the IDC a better target for small molecule inhibitors.

Some residues within the IDC are widely conserved in all bacterial species, some are conserved only among the Gram positive bacteria or in Gram negative bacteria, whereas other residues are specific to a particular species. For example, residues V189, Q192, G193, Q195, G196, I197, D199, L200, I201, V203, S204, G205, E206, V207, N208, L209, D210, M226, G227, I228, L261, M262, N263, T265, G295, T296, V297, T309, V310, and I311 are located within 6 Å of the IDC of *Sa*FtsZ. The corresponding residues in *Ec*FtsZ are shown in **Table 4**. Of these, N208, D210, G227, and G295 are conserved throughout bacteria that have FtsZ; G193, Q195, I197, L200, I201, M226, T309, and V310 are conserved mostly in Gram-positive species, and the remaining residues are not conserved (**Figure 3C**). These residues are involved in formation of different bonds with the small molecules–hydrogen bonds, hydrophobic, van der Waals, amide bonds or other types of interactions–and depend upon the chemical nature of the inhibitors and the interacting residues. For example, V207 and N263 are mainly involved in hydrogen bonding with PC190723, while L200 and I311 form hydrophobic interactions (Matsui et al., 2012). The size of the IDC, the number of amino acid residues and their types vary among different bacterial species. For example, a multiple sequence alignment of IDCs from 12 bacteria showed that 6–12 residues are conserved between Gram-positive and Gram-negative species, whereas more than 12 residues are conserved when aligned among only Gram positive bacteria.

Although the IDC mostly consists of hydrophobic residues, it also contains several conserved hydrophilic residues that are important for interaction with small molecule inhibitors. Similarly, many residues are important for interaction with multiple inhibitors. For example, residues in *Ec*FtsZ such as G191, G195, L199, M206, N207, V208, N263, S297, R307 and T309 and their equivalent residues in both *B. subtilis* and *S. aureus* (Q192, G196, L200, V207, N208, L209, N263, V297, V307, and T309 in the latter species) mostly interact with more than one FtsZ inhibitor (**Figure 4A** and **Table 2**). Our analysis of the published literature suggests that most FtsZ inhibitors that target the IDC have higher IC_{50}/MIC ratios than inhibitors that target the NBD (**Figure 4B**). Although IDCs from different bacteria are highly hydrophobic, their lower sequence conservation and variable cleft openings should potentially facilitate development of species-specific antibacterial agents.

IDC Size and Conformational Flexibility

Structural organization of the IDC indicates that the cleft has a specific size and a specific cleft opening. The cleft opening changes for different conformers of FtsZ such as GDP/GTP bound forms, and monomeric/polymeric FtsZ. Further, the size of the cleft opening differs in different bacterial species. Recent analysis of crystal structures of diverse FtsZs by Kusuma et al. indicated that IDC size depends upon the curvature of H7: if its curvature increases, the size of the IDC opening decreases, and vice-versa (**Figure 5**) (Kusuma et al., 2019). Using *in silico* analysis, they further measured the cleft opening size and the curvature of the H7 helix in *Staphylococcus* and non-*Staphylococcus* FtsZs, providing clues to the molecular accessibility of IDCs from different bacterial species (Kusuma et al., 2019). Their analysis shows that the curvature of H7 in *Sa*FtsZ is 140.3° (PDB ID: 3WGN) and the cleft opening size is 15.9 Å, whereas, in *Bs*FtsZ it is 164.5° (PDB ID: 2RHO) and 7.5 Å, respectively. The same study showed that the drug-binding pocket is also subject to species-level variations: *S. aureus* has the widest cleft opening (∼15 Å), whereas in *B. subtilis, M. tuberculosis, A. aeolicus, and P. aeruginosa* the cleft opening size is 9–10 Å. The IDC binder PC190723 has a size of 14.1 Å, with higher affinity for *Sa*FtsZ than *Bs*FtsZ. This wider cleft opening of *Sa*FtsZ vs. *Bs*FtsZ probably facilitates PC190723 entry and binding, and may be the major reason why it inhibits *S. aureus* cell division more effectively than that of *B. subtilis*.

Similarly, molecular dynamic simulations indicate that in the GTP bound state, the H7 helix is twisted backward and the T7 loop shifts downward, opening the cleft, whereas in GDP bound FtsZ the H7-helix is relaxed and the T7 loop shifts upward, closing the cleft's opening. The size of the cleft opening in GDP and GTP bound *Sa*FtsZ varies between 15 and 20 Å (Kusuma et al., 2019). This model is supported by fluorescence anisotropy experiments showing that a fluorescent analog of PC190723, a nitrobenzoxadiazole probe, specifically binds to the polymeric form of FtsZ (Artola et al., 2017). Molecular dynamics simulations suggest that in monomeric FtsZ the cleft is in a closed or relaxed conformation, preventing the probe from interacting with FtsZ, whereas in polymeric FtsZ the cleft is in the open or tense conformation (Wagstaff et al., 2017; Schumacher et al., 2020), allowing interaction with FtsZ and resulting in fluorescence. *In silico* analysis of the

PC190723 binding pocket in the IDC in different bacterial species showed that the microenvironment of the binding pocket affects the drug's affinity toward FtsZ (Miguel et al., 2015). Analysis of FtsZ crystal structures and molecular dynamics trajectories showed that the conformation of the PC190723 binding pocket depends upon multiple factors such as bacterial species, genetic alterations, allosteric binding and polymerization state (Miguel et al., 2015). In particular, FtsZ polymerization and allosteric binding of the guanosine nucleotide may play a crucial role in stabilizing the PC190723 pocket. For example, for PC190723, the GDP-bound *Sa*FtsZ has a pocket score of -10.75 (PDB ID: 3VO8), whereas FtsZ without nucleotide has a pocket score of -4.29 (PDB ID 3VO9). Similarly, amino acid substitutions G193D, G196C, and N263K in *Sa*FtsZ change the microenvironment of the binding pocket, significantly affecting the binding of PC190723 and leading to drug resistance (Haydon et al., 2008; Miguel et al., 2015).

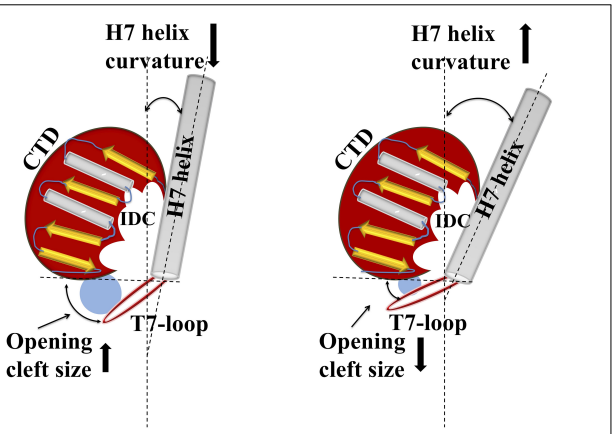

FIGURE 5 | Structural relationship between IDC opening size and helix H7 of FtsZ. Cartoon representation shows how alterations in helix H7 curvature influence IDC opening size. Increased curvature of helix H7 yields a smaller cleft opening, whereas decreased H7 curvature leads to a larger cleft opening size.

IDC INHIBITORS

Inhibitors that are known to interact with the IDC have been identified by molecular docking, simulation studies, mutational analysis, NMR and crystallographic studies. In addition, FtsZ inhibitors such as Ruthenium red, totarol, sanguinarine, OTBA, *Dichamanetin* and viriditoxin inhibit or promote FtsZ bundling, but the exact binding sites of these drugs on FtsZ are still not known (Santra et al., 2004; Beuria et al., 2005; Urgaonkar et al., 2005; Jaiswal et al., 2007; Beuria et al., 2009). Depending on their structure, we have characterized the IDC inhibitors in seven major groups, which are described below (**Table 1**).

BENZAMIDES

3-MBA, PC190723, and Derivatives

Ohashi et al. originally showed that a benzamide derivative, 3-MBA (3-Methoxybenzamide), inhibits the proliferation of bacteria by targeting FtsZ (Ohashi et al., 1999). Although 3-MBA has low antibacterial activity (MIC = 2048 μg/mL), it provided a strong starting point for FtsZ-targeted fragment-based drug discovery. Screening more than 500 benzamide analogs led to the discovery of the aforementioned PC190723, which contains a thiazolopyridine moiety fused to the benzamide by an ether linkage that makes it ∼2000 times more potent than the parent 3-MBA (MIC = 0.5–1 μg/ml). Molecular docking and X-ray crystallography demonstrated that PC190723 binds to the IDC, interacting specifically with R191, Q192, N263, V307, and T309 in *Bs*FtsZ (Haydon et al., 2008). Similarly, crystallography showed that PC190723 binding site in *Sa*FtsZ comprises Q192, G193,G196, I197, D199, L200, V203, G205, V207, N208, L209, M226, G227, I228, N263, G295, T296, T309, V310, and I311 (**Table 4**) (Matsui et al., 2012). PC190723 binding to the IDC disrupts the normal assembly of the Z ring by causing multiple FtsZ aggregates to distribute throughout the cell that are not able to form a coherent Z ring (Haydon et al., 2008).

Not surprisingly, *S. aureus* developed resistance to PC190723 by altering *Sa*FtsZ residues R191 G193, G196, V214, N263, or G266. G196 mainly interacts with the thiazolopyridine moiety and changes at this residue are commonly found in PC190723-resistant *S. aureus*. Interestingly, however, some PC190723-resistant mutants such as R191P and G196A in SaFtsZ and G196S in BsFtsZ remain sensitive to 3-MBA, suggesting that the less specific 3-MBA can still bind to an IDC pocket that occludes PC190723 binding (Adams et al., 2016). Moreover, some substitutions in FtsZ that render cells non-susceptible to PC190723, such as R191P, G193D, and G266S, at the same time confer benzamide dependence for normal cell division (Adams et al., 2016), although the mechanism for this drug dependent function of FtsZ is not clear. Interestingly, a 3-MBA-resistant mutant (A47) remains susceptible to PC190723 (Haydon et al., 2008).

A notable advance in optimizing benzamide action against FtsZ was the replacement of the chlorine atom on the pyridyl ring of PC190723 with a CF3 group, exemplified by a derivative called TXA707, which increases the drug's metabolic stability and anti-staphylococcal activity (MIC: 0.25–2 μg/ml). Nonetheless, TXA707 is less effective on FtsZs with residue changes at G196 and others that mediate resistance, probably for the reason discussed above. A modification made in TXA707, in which a five membered oxazole and six membered phenyl ring (i.e., TXA6101) are flexibly linked, not only improved the binding affinity but also increased its activity against both wild-type methicillin resistant *S. aureus* (MRSA) and mutants carrying residue changes at FtsZ G196 (MIC = 0.125 μg/mL and 1 μg/mL, respectively) (Fujita et al., 2017). Crystallography and biochemical studies showed that both TXA707 and TXA6101 interact with the IDC. TXA6101 induces a conformational rearrangement of I197, M226, and I311 that leads to the formation of an inner hydrophobic pocket, with M226 acting as a gate that opens access to the pocket (Fujita et al., 2017).

Further advances have been made using improved benzamide prodrugs. TXY541 is a prodrug of PC190723 that is 143-times more soluble in an aqueous acid vehicle than PC190723 (Kaul et al., 2013). A prodrug of TXA707, TXA709, is structurally similar to TXY541 except that TXA709 contains a CF3 group instead of Cl group on the pyridyl ring, which increases the metabolic stability of the compound. Currently, TXA709 is in phase-I clinical trials. Recent reports showed that clinically isolated MRSA display resistance toward TXA709 at a frequency of 1 x 10^{-8}, which is similar to that for PC190723. TXA709-resistant isolates carried mutations in FtsZ at G196S, N263K, G193D, G196C, and G196A, similar to residues that confer *S. aureus* resistance to PC190723 (Kaul et al., 2015).

In another study of benzamides, Bi et al. designed and synthesized a series of 3-substituted 2,6-difluorobenzamide derivatives, of which a chloroalkoxy derivative (**7**), a 3-bromoalkoxy derivative (**12**) and a 3-alkyloxy derivative (**17**) exhibited good antibacterial activity against *B. subtilis* and susceptible/resistant *S. aureus* (Bi et al., 2017). Using structure-based drug design to target the IDC, they designed and synthesized a series of isoxazole (isoxazol-3-yl- and isoxazol-5-yl) containing benzamide derivatives. Some of these isoxazol-5-yl benzamide derivatives (B14) were ∼32 fold more potent against *B. subtilis* than PC190723 (Bi et al., 2018). In another study, Bi et al synthesized a series of 1, 3, 4-oxadiazol-2-one containing benzamide derivatives. Out of many derivatives, compound A14 showed the highest antibacterial activity against Gram positive bacteria (MIC 0.125-1 μg/mL) and less cytotoxicity against HeLa cells (IC_{50} > 64 μg/mL). *In silico* docking revealed that compound A14 binds to the IDC (Bi et al., 2019). A recent study of benzodioxane-benzamides identified a derivative (compound 8) with very high potency against MRSA and *B. subtilis*, with MICs at or below 0.1 μg/ml, good solubility, and very low toxicity to human cells. Like the original PC190723 (Haydon et al., 2008), compound 8 caused the delocalization of Z rings in *B. subtilis* into subcellular foci that were unable to function in cell division (Straniero et al., 2021) (**Figure 6**).

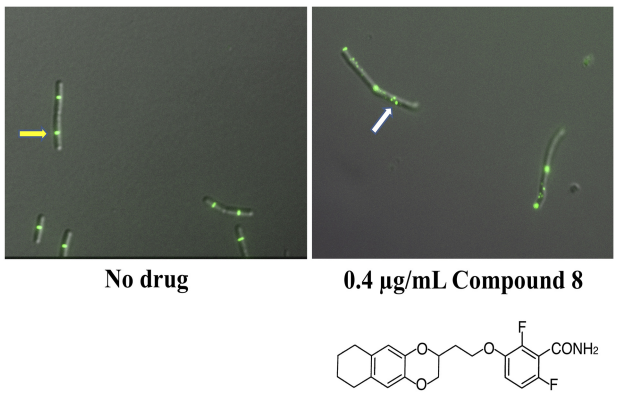

FIGURE 6 | Benzamide derivatives disrupt Z-rings by redistributing FtsZ to multiple cellular foci. Shown are micrographs of *B. subtilis* cells with fluorescently labeled Z-rings, grown with either no drug added or after 90 min incubation with compound 8, a benzodioxane-benzamide derivative (diagrammed below). Reproduced from Straniero et al. (2021), under Creative Commons License CC BY 4.0. The yellow arrow highlights a functional and morphologically normal Z-ring; the white arrow highlights disrupted FtsZ localization as multiple foci.

3-Aminobenzamide Derivatives

Using cell-based screening, Lui et al screened 47 derivatives of 3-aminobenzamide and showed that their compound 28 interacts with the FtsZ IDC. This compound exhibits high antibacterial activity (MIC 0.5–1 μg/mL against *S. aureus*) and less cytotoxicity ($IC_{50} \geq 100$ μM, mouse L929 cell line) and worked in synergy with β-lactam antibiotics. Molecular docking studies showed that the C3 amino group of compound 28 interacts with the hydroxyl group of T309 in *Sa*FtsZ. The other *Sa*FtsZ residues in its proximity are G193, G196, M262, and N263 (**Table 4**). They also found that the M262I residue change is resistant to this molecule (Lui et al., 2019).

Fluorescent Benzamide Derivatives That Bind to the IDC

Recently, Ferrer-González et al. developed a structure-guided fluorescent benzamide derivative by conjugating BODIPY to an oxazole benzamide FtsZ inhibitor (BOFP). BOFP binds to FtsZ from both Gram positive and Gram negative bacteria with K_ds of 0.6–4.6 and 0.2–0.8 μM, respectively (Ferrer-Gonzalez et al., 2019). BOFP binds to the IDC, where the BODIPY moiety interacts with residues I228 and V307 of *Bs*FtsZ (**Table 4**). As it can label FtsZs within diverse bacteria, BOFP holds great promise for the screening of non-fluorescent FtsZ inhibitors and determining whether they perturb Z ring assembly in cells. In a recent study, Huecas et al. developed a competitive binding assay using specific high-affinity fluorescent probes to screen allosteric compounds that can interact with the IDC and inhibit FtsZ assembly. The probes displayed higher anisotropy in the presence of FtsZ polymer, where the IDC is open, compared with FtsZ monomers, where the IDC is closed. The specificity of this probe was assessed using a competitive assay with PC190723. The study demonstrated that the anisotropy of the probe decreased considerably upon binding of the IDC specific inhibitor PC190723, whereas it did not change upon binding of non-specific inhibitors. Thus, this probe can be used to identify inhibitors that specifically bind to the IDC (Artola et al., 2017; Huecas et al., 2021).

QUINOLINE RING COMPOUNDS

Quinolinium derivatives have been widely used as therapeutics due to their antibacterial potency. Here, we describe recent developments in quinolinium molecules that target FtsZ. Berberine, a quinolinium derivative, was first described by Domadia et al. (2008) as an FtsZ interacting molecule and FtsZ inhibitor (Domadia et al., 2008). Since then, several other quinolinium derivatives were identified or synthesized that interact with the IDC and inhibit FtsZ function.

Berberine and Its Derivatives

Berberine is a benzylisoquinoline alkaloid that has been used as an antimicrobial therapeutic for centuries. After identification of its interaction with FtsZ, Wong et al. used *in silico* structure-based design to synthesize a number of 9-phenoxyalkyl berberine derivatives that bind to the IDC of *Sa*FtsZ (Sun et al., 2014). A positively charged amine on these derivatives interacts with *Sa*FtsZ residue D199 and a C-9 methoxy binds to several hydrophobic residues (I228, V230 and V307) in the IDC. Modifications of these two moieties make the derivatives more potent than berberine (MIC = 100–400 μg/mL) and enable them to inhibit growth of MRSA and vancomycin-resistant Enterococci (VRE), with MICs of 2–8 μg/mL and 4–16 μg/mL, respectively. These compounds also exhibit moderate antimicrobial activity against Gram negative strains such as *E. coli* (MIC 32–128 μg/mL). Similarly, 9-phenoxy berberine derivatives inhibit FtsZ GTPase activity (IC_{50} 37.8 – 63.7 μM) more potently than the parent berberine molecule (IC_{50} = 272 μM) and showed similar effects on FtsZ polymerization. This confirms that the substitution of the 9-phenoxy group in berberine increases its affinity toward FtsZ and its antibacterial activity.

Thiazole Orange Derivatives

Quinolines fused with a thiazole orange derivative confer broad spectrum antibacterial activities. Among them, 2-((E)-4- Hydroxystyryl)-1-methyl-4-((Z)-(3-methylbenzo[d]thiazol-2 (3H)-ylidene) methyl) quinolin-1-ium iodide (1) (compound-1) exhibits high antibacterial activity against *S. aureus* (MIC ∼ 1.5–3 μg/mL), other *staphylococci* (MIC ∼ 0.75–3.0 μg/mL) and *E. coli* (MIC ∼ 1.5 μg/mL). This compound enhances FtsZ bundling at lower concentrations (10 nm – 90 nm), inhibits GTPase activity (IC_{50} = 5 μg/mL) and is significantly less toxic to mammalian cells (IC_{50} = 98.15 μM). Molecular docking studies showed that it binds to the IDC of *Sa*FtsZ through both hydrophobic interactions at residues L200, M226, I228, L261, V297, L302, V307, and I311 and hydrogen bonding to V203 and L209 (**Table 4**) (Sun et al., 2017b).

Quinolinium and Quinolone Derivatives

High throughput phenotypic screening by the NIH screened 215,110 molecules against the *M. tuberculosis* (Mtb) H37Rv strain and the data are freely available. Using the results from this screen, Mathew and coworkers found that quinoline and quinazoline can inhibit *Mtb*FtsZ functions (Mathew et al., 2013). Subsequently, Cai et al. synthesized a series of 1-methylquinolinium derivatives (c1-c15) by combining an indole fragment at the 2-position with different amino groups at the 4-position (Cai et al., 2019). These compounds strongly inhibited FtsZ activity and growth of MRSA and VRE, with MIC values between 1 and 4 μg/mL. C2 and c9 derivatives enhanced bactericidal activity with an MIC of 1 μg/mL in *S. aureus* (ATCC 29213). Both compounds possess a common piperidine group at the 4-position of the 1-methylquinolinium core that might increase its antibacterial properties compared with other indole-quinolinium derivatives. Molecular docking studies predicted that these derivatives bind to the IDC of *Sa*FtsZ mostly through hydrophobic interactions with residues Q192, G196, L200, V203, L209, M226, G227, I228, and V297 and electrostatic interaction with D199 (**Table 4**).

Several quinolone and quinoline derivatives exhibited antibacterial activity against Gram positive and Gram negative bacteria (Piddock and Walters, 1992; Aldred et al., 2014; Zhang et al., 2018). Sun et al. synthesized a series of quinoline derivatives containing the unique quaternary pyridinium core, many of which demonstrated antibacterial activities (Sun et al., 2017a). These compounds interacted hydrophobically with FtsZ residues D199, L200, V297, and V307, and the imino group of these derivatives could hydrogen-bond with FtsZ T309. These compounds showed ∼50-fold better antibacterial activity against *B. subtilis* (MIC ∼2–8 μg/mL) compared with berberine (MIC = 128 μg/mL). In their next study, Sun et al. synthesized sixteen 3-methylbenzo[d]thaizol-methylquinolinium derivatives with different groups added to the ortho-position of the 1-methylquinolinium core (Sun et al., 2018). One of the derivatives, A2, showed strong antibacterial activity (MIC = 1.5 μg/mL) by inhibiting FtsZ functions, and like the others, exhibited low toxicity toward mammalian cells (IC50 = 78.25 μM) (Sun et al., 2018). A docking study showed that A2 interacts with residues D199, L200, M226, I228, V297, T309, and I311 of *Sa*FtsZ (Sun et al., 2018).

From previous studies, it was clear that thiazole and quinolinium groups are important for antibacterial activity. Li et al. synthesized various thiazole-quinolinium derivatives and evaluated their antibacterial activities against Gram positive and Gram negative species (Li et al., 2015). All compounds showed good antibacterial activity (MIC 1–32 μg/mL) against *S. aureus*. A methyl group substitution at the quinolinium ring resulted in better antibacterial potency than the bulky indolyl group. These derivatives were effective against antibiotic resistant strains, did not induce antibiotic resistance, and showed less cytotoxicity toward mammalian cells (16HBE, HK-2 L929 with IC50 12–26 μg/mL). Molecular docking studies determined that thiazole-quinolinium derivatives interact with the IDC through numerous hydrophobic bonds with residues D199, L200, M226, I228, V297 and van der Waals interactions with Q195, V310, G205, and I311 of *SaFtsZ* (**Table 4**).

BENZOPYRONE RING COMPOUNDS (COUMARIN AND ITS DERIVATIVES)

Compounds harboring a benzopyrone ring are known to inhibit assembly and GTPase activity of FtsZ. Coumarin (1, 2- benzopyrone) is a natural polyphenolic compound with a benzopyrone ring (Detsi et al., 2017). Duggirala et al. screened several natural compounds including benzopyrone derivatives and showed that coumarins, specifically scopoletin and daphnetin, inhibit FtsZ polymerization and GTPase activity. Molecular docking studies showed that coumarin binds to the IDC via its interaction with highly conserved amino acids such as N207, D209, and D212 in the T7 loop of *Ec*FtsZ (Duggirala et al., 2014). In the case of scopoletin,

the hydroxyl group of coumarin interacts with *Ec*FtsZ residue G204 and the keto group interacts with N207 via hydrogen bonding, whereas daphnetin interacts with G104. In other coumarin derivatives such as umbelliferone and 7-diethylamino-4-methyl coumarin, an oxygen group interacts with N207 and F210 of *Ec*FtsZ. The anti-tubercular activity of coumarin derivatives is reviewed elsewhere (Keri et al., 2015). Apart from the IDC, coumarin derivatives might also interact with the NBD of FtsZ in different organisms. Molecular docking studies revealed that most coumarin derivatives interact with the NBD of *Mycobacterium smegmatis* FtsZ via hydrogen bonding with residues N41, G103 and R140 (Sridevi et al., 2017).

PHENYLPROPANOIDS (CINNAMALDEHYDE AND ITS DERIVATIVES)

Plant-derived natural products are attractive for antibiotic development because they often are less toxic to mammalian cells. Phenylpropanoids are a group of natural organic compounds that are synthesized by plants using phenylalanine and tyrosine. Most phenylpropanoid derivatives possess antibacterial activity, and include cinnamic acid, p-coumaric acid, caffeic acid, chlorogenic acid, eugenol, and ferulic acid (Puupponen-Pimia et al., 2001; Hemaiswarya and Doble, 2009, 2010). These compounds inhibit GTPase activity of FtsZ and are able to disassemble preformed FtsZ polymers with varying effectiveness. For example, the IC_{50} values of FtsZ assembly for eugenol, ferulic acids and 3, 4-dimethoxycinnamic acids are more than 250 μM, whereas cholinergic acid, cinnamic acid, p-coumaric acid and caffeic acid have IC_{50} values of 70 μM, 238 μM, 190 μM, and 106 μM, respectively.

Molecular docking studies indicate that all the phenylpropanoids interact with the T7-loop of IDC. For example, chlorogenic acid, 3, 4-dimethoxycinnamic acid, 2, 4, 5-trimethoxycinnamic acid and ferulic acid interact with residues A11, G36, N207, V208, D209, and F210 of *Ec*FtsZ via hydrogen bonds and P203, N207 *via* hydrophobic bonds (Hemaiswarya et al., 2011). Other phenylpropanoids such as cinnamic acid, p-coumaric acid and caffeic acid bind to M206 and T296 of *Ec*FtsZ through hydrogen bonding. Among phenylpropanoid derivatives, chlorogenic and caffeic acid possesses two hydroxyl groups on their benzene ring, making them more hydrophilic than the other compounds containing methoxy substituents, resulting in higher affinity toward FtsZ (Hemaiswarya et al., 2011). Thus, the presence of hydroxyl groups in phenylpropanoids favor hydrogen bonding with the side chains of FtsZ active site residues that makes the compounds more effective.

Cinnamaldehyde, a phenylpropanoid, exhibits broad spectrum antibacterial activity against diverse species such as *E. coli* (MIC ∼ 1000 μg/mL), *B. subtilis* (MIC ∼ 500 μg/mL) and MRSA (MIC ∼ 250 μg/mL) (Domadia et al., 2007). It contains an aromatic benzene ring with an α, β-unsaturated carbonyl moiety and inhibits FtsZ assembly and GTPase activity in a dose dependent manner (Li and Ma, 2015). *In silico* docking and STD NMR spectroscopy showed that H2 and H3 of cinamaldehyde interact with residues G295 and V208 of FtsZ. The aromatic ring of cinamaldehyde is in close proximity to the aliphatic side chains of residues F203, M206, N207, and V208, whereas its carbonyl group is in close proximity to the side chain of N203, the guanidium group of R202 and the hydroxyl group of S297 (Domadia et al., 2007). These studies suggest that cinnamaldehyde preferably interacts with the IDC of FtsZ. Furthermore, multiple sequence alignment shows that the cinnamaldehyde-interacting residues such as G295, V208, R202, N263, and S297 are conserved among FtsZs from different bacterial species.

TAXANE RING COMPOUNDS

The structural kinship between FtsZ and tubulin suggest that some microtubule targeting drugs might also target FtsZ, and taxanes are attractive candidates. Indeed, a screen of 120 taxane derivatives identified several taxanes that bind to FtsZ and exhibit effective anti-tubercular activity (Huang et al., 2006). Among those, SB-RA-2001, a derivative of a non-cytotoxic taxane, contains a 3-naphtha-2yl acryloyl group at the C13 position and showed promising anti-tubercular activity against both drug sensitive and resistant *M. tuberculosis* strains. *In silico* docking studies revealed that this compound binds to the IDC of FtsZ at the PC190723 interaction site (Singh et al., 2014). The SB-RA-2001 binding pocket in *Bs*FtsZ includes residues R29, E32, N33, N188, R191, Q192, Q195, G196, D199, I230, N263, T265, N299, N301, L302, K303, E305, V307, T309 (**Table 4**) of which many are present in the IDC. Its major interaction with *Bs*FtsZ is via hydrogen bonding with residues E305, R191, Q192, N188, and N33. Structural alignment of the taxane binding site on FtsZ and the paclitaxel binding site on tubulin indicated that no identical residues exist between these two sites.

OTHER SMALL MOLECULES WITH SIMPLE AND COMPLEX RING GROUPS

Apart from molecules discussed above, there are several other small molecules with different size and ring structures that are reported to interact with the IDC.

Plumbagin

Plumbagin (5-hydroxy-2-methyl-4, 4-naphthoquinone) is a naturally occurring naphthoquinone originally isolated from the plumbago plant (de Paiva et al., 2003; Aziz et al., 2008). It inhibits proliferation of diverse species such as *S. aureus, P. aeruginosa*, *B. subtilis* (MIC∼29 μM), *Proteus vulgaris* and *M. smegmatis* (MIC ∼ 31 μM) (de Paiva et al., 2003; Mathew et al., 2010). Plumbagin binds to *Bs*FtsZ and inhibits its assembly and GTPase activity (Bhattacharya et al., 2013). *In vitro* and

in silico assessment studies demonstrated that the plumbagin binding site is distinct from the NBD in *Bs*FtsZ (Bhattacharya et al., 2013). The residues of *Bs*FtsZ that constitute the plumbagin binding site include the H7 helix and other residues in the IDC such as R191, Q192, Q195, G196, D199, N263, T265, N299, V307, and T309 (**Table 4**). Of these, R191, Q195, D199, and N299 of *Bs*FtsZ are involved in hydrogen bonding with plumbagin (Bhattacharya et al., 2013). Mutational studies confirmed that D199 and V307 of *Bs*FtsZ play an important role in plumbagin binding. *In silico* studies showed that the plumbagin binding site in *Ec*FtsZ includes residues G21, M104, T132, P134, E138, R142, N165, F182, A185, and L189 (Bhattacharya et al., 2013). Notably, these residues are in a completely different part of FtsZ than the plumbagin binding pocket of *Bs*FtsZ, suggesting that FtsZs of different bacteria may have different ligand binding properties.

Fungal Compounds

Since the discovery of penicillin, it is well known that bioactive molecules of fungi show strong antimicrobial properties. While screening 58 fungal compounds from 24 different genera, Wu et al. found that *Penicillium cataractum* SYPF 7131 has strong antibacterial activity against *S. aureus* (Wu et al., 2018). Out of the 8 known and unknown isolates from its fermentation broth, 3 compounds showed effective antibacterial activity (MIC 10–65 μg/mL) and strong interaction with FtsZ. An *in silico* study suggested that these compounds interact with the IDC of *Sa*FtsZ by hydrogen bonding with residues G205, N263, T309, L209, G196, G227, and G193, and hydrophobic interaction with L200, L209, I311 L261, V307, V203, I228, I311 V297, and V203 (**Table 4**).

Doxorubicin

Doxorubicin is an anthracycline antibiotic which inhibits bacterial proliferation with moderate inhibition against *E. coli* (MIC 40 μM) and strong inhibition against *S. aureus* (MBC 5 μM). In the presence of doxorubicin, *E. coli* becomes highly filamentous without affecting chromosome segregation, indicating a cell division defect. Panda et al. showed that doxorubicin binds to a site in FtsZ distinct from the NBD. The amino sugar region of doxorubicin sits in a polar cavity and involves hydrogen-bond interactions with E32, R33, and D187 of *Ec*FtsZ, whereas the ethyloxy side chain involves hydrogen-bond interaction with E305 (Panda et al., 2015). The hydrophobic part of the molecule (the aromatic rings) sits in a cavity lined by hydrophobic residues of FtsZ, *e.g.,* V171, V188, M225, V229, and L248. The binding site contains many highly conserved residues, including E32, R33, V171, D187, V188, M225, G226, P247, L248, M302, N303, E305, and R307.

CCR-11

Rhodanine derivatives can perturb the assembly of FtsZ polymers and inhibit bacterial proliferation. Singh et al. screened a library of 151 rhodanine derivatives, of which 8 compounds showed good antibacterial activity (MIC ∼2 μM) and 3 specifically inhibited division of *B. subtilis* cells (Singh et al., 2012). One of these molecules, CCR-11, interacts with FtsZ with a Kd of 1.5 ± 0.3 μM and inhibits FtsZ assembly and GTPase activity. Docking studies revealed that CCR-11 binds to the IDC. The fluorine atoms of the CCR-11 trifluoromethylphenyl side chain interact with *Bs*FtsZ T203 and CCR-11 also interacts with *Bs*FtsZ G205, I207, L272, V275, and I298 through hydrophobic interactions. The thiazolidine ring of CCR-11 interacts with T203 and D199 of *Bs*FtsZ. CCR-11 inhibited HeLa cell proliferation with an IC_{50} value of 18.1 ± 0.2 μM, which is 6 times higher than the MIC (3 μM) of CCR11 on *B. subtilis* (Singh et al., 2012).

Bt-Benzo-29

Ray et al. screened 100 benzamidazole compounds for them) ability to elongate *B. subtilis* cells, out of which one compound, N-(4-sec-butylphenyl)-2- (thiophen-2-yl)-1H-benzo[d]imidazole-4-carboxamide (BT-benzo-29), causes cell filamentation. BT-benzo-29 inhibits FtsZ functions by interacting with FtsZ (Kd = 24 ± 3 μM) and inhibits proliferation of *B. subtilis* with an MIC of 17 μM (Ray et al., 2015). A molecular docking study proposed that BT-benzo-29 binds to the *Bs*FtsZ C-terminal portion of the globular domain, near the T7 loop. The interaction involves hydrogen bonding with L206 and S296 and hydrophobic interactions with D199, T203, P204, G205, L206, N208, L270, S271, L272, V275, S296, V297, I298, and E300 residues (Ray et al., 2015). Mutational studies showed that L272A and V275A mutants had weaker inhibitory effects on the assembly and GTPase activity. Unfortunately, BT-benzo-29 inhibits HeLa cell proliferation with an IC_{50} 17 ± 2 μM, only ∼4 times higher than the IC_{50} for *B. subtilis*.

Tiplaxtinin

Tiplaxtinin is an indole oxoacetic acid derivative (Elokdah et al., 2004). Using a cell based screen of 250 compounds, Sun et al. identified Tiplaxtinin as a bacterial cell division inhibitor (Sun et al., 2017c). Tiplaxtinin has strong antibacterial activity against Gram-positive pathogens, with MICs of 4.55–9.10 μM (2–4 μg/mL). Both *in vitro* and *in vivo* findings indicate that tiplaxtinin is capable of effectively disrupting dynamic assembly of FtsZ, GTPase function and Z-ring formation; tiplaxtinin-induced multiple FtsZ foci in *B. subtilis* cells is similar to the *in vivo* effects of benzamides. Molecular docking studies of this compound in *Sa*FtsZ revealed that tiplaxtinin binds near the T7-loop and H7 helix in the IDC region. The trifluoromethoxy group of tiplaxtinin forms hydrogen bonds with G193 and G227 and halogen bonds with V189, Q192, G193, and M226 (Sun et al., 2017c). Similarly, the carbonyl group interacts with T265 through a hydrogen bond. Tiplaxtinin also interacts with V189, Q192, G193 D199, L200, L209, M226, G227, I228, and V297 residues via hydrophobic interactions (**Table 4**).

SMALL INHIBITORY PEPTIDES THAT BIND NEAR THE IDC

Cathelin related antimicrobial peptide (CRAMP) is present in multicellular organisms and helps the innate immune system in the fight against microbes (Bergman et al., 2006). Like many antimicrobial peptides, CRAMP has an amphipathic α helical conformation. The active part of CRAMP consists of 18 amino

acid residues from 16 to 33 (GEKLKKIGQKIKNFFQKL), which inhibits bacterial proliferation (MIC 20–50 μM) and GTPase activity of FtsZ in concentration dependent manner (IC50 ∼ 70 ± 14 μM) (Ray et al., 2014). Molecular docking studies suggest that both hydrophobic and hydrophilic amino acid residues of CRAMP can bind to the T7 loop (L206, I207, N208, and D210) and C-terminal residues adjacent to T7 loop. CRAMP binding to FtsZ is stabilized through salt bridges, hydrogen bonding, hydrophilic and hydrophobic interactions. K25 of CRAMP binds to D210 of T7 loop through a salt bridge and the G16, K27, K32 of CRAMP form hydrogen bonds with both R286 and D287 residues of FtsZ.

Another small FtsZ-inhibitory peptide is MciZ, a 40-aa peptide produced during sporulation of *B. subtilis*. MciZ interacts directly with FtsZ, inhibiting FtsZ polymerization and Z ring assembly *in vivo* (Handler et al., 2008; Ray et al., 2013). Using crystallography and computational techniques, Bisson-Filho et al. demonstrated that MciZ interacts with the C-terminal domain of FtsZ and thus does not bind to the NBD (Bisson-Filho et al., 2015). However, MciZ does not bind to the IDC either, and instead interacts with H10 and beta strand 9 of FtsZ. This results in occlusion of subunit-subunit contacts that causes capping of the growing FtsZ protofilament end (Araujo-Bazan et al., 2019). Other peptide inhibitors of FtsZ, including Kil from bacteriophage lambda and GP0.4 from bacteriophage T7, disrupt assembly of *Ec*FtsZ protofilaments, but their binding sites on FtsZ are not yet known (Kiro et al., 2013; Haeusser et al., 2014; Hernandez-Rocamora et al., 2015).

CONCLUSION AND FUTURE PERSPECTIVES

We have described many small molecules that can interact with the IDC of FtsZ. Despite structurally mapping to the taxol and colchicine binding sites in tubulin, the IDC shares a low level of sequence and structural similarities with tubulin, reducing the likelihood that small molecules targeting the IDC will be toxic to mammalian cells. Molecules targeting the FtsZ NBD, on the other hand, are likely to have adverse effects on tubulin, and thus mammalian cells.

In most species, the IDC in FtsZ extends from residues 186 to 320 in *Ec*FtsZ. However, there are only a handful of residues that are specifically involved in interacting with small molecules (**Table 2**). Many of these residues are hydrophobic and favor interaction with small molecules, making the IDC a good druggable site. Fortunately, a few of these residues are conserved in both Gram positive and Gram negative bacteria and are essential for FtsZ functions. For example, G191 of *Ec*FtsZ is important for FtsZ assembly and G193 and G196 of *Sa*FtsZ are essential for interaction with anti-FtsZ drugs. Not surprisingly, alterations to any of these residues either inhibit FtsZ assembly or result in drug resistance. The G196A substitution in *Sa*FtsZ remains sensitive to 3-MBA despite conferring resistance to PC190723, suggesting that acquiring drug resistance comes with a fitness cost. It is notable that the V307 residue in FtsZ is important for FtsZ interaction with several drug classes including benzamides, plumbagin, quinolines, taxanes (SB-RA-2001), and berberine derivatives. Likewise, the T7-loop residue M206 of *Ec*FtsZ interacts with phenylpropanoid derivatives, and additional residues in the T7-loop interact with other drug molecules. Although the specter of resistant mutations is a significant challenge, molecules targeting the T7 loop may be less likely to induce resistant mutations because of its requirement in GTP hydrolysis.

Apart from the differences in residues among bacterial FtsZs, the size of the IDC and the cleft opening also varies in different bacterial species, with PC190723 binding to the larger cleft opening in *Sa*FtsZ with high affinity, and to the smaller cleft opening in *Bs*FtsZ with very low affinity. As a result, compounds can be tailored for specific species by targeting their IDCs. The limited number of FtsZ crystal structures and the lack of understanding of drug binding pockets in FtsZ have so far hindered such fine tuning, and consequently anti-FtsZ drugs are not yet ready for the clinic. Most of the IDC-drug interaction studies rely on *in silico* studies, whereas only a few drug molecules such as PC190723 and some of its derivatives have been subject to experimental genetic and structural studies. Nonetheless, recently reported derivatives of PC190723 exhibit very low MICs on important Gram-positive pathogens and have low toxicity profiles. Targeting FtsZs in Gram-negative pathogens will be more challenging because of increased barriers to permeability due to the outer membrane, but the small size of many of the compounds reviewed here, along with combination therapy using adjuvants that perturb the outer membrane and/or drug efflux pumps, provide promising future avenues (Khare et al., 2019). Continued development of better small molecule inhibitors that target FtsZ, as well as discovery of small molecules that can inhibit the activity of other conserved bacterial cell division proteins, will require continued collaboration between medicinal chemists, structural biologists and microbiologists.

AUTHOR CONTRIBUTIONS

All authors listed have made a substantial, direct and intellectual contribution to the work, and approved it for publication.

FUNDING

WM was funded by National Institutes of Health grant GM131705 and TB was funded by the Department of Biotechnology, India (BT/PR21546/BRB/10/1560/2016). PP was supported by a junior research fellowship from University Grants Commission, India.

REFERENCES

Acharya, B. R., Bhattacharyya, B., and Chakrabarti, G. (2008). The natural naphthoquinone plumbagin exhibits antiproliferative activity and disrupts the microtubule network through tubulin binding. *Biochemistry* 47, 7838–7845. doi: 10.1021/bi800730q

Adams, D. W., Wu, L. J., and Errington, J. (2016). A benzamide-dependent ftsZ mutant reveals residues crucial for Z-ring assembly. *Mol. Microbiol.* 99, 1028–1042. doi: 10.1111/mmi.13286

Addinall, S. G., Bi, E., and Lutkenhaus, J. (1996). FtsZ ring formation in fts mutants. *J. Bacteriol.* 178, 3877–3884. doi: 10.1128/jb.178.13.3877-3884.1996

Aldred, K. J., Kerns, R. J., and Osheroff, N. (2014). Mechanism of quinolone action and resistance. *Biochemistry* 53, 1565–1574. doi: 10.1021/bi500564

Allard, J. F., and Cytrynbaum, E. N. (2009). Force generation by a dynamic Z-ring in *Escherichia coli* cell division. *Proc. Natl. Acad. Sci. U.S.A.* 106, 145–150. doi: 10.1073/pnas.0808657106

Anderson, D. E., Gueiros-Filho, F. J., and Erickson, H. P. (2004). Assembly dynamics of FtsZ rings in *Bacillus subtilis* and *Escherichia coli* and effects of FtsZ-regulating proteins. *J. Bacteriol.* 186, 5775–5781. doi: 10.1128/JB.186.17.5775-5781.2004

Araujo-Bazan, L., Huecas, S., Valle, J., Andreu, D., and Andreu, J. M. (2019). Synthetic developmental regulator MciZ targets FtsZ across *Bacillus* species and inhibits bacterial division. *Mol. Microbiol.* 111, 965–980. doi: 10.1111/mmi.14198

Artola, M., Ruiz-Avila, L. B., Ramirez-Aportela, E., Martinez, R. F., Araujo-Bazan, L., Vazquez-Villa, H., et al. (2017). The structural assembly switch of cell division protein FtsZ probed with fluorescent allosteric inhibitors. *Chem. Sci.* 8, 1525–1534. doi: 10.1039/c6sc03792e

Artola, M., Ruiz-Avila, L. B., Vergonos, A., Huecas, S., Araujo-Bazan, L., Martin-Fontecha, M., et al. (2015). Effective GTP-replacing FtsZ inhibitors and antibacterial mechanism of action. *ACS Chem. Biol.* 10, 834–843. doi: 10.1021/cb500974d

Aziz, M. H., Dreckschmidt, N. E., and Verma, A. K. (2008). Plumbagin, a medicinal plant-derived naphthoquinone, is a novel inhibitor of the growth and invasion of hormone-refractory prostate cancer. *Cancer Res.* 68, 9024–9032. doi: 10.1158/0008-5472.CAN-08-2494

Battaje, R. R., and Panda, D. (2017). Lessons from bacterial homolog of tubulin, FtsZ for microtubule dynamics. *Endocr. Relat. Cancer* 24, T1–T21. doi: 10.1530/ERC-17-0118

Beall, B., and Lutkenhaus, J. (1991). FtsZ in *Bacillus subtilis* is required for vegetative septation and for asymmetric septation during sporulation. *Genes Dev.* 5, 447–455. doi: 10.1101/gad.5.3.447

Bergman, P., Johansson, L., Wan, H., Jones, A., Gallo, R. L., Gudmundsson, G. H., et al. (2006). Induction of the antimicrobial peptide CRAMP in the blood-brain barrier and meninges after meningococcal infection. *Infect. Immun.* 74, 6982–6991. doi: 10.1128/IAI.01043-06

Beuria, T. K., Santra, M. K., and Panda, D. (2005). Sanguinarine blocks cytokinesis in bacteria by inhibiting FtsZ assembly and bundling. *Biochemistry* 44, 16584–16593.

Beuria, T. K., Singh, P., Surolia, A., and Panda, D. (2009). Promoting assembly and bundling of FtsZ as a strategy to inhibit bacterial cell division: a new approach for developing novel antibacterial drugs. *Biochem. J.* 423, 61–69. doi: 10.1042/BJ20090817

Bhattacharya, A., Jindal, B., Singh, P., Datta, A., and Panda, D. (2013). Plumbagin inhibits cytokinesis in *Bacillus subtilis* by inhibiting FtsZ assembly–a mechanistic study of its antibacterial activity. *FEBS J.* 280, 4585–4599. doi: 10.1111/febs.12429

Bi, E. F., and Lutkenhaus, J. (1991). FtsZ ring structure associated with division in *Escherichia coli*. *Nature* 354, 161–164. doi: 10.1038/354161a0

Bi, F., Guo, L., Wang, Y., Venter, H., Semple, S. J., Liu, F., et al. (2017). Design, synthesis and biological activity evaluation of novel 2,6-difluorobenzamide derivatives through FtsZ inhibition. *Bioorg. Med. Chem. Lett.* 27, 958–962. doi: 10.1016/j.bmcl.2016.12.081

Bi, F., Song, D., Qin, Y., Liu, X., Teng, Y., Zhang, N., et al. (2019). Discovery of 1,3,4-oxadiazol-2-one-containing benzamide derivatives targeting FtsZ as highly potent agents of killing a variety of MDR bacteria strains. *Bioorg. Med. Chem.* 27, 3179–3193. doi: 10.1016/j.bmc.2019.06.010

Bi, F., Song, D., Zhang, N., Liu, Z., Gu, X., Hu, C., et al. (2018). Design, synthesis and structure-based optimization of novel isoxazole-containing benzamide derivatives as FtsZ modulators. *Eur. J. Med. Chem.* 159, 90–103. doi: 10.1016/j.ejmech.2018.09.053

Bisson-Filho, A. W., Discola, K. F., Castellen, P., Blasios, V., Martins, A., Sforca, M. L., et al. (2015). FtsZ filament capping by MciZ, a developmental regulator of bacterial division. *Proc. Natl. Acad. Sci. U.S.A.* 112, E2130–E2138. doi: 10.1073/pnas.1414242112

Bisson-Filho, A. W., Hsu, Y. P., Squyres, G. R., Kuru, E., Wu, F., Jukes, C., et al. (2017). Treadmilling by FtsZ filaments drives peptidoglycan synthesis and bacterial cell division. *Science* 355, 739–743. doi: 10.1126/science.aak9973

Borges, A., Ferreira, C., Saavedra, M. J., and Simoes, M. (2013). Antibacterial activity and mode of action of ferulic and gallic acids against pathogenic bacteria. *Microb. Drug Resist.* 19, 256–265. doi: 10.1089/mdr.2012.0244

Bramhill, D., and Thompson, C. M. (1994). GTP-dependent polymerization of *Escherichia coli* FtsZ protein to form tubules. *Proc. Natl. Acad. Sci. U.S.A.* 91, 5813–5817. doi: 10.1073/pnas.91.13.5813

Bramkamp, M., Emmins, R., Weston, L., Donovan, C., Daniel, R. A., and Errington, J. (2008). A novel component of the division-site selection system of *Bacillus subtilis* and a new mode of action for the division inhibitor MinCD. *Mol. Microbiol.* 70, 1556–1569. doi: 10.1111/j.1365-2958.2008.06501.x

Buske, P. J., and Levin, P. A. (2012). Extreme *C terminus* of bacterial cytoskeletal protein FtsZ plays fundamental role in assembly independent of modulatory proteins. *J. Biol. Chem.* 287, 10945–10957. doi: 10.1074/jbc.M111.330324

Cai, S., Yuan, W., Li, Y., Huang, X., Guo, Q., Tang, Z., et al. (2019). Antibacterial activity of indolyl-quinolinium derivatives and study their mode of action. *Bioorg. Med. Chem.* 27, 1274–1282. doi: 10.1016/j.bmc.2019.02.024

Carro, L. (2019). Recent progress in the development of small-molecule FtsZ inhibitors as chemical tools for the development of novel antibiotics. *Antibiotics (Basel)* 8:217. doi: 10.3390/antibiotics8040217

Casiraghi, A., Suigo, L., Valoti, E., and Straniero, V. (2020). Targeting bacterial cell division: a binding site-centered approach to the most promising inhibitors of the essential protein FtsZ. *Antibiotics (Basel)* 9:69. doi: 10.3390/antibiotics9020069

Chakraborti, S., Das, L., Kapoor, N., Das, A., Dwivedi, V., Poddar, A., et al. (2011). Curcumin recognizes a unique binding site of tubulin. *J. Med. Chem.* 54, 6183–6196. doi: 10.1021/jm2004046

Chan, F. Y., Sun, N., Neves, M. A., Lam, P. C., Chung, W. H., Wong, L. K., et al. (2013). Identification of a new class of FtsZ inhibitors by structure-based design and in vitro screening. *J. Chem. Inf. Model.* 53, 2131–2140. doi: 10.1021/ci400203f

Chang, M. Y., and Shen, Y. L. (2014). Linalool exhibits cytotoxic effects by activating antitumor immunity. *Molecules* 19, 6694–6706. doi: 10.3390/molecules19056694

Cohan, M. C., Eddelbuettel, A. M. P., Levin, P. A., and Pappu, R. V. (2020). Dissecting the functional contributions of the intrinsically disordered C-terminal tail of *Bacillus subtilis* FtsZ. *J. Mol. Biol.* 432, 3205–3221. doi: 10.1016/j.jmb.2020.03.008

Dai, K., and Lutkenhaus, J. (1991). ftsZ is an essential cell division gene in *Escherichia coli*. *J. Bacteriol.* 173, 3500–3506. doi: 10.1128/jb.173.11.3500-3506.1991

de Boer, P., Crossley, R., and Rothfield, L. (1992). The essential bacterial cell-division protein FtsZ is a GTPase. *Nature* 359, 254–256. doi: 10.1038/359254a0

de Paiva, S. R., Figueiredo, M. R., Aragao, T. V., and Kaplan, M. A. (2003). Antimicrobial activity in vitro of plumbagin isolated from *Plumbago* species. *Mem. Inst. Oswaldo. Cruz.* 98, 959–961. doi: 10.1590/s0074-02762003000700017

de Pereda, J. M., Leynadier, D., Evangelio, J. A., Chacon, P., and Andreu, J. M. (1996). Tubulin secondary structure analysis, limited proteolysis sites, and homology to FtsZ. *Biochemistry* 35, 14203–14215. doi: 10.1021/bi961357b

de Souza, S. M., Delle Monache, F., and Smania, A. Jr. (2005). Antibacterial activity of coumarins. *Z. Naturforsch. C. J. Biosci.* 60, 693–700. doi: 10.1515/znc-2005-9-1006

Detsi, A., Kontogiorgis, C., and Hadjipavlou-Litina, D. (2017). Coumarin derivatives: an updated patent review (2015-2016). *Expert Opin. Ther. Pat.* 27, 1201–1226. doi: 10.1080/13543776.2017.1360284

Dhaked, H. P., Bhattacharya, A., Yadav, S., Dantu, S. C., Kumar, A., and Panda, D. (2016). Mutation of Arg191 in FtsZ impairs cytokinetic abscission of *Bacillus subtilis* cells. *Biochemistry* 55, 5754–5763. doi: 10.1021/acs.biochem.6b00493

Din, N., Quardokus, E. M., Sackett, M. J., and Brun, Y. V. (1998). Dominant C-terminal deletions of FtsZ that affect its ability to localize in *Caulobacter* and its interaction with FtsA. *Mol. Microbiol.* 27, 1051–1063. doi: 10.1046/j.1365-2958.1998.00752.x

Domadia, P., Swarup, S., Bhunia, A., Sivaraman, J., and Dasgupta, D. (2007). Inhibition of bacterial cell division protein FtsZ by cinnamaldehyde. *Biochem. Pharmacol.* 74, 831–840. doi: 10.1016/j.bcp.2007.06.029

Domadia, P. N., Bhunia, A., Sivaraman, J., Swarup, S., and Dasgupta, D. (2008). Berberine targets assembly of *Escherichia coli* cell division protein FtsZ. *Biochemistry* 47, 3225–3234. doi: 10.1021/bi7018546

Duggirala, S., Nankar, R. P., Rajendran, S., and Doble, M. (2014). Phytochemicals as inhibitors of bacterial cell division protein FtsZ: coumarins are promising candidates. *Appl. Biochem. Biotechnol.* 174, 283–296. doi: 10.1007/s12010-014-1056-2

Duman, R., Ishikawa, S., Celik, I., Strahl, H., Ogasawara, N., Troc, P., et al. (2013). Structural and genetic analyses reveal the protein SepF as a new membrane anchor for the Z ring. *Proc. Natl. Acad. Sci. U.S.A.* 110, E4601–E4610. doi: 10.1073/pnas.1313978110

Elokdah, H., Abou-Gharbia, M., Hennan, J. K., McFarlane, G., Mugford, C. P., Krishnamurthy, G., et al. (2004). Tiplaxtinin, a novel, orally efficacious inhibitor of plasminogen activator inhibitor-1: design, synthesis, and preclinical characterization. *J. Med. Chem.* 47, 3491–3494. doi: 10.1021/jm049766q

Erickson, H. P. (1995). FtsZ, a prokaryotic homolog of tubulin? *Cell* 80, 367–370. doi: 10.1016/0092-8674(95)90486-7

Erickson, H. P. (1998). Atomic structures of tubulin and FtsZ. *Trends Cell Biol.* 8, 133–137. doi: 10.1016/s0962-8924(98)01237-9

Erickson, H. P., Anderson, D. E., and Osawa, M. (2010). FtsZ in bacterial cytokinesis: cytoskeleton and force generator all in one. *Microbiol. Mol. Biol. Rev.* 74, 504–528. doi: 10.1128/MMBR.00021-10

Eroglu, C., Secme, M., Bagci, G., and Dodurga, Y. (2015). Assessment of the anticancer mechanism of ferulic acid via cell cycle and apoptotic pathways in human prostate cancer cell lines. *Tumour. Biol.* 36, 9437–9446. doi: 10.1007/s13277-015-3689-3

Fang, Z., Zheng, S., Chan, K. F., Yuan, W., Guo, Q., Wu, W., et al. (2019). Design, synthesis and antibacterial evaluation of 2,4-disubstituted-6-thiophenyl-pyrimidines. *Eur. J. Med. Chem.* 161, 141–153. doi: 10.1016/j.ejmech.2018.10.039

Ferrer-Gonzalez, E., Fujita, J., Yoshizawa, T., Nelson, J. M., Pilch, A. J., Hillman, E., et al. (2019). Structure-guided design of a fluorescent probe for the visualization of FtsZ in clinically important gram-positive and gram-negative bacterial pathogens. *Sci. Rep.* 9:20092. doi: 10.1038/s41598-019-56557-x

Finn, G. J., Creaven, B., and Egan, D. A. (2001). Study of the in vitro cytotoxic potential of natural and synthetic coumarin derivatives using human normal and neoplastic skin cell lines. *Melanoma Res.* 11, 461–467. doi: 10.1097/00008390-200110000-00004

Fujita, J., Maeda, Y., Mizohata, E., Inoue, T., Kaul, M., Parhi, A. K., et al. (2017). Structural flexibility of an inhibitor overcomes drug resistance mutations in *Staphylococcus aureus* FtsZ. *ACS Chem. Biol.* 12, 1947–1955. doi: 10.1021/acschembio.7b00323

Gardner, K. A., Moore, D. A., and Erickson, H. P. (2013). The C-terminal linker of *Escherichia coli* FtsZ functions as an intrinsically disordered peptide. *Mol. Microbiol.* 89, 264–275. doi: 10.1111/mmi.12279

Guo, Z., Li, B., Cheng, L. T., Zhou, S., McCammon, J. A., and Che, J. (2015). Identification of protein-ligand binding sites by the level-set variational implicit-solvent approach. *J. Chem. Theory Comput.* 11, 753–765. doi: 10.1021/ct500867u

Haeusser, D. P., Hoashi, M., Weaver, A., Brown, N., Pan, J., Sawitzke, J. A., et al. (2014). The Kil peptide of bacteriophage lambda blocks *Escherichia coli* cytokinesis via ZipA-dependent inhibition of FtsZ assembly. *PLoS Genet.* 10:e1004217. doi: 10.1371/journal.pgen.1004217

Haeusser, D. P., and Margolin, W. (2016). Splitsville: structural and functional insights into the dynamic bacterial Z ring. *Nat. Rev. Microbiol.* 14, 305–319.

Haeusser, D. P., Schwartz, R. L., Smith, A. M., Oates, M. E., and Levin, P. A. (2004). EzrA prevents aberrant cell division by modulating assembly of the cytoskeletal protein FtsZ. *Mol. Microbiol.* 52, 801–814. doi: 10.1111/j.1365-2958.2004.04016.x

Hale, C. A., and de Boer, P. A. (1997). Direct binding of FtsZ to ZipA, an essential component of the septal ring structure that mediates cell division in *E. coli*. *Cell* 88, 175–185. doi: 10.1016/s0092-8674(00)81838-3

Handler, A. A., Lim, J. E., and Losick, R. (2008). Peptide inhibitor of cytokinesis during sporulation in *Bacillus subtilis*. *Mol. Microbiol.* 68, 588–599. doi: 10.1111/j.1365-2958.2008.06173.x

Haranahalli, K., Tong, S., and Ojima, I. (2016). Recent advances in the discovery and development of antibacterial agents targeting the cell-division protein FtsZ. *Bioorg. Med. Chem.* 24, 6354–6369. doi: 10.1016/j.bmc.2016.05.003

Haydon, D. J., Stokes, N. R., Ure, R., Galbraith, G., Bennett, J. M., Brown, D. R., et al. (2008). An inhibitor of FtsZ with potent and selective anti-staphylococcal activity. *Science* 321, 1673–1675. doi: 10.1126/science.1159961

Hemaiswarya, S., and Doble, M. (2009). Synergistic interaction of eugenol with antibiotics against Gram negative bacteria. *Phytomedicine* 16, 997–1005. doi: 10.1016/j.phymed.2009.04.006

Hemaiswarya, S., and Doble, M. (2010). Synergistic interaction of phenylpropanoids with antibiotics against bacteria. *J. Med. Microbiol.* 59(Pt 12), 1469–1476. doi: 10.1099/jmm.0.022426-0

Hemaiswarya, S., Soudaminikkutty, R., Narasumani, M. L., and Doble, M. (2011). Phenylpropanoids inhibit protofilament formation of *Escherichia coli* cell division protein FtsZ. *J. Med. Microbiol.* 60(Pt 9), 1317–1325. doi: 10.1099/jmm.0.030536-0

Hernandez-Rocamora, V. M., Alfonso, C., Margolin, W., Zorrilla, S., and Rivas, G. (2015). Evidence that bacteriophage lambda kil peptide inhibits bacterial cell division by disrupting FtsZ protofilaments and sequestering protein subunits. *J. Biol. Chem.* 290, 20325–20335. doi: 10.1074/jbc.M115.653329

Hsin, J., Gopinathan, A., and Huang, K. C. (2012). Nucleotide-dependent conformations of FtsZ dimers and force generation observed through molecular dynamics simulations. *Proc. Natl. Acad. Sci. U.S.A.* 109, 9432–9437. doi: 10.1073/pnas.1120761109

Huang, Q., Kirikae, F., Kirikae, T., Pepe, A., Amin, A., Respicio, L., et al. (2006). Targeting FtsZ for antituberculosis drug discovery: noncytotoxic taxanes as novel antituberculosis agents. *J. Med. Chem.* 49, 463–466. doi: 10.1021/jm050920y

Huecas, S., Araujo-Bazan, L., Ruiz, F. M., Ruiz-Avila, L. B., Martinez, R. F., Escobar-Pena, A., et al. (2021). Targeting the FtsZ allosteric binding site with a novel fluorescence polarization screen, cytological and structural approaches for antibacterial discovery. *J. Med. Chem.* 64, 5730–5745. doi: 10.1021/acs.jmedchem.0c02207

Jaiswal, R., Beuria, T. K., Mohan, R., Mahajan, S. K., and Panda, D. (2007). Totarol inhibits bacterial cytokinesis by perturbing the assembly dynamics of FtsZ. *Biochemistry* 46, 4211–4220. doi: 10.1021/bi602573e

Jindal, B., and Panda, D. (2013). Understanding FtsZ assembly: cues from the behavior of its N- and C-terminal domains. *Biochemistry* 52, 7071–7081. doi: 10.1021/bi400129j

Kaul, M., Mark, L., Zhang, Y., Parhi, A. K., LaVoie, E. J., and Pilch, D. S. (2013). Pharmacokinetics and in vivo antistaphylococcal efficacy of TXY541, a 1-methylpiperidine-4-carboxamide prodrug of PC190723. *Biochem. Pharmacol.* 86, 1699–1707. doi: 10.1016/j.bcp.2013.10.010

Kaul, M., Mark, L., Zhang, Y., Parhi, A. K., Lyu, Y. L., Pawlak, J., et al. (2015). TXA709, an FtsZ-targeting benzamide prodrug with improved pharmacokinetics and enhanced in vivo efficacy against methicillin-resistant *Staphylococcus aureus*. *Antimicrob. Agents Chemother.* 59, 4845–4855. doi: 10.1128/AAC.00708-15

Kaul, M., Zhang, Y., Parhi, A. K., Lavoie, E. J., and Pilch, D. S. (2014). Inhibition of RND-type efflux pumps confers the FtsZ-directed prodrug TXY436 with activity against Gram-negative bacteria. *Biochem. Pharmacol.* 89, 321–328. doi: 10.1016/j.bcp.2014.03.002

Kaur, S., Modi, N. H., Panda, D., and Roy, N. (2010). Probing the binding site of curcumin in *Escherichia coli* and *Bacillus subtilis* FtsZ–a structural insight to unveil antibacterial activity of curcumin. *Eur. J. Med. Chem.* 45, 4209–4214. doi: 10.1016/j.ejmech.2010.06.015

Keffer, J. L., Huecas, S., Hammill, J. T., Wipf, P., Andreu, J. M., and Bewley, C. A. (2013). Chrysophaentins are competitive inhibitors of FtsZ and inhibit Z-ring formation in live bacteria. *Bioorg. Med. Chem.* 21, 5673–5678. doi: 10.1016/j.bmc.2013.07.033

Kellogg, E. H., Hejab, N. M. A., Howes, S., Northcote, P., Miller, J. H., Diaz, J. F., et al. (2017). Insights into the distinct mechanisms of action of taxane and non-taxane microtubule stabilizers from cryo-EM structures. *J. Mol. Biol.* 429, 633–646. doi: 10.1016/j.jmb.2017.01.001

Keri, R. S., Sasidhar, B. S., Nagaraja, B. M., and Santos, M. A. (2015). Recent progress in the drug development of coumarin derivatives as potent antituberculosis agents. *Eur. J. Med. Chem.* 100, 257–269. doi: 10.1016/j.ejmech.2015.06.017

Khare, S., Hsin, J., Sorto, N. A., Nepomuceno, G. M., Shaw, J. T., Shi, H., et al. (2019). FtsZ-Independent mechanism of division inhibition by the small molecule PC190723 in *Escherichia coli*. *Adv. Biosyst.* 3:e1900021. doi: 10.1002/adbi.201900021

Kiro, R., Molshanski-Mor, S., Yosef, I., Milam, S. L., Erickson, H. P., and Qimron, U. (2013). Gene product 0.4 increases bacteriophage T7 competitiveness by inhibiting host cell division. *Proc. Natl. Acad. Sci. U.S.A.* 110, 19549–19554. doi: 10.1073/pnas.1314096110

Krupka, M., and Margolin, W. (2018). Unite to divide: oligomerization of tubulin and actin homologs regulates initiation of bacterial cell division. *F1000Res.* 7:235.

Kusuma, K. D., Griffith, R., Harry, E. J., Bottomley, A. L., and Ung, A. T. (2019). In silico analysis of FtsZ crystal structures towards a new target for antibiotics. *Aust. J. Chem.* 72, 184–193. doi: 10.1071/CH18347

Lan, G., Wolgemuth, C. W., and Sun, S. X. (2007). Z-ring force and cell shape during division in rod-like bacteria. *Proc. Natl. Acad. Sci. U.S.A.* 104, 16110–16115. doi: 10.1073/pnas.0702925104

Li, X., and Ma, S. (2015). Advances in the discovery of novel antimicrobials targeting the assembly of bacterial cell division protein FtsZ. *Eur. J. Med. Chem.* 95, 1–15. doi: 10.1016/j.ejmech.2015.03.026

Li, Y., Sun, N., Ser, H.-L., Long, W., Li, Y., Chen, C., et al. (2015). Antibacterial activity evaluation and mode of action study of novel thiazole-quinolinium derivatives. *RSC Adv.* 10, 15000–15014. doi: 10.1039/D0RA00691B

Lou, Z., Wang, H., Rao, S., Sun, J., Chaoyang, m, and Li, J. (2012). P-Coumaric acid kills bacteria through dual damage mechanisms. *Food Control* 25, 550–554. doi: 10.1016/j.foodcont.2011.11.022

Löwe, J. (1998). Crystal structure determination of FtsZ from *Methanococcus jannaschii*. *J. Struct. Biol.* 124, 235–243. doi: 10.1006/jsbi.1998.4041

Löwe, J., and Amos, L. A. (1998). Crystal structure of the bacterial cell-division protein FtsZ. *Nature* 391, 203–206. doi: 10.1038/34472

Löwe, J., and Amos, L. A. (1999). Tubulin-like protofilaments in Ca2+-induced FtsZ sheets. *EMBO J.* 18, 2364–2371. doi: 10.1093/emboj/18.9.2364

Lu, C., Reedy, M., and Erickson, H. P. (2000). Straight and curved conformations of FtsZ are regulated by GTP hydrolysis. *J. Bacteriol.* 182, 164–170. doi: 10.1128/JB.182.1.164-170.2000

Lu, C., Stricker, J., and Erickson, H. P. (1998). FtsZ from *Escherichia coli*, *Azotobacter vinelandii*, and *Thermotoga maritima*–quantitation, GTP hydrolysis, and assembly. *Cell Motil. Cytoskeleton* 40, 71–86. doi: 10.1002/(SICI)1097-0169199840:1<71::AID-CM7<3.0.CO;2-I

Lu, Y., Chen, J., Xiao, M., Li, W., and Miller, D. D. (2012). An overview of tubulin inhibitors that interact with the colchicine binding site. *Pharm. Res.* 29, 2943–2971. doi: 10.1007/s11095-012-0828-z

Lui, H. K., Gao, W., Cheung, K. C., Jin, W. B., Sun, N., Kan, J. W. Y., et al. (2019). Boosting the efficacy of anti-MRSA beta-lactam antibiotics via an easily accessible, non-cytotoxic and orally bioavailable FtsZ inhibitor. *Eur. J. Med. Chem.* 163, 95–115. doi: 10.1016/j.ejmech.2018.11.052

Ma, S., and Ma, S. (2012). The development of FtsZ inhibitors as potential antibacterial agents. *ChemMedChem* 7, 1161–1172. doi: 10.1002/cmdc.201200156

Ma, X., and Margolin, W. (1999). Genetic and functional analyses of the conserved C-terminal core domain of *Escherichia coli* FtsZ. *J. Bacteriol.* 181, 7531–7544.

Mathew, B., Hobrath, J. V., Ross, L., Connelly, M. C., Lofton, H., Rajagopalan, M., et al. (2016). Screening and development of new inhibitors of FtsZ from *M. Tuberculosis*. *PLoS One* 11:e0164100. doi: 10.1371/journal.pone.0164100

Mathew, B., Ross, L., and Reynolds, R. C. (2013). A novel quinoline derivative that inhibits mycobacterial FtsZ. *Tuberculosis (Edinb.)* 93, 398–400. doi: 10.1016/j.tube.2013.04.002

Mathew, R., Kruthiventi, A. K., Prasad, J. V., Kumar, S. P., Srinu, G., and Chatterji, D. (2010). Inhibition of mycobacterial growth by plumbagin derivatives. *Chem. Biol. Drug Des.* 76, 34–42. doi: 10.1111/j.1747-0285.2010.00987.x

Matsui, T., Lallo, S., Nisa, K., and Morita, H. (2017). Filamenting temperature-sensitive mutant Z inhibitors from *Glycyrrhiza glabra* and their inhibitory mode of action. *Bioorg. Med. Chem. Lett.* 27, 1420–1424. doi: 10.1016/j.bmcl.2017.01.095

Matsui, T., Yamane, J., Mogi, N., Yamaguchi, H., Takemoto, H., Yao, M., et al. (2012). Structural reorganization of the bacterial cell-division protein FtsZ from *Staphylococcus aureus*. *Acta Crystallogr. D Biol. Crystallogr.* 68(Pt 9), 1175–1188. doi: 10.1107/S0907444912022640

Miguel, A., Hsin, J., Liu, T., Tang, G., Altman, R. B., and Huang, K. C. (2015). Variations in the binding pocket of an inhibitor of the bacterial division protein FtsZ across genotypes and species. *PLoS Comput. Biol.* 11:e1004117. doi: 10.1371/journal.pcbi.1004117

Mukherjee, A., Dai, K., and Lutkenhaus, J. (1993). *Escherichia coli* cell division protein FtsZ is a guanine nucleotide binding protein. *Proc. Natl. Acad. Sci. U.S.A.* 90, 1053–1057. doi: 10.1073/pnas.90.3.1053

Mukherjee, A., and Lutkenhaus, J. (1994). Guanine nucleotide-dependent assembly of FtsZ into filaments. *J. Bacteriol.* 176, 2754–2758. doi: 10.1128/jb.176.9.2754-2758.1994

Ng, L. T., and Wu, S. J. (2011). Antiproliferative activity of *Cinnamomum cassia* constituents and effects of pifithrin-alpha on their apoptotic signaling pathways in Hep G2 Cells. *Evid. Based Complement Alternat. Med.* 2011:492148. doi: 10.1093/ecam/nep220

Nguyen, L. T., Oikonomou, C. M., Ding, H. J., Kaplan, M., Yao, Q., Chang, Y. W., et al. (2019). Simulations suggest a constrictive force is required for Gram-negative bacterial cell division. *Nat. Commun.* 10:1259. doi: 10.1038/s41467-019-09264-0

Niero, E. L., and Machado-Santelli, G. M. (2013). Cinnamic acid induces apoptotic cell death and cytoskeleton disruption in human melanoma cells. *J. Exp. Clin. Cancer Res.* 32:31. doi: 10.1186/1756-9966-32-31

Nogales, E., Downing, K. H., Amos, L. A., and Löwe, J. (1998a). Tubulin and FtsZ form a distinct family of GTPases. *Nat. Struct. Biol.* 5, 451–458. doi: 10.1038/nsb0698-451

Nogales, E., Wolf, S. G., and Downing, K. H. (1998b). Structure of the alpha beta tubulin dimer by electron crystallography. *Nature* 391, 199–203. doi: 10.1038/34465

Nussbaum, P., Gerstner, M., Dingethal, M., Erb, C., and Albers, S. V. (2021). The archaeal protein SepF is essential for cell division in *Haloferax volcanii*. *Nat. Commun.* 12:3469. doi: 10.1038/s41467-021-23686-9

Ohashi, Y., Chijiiwa, Y., Suzuki, K., Takahashi, K., Nanamiya, H., Sato, T., et al. (1999). The lethal effect of a benzamide derivative, 3-methoxybenzamide, can be suppressed by mutations within a cell division gene, ftsZ, in *Bacillus subtilis*. *J. Bacteriol.* 181, 1348–1351. doi: 10.1128/JB.181.4.1348-1351.1999

Oncul, S., and Ercan, A. (2017). Discrimination of the effects of doxorubicin on two different breast cancer cell lines on account of multidrug resistance and apoptosis. *Indian J. Pharm. Sci.* 79, 599–607. doi: 10.4172/pharmaceutical-sciences.1000268

Ortiz, C., Natale, P., Cueto, L., and Vicente, M. (2016). The keepers of the ring: regulators of FtsZ assembly. *FEMS Microbiol. Rev.* 40, 57–67.

Panda, D., Bhattacharya, D., Gao, Q. H., Oza, P. M., Lin, H. Y., Hawkins, B., et al. (2016). Identification of agents targeting FtsZ assembly. *Future Med. Chem.* 8, 1111–1132. doi: 10.4155/fmc-2016-0041

Panda, P., Taviti, A. C., Satpati, S., Kar, M. M., Dixit, A., and Beuria, T. K. (2015). Doxorubicin inhibits *E. coli* division by interacting at a novel site in FtsZ. *Biochem. J.* 471, 335–346. doi: 10.1042/BJ20150467

Pichoff, S., and Lutkenhaus, J. (2002). Unique and overlapping roles for ZipA and FtsA in septal ring assembly in *Escherichia coli*. *EMBO J.* 21, 685–693. doi: 10.1093/emboj/21.4.685

Piddock, L. J., and Walters, R. N. (1992). Bactericidal activities of five quinolones for *Escherichia coli* strains with mutations in genes encoding the SOS response or cell division. *Antimicrob. Agents Chemother.* 36, 819–825. doi: 10.1128/aac.36.4.819

Pinho, M. G., and Errington, J. (2003). Dispersed mode of *Staphylococcus aureus* cell wall synthesis in the absence of the division machinery. *Mol. Microbiol.* 50, 871–881. doi: 10.1046/j.1365-2958.2003.03719.x

Plaza, A., Keffer, J. L., Bifulco, G., Lloyd, J. R., and Bewley, C. A. (2010). Chrysophaentins A-H, antibacterial bisdiarylbutene macrocycles that inhibit the bacterial cell division protein FtsZ. *J. Am. Chem. Soc.* 132, 9069–9077. doi: 10.1021/ja102100h

Prota, A. E., Bargsten, K., Northcote, P. T., Marsh, M., Altmann, K. H., Miller, J. H., et al. (2014). Structural basis of microtubule stabilization by laulimalide and peloruside A. *Angew Chem. Int. Ed. Engl.* 53, 1621–1625. doi: 10.1002/anie.201307749

Puupponen-Pimia, R., Nohynek, L., Meier, C., Kahkonen, M., Heinonen, M., Hopia, A., et al. (2001). Antimicrobial properties of phenolic compounds from berries. *J. Appl. Microbiol.* 90, 494–507. doi: 10.1046/j.1365-2672.2001.01271.x

Raghav, D., Ashraf, S. M., Mohan, L., and Rathinasamy, K. (2017). Berberine induces toxicity in HeLa cells through perturbation of microtubule polymerization by binding to tubulin at a unique site. *Biochemistry* 56, 2594–2611. doi: 10.1021/acs.biochem.7b00101

Rai, D., Singh, J. K., Roy, N., and Panda, D. (2008). Curcumin inhibits FtsZ assembly: an attractive mechanism for its antibacterial activity. *Biochem. J.* 410, 147–155. doi: 10.1042/BJ20070891

Ramirez-Diaz, D. A., Merino-Salomon, A., Meyer, F., Heymann, M., Rivas, G., Bramkamp, M., et al. (2021). FtsZ induces membrane deformations via torsional stress upon GTP hydrolysis. *Nat. Commun.* 12:3310. doi: 10.1038/s41467-021-23387-3

Rastogi, N., Domadia, P., Shetty, S., and Dasgupta, D. (2008). Screening of natural phenolic compounds for potential to inhibit bacterial cell division protein FtsZ. *Indian J. Exp. Biol.* 46, 783–787.

Ravelli, R. B., Gigant, B., Curmi, P. A., Jourdain, I., Lachkar, S., Sobel, A., et al. (2004). Insight into tubulin regulation from a complex with colchicine and a stathmin-like domain. *Nature* 428, 198–202. doi: 10.1038/nature02393

Ray, S., Dhaked, H. P., and Panda, D. (2014). Antimicrobial peptide CRAMP (16-33) stalls bacterial cytokinesis by inhibiting FtsZ assembly. *Biochemistry* 53, 6426–6429. doi: 10.1021/bi501115p

Ray, S., Jindal, B., Kunal, K., Surolia, A., and Panda, D. (2015). BT-benzo-29 inhibits bacterial cell proliferation by perturbing FtsZ assembly. *FEBS J.* 282, 4015–4033. doi: 10.1111/febs.13403

Ray, S., Kumar, A., and Panda, D. (2013). GTP regulates the interaction between MciZ and FtsZ: a possible role of MciZ in bacterial cell division. *Biochemistry* 52, 392–401. doi: 10.1021/bi301237m

Romberg, L., Simon, M., and Erickson, H. P. (2001). Polymerization of Ftsz, a bacterial homolog of tubulin. is assembly cooperative? *J. Biol. Chem.* 276, 11743–11753. doi: 10.1074/jbc.M009033200

Rowlett, V. W., and Margolin, W. (2015). The Min system and other nucleoid-independent regulators of Z ring positioning. *Front. Microbiol.* 6:478. doi: 10.3389/fmicb.2015.00478

Ruiz-Avila, L. B., Huecas, S., Artola, M., Vergonos, A., Ramirez-Aportela, E., Cercenado, E., et al. (2013). Synthetic inhibitors of bacterial cell division targeting the GTP-binding site of FtsZ. *ACS Chem. Biol.* 8, 2072–2083. doi: 10.1021/cb400208z

Sanderson, J. T., Clabault, H., Patton, C., Lassalle-Claux, G., Jean-Francois, J., Pare, A. F., et al. (2013). Antiproliferative, antiandrogenic and cytotoxic effects of novel caffeic acid derivatives in LNCaP human androgen-dependent prostate cancer cells. *Bioorg. Med. Chem.* 21, 7182–7193. doi: 10.1016/j.bmc.2013.08.057

Santra, M. K., Beuria, T. K., Banerjee, A., and Panda, D. (2004). Ruthenium red-induced bundling of bacterial cell division protein, FtsZ. *J. Biol. Chem.* 279, 25959–25965. doi: 10.1074/jbc.M312473200

Scheffers, D. J., de Wit, J. G., den Blaauwen, T., and Driessen, A. J. (2002). GTP hydrolysis of cell division protein FtsZ: evidence that the active site is formed by the association of monomers. *Biochemistry* 41, 521–529. doi: 10.1021/bi011370i

Schumacher, M. A., Ohashi, T., Corbin, L., and Erickson, H. P. (2020). High-resolution crystal structures of *Escherichia coli* FtsZ bound to GDP and GTP. *Acta Crystallogr. F Struct. Biol. Commun.* 76(Pt 2), 94–102. doi: 10.1107/S2053230X20001132

Singh, D., Bhattacharya, A., Rai, A., Dhaked, H. P., Awasthi, D., Ojima, I., et al. (2014). SB-RA-2001 inhibits bacterial proliferation by targeting FtsZ assembly. *Biochemistry* 53, 2979–2992. doi: 10.1021/bi401356y

Singh, P., Jindal, B., Surolia, A., and Panda, D. (2012). A rhodanine derivative CCR-11 inhibits bacterial proliferation by inhibiting the assembly and GTPase activity of FtsZ. *Biochemistry* 51, 5434–5442. doi: 10.1021/bi201813u

Squyres, G. R., Holmes, M. J., Barger, S. R., Pennycook, B. R., Ryan, J., Yan, V. T., et al. (2021). Single-molecule imaging reveals that Z-ring condensation is essential for cell division in *Bacillus subtilis*. *Nat. Microbiol.* 6, 553–562.

Sridevi, D., Sudhakar, K. U., Ananthathatmula, R., Nankar, R. P., and Doble, M. (2017). Mutation at G103 of MtbFtsZ altered their sensitivity to coumarins. *Front. Microbiol.* 8:578. doi: 10.3389/fmicb.2017.00578

Steinmetz, M. O., and Prota, A. E. (2018). Microtubule-targeting agents: strategies to hijack the cytoskeleton. *Trends Cell Biol.* 28, 776–792. doi: 10.1016/j.tcb.2018.05.001

Straniero, V., Sebastian-Perez, V., Suigo, L., Margolin, W., Casiraghi, A., Hrast, M., et al. (2021). Computational design and development of benzodioxane-benzamides as potent inhibitors of FtsZ by exploring the hydrophobic subpocket. *Antibiotics (Basel)* 10:442. doi: 10.3390/antibiotics10040442

Stricker, J., Maddox, P., Salmon, E. D., and Erickson, H. P. (2002). Rapid assembly dynamics of the *Escherichia coli* FtsZ-ring demonstrated by fluorescence recovery after photobleaching. *Proc. Natl. Acad. Sci. U.S.A.* 99, 3171–3175. doi: 10.1073/pnas.052595099

Sun, N., Chan, F. Y., Lu, Y. J., Neves, M. A., Lui, H. K., Wang, Y., et al. (2014). Rational design of berberine-based FtsZ inhibitors with broad-spectrum antibacterial activity. *PLoS One* 9:e97514. doi: 10.1371/journal.pone.0097514

Sun, N., Du, R. L., Zheng, Y. Y., Guo, Q., Cai, S. Y., Liu, Z. H., et al. (2018). Antibacterial activity of 3-methylbenzo[d]thiazol-methylquinolinium derivatives and study of their action mechanism. *J. Enzyme Inhib. Med. Chem.* 33, 879–889. doi: 10.1080/14756366.2018.1465055

Sun, N., Du, R. L., Zheng, Y. Y., Huang, B. H., Guo, Q., Zhang, R. F., et al. (2017a). Antibacterial activity of N-methylbenzofuro[3,2-b]quinoline and N-methylbenzoindolo[3,2-b]-quinoline derivatives and study of their mode of action. *Eur. J. Med. Chem.* 135, 1–11. doi: 10.1016/j.ejmech.2017.04.018

Sun, N., Lu, Y. J., Chan, F. Y., Du, R. L., Zheng, Y. Y., Zhang, K., et al. (2017b). A thiazole orange derivative targeting the bacterial protein FtsZ shows potent antibacterial activity. *Front. Microbiol.* 8:855. doi: 10.3389/fmicb.2017.00855

Sun, N., Zheng, Y. Y., Du, R. L., Cai, S. Y., Zhang, K., So, L. Y., et al. (2017c). New application of tiplaxtinin as an effective FtsZ-targeting chemotype for an antimicrobial study. *Medchemcomm* 8, 1909–1913. doi: 10.1039/c7md00387k

Taviti, A. C., and Beuria, T. K. (2017). MinD directly interacting with FtsZ at the H10 helix suggests a model for robust activation of MinC to destabilize FtsZ polymers. *Biochem. J.* 474, 3189–3205. doi: 10.1042/BCJ20170357

Tripathy, S., and Sahu, S. K. (2019). FtsZ inhibitors as a new genera of antibacterial agents. *Bioorg. Chem.* 91:103169. doi: 10.1016/j.bioorg.2019.103169

Trusca, D., Scott, S., Thompson, C., and Bramhill, D. (1998). Bacterial SOS checkpoint protein SulA inhibits polymerization of purified FtsZ cell division protein. *J. Bacteriol.* 180, 3946–3953. doi: 10.1128/JB.180.15.3946-3953.1998

Urgaonkar, S., La Pierre, H. S., Meir, I., Lund, H., RayChaudhuri, D., and Shaw, J. T. (2005). Synthesis of antimicrobial natural products targeting FtsZ: (+/−)-dichamanetin and (+/−)-2′ ′-hydroxy-5′ ′-benzylisouvarinol-B. *Org. Lett.* 7, 5609–5612. doi: 10.1021/ol052269z

van den Ent, F., Amos, L., and Löwe, J. (2001). Bacterial ancestry of actin and tubulin. *Curr. Opin. Microbiol.* 4, 634–638. doi: 10.1016/s1369-5274(01)00262-4

Vaughan, S., Wickstead, B., Gull, K., and Addinall, S. G. (2004). Molecular evolution of FtsZ protein sequences encoded within the genomes of archaea, bacteria, and eukaryota. *J. Mol. Evol.* 58, 19–29. doi: 10.1007/s00239-003-2523-5

Wagstaff, J. M., Tsim, M., Oliva, M. A., Garcia-Sanchez, A., Kureisaite-Ciziene, D., Andreu, J. M., et al. (2017). A polymerization-associated structural switch in FtsZ that enables treadmilling of model filaments. *mBio* 8:e00254-17. doi: 10.1128/mBio.00254-17

Wang, M., Fang, C., Ma, B., Luo, X., and Hou, Z. (2020). Regulation of cytokinesis: FtsZ and its accessory proteins. *Curr. Genet.* 66, 43–49. doi: 10.1007/s00294-019-01005-6

White, E. L., Suling, W. J., Ross, L. J., Seitz, L. E., and Reynolds, R. C. (2002). 2-Alkoxycarbonylaminopyridines: inhibitors of *Mycobacterium tuberculosis* FtsZ. *J. Antimicrob. Chemother.* 50, 111–114. doi: 10.1093/jac/dkf075

White, M. L., and Eswara, P. J. (2021). ylm has more than a (Z Anchor) ring to It! *J. Bacteriol.* 203:e00460-20. doi: 10.1128/JB.00460-20

Whitley, K. D., Jukes, C., Tregidgo, N., Karinou, E., Almada, P., Cesbron, Y., et al. (2021). FtsZ treadmilling is essential for Z-ring condensation and septal constriction initiation in *Bacillus subtilis*. *Nat. Commun.* 12:2448.

Wu, Y. Y., Zhang, T. Y., Zhang, M. Y., Cheng, J., and Zhang, Y. X. (2018). An endophytic Fungi of *Ginkgo biloba* L. produces antimicrobial metabolites as potential inhibitors of FtsZ of *Staphylococcus aureus*. *Fitoterapia* 128, 265–271. doi: 10.1016/j.fitote.2018.05.033

Yang, X., Lyu, Z., Miguel, A., McQuillen, R., Huang, K. C., and Xiao, J. (2017). GTPase activity-coupled treadmilling of the bacterial tubulin FtsZ organizes septal cell wall synthesis. *Science* 355, 744–747. doi: 10.1126/science.aak9995

Yao, Q., Jewett, A. I., Chang, Y. W., Oikonomou, C. M., Beeby, M., Iancu, C. V., et al. (2017). Short FtsZ filaments can drive asymmetric cell envelope constriction at the onset of bacterial cytokinesis. *EMBO J.* 36, 1577–1589. doi: 10.15252/embj.201696235

Yu, H. H., Kim, K. J., Cha, J. D., Kim, H. K., Lee, Y. E., Choi, N. Y., et al. (2005). Antimicrobial activity of berberine alone and in combination with ampicillin or oxacillin against methicillin-resistant *Staphylococcus aureus*. *J. Med. Food* 8, 454–461. doi: 10.1089/jmf.2005.8.454

Zhang, G. F., Zhang, S., Pan, B., Liu, X., and Feng, L. S. (2018). 4-Quinolone derivatives and their activities against Gram positive pathogens. *Eur. J. Med. Chem.* 143, 710–723. doi: 10.1016/j.ejmech.2017.11.082

Zheng, Y. Y., Du, R. L., Cai, S. Y., Liu, Z. H., Fang, Z. Y., Liu, T., et al. (2018). Study of benzofuroquinolinium derivatives as a new class of potent antibacterial agent and the mode of inhibition targeting FtsZ. *Front. Microbiol.* 9:1937. doi: 10.3389/fmicb.2018.01937

Conflict of Interest: The authors declare that the research was conducted in the absence of any commercial or financial relationships that could be construed as a potential conflict of interest.

Publisher's Note: All claims expressed in this article are solely those of the authors and do not necessarily represent those of their affiliated organizations, or those of the publisher, the editors and the reviewers. Any product that may be evaluated in this article, or claim that may be made by its manufacturer, is not guaranteed or endorsed by the publisher.

frontiers in Microbiology

ORIGINAL RESEARCH
published: 13 September 2021
doi: 10.3389/fmicb.2021.695572

Functional Characterization of the Cell Division Gene Cluster of the Wall-less Bacterium *Mycoplasma genitalium*

Carlos Martínez-Torró[1†], Sergi Torres-Puig[1†], Marina Marcos-Silva[1], Marta Huguet-Ramón[1], Carmen Muñoz-Navarro[1], Maria Lluch-Senar[2], Luis Serrano[2], Enrique Querol[1], Jaume Piñol[1] and Oscar Q. Pich[1,3*]*

[1]Departament de Bioquímica i Biologia Molecular, Institut de Biotecnologia i Biomedicina, Universitat Autònoma de Barcelona, Barcelona, Spain, [2]EMBL/CRG Systems Biology Research Unit, Centre for Genomic Regulation (CRG), The Barcelona Institute of Science and Technology, Barcelona, Spain, [3]Laboratori de Recerca en Microbiologia i Malalties Infeccioses, Institut d'Investigació i Innovació Parc Taulí (I3PT), Hospital Universitari Parc Taulí, Universitat Autònoma de Barcelona, Sabadell, Spain

OPEN ACCESS

Edited by:
Joe Lutkenhaus, University of Kansas Medical Center Research Institute, United States

Reviewed by:
William Margolin, University of Texas Health Science Center at Houston, United States
Iain G. Duggin, University of Technology Sydney, Australia

***Correspondence:**
Jaume Piñol
jaume.pinyol@uab.cat
Oscar Q. Pich
oquijada@tauli.cat

[†]*These authors have contributed equally to this work*

Specialty section:
This article was submitted to Microbial Physiology and Metabolism, a section of the journal Frontiers in Microbiology

Received: *15 April 2021*
Accepted: *10 August 2021*
Published: *13 September 2021*

Citation:
Martínez-Torró C, Torres-Puig S, Marcos-Silva M, Huguet-Ramón M, Muñoz-Navarro C, Lluch-Senar M, Serrano L, Querol E, Piñol J and Pich OQ (2021) Functional Characterization of the Cell Division Gene Cluster of the Wall-less Bacterium Mycoplasma genitalium. Front. Microbiol. 12:695572. doi: 10.3389/fmicb.2021.695572

It is well-established that FtsZ drives peptidoglycan synthesis at the division site in walled bacteria. However, the function and conservation of FtsZ in wall-less prokaryotes such as mycoplasmas are less clear. In the genome-reduced bacterium *Mycoplasma genitalium*, the cell division gene cluster is limited to four genes: *mraZ*, *mraW*, MG_223, and *ftsZ*. In a previous study, we demonstrated that *ftsZ* was dispensable for growth of *M. genitalium* under laboratory culture conditions. Herein, we show that the entire cell division gene cluster of *M. genitalium* is non-essential for growth *in vitro*. Our analyses indicate that loss of the *mraZ* gene alone is more detrimental for growth of *M. genitalium* than deletion of *ftsZ* or the entire cell division gene cluster. Transcriptional analysis revealed a marked upregulation of *ftsZ* in the *mraZ* mutant. Stable isotope labeling by amino acids in cell culture (SILAC)-based proteomics confirmed the overexpression of FtsZ in MraZ-deprived cells. Of note, we found that *ftsZ* expression was upregulated in non-adherent cells of *M. genitalium*, which arise spontaneously at relatively high rates. Single cell analysis using fluorescent markers showed that FtsZ localization varied throughout the cell cycle of *M. genitalium* in a coordinated manner with the chromosome and the terminal organelle (TMO). In addition, our results indicate a possible role for the RNA methyltransferase MraW in the regulation of FtsZ expression at the post-transcriptional level. Altogether, this study provides an extensive characterization of the cell division gene cluster of *M. genitalium* and demonstrates the existence of regulatory elements controlling FtsZ expression at the temporal and spatial level in mycoplasmas.

Keywords: mycoplasmas, cell division, regulation, single cell analysis, FtsZ localization, cell cycle

INTRODUCTION

Cell division plays a central role in the life of all prokaryotic and eukaryotic organisms and it requires the coordinated action of multiple proteins and regulatory circuits. In bacteria, most genes necessary for cytokinesis and peptidoglycan wall biosynthesis are encoded in the division and cell wall (*dcw*) gene cluster. Organization and length of the *dcw* gene cluster are

exquisitely conserved across phylogenetically distant species. As an exception, several genes that lie within the *dcw* gene cluster of Gram-negative and Gram-positive rods, are located elsewhere in the chromosome in Gram-positive cocci (Pucci et al., 1997). Based on this observation, a relationship between the structure of the *dcw* gene cluster and cell morphology was proposed. The underlying mechanism in this relationship, which involves the co-translational assembly of the protein complexes involved in cell division, is referred to as genomic channeling (Mingorance et al., 2004). In mycoplasmas, the *dcw* gene cluster is usually limited to four genes: *mraZ*, *mraW*, MG_223, and *ftsZ* (**Figure 1A**; Alarcón et al., 2007). Mycoplasmas are phylogenetically related to Gram-positive bacteria, but they have lost the peptidoglycan biosynthesis genes as a result of an extensive genome reduction. Although mycoplasma cells are typically spherical, the presence in some species of a tip structure instrumental for cytoadherence, results in an elongated, flask-shaped morphology.

The function of *mraZ* and *mraW*, the first two genes of the *dcw* gene cluster, has been elusive for many years. A comprehensive study in *Escherichia coli* revealed that MraZ is a transcriptional repressor that controls its own expression and that of other genes of the *dcw* gene cluster (Eraso et al., 2014). In the same study, the authors found that MraZ binds to conserved sequences, designated as MraZ boxes, within the upstream region of the *dcw* gene cluster. Perhaps surprisingly, loss of MraZ was not associated with any apparent phenotype in this model bacterium. In spite of this, an antagonistic effect between MraZ and MraW was disclosed. MraW is an RNA methyltransferase that targets the 16S ribosomal RNA (Kimura and Suzuki, 2010). Characterization of an *mraW* mutant in *E. coli* demonstrated an altered non-AUG initiation and a decreased translation fidelity, suggesting that MraW could play a role in start codon selection and recognition of classic STOP codons. In *Staphylococcus aureus*, *mraW* mutants also exhibit an anomalous translation fidelity, along with a reduced growth rate and an increased sensitivity to oxidative stress (Kyuma et al., 2015). More recently, the MraW protein was found to also methylate DNA and alter gene expression in *E. coli* (Xu et al., 2019). Of note, loss of MraW increases the expression of MraZ, which supports the antagonistic activity between these two proteins described earlier (Eraso et al., 2014; Xu et al., 2019).

By contrast, the function of the ancestral homologue of tubulin, FtsZ, is much better established. FtsZ polymerizes and depolymerizes through GTP hydrolysis and forms a ring-like structure at the midcell known as the Z-ring that subsequently contracts during septation (Adams and Errington, 2009; Busiek and Margolin, 2015). The Z-ring recruits cell division proteins and septal peptidoglycan synthesizing enzymes to the division site, and constitutes the scaffold of the bacterial divisome (Errington et al., 2003). In *E. coli*, FtsA is the first protein known to be recruited to the septal ring and it is important for the stability of FtsZ (Vicente and Rico, 2006). Of note, the ratio of FtsZ and FtsA is critical for the proper functioning of the cell division apparatus (Dai and Lutkenhaus, 1992; Dewar et al., 1992). In fact, it has been recently demonstrated that cell division in the Gram-positive bacterium *Bacillus subtilis* is mediated by filaments of FtsZ and FtsA, which treadmill circumferentially around the division ring, driving the motion of the peptidoglycan synthesizing enzymes (Bisson-Filho et al., 2017).

Because of its pivotal role in cell division, FtsZ expression is controlled at multiple levels (Robin et al., 1990). Similarly, septal ring formation and localization are tightly regulated (Vicente et al., 1998). The complex regulation observed within the *dcw* gene cluster has a fundamental biological role and accordingly, dissociation of *ftsZ* expression from its natural regulatory signals leads to important alterations in the physiology of cell division. However, so far, very little is known regarding the factors controlling FtsZ expression, localization, and function in mycoplasmas. The cell division gene cluster has an operonic structure in *Mycoplasma genitalium* and the close related species *Mycoplasma pneumoniae* (Benders et al., 2005). On the other hand, the N-terminal region of FtsZ from *Mycoplasma pulmonis* could function for cell division in *E. coli* suppressor strains, provided that the C-terminal tail is replaced (Osawa and Erickson, 2006). In addition, in *Mycoplasma hominis*, FtsZ protofilaments can form spiral structures similar to Z-spirals of *B. subtilis* and *E. coli*, suggesting also a functional role of FtsZ in cell division (Vishnyakov et al., 2009). Recent data also suggest that FtsZ stability is controlled by the Lon protease in *M. pneumoniae* (Burgos et al., 2020).

Remarkably, while the *ftsZ* gene is essential in most bacteria (Beall and Lutkenhaus, 1991; Dai and Lutkenhaus, 1991), it is dispensable in cell wall-deficient derivatives of some Gram-positive and Gram-negative bacteria known as L-forms (Mercier et al., 2014). Similarly, bacteria from the *Planctomycetes* and Chlamydiae superphylum lack the FtsZ protein (Pilhofer et al., 2008). In a previous study, our laboratory demonstrated that *ftsZ* was non-essential for *in vitro* growth of *M. genitalium* (Lluch-Senar et al., 2010), raising important questions as to the conservation of *ftsZ* in mycoplasmas. In keeping with this, other species phylogenetically related to *M. genitalium* such as *Mycoplasma mobile* or *Ureaplasma urealyticum*, do not code for a homolog of the *ftsZ* gene (Glass et al., 2000; Jaffe et al., 2004). Therefore, what is the role of the cell division genes in mycoplasmas? We have addressed this question by constructing and characterizing several cell division mutants in the genome-reduced bacterium *M. genitalium*.

Abbreviations: SEM, Scanning electron microscopy; TMO, Terminal organelle; WGS, Whole genome sequencing.

MATERIALS AND METHODS

Bacterial Strains and Culture Conditions

All *M. genitalium* strains were grown in SP-4 broth at 37°C in a 5% CO_2 atmosphere in tissue culture flasks. SP-4 plates were prepared supplementing the medium with 0.8% agar (BD). Chloramphenicol (17 μg ml^{-1}) or tetracycline (3 μg ml^{-1}) were added for mutant selection. All *M. genitalium* strains used in this work are listed in the **Supplementary Table S1**. *Escherichia coli* strain XL-1 Blue was used for cloning and

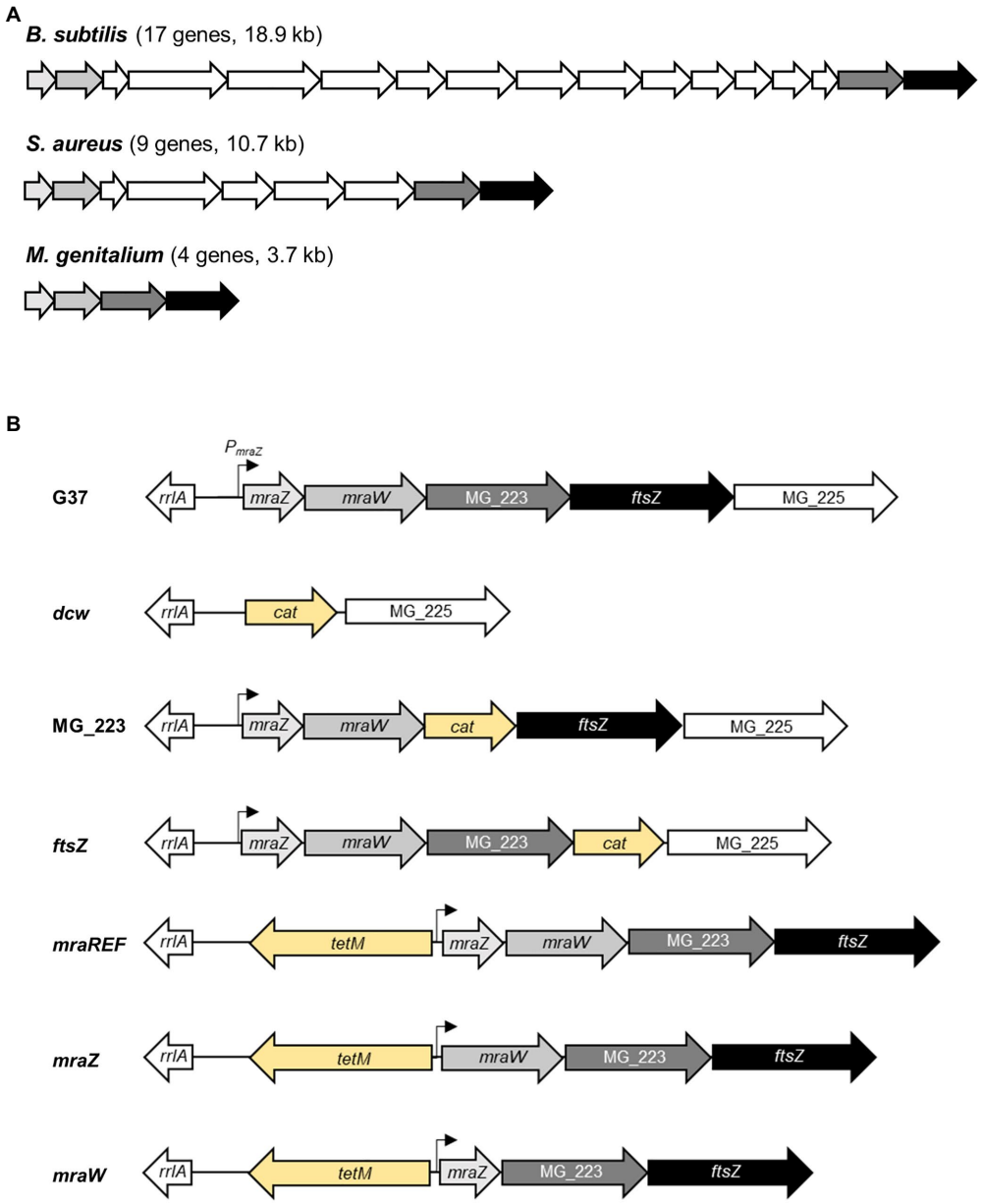

FIGURE 1 | Overview of the *dcw* gene cluster organization in selected bacteria. Scheme depicting the *dcw* gene cluster of three representative species of the Firmicutes phylum **(A)**. *Bacillus subtilis* (17 genes, 18.9 kb), *Staphylococcus aureus* (nine genes, 10.7 kb), and *Mycoplasma genitalium* (four genes, 3.7 kb). **(B)** Scheme of the cell division gene cluster in the different *M. genitalium* mutants created in this study. The promoter region of the *mraZ* gene (P_{mraZ}) was characterized in a previous report (Benders et al., 2005). The *tetM* or *cat* markers (in yellow) were introduced to select for the intended mutants.

plasmid propagation. The strain was grown in Luria Bertani (LB) or LB agar plates containing 100 μg ml^{-1} ampicillin, 40 μg ml^{-1} X-Gal, and 24 μg ml^{-1} Isopropyl β-D-1-thiogalactopyranoside (IPTG) when needed.

DNA Manipulation

Plasmid DNA was obtained using 5Prime kit. PCR products were purified from agarose gels using Nucleospin Gel and PCR Clean-up kit (Macherey-Nagel) and digested with the corresponding restriction enzymes (Fermentas) when necessary. All primers used in this study are listed in the **Supplementary Table S2**. Plasmids for *M. genitalium* transformation were obtained using the GenElute HP Midiprep kit (Sigma).

Mutant Construction and Screening

A detailed explanation of the methodology, including primers and plasmids, used to generate the different mutants created in this study is supplied in the **Supplementary Material**. Integrity of the chromosome in the mutant strains, other than

the intended deletions, was assessed and confirmed by whole genome sequencing (WGS; **Supplementary Table S3**). Transformation of *M. genitalium* was carried out as previously described (Torres-Puig et al., 2015). Screening for mutants was performed using cell lysates as template for PCR or sequencing reactions. Cell lysates were obtained by centrifugation of 1.5 ml cell cultures, disruption of pellets using 30 µl of Lysis Buffer (Tris-HCl 0.1 M pH8.5, Tween-20 0.05%, and proteinase K 0.25 mg ml^{-1}), and incubation for 1 h at 37°C followed by inactivation at 95°C for 10 min.

DNA Sequencing

DNA sequencing reactions were performed using BigDye® v3.1 Cycle Sequencing kit using 2.5 µl of genomic DNA or *M. genitalium* lysate, following manufacturer's instructions. All reactions were analyzed in an ABI PRISM 3130xl Genetic Analyzer at the Servei de Genòmica i Bioinformàtica (UAB).

Growth Rate Quantification

Growth rates of *M. genitalium* cultures were determined using an adaptation of the colorimetric protocol described by Karr et al. (2012). Strains were grown to mid-log phase in 25 cm^2 flasks with 5 ml SP4. Attached cells were scraped off, recovered by centrifugation at 12,000 rpm, and resuspended in 3 ml of fresh SP4. Then, 300 µl of the cellular suspension were inoculated in four different wells of a 96-well plate. Each of these wells constitutes the first sample of four technical repeats. About 100 µl of the first well (sample 1) were inoculated into the next well (sample 2) already containing 200 µl of fresh SP4, thus diluting 1/3 the initial concentration. This process was repeated four more times (samples 3, 4, 5, and 6), achieving a final dilution of 1/243. The 96-well plate was sealed with transparent tape, placed into a Tecan Sunrise Absorbance Microplate Reader (Tecan), and incubated at 37°C for 7 days. As *M. genitalium* grows, the bacterial metabolism acidifies the culture medium changing the color of the phenol red indicator from red (pH 7.8) to yellow (pH 6), which was detected by measuring the absorbance at 550 nm. For each analysis, readings were taken every 30 min for up to 8 days (total of 400 reads per well). The readings were stored in an Excel datasheet and analyzed once the experiment was completed, and a curve was plotted for each dilution and the inflection point was inferred. Next, the inflection points were plotted in a graphic, using the Napierian logarithm of the dilution as the *x* coordinate for each dilution. Once all the inflection points were plotted, the slope (μ, growth rate constant) was inferred by linear regression, and the doubling time (g) was obtained and according to the general equation for exponential growth of bacteria [$g = \ln 2/(1/\mu)$].

RNA-Seq

RNA-Seq analyses were performed as previously described (Torres-Puig et al., 2018; Martínez-Torró et al., 2020). Mid-log phase cultures of *M. genitalium* were scraped off in 1 ml of fresh SP-4 and reinoculated in two new 25 cm^2 tissue culture flasks with fresh SP-4 medium for 6 h. Then, cells were lysed, and total RNA was extracted using the miRNeasy Mini Kit (Qiagen). RNA libraries were prepared with TruSeq Stranded Total RNA Library Prep Kit (Illumina) and analyzed using a HiSeq 3000 System (Illumina) at the Genomics Unit from the Centre for Genomic Regulation (CRG), Barcelona. cDNA clusters were immobilized in sequencing lanes of 2 × 50 reads. Reverse and complementary were computed for sequences coming from Read1 primer. Data analysis and sequence alignment were performed using Bowtie2 (Langmead and Salzberg, 2012) in the End-to-End mode and Forward-Forward paired-ends. Sequences were piled up using SAMtools (Li et al., 2009) with no limited set to the number of sequences in the alignment. Counts in the different ORFs were performed with a standalone version of featureCounts program (Liao et al., 2014) without counting the multi-mapping reads and disabling multi-overlapping reads.

Counted features were then submitted to the R/Bioconductor package DESeq2 (Love et al., 2014) for statistical analysis. DESeq2 analysis used a parametric fitType and a zero-mean normal prior on the non-intercept coefficients. Data were sorted by log2 fold change, and statistical significance was set at the common threshold value of $p < 0.05$. Three independent biological repeats of each strain or condition were analyzed.

qRT-PCR

RNA was extracted from mid-log phase cultures of *M. genitalium* using the RNAqueous Kit (Thermo Fisher Scientific) and then treated with Turbo DNase (Thermo Fisher Scientific) following the manufacturer's instructions. Reverse transcription was performed with iScript Reverse Transcriptase (Bio-Rad) and random primers as previously described (Torres-Puig et al., 2015). Primers used for qPCR are listed in **Supplementary Table S2** and they were designed using Primer3 software. qPCR was performed with iTaq polymerase (Bio-Rad) and SYBR green in CFX96 or CFX384 PCR instruments (Bio-Rad). Relative gene expression was calculated using the Pfaffl method (Pfaffl, 2001). Differential gene expression was judged based on the common arbitrary 2-fold cutoff. Data presented in the manuscript correspond to the analysis of RNAs isolated from three independent biological repeats.

Quantification of Protein Abundance

Differences in relative protein abundance were assessed by stable isotope labeling by amino acids in cell culture (SILAC). To this end, *M. genitalium* cultures were grown to mid-log phase in 25 cm^2 flasks on Hayflick's medium with 15 mM of light (^{12}C) or heavy (^{13}C) lysine. Once grown, cells were split (1:10) and cultured in the same conditions. Then, cells were washed with PBS, scraped off, and pellets stored at −80°C. Protein lysates were prepared as previously described (Sabidó et al., 2012). Protein quantification was performed using the Pierce BCA Protein Assay Kit (Thermo Fisher Scientific), and protein extracts from heavy and light media cultures were mixed at a 1:1 ratio. Samples were then reduced with dithiothreitol (150 nmol, 1 h, 37°C) and alkylated in the dark with iodoacetamide (300 nmol, 30 min, 25°C). The resulting protein extract was diluted 1/3 with 200 mM NH_4HCO_3 and digested with 5 µg LysC (Wako)

overnight at 37°C. Finally, the peptide mix was acidified with formic acid and desalted with a homemade Empore C18 column (3 M, St. Paul, MN, United States; Rappsilber et al., 2007). Samples were analyzed using an LTQ-Orbitrap Velos Pro mass spectrometer (Thermo Fisher Scientific, San Jose, CA, United States) coupled to an EasyLC [Thermo Fisher Scientific (Proxeon), Odense, Denmark]. Peptides were loaded directly onto the analytical 25-cm column with an inner diameter of 75 µm and packed with 5-µm C18 particles (Nikkyo Technos Co. Ltd., Japan). Chromatographic gradients started at 97% buffer A and 3% buffer B, with a flow rate of 250 nl/min, and gradually increased to 65% buffer A/35% buffer B over 360 min. After each analysis, the column was washed for 10 min with 10% buffer A/90% buffer B. Buffer A: 0.1% formic acid in water. Buffer B: 0.1% formic acid in acetonitrile. The mass spectrometer was operated in positive ionization mode with a nanospray voltage set at 2.2 kV and source temperature at 250°C. Ultramark 1621 for the FT mass analyzer was used for external calibration prior to the analyses. Moreover, an internal calibration was also performed using the background polysiloxane ion signal at *m*/*z* 445.1200. The instrument was operated in data-dependent acquisition (DDA) mode and full MS scans with one micro scan at a resolution of 60,000 were used over a mass range of *m*/*z* 350–2,000 with detection in the Orbitrap. Auto gain control (AGC) was set to 10^6, and dynamic exclusion (60 s) and charge state filtering disqualifying singly charged peptides were carried out. In each cycle of DDA analysis, following each survey scan, the top 10 most intense ions with multiple charged ions above a threshold ion count of 5,000 were selected for fragmentation at normalized collision energy of 35%. Fragment ion spectra produced *via* collision-induced dissociation (CID) were acquired in the ion trap, AGC was set to $5e^4$, with an isolation window of 2.0 *m*/*z*, activation time of 0.1 ms, and maximum injection time of 100 ms. All data were acquired with Xcalibur software v2.2. The MaxQuant software suite (v1.4.0.5) was used for peptide identification and SILAC protein quantitation (Cox and Mann, 2008). The data were searched against an in-house generated database containing all *M. genitalium* proteins.

Scanning Electron Microscopy

Mycoplasma genitalium cultures were grown to mid-log phase over glass coverslips. Samples were fixed, dehydrated, and critical point dried as previously described (Pich et al., 2008). Coverslips were then sputter coated with gold and examined in a Merlin (Zeiss) scanning electron microscope (SEM). SEM micrographs were analyzed with the ImageJ software to determine the frequency of cells in division. To this end, we determined the number of terminal organelles (TMOs) per cell. As mycoplasma cells duplicate the tip structure during cell division, cells with one TMO were classified as non-dividing, while cells with two or more TMOs were classified as dividing. On the other hand, we measured the length of single cells from the tip of the TMO to the opposite pole. In addition, we determined the length of cytokinetic cells by measuring the distance from the tip of one TMO to the tip of the opposite TMO. For this analysis, only cells with one TMO at each cell pole were considered.

Phase Contrast and Fluorescence Microscopy

Mycoplasma genitalium cells were grown in filtered SP-4 medium (0.22 µm) on IBIDI chamber slides for 16 h, washed once with 1 × PBS, and visualized on an inverted Nikon Eclipse TE 2000-E microscope. For the analysis of the mg191ftsZCh non-adherent mutant, IBIDI chamber slides were previously treated with 0.2 mg/ml poly-L-lysine hydrobromide (Sigma-Aldrich) solution, allowing surface adherence. In addition, cells were passed 10 times through a 25-gauge syringe to break the aggregates. Hoechst 33342 0.01 mg ml^{-1} was added when necessary. All strains were grown and visualized under the same conditions. Phase contrast, enhanced yellow fluorescent protein (eYFP), 4',6-diamidino-2-phenylindole (DAPI), and TRITC epifluorescence images were captured with a Digital Sight DS-SMC Nikon camera controlled by NIS-Elements BR software. Images were analyzed using ImageJ software and GDSC plug-in.

RESULTS

Deletion of the Entire Cell Division Gene Cluster of *Mycoplasma genitalium*

Previously, we demonstrated that the *ftsZ* gene was non-essential in *M. genitalium* (Lluch-Senar et al., 2010). Based on this finding, we speculated whether the entire cell division gene cluster could be dispensable in this wall-less bacterium. To ascertain this, we replaced the four genes of the cell division gene cluster of *M. genitalium* by the chloramphenicol resistance marker (**Figure 1B**). We recovered several chloramphenicol resistant transformants and confirmed the deletion of the entire gene cluster (3.7 kb) by PCR and sequencing. We found that the duplication time of the resulting *dcw* mutant was significantly longer (10.13 ± 0.33 h) than that of the wild-type strain (8.38 ± 0.28 h; **Figure 2A**). In addition, SEM analyses revealed an increased frequency of cells in division in the *dcw* mutant (30.53%) as compared to the wild-type strain (13.35%; **Figure 2B**).

Characterization of Cell Division Mutants of *Mycoplasma genitalium*

To dissect and better understand the phenotype of the *dcw* mutant, we created strains defective for each gene of the cell division gene cluster by allelic exchange. First, we obtained mutants for the MG_223 and *ftsZ* genes using the chloramphenicol resistance marker for selection (**Figure 1B**; **Supplementary Material**). Our analyses revealed that the growth rate of the *ftsZ* mutant (8.29 ± 0.09 h) was comparable to that of the wild-type strain (8.38 ± 0.28 h; **Figure 2A**). By contrast, the duplication time of the MG_223 mutant increased significantly (9.80 ± 0.56 h). SEM analyses revealed an increased frequency of cells in division in both mutant strains (*ftsZ*, 22.44%; MG_223, 29.15%; **Figure 2B**).

Next, we created mutants lacking either *mraZ* or *mraW*. In this case, to preserve the operonic structure of the gene cluster, the antibiotic resistance marker was placed at the 5' end of the

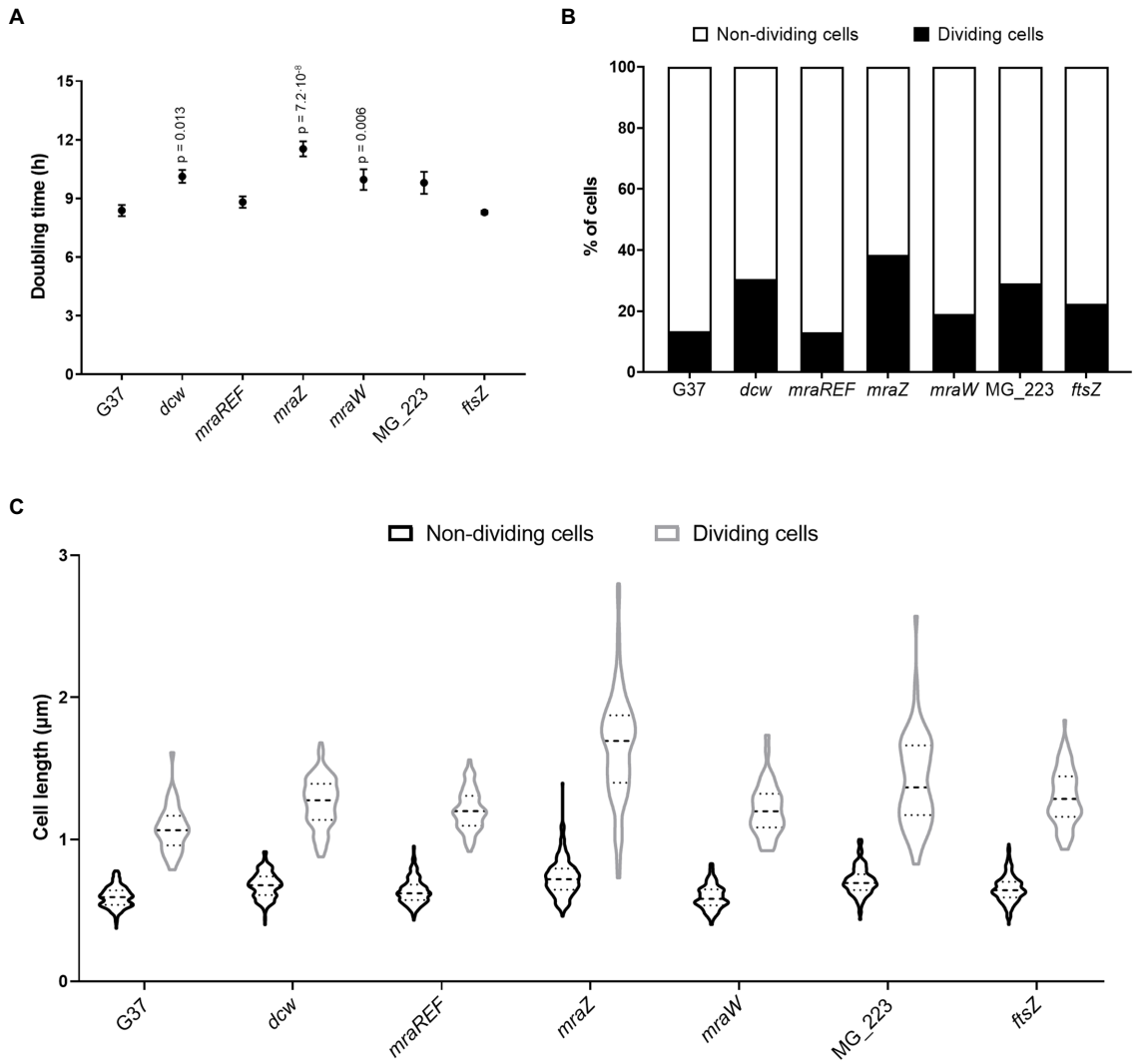

FIGURE 2 | Cell fitness analysis of the wild-type strain and several *M. genitalium* mutants. Growth rates **(A)** and percentage of cells in division **(B)** of different *M. genitalium* mutants of the cell division gene cluster. Statistical significance was assessed using the Student's *t*-test and the value of *p* of significant values ($p < 0.05$) is indicated above each data point. An average of 900 cells for each strain were analyzed **(C)**. Graph depicting the length of single or cytokinetic cells. An average of 320 cells for each strain were measured.

mraZ UTR (**Figure 1B**; **Supplementary Material**). For control purposes, we also created a reference strain, designated *mraREF*, carrying the selectable marker in the same chromosomal location, but with an intact cell division gene cluster (**Figure 1B**; **Supplementary Material**). Cells from the *mraREF* strain grew at a similar rate (8.81 ± 0.29 h) than those of the wild-type strain (8.38 ± 0.28 h; **Figure 2A**). However, the duplication time increased significantly upon the loss of MraZ (11.54 ± 0.38 h). Cells from the *mraW* null mutant duplicated at a slower rate (9.96 ± 0.53 h), indicating that the absence of MraW is also detrimental for growth. All the mutant strains obtained were examined by genome resequencing for the presence of mutations other than those introduced by genetic manipulation. No major genome rearrangements like large deletions or translocations were detected in all the analyzed strains. However, all the strains showed the presence of small variants like SNPs or INDELS in different frequencies. Many of these variants were also identified in the G37 strain. All new variants were found in recombinogenic, variable repeated regions, being most of them in non-coding genome locations, thus supporting the absence of additional mutations that could impact on the phenotype of the *dcw* strains (**Supplementary Material**).

Scanning electron microscopy analyses revealed a slight increase in the frequency of cells in division in the *mraW* mutant (19.0%) when compared to the wild-type (13.35%) or the *mraREF* strains (12.99%; **Figure 2B**). Remarkably, the frequency of dividing cells found in the *mraZ* mutant was markedly high (38.44%). Moreover, we observed that cytokinetic cells from the *mraZ* mutant were markedly elongated (**Figures 3A,B**). Quantitative analysis confirmed that cells in

cytokinesis from the *mraZ* mutant were longer (1.651 ± 0.372 μm, $n = 96$) than those of the wild-type strain (1.118 ± 0.177 μm, $n = 24$; **Figure 2C**). By contrast, analyses of the other cell division mutants obtained in this study did not reveal morphological changes in the cytokinetic cells (**Figure 2C**).

Transcriptional Analysis of the Cell Division Gene Cluster in Different Mutant Backgrounds

Previous studies in *E. coli* indicated that MraZ is a transcriptional repressor (Eraso et al., 2014). Therefore, we conducted a genome-wide transcriptional analysis in *M. genitalium* by RNA-Seq to identify transcriptional changes in the *mraZ* mutant (**Table 1**). Our transcriptomic data revealed that *mraW*, *ftsZ*, and the MG_223 gene were significantly upregulated in the absence of MraZ. By contrast, the transcription was largely unaffected in both the *mraW* mutant and the *mraREF* control strain. qRT-PCR analyses confirmed the increased expression of the cell division genes in the absence of MraZ (**Figure 4**). To confirm that the altered gene expression observed in the *mraZ* mutant was due to the loss of the MraZ protein, we reintroduced an ectopic copy of the *mraZ* gene under the control of its native promoter. Of note, several complementation attempts with a transposon encoded copy of the *mraZ* gene, alone or in combination with *mraW*, were unsuccessful. However, insertion of the *mraZ* gene at the end of the cell division gene cluster in the *mraZ* mutant restored the transcriptional levels of *mraW*, *ftsZ*, and the MG_223 gene (**Figure 4**; **Supplementary Figure S1**). On the other hand, we also assessed transcription of the cell division gene cluster in a mutant strain lacking the *mg191* gene, which codes for the major cytoadhesin P140 of *M. genitalium*. Cells from the *mg191* mutant are pleomorphic and grow in suspension as large cell aggregates (Burgos et al., 2006). This non-adherent mutant was analyzed to shed some light on the connection between cell division and adherence in *M. genitalium*. In this sense, in a previous study (Lluch-Senar et al., 2010), we showed that, in contrast to WT cells, an *ftsZ* mutant could not generate non-adherent variants. Based on this observation, we hypothesized that non-adherent mutants rely exclusively on the cell division cluster for division. Remarkably, transcriptional analysis of the *mg191* mutant revealed a significant upregulation of the cell division gene cluster (**Figure 4**).

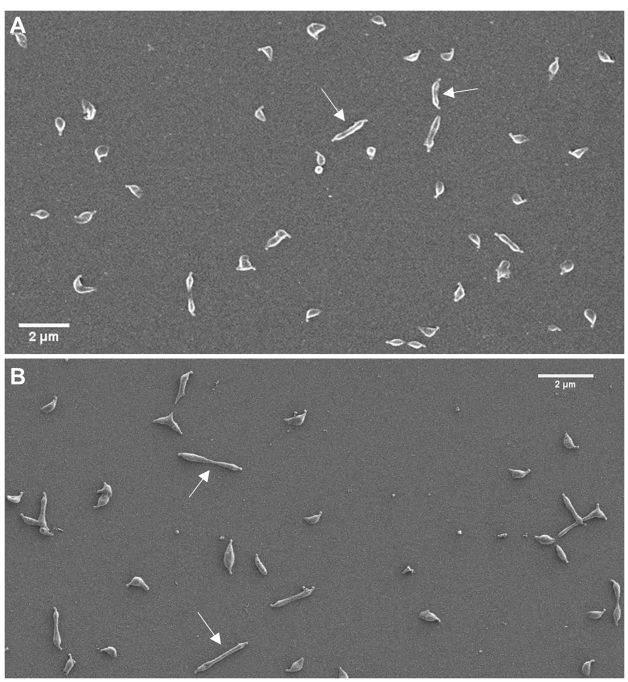

FIGURE 3 | Characterization of cell morphology of the *mraZ* mutant. Scanning electron micrographs of the wild-type strain **(A)** and the *mraZ* mutant **(B)**. White arrows indicate some cells in cytokinesis.

Proteome Analysis of the *mraZ* and *mraW* Mutants

Next, we wondered whether the transcriptional changes observed in the *mraZ* null mutant were conserved at the protein level. To this end, we determined the proteome profile of the *mraZ* mutant by SILAC (**Supplementary Tables S4** and **S5**). Our analyses demonstrated a marked increase in the cellular levels of MraW (14.3-fold) and FtsZ (25-fold; **Table 2**). Along the same lines, expression of the MG_223 protein could only be detected when MraZ was absent.

We also investigated the presence of proteomic changes in the *mraW* mutant (**Supplementary Tables S6** and **S7**). We found that several proteins, including a number of DNA and RNA methyltransferases, were differentially expressed in the absence of MraW. As these changes in protein abundance were not accompanied by changes in mRNA levels, we anticipate that MraW may modulate protein expression at the post-transcriptional level. Of note, we found that the levels of the FtsZ protein were slightly higher (by 2-fold) in the *mraW* mutant (**Table 2**).

FtsZ Expression and Localization Dynamics

Previous attempts in our laboratory to monitor FtsZ expression in *M. genitalium* using fluorescent markers were unsuccessful. In these studies, we characterized mutant strains carrying an

TABLE 1 | Transcriptional changes in the *mraZ* and *mraW* mutants by RNA-Seq.

Gene	*mraZ*		*mraW*	
	Log2 fold change	*p*	Log2 fold change	*p*
mraZ	**−4.64**	**0**	0.10	0.24
mraW	**3.02**	**0**	**−3.84**	**0**
MG_223	**2.08**	**2×10^{-139}**	−0.21	0.02
ftsZ	**2.34**	**9.3×10^{-218}**	−0.21	0.03

Transcriptional changes in the cell division gene cluster identified by RNA-Seq in the mraZ and mraW mutants. Changes that are statistically significant (value of $p < 0.05$) and biologically relevant (above or below the log2 ± 1 arbitrary cutoff) are highlighted in bold. Data were obtained from the analysis of three independent biological repeats of each mutant.

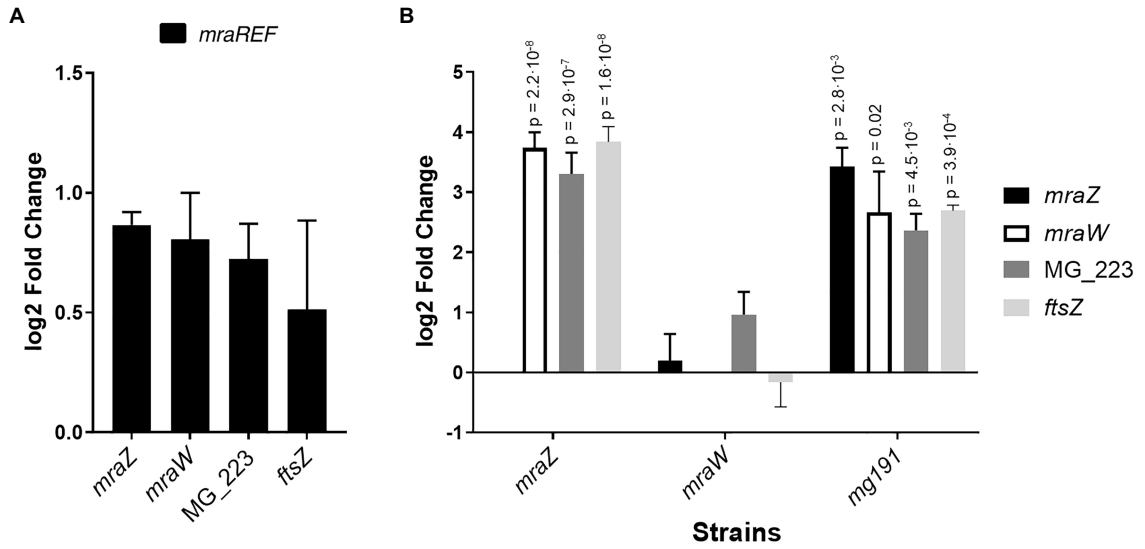

FIGURE 4 | Transcriptional analysis of the cell division gene cluster of several *M. genitalium* mutants by qRT-PCR. Transcriptional changes of the cell division gene cluster in the *mraREF* mutant **(A)** or the *mraZ*, *mraW*, and *mg191* mutants **(B)** compared to the wild-type strain. Bars represent the average log2 fold change of at least three independent biological repeats. Statistical significance was assessed using the Student's *t*-test, and the value of *p* of biologically significant values (log2 ± 1) is stated above the corresponding bar if significant (value of $p < 0.05$).

TABLE 2 | Comparative analysis of the abundance of cell division proteins in the wild-type strain and the *mraZ* and *mraW* mutants by stable isotope labeling by amino acids in cell culture (SILAC).

Locus tag	Gene	Gene product	G37	mraZ		mraW	
			AUC	AUC	FC	AUC	FC
MG_221	*mraZ*	Transcriptional regulator MraZ	4.12×10^8	ND	–	4.65×10^8	–
MG_222	*mraW*	Ribosomal RNA small subunit methyltransferase H	4.17×10^7	5.95×10^8	**14.28**	ND	–
MG_223	–	Uncharacterized protein	ND	7.88×10^6	–	ND	–
MG_224	*ftsZ*	Cell division protein	4.40×10^6	1.10×10^8	**24.96**	8.50×10^6	1.93

Area under the curve (AUC) of the four proteins encoded in the cell division gene cluster in the wild-type (G37) and the mraZ and mraW mutants. Fold-change (FC) with respect to the G37 strain is indicated. Biologically significant fold changes (>2 and <0.5) are highlighted in bold. ND stands for not detected.

ftsZ-mcherry fusion at its native locus, that is, at the 3' end of the cell division gene cluster (**Figure 5**). Presumably, FtsZ expression was too low to allow detection of the fluorescent fusion in single cells. However, we hypothesized that the increased levels of FtsZ expression observed in the *mraZ* mutant could facilitate the visualization of this protein in live cells. Therefore, we assessed FtsZ-mCherry expression in MraZ-deprived cells (**Supplementary Material**) and found a large number (56.63%) of fluorescent cells, although at different extents (**Figure 5**). The presence of non-fluorescent cells suggests that the expression and assembly of FtsZ are under the control of other factors in addition to MraZ (Burgos et al., 2020). Separately, we assessed FtsZ expression in the absence of MraW and observed that a small subset of cells (1.58%) exhibited mCherry fluorescence (**Figure 5**). This result is in keeping with the increased amount of FtsZ identified in the *mraW* mutant by proteomics analysis. On the other hand, we tested whether the FtsZ-mCherry fusion was visible in the P140 adhesin mutant. In agreement with the transcriptional data, we observed that some cells exhibited a conspicuous FtsZ-associated fluorescence (**Figure 5**).

A detailed analysis of the *mraZ* mutant revealed that FtsZ foci displayed a polar location. Of note, *M. genitalium* cells are polar because they exhibit a TMO instrumental for cytoadherence. For this reason, we wanted to test whether FtsZ foci co-localized with the TMO of this bacterium. To this end, we tagged P65, a protein that localizes at the distal end of the TMO (Burgos et al., 2008). Introduction of an eYFP fluorescent marker at the P65 native locus (MG_217) allowed the identification of sharp P65-eYFP foci, providing a way to unambiguously identify the cell pole containing the TMO (**Figure 6**). We found that FtsZ clustered at the cell pole opposite to P65 in cells showing a single P65 focus. This is important because as mycoplasma cells duplicate the TMO prior to cytokinesis (Miyata and Seto, 1999), some cells displayed two separate P65 foci. In addition, we observed that the intensity and localization of the FtsZ foci varied through the cell division cycle. Based on the localization of the two tagged proteins

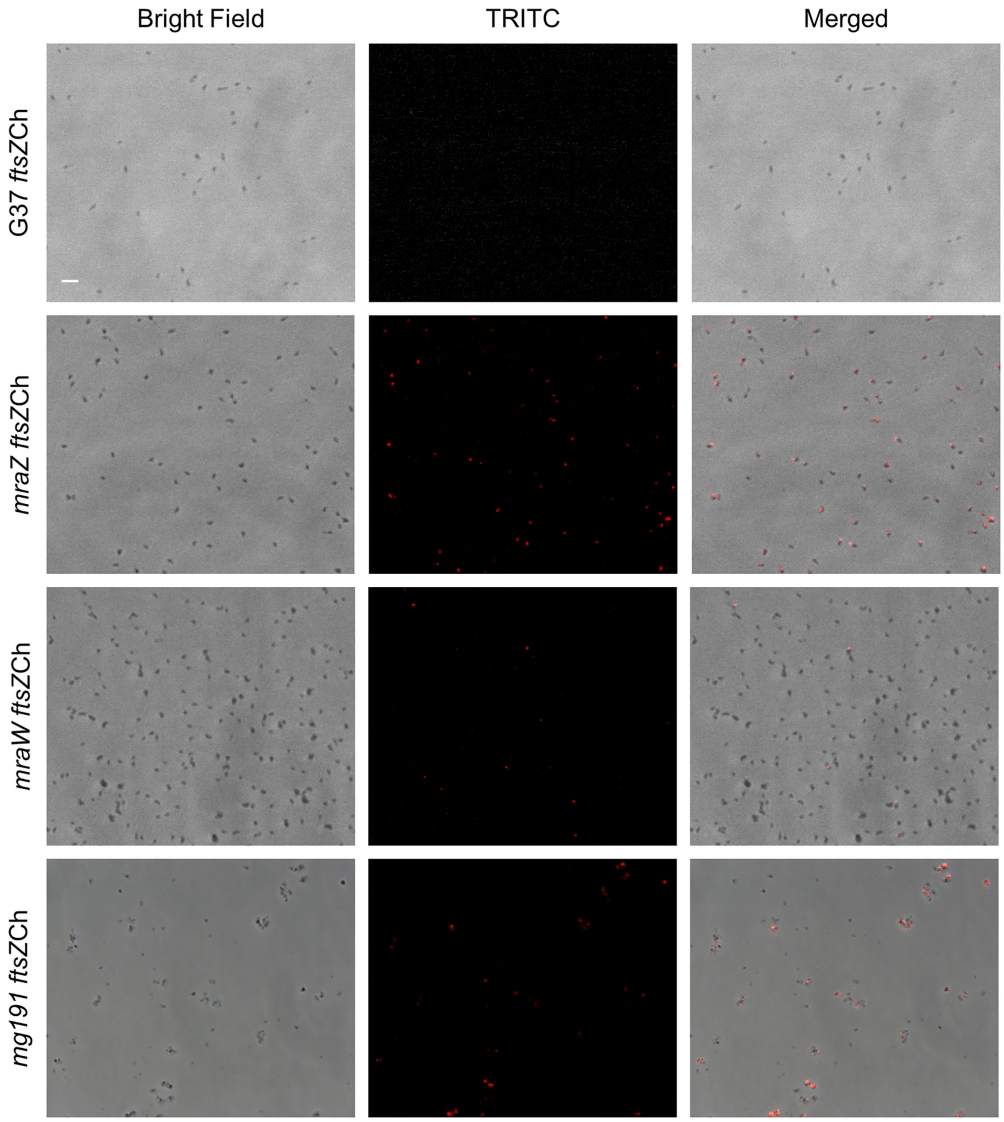

FIGURE 5 | Single cell analysis of FtsZ expression in different *M. genitalium* mutants. Fluorescence microscopy images showing FtsZ-mCherry localization in live cells from the wild-type strain, *mraZ*, *mraW*, and *mg191* mutants. Each row contains the phase contrast, TRITC channel, and the resulting overlay, respectively. The scale bar represents 2 μm. All images are shown at the same magnification.

(FtsZ and P65) and the chromosome stained with Hoechst 33258, we recognized eight different stages throughout the cell cycle (**Figure 7**). Non-dividing cells (stage 1) exhibit a single P65 focus and FtsZ signal is weak. In time, FtsZ is recruited at the cell pole opposite to the TMO (stage 2). Prior to cytokinesis, a new P65 focus forms close to the pre-existent focus (stage 3). Then, one of these P65 foci migrates to the opposite cell pole and localizes near the FtsZ focus (stage 4). Next, likely coinciding with chromosome segregation, FtsZ leaves the polar location and moves to the midcell to form a diffuse band (stage 5). As cytokinesis proceeds, FtsZ signal decreases (stage 6) and daughter cells display small FtsZ foci with marginal fluorescence (stage 7). Finally, daughter cells separate and FtsZ signal disappears (stage 8), but soon after, FtsZ accumulation starts within the cell body (stage 1).

DISCUSSION

Mycoplasmas are wall-less bacteria that divide by binary fission. So far, the factors mediating and coordinating cell division in these genome-reduced bacteria are poorly understood. Typically, the cell division gene cluster of mycoplasmas comprises four genes, including *ftsZ*. In walled bacteria, it is well-established that FtsZ drives peptidoglycan synthesis at the division site (Bisson-Filho et al., 2017). However, the conservation in mycoplasmas of FtsZ and other cell division related proteins, such as MraZ or MraW, is puzzling. In this study, we constructed and characterized several cell division mutants of *M. genitalium*. We found that deletion of *mraZ* induces a strong activation of the other genes of the cell division gene cluster. Hence, our results indicate that MraZ functions as a transcriptional repressor.

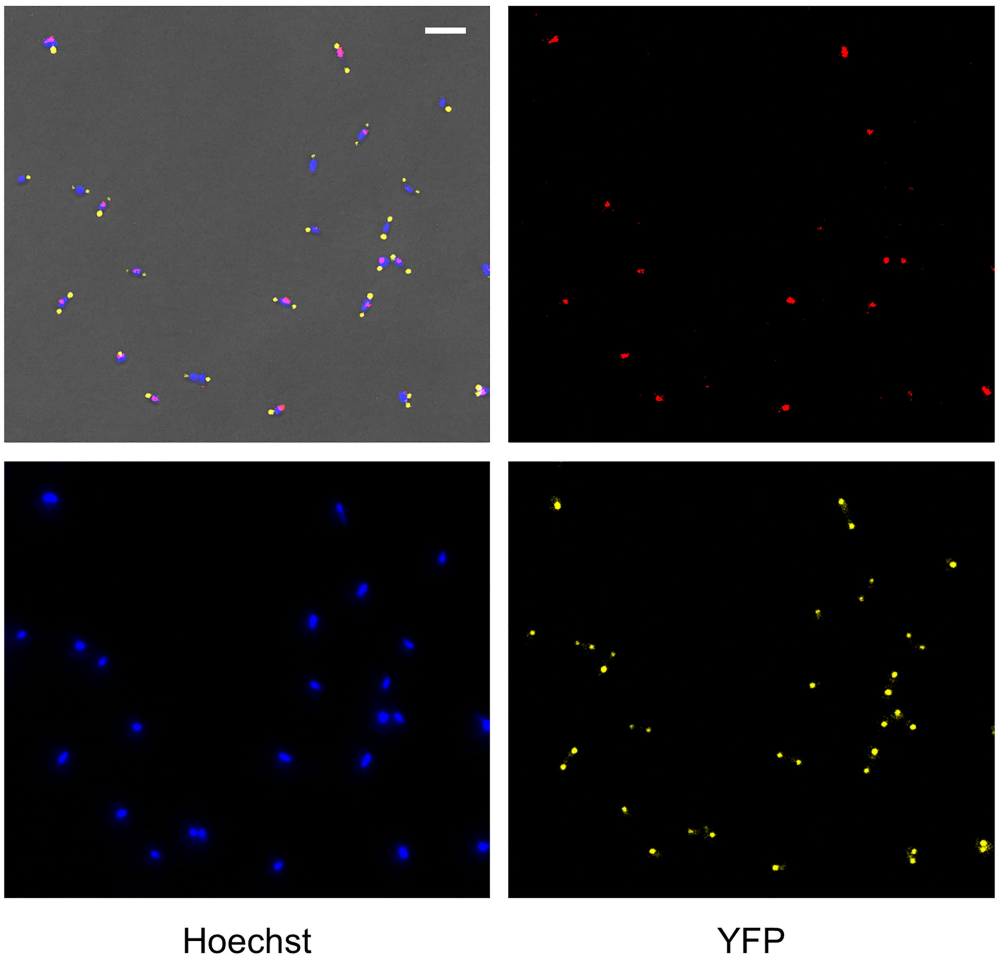

FIGURE 6 | Single cell analysis of FtsZ, P65, and chromosome localization in the *mraZ* mutant. Fluorescence microscopy analysis showing FtsZ-mCherry, P65-eYFP, and chromosome localization in live cells of *M. genitalium*. Each panel shows the TRITC, 4',6-diamidino-2-phenylindole (DAPI), and eYFP images or a combination of the three channels and the phase contrast. The scale bar represents 2 μm. All images are shown at the same magnification.

This finding correlates well with proteomics data showing that MraW, FtsZ, and MG_223 proteins are overexpressed in the absence of MraZ. Altogether, our results substantiate the repressor role of MraZ previously documented by Eraso et al. (2014). Unlike in *E. coli*, MraZ depletion in *M. genitalium* results in a clear phenotype. The *mraZ* mutant exhibits a significant growth delay, important morphological alterations, and a high frequency of cells stuck in cytokinesis. These data indicate that expression of the cell division proteins of *M. genitalium* at relative high levels throughout the cell cycle is largely detrimental.

A previous study in *Mycoplasma gallisepticum* revealed that MraZ overexpression induces a characteristic cell filamentation (Fisunov et al., 2016), which is reminiscent to the phenotype described in the *mraZ* mutant of *M. genitalium*. Moreover, the filamentation described in *M. gallisepticum* was also associated with increased levels of FtsZ. In the same study, the authors define a binding site for MraZ in Mollicutes, characterized by a series of direct repeats of the sequence AAAGTG[T/G]. The only occurrence of this motif in the chromosome of *M. genitalium* lays within the promoter region of the *mraZ* gene. This finding is consistent with the lack of transcriptional changes outside the cell division gene cluster in our *mraZ* mutant. Of note, complementation of the *mraZ* mutant of *M. genitalium* could only be achieved in *cis*, that is, reintroducing a copy of the *mraZ* gene at an ectopic site within the cell division gene cluster. This result reveals a complex interplay between the relative location of the *mraZ* gene in the chromosome and MraZ activity. In this sense, our results indicate that the repressor role of MraZ requires a transcriptional linkage between the *mraZ* gene, the MraZ operator, and the cell division gene cluster.

On the other hand, we found that cultures of the *mraW* mutant grew at a slower rate than those of the wild-type strain. More importantly, we could detect FtsZ-mCherry fluorescence in a small subset of cells from this mutant. This fact is relevant because we could not detect FtsZ-mCherry expression in the wild-type background. Thus, MraW may

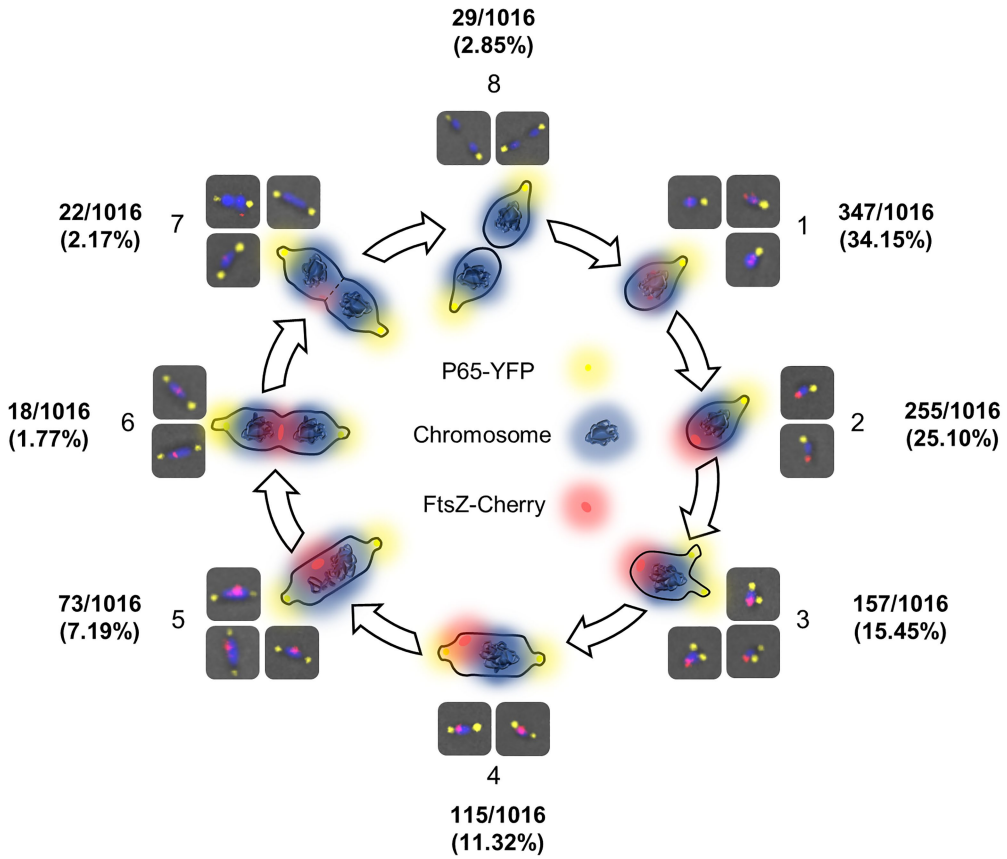

FIGURE 7 | FtsZ localization dynamics throughout the cell cycle of *M. genitalium*. Scheme depicting different stages of the *M. genitalium* cell cycle based on the localization of FtsZ foci relative to the terminal organelle (TMO) and the chromosome. In this model, FtsZ accumulates at the cell body (1) and clusters at the cell pole opposite to the TMO (2). Then, the TMO duplicates (3) and one TMO moves to the opposite cell pole (4). Next, FtsZ foci move to the midcell (5). Finally, cytokinesis starts (6) and the FtsZ signal decreases (7) until the process is completed (8).

play a role in regulating FtsZ expression in *M. genitalium*. This regulation must take place at the post-transcriptional level, as no transcriptional changes could be detected in the *mraW* mutant. In agreement with these data, our proteomics analysis revealed a slight increase of FtsZ levels in the absence of MraW. Of note, FtsZ expression in the *mraW* mutant is expected to be low because of the repressor activity of MraZ. The differential expression of several methyltransferases in the *mraW* mutant was also noticeable, which may represent a response of *M. genitalium* to the loss of the methyltransferase activity of MraW. The existence of species with orphan *mraW* genes supports a role for MraW independent from MraZ function in the regulation of cell division. It has been reported that MraW methylates the C1402 residue of the 16S rRNA (Kimura and Suzuki, 2010). This residue is involved in translation initiation and its mutation in *E. coli* leads to an increased doubling time (Jemiolo et al., 1985). Moreover, the loss of MraW function has been directly related to an altered translation fidelity (Kyuma et al., 2015), DNA methylation, and regulation of gene expression (Xu et al., 2019). Our RNA-Seq data from the *mraW* mutant suggest that MraW does not regulate gene expression in *M. genitalium*. However, whether MraW has a role in DNA or rRNA methylation in this bacterium still needs to be fully addressed.

The increased levels of FtsZ expression in the *mraZ* mutant allowed us to visualize this protein in single cells and to determine the FtsZ dynamics throughout the cell cycle of *M. genitalium*. We found that FtsZ clusters at the cell pole opposite to the TMO. When TMOs duplicate and migrate to the opposite cell pole, FtsZ-associated foci move toward the midcell. Intensity of the FtsZ foci decreases when they arrive at the midcell and the two chromosomes start to segregate. This pattern strongly suggests that FtsZ might play an active role in cell division and facilitates cytokinesis in *M. genitalium*. In addition, the localization of FtsZ protein during the cell cycle seems to be tightly regulated. Although the presence of a Min system (Lutkenhaus, 2007; Rowlett and Margolin, 2015) has not been described in mycoplasmas, it is presumed that unidentified regulatory factors inhibit the formation of a Z-ring close to the TMO. Interestingly, *M. genitalium* codes for a DivIVA domain-containing protein (MG211), a key component of the Min system of *B. subtilis* (Edwards and Errington, 1997). In addition, we observed that FtsZ foci were sometimes located between two DNA foci, suggesting that nucleoid occlusion is also in place in *M. genitalium*.

Altogether, the distinct localization of the FtsZ protein throughout the cell cycle suggests the existence of unknown factors regulating cell division in this genome-reduced bacterium. These underlying regulatory mechanisms coordinate the cytokinesis process with chromosome segregation (Seto and Miyata, 1999).

The results of our study indicate that the cell division gene cluster of *M. genitalium* plays a minor role during *in vitro* propagation of wild-type cells. This is consistent with previous reports showing that motility seems to be the primary force facilitating cytokinesis in *M. pneumoniae*, a close relative species (Hasselbring et al., 2006). A few years ago, we documented that deletion of the *ftsZ* gene abrogated the occurrence of non-adherent phase variants in *M. genitalium* (Lluch-Senar et al., 2010). These non-adherent variants arise at relatively high frequencies and may play an important role to evade the immune response during infection (Burgos et al., 2018). Based on this observation, we proposed that FtsZ could be important for cell division in non-adherent cells of *M. genitalium*. Of note, non-adherent derivatives of *M. genitalium* are non-motile, largely pleomorphic and grow as large cell aggregates (Burgos et al., 2006). In the current study, we provide evidence that the cell division gene cluster is upregulated in a non-adherent mutant of *M. genitalium*. This finding is in agreement with our previous hypothesis that FtsZ and the formation of a rudimentary divisome may be required when gliding motility is unfeasible. Therefore, the strict parasitic lifestyle of *M. genitalium* and the intricate strategy to escape immune surveillance, likely imposes the conservation of the cell division gene cluster in this wall-less bacterium. Remarkably, most *Mycoplasma* species are non-motile, which may also enforce the conservation of the cell division genes. Supporting this notion, a recent report has demonstrated that *ftsZ* is important to restore cell morphology and proficiency of cell division in synthetic minimal cells (Pelletier et al., 2021).

DATA AVAILABILITY STATEMENT

The original contributions presented in the study are publicly available. This data can be found here: National Center for Biotechnology Information (NCBI) BioProject database under accession number PRJNA750275.

AUTHOR CONTRIBUTIONS

CM-T, ST-P, ML-S, LS, EQ, JP, and OQP contributed to conception and design of the study. CM-T, ST-P, MM-S, MH-R, CM-N, ML-S, and OQP performed the experiments. CM-T and ST-P performed the statistical analysis. CM-T and OQP wrote the first draft of the manuscript. ST-P, EQ, and JP wrote some parts of the manuscript. All authors contributed to the article and approved the submitted version.

FUNDING

This work was supported by the grant BIO2017-84166-R from the Ministerio de Ciencia, Innovación y Universidades.

ACKNOWLEDGMENTS

We are grateful to the staff of the Servei de Genòmica i Bioinformàtica (UAB), the Genomics Unit (CRG) and the Proteomics Unit (CRG), for performing Sanger sequencing, RNA-Seq and SILAC analyses, respectively. In addition, we are thankful to the thesis committee of CM-T and the two reviewers of this manuscript for their helpful comments and constructive discussion. Finally, CM-T and MM-S want to acknowledge a PIF fellowship from the UAB and a FI predoctoral fellowship from the Generalitat de Catalunya, respectively.

SUPPLEMENTARY MATERIAL

The Supplementary Material for this article can be found online at: https://www.frontiersin.org/articles/10.3389/fmicb.2021.695572/full#supplementary-material

REFERENCES

Adams, D., and Errington, J. (2009). Bacterial cell division: assembly, maintenance and disassembly of the Z ring. *Nat. Rev. Microbiol.* 7, 642–653. doi: 10.1038/nrmicro2198

Alarcón, F., de Vasconcelos, A. T. R., Yim, L., and Zaha, A. (2007). Genes involved in cell division in mycoplasmas. *Genet. Mol. Biol.* 30, 174–181. doi: 10.1590/S1415-47572007000200003

Beall, B., and Lutkenhaus, J. (1991). FtsZ in *Bacillus subtilis* is required for vegetative septation and for asymmetric septation during sporulation. *Genes Dev.* 5, 447–455. doi: 10.1101/gad.5.3.447

Benders, G. A., Powell, B. C., and Hutchison, C. A. (2005). Transcriptional analysis of the conserved ftsZ gene cluster in *Mycoplasma genitalium* and *Mycoplasma pneumoniae*. *J. Bacteriol.* 187, 4542–4551. doi: 10.1128/JB.187.13.4542-4551.2005

Bisson-Filho, A. W., Hsu, Y. P., Squyres, G. R., Kuru, E., Wu, F., Jukes, C., et al. (2017). Treadmilling by FtsZ filaments drives peptidoglycan synthesis and bacterial cell division. *Science* 355, 739–743. doi: 10.1126/science.aak9973

Burgos, R., Pich, O. Q., Ferrer-Navarro, M., Baseman, J. B., Querol, E., and Piñol, J. (2006). *Mycoplasma genitalium* P140 and P110 cytadhesins are reciprocally stabilized and required for cell adhesion and terminal-organelle development. *J. Bacteriol.* 188, 8627–8637. doi: 10.1128/JB.00978-06

Burgos, R., Pich, O. Q., Querol, E., and Piñol, J. (2008). Deletion of the *Mycoplasma genitalium* MG_217 gene modifies cell gliding behaviour by altering terminal organelle curvature. *Mol. Microbiol.* 69, 1029–1040. doi: 10.1111/j.1365-2958.2008.06343.x

Burgos, R., Weber, M., Martinez, S., Lluch-Senar, M., and Serrano, L. (2020). Protein quality control and regulated proteolysis in the genome-reduced organism *Mycoplasma pneumoniae*. *Mol. Syst. Biol.* 16:e9530. doi: 10.15252/msb.20209530

Burgos, R., Wood, G. E., Iverson-Cabral, S. L., and Totten, P. A. (2018). *Mycoplasma genitalium* nonadherent phase variants arise by multiple mechanisms and escape antibody-dependent growth inhibition. *Infect. Immun.* 86:e00866-17. doi: 10.1128/IAI.00866-17

Busiek, K. K., and Margolin, W. (2015). Bacterial actin and tubulin homologs in cell growth and division. *Curr. Biol.* 25, R243–R254. doi: 10.1016/j.cub.2015.01.030

Cox, J., and Mann, M. (2008). MaxQuant enables high peptide identification rates, individualized p.p.b.-range mass accuracies and proteome-wide protein quantification. *Nat. Biotechnol.* 26, 1367–1372. doi: 10.1038/nbt.1511

Dai, K., and Lutkenhaus, J. (1991). ftsZ is an essential cell division gene in *Escherichia coli*. *J. Bacteriol.* 173, 3500–3506. doi: 10.1128/jb.173.11.3500-3506.1991

Dai, K., and Lutkenhaus, J. (1992). The proper ratio of FtsZ to FtsA is required for cell division to occur in *Escherichia coli*. *J. Bacteriol.* 174, 6145–6151. doi: 10.1128/jb.174.19.6145-6151.1992

Dewar, S. J., Begg, K. J., and Donachie, W. D. (1992). Inhibition of cell division initiation by an imbalance in the ratio of FtsA to FtsZ. *J. Bacteriol.* 174, 6314–6316. doi: 10.1128/jb.174.19.6314-6316.1992

Edwards, D. H., and Errington, J. (1997). The *Bacillus subtilis* DivIVA protein targets to the division septum and controls the site specificity of cell division. *Mol. Microbiol.* 24, 905–915. doi: 10.1046/j.1365-2958.1997.3811764.x

Eraso, J. M., Markillie, L. M., Mitchell, H. D., Taylor, R. C., Orr, G., and Margolin, W. (2014). The highly conserved MraZ protein is a transcriptional regulator in *Escherichia coli*. *J. Bacteriol.* 196, 2053–2066. doi: 10.1128/JB.01370-13

Errington, J., Daniel, R. A., and Scheffers, D.-J. (2003). Cytokinesis in bacteria. *Microbiol. Mol. Biol. Rev.* 67, 52–65. doi: 10.1128/MMBR.67.1.52-65.2003

Fisunov, G. Y., Evsyutina, D. V., Semashko, T. A., Arzamasov, A. A., Manuvera, V. A., Letarov, A. V., et al. (2016). Binding site of MraZ transcription factor in mollicutes. *Biochimie* 125, 59–65. doi: 10.1016/j.biochi.2016.02.016

Glass, J., Lefkowitz, E., Glass, J., Heiner, C. R., Chen, E. Y., and Cassell, G. H. (2000). The complete sequence of the mucosal pathogen *Ureaplasma urealyticum*. *Nature* 407, 757–762. doi: 10.1038/35037619

Hasselbring, B. M., Jordan, J. L., Krause, R. W., and Krause, D. C. (2006). Terminal organelle development in the cell wall-less bacterium *Mycoplasma pneumoniae*. *Proc. Natl. Acad. Sci. U. S. A.* 103, 16478–16483. doi: 10.1073/pnas.0608051103

Jaffe, J. D., Stange-Thomann, N., Smith, C., DeCaprio, D., Fisher, S., Butler, J., et al. (2004). The complete genome and proteome of *Mycoplasma* mobile. *Genome Res.* 14, 1447–1461. doi: 10.1101/gr.2674004

Jemiolo, D. K., Zwieb, C., and Dahlberg, A. E. (1985). Point mutations in the 3' minor domain of 16S rRNA of *E. coli*. *Nucleic Acids Res.* 13, 8631–8643. doi: 10.1093/nar/13.23.8631

Karr, J. R., Sanghvi, J. C., MacKlin, D. N., Gutschow, M. V., Jacobs, J. M., Bolival, B., et al. (2012). A whole-cell computational model predicts phenotype from genotype. *Cell* 150, 389–401. doi: 10.1016/j.cell.2012.05.044

Kimura, S., and Suzuki, T. (2010). Fine-tuning of the ribosomal decoding center by conserved methyl-modifications in the *Escherichia coli* 16S rRNA. *Nucleic Acids Res.* 38, 1341–1352. doi: 10.1093/nar/gkp1073

Kyuma, T., Kimura, S., Hanada, Y., Suzuki, T., Sekimizu, K., and Kaito, C. (2015). Ribosomal RNA methyltransferases contribute to *Staphylococcus aureus* virulence. *FEBS J.* 282, 2570–2584. doi: 10.1111/febs.13302

Langmead, B., and Salzberg, S. (2012). Fast gapped-read alignment with bowtie 2. *Nat. Methods* 9, 357–359. doi: 10.1038/nmeth.1923

Li, H., Handsaker, B., Wysoker, A., Fennell, T., Ruan, J., Homer, N., et al. (2009). The sequence alignment/map format and SAMtools. *Bioinformatics* 25, 2078–2079. doi: 10.1093/bioinformatics/btp352

Liao, Y., Smyth, G. K., and Shi, W. (2014). featureCounts: an efficient general purpose program for assigning sequence reads to genomic features. *Bioinformatics* 30, 923–930. doi: 10.1093/bioinformatics/btt656

Lluch-Senar, M., Querol, E., and Piñol, J. (2010). Cell division in a minimal bacterium in the absence of ftsZ. *Mol. Microbiol.* 78, 278–289. doi: 10.1111/j.1365-2958.2010.07306.x

Love, M. I., Huber, W., and Anders, S. (2014). Moderated estimation of fold change and dispersion for RNA-seq data with DESeq2. *Genome Biol.* 15:550. doi: 10.1186/s13059-014-0550-8

Lutkenhaus, J. (2007). Assembly dynamics of the bacterial MinCDE system and spatial regulation of the Z ring. *Annu. Rev. Biochem.* 76, 539–562. doi: 10.1146/annurev.biochem.75.103004.142652

Martínez-Torró, C., Torres-Puig, S., Monge, M., Sánchez-Alba, L., González-Martín, M., Marcos-Silva, M., et al. (2020). Transcriptional response to metal starvation in the emerging pathogen *Mycoplasma genitalium* is mediated by fur-dependent and – independent regulatory pathways. *Emerg. Microbes Infect.* 9, 5–19. doi: 10.1080/22221751.2019.1700762

Mercier, R., Kawai, Y., and Errington, J. (2014). General principles for the formation and proliferation of a wall-free (L-form) state in bacteria. *eLife* 3:e04629. doi: 10.7554/eLife.04629

Mingorance, J., Tamames, J., and Vicente, M. (2004). Genomic channeling in bacterial cell division. *J. Mol. Recognit.* 17, 481–487. doi: 10.1002/jmr.718

Miyata, M., and Seto, S. (1999). Cell reproduction cycle of *Mycoplasma*. *Biochimie* 81, 873–878. doi: 10.1016/S0300-9084(99)00209-6

Osawa, M., and Erickson, H. P. (2006). FtsZ from divergent foreign bacteria can function for cell division in *Escherichia coli*. *J. Bacteriol.* 188, 7132–7140. doi: 10.1128/JB.00647-06

Pelletier, J. F., Sun, L., Wise, K. S., Assad-Garcia, N., Karas, B. J., Deerinck, T. J., et al. (2021). Genetic requirements for cell division in a genomically minimal cell. *Cell* 184, 2430.e16–2440.e16. doi: 10.1016/J.cell.2021.03.008

Pfaffl, M. W. (2001). A new mathematical model for relative quantification in real-time RT-PCR. *Nucleic Acids Res.* 29:e45. doi: 10.1093/nar/29.9.e45

Pich, O. Q., Burgos, R., Ferrer-Navarro, M., Querol, E., and Piñol, J. (2008). Role of *Mycoplasma genitalium* MG218 and MG317 cytoskeletal proteins in terminal organelle organization, gliding motility and cytadherence. *Microbiology* 154, 3188–3198. doi: 10.1099/mic.0.2008/020636-0

Pilhofer, M., Rappl, K., Eckl, C., Bauer, A. P., Ludwig, W., Schleifer, K. H., et al. (2008). Characterization and evolution of cell division and cell wall synthesis genes in the bacterial phyla Verrucomicrobia, Lentisphaerae, Chlamydiae, and Planctomycetes and phylogenetic comparison with rRNA genes. *J. Bacteriol.* 190, 3192–3202. doi: 10.1128/JB.01797-07

Pucci, M. J., Thanassi, J. A., Discotto, L. F., Kessler, R. E., and Dougherty, T. J. (1997). Identification and characterization of cell wall-cell division gene clusters in pathogenic gram-positive cocci. *J. Bacteriol.* 179, 5632–5635. doi: 10.1128/jb.179.17.5632-5635.1997

Rappsilber, J., Mann, M., and Ishihama, Y. (2007). Protocol for micro-purification, enrichment, pre-fractionation and storage of peptides for proteomics using StageTips. *Nat. Protoc.* 2, 1896–1906. doi: 10.1038/nprot.2007.261

Robin, A., Joseleau-Petit, D., and D'Ari, R. (1990). Transcription of the ftsZ gene and cell division in *Escherichia coli*. *J. Bacteriol.* 172, 1392–1399. doi: 10.1128/jb.172.3.1392-1399.1990

Rowlett, V. W., and Margolin, W. (2015). The min system and other nucleoid-independent regulators of Z ring positioning. *Front. Microbiol.* 6:478. doi: 10.3389/fmicb.2015.00478

Sabidó, E., Quehenberger, O., Shen, Q., Chang, C. Y., Shah, I., Armando, A. M., et al. (2012). Targeted proteomics of the eicosanoid biosynthetic pathway completes an integrated genomics-proteomics-metabolomics picture of cellular metabolism. *Mol. Cell. Proteomics* 11:M111.014746. doi: 10.1074/mcp.M111.014746

Seto, S., and Miyata, M. (1999). Partitioning, movement, and positioning of nucleoids in *Mycoplasma capricolum*. *J. Bacteriol.* 181, 6073–6080. doi: 10.1128/JB.181.19.6073-6080.1999

Torres-Puig, S., Broto, A., Querol, E., Piñol, J., and Pich, O. Q. (2015). A novel sigma factor reveals a unique regulon controlling cell-specific recombination in *Mycoplasma genitalium*. *Nucleic Acids Res.* 43, 4923–4936. doi: 10.1093/nar/gkv422

Torres-Puig, S., Martínez-Torró, C., Granero-Moya, I., Querol, E., Piñol, J., and Pich, O. Q. (2018). Activation of σ20-dependent recombination and horizontal gene transfer in *Mycoplasma genitalium*. *DNA Res.* 25, 383–393. doi: 10.1093/dnares/dsy011

Vicente, M., Gomez, M. J., and Ayala, J. A. (1998). Regulation of transcription of cell division genes in the *Eschericia coli dcw* cluster. *Cell. Mol. Life Sci.* 54, 317–324. doi: 10.1007/s000180050158

Vicente, M., and Rico, A. I. (2006). The order of the ring: assembly of *Escherichia coli* cell division components. *Mol. Microbiol.* 61, 5–8. doi: 10.1111/j.1365-2958.2006.05233.x

Vishnyakov, I. E., Borchsenius, S. N., Basovskii, Y. I., Levitskiĭ, S. A., Lazarev, V. N., Snigirevskaia, E. S., et al. (2009). Localization of division protein FtsZ in *Mycoplasma hominis*. *Cell Tiss. Biol.* 3, 254–262. doi: 10.1134/S1990519X09030079

Xu, X., Zhang, H., Huang, Y., Zhang, Y., Wu, C., Gao, P., et al. (2019). Beyond a ribosomal RNA methyltransferase, the wider role of MraW in DNA

methylation, motility and colonization in *Escherichia coli* O157:H7. *Front. Microbiol.* 10:2520. doi: 10.3389/fmicb.2019.02520

Conflict of Interest: The authors declare that the research was conducted in the absence of any commercial or financial relationships that could be construed as a potential conflict of interest.

Publisher's Note: All claims expressed in this article are solely those of the authors and do not necessarily represent those of their affiliated organizations, or those of the publisher, the editors and the reviewers. Any product that may be evaluated in this article, or claim that may be made by its manufacturer, is not guaranteed or endorsed by the publisher.

frontiers in Microbiology

REVIEW
published: 18 October 2021
doi: 10.3389/fmicb.2021.737396

The Pneumococcal Divisome: Dynamic Control of *Streptococcus pneumoniae* Cell Division

Nicholas S. Briggs[1], Kevin E. Bruce[2], Souvik Naskar[3], Malcolm E. Winkler[2] and David I. Roper[1]**

[1] School of Life Sciences, University of Warwick, Coventry, United Kingdom, [2] Department of Biology, Indiana University Bloomington, Bloomington, IN, United States, [3] Department of Infectious Disease, Imperial College London, London, United Kingdom

OPEN ACCESS

Edited by:
Martin Loose, Institute of Science and Technology Austria (IST Austria), Austria

Reviewed by:
Orietta Massidda, University of Trento, Italy
Anders P. Hakansson, Lund University, Sweden
Cecile Morlot, Délégation Alpes, Center for the National Scientific Research (CNRS), France

***Correspondence:**
David I. Roper
david.roper@warwick.ac.uk
Malcolm E. Winkler
winklerm@indiana.edu

Specialty section:
This article was submitted to Microbial Physiology and Metabolism, a section of the journal Frontiers in Microbiology

Received: *06 July 2021*
Accepted: *15 September 2021*
Published: *18 October 2021*

Citation:
Briggs NS, Bruce KE, Naskar S, Winkler ME and Roper DI (2021) The Pneumococcal Divisome: Dynamic Control of Streptococcus pneumoniae Cell Division. Front. Microbiol. 12:737396. doi: 10.3389/fmicb.2021.737396

Cell division in *Streptococcus pneumoniae* (pneumococcus) is performed and regulated by a protein complex consisting of at least 14 different protein elements; known as the divisome. Recent findings have advanced our understanding of the molecular events surrounding this process and have provided new understanding of the mechanisms that occur during the division of pneumococcus. This review will provide an overview of the key protein complexes and how they are involved in cell division. We will discuss the interaction of proteins in the divisome complex that underpin the control mechanisms for cell division and cell wall synthesis and remodelling that are required in *S. pneumoniae*, including the involvement of virulence factors and capsular polysaccharides.

Keywords: *Streptococcus pneumoniae* (pneumococcus), cell division, peptidoglycan (PG) synthesis, FtsZ, antibiotic resistance

INTRODUCTION

Bacterial cell division is a fundamental and highly regulated process. It is heavily reliant on the coordination of peptidoglycan (PG) synthesis outside the cell membrane with molecular events occurring inside the cell, such as chromosome replication and separation, as well as membrane invagination and septation (Egan and Vollmer, 2013). Coordination between these components is critical for successful cell division, as many of the control checkpoints rely on signals from the cytoplasmic face of the membrane being used to regulate events outside the cell (Trusca et al., 1998; Haeusser and Margolin, 2016; Willis and Huang, 2017; Egan et al., 2020). This includes degradation or remodelling of the "old" cell wall PG sacculus outside the cell membrane and the creation of new PG for daughter cells (Typas et al., 2012; Massidda et al., 2013; Egan et al., 2020). PG is a three-dimensional mesh of glycan strands crosslinked together by short peptide stems [reviewed in Vollmer et al. (2019) for *Streptococcus pneumoniae*, and in Vollmer et al. (2008) more generally]. PG provides cell shape and resistance to turgor pressure and is a distinctive structural and chemical feature of bacteria, making it a widely used antibiotic target (Macheboeuf et al., 2006; den Blaauwen et al., 2014; Bush and Bradford, 2016). The biosynthesis of PG is a complex process performed by dedicated enzymes and protein complexes that begins in the cytoplasm and continues outside the cell membrane (Typas et al., 2012). Disruption of PG biosynthesis by inhibition of the enzymes responsible for its formation or sequestration of a key substrate intermediate, can be lethal to bacteria and has been the basis for life saving β-lactam chemotherapy for decades (Bush and Bradford, 2016).

Additionally, proper growth and division requires the coordinated remodelling of existing PG by dedicated PG hydrolases that degrade and modify its polymeric form, thus enabling growth and division. At present there is a significant lack of understanding of this process, particularly with regards to the required coordination of cell division with new cell wall PG biosynthesis. This is a subject of fundamental biological interest and may also provide further insight into future antimicrobial disruption of this vital process (Macheboeuf et al., 2006; den Blaauwen et al., 2014; Fisher and Mobashery, 2020). Previous microbiological investigation of bacterial cell morphology, encompassing detailed genetic, biochemical and advanced microscopy studies, has already provided a wealth of information on the identity of the key proteins and macromolecules in the divisome generally (Typas et al., 2012; Egan and Vollmer, 2013; Haeusser and Margolin, 2016; Du and Lutkenhaus, 2017, 2019; Egan et al., 2020). Moreover, the field of bacterial cell biology has undergone a renaissance recently, in particular enabled by the technique of fluorescent D-amino acid (FDAA)-based PG labelling, enabling visualisation of the coordination of events between cell division and PG biosynthesis (Kuru et al., 2012, 2019; Hsu et al., 2017, 2019). Studies have been carried out in a number of model organisms, including rod-shaped *Escherichia coli* and *Bacillus subtilis,* as well as those with particular morphological and biomedical interest (Eswara and Ramamurthi, 2017; Hsu et al., 2019). In addition, metabolic labelling has been achieved using azide-bound D-Ala-D-Ala incorporation to allow Direct Stochastic Optical Reconstruction Microscopy (dSTORM) analysis of PG synthesis with very high resolution (Trouve et al., 2021). Besides dSTORM, other microscopy advances such as the use of 3D-Structured Illumination Microscopy (3D-SIM; Tsui et al., 2014; Perez et al., 2021b) and Total Internal Reflection Fluorescence Microscopy (TIRFm; Zhao et al., 2018; Perez et al., 2019; Squyres et al., 2021) have contributed studies of division and motion in relatively small bacterial cells. Many of the key cell division proteins are highly conserved in these organisms, underlying their essentiality and universality, although their functions can vary between species.

Here, we focus on the Gram-positive, human commensal bacterium *Streptococcus pneumoniae* (pneumococcus), the classical model for bacterial transformation (Griffith, 1928) and capsule formation (Geno et al., 2015). This opportunistic human respiratory pathogen resides within the nasopharynx of a healthy individual, often without symptoms, from early after birth (Austrian, 1986). Infections occur when, in an immunocompromised or virally infected individual, pneumococcus migrates to the sterile lining of the alveoli, where it causes inflammation and activation of sputum-producing neutrophils (Weiser et al., 2018) leading to pneumonia symptoms. Once invaginated by the alveoli epithelium, the bacteria can also enter the blood stream and cross the blood-brain barrier to cause bacterial meningitis (Koedel et al., 2002), making pneumococcal infection a serious clinical issue. Pneumococcal disease is compounded by the presence of over 90 distinct strains with different capsule serotypes (Jefferies et al., 2004; Hausdorff et al., 2005), allowing pneumococcus to circumvent the actions of the currently available vaccines, which are based on a limited number of capsule serotypes (Shapiro et al., 1991; Lynch and Zhanel, 2010; Moffitt et al., 2011). This combined with the increasing prevalence of drug resistant pneumococcus [31% of worldwide cases were resistant to one or more antibiotics in 2018 (Centers for Disease Control and Prevention, 2018)] has driven the recent surge of research into pneumococcal cell division as a potential target for future chemotherapeutic strategies governing the development of next-generation antibiotics.

Although less well characterised than rod-shaped bacteria, many details of cell division in ovoid-shaped bacteria such as pneumococcus are known (Zapun et al., 2008b; Massidda et al., 2013; Pinho et al., 2013; Vollmer et al., 2019). The characteristic prolate ellipsoid shape is produced by coordinated PG assembly at midcell, producing the new cell-hemispheres in between old hemispheres. Initially, PG synthesis proteins are recruited to the FtsZ rings at the equator of the newly formed daughter cells at the beginning of division (**Figures 1A**, **2**; Fleurie et al., 2014b; Tsui et al., 2014; Perez et al., 2019) and PG synthesis occurs via two separate modes, termed septal and peripheral (Hakenbeck et al., 2012; Berg et al., 2013; Land et al., 2013; Tsui et al., 2014; Straume et al., 2017). Septal synthesis produces the cell wall separating the new daughter cells, while peripheral synthesis is responsible for cell elongation (Berg et al., 2013; Tsui et al., 2014; Philippe et al., 2015; Straume et al., 2017). In pneumococcus the septal and peripheral machineries both remain at midcell throughout division, but form spatially distinct concentric rings as division proceeds, with the septal machine moving with FtsZ to the inner edge of the constricting septal annulus, whilst the peripheral machine remains in the outer ring (**Figures 1B,C**, **3**, top; Land et al., 2013; Tsui et al., 2014, 2016; Rued et al., 2017; Sharifzadeh et al., 2017, 2020; Perez et al., 2021b). Concentric rings of newly synthesised PG consistent with this model were recently visualised by both 3D-SIM (Perez et al., 2021b) and by dSTORM (Trouve et al., 2021). As division begins, a portion of FtsZ, EzrA, and FtsA begin to migrate to the equatorial sites of the developing daughter cells, guided by MapZ (also called LocZ) (**Figure 1**; Fleurie et al., 2014a; Holečková et al., 2014; Perez et al., 2019). This process is discussed further below. Finally, as septum formation finishes and cell separation occurs, PG synthesis proteins migrate to the FtsZ rings at the equators of the newly formed daughter cells (**Figure 1D**).

This process contrasts with division in other cocci bacteria such as *Staphylococcus aureus*, which forms a divisional transverse septum spanning the axis of the cell, before "popping" open into two hemispherical daughter cells that are then able to rebuild the rest of their cocci shape (Tzagoloff and Novick, 1977; Pinho et al., 2013; Monteiro et al., 2015; Saraiva et al., 2020). This has been described as formation of a "pie crust" immediately prior to division, which has been extensively characterised using atomic force and other microscopy techniques (Turner et al., 2010; Monteiro et al., 2015; Viljoen et al., 2020). It should also be noted that *S. aureus* undergoes a much shorter elongation stage than pneumococcus, making them not truly spherical (Monteiro et al., 2015; Pereira et al., 2016; Reichmann et al., 2019). This makes pneumococcus an interesting subject of study, as even in

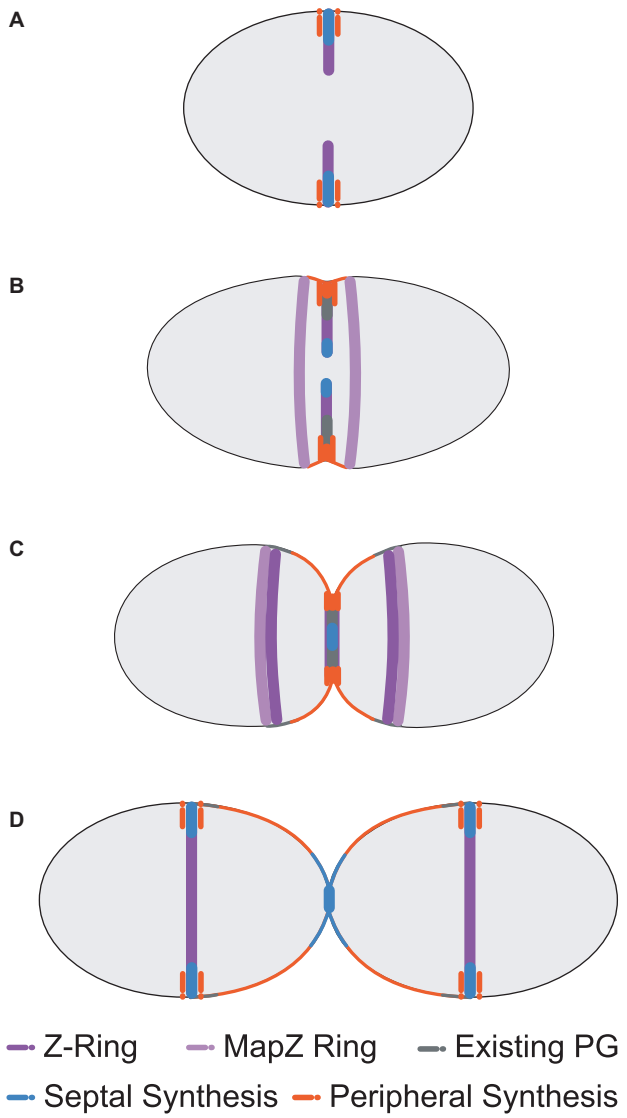

FIGURE 1 | Pneumococcal cell division morphology. Following the initial formation of the Z-ring and divisome machinery, septal and peripheral PG synthetic complexes begin to make new PG as invagination begins **(A)**. Two concentric rings of newly synthesised PG surrounding the existing sacculus form as a result, whilst a portion of MapZ, FtsZ, EzrA, and FtsA (MapZ Ring) begin to migrate to the new equators. For simplicity, newly synthesised peripheral PG is drawn as a single orange colour, but likely consists of some mixture of newly synthesised peripheral PG attached to remodelled septal PG (see Trouve et al., 2021) **(B)**. Septal PG synthesis continues to close the central septum whilst peripheral PG synthesis continues to elongate the cell from midcell **(C)**. This process continues until the septum is closed. The divisome machinery then migrates to the midcells of the newly formed daughter cells and the cycle repeats **(D)**. Note that pneumococcus exists natively as encapsulated cells that are often in chains of divided cells (Barendt et al., 2009).

the absence of an MreB homolog that is commonly associated with rod-shaped elongation (Land and Winkler, 2011; Philippe et al., 2014), it still exhibits a prolonged elongation phase during division (Wheeler et al., 2011), something not traditionally seen in other cocci bacteria. Although many pneumococcal division proteins are conserved in bacteria with different morphologies (such as rod-shaped *B. subtilis* or coccoid-shaped *S. aureus*) (Pinho et al., 2013), they seem to play different roles and have different spatiotemporal interactions. Moreover, the accepted notion of "sequential assembly" of the divisome components as seen in *E. coli* (Buddelmeijer and Beckwith, 2002) has not yet been demonstrated; but is still implied in *S. pneumoniae*. This article aims to update and consolidate the current understanding of the pneumococcal cell division, as outlined in **Figure 1** beyond previous excellent reviews (Massidda et al., 2013; Pinho et al., 2013; Philippe et al., 2014; Vollmer et al., 2019).

EARLY-STAGE ASSEMBLY

In *S. pneumoniae*, the initial FtsZ-ring assembly at the equators of newly divided daughter cells organises all of the components required for cell division, septal and peripheral PG synthesis and chromosome segregation (**Figure 2**; Fleurie et al., 2014b; Tsui et al., 2014; Perez et al., 2019, 2021b). In this regard, the pneumococcal FtsZ-ring assembly resembles the predivisional PG complexes at the septa of rod-shaped bacteria (Buddelmeijer and Beckwith, 2002; den Blaauwen et al., 2008). Assembly of equatorial FtsZ rings begins even before division is complete, resulting in a distinctive pattern of three FtsZ rings (one at the old septum and two at the future equators) in late divisional cells (**Figure 1C**; Land et al., 2013; Jacq et al., 2015). In pneumococcus, the initial equatorial FtsZ-ring assembly surrounds the undivided bacterial chromosome (Tsui et al., 2014). Canonical nucleoid occlusion and Min systems found in rod-shaped bacteria are absent in pneumococcus, and replaced by the CcrZ and MapZ systems described below (Fleurie et al., 2014a; Holečková et al., 2014; Gallay et al., 2021). The initial stages of divisome assembly are broadly conserved in nearly all bacterial species. FtsZ, the homolog of eukaryotic tubulin, localises to the inner side of the cytoplasmic membrane via FtsA (Pichoff and Lutkenhaus, 2005; Mura et al., 2017). FtsZ monomers form short protofilaments at the midcell and move circumferentially around the short axis of the cell via a rapid GTP-dependent polymerisation and depolymerisation treadmilling mechanism, similar to that of eukaryotic tubulin (Dai and Lutkenhaus, 1991; Adams and Errington, 2009; Erickson et al., 2010; Meier and Goley., 2014; Haeusser and Margolin, 2016; Bisson-Filho et al., 2017; Yang et al., 2017; Perez et al., 2019). FtsZ treadmilling velocity appears to be controlled by the manner of membrane anchoring, and FtsZ GTPase activity (Bisson-Filho et al., 2017; Yang et al., 2017; Perez et al., 2019; García-Soriano et al., 2020) is important for correct divisome formation (Yang et al., 2017; Du and Lutkenhaus, 2019).

FtsA, also referred to as bacterial actin, is able to form its own filaments by binding ATP *in vitro* (Szwedziak et al., 2012). Co-localisation of FtsZ and FtsA, indicative of interaction, has been observed at all stages of cell division (Perez et al., 2019), unlike in other model bacteria, such as *E. coli* and *B. subtilis*, where inactivation of FtsA causes filamentation rather than the cell lysis seen in pneumococcus (see Mura et al., 2017). A predicted amphipathic helix at the C-terminus of FtsA is

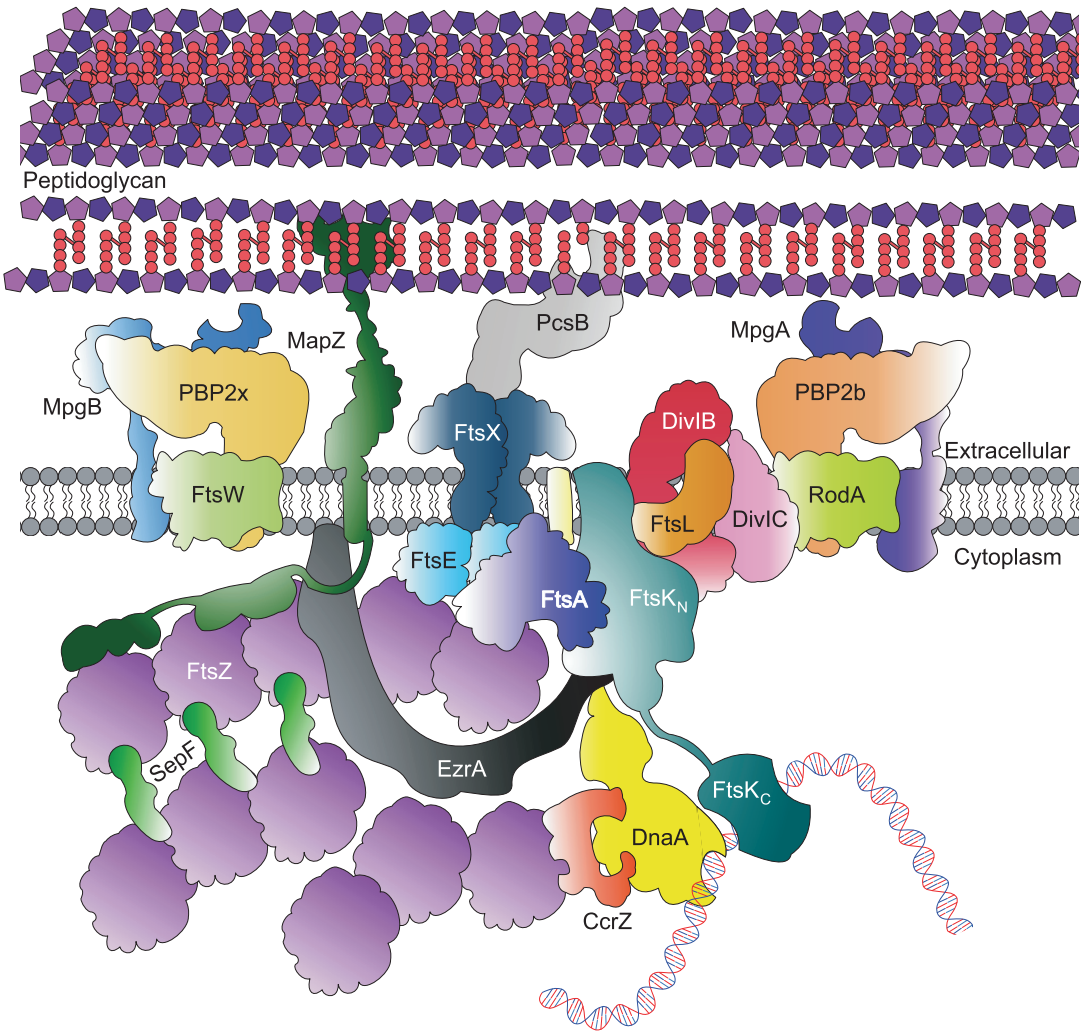

FIGURE 2 | Core pneumococcal divisome components at equators of predivisional cells. For simplicity, components that localise to the equatorial ring, including Class A PBPs, the Rod complex and regulatory proteins are not shown here; but depicted in **Figure 3**.

thought to lay against the membrane to facilitate its role as an FtsZ anchor (Pichoff and Lutkenhaus, 2005). ATP binding causes a conformational change at the C-terminus, which exposes the amphipathic helix and promotes membrane association and polymerisation (Krupka et al., 2014). Although FtsZ and FtsA bear homology to eukaryotic cytoskeletal components, there has as yet been no evidence to suggest the presence of motor proteins similar to myosin or kinesin. Besides simply anchoring FtsZ to cell membranes, pneumococcal FtsA seems to play regulatory roles in coordinating septal and peripheral growth at midcells (Mura et al., 2017).

Besides FtsA, EzrA, SepF, and ZapA may also play roles in anchoring pneumococcal FtsZ filaments and bundles to cell membranes. Like FtsA, EzrA is essential in *S. pneumoniae* (Thanassi et al., 2002; van Opijnen et al., 2009; Perez et al., 2021a). EzrA is a bitopic protein, whose cytoplasmic domain forms a spectrin-like coiled-coil structure (Cleverley et al., 2014). Dimers of EzrA spectrin-like molecules have been proposed to form arch structures in the cytoplasm that bind to FtsZ and modulate lateral interactions of the bundles (Cleverley et al., 2014). Along with FtsA, pneumococcal EzrA is found in treadmilling nascent FtsZ filaments and bundles that move out with MapZ toward the equators of daughter cells (Perez et al., 2019). This association argues against EzrA acting as a negative regulator that promotes FtsZ depolymerisation as reported in *B. subtilis* (Levin et al., 1999). Instead, pneumococcal EzrA is required for pneumococcal FtsZ ring formation (Perez et al., 2021a). In support of this hypothesis, *B. subtilis* EzrA, ZapA, and SepF have been shown to condense treadmilling FtsZ filaments at midcell into an FtsZ ring that can help promote cell division and septal PG synthesis (Squyres et al., 2021). In pneumococcus, SepF rings are proposed to sit perpendicular to the FtsZ filaments and group them into bundles (Singh et al., 2008; Duman et al., 2013). This plays a role in efficient cell division, as the absence of SepF results in cells displaying Z-ring constriction defects (Mura et al., 2017). Although it remains to be determined, it is likely that the

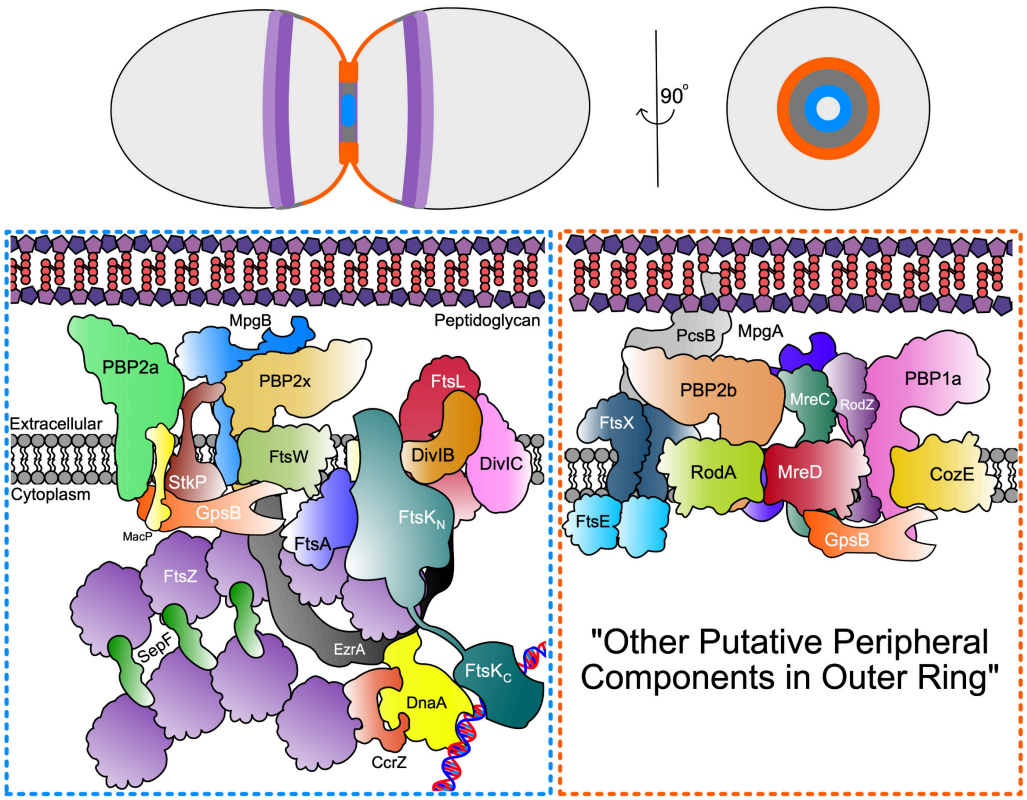

FIGURE 3 | Septal and Peripheral PG synthesis components. (Top) Organisation of FtsZ Ring (dark purple) and MapZ ring (light purple) as well as septal (blue) and periphery (orange) PG synthases represented across the longitudinal and transverse plan of the pneumococcal cell. (Bottom) Schematic representation of the spatial and functional separation of divisome machinery between septal (blue box) and peripheral (orange box) machinery located in the inner and outer PG synthesis rings at opposite edges of the midcell annular disk. The organisation of the outer peripheral ring is unknown and may contain additional components, thus denoted here as "other putative peripheral components in outer ring".

pneumococcal SepF and ZapA homologs also act to bundle FtsZ filaments to form fibres, in much the same way that ZipA does in *E. coli* (Hamoen et al., 2006; Duman et al., 2013; Krupka et al., 2018). Pneumococcal ZapA is not essential (Thanassi et al., 2002) and has not yet been fully characterised, however, *B. subtilis* ZapA was shown to promote FtsZ bundle formation (Gueiros-Filho and Losick, 2002). Though it remains to be determined, it is likely that pneumococcal EzrA, SepF, and ZapA modulate the formation of FtsZ filaments during condensation of the mature FtsZ ring.

As mentioned above, pneumococcal MapZ has been shown to guide treadmilling FtsZ filaments and bundles throughout the division cycle from the septum to the equators of daughter cells (Fleurie et al., 2014a; Holečková et al., 2014; Perez et al., 2019). However, pneumococcal MapZ is not an essential protein, and in its absence, treadmilling FtsZ filaments and bundles move by a streaming failsafe mechanism imprecisely to daughter cells (Perez et al., 2019). This results in frequently misaligned FtsZ rings (Fleurie et al., 2014a; Holečková et al., 2014; Perez et al., 2019). In contrast, MapZ acts more like a beacon in *Streptococcus mutans* cells, where MapZ first moves to equators without nascent FtsZ filaments and bundles followed by streaming of FtsZ from the septum (Li et al., 2018). MapZ is a bitopic membrane protein that binds to the extracellular PG layer via its C-terminus, whilst its N-terminus associates with the cytoplasmic FtsZ (Fleurie et al., 2014a; Hosek et al., 2020). Interestingly, it appears that the C-terminal region of FtsZ is not required for its association with MapZ, but is required for associations with FtsA; the classical membrane anchor for the Z-ring (Hosek et al., 2020). At the start of division, the MapZ ring at the midcell of the predivisional cell splits into two rings on both sides of the developing septum, binds FtsZ, FtsA, and EzrA in increasing amounts, and moves toward the future equators of the daughter cells (**Figure 1**; Fleurie et al., 2014a; Holečková et al., 2014; Perez et al., 2019). It is postulated, but not experimentally established, that the progressive movement of the MapZ/FtsZ/FtsA/EzrA plane is driven by peripheral PG elongation synthesis. A further important consideration is the manner in which MapZ recognises the midcell and other proteins, a phenomenon which remains unknown at this point. One interesting hypothesis is that distinct regions of the lipid membrane, comprised of different lipids according to cell geometry, could serve as markers for localisation of membrane proteins such as pneumococcal MapZ (Calvez et al., 2019), however, this remains to be shown experimentally.

LATE-STAGE ASSEMBLY

In *E. coli*, following the establishment of the FtsZ-ring, there is an ordered assembly of divisome component proteins starting with FtsEX (Pichoff et al., 2019). However, the order of assembly of the divisome at the equators of predivisional pneumococcal cells has not yet been established. With the exception of FtsN, homologs of the *E. coli* divisome proteins are present in *S. pneumoniae*, and it seems likely that the pneumococcal divisome assembles in the same order, which will be assumed here. Notably, at a point early after the start of division, septal and peripheral PG synthesis proteins separate into concentric rings (Perez et al., 2021b). During this separation, some proteins remain in the closing inner-ring septal PG synthesis machine, including FtsZ and PBP2x, while other proteins partition and remain in the outer-ring peripheral PG synthesis machine, including PBP2b, FtsX, and PBP2x (Perez et al., 2021b).

FtsE and FtsX are likely to be the next proteins to assemble into the nascent pneumococcal divisome. The membrane-spanning FtsX assembles into a dimer with overall predicted structural homology to the ABC transporter MacB (Leeuw et al., 1999), though it has no known role in transporting substrates; whilst the ATPase FtsE (Alcorlo et al., 2020) associates with the cytoplasmic side of FtsX. In pneumococcus, FtsEX forms a complex with the extracellular PG hydrolase, PcsB (Sham et al., 2011, 2013; Bartual et al., 2014). Like FtsX and FtsE, PcsB itself is essential in pneumococcus, as cells depleted of PcsB show misplaced newly formed cell walls, as well as partially divided cells that are still joined by their sacculus (Barendt et al., 2009; Bartual et al., 2014). Although likely to form a complex with FtsEX, based upon similarity to *E. coli* (Cook et al., 2020) and *B. subtilis* (Meisner et al., 2013) homologs, it is not yet known at which stage in cell division PcsB associates with FtsEX. Furthermore, FtsX is found in the outer peripheral PG synthesis ring as division progresses (Perez et al., 2021b), indicating that FtsEX-PcsB mediates peripheral PG elongation synthesis, analogous to FtsEX-CwlO in *B. subtilis* (Meisner et al., 2013). Thus, it is possible that FtsEX plays an early role in divisome assembly and a later role in peripheral PG remodelling. After PcsB associates with FtsEX, ATP binding and hydrolysis by FtsE is thought to provide the driving force for the mechanotransmission that activates PcsB (Sham et al., 2013; Pichoff et al., 2019; Rued et al., 2019), but how this is regulated is as yet unclear. The X-ray crystal structure of pneumococcal PcsB shows a coiled-coil domain preceding the hydrolytic CHAP domain which houses the active site Cys (Bartual et al., 2014). The PcsB coiled-coil domain interacts with the large extracellular loop domain of FtsX (Rued et al., 2019). Unlike the EnvC hydrolase of *E. coli*, PcsB is catalytically active, provided that the coiled-coil domain is removed, suggesting a control mechanism for its activity (Bartual et al., 2014; Rued et al., 2019).

Following the recruitment of the FtsEX-PcsB subcomplex, further divisome components are likely recruited in a highly ordered manner. FtsK may be another early addition, serving as a motor to separate the chromosomal DNA across the septal site (Aussel et al., 2002). Several structures of the hexameric motor domain of FtsK have been solved for the *Pseudomonas aeruginosa* protein; which describe an ATP-dependent "inchworm" mechanism of translocation in which each subunit is in one of six conformational states (Massey et al., 2006; Jean et al., 2020). The rest of this protein remains challenging to study crystallographically due to the predicted long disordered region between the polytopic membrane anchor and the motor domain. This spacer region could play a role in positioning the DNA strands exiting the motor such that each daughter cell receives a complete chromosome before septation completes. Several assays have been conducted on purified FtsK from *E. coli*, which demonstrate the speed with which this motor is able to reposition DNA, whilst also observing that the DNA sequence is sufficient only to influence FtsK directionality (Pease et al., 2005). Since pneumococcus does not possess the Min or nucleoid occlusion systems, the role of FtsK may be different from that of *E. coli* FtsK, and more analogous to SpoIIIE in *B. subtilis* sporulation (Khanna et al., 2020).

Following FtsK binding, the conserved DivIBC-FtsL subcomplex is likely recruited to the divisome. Homologous to the FtsQLB complex in *E. coli* (where DivIB is FtsQ and DivIC is FtsB), the full complex has been suggested to form in pneumococcus only during septation, despite the components being present throughout the cell cycle (Noirclerc-Savoye et al., 2005). DivIC binds FtsL via its extracellular coiled-coil domains (Masson et al., 2009) and may also have a role in stabilising FtsL (Sievers and Errington, 2000; Wadenpohl and Bramkamp, 2010), though its exact function in many organisms remains unclear. In *B. subtilis*, DivIC reportedly protects FtsL against RasP cleavage by shifting the oligomeric state of FtsL to a dimeric form (Wadenpohl and Bramkamp, 2010). Given that the homologous protease RseP from *E. coli* uses zinc as a co-factor (Hizukuri et al., 2017), it is possible that zinc availability may be an important and unexplored regulator of this stage of pneumococcal cell division. FtsL is essential in *E. coli* and is thought to play a role in zinc sensitivity and by extension, membrane permeability (Guzman et al., 1992; Blencowe et al., 2011). Although the role of pneumococcal FtsL is unknown, the conservation of this complex across all bacteria makes it likely that FtsL's function is also conserved. The membrane spanning protein DivIB has also been shown to interact with DivIC-FtsL via its central β-domain, and is not essential for growth unlike FtsQ in *E. coli*; with deletion of the gene leading to long chains of pneumococcal cells, as well as cells with impaired septa in rich media (Gouëllec et al., 2008). FtsL is rapidly degraded in the absence of DivIB, suggesting that the latter serves to stabilise the former, either physically or by other means (Gouëllec et al., 2008). Interestingly, the full DivIBC-FtsL subcomplex only co-localises in pneumococcus during septation (Noirclerc-Savoye et al., 2005). DivIB and FtsL localise to the midcell only during septation, whereas DivIC follows the localisation pattern of the FtsW-PBP2x complex, residing always at the septal site until late in division (Noirclerc-Savoye et al., 2005). This could indicate that the function of the DivIBC-FtsL complex at the site of division is controlled, at least in part, by DivIC; and that DivC is involved in the recruitment of the PG synthesis subcomplex FtsW-PBP2x. It has also been shown in other bacteria that the DivIBC-FtsL subcomplex homologs are involved in the

regulation of PG synthases (Boes et al., 2019; Marmont and Bernhardt, 2020).

At some point in the assembly of the divisome, the newly discovered protein CcrZ interacts with FtsZ and couples cell division to DNA replication in pneumococcus and other *Firmicutes* (Gallay et al., 2021). At the midcell, the origin of replication is bound by DnaA, which CcrZ stimulates to start replication, after which the newly replicated origins segregate to daughter cells. CcrZ remains at the septum with the replication machinery throughout division and moves to the equatorial FtsZ rings of daughter cells only after replication is complete. In this way, CcrZ stimulates new rounds of replication when replicated chromosomes are correctly positioned, thereby preventing guillotining of chromosomes (Gallay et al., 2021). This mechanism ensures that DNA replication occurs just a single time in the cell cycle.

FINAL-STAGE ASSEMBLY

In the final phase of divisome assembly, it is crucial for the cell to start producing more PG alongside the membrane extension so that the overall shape and rigidity of the daughter cells can be maintained. In pneumococcus, there are two major PG synthase complexes that facilitate this process: FtsW-PBP2x and RodA-PBP2b, which mainly carry out septal and peripheral PG synthesis, respectively (Berg et al., 2014; Tsui et al., 2014; Perez et al., 2019, 2021b). PBP2x, however, was recently shown to remain partially localised to the periphery of the septum during constriction, suggesting that it might participate in enlargement of the septal annular ring or in peripheral PG synthesis (Perez et al., 2021b). Each of these PG synthase complexes consists of a shape, elongation, division, sporulation (SEDS) family glycosyltransferase (FtsW; RodA) with a cognate Class B PBP (PBP2x; PBP2b) (Gérard et al., 2002; Fraipont et al., 2011; Zapun et al., 2012; Sjodt et al., 2018, 2020). The FtsW-PBP2x complex migrates circumferentially around the septal FtsZ ring leading to invagination between daughter cells (Perez et al., 2019). FtsW-PBP2x complex movement is driven by septal PG synthesis itself and is not directly dependent on treadmilling of FtsZ filaments and bundles (Perez et al., 2019).

As in other bacteria (den Blaauwen et al., 2008; Rohs et al., 2018), pneumococcal RodA-PBP2b is part of an elongasome "Rod" complex, which in pneumococcus, contains several regulatory and organising proteins, including MreC, MreD, and RodZ, but not MreB (Land and Winkler, 2011; Land et al., 2013; Philippe et al., 2014; Tsui et al., 2016; Stamsås et al., 2017; Straume et al., 2017; Zheng et al., 2017; Winther et al., 2021). This complex in pneumococcus carries out a form of sidewall synthesis that pushes new peripheral PG out from an outer ring at the midcell, and participates in cell elongation (**Figure 3**; Tsui et al., 2014; Perez et al., 2021b; Trouve et al., 2021). Several investigations show that septal and peripheral PG synthesis occur concurrently throughout most of the pneumococcal cell cycle, instead of as separate elongation and septal-closure phases (Wheeler et al., 2011; Tsui et al., 2014; Perez et al., 2021b; Trouve et al., 2021). Although septal and peripheral PG synthesis occur separately and are catalysed by distinct synthases (Tsui et al., 2014; Perez et al., 2021b; Trouve et al., 2021), protein interaction profiles and phenotypes of mutants lacking certain proteins, such as those for GpsB (Rued et al., 2017; Cleverley et al., 2019), suggest mechanisms for coordination of septal and peripheral PG synthesis to give final cell shapes and sizes. Another important regulatory protein, DivIVA, seems to mediate division, cell morphology (possibly through PG peripheral synthesis), and chromosome segregation in *S. pneumoniae* (Vollmer et al., 2019); however, since its exact function remains unknown (Fadda et al., 2007; Fleurie et al., 2014b; Straume et al., 2017), it is not included in **Figure 3**.

Besides the Class B enzymes, PBP2x and PBP2b, mediators of septal and peripheral PG synthesis, respectively, the Class A PBPs, PBP1a, PBP2a, and PBP1b, also play roles in PG synthesis and PG repair in pneumococcus [recently reviewed in Straume et al. (2021)]. Unlike the Class B PBPs, Class A PBPs are bifunctional enzymes and contain a glycosyltransferase (GT) and transpeptidase (TP) domain in the same polypeptide chain separated into distinct domains (Straume et al., 2021). Like most bacteria, pneumococcus contains a pair of Class A PBPs, PBP1a, and PBP2a, whose simultaneous deletion results in a synthetic lethal phenotype (Straume et al., 2021). Mutants lacking PBP2a or PBP1b generally show minimal cell morphology defects in culture, whereas mutants of the progenitor D39 serotype 2 strain lacking PBP1a form narrower, slightly longer cells under some culture conditions (Land and Winkler, 2011). Genetic suppression patterns strongly implicate PBP1a in peripheral PG synthesis (Land and Winkler, 2011; Tsui et al., 2016). In addition, PBP1a localises in rings at the midcell in the same patterns as PBP2b and MreC, which mediate peripheral PG synthesis (**Figure 3**; Tsui et al., 2014). In contrast, Class A PBPs that mediate sidewall elongation of rod-shaped bacteria localise diffusely over the bodies of cells (Rohs et al., 2018). High-level penicillin resistance in pneumococcus is due to mutagenic alterations in the *pbp2x*, *pbp2b*, and *pbp1a* genes (Barcus et al., 1995; Chesnel et al., 2005; Zapun et al., 2008a; Hakenbeck et al., 2012).

Consistent with a role in peripheral PG synthesis, PBP1a interacts with the polytopic membrane protein CozE, a member of the MreCD-Rod complex, which directs PBP1a to the midcell elongasome (Fenton et al., 2016). A *S. aureus* CozEb paralog of pneumococcal CozE has also recently been reported and suggested to play a role in cell-shape homeostasis (Stamsås et al., 2018). Much less is known about the function of PBP2a and PBP1b in pneumococcus. PBP2a activity was reported to be activated by phosphorylated MacP protein (Fenton et al., 2018). MacP is phosphorylated by the Serine/Threonine protein kinase StkP, which interacts with and phosphorylates a number of proteins involved in pneumococcal cell division and PG synthesis (Fleurie et al., 2012, 2014b; Grangeasse, 2016; Manuse et al., 2016). Besides phosphorylated MacP, PBP2a directly interacts with the regulatory protein GpsB (Cleverley et al., 2019) which also positively regulates the levels of StkP-mediated protein phosphorylation (Fleurie et al., 2014b; Rued et al., 2017). It has been postulated that phosphorylation of MacP by StkP activates PBP2a in septal PG synthesis (Fenton et al., 2018),

however, more generally, the roles of protein phosphorylation in pneumococcus remain unclear; though likely important. Problematically, phosphoablative and phosphomimetic mutants of phosphorylated cell division and PG synthesis proteins do not uniformly show phenotypes in exponentially growing cultures (Fleurie et al., 2012; Grangeasse, 2016; Manuse et al., 2016; Zheng et al., 2017); suggesting other factors such as genetic background, culture conditions, growth phase, and/or cell stress may modulate the phenotypic effects of protein phosphorylation.

The recent discovery of primary PG synthases consisting of Class B PBPs and cognate SEDS proteins (Taguchi et al., 2019; Sjodt et al., 2020), has raised the question of whether Class A PBPs play direct roles in PG synthesis (Straume et al., 2020, 2021; Pazos and Vollmer, 2021). In support of this, there is strong evidence that Class A PBPs interact with cell division and PG synthesis proteins and account for a considerable amount of PG synthesis in exponentially growing, non-stressed cells (Pazos and Vollmer, 2021; Straume et al., 2021). However, recent results in *E. coli* and *S. pneumoniae* implicate Class A PBPs in PG repair in cells subjected to cell wall stresses (Straume et al., 2020; Vigouroux et al., 2020). In pneumococcus, inhibition of the septal synthetic complex FtsW-PBP2x results in the cells becoming resistant to cleavage by exogenously added PG hydrolase CbpD (Straume et al., 2020). Under the conditions used here, only PBP2x was being inhibited by oxacillin. When combined with other localisation studies showing CbpD binding to the septal region (Eldholm et al., 2010), a remodelling role for the Class A PBPs can be suggested; one which alters the crosslinking of septal PG strands to protect the sacculus from degradation by CbpD (Straume et al., 2020).

As noted in two recent reviews, the roles of Class A PBPs in normal PG synthesis and in PG repair of damaged cell wall during stress conditions are not mutually exclusive (Pazos and Vollmer, 2021; Straume et al., 2021). In this regard, an interesting hypothesis (Straume et al., 2021) was recently put forward that during septal and peripheral PG synthesis, pneumococcal Class A PBPs act in concert to the Class B PBP-SEDS synthases to lay down a separate internal layer of PG, characterised by a dense PG mesh of randomly orientated strands (Pasquina-Lemonche et al., 2020). In the septal division plane, this disordered internal layer is built on top of the ordered concentric rings of PG strands synthesised by Class B-SEDS synthases, such as PBP2x-FtsW, in pneumococcus and other *Firmicutes* (Pasquina-Lemonche et al., 2020; Straume et al., 2021). Whether this internal layer of PG is synthesised primarily by Class A PBPs alone as postulated, or results from the extensive remodelling of ordered PG synthesised by a combination of Class B PBP-SEDS and Class A PBPs remains to be determined.

Remodelling of PG by hydrolases is required to release nascent glycan strands from their lipid anchors and to cleave amide bonds in muropeptides to allow integration of newly synthesised peptidoglycan strands (Massidda et al., 2013; Vollmer et al., 2019). A recent model suggests that remodelling of septal PG and integration with newly synthesised peripheral PG occurs throughout the cell division cycle (Trouve et al., 2021). According to this model, the final peripheral PG then consists of a patchwork of PG synthesised by both machines: septal PG at the outer edge of the septal annulus is cleaved by PG hydrolases in a concerted manner, and woven into the newly synthesised peripheral PG. Consistent with this model, PBP2x and PBP2b arrive concurrently at new division sites (Tsui et al., 2014), inhibition of PBP2x alters cell shape in pre-divisional cells (Philippe et al., 2015), and concentric PG synthesis rings are observed at very early stages of the cell cycle (Perez et al., 2021b; Trouve et al., 2021).

However, the pulse-chase PG labelling data used to support this model can alternatively be interpreted to indicate that peripheral PG synthesis starts before septal PG synthesis in newly divided cells. This alternative interpretation was also proposed in a previous study showing that in terms of geometry, cell elongation precedes separation in ovococci bacteria (Wheeler et al., 2011). Further studies are needed to determine the timing and extent of remodelling at the junction of septal and peripheral PG. A leading candidate for a remodelling endopeptidase in this process is the essential FtsEX-PcsB discussed above, which localises to the outer peripheral synthesis ring of the septal annulus (Perez et al., 2021b). Other PG endopeptidases that participate in pneumococcal PG remodelling are currently unknown, but antibiotic and cell wall stress conditions induce the transcription of the WalRK regulon, which includes PcsB as well as putative PG binding proteins of unknown functions (Ng and Winkler, 2004; Ng et al., 2005).

Two other PG hydrolases have been identified that release glycan chains from lipid precursors in the separate septal and peripheral PG synthesis nanomachines. Lack of MpgB [previously PMP23 (Jacq et al., 2018)] leads to aberrant localisation of divisome proteins as well as septal defects, whilst MpgA (previously MltG^{Spn}) localises to and is linked genetically to the peripheral PG synthesis machinery (Tsui et al., 2016). A new paper demonstrates that both MpgB and MpgA are muramidases with different points of glycan chain cleavage (Taguchi et al., 2021). MpgB cleaves nascent peptidoglycan at the MurNAc-GlcNAc closest to the lipid anchor. In contrast, MpgA shows homology to *E. coli* MltG, including a LysM domain that specifies the cleavage site such that the MpgA cleaves after every seventh dipeptide from the lipid anchor at the periphery (Taguchi et al., 2021). Whilst not essential, the mutant MpgA lacking the LysM domain is not fully functional in pneumococcal cells (Taguchi et al., 2021), therefore the separation between septal and peripheral PG synthesis machinery is also seen for remodelling PG hydrolases, resulting in a different biochemical environment at each site. Finally, unlike in *E. coli* and *B. subtilis* where about 50% of PG is turned over and recycled per generation during growth, there is minimal turnover of "old" PG by pneumococcus during planktonic growth and in host-relevant biofilms (Boersma et al., 2015). Minimal release of PG breakdown products from turnover may be a strategy that pneumococcus uses to avoid alerting the host innate immune system to its presence.

OTHER DIVISION CONSIDERATIONS

It should also be noted that, despite sharing some morphology events with rod-shaped bacteria, Gram-positive bacteria,

including pneumococcus, do not encode an FtsN homolog found in Gram-negative organisms. In *E. coli*, this essential protein is known to interact with PBP1b, PBP3 and the FtsQLB complex (Müller et al., 2007; Liu et al., 2015), but also with FtsA, which is able to recruit FtsN to the septal site and allow it to activate PBP3 (Busiek and Margolin, 2014). This protein appears to act as a kind of checkpoint for septal constriction, since only after the binding of FtsN does septal PG synthesis appear to begin (Liu et al., 2015). This raises the interesting question of whether there is an equivalent control mechanism in Gram-positive organisms such as pneumococcus. At present, this is a question that remains unanswered. Moreover, the relationship between FtsZ treadmilling and the movement of septal PG synthases show distinct differences in *E. coli* (Yang et al., 2021), *B. subtilis* (Bisson-Filho et al., 2017), and *S. pneumoniae* (Perez et al., 2019), along with numerous similarities (McCausland et al., 2021).

Another important area that is not well understood is the effect of the extracellular capsule on pneumococcal cell division. As noted above, the pneumococcal pangenome specifies over 90 different capsular polysaccharides in the different serotype strains of *S. pneumoniae*. In addition, non-encapsulated pneumococcus strains are emerging as pathogens (Bradshaw and McDaniel, 2019). When present, the capsule is the single most important virulence factor of *S. pneumoniae*, allowing avoidance of opsonisation by phagocytotic cells of the innate immune system (Weiser et al., 2018). Multivalent capsule-based adult and conjugated vaccines provide significant protection against pneumococcal infections (Lynch and Zhanel, 2010; Moffitt et al., 2011). Depending on the serotype, the capsular polysaccharides may be linked to the membrane, covalently bound to the cell wall, or fully ejected into the extracellular space (Sørensen et al., 1990; Cartee et al., 2005); all of which could potentially provide different mechanisms for their involvement in cell division. Links have also been made between virulence and the roles of teichoic acids in *S. pneumoniae* (Vollmer et al., 2019), though any specific involvement of these crucial cell wall components and pneumococcal division has as yet not been demonstrated. However, a recent report shows that the degree and location of external modifications of PG-bound polyrhamnose of *S. mutans*, which lacks teichoic acids, controls PG hydrolase activity and placement of the axis of cell division (Zamakhaeva et al., 2021). It remains to be determined whether other ovococcal species like *S. pneumoniae* use undermodification of wall teichoic acids or exopolysaccharides to cue division (Winkler, 2021).

In this regard, presence of the serotype 2 capsule, which is covalently linked to the PG of the progenitor D39 strain, reduces the phenotypes observed for mutants defective in cell division or PG synthesis compared to an isogenic unencapsulated derivative (Barendt et al., 2009). This phenotype dampening is general and not confined to specific steps in division or PG synthesis. The mechanisms underlying phenotype dampening by the serotype 2 capsule are not understood and could involve physical constraint by the capsule that changes the timing of division or regulatory mechanisms analogous to the recently described RocS system that coordinates proper chromosome segregation and division with capsule biosynthesis (Mercy et al., 2019).

CONCLUDING REMARKS

Pneumococcal cell division is a complex and dynamic process of distinct microbiological and biomedical importance. Cell division and PG synthesis of ovoid-shaped pneumococcus have emerged as models, with distinct mechanisms and components compared to rod-shaped and spherical model bacteria. Dynamic interactions amongst the protein components that form the broader divisome result in the formation and dissolution of many subcomplexes that facilitate the intricate morphological and biochemical changes inherently essential to the division process. This dynamic process has recently become clearer through an elegant combination of genetic and biochemical approaches, augmented by novel cell wall labelling and high-resolution microscopy studies. At its core, cell wall PG must be broken, remodelled, and resynthesised by these protein complexes in a precise order whilst also coordinating with the membrane synthesis to continue providing structure to the cell.

AUTHOR CONTRIBUTIONS

NB drew the figures. All authors wrote and contributed to the manuscript. MW and DR coordinated preparation of the final manuscript.

FUNDING

Funding for this work was provided by the National Institutes of Health (United States) grant R35GM131767 to MW. NB was supported by a Ph.D. studentship to the Midlands Integrative Biosciences Training Partnership (MIBTP) BBSRC grant BB/J014532/1. Research in the laboratory of DR was supported by MRC grants G1100127, G0400848, Mr/N002679/1, and BBSRC grant BB/N003241/1.

ACKNOWLEDGMENTS

We thank Amilcar Perez and Tiffany Tsui for comments on this review. SN was supported by MRC Doctoral Training Partnership grant MR/N014294/1 and a Medical and Life Sciences Research fund award.

REFERENCES

Adams, D. W., and Errington, J. (2009). Bacterial cell division: assembly, maintenance and disassembly of the Z ring. *Nat. Rev. Microbiol.* 7, 642–653. doi: 10.1038/nrmicro2198

Alcorlo, M., Straume, D., Lutkenhaus, J., Håvarstein, L. S., and Hermoso, J. A. (2020). Structural characterization of the essential cell division protein FtsE and its interaction with FtsX in *Streptococcus pneumoniae*. *mBio* 11:e01488-20.

Aussel, L., Barre, F.-X., Aroyo, M., Stasiak, A., Stasiak, A. Z., and Sherratt, D. (2002). FtsK is a DNA motor protein that activates chromosome dimer

resolution by switching the catalytic state of the XerC and XerD recombinases. *Cell* 108, 195–205. doi: 10.1016/s0092-8674(02)00624-4

Austrian, R. (1986). Some aspects of the pneumococcal carrier state. *J Antimicrob Chemother*. 18, 35–45. doi: 10.1093/jac/18.supplement_a.35

Barcus, V. A., Ghanekar, K., Yeo, M., Coffey, T. J., and Dowson, C. G. (1995). Genetics of high level penicillin resistance in clinical isolates of *Streptococcus pneumoniae*. *FEMS Microbiol Lett*. 126, 299–303. doi: 10.1111/j.1574-6968.1995.tb07433.x

Barendt, S. M., Land, A. D., Sham, L.-T., Ng, W.-L., Tsui, H. T., Arnold, R. J., et al. (2009). Influences of capsule on cell shape and chain formation of wild-type and pcsB mutants of serotype 2 *Streptococcus pneumoniae*. *J. Bacteriol.* 191, 3024–3040. doi: 10.1128/jb.01505-08

Bartual, S. G., Straume, D., Stamsås, G. A., Muñoz, I. G., Alfonso, C., Martínez-Ripoll, M., et al. (2014). Structural basis of PcsB-mediated cell separation in *Streptococcus pneum*oniae. *Nat. Commun.* 5:3842.

Berg, K. H., Stamsås, G. A., Straume, D., and Håvarstein, L. S. (2013). Effects of low PBP2b levels on cell morphology and peptidoglycan composition in *Streptococcus pneumoniae* R6. *J. Bacteriol.* 195, 4342–4354. doi: 10.1128/jb.00184-13

Berg, K. H., Straume, D., and Håvarstein, L. S. (2014). The function of the transmembrane and cytoplasmic domains of pneumococcal penicillin-binding proteins 2x and 2b extends beyond that of simple anchoring devices. *Microbiology* 160, 1585–1598. doi: 10.1099/mic.0.078535-0

Bisson-Filho, A. W., Hsu, Y.-P., Squyres, G. R., Kuru, E., Wu, F., Jukes, C., et al. (2017). Treadmilling by FtsZ filaments drives peptidoglycan synthesis and bacterial cell division. *Science* 355, 739–743. doi: 10.1126/science.aak9973

Blencowe, D. K., al Jubori, S., and Morby, A. P. (2011). Identification of a novel function for the FtsL cell division protein from *Escherichia coli*. *Biochem. Biophys. Res. Commun.* 411, 44–49. doi: 10.1016/j.bbrc.2011.06.083

Boersma, M. J., Kuru, E., Rittichier, J., VanNieuwenhze, M. S., Brun, Y., and Winkler, M. E. (2015). Minimal peptidoglycan (PG) turnover in wild-type and PG hydrolase and cell division mutants of *Streptococcus pneumoniae* D39 growing planktonically and in host-relevant biofilms. *J Bacteriol.* 197, 3472–3485. doi: 10.1128/jb.00541-15

Boes, A., Olatunji, S., Breukink, E., and Terrak, M. (2019). Regulation of the peptidoglycan polymerase activity of PBP1b by antagonist actions of the core divisome proteins FtsBLQ and FtsN. *mBio* 10:e01912-18.

Bradshaw, J. L., and McDaniel, L. S. (2019). Selective pressure: Rise of the nonencapsulated pneumococcus. *PLoS Pathog* 15:e1007911. doi: 10.1371/journal.ppat.1007911

Buddelmeijer, N., and Beckwith, J. (2002). Assembly of cell division proteins at the *E. coli* cell center. *Curr. Opin. Microbiol.* 5, 553–557. doi: 10.1016/s1369-5274(02)00374-0

Bush, K., and Bradford, P. A. (2016). β-Lactams and β-Lactamase inhibitors: an overview. *Cold Spring Harb. Perspect Med.* 6:a025247. doi: 10.1101/cshperspect.a025247

Busiek, K. K., and Margolin, W. (2014). A role for FtsA in SPOR-independent localization of the essential *Escherichia coli* cell division protein FtsN. *Mol. Microbiol.* 92, 1212–1226. doi: 10.1111/mmi.12623

Calvez, P., Jouhet, J., Vié, V., Durmort, C., and Zapun, A. (2019). Lipid phases and cell geometry during the cell cycle of *Streptococcus pneumoniae*. *Front. Microbiol.* 10:351. doi: 10.3389/fmicb.2019.00351

Cartee, R. T., Forsee, W. T., and Yother, J. (2005). Initiation and synthesis of the *Streptococcus pneumoniae* Type 3 capsule on a phosphatidylglycerol membrane anchor. *J. Bacteriol.* 187, 4470–4479. doi: 10.1128/jb.187.13.4470-4479.2005

Centers for Disease Control and Prevention (2018). *Active Bacterial Core Surveillance Report, Emerging Infections Program Network, Streptococcus pneumoniae, 2018*. Atlanta, GA: Centers for Disease Control and Prevention.

Chesnel, L., Carapito, R., Croizé, J., Dideberg, O., Vernet, T., and Zapun, A. (2005). Identical Penicillin-Binding Domains in Penicillin-Binding Proteins of *Streptococcus pneumoniae* Clinical Isolates with Different Levels of β-Lactam Resistance. *Antimicrob. Agents Chemother.* 49, 2895–2902. doi: 10.1128/aac.49.7.2895-2902.2005

Cleverley, R. M., Barrett, J. R., Baslé, A., Bui, N. K., Hewitt, L., Solovyova, A., et al. (2014). Structure and function of a spectrin-like regulator of bacterial cytokinesis. *Nat. Commun.* 5:5421.

Cleverley, R. M., Rutter, Z. J., Rismondo, J., Corona, F., Tsui, H.-C. T., Alatawi, F. A., et al. (2019). The cell cycle regulator GpsB functions as cytosolic adaptor for multiple cell wall enzymes. *Nat. Commun.* 10:261.

Cook, J., Baverstock, T. C., McAndrew, M. B. L., Stansfeld, P. J., Roper, D. I., and Crow, A. (2020). Insights into bacterial cell division from a structure of EnvC bound to the FtsX periplasmic domain. *Proc. Natl. Acad. Sci. U S A.* 117, 28355–28365. doi: 10.1073/pnas.2017134117

Dai, K., and Lutkenhaus, J. (1991). ftsZ is an essential cell division gene in *Escherichia coli*. *J Bacteriol.* 173, 3500–3506. doi: 10.1128/jb.173.11.3500-3506.1991

den Blaauwen, T., Andreu, J. M., and Monasterio, O. (2014). Bacterial cell division proteins as antibiotic targets. *Bioorganic Chem.* 55, 27–38. doi: 10.1016/j.bioorg.2014.03.007

den Blaauwen, T., de Pedro, M. A., Nguyen-Distèche, M., and Ayala, J. A. (2008). Morphogenesis of rod-shaped sacculi. *FEMS Microbiol. Rev.* 32, 321–344. doi: 10.1111/j.1574-6976.2007.00090.x

Du, S., and Lutkenhaus, J. (2017). Assembly and activation of the *Escherichia coli* divisome. *Mol. Microbiol.* 102, 177–187.

Du, S., and Lutkenhaus, J. (2019). At the Heart of Bacterial Cytokinesis: the Z Ring. *Trends Microbiol.* 27, 781–791. doi: 10.1016/j.tim.2019.04.011

Duman, R., Ishikawa, S., Celik, I., Strahl, H., Ogasawara, N., Troc, P., et al. (2013). Structural and genetic analyses reveal the protein SepF as a new membrane anchor for the Z ring. *Proc. Natl. Acad. Sci. U S A.* 110, E4601–E4610.

Egan, A. J. F., Errington, J., and Vollmer, W. (2020). Regulation of peptidoglycan synthesis and remodelling. *Nat. Rev. Microbiol.* 18, 446–460. doi: 10.1038/s41579-020-0366-3

Egan, A. J. F., and Vollmer, W. (2013). The physiology of bacterial cell division. *Ann. N Y Acad Sci.* 1277, 8–28. doi: 10.1111/j.1749-6632.2012.06818.x

Eldholm, V., Johnsborg, O., Straume, D., Ohnstad, H. S., Berg, K. H., Hermoso, J. A., et al. (2010). Pneumococcal CbpD is a murein hydrolase that requires a dual cell envelope binding specificity to kill target cells during fratricide. *Mol. Microbiol.* 76, 905–917. doi: 10.1111/j.1365-2958.2010.07143.x

Erickson, H. P., Anderson, D. E., and Osawa, M. (2010). FtsZ in bacterial cytokinesis: cytoskeleton and force generator all in one. *Microbiol. Mol. Biol. Rev. MMBR.* 74, 504–528. doi: 10.1128/mmbr.00021-10

Eswara, P. J., and Ramamurthi, K. S. (2017). Bacterial cell division: nonmodels poised to take the spotlight. *Annu. Rev. Microbiol.* 71, 393–411. doi: 10.1146/annurev-micro-102215-095657

Fadda, D., Santona, A., D'Ulisse, V., Ghelardini, P., Ennas, M. G., Whalen, M. B., et al. (2007). *Streptococcus pneumoniae* DivIVA: localization and interactions in a MinCD-Free Context. *J. Bacteriol.* 189, 1288–1298. doi: 10.1128/jb.01168-06

Fenton, A. K., El Mortaji, L., Lau, D. T. C., Rudner, D. Z., and Bernhardt, T. G. (2016). CozE is a member of the MreCD complex that directs cell elongation in *Streptococcus pneumoniae*. *Nat. Microbiol.* 2:16237.

Fenton, A. K., Manuse, S., Flores-Kim, J., Garcia, P. S., Mercy, C., Grangeasse, C., et al. (2018). Phosphorylation-dependent activation of the cell wall synthase PBP2a in *Streptococcus pneumoniae* by MacP. *Proc Natl Acad Sci. U S A.* 115, 2812–2817. doi: 10.1073/pnas.1715218115

Fisher, J. F., and Mobashery, S. (2020). Constructing and deconstructing the bacterial cell wall. *Protein Sci.* 29, 629–646. doi: 10.1002/pro.3737

Fleurie, A., Cluzel, C., Guiral, S., Freton, C., Galisson, F., Zanella-Cleon, I., et al. (2012). Mutational dissection of the S/T-kinase StkP reveals crucial roles in cell division of *Streptococcus pneumoniae*. *Mol. Microbiol.* 83, 746–758. doi: 10.1111/j.1365-2958.2011.07962.x

Fleurie, A., Manuse, S., Zhao, C., Campo, N., Cluzel, C., Lavergne, J.-P., et al. (2014b). Interplay of the Serine/Threonine-Kinase StkP and the paralogs DivIVA and GpsB in pneumococcal cell elongation and division. *PLoS Genet* 10:e1004275. doi: 10.1371/journal.pgen.1004275

Fleurie, A., Lesterlin, C., Manuse, S., Zhao, C., Cluzel, C., Lavergne, J.-P., et al. (2014a). MapZ marks the division sites and positions FtsZ rings in *Streptococcus pneumoniae*. *Nature* 516, 259–262. doi: 10.1038/nature13966

Fraipont, C., Alexeeva, S., Wolf, B., van der Ploeg, R., Schloesser, M., den Blaauwen, T., et al. (2011). The integral membrane FtsW protein and peptidoglycan synthase PBP3 form a subcomplex in *Escherichia coli*. *Microbiology.* 157, 251–259. doi: 10.1099/mic.0.040071-0

Gallay, C., Sanselicio, S., Anderson, M. E., Soh, Y. M., Liu, X., Stamsås, G. A., et al. (2021). CcrZ is a pneumococcal spatiotemporal cell cycle regulator that

interacts with FtsZ and controls DNA replication by modulating the activity of DnaA. *Nat. Microbiol.* 6, 1175–1187. doi: 10.1038/s41564-021-00949-1

García-Soriano, D. A., Heermann, T., Raso, A., Rivas, G., and Schwille, P. (2020). The speed of FtsZ treadmilling is tightly regulated by membrane binding. *Sci. Rep.* 10:10447.

Geno, K. A., Gilbert, G. L., Song, J. Y., Skovsted, I. C., Klugman, K. P., Jones, C., et al. (2015). Pneumococcal capsules and their types: past. present, and future. *Clin. Microbiol. Rev.* 28, 871–899. doi: 10.1128/cmr.00024-15

Gérard, P., Vernet, T., and Zapun, A. (2002). Membrane Topology of the *Streptococcus pneumoniae* FtsW Division Protein. *J. Bacteriol.* 184, 1925–1931. doi: 10.1128/jb.184.7.1925-1931.2002

Gouëllec, A. L., Roux, L., Fadda, D., Massidda, O., Vernet, T., and Zapun, A. (2008). Roles of pneumococcal DivIB in cell division. *J Bacteriol.* 190, 4501–4511. doi: 10.1128/jb.00376-08

Grangeasse, C. (2016). Rewiring the pneumococcal cell cycle with serine/threonine- and tyrosine-kinases. *Trends Microbiol.* 24, 713–724. doi: 10.1016/j.tim.2016.04.004

Griffith, F. (1928). The significance of pneumococcal types. *Epidemiol. Infect.* 27, 113–159. doi: 10.1017/s0022172400031879

Gueiros-Filho, F. J., and Losick, R. (2002). A widely conserved bacterial cell division protein that promotes assembly of the tubulin-like protein FtsZ. *Genes Dev.* 16, 2544–2556. doi: 10.1101/gad.1014102

Guzman, L.-M., Barondess, J. J., and Beckwith, J. (1992). FtsL, an essential cytoplasmic membrane protein involved in cell division in *Escherichia coli*. *J. Bacteriol.* 174, 7717–7728. doi: 10.1128/jb.174.23.7717-7728.1992

Haeusser, D. P., and Margolin, W. (2016). Splitsville: structural and functional insights into the dynamic bacterial Z ring. *Nat. Rev. Microbiol.* 14, 305–319. doi: 10.1038/nrmicro.2016.26

Hakenbeck, R., Brückner, R., Denapaite, D., and Maurer, P. (2012). Molecular mechanisms of β-lactam resistance in *Streptococcus pneumoniae*. *Future Microbiol.* 7, 395–410. doi: 10.2217/fmb.12.2

Hamoen, L. W., Meile, J.-C., Jong, W. D., Noirot, P., and Errington, J. (2006). SepF, a novel FtsZ-interacting protein required for a late step in cell division. *Mol. Microbiol.* 59, 989–999. doi: 10.1111/j.1365-2958.2005.04987.x

Hausdorff, W. P., Feikin, D. R., and Klugman, K. P. (2005). Epidemiological differences among pneumococcal serotypes. *Lancet Infect Dis.* 5, 83–93. doi: 10.1016/s1473-3099(05)70083-9

Hizukuri, Y., Akiyama, K., and Akiyama, Y. (2017). "Chapter One - biochemical characterization of function and structure of RseP, an Escherichia coli S2P Protease," in *Methods in Enzymology*, ed. M. H. Gelb (Cambridge, MA: Academic Press).

Holečková, N., Doubravová, L., Massidda, O., Molle, V., Buriánková, K., Benada, O., et al. (2014). LocZ is a new cell division protein involved in proper septum placement in *Streptococcus pneumoniae*. *mBio* 6:e01700-14.

Hosek, T., Bougault, C. M., Lavergne, J.-P., Martinez, D., Ayala, I., Fenel, D., et al. (2020). Structural features of the interaction of MapZ with FtsZ and membranes in *Streptococcus pneumoniae*. *Sci. Rep.* 10:4051.

Hsu, Y.-P., Booher, G., Egan, A., Vollmer, W., and VanNieuwenhze, M. S. (2019). d-Amino acid derivatives as in situ probes for visualizing bacterial peptidoglycan biosynthesis. *Acc. Chem. Res.* 52, 2713–2722. doi: 10.1021/acs.accounts.9b00311

Hsu, Y.-P., Rittichier, J., Kuru, E., Yablonowski, J., Pasciak, E., Tekkam, S., et al. (2017). Full color palette of fluorescent D-amino acids for in situ labeling of bacterial cell walls. *Chem. Sci.* 8, 6313–6321. doi: 10.1039/c7sc01800b

Jacq, M., Adam, V., Bourgeois, D., Moriscot, C., Di Guilmi, A. M., Vernet, T., et al. (2015). Remodeling of the Z-Ring nanostructure during the *Streptococcus pneumoniae* cell cycle revealed by photoactivated localization microscopy. *mBio* 6:e01108-5.

Jacq, M., Arthaud, C., Manuse, S., Mercy, C., Bellard, L., Peters, K., et al. (2018). The cell wall hydrolase Pmp23 is important for assembly and stability of the division ring in Streptococcus pneumoniae. *Sci. Rep.* 8:7591.

Jean, N. L., Rutherford, T. J., and Löwe, J. (2020). FtsK in motion reveals its mechanism for double-stranded DNA translocation. *Proc. Natl. Acad. Sci. U S A.* 117, 14202–14208. doi: 10.1073/pnas.2001324117

Jefferies, J. M. C., Smith, A., Clarke, S. C., Dowson, C., and Mitchell, T. J. (2004). Genetic analysis of diverse disease-causing pneumococci indicates high levels of diversity within serotypes and capsule switching. *J. Clin. Microbiol.* 42, 5681–5688. doi: 10.1128/jcm.42.12.5681-5688.2004

Khanna, K., Lopez-Garrido, J., and Pogliano, K. (2020). Shaping an endospore: architectural transformations during *Bacillus subtilis* sporulation. *Annu. Rev. Microbiol.* 74, 361–386.

Koedel, U., Scheld, W. M., and Pfister, H.-W. (2002). Pathogenesis and pathophysiology of pneumococcal meningitis. *Lancet Infect Dis.* 2, 721–736. doi: 10.1016/s1473-3099(02)00450-4

Krupka, M., Cabré, E. J., Jiménez, M., Rivas, G., Rico, A. I., and Vicente, M. (2014). Role of the FtsA C Terminus as a switch for polymerization and membrane association. *mBio* 5:e02221.

Krupka, M., Sobrinos-Sanguino, M., Jiménez, M., Rivas, G., and Margolin, W. (2018). ZipA organizes FtsZ polymers into dynamic ring-like protofilament structures *Escherichia coli*. *mBio* 9:e1008-18.

Kuru, E., Hughes, H. V., Brown, P. J., Hall, E., Tekkam, S., Cava, F., et al. (2012). In situ probing of newly synthesized peptidoglycan in live bacteria with fluorescent d-amino acids. *Angew Chem.* 124, 12687–12691. doi: 10.1002/ange.201206749

Kuru, E., Radkov, A., Meng, X., Egan, A., Alvarez, L., Dowson, A., et al. (2019). Mechanisms of incorporation for d-amino acid probes that target peptidoglycan biosynthesis. *ACS Chem. Biol.* 14, 2745–2756. doi: 10.1021/acschembio.9b00664

Land, A. D., Tsui, H.-C. T., Kocaoglu, O., Vella, S. A., Shaw, S. L., Keen, S. K., et al. (2013). Requirement of essential Pbp2x and GpsB for septal ring closure in *Streptococcus pneumoniae* D39. *Mol. Microbiol.* 90, 939–955. doi: 10.1111/mmi.12408

Land, A. D., and Winkler, M. E. (2011). The requirement for pneumococcal MreC and MreD is relieved by inactivation of the gene encoding PBP1a. *J. Bacteriol.* 193, 4166–4179. doi: 10.1128/jb.05245-11

Leeuw, E. D., Graham, B., Phillips, G. J., Hagen-Jongman, C. M. T., Oudega, B., and Luirink, J. (1999). Molecular characterization of *Escherichia coli* FtsE and FtsX. *Mol. Microbiol.* 31, 983–993. doi: 10.1046/j.1365-2958.1999.01245.x

Levin, P. A., Kurtser, I. G., and Grossman, A. D. (1999). Identification and characterization of a negative regulator of FtsZ ring formation in *Bacillus subtilis*. *Proc. Natl. Acad. Sci. U S A.* 96, 9642–9647. doi: 10.1073/pnas.96.17.9642

Li, Y., Shao, S., Xu, X., Su, X., Sun, Y., and Wei, S. (2018). MapZ forms a stable ring structure that acts as a nanotrack for ftsz treadmilling in *Streptococcus mutans*. *ACS Nano.* 12, 6137–6146.

Liu, B., Persons, L., Lee, L., and de Boer, P. A. J. (2015). Roles for both FtsA and the FtsBLQ subcomplex in FtsN-stimulated cell constriction in *Escherichia coli*. *Mol Microbiol.* 95, 945–970. doi: 10.1111/mmi.12906

Lynch, J. P. I., and Zhanel, G. G. (2010). *Streptococcus pneumoniae*: epidemiology and risk factors, evolution of antimicrobial resistance, and impact of vaccines. *Curr. Opin. Pulm Med.* 16, 217–225.

Macheboeuf, P., Contreras-Martel, C., Job, V., Dideberg, O., and Dessen, A. (2006). Penicillin binding proteins: key players in bacterial cell cycle and drug resistance processes. *FEMS Microbiol. Rev.* 30, 673–691. doi: 10.1111/j.1574-6976.2006.00024.x

Manuse, S., Fleurie, A., Zucchini, L., Lesterlin, C., and Grangeasse, C. (2016). Role of eukaryotic-like serine/threonine kinases in bacterial cell division and morphogenesis. *FEMS Microbiol. Rev.* 40, 41–56. doi: 10.1093/femsre/fuv041

Marmont, L. S., and Bernhardt, T. G. (2020). A conserved subcomplex within the bacterial cytokinetic ring activates cell wall synthesis by the FtsW-FtsI synthase. *Proc. Natl. Acad. Sci. U S A.* 117, 23879–23885. doi: 10.1073/pnas.2004598117

Massey, T. H., Mercogliano, C. P., Yates, J., Sherratt, D. J., and Löwe, J. (2006). Double-Stranded DNA translocation: structure and mechanism of hexameric FtsK. *Mol. Cell.* 23, 457–469. doi: 10.1016/j.molcel.2006.06.019

Massidda, O., Nováková, L., and Vollmer, W. (2013). From models to pathogens: how much have we learned about *Streptococcus pneumoniae* cell division? *Environ. Microbiol.* 15, 3133–3157. doi: 10.1111/1462-2920.12189

Masson, S., Kern, T., Gouëllec, A. L., Giustini, C., Simorre, J.-P., Callow, P., et al. (2009). Central domain of DivIB caps the C-terminal regions of the FtsL/DivIC Coiled-coil Rod. *J. Biol. Chem.* 284, 27687–27700. doi: 10.1074/jbc.m109.019471

McCausland, J. W., Yang, X., Squyres, G. R., Lyu, Z., Bruce, K. E., Lamanna, M. M., et al. (2021). Treadmilling FtsZ polymers drive the directional movement of SPG-Synthesis enzymes via a brownian ratchet mechanism. *Nat. Commun.* 12:609.

Meier, E. L., and Goley. (2014). Form and function of the bacterial cytokinetic ring. *Curr. Opin. Cell Biol.* 26, 19–27. doi: 10.1016/j.ceb.2013.08.006

Meisner, J., Llopis, P. M., Sham, L.-T., Garner, E., Bernhardt, T. G., and Rudner, D. Z. (2013). FtsEX is required for CwlO peptidoglycan hydrolase activity during cell wall elongation in *Bacillus subtilis*. *Mol. Microbiol.* 89, 1069–1083. doi: 10.1111/mmi.12330

Mercy, C., Ducret, A., Slager, J., Lavergne, J.-P., Freton, C., Nagarajan, S. N., et al. (2019). RocS drives chromosome segregation and nucleoid protection in *Streptococcus pneumoniae*. *Nat. Microbiol.* 4, 1661–1670. doi: 10.1038/s41564-019-0472-z

Moffitt, K. L., Gierahn, T. M., Lu, Y., Gouveia, P., Alderson, M., Flechtner, J. B., et al. (2011). TH17-Based vaccine design for prevention of *Streptococcus pneumoniae* colonization. *Cell Host Microbe* 9, 158–165. doi: 10.1016/j.chom.2011.01.007

Monteiro, J. M., Fernandes, P. B., Vaz, F., Pereira, A. R., Tavares, A. C., Ferreira, M. T., et al. (2015). Cell shape dynamics during the staphylococcal cell cycle. *Nat. Commun.* 6:8055.

Müller, P., Ewers, C., Bertsche, U., Anstett, M., Kallis, T., Breukink, E., et al. (2007). The essential cell division protein FtsN interacts with the murein (Peptidoglycan) synthase PBP1B in *Escherichia coli*. *J. Biol. Chem.* 282, 36394–36402. doi: 10.1074/jbc.m706390200

Mura, A., Fadda, D., Perez, A. J., Danforth, M. L., Musu, D., Rico, A. I., et al. (2017). Roles of the essential protein FtsA in cell growth and division in *Streptococcus pneumoniae*. *J. Bacteriol.* 199, e608–e616.

Ng, W.-L., Tsui, H.-C. T., and Winkler, M. E. (2005). Regulation of the pspA virulence factor and essential pcsB murein biosynthetic genes by the phosphorylated VicR (YycF) response regulator in *Streptococcus pneumoniae*. *J. Bacteriol.* 187, 7444–7459. doi: 10.1128/jb.187.21.7444-7459.2005

Ng, W.-L., and Winkler, M. E. (2004). Singular structures and operon organizations of essential two-component systems in species of *Streptococcus*. *Microbiology* 150, 3096–3098. doi: 10.1099/mic.0.27550-0

Noirclerc-Savoye, M., Gouëllec, A. L., Morlot, C., Dideberg, O., Vernet, T., and Zapun, A. (2005). In vitro reconstitution of a trimeric complex of DivIB, DivIC and FtsL, and their transient co-localization at the division site in *Streptococcus pneumoniae*. *Mol. Microbiol.* 55, 413–424. doi: 10.1111/j.1365-2958.2004.04408.x

Pasquina-Lemonche, L., Burns, J., Turner, R. D., Kumar, S., Tank, R., Mullin, N., et al. (2020). The architecture of the Gram-positive bacterial cell wall. *Nature* 582, 294–297.

Pazos, M., and Vollmer, W. (2021). Regulation and function of class a Penicillin-binding proteins. *Curr. Opin. Microbiol.* 60, 80–87. doi: 10.1016/j.mib.2021.01.008

Pease, P. J., Levy, O., Cost, G. J., Gore, J., Ptacin, J. L., Sherratt, D., et al. (2005). Sequence-Directed DNA translocation by purified FtsK. *Science* 307, 586–590. doi: 10.1126/science.1104885

Pereira, A., Hsin, J., Król, E., Tavares, A. C., Flores, P., Hoiczyk, E., et al. (2016). FtsZ-Dependent elongation of a coccoid bacterium. *mBio* 7:e00908-16.

Perez, A. J., Cesbron, Y., Shaw, S. L., Villicana, J. B., Tsui, H.-C. T., Boersma, M. J., et al. (2019). Movement dynamics of divisome proteins and PBP2x:FtsW in cells of *Streptococcus pneumoniae*. *Proc. Natl. Acad. Sci. U S A.* 116, 3211–3220. doi: 10.1073/pnas.1816018116

Perez, A. J., Boersma, M. J., Bruce, K. E., Lamanna, M. M., Shaw, S. L., Tsui, H.-C. T., et al. (2021b). Organization of peptidoglycan synthesis in nodes and separate rings at different stages of cell division of *Streptococcus pneumoniae*. *Mol. Microbiol.* 115, 1152–1169. doi: 10.1111/mmi.14659

Perez, A. J., Bazan Vollicana, J., Tsui, H.-C. T., Danforth, M. L., Benedet, M., Massidda, O., et al. (2021a). FtsZ-ring regulation and cell division are mediated by essential EzrA and accessory proteins ZapA, ZapJ, and SepF in *Streptococcus pneumoniae*. *Front. Microbiol.*

Philippe, J., Gallet, B., Morlot, C., Denapaite, D., Hakenbeck, R., Chen, Y., et al. (2015). Mechanism of β-Lactam action in *Streptococcus pneumoniae*: the piperacillin paradox. *Antimicrob. Agents Chemother.* 59, 609–621. doi: 10.1128/aac.04283-14

Philippe, J., Vernet, T., and Zapun, A. (2014). The elongation of ovococci. *Microb Drug Resist.* 20, 215–221. doi: 10.1089/mdr.2014.0032

Pichoff, S., Du, S., and Lutkenhaus, J. (2019). Roles of FtsEX in cell division. *Res. Microbiol.* 170, 374–380. doi: 10.1016/j.resmic.2019.07.003

Pichoff, S., and Lutkenhaus, J. (2005). Tethering the Z ring to the membrane through a conserved membrane targeting sequence in FtsA. *Mol. Microbiol.* 55, 1722–1734. doi: 10.1111/j.1365-2958.2005.04522.x

Pinho, M. G., Kjos, M., and Veening, J.-W. (2013). How to get (a)round: mechanisms controlling growth and division of coccoid bacteria. *Nat. Rev. Microbiol.* 11, 601–614. doi: 10.1038/nrmicro3088

Reichmann, N. T., Tavares, A. C., Saraiva, B. M., Jousselin, A., Reed, P., Pereira, A. R., et al. (2019). SEDS–bPBP pairs direct lateral and septal peptidoglycan synthesis in *Staphylococcus aureus*. *Nat. Microbiol.* 4, 1368–1377. doi: 10.1038/s41564-019-0437-2

Rohs, P. D. A., Buss, J., Sim, S. I., Squyres, G. R., Srisuknimit, V., Smith, M., et al. (2018). A central role for PBP2 in the activation of peptidoglycan polymerization by the bacterial cell elongation machinery. *PLoS Genet.* 14:e1007726. doi: 10.1371/journal.pgen.1007726

Rued, B. E., Alcorlo, M., Edmonds, K. A., Martínez-Caballero, S., Straume, D., Fu, Y., et al. (2019). Structure of the large extracellular loop of FtsX and Its interaction with the essential peptidoglycan hydrolase PcsB in *Streptococcus pneumoniae*. *mBio* 10:e02622-18.

Rued, B. E., Zheng, J. J., Mura, A., Tsui, H.-C. T., Boersma, M. J., Mazny, J. L., et al. (2017). Suppression and synthetic-lethal genetic relationships of ΔgpsB mutations indicate that GpsB mediates protein phosphorylation and penicillin-binding protein interactions in *Streptococcus pneumoniae* D39. *Mol. Microbiol.* 103, 931–957. doi: 10.1111/mmi.13613

Saraiva, B. M., Sorg, M., Pereira, A. R., Ferreira, M. J., Caulat, L. C., Reichmann, N. T., et al. (2020). Reassessment of the distinctive geometry of *Staphylococcus aureus* cell division. *Nat. Commun.* 11:4097.

Sham, L.-T., Barendt, S. M., Kopecky, K. E., and Winkler, M. E. (2011). Essential PcsB putative peptidoglycan hydrolase interacts with the essential FtsXSpn cell division protein in *Streptococcus pneumoniae* D39. *Proc Natl Acad Sci. U S A.* 108, E1061–E1069.

Sham, L.-T., Jensen, K. R., Bruce, K. E., and Winkler, M. E. (2013). Involvement of FtsE ATPase and FtsX extracellular loops 1 and 2 in FtsEX-PcsB complex function in cell division of *Streptococcus pneumoniae* D39. *mBio* 4:e00431-13.

Shapiro, Berg, A. T., Austrian, R., Schroeder, D., Parcells, V., Margolis, A., et al. (1991). The protective efficacy of polyvalent pneumococcal polysaccharide vaccine. *N. Engl. J. Med.* 325, 1453–1460. doi: 10.1056/nejm199111213252101

Sharifzadeh, S., Boersma, M. J., Kocaoglu, O., Shokri, A., Brown, C. L., Shirley, J. D., et al. (2017). Novel electrophilic scaffold for imaging of essential penicillin-binding proteins in *Streptococcus pneumoniae*. *ACS Chem. Biol.* 12, 2849–2857. doi: 10.1021/acschembio.7b00614

Sharifzadeh, S., Brown, N. W., Shirley, J. D., Bruce, K. E., Winkler, M. E., and Carlson, E. E. (2020). Chemical tools for selective activity profiling of bacterial penicillin-binding proteins. *Methods Enzymol.* 638, 27–55. doi: 10.1016/bs.mie.2020.02.015

Sievers, J., and Errington, J. (2000). The *Bacillus subtilis* cell division protein FtsL localizes to sites of septation and interacts with DivIC. *Mol. Microbiol.* 36, 846–855. doi: 10.1046/j.1365-2958.2000.01895.x

Singh, J. K., Makde, R. D., Kumar, V., and Panda, D. (2008). SepF increases the assembly and bundling of FtsZ polymers and stabilizes FtsZ protofilaments by binding along its length. *J. Biol. Chem.* 283, 31116–31124. doi: 10.1074/jbc.m805910200

Sjodt, M., Brock, K., Dobihal, G., Rohs, P. D. A., Green, A. G., Hopf, T. A., et al. (2018). Structure of the peptidoglycan polymerase RodA resolved by evolutionary coupling analysis. *Nature* 556, 118–121. doi: 10.1038/nature25985

Sjodt, M., Rohs, P. D. A., Gilman, M. S. A., Erlandson, S. C., Zheng, S., Green, A. G., et al. (2020). Structural coordination of polymerization and crosslinking by a SEDS–bPBP peptidoglycan synthase complex. *Nat. Microbiol.* 5, 813–820. doi: 10.1038/s41564-020-0687-z

Sørensen, U. B. S., Henrichsen, J., Chen, H.-C., and Szu, S. C. (1990). Covalent linkage between the capsular polysaccharide and the cell wall peptidoglycan of *Streptococcus pneumoniae* revealed by immunochemical methods. *Microb Pathog.* 8, 325–334. doi: 10.1016/0882-4010(90)90091-4

Squyres, G. R., Holmes, M. J., Barger, S. R., Pennycook, B. R., Ryan, J., Yan, V. T., et al. (2021). Single-molecule imaging reveals that Z-ring condensation is essential for cell division in Bacillus subtilis. *Nat. Microbiol.* 6, 553–562. doi: 10.1038/s41564-021-00878-z

Stamsås, G. A., Myrbråten, I. S., Straume, D., Salehian, Z., Veening, J.-W., Håvarstein, L. S., et al. (2018). CozEa and CozEb play overlapping and essential

roles in controlling cell division in *Staphylococcus aureus*. *Mol. Microbiol.* 109, 615–632. doi: 10.1111/mmi.13999

Stamsås, G. A., Straume, D., Winther, A. R., Kjos, M., Frantzen, C. A., and Håvarstein, L. S. (2017). Identification of EloR (Spr1851) as a regulator of cell elongation in *Streptococcus pneumoniae*. *Mol. Microbiol.* 105, 954–967. doi: 10.1111/mmi.13748

Straume, D., Piechowiak, K. W., Kjos, M., and Håvarstein, L. S. (2021). Class A PBPs: It is time to rethink traditional paradigms. *Mol. Microbiol.* 116, 41–52. doi: 10.1111/mmi.14714

Straume, D., Piechowiak, K. W., Olsen, S., Stamsås, G. A., Berg, K. H., Kjos, M., et al. (2020). Class A PBPs have a distinct and unique role in the construction of the pneumococcal cell wall. *Proc. Natl. Acad. Sci. U S A.* 117, 6129–6138. doi: 10.1073/pnas.1917820117

Straume, D., Stamsås, G. A., Berg, K. H., Salehian, Z., and Håvarstein, L. S. (2017). Identification of pneumococcal proteins that are functionally linked to penicillin-binding protein 2b (PBP2b). *Mol. Microbiol.* 103, 99–116. doi: 10.1111/mmi.13543

Szwedziak, P., Wang, Q., Freund, S. M., and Löwe, J. (2012). FtsA forms actin-like protofilaments. *EMBO J.* 31, 2249–2260. doi: 10.1038/emboj.2012.76

Taguchi, A., Page, J., Tsui, H.-C. T., Winkler, M. E., and Walker, S. (2021). Biochemical reconstitution defines new functions for membrane-bound glycosidases in assembly of the bacterial cell wall. *Proc. Natl. Acad. Sci. U S A.* 118:e2103740118.

Taguchi, A., Welsh, M. A., Marmont, L. S., Lee, W., Sjodt, M., Kruse, A. C., et al. (2019). FtsW is a peptidoglycan polymerase that is functional only in complex with its cognate penicillin-binding protein. *Nat. Microbiol.* 4, 587–594. doi: 10.1038/s41564-018-0345-x

Thanassi, J. A., Hartman-Neumann, S. L., Dougherty, T. J., Dougherty, B. A., and Pucci, M. J. (2002). Identification of 113 conserved essential genes using a high-throughput gene disruption system in *Streptococcus pneumoniae*. *Nucleic Acids Res.* 30, 3152–3162. doi: 10.1093/nar/gkf418

Trouve, J., Zapun, A., Arthaud, C., Durmort, C., Guilmi, A. M. D., Söderström, B., et al. (2021). Nanoscale dynamics of peptidoglycan assembly during the cell cycle of *Streptococcus pneumoniae*. *Curr. Biol.* 31, 2844–2856. doi: 10.1016/j.cub.2021.04.041

Trusca, D., Scott, S., Thompson, C., and Bramhill, D. (1998). Bacterial SOS checkpoint protein SulA inhibits polymerization of purified FtsZ cell division protein. *J. Bacteriol.* 180, 3946–3953. doi: 10.1128/jb.180.15.3946-3953.1998

Tsui, H.-C. T., Boersma, M. J., Vella, S. A., Kocaoglu, O., Kuru, E., Peceny, J. K., et al. (2014). Pbp2x localizes separately from Pbp2b and other peptidoglycan synthesis proteins during later stages of cell division of *Streptococcus pneumoniae* D39. *Mol. Microbiol.* 94, 21–40. doi: 10.1111/mmi.12745

Tsui, H.-C. T., Zheng, J. J., Magallon, A. N., Ryan, J. D., Yunck, R., Rued, B. E., et al. (2016). Suppression of a deletion mutation in the gene encoding essential PBP2b reveals a new lytic transglycosylase involved in peripheral peptidoglycan synthesis in *Streptococcus pneumoniae* D39. *Mol. Microbiol.* 100, 1039–1065. doi: 10.1111/mmi.13366

Turner, R. D., Ratcliffe, E. C., Wheeler, R., Golestanian, R., Hobbs, J. K., and Foster, S. J. (2010). Peptidoglycan architecture can specify division planes in *Staphylococcus aureus*. *Nat. Commun.* 1:26.

Typas, A., Banzhaf, M., Gross, C. A., and Vollmer, W. (2012). From the regulation of peptidoglycan synthesis to bacterial growth and morphology. *Nat. Rev. Microbiol.* 10, 123–136. doi: 10.1038/nrmicro2677

Tzagoloff, H., and Novick, R. (1977). Geometry of cell division in *Staphylococcus aureus*. *J. Bacteriol.* 129, 343–350. doi: 10.1128/jb.129.1.343-350.1977

van Opijnen, T., Bodi, K. L., and Camilli, A. (2009). Tn-seq: high-throughput parallel sequencing for fitness and genetic interaction studies in microorganisms. *Nat. Methods* 6, 767–772. doi: 10.1038/nmeth.1377

Vigouroux, A., Cordier, B., Aristov, A., Alvarez, L., Özbaykal, G., Chaze, T., et al. (2020). Class-A penicillin binding proteins do not contribute to cell shape but repair cell-wall defects. Akhmanova A, Xiao J, Xiao J, Dörr T, editors. *eLife* 9:e51998.

Viljoen, A., Foster, S. J., Fantner, G. E., Hobbs, J. K., and Dufrêne, Y. F. (2020). Scratching the surface: bacterial cell envelopes at the nanoscale. *mBio* 11:e03020-19.

Vollmer, W., Blanot, D., and De Pedro, M. A. (2008). Peptidoglycan structure and architecture. *FEMS Microbiol. Rev.* 32, 149–167. doi: 10.1111/j.1574-6976.2007.00094.x

Vollmer, W., Massidda, O., and Tomasz, A. (2019). The Cell Wall of *Streptococcus pneumoniae*. *Microbiol. Spectr.* 7. doi: 10.1128/microbiolspec.GPP3-0018-2018

Wadenpohl, I., and Bramkamp, M. (2010). DivIC stabilizes FtsL against RasP Cleavage. *J. Bacteriol.* 192, 5260–5263. doi: 10.1128/jb.00287-10

Weiser, J. N., Ferreira, D. M., and Paton, J. C. (2018). *Streptococcus pneumoniae* : transmission, colonization and invasion. *Nat. Rev. Microbiol.* 16, 355–367. doi: 10.1038/s41579-018-0001-8

Wheeler, R., Mesnage, S., Boneca, I. G., Hobbs, J. K., and Foster, S. J. (2011). Super-resolution microscopy reveals cell wall dynamics and peptidoglycan architecture in ovococcal bacteria. *Mol. Microbiol.* 82, 1096–1109. doi: 10.1111/j.1365-2958.2011.07871.x

Willis, L., and Huang, K. C. (2017). Sizing up the bacterial cell cycle. *Nat. Rev. Microbiol.* 15, 606–620. doi: 10.1038/nrmicro.2017.79

Winkler, M. E. (2021). Undermodification cues division. *Nat. Chem. Biol.* 17, 841–843. doi: 10.1038/s41589-021-00818-2

Winther, A. R., Kjos, M., Herigstad, M. L., Håvarstein, L. S., and Straume, D. (2021). EloR interacts with the lytic transglycosylase MltG at midcell in *Streptococcus pneumoniae* R6. *J. Bacteriol.* 203, e691–e620.

Yang, X., Lyu, Z., Miguel, A., McQuillen, R., Huang, K. C., and Xiao, J. (2017). GTPase activity–coupled treadmilling of the bacterial tubulin FtsZ organizes septal cell wall synthesis. *Science* 355, 744–747. doi: 10.1126/science.aak9995

Yang, X., McQuillen, R., Lyu, Z., Phillips-Mason, P., De La Cruz, A., McCausland, J. W., et al. (2021). A two-track model for the spatiotemporal coordination of bacterial septal cell wall synthesis revealed by single-molecule imaging of FtsW. *Nat. Microbiol.* 6, 584–593. doi: 10.1038/s41564-020-00853-0

Zamakhaeva, S., Chaton, C. T., Rush, J. S., Ajay Castro, S., Kenner, C. W., Yarawsky, A. E., et al. (2021). Modification of cell wall polysaccharide guides cell division in *Streptococcus mutans*. *Nat. Chem. Biol.* 17, 878–887. doi: 10.1038/s41589-021-00803-9

Zapun, A., Vernet, T., and Pinho, M. G. (2008b). The different shapes of cocci. *FEMS Microbiol. Rev.* 32, 345–360. doi: 10.1111/j.1574-6976.2007.00098.x

Zapun, A., Contreras-Martel, C., and Vernet, T. (2008a). Penicillin-binding proteins and β-lactam resistance. *FEMS Microbiol. Rev.* 32, 361–385. doi: 10.1111/j.1574-6976.2007.00095.x

Zapun, A., Noirclerc-Savoye, M., Helassa, N., and Vernet, T. (2012). Peptidoglycan assembly machines: the biochemical evidence | microbial drug resistance. *Microb Drug Resist.* 18, 256–260. doi: 10.1089/mdr.2011.0236

Zhao, Z., Zhao, Y., Zhuang, X.-Y., Lo, W.-C., Baker, M. A. B., Lo, C.-J., et al. (2018). Frequent pauses in *Escherichia coli* flagella elongation revealed by single cell real-time fluorescence imaging. *Nat. Commun.* 9:1885.

Zheng, J. J., Perez, A. J., Tsui, H.-C. T., Massidda, O., and Winkler, M. E. (2017). Absence of the KhpA and KhpB (JAG/EloR) RNA-binding proteins suppresses the requirement for PBP2b by overproduction of FtsA in *Streptococcus pneumoniae* D39. *Mol. Microbiol.* 106, 793–814. doi: 10.1111/mmi.13847

Conflict of Interest: The authors declare that the research was conducted in the absence of any commercial or financial relationships that could be construed as a potential conflict of interest.

Publisher's Note: All claims expressed in this article are solely those of the authors and do not necessarily represent those of their affiliated organizations, or those of the publisher, the editors and the reviewers. Any product that may be evaluated in this article, or claim that may be made by its manufacturer, is not guaranteed or endorsed by the publisher.

frontiers in Microbiology

ORIGINAL RESEARCH
published: 02 December 2021
doi: 10.3389/fmicb.2021.780864

FtsZ-Ring Regulation and Cell Division Are Mediated by Essential EzrA and Accessory Proteins ZapA and ZapJ in *Streptococcus pneumoniae*

*Amilcar J. Perez[1], Jesus Bazan Villicana[1], Ho-Ching T. Tsui[1], Madeline L. Danforth[1], Mattia Benedet[2], Orietta Massidda[2] and Malcolm E. Winkler[1]**

[1] Department of Biology, Indiana University Bloomington, Bloomington, IN, United States, [2] Department of Cellular, Computational and Integrative Biology (CIBIO), University of Trento, Trento, Italy

OPEN ACCESS

Edited by:
Shishen Du,
Wuhan University, China

Reviewed by:
Leendert Hamoen,
University of Amsterdam, Netherlands
Richard A. Daniel,
Newcastle University, United Kingdom

***Correspondence:**
Malcolm E. Winkler
winklerm@indiana.edu

Specialty section:
This article was submitted to Microbial Physiology and Metabolism, a section of the journal Frontiers in Microbiology

Received: *21 September 2021*
Accepted: *22 October 2021*
Published: *02 December 2021*

Citation:
Perez AJ, Villicana JB, Tsui H-CT, Danforth ML, Benedet M, Massidda O and Winkler ME (2021) FtsZ-Ring Regulation and Cell Division Are Mediated by Essential EzrA and Accessory Proteins ZapA and ZapJ in Streptococcus pneumoniae. Front. Microbiol. 12:780864. doi: 10.3389/fmicb.2021.780864

The bacterial FtsZ-ring initiates division by recruiting a large repertoire of proteins (the divisome; Z-ring) needed for septation and separation of cells. Although FtsZ is essential and its role as the main orchestrator of cell division is conserved in most eubacteria, the regulators of Z-ring presence and positioning are not universal. This study characterizes factors that regulate divisome presence and placement in the ovoid-shaped pathogen, *Streptococcus pneumoniae* (*Spn*), focusing on FtsZ, EzrA, SepF, ZapA, and ZapJ, which is reported here as a partner of ZapA. Epi-fluorescence microscopy (EFm) and high-resolution microscopy experiments showed that FtsZ and EzrA co-localize during the entire *Spn* cell cycle, whereas ZapA and ZapJ are late-arriving divisome proteins. Depletion and conditional mutants demonstrate that EzrA is essential in *Spn* and required for normal cell growth, size, shape homeostasis, and chromosome segregation. Moreover, EzrA(*Spn*) is required for midcell placement of FtsZ-rings and PG synthesis. Notably, overexpression of EzrA leads to the appearance of extra Z-rings in *Spn*. Together, these observations support a role for EzrA as a positive regulator of FtsZ-ring formation in *Spn.* Conversely, FtsZ is required for EzrA recruitment to equatorial rings and for the organization of PG synthesis. In contrast to EzrA depletion, which causes a bacteriostatic phenotype in *Spn*, depletion of FtsZ results in enlarged spherical cells that are subject to LytA-dependent autolysis. Co-immunoprecipitation and bacterial two-hybrid assays show that EzrA(*Spn*) is in complexes with FtsZ, Z-ring regulators (FtsA, SepF, ZapA, MapZ), division proteins (FtsK, StkP), and proteins that mediate peptidoglycan synthesis (GpsB, aPBP1a), consistent with a role for EzrA at the interface of cell division and PG synthesis. In contrast to the essentiality of FtsZ and EzrA, ZapA and SepF have accessory roles in regulating pneumococcal physiology. We further show that ZapA interacts with a non-ZapB homolog, named here as ZapJ, which

is conserved in *Streptococcus* species. The absence of the accessory proteins, ZapA, ZapJ, and SepF, exacerbates growth defects when EzrA is depleted or MapZ is deleted. Taken together, these results provide new information about the spatially and temporally distinct proteins that regulate FtsZ-ring organization and cell division in *Spn*.

Keywords: EzrA function, FtsZ-ring formation, MapZ(LocZ), SepF, ZapA, ZapJ (Spd_1350), localization of peptidoglycan synthesis

INTRODUCTION

Bacterial cell division initiates by polymerization of the highly conserved and essential tubulin-like protein FtsZ into a dynamic Z-ring composed of FtsZ treadmilling filaments (Bi and Lutkenhaus, 1991; Lutkenhaus et al., 2012; Haeusser and Margolin, 2016; Bisson-Filho et al., 2017; Yang et al., 2017; Perez et al., 2019). The dynamic Z-ring recruits a large number of proteins into the divisome needed for septal peptidoglycan (PG) synthesis, septation, and separation of cells (Den Blaauwen et al., 2003; Aarsman et al., 2005; Gamba et al., 2009; Trip and Scheffers, 2015). Many studies of FtsZ-ring regulation and cell division have been performed on model rod-shaped bacteria, including *Escherichia coli* (*Eco*; Gram-negative), *Bacillus subtilis* (*Bsu*; Gram-positive), and *Caulobacter crescentus* (*Ccr*; Gram-negative) (Thanbichler and Shapiro, 2006; Coltharp et al., 2016, Yu et al., 2021). In these bacteria, the position of the Z-ring is dictated largely by negative regulatory systems (Min and nucleoid occlusion in *Bsu* and *Eco* and MipZ in *Ccr*); yet, a many other bacteria with different cell shapes do not follow the paradigms from these model rod-shaped bacteria (reviewed by Monahan et al., 2014). *Streptococcus pneumoniae* (*Spn*; pneumococcus) is a low-GC Gram-positive, ovoid-shaped commensal bacterium that can act as a drug-resistant, opportunistic pathogen and serious threat to human health (Weiser et al., 2018). *Spn* and other species of *Streptococci* lack Min and nucleoid occlusion systems and form Z-rings over the nucleoid at early stages of division (Land et al., 2013). The mechanisms leading to midcell Z-ring placement and regulation in cell division and septal PG synthesis have only recently begun to be understood in ovoid-shaped bacteria like *Spn* (Briggs et al., 2021), despite their potential to reveal vulnerabilities for the discovery of new antibiotics and vaccines.

The ovoid shape of *Spn* is maintained by a thick PG layer that provides protection against osmotic stress-induced cell lysis (Vollmer et al., 2019). Morphogenesis of the cell wall into an ovoid shape is achieved through the activities and coordination of two PG synthesis systems that occur at the midcell plane, where the FtsZ-ring assembles (**Supplementary Figure 1A**). Septal peptidoglycan synthesis (sPG) is carried out in part by the bPBP2x:FtsW PG synthase that inserts PG at the leading edge of the closing septal annulus (Perez et al., 2021). Peripheral PG (pPG) synthesis is mediated by the bPBP2b:RodA synthase pair that catalyzes cellular elongation pushing outward from the midcell ring (**Supplementary Figure 1A**, middle). In pneumococcus, the sPG and pPG syntheses occur nearly simultaneously throughout the cell cycle (Wheeler et al., 2011; Perez et al., 2021; Trouve et al., 2021). Unlike rod-shaped *Bsu* and *Eco*, *Spn* lacks MreB actin-like proteins to organize lateral cell-wall synthesis (Vollmer et al., 2019). In *Spn*, FtsZ and its closely associated proteins initially organize the sPG and pPG synthesis machines in a single ring at the equators of newly divided cells (**Supplementary Figure 1A**, top) (Massidda et al., 2013; Briggs et al., 2021; Perez et al., 2021). As septation and elongation begin, the Z-ring moves as an inner ring at the leading edge of the closing septal annulus, while pPG synthesis occurs in a separate outer ring lacking FtsZ at the base of the septal annulus (**Supplementary Figure 1A**, middle) (Perez et al., 2021). Thus, FtsZ-ring regulation initially organizes both cell division and elongation in *Spn*.

In ovoid-shaped bacteria, such as *Spn*, MapZ (LocZ) positively regulates FtsZ-ring placement at the equators of daughter cells (Fleurie et al., 2014a; Holeckova et al., 2015). MapZ-rings bound to PG split from the initial midcell Z-ring of newly divided cells and are moved, presumably by pPG synthesis, toward the future equators of daughter cells (**Supplementary Figure 1A**, middle (Fleurie et al., 2014a; Holeckova et al., 2015). Recent dynamic studies demonstrate that the MapZ-ring forms a stable structure in *Streptococcus* species (Li et al., 2018; Perez et al., 2019). In *Spn*, the MapZ-ring guides nascent treadmilling FtsZ filaments and bundles continuously from the earliest stage of division over an approximate ≈9-min period out to the future equatorial rings (Perez et al., 2019). With time, the amount of FtsZ associated with MapZ-rings increases, while the amount of septal FtsZ decreases and disappears before septation is complete (Tsui et al., 2014; Perez et al., 2019). In contrast, *Streptococcus mutans* (*Smu*) MapZ seems to move toward future equators in the absence of nascent FtsZ filaments and bundles (Li et al., 2018). Once MapZ has reached the new equators, FtsZ filaments/bundles rapidly stream from the septum to the equatorial MapZ-ring (Li et al., 2018).

Along with MapZ, chromosome segregation positively regulates Z-ring placement in *Spn*, as indicated by misplaced Z-rings in Δ*mapZ* or Δ*smc* mutants (van Raaphorst et al., 2017). However, Δ*mapZ* and Δ*smc* are not synthetically lethal (van Raaphorst et al., 2017). Other Z-ring-associated proteins or regulators in *Spn* have recently been studied, including FtsA, SepF, RocS, and CcrZ (Mura et al., 2016; Zheng et al., 2017; Mercy et al., 2019; Gallay et al., 2021), but besides FtsA, none has been shown to be essential. Therefore, it has remained an unanswered question whether other essential components are involved in Z-ring assembly and PG synthesis in *Spn*. In this work, we elucidate the relationship of the key Z-ring regulators EzrA and ZapA that were first identified in *Bsu*.

EzrA is conserved in low-GC, Gram-positive bacteria (Levin et al., 1999). The 2D-protein topology of EzrA consists of an

N-terminus transmembrane domain followed by cytoplasmic C-terminus, whose crystal structure consists of spectrin-like repeats (Haeusser et al., 2007; Cleverley et al., 2014; Land et al., 2014). Cellular and *in vitro* studies suggested that a primary function of EzrA(*Bsu*) is to inhibit aberrant FtsZ assembly and division at cell poles, thereby acting as a negative Z-ring regulator (Chung et al., 2007; Land et al., 2014). Yet, contrary to acting as a negative regulator, EzrA(*Bsu*) is among the first group of proteins to localize at the midcell, simultaneously with FtsZ, FtsA, and ZapA, but prior to GpsB, Pbp2b, FtsL, DivIVB, and DivIVA (Gamba et al., 2009). EzrA(*Bsu*) midcell localization is dependent on FtsZ as well as the EzrA(*Bsu)*-QNR motif that is conserved in all EzrA homolog proteins (Haeusser et al., 2007). At the midcell, EzrA(*Bsu)*, ZapA, and SepF function to condense treadmilling FtsZ-filaments into an FtsZ-ring that can then act to promote cell division and sPG synthesis in *Bsu* (Squyres et al., 2021). The presence of EzrA(*Bsu*) decreases FtsZ subunit lifetimes and FtsZ filament lengths without affecting FtsZ-treadmilling speeds (Squyres et al., 2021). In addition to regulating Z-ring dynamics, fluorescent microscopy and bacterial two-hybrid (B2H) assays suggest that EzrA(*Bsu*) acts in concert with other cell division proteins, including GpsB(*Bsu*), to shuttle the major class A penicillin-binding protein (aPBP1) from the elongation to the division machinery in *Bsu* (Claessen et al., 2008). Interactions between GpsB(*Bsu*) and EzrA(*Bsu*) have been shown by B2H assays (Claessen et al., 2008; Pompeo et al., 2015).

Additional studies of EzrA functions have been performed in coccus-shaped *Staphylococcus aureus* (*Sau*) and ovococcus-shaped *Streptococcus mutans* (*Smu*). Biochemical studies showed that the N-terminal domain of EzrA(*Sau*) interacts with the C-terminal tail of FtsZ(*Sau*) (Son and Lee, 2013). Physiological studies by two different groups contest the essentiality of EzrA*(Sau)* (Jorge et al., 2011; Steele et al., 2011). One study concluded from depletion experiments that EzrA*(Sau)* is required for *Sau* cell growth (Steele et al., 2011). B2H assays in this study further indicated that EzrA(*Sau*) interacts with itself and potentially interacts directly with numerous division and PG synthesis proteins, including FtsZ, FtsA, FtsL, FtsW, DivIB, DivIC, PBP1, PBP2, PBP3, SepF, GpsB, and RodA (Steele et al., 2011). By contrast, a second study concluded that EzrA(*Sau*) is not essential, based on multiple depletion approaches of EzrA(*Sau*) in different *Sau* genetic backgrounds; rather, EzrA(*Sau*) is important for cell size homeostasis (Jorge et al., 2011). The second study also showed by B2H assays that EzrA(*Sau*) interacts with itself, PBP1, and PBP2. In *Smu*, a species distantly related to *Spn* (Richards et al., 2014), EzrA(*Smu*) is not essential, and deletion of EzrA(*Smu*) results in an increased doubling time (≈1.7-fold), shorter and wider cells, and irregular localization of FtsZ compared to wild-type (WT) cells (Xiang et al., 2019). However, a comprehensive study of EzrA(*Smu*) in cell division and PG synthesis has not been reported.

EzrA(*Spn*) was classified as essential by transposon-sequencing (Tn-Seq) screens (van Opijnen et al., 2009), high-throughput gene disruption assays (Thanassi et al., 2002), and CRISPRi experiments (Liu et al., 2017). The spectrin-repeat structure *of* EzrA(*Bsu*) (Cleverley et al., 2014) is conserved in EzrA(*Spn*) based on modeling with the Phyre2 program (**Supplementary Figure 1D**) (Kelley et al., 2015). Coiled-coil analysis demonstrates that EzrA(*Spn*) has four coiled-coil repeats in addition to the transmembrane domain (**Supplementary Figure 1C**), similar to EzrA(*Bsu*) (Land et al., 2014). The topology of EzrA(*Spn*) has an extracellular N-terminus attached to a transmembrane domain (amino acids 5-27) followed by the large intracellular spectrin-like domain in the C-terminus (amino acids 28-575; **Supplementary Figure 1E**).

Bacterial two-hybrid and surface plasmon resonance experiments showed that EzrA(*Spn*) interacts with GpsB, DivIVA, and FtsZ (Fleurie et al., 2014b; Rued et al., 2017). Co-immunoprecipitation (Co-IP) experiments further demonstrated that EzrA(*Spn*) is in a complex with FtsZ, GpsB, and StkP in *Spn* cells, and it was postulated that EzrA(*Spn*) acts as a bridge connecting FtsZ to other cell division proteins (Rued et al., 2017). TIRF microscopy (TIRFm) of EzrA(*Spn*)-GFP expressed from its native chromosomal locus showed that EzrA(*Spn*) and FtsA move circumferentially at ≈30 nm/s with treadmilling FtsZ filaments/bundles in nascent rings containing MapZ that move toward the future equators of dividing daughter cells (Perez et al., 2019). Strikingly, in Δ*mapZ* mutants, EzrA(*Spn*), presumably associated with FtsZ filaments/bundles, streams from division septa to equators and other positions in daughter cells, indicating a failsafe mechanism for Z-ring placement when MapZ is absent (Perez et al., 2019). In addition, at a semi-permissive temperature (37°C), the temperature-sensitive *ezrA*(T506I) mutant forms cells with larger diameters in which the regular spacing of nodes of PG synthesis are disrupted (Perez et al., 2021). Other roles of EzrA(*Spn*) in Z-ring placement, growth, morphology, and viability have not yet been described.

Unlike Gram-positive EzrA, ZapA is well conserved in both Gram-positive and Gram-negative bacteria, where its role in Z-ring bundling and ordering has been established (Caldas et al., 2019). While ZapA, SepF, and EzrA are not individually essential in *Bsu*, combined mutations result in synthetic-lethal phenotypes, including *ezrA* and *sepF* (Duman et al., 2013), *ftsA* and *sepF* (Ishikawa et al., 2006), and *zapA* and *ezrA* (Gueiros-Filho and Losick, 2002). Besides regulating Z-ring dynamics in *E. coli*, ZapA is part of a multilayered network of proteins that connect and coordinate the Z-ring to the chromosome *via* ZapB and MatP (Buss et al., 2015). In contrast, nothing has been reported about ZapA(*Spn*) function or whether ZapA(*Spn*) has a partner subunit, since ZapB homologs are absent in *Spn.*

In this paper, we fill in some of these gaps about EzrA(*Spn*) and ZapA(*Spn*) functions and interactions. We report the association of FtsZ and EzrA during the entire *Spn* cell cycle. We also characterize the essential intertwined roles of FtsZ and EzrA in *Spn* cell division and organizing PG synthesis. We show that depletion of EzrA(*Spn*) is required for midcell Z-ring divisome assembly, whereas overexpression of EzrA(*Spn*) leads to the appearance of extra Z-rings in cells, opposite to the phenotypes observed in *Bsu* (Haeusser et al., 2004). Our combined results are consistent with a role for EzrA(*Spn*) as a positive, rather than a negative, regulator of FtsZ-ring formation in *Spn.* In addition, Co-IP and B2H experiments show that EzrA(*Spn*) is found in complexes with numerous proteins, including FtsZ, Z-ring regulators, division proteins, and

PG synthesis proteins. This versatility of EzrA(*Spn*) in forming multicomponent complexes, possibly through direct interactions, is consistent with EzrA(*Spn*) acting to link and modulate cell division and PG synthesis. Finally, we discovered the interaction partner (ZapJ) of ZapA(*Spn*) and show that non-essential ZapA, ZapJ, and SepF act as accessory proteins to essential EzrA, possibly by forming a spatially separated network of positive Z-ring regulators.

MATERIALS AND METHODS

Complete descriptions of the following materials and methods used in this study are contained in ***Supplementary Material*** based on the references indicated: EzrA(*Spn*) structure modeling (Kelley et al., 2015; PyMol); construction of bacterial strains and growth conditions (**Supplementary Tables 1, 2**; Lanie et al., 2007; Tsui et al., 2010, 2014; Land et al., 2013); growth of merodiploid strains and Zn-dependent depletion (Jacobsen et al., 2011; Tsui et al., 2014, 2016); cell fixation and adherence to coverslips for fluorescence microscopy (Fm) (Tsui et al., 2016); characterization of antibodies for immunofluorescence microscopy (IFM) (**Supplementary Table 5**; Land et al., 2013; Tsui et al., 2014, 2016); analysis of 2D-epifluorescence microscopy (EFm) images (Land et al., 2013; Tsui et al., 2014; Perez et al., 2019); 3D-SIM IFM (Land et al., 2013; Tsui et al., 2014); TIRF microscopy (TIRFm) (Grimm et al., 2015; Perez et al., 2019); 3D-SIM of FDAA-labeled cells expressing EzrA(*Spn*)-sfGFP (Perez et al., 2021); measurements of cell dimensions by phase-contrast microscopy (PCm); quantitative Western blotting (Lara et al., 2005; Wayne et al., 2010; Land and Winkler, 2011; Beilharz et al., 2012; Cleverley et al., 2019); Live/Dead staining of *ezrA* and other mutants (Wayne et al., 2012; Sham et al., 2013); DAPI staining for nucleiod content (Perez et al., 2019); FDAA pulse-chase labeling in depletion experiments (Boersma et al., 2015; Perez et al., 2021); co-immunoprecipitation (Co-IP) assays (Rued et al., 2017); bacterial two-hybrid (B2H) assays (**Supplementary Tables 6, 7**); Karimova et al., 2005; Rued et al., 2017; Cleverley et al., 2019); and mass spectrometry (MS) to identify ZapJ (Spd_1350) (Sham et al., 2011; Zheng et al., 2017).

RESULTS

Localization of EzrA and FtsZ Is Highly Correlated During the Entire *Spn* Cell Cycle

The strong association of EzrA(*Spn*) and FtsZ(*Spn*) was demonstrated from co-IP experiments showing that EzrA as bait can pull down FtsZ in *Spn* extracts without the cross-linking procedure (**Figure 1C**). To determine the spatiotemporal relationship of EzrA relative to FtsZ during the *Spn* cell cycle, we performed EFm on live cells expressing fluorescent-protein fusions of FtsZ and EzrA and IFM on fixed cells expressing epitope-tagged FtsZ and EzrA, as described in section "Materials and Methods." Unless otherwise noted, all strains in this study did not show detectable growth or cell shape defects when fusion proteins were expressed as the only copy in the cell from native promoters (**Supplementary Table 1** and data not shown). Linkers in fusion constructs are omitted in the text for simplicity, but are listed in **Supplementary Tables 1, 2**.

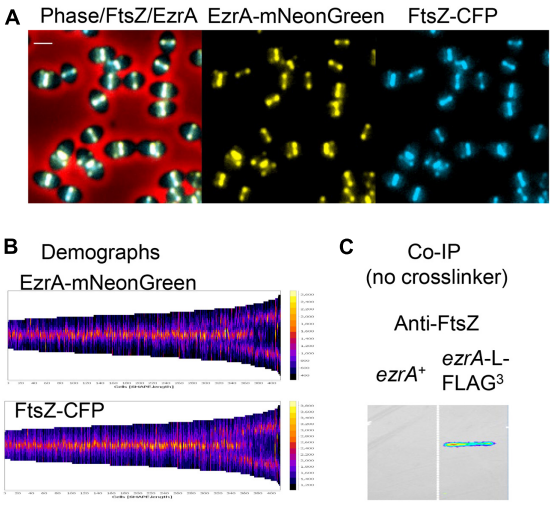

FIGURE 1 | Highly correlated localization patterns of FtsZ and EzrA during the *Spn* cell cycle. Cells from at least two independent biological replicates were collected at $OD_{620} \approx 0.1–0.2$ and prepared for microscopy or co-IP as described in section "Materials and Methods." **(A)** Representative field of live cells expressing EzrA-mNeonGreen and FtsZ-CFP (IU14153). Scale bar is 1.0 μm. **(B)** Demographs showing FtsZ and EzrA localization from shorter pre-divisional cells (left side) to longer post-divisional cells (right side). **(C)** Membrane probed with anti-FtsZ showing EzrA-$FLAG^3$ (IU5456) can co-IP FtsZ from non-crosslinked *Spn* cells relative to untagged $EzrA^+$ (IU10447).

In live cells of strain IU14153, C-terminal fusion proteins EzrA-mNeonGreen and FtsZ-CFP showed complete overlap by EFm (**Figure 1A**). Demographs generated with MicrobeJ (Ducret et al., 2016) of fields of these unsynchronized cells at different stages of division confirmed overlap of EzrA and FtsZ and indicated simultaneous movement of the proteins from septa to developing equators of daughter cells, including the stage at which three bands are present (**Figure 1B**). Likewise, 2D-IFM images of fixed cells expressing epitope-tagged EzrA-HA and FtsZ-Myc (strains IU7223 or IU9713) indicated overlap at all stages of cell division (**Supplementary Figure 2A**, left). Cells were retrospectively binned into four stages, and fluorescence signals of EzrA-HA, FtsZ-Myc, and DNA nucleoids (DAPI) were averaged as described previously (Land et al., 2013; **Supplementary Figure 2B**). This quantitative analysis confirmed overlap of EzrA and FtsZ throughout the cell cycle (**Supplementary Figures 2B,C**). Averaged images at each division stage indicated that the EzrA-ring is slightly larger than the FtsZ-ring, similar to the slightly larger FtsA-ring in relation to the FtsZ-ring (Mura et al., 2016). This conclusion was confirmed by Student t-test analysis of the distributions of band diameters in each cell (**Supplementary Figure 2C**) (see Tsui et al., 2014). This slight difference in diameters coincides with location of the C-terminus of EzrA closer to the membrane than FtsZ (**Supplementary Figures 1C,D**), whose apparent distance

is likely enhanced by the length of the fluorescently labeled antibodies used in IFM.

High-resolution 3D-SIM IFM images (**Supplementary Figure 3**) confirmed and extended results from 2D-EFm. For each stage of division, > 20 cells were examined by 3D-SIM. Stage 1 cells show highly correlated spatial organization of EzrA and FtsZ, with the diameter of EzrA slightly larger than that of FtsZ in rotated images (**Supplementary Figure 3**). Most EzrA and FtsZ are visible at the septa of all Stage 2 cells examined, and in ≈35% of cells, faint rings containing EzrA and FtsZ are detected in nascent rings moving toward the equatorial regions of daughter cells (arrow, **Supplementary Figure 3**, Stage 2) (Perez et al., 2019). Later in division, EzrA and FtsZ locate in a characteristic three-ring pattern at the septum and the equators of daughter cells over the separating nucleoid (**Supplementary Figure 3**, Stages 2.5 and 3). In Stage 4 cells, most EzrA and FtsZ locate to the new equatorial rings of the daughter cells, sometimes leaving a small dot of each protein at the closing septum (**Supplementary Figures 2B, 3**).

We extended these analyses to further characterize FtsZ and EzrA localization in a Δ*mapZ* mutant. Certain FtsZ-GFP fusions are partially functional in Δ*mapZ* mutants, resulting in more severe morphological defects than in strains containing Δ*mapZ* alone (Perez et al., 2019). We did not observe these compounded defects in a Δ*mapZ* mutant expressing epitope-tagged EzrA-HA and FtsZ-Myc by PCm or growth curve analysis (**Supplementary Figure 2A**, right and data not shown). Previously, we showed that in the absence of MapZ, EzrA moves to daughter cells by a delayed and aberrant streaming mechanism that was rarely (1%) seen in WT cells (Perez et al., 2019). This secondary, failsafe mechanism is responsible for placement of Z-rings near the equators of most, but not all, Δ*mapZ* daughter cells (**Supplementary Figure 2A**, right). EzrA and FtsZ co-localized during delayed streaming in late-divisional Δ*mapZ* cells, as observed by 2D-EFm (**Supplementary Figures 2A,B**, stage 4) and at high resolution by 3D-SIM (**Supplementary Figure 4**). Together, these results confirm that a tight association between EzrA and FtsZ filaments/bundles is maintained during this alternate failsafe streaming mechanism.

Previously, we reported that EzrA or FtsA moves circumferentially at the same velocity as treadmilling FtsZ filaments/bundles in nascent rings or early equatorial rings during the *Spn* cell division (Perez et al., 2019). By contrast, the density of molecules was too great in septal rings or fully developed equatorial rings to determine dynamic patterns by TIRFm. We further evaluated how tightly associated dynamic patterns of EzrA are with FtsZ or FtsA in developing equatorial or nascent rings. In these experiments, we performed dual-color TIRFm where we tracked native locus-expressed FtsZ-sfGFP or GFP-FtsA alongside EzrA-HaloTag (EzrA-HT) labeled to saturation with the HaloTag JF549 ligand (Grimm et al., 2015; Perez et al., 2019). Kymographs along equatorial and nascent-ring planes indicate that for the most part, the movement of FtsZ filaments/bundles or FtsA in FtsZ filaments/bundles mirrored that of EzrA in time and space, indicating a strong dynamic association (**Supplementary Figure 5**). In addition, we observed some events consistent with unassociated EzrA, as indicated by lack of FtsZ or FtsA and vertical EzrA traces (magenta lines, **Supplementary Figure 5**). Together, we conclude that EzrA is tightly associated with circumferentially moving FtsZ filaments/bundles that also contain FtsA, although some EzrA is not associated with moving FtsZ filaments/bundles.

EzrA and PG Synthesis Show Different Localization Patterns in *Spn*

Several reports suggest that EzrA is associated with PBPs and PG synthesis in *Bsu* and *Sau* (Claessen et al., 2008; Jorge et al., 2011; Steele et al., 2011). In *Spn*, PG synthesis enzymes and activity localize late in division from septa to new equatorial FtsZ-rings in daughter cells (Tsui et al., 2010; Land et al., 2013; Perez et al., 2019). Given the strong association between FtsZ and EzrA described above, we postulated that EzrA would precede PG synthesis to the new equatorial rings of daughter cells. To localize EzrA relative to PG synthesis, we carried out short pulse (2.5 min) labeling with a fluorescent D-amino acid (FDAA) in a strain expressing EzrA-sfGFP from the *ezrA* native locus (strain IU10254) as described in *Materials and Methods* (**Supplementary Figure 6**). FDAAs are incorporated into the PG in regions of active PBP transpeptidase activity (Kuru et al., 2012; Tsui et al., 2014; Boersma et al., 2015). Cells were binned by division stage, and average fluorescence intensities were quantitated as described above for EFm images (**Supplementary Figure 2**). Statistical analysis of labeling widths shows that the FDAA labeling was greater than the EzrA width at all division stages (**Supplementary Figure 6B**). In early stage-1 and -2 cells, PG synthesis and EzrA are confined to division septa. In later stage-3 and -4 cells, EzrA shows the same pattern reported previously for FtsZ (Land et al., 2013). PG synthesis remains confined to the septum, while a substantial amount of EzrA has moved to the equators of daughter cells (**Supplementary Figure 6A**). By stage 4, little EzrA remains at the septum compared to small region of PG synthesis.

3D-SIM images of vertically oriented cells confirm the separation of the FDAA labeling and EzrA in early-stage 1 and 2 cells (**Supplementary Figure 6C**). In stage 1 cells, the separation is small and consistent with the fact that PG synthesis occurs outside of cells, whereas the sfGFP-fused C-terminus of EzrA is inside the cell near the membrane (**Supplementary Figures 1D, 6C**). The increased separation of labeling in stage 2 cells is consistent with the recent report that the contracting FtsZ-ring tracks with an inner ring of sPG synthesis at the leading edge of the septal annulus, while an outer concentric ring of pPG elongation synthesis remains at the outer edge of the septal disk (Perez et al., 2021). We conclude that EzrA is tracking in a pattern reported before for FtsZ and FtsA that is different from that of PG synthesis.

EzrA Is Essential in *Spn*

To directly test the essentiality of EzrA(*Spn*), we performed assays for recovery of colonies following transformation with amplicons containing null mutations, as described in section "Materials and Methods." We transformed an amplicon containing a null Δ*ezrA*<>*aad9* allele, where the *ezrA* ORF is replaced by an

ORF imparting spectinomycin resistance, into an unencapsulated derivative of strain D39W (IU1945; D39 Δ*cps*) and compared the number of transformants with a positive-control amplicon (Δ*purR*<>*aad9*) and a negative-control amplicon (Δ*ftsZ*::*aad9*) (**Table 1**). Following 24 h of incubation, the Δ*purR* control showed many transformants, while Δ*ezrA* or Δ*ftsZ* showed none (**Table 1**, column 1). After 48 h of incubation, a limited number of small, variable-sized transformant colonies, indicative of potential suppressor mutations, were observed for Δ*ezrA*, but not Δ*ftsZ* (**Table 1**). These potential Δ*ezrA* transformants showed similar cell growth as the EzrA depletion strains described next; however, they were unstable and could not be recovered after storage and were not further characterized here.

EzrA(*Bsu*) is conditionally essential in the presence of certain antibiotics (Gamba et al., 2015). Consequently, we repeated the transformation assay with an amplicon containing a Δ*ezrA*::P_c-*erm* deletion–insertion null mutation into the D39 Δ*cps Spn* strain, selecting for erythromycin resistance. We obtained no Δ*ezrA*::P_c-*erm* transformants after 24 of incubation (data not shown), similar to the results for the Δ*ezrA*<>*aad9* amplicon (**Table 1**). Finally, we repeated the transformation assay for the Δ*ezrA*<>*aad9* amplicon into laboratory strain R6 (strain EL59), which has acquired numerous mutations compared to its D39W progenitor strain (Lanie et al., 2007). Mutations in the R6 strain genetic background suppress the essentiality of numerous genes involved in PG synthesis, including Δ*mreC*, Δ*gpsB*, Δ*mltG*, and Δ*stkP* (Land and Winkler, 2011; Rued et al., 2017; Straume et al., 2017). However, transformation of the Δ*ezrA*<>*aad9* amplicon into strain R6 gave no colonies after 20 h of incubation (data not shown), similar to the D39 Δ*cps* strain (**Table 1**). Attempts to delete *ezrA* in the commonly used Rx1 background were also unsuccessful (Massidda et al., 2013). Together, these results show that EzrA(*Spn*) is essential and not conditionally lethal.

To determine phenotypes caused by EzrA(*Spn)* depletion, we constructed a Δ*ezrA*//P_{Zn}-*ezrA*$^+$ merodiploid strain (IU8799) by moving a Δ*ezrA*<>*aad9* deletion into a *ezrA*$^+$//P_{Zn}-*ezrA*$^+$ strain (IU8795) containing an ectopic copy of *ezrA*$^+$ under control of a Zn^{2+}-inducible promoter in the *bgaA* gene (see **Supplementary Table 1**). Consistent with EzrA(*Spn*) essentiality, transformation of the *ezrA*$^+$//P_{Zn}-*ezrA*$^+$ merodiploid with the Δ*ezrA*<>*aad9* amplicon only resulted in many colonies when Zn (0.5 mM $ZnCl_2$ and 0.05 mM $MnSO_4$) was added to selection plates (**Table 1**, middle columns). Without added Zn, only a few putative suppressor mutants were detected. Likewise, transformation of a comparable *ftsZ*$^+$//P_{Zn}-*ftsZ*$^+$ merodiploid with a Δ*ftsZ*::*aad9* amplicon only resulted in colonies when Zn was added (**Table 1**, right columns).

EzrA Is Required for Normal Cell Growth, Size, and Shape Homeostasis in *Spn*

To characterize EzrA depletion phenotypes, we performed growth curve analyses and PCm on cells depleted for EzrA in BHI broth, as described in section "Materials and Methods." Growth rates and yields of an EzrA merodiploid (Δ*ezrA*//P_{Zn}-*ezrA*$^+$) strain were dependent on the concentration Zn ($ZnCl_2$ + 1/10 $MnSO_4$) in cultures, where Mn^{2+} was added to prevent Zn^{2+} toxicity (see section "Materials and Methods"; **Figure 2A** and **Supplementary Figure 7A**; Jacobsen et al., 2011). Depletion growth curves depended on OD_{620} at which Zn was omitted from cultures containing 0.5 mM Zn (**Supplementary Figure 7B**), consistent with the requirement of EzrA for growth. Although cultures containing 0.3–0.5 mM Zn grew, similarly (**Supplementary Figure 7A**), only 0.5 mM fully complemented cell shape and was used in depletion experiments started at OD_{620} ≈0.01–0.05 (**Supplementary Figures 7B,C**). Finally, a merodiploid strain ectopically expressing EzrA fused to a $FLAG^3$ epitope tag (Δ*ezrA*//P_{Zn}-*ezrA*-$FLAG^3$) grew, similarly, to the Δ*ezrA*//P_{Zn}-*ezrA*$^+$ strain in 0.5 mM Zn and after Zn was removed, after which OD_{620} stopped increasing in ≈3 h (**Supplementary Figure 7C**).

After depletion of EzrA or EzrA-L-$FLAG^3$ for 1 h or longer, cell shapes became distorted and non-uniform (**Figure 2B**). With time, the median aspect ratio of EzrA-depleted cells decreased compared to the non-depleted control cells, and cells appeared as irregular spheroids with variable relative volumes (**Figure 2B** and **Supplementary Figure 8**). Quantitative Western blotting showed that ectopic EzrA-L-$FLAG^3$ in the presence of

TABLE 1 | Relative transformation of Δ*ezrA* or Δ*ftsZ* amplicon into *Spn* D39 Δ*cps*[a,b].

Amplicon	Number of colonies in recipient strain after 16-20 h incubation				
	D39 Δ*cps*	D39 Δ*cps bgaA*'::P_{Zn}-*ezrA*$^+$		D39 Δ*cps bgaA*'::P_{Zn}-*ftsZ*$^+$	
		+Zn	-Zn	+Zn	-Zn
1. Δ*ezrA*<>*aad9*	0[d]	> 300	< 15[c,d]	0	0
2. Δ*ftsZ*::*aad9*	0	0	0	> 300	0
3. Δ*purR*::*aad9*	> 300	>300	> 300	NT	NT

[a] *D39 Δcps (IU1945), D39 Δcps bgaA'::P_{Zn}-ezrA$^+$ (IU8795), D39 Δcps bgaA'::P_{Zn}-ftsZ$^+$ (IU8122) were grown and transformed as described in section "Materials and Methods." Transformation reactions requiring $ZnCl_2$ were grown (for 1 h before addition of ΔezrA or ΔftsZ amplicon), transformed, and plated in the presence of 0.5 mM $ZnCl_2$ and 0.05 mM $MnSO_4$ for transformation with ΔezrA<>aad9 amplicons or 0.3 mM $ZnCl_2$ and 0.03 mM $MnSO_4$ for transformation with ΔftsZ::aad9 amplicon. Numbers of colonies indicated were obtained from 1 ml of transformation mix. Data are representative of three biological replicates with similar results.*

[b] *NT, not tested.*

[c] *After 24 h of incubation, < 15 colonies were obtained which were variable in size, dull, and underneath agar. These colonies remained very tiny upon streaking. They were unstable and could not be recovered after storage.*

[d] *< 50 colonies were obtained after 48 h of incubation. They were unstable and could not be recovered after storage.*

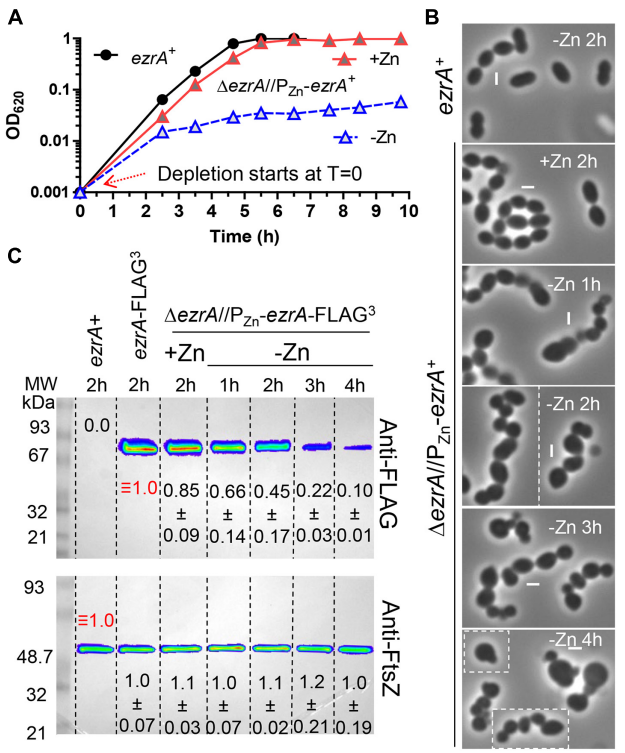

FIGURE 2 | Depletion of EzrA results in severe growth, size, and shape defects. EzrA depletion in untagged-strain, IU8799 (Δ*ezrA*//*bgaA*::P_{Zn}-*ezrA*$^+$) in **(A)** and **(B)** or tagged-strain, IU9572 (Δ*ezrA*//*bgaA*::P_{Zn}-*ezrA*-FLAG^3) in **(C)**. **(A)** Representative growth curves after resuspension in BHI broth containing or lacking $ZnCl_2$ show EzrA-depletion results in bacteriostatic-like growth. IU8799 and IU1945 (WT parent) were grown exponentially in BHI broth supplemented with 0.5 mM $ZnCl_2$ and 0.05 mM $MnSO_4$ to $OD_{620} \approx 0.1$, spun, and resuspended to $OD_{620} \approx 0.001$ for this growth curve. **(B)** Representative PCm images of wild-type (IU1945) or EzrA depletion strain (IU8799) after resuspension in BHI broth supplemented with, or lacking supplemented $ZnCl_2$ for 1, 2, 3, or 4 h. Resuspension volumes were adjusted in BHI broth supplemented with or without 0.5 mM $ZnCl_2$ and 0.05 mM $MnSO_4$ to $OD_{620} \approx 0.36$ (for $T = 1$ h time-point) or 0.012 (for $T = 2$, 3, and 4 h time-points). Experiments were performed three times with similar results. See **Supplementary Figure 8** for quantitation. **(C)** Representative western blots of gels containing extracts of IU1945 (wild-type), IU5456 (*ezrA*-FLAG^3), or IU9572 (Δ*ezrA*//P_{Zn}-*ezrA*-FLAG^3). Western blotting using anti-FLAG antibody or anti-FtsZ are described in section "Materials and Methods" and **Supplementary Materials**. Protein amounts of $ZnCl_2$-induced and $ZnCl_2$-depleted strains relative to IU5456 (*ezrA*-FLAG^3 native) for EzrA-FLAG^3 levels or IU1945 (untagged parent isolate) for FtsZ, levels were quantified and are from at least 3 independent biological replicates experiments (± standard deviations).

0.5 mM Zn was expressed at 85% of the cellular amount of EzrA-L-FLAG^3 expressed from the native chromosomal locus (**Figure 2C**). Depletion of EzrA-L-FLAG^3 for 1 to 4 h reduced the relative cellular amount to 66% and to 10%, respectively (**Figure 2C**). At 3 h of depletion, when cultures stopped growing (**Figure 2A** and **Supplementary Figure 7C**), the relative amount of EzrA-L-FLAG^3 was ≈22% of that in cells expressing EzrA-L-FLAG^3 from the native locus (**Figure 2C**). Distorted cells depleted of EzrA did not appear to lyse, and cell debris was not observed by PCm. Viability staining with the LIVE/DEAD *Bac*Light procedure, as described in *Materials and Methods*, showed that > 90% of non-growing, distorted cells lacking EzrA were stained as viable for 3, 4, and 7 h after depletion (**Supplementary Table 3**). Consistent with this conclusion, CFUs of Δ*ezrA*//P_{Zn}-*ezrA* cells depleted of EzrA for 4 or 8 h without Zn were recovered on plates containing Zn with no decrease or increase in CFU/mL throughout the depletion time course (data not shown). Thus, EzrA is required for *Spn* cell size and shape homeostasis, although prolonged depletion of EzrA under these culture conditions is bacteriostatic and not bactericidal.

Finally, we determined the effects of the EzrA(ΔTM) and EzrA(ΔQNR motif) or EzrA(QND motif) mutant variants, which mediate membrane anchoring and medial localization, respectively, in *Bsu* (**Supplementary Figures 1C, 9A**) (Land et al., 2014). We expressed EzrA(ΔTM) (deletion of amino acids 2-26; strain IU11123), EzrA(ΔQNR) (deletion of amino acids 510-516 (deletion of amino acids 510-516; strain 10909), and EzrA(QND motif) (*ezrA*(R515D); strain IU10901) from the native locus of a merodiploid strain ectopically expressing $ezrA^+$ from the P_{Zn} promoter (**Supplementary Table 1**). Depletion of EzrA$^+$ showed that *ezrA*(ΔTM) and *ezrA*(ΔQNR) caused the same growth defects as Δ*ezrA* (**Supplementary Figure 9B**), whereas *ezrA*(QND) strains grew like WT (data not shown). sfGFP fused to the C-terminus of EzrA(QND), EzrA(ΔQNR), or EzrA(ΔTM) in comparable EzrA$^+$ merodiploid strains showed that EzrA(QND)-sfGFP and EzrA(ΔQNR)-sfGFP were expressed at nearly the same level as EzrA$^+$-sfGFP upon EzrA$^+$ depletion, whereas EzrA(ΔTM)-sfGFP was expressed at only 30% of the WT level (**Supplementary Figure 9C**). Moreover, the ectopic expression of EzrA(ΔTM)-FLAG^3 at the WT level did not complement a Δ*ezrA* mutation, confirming that the TM domain is required for EzrA function (data not shown). EzrA(ΔQNR)-sfGFP and EzrA(ΔTM)-sfGFP were highly mislocalized upon depletion of EzrA$^+$ in merodiploid strains (**Supplementary Figure 9D**). Remaining midcell rings containing EzrA(ΔQNR)-sfGFP or EzrA(ΔTM)-sfGFP may reflect dimer formation with residual EzrA$^+$ after depletion. In contrast, EzrA(QND motif)-sfGFP largely localized normally to midcell and equatorial bands in irregularly shaped cells (**Supplementary Figure 9D**). In addition, the *ezrA*(QND)//P_{Zn}-$ezrA^+$ mutant was temperature sensitive for growth at 42°C in the absence of Zn (data not shown). We conclude that the TM domain of EzrA is required for membrane localization and possibly protein stability, while the QNR motif localizes EzrA to the septal and equatorial rings of *Spn* cells. While not necessary for ring localization, amino acid R515 in the QNR motif of EzrA(*Spn*) is required for full function.

EzrA Is Required for Normal Chromosome Segregation in *Spn*

Depletion of EzrA often results in larger cells attached to smaller cells (**Figure 2B**), reminiscent of minicells containing guillotined DNA or no DNA produced by division site placement mutants (Wu and Errington, 2004; Bernhardt and de Boer,

2005). To test this idea, we stained the DNA of cells from WT, EzrA-complemented, or EzrA-depleted cultures with DAPI as described in *Materials and Methods*. We counted nucleated and anucleate cells that were at pre-divisional (stage 1) or post-divisional (stage 4) stages (n = 400 per condition) based on PCm (**Supplementary Figure 10**). Depletion of EzrA resulted in a relatively high number (3.25% of cells detected by PCm) of cells lacking nucleoids compared to WT (none) or EzrA-complemented strains (<0.25%) (arrows, **Supplementary Figure 10**; **Supplementary Table 4**). By comparison, cells lacking MapZ, which plays a role in positioning FtsZ-rings at the equators of daughter cells (Fleurie et al., 2014a; Holeckova et al., 2015; Perez et al., 2019), displayed only about 0.5% anucleate cells, which was greater than WT but far fewer than in EzrA-depleted cells (**Supplementary Table 4**). These results indicate that EzrA plays an important role in chromosome segregation, likely by modulating Z-ring placement and organization, analogous to Z-ring regulators in rod-shaped bacteria.

EzrA Is Required for the Midcell Placement of FtsZ-Rings in *Spn*

EzrA regulates FtsZ-ring number and position in *Bsu* cells. In the absence of EzrA, *Bsu* cells contain two extra parallel Z-rings per cell length (Levin et al., 1999). To determine the role of EzrA in regulating the presence and position of FtsZ-rings in *Spn*, we performed 2D-IFM using the anti-FtsZ(*Spn*) antibody in EzrA-depleted cells (Lara et al., 2005). The majority of pre-divisional (stage 1) cells of WT, EzrA-complemented (+Zn), and EzrA-depleted (1 h) cells contained normally placed FtsZ-rings at midcell (see **Figures 1A**, **3A**). In contrast, after 2 h of EzrA depletion, the majority of cells lacked identifiable Z-rings (**Figure 3A**). Cells classified as "FtsZ other" did not contain obvious Z-rings but did show the presence of FtsZ-labeling, and cells classified as "no FtsZ detected" lacked FtsZ labeling and appeared opaque by PCm, which may indicate an inability to be permeabilized and take up antibodies (data not shown). Nevertheless, comparison of cells with the FtsZ signal indicates that at 2 or 3 h after EzrA depletion, less than half of pre-divisional cells have Z-ring structures, while 90% of WT and 70% of EzrA-complemented cells contain Z-rings (**Figure 3A**), indicating that EzrA is necessary for FtsZ-ring formation in *Spn*. 3D-SIM IFM confirmed this conclusion at higher resolution than 2D-IFM. Among the patterns of FtsZ labeling in cells depleted for EzrA for 3 h, we observed diffuse localization and aberrant, twisted Z-ring structures, as well as cells lacking labeling patterns (**Figure 3C**).

To determine if EzrA influences positioning of FtsZ-rings in *Spn*, we determined the relative position of Z-rings in cells from **Figure 3A**. We measured the distance of Z-rings to the nearest cell pole normalized to cell length, where 0.5 indicates exact midcell placement. Fifty percent of WT and EzrA-complemented (+Zn) cells had FtsZ-rings positioned between 0.45 and 0.5 (**Figure 3B**). Cells depleted of EzrA for 1 or 2 h maintained Z-rings near this midcell range. By 3 h of EzrA depletion, the median (0.38) and distributions started to trend downward. Z-rings were significantly out of the midcell region at 3 h, indicating that the presence of EzrA also influences placement of Z-rings in *Spn*.

We confirmed these conclusions by tracking FtsZ-GFP expressed from the native chromosomal locus in live cells complemented or depleted for EzrA (**Figure 4** and **Supplementary Figure 11**). Defects in midcell localization and correct plane placement of FtsZ-GFP were apparent by 1 h of EzrA depletion (**Figure 4B** and **Supplementary Figure 11B**). By 3 h of EzrA depletion, polar placement of FtsZ-GFP band structures or condensed foci were observed (**Figure 4B** and **Supplementary Figure 11C**). Demographs of FtsZ-GFP in a population of EzrA-depleted cells revealed major delocalization of FtsZ-GFP as a function of relative cell length (**Figure 4B**). Localization of FtsZ-GFP to equatorial rings became aberrant at 2 h of EzrA depletion, while FtsZ-GFP localization in the whole population became aberrant at 3 h (**Supplementary Figure 11B**). We also observed that the culture density of strains expressing FtsZ-GFP began to drop after about 4 h of EzrA depletion, in contrast to strains expressing $FtsZ^+$, indicating an aberration caused by the FtsZ-GFP fusion upon extended EzrA depletion (**Supplementary Figure 11A**). We conclude from these combined IFM and GFP imaging experiments that EzrA is required for the presence and localization of FtsZ in *Spn*, in contrast to *Bsu* where the absence of EzrA leads to the formation of additional FtsZ-rings (Levin et al., 1999).

EzrA Is Required for the Midcell Peptidoglycan Synthesis in *Spn*

In pre-divisional and early divisional *Spn* cells, PG synthesis occurs at a midcell ring initially organized by FtsZ and FtsA (**Supplementary Figure 1**) (see Briggs et al., 2021). As septation proceeds, FtsZ continues to organize the inner ring of sPG synthesis that closes the septum, while pPG remains in an outer ring that lacks FtsZ (Briggs et al., 2021; Perez et al., 2021). Given that FtsZ organizes PG synthesis at different stages of division in *Spn*, we predicted aberrant PG synthesis patterns upon depletion of EzrA that mirrored those of FtsZ described above (**Figures 3**, **4**, and **Supplementary Figure 11**). To detect regions of active PBP TP activity, we labeled cells sequentially with two colors of FDAAs (**Supplementary Figure 12A**). Cells were labeled with a "long pulse" of HADA FDAA at the start of EzrA depletion or continued synthesis in merodiploid strains, as described in *Materials and Methods*. After 1, 2, or 3 h, cells were washed and a second TADA FDAA was added for a short pulse (5–18 min depending on strains or conditions, **Supplementary Figure 12A**), indicating regions of new PG synthesis. Cells observed by PCm and EFm showed patterns of TADA labeling (**Figure 5A** and **Supplementary Figures 12A–C**) similar to those of FtsZ with increasing EzrA depletion (**Figure 3A**). At 1 h of EzrA depletion, most TADA labeling was at midcell rings of pre-divisional and post-divisional cells, but by 2 h and beyond of EzrA depletion, TADA labeling was increasingly seen in polar foci and other aberrant and diffuse patterns (**Figure 5A**). 3D-SIM images captured

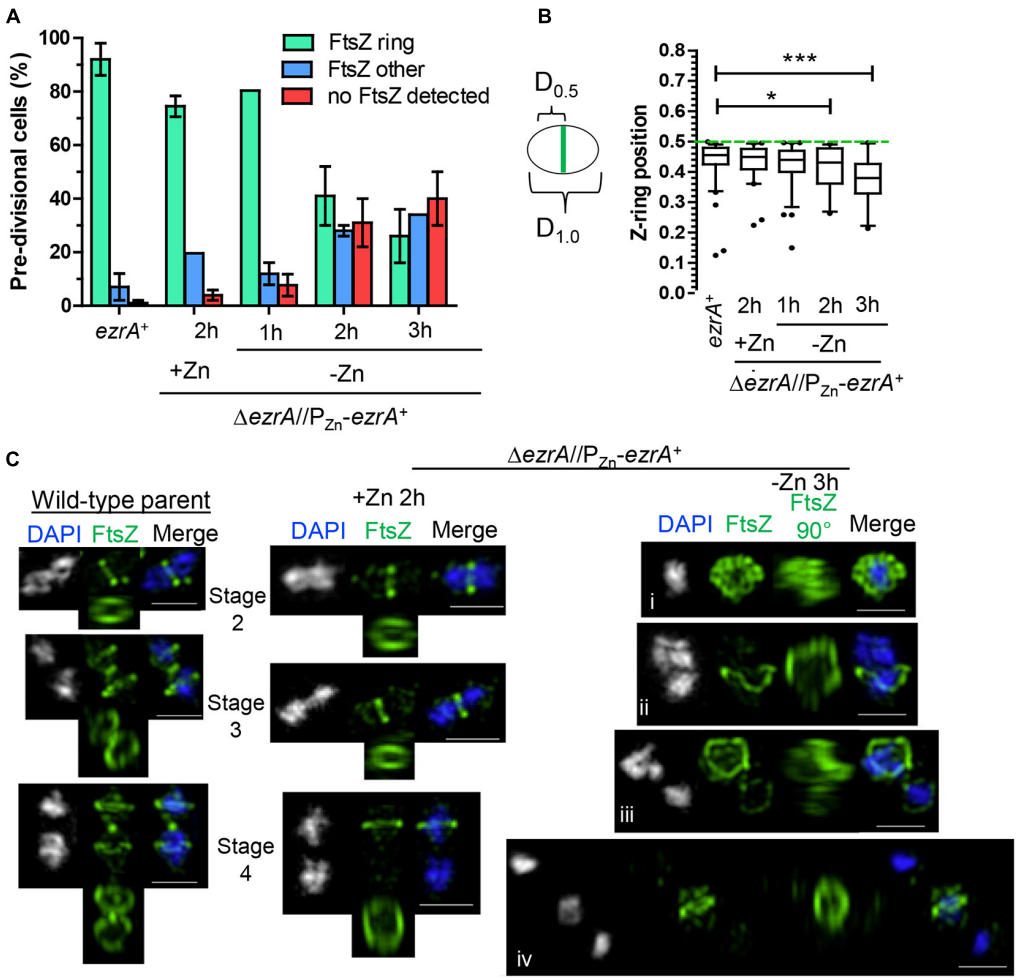

FIGURE 3 | EzrA depletion results in cells lacking Z-rings or aberrations in Z-ring positions. Wild-type (IU1945; *ezrA*$^{+}$) and *ezrA* depletion strain (IU8799+Zn; Δ*ezrA*//*bgaA*::P_{Zn}-*ezrA*$^{+}$) were grown exponentially (+Zn; 0.5 mM $ZnCl_2$ and 0.05 mM $MnSO_4$), and IU8799 was depleted of EzrA by shifting cells to BHI broth lacking $ZnCl_2$ and $MnSO_4$ as described in *Materials and Methods*. EzrA depleted cells were obtained at appropriate time points, prepared for IFM, and analyzed. Native FtsZ proteins were detected *via* anti-FtsZ antibodies as described in **Supplementary Table 5**. **(A)** Pre-divisional cells (stage 1) or post-divisional cells (daughters of stage 4) were binned into three different categories based on FtsZ localization events from 2D-EFm images. The bar is the mean percentage ± the SD for two separate IFM fields of one biological replicate. The different color bars represent cells that contained FtsZ-rings (green), FtsZ other (blue), or no FtsZ detected (red). The experiment was performed two independent times with similar results. **(B)** Box-and-whisker plots (whiskers, 5 and 95 percentile) of the FtsZ-ring position relative to whole cell length in cells which contained rings in **(A)**. The smaller distance of the Z-ring to the cell pole was measured and divided by the whole cell length to determine Z-ring position. Green dotted line indicates $D = 0.5$, a precisely midcell measured Z-ring. Data are from one biological replicate for a subset of cells that contained rings in **(A)**. (*ezrA*$^{+}$, $n = 86$ cells; +Zn 2 h, $n = 65$ cells; -Zn 1 h, $n = 72$ cells; -Zn 2 h, $n = 35$ cells; -Zn 3 h, $n = 24$ cells). *p*-values obtained with Mann–Whitney two-tailed unpaired t-test are for comparisons between *ezrA*$^{+}$ and other conditions. * and *** indicate $p < 0.05$ and < 0.001, respectively. **(C)** 3D-SIM examples of FtsZ-labeled cells shows EzrA-depletion leads to major aberrances in FtsZ-ring presence, FtsZ-ring placement, and FtsZ-structure. More than 20 cells were analyzed per condition (wild-type, Δ*ezrA*//P_{Zn}-*ezrA*$^{+}$ +Zn, Δ*ezrA*//P_{Zn}-*ezrA*$^{+}$ -Zn 3 h). Left panels show wild-type cells. Middle panel shows EzrA complemented cells. Further right panels show different aberrances in FtsZ structures during EzrA depletion, (i) FtsZ diffuse, (ii) FtsZ aberrant twisted rings, (iii) aberrant stage 4 like cells, (iv) two outer cells without labeling containing intense DAPI staining while the middle cell contains semi-diffuse DAPI and normal Z-ring.

details of these aberrant PG synthesis patterns, notably rings or puncta of TADA labeling at distal poles, diffuse TADA labeling, and aberrantly placed planes of TADA labeling in EzrA-depleted cells (**Supplementary Figures 13B,C**). As expected from these results, the placement of medial TADA-rings, when present, showed the same trend as FtsZ-rings in being located away from the exact midcell the longer EzrA was depleted (**Figures 3B**, **5B**). Together, these results indicate that PG synthesis tracks with the mislocalization of FtsZ that occurs when EzrA is depleted, possibly contributing to the diverse, aberrant cell shapes that occur.

Overexpression of EzrA Leads to Extra Z-Rings in *Spn*

The essentiality of EzrA(*Spn*) and the dependence of FtsZ-ring formation on EzrA (**Figures 3**, **4**) suggest that EzrA(*Spn*) is a positive regulator of FtsZ-ring formation, unlike EzrA(*Bsu*)

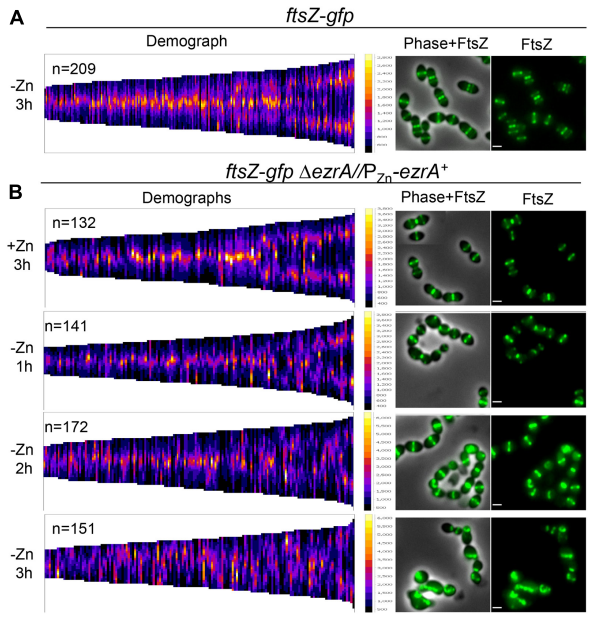

FIGURE 4 | Severe defects in FtsZ-GFP localization upon EzrA depletion in live cells. FtsZ-GFP was localized in live wild-type cells [*ftsZ-gfp*; IU8845 in **(A)**] or live EzrA depletion strain [*ftsZ-gfpΔezrA//*P$_{Zn}$-*ezrA*$^+$*;* IU8908 in **(B)**] grown and visualized in BHI broth at OD$_{620}$≈0.05–0.15 using EFm. EzrA depletion strain was complemented (+Zn; 0.5 mM $ZnCl_2$ and 0.05 mM $MnSO_4$). Alternatively, EzrA-depleted cells were visualized at 1, 2, or 3 h, upon removal of supplemented Zn/Mn from the BHI broth. Demographs assembled in MicrobeJ (Ducret et al., 2016) showing FtsZ-GFP intensity (left panels) and representative fields (right panels) are shown. Data are from two independent biological replicates in which (*n*) number of cells were analyzed.

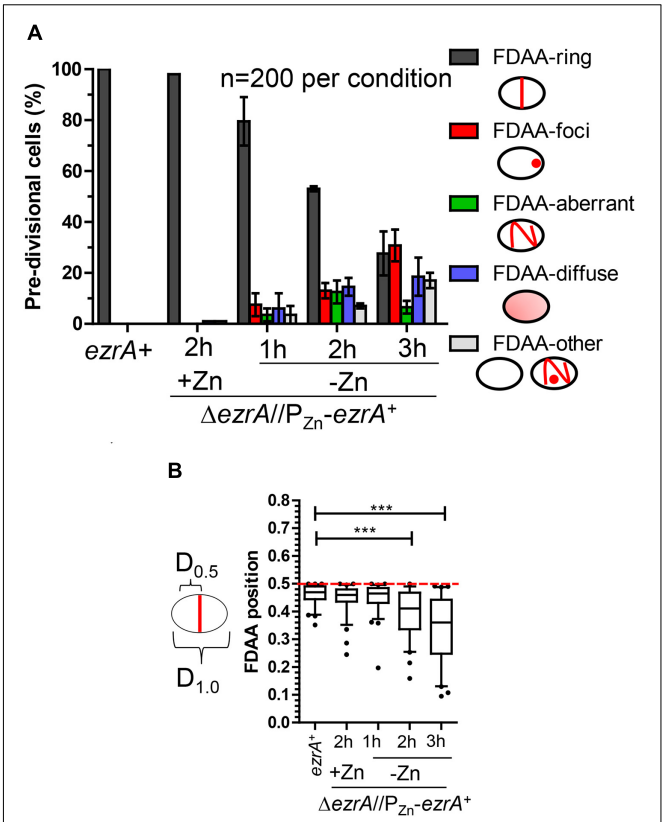

FIGURE 5 | Quantification of 2D-FDAA labeling patterns of EzrA depleted pre-divisional cells which were pulse-chase labeled. Strains used IU1945 (wild-type cells) and IU8799 (Δ*ezrA//*P$_{Zn}$-*ezrA*$^+$). Cells were grown and labeled as described in **Supplementary Figure 12A**. **(A)** Categorical bar graph showing different labeling characteristics with the short-pulse FDAA (TADA). Average values are represented by the colored bars, and error bars are for a SD of two different biological replicates in which 100 cells were counted per experiment. **(B)** Box-and-whisker plots (whiskers, 5 and 95 percentile) showing the position of FDAA-rings relative to whole cell length were determined in cells which contained FDAA-rings in **(A)**. Red dotted line indicates $D = 0.5$, a precisely midcell measured Z-ring. *p*-values obtained with Mann–Whitney two-tailed unpaired *t*-test are for comparisons between *ezrA*$^+$ and other conditions. *** indicate $p < 0.001$.

which is a negative regulator (Levin et al., 1999). To test this hypothesis, we overexpressed EzrA to see if extra FtsZ-rings appear in *Spn*. To this end, we introduced copies of P$_{Zn}$-*ezrA*$^+$ into two different ectopic sites in an *Spn* strain containing *ftsZ*-CFP at the native chromosomal locus (strain IU13700). In the BHI medium without added Zn, FtsZ-CFP localized normally in the *ftsZ*-CFP or *ezrA*$^+$ merodiploid strain (-Zn, **Figure 6**), whereas overexpression of EzrA resulted in 90% of cells showing elongated, wider chains of cells containing multiple FtsZ-CFP rings (arrows, **Figure 6**). We corroborated this conclusion using a different construct grown in the C+Y medium. FtsZ-sfGFP was expressed at the native locus in a merodiploid strain containing an ectopic copy of P$_{Zn}$-*ezrA*$^+$ (strain IU14224). The *ftsZ-sfgfp* control strain with or without Zn and the *ftsZ-sfgfp*//P$_{Zn}$-*ezrA*$^+$ merodiploid strain without Zn showed the expected pattern of FtsZ-rings (**Supplementary Figure 14**). Overexpression of EzrA by the addition of 0.25 or 0.5 mM Zn again caused formation of chains of elongated, wider cells containing multiple FtsZ-sfGFP rings (arrows, **Supplementary Figure 14**). Note that in the C+Y medium, the addition of 0.5 mM Zn and 0.05 mM Mn led to cell debris, indicative of lysis in both *ezrA*$^+$ and EzrA-overexpression cells. However, multiple FtsZ-sfGFP rings were only present in EzrA-overexpression cells and not in WT *ezrA*$^+$ cells. These combined experiments confirm that the appearance of multiple FtsZ-rings upon EzrA overexpression is not tag, construct, or medium dependent. We conclude that overexpression of EzrA in *Spn* does indeed leads to increased formation of parallel FtsZ-rings, consistent with EzrA acting as a positive regulator of FtsZ-ring formation in *Spn* cells.

FtsZ Depletion Results in Enlarged, Dead Spherical Cells That Are Subject to LytA-Dependent Autolysis

To study the relationship between FtsZ and EzrA in *Spn*, we further characterized the phenotypes caused by FtsZ depletion under our culture conditions. We constructed a strain expressing FtsZ-Myc from the chromosomal locus (IU7223) and a Δ*ftsZ* merodiploid strain expressing FtsZ$^+$ or FtsZ-Myc from an

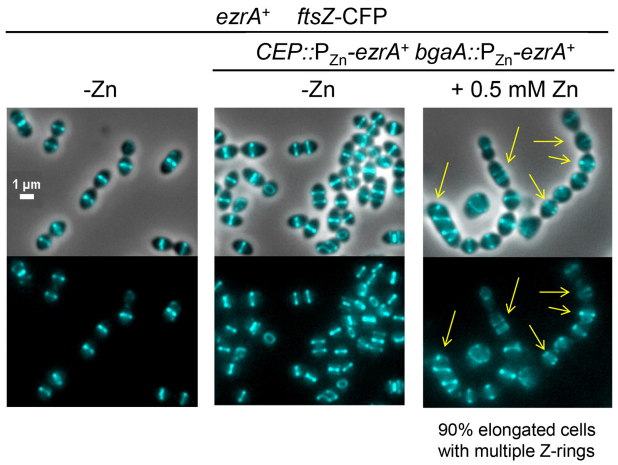

FIGURE 6 | Overexpression of EzrA leads to extra Z-rings in cells expressing FtsZ-CFP in BHI. FtsZ-CFP was localized in otherwise wild-type cells (IU13406) or *ezrA* merodiploid strain (IU13700; *ftsZ-cfp ezrA*$^+$//CEP::P_{Zn}-*ezrA*$^+$//*bgaA*::P_{Zn}-*ezrA*$^+$) in BHI 37°C 5% CO_2. Cells were grown from OD_{620}≈0.003 without supplemented $ZnCl_2$ (- Zn) or supplemented with $ZnCl_2$ (0.5 mM $ZnCl_2$ and 0.05 $MnSO_4$) to overexpress *ezrA*$^+$. Yellow arrows point to cells with extra Z-rings. Images were obtained after 4 h of growth in the presence of $ZnCl_2$/$MnSO_4$. Ninety percent of the cell population of EzrA-overexpressed cells were elongated and contained multiple Z-rings.

ectopic site (IU8124 or IU8237, respectively). Induction of FtsZ$^+$ or FtsZ-Myc with 0.3 mM Zn fully complemented the Δ*ftsZ* mutation in the merodiploid strains for growth and cell morphology (**Figures 7A,B**, and **Supplementary Figures 15A,B**). Western blotting indicated that ectopic FtsZ-Myc was expressed at 80% in the merodiploid compared to FtsZ-Myc expressed from the chromosome (**Figure 7C**). Depletion of FtsZ$^+$ or FtsZ-Myc resulted in a rapid cessation of growth, rounding of cells to spheroids, enlargement of relative cell volumes (≈ 4 ×), and a decrease in OD_{620} indicative of cell autolysis (**Figures 7A,B** and **Supplementary Figures 15A,B**). These phenotypes are similar to the aberrant, heterogeneous, exploding cells reported previously for CRIPSRi- or IPTG-regulated depletion of FtsZ in strain D39V (Liu et al., 2017; Gallay et al., 2021). Western blotting indicated that FtsZ-Myc cellular amount was reduced rapidly to < 10% within 1 h of depletion (**Figure 7C**). Titration with 0.135 mM Zn showed the relative expression of FtsZ-Myc at 3 h of growth to be at ≈23%, which was sufficient to allow continued growth without lysis (data not shown). Autolysis, but not cell shape defect upon FtsZ depletion, was abrogated by a Δ*lytA* mutation, indicating that autolysis of spheroidal lacking FtsZ was mediated by induction of the LytA amidase activity (**Figure 7A**). Nevertheless, CFU counting showed that the viability of the spheroid FtsZ-depleted Δ*lytA* cells decreased at a similar rate as in the *lytA*$^+$ cells that were lysing (**Supplementary Figure 15A**). In FtsZ-depleted *lytA*$^+$ and Δ*lytA* cells, CFU/mL counts at 7 h of depletion dropped to ≈1% to 3% compared to CFU counts at 1 to 3 h of depletion. We concluded that, as expected, FtsZ depletion in *Spn* is lethal and results in LytA-induced autolysis and loss of viability that is independent of LytA autolysis.

EzrA Recruitment to Equatorial Rings and Organized Peptidoglycan Synthesis Require FtsZ

We determined the organization of EzrA upon FtsZ depletion in a doubly epitope-tagged merodiploid strain expressing EzrA-HA from the native chromosomal locus and FtsZ-Myc ectopically (strain IU8237). We averaged 2D-EFm IFM images of dually labeled cells at different stages of division (**Figure 8A**). After 1 h of FtsZ depletion, FtsZ localization started to become disorganized, while EzrA-rings remained at midcell septa but failed to appear at the equators of daughter cells in stage 3 and 4 divisional cells (arrows, **Figure 8A**), compared to WT cells (in strain IU7223; see **Supplementary Figure 2B**). After 2 h of FtsZ depletion, a band of EzrA remained at septa and only weakly appeared at equators compared to EzrA-complemented (+Zn) cells, while FtsZ became severely disorganized (**Figure 8A** and **Supplementary Figure 16**). 3D-SIM images confirmed these conclusions (**Supplementary Figure 17**). Although some cells were able to complete a cycle of division and chromosome segregation, EzrA remained at septa in rings or diffuse areas and was not recruited to the equators of daughter cells (bottom, **Supplementary Figure 17**). Enlarged, spheroidal cells depleted of FtsZ contained diffuse regions of nucleoid staining, consistent with defects in chromosome organization and segregation (**Supplementary Figure 17**). This lack of EzrA-rings at future division sites supports the conclusions that FtsZ is required for initial recruitment of EzrA to equatorial rings of daughter cells.

Although EzrA was absent from equatorial rings during FtsZ depletion, many pre-divisional cells still contained EzrA-rings but lacked FtsZ labeling, which was obscured by the image averaging used in **Figure 8A**. To circumvent this issue, we counted co-localization events of EzrA-rings and FtsZ-rings during FtsZ depletion in pre-divisional cells (**Figure 8B**). WT cells displayed Z-ring and EzrA-ring colocalization in nearly all cells, whereas FtsZ-complemented strains (+Zn) showed ≈60% EzrA and FtsZ co-localization in pre-divisional cells (**Figure 8B**), consistent with the slightly lower expression of FtsZ detected in Western blots (**Figure 7C**). Depletion of FtsZ for 1 or 2 h showed a large, increasing drop of EzrA-ring and FtsZ-ring colocalization (**Figure 8B**). Concomitantly, after severe depletion of FtsZ for 2 h, a majority (≈80%) of cells lacked both EzrA- and FtsZ-rings (**Figure 8B**). In addition, we examined the localization pattern of FtsA upon FtsZ depletion since FtsA, similar to EzrA, co-localizes with FtsZ at all stages of cell division (Mura et al., 2016). Co-localization experiments of FLAG-FtsA upon FtsZ-Myc depletion led to a similar result (**Supplementary Figure 18**). Together, these data indicate that once assembled, EzrA- and FtsA-ring structures can persist in the absence of FtsZ-rings, but assembly of new EzrA and FtsA-rings requires the presence of FtsZ (**Figure 8C**).

Finally, a similar conclusion was reached about the organization of PG synthesis upon FtsZ depletion. Merodiploid Δ*ftsZ*//P_{Zn}-*ftsZ*$^+$ cells labeled with one color of FDAA for

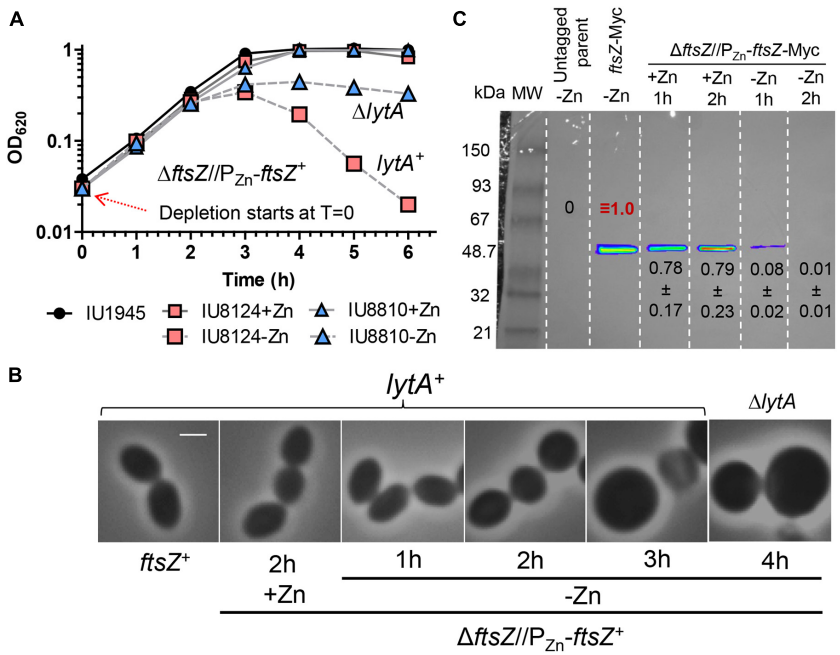

FIGURE 7 | Depletion of FtsZ results in enlarged spherical cell morphology followed by LytA induced lysis. Strains IU1945 (wild-type parent), IU8124 (Δ*ftsZ*//P_{Zn}-*ftsZ*$^+$), IU8237 (Δ*ftsZ*//P_{Zn}-*ftsZ*-Myc), and IU8810 (Δ*ftsZ*//P_{Zn}-*ftsZ* Δ*lytA*) were grown exponentially in BHI broth supplemented with 0.3 mM $ZnCl_2$ and 0.03 mM $MnSO_4$ to $OD_{620} \approx 0.1$, spun, and resuspended in BHI broth supplemented with or without 0.3 mM $ZnCl_2$ and 0.03 mM $MnSO_4$. **(A)** Representative growth curves after resuspension in BHI broth at $OD_{620} \approx 0.012$ containing or lacking $ZnCl_2$. Red arrow indicates when depletion of $ZnCl_2$ started. **(B)** Representative images of wild-type (IU1945) or FtsZ depletion strains (IU8124; *lytA*$^+$ and IU8810; Δ*lytA*) after resuspension in BHI broth supplemented with, or lacking $ZnCl_2$ for 1, 2, 3, and 4 h. Resuspension $OD_{620} \approx 0.36$ (for $T = 1$ h time point) or 0.012 (for $T = 2$, 3 or 4 h time point). The experiment was performed at least two separate times with similar results. Scale bar = 1 μm. See **Supplementary Figure 15B** for cell size measurements and statistical analysis. **(C)** Representative Western blot membranes containing extracts of IU1945 (untagged parent), IU7223 (*ftsZ*-Myc), or IU8237 (Δ*ftsZ*//P_{Zn}-*ftsZ*-Myc) mutant strains. Western blotting using the anti-Myc antibody is described in *Materials and Methods*. Protein amounts of $ZnCl_2$-induced and $ZnCl_2$-depleted strains relative to IU7223 (*ftsZ*-Myc expressed from the native promoter) were determined and quantified as detailed in section "Materials and Methods" and are from either two or three independent biological replicate experiments (± SD).

a long pulse to indicate regions of "old" PG were washed and labeled with a short pulse of a second color of FDAA to indicate regions of "new" PG synthesis (**Supplementary Figure 19A**) and examined by 2D-EFm (**Supplementary Figures 19B, 20**) or by 3D-SIM (**Supplementary Figure 19C**). After 1 h of FtsZ depletion, new PG synthesis was still occurring in rings at midcell regions. By 2 h of FtsZ depletion, organized FDAA-rings of new PG synthesis were largely absent (**Supplementary Figure 19B**), and only aberrant, diffuse FDAA-labeling patterns at old division sites and elsewhere were present in FtsZ-depleted in cells (**Supplementary Figures 19C, 20**). We conclude that FtsZ is required for organizing PG synthesis at septa and equators of dividing *Spn* cells, but PG synthesis continues in a diffusive manner in the absence of this organization.

EzrA Interaction Profiles Suggest That EzrA Functions at the Interface Between Z-Ring Regulation and Peptidoglycan Synthesis and Cell Division in *Spn*

Previously, it was shown that pneumococcal EzrA interacts with FtsZ in B2H experiments and in biochemical assays using surface plasmon resonance detection (Fleurie et al., 2014b; Rued et al., 2017). We further determined complexes that contain EzrA in *Spn* cells by co-IP (**Figures 1C, 9**) and potential direct interactors of EzrA(*Spn*) by B2H assays (**Supplementary Figure 21**). For Co-IP assays, chromosomal expressed EzrA-L-$FLAG^3$ in extracts of cells was the bait that bound magnetic FLAG-tag beads, and an extract from cells expressing untagged EzrA was used as the negative control (**Figure 1C**). Even without cross linking, EzrA pulled down FtsZ, indicative of a complex containing FtsZ and EzrA. B2H assays confirmed direct binding between EzrA and FtsZ in both B2H constructs (**Supplementary Figure 21**; Fleurie et al., 2014b; Rued et al., 2017).

EzrA was reported to interact with several cell division proteins in other bacteria, especially in B2H assays (Claessen et al., 2008; Jorge et al., 2011; Steele et al., 2011; Pompeo et al., 2015). To identify complexes that contain EzrA, we performed co-IP experiments on extracts of cross-linked *Spn* cells, as described in section "Materials and Methods." All strains used in these experiments expressed untagged EzrA (negative control) or epitope-tagged EzrA-$FLAG^3$ (bait) (**Table 2**) or other FLAG-tagged bait proteins (**Table 3**) in combination with prey proteins that were epitope tagged with -HA or -Myc (**Figure 9**; **Supplementary Figures 22–24**).

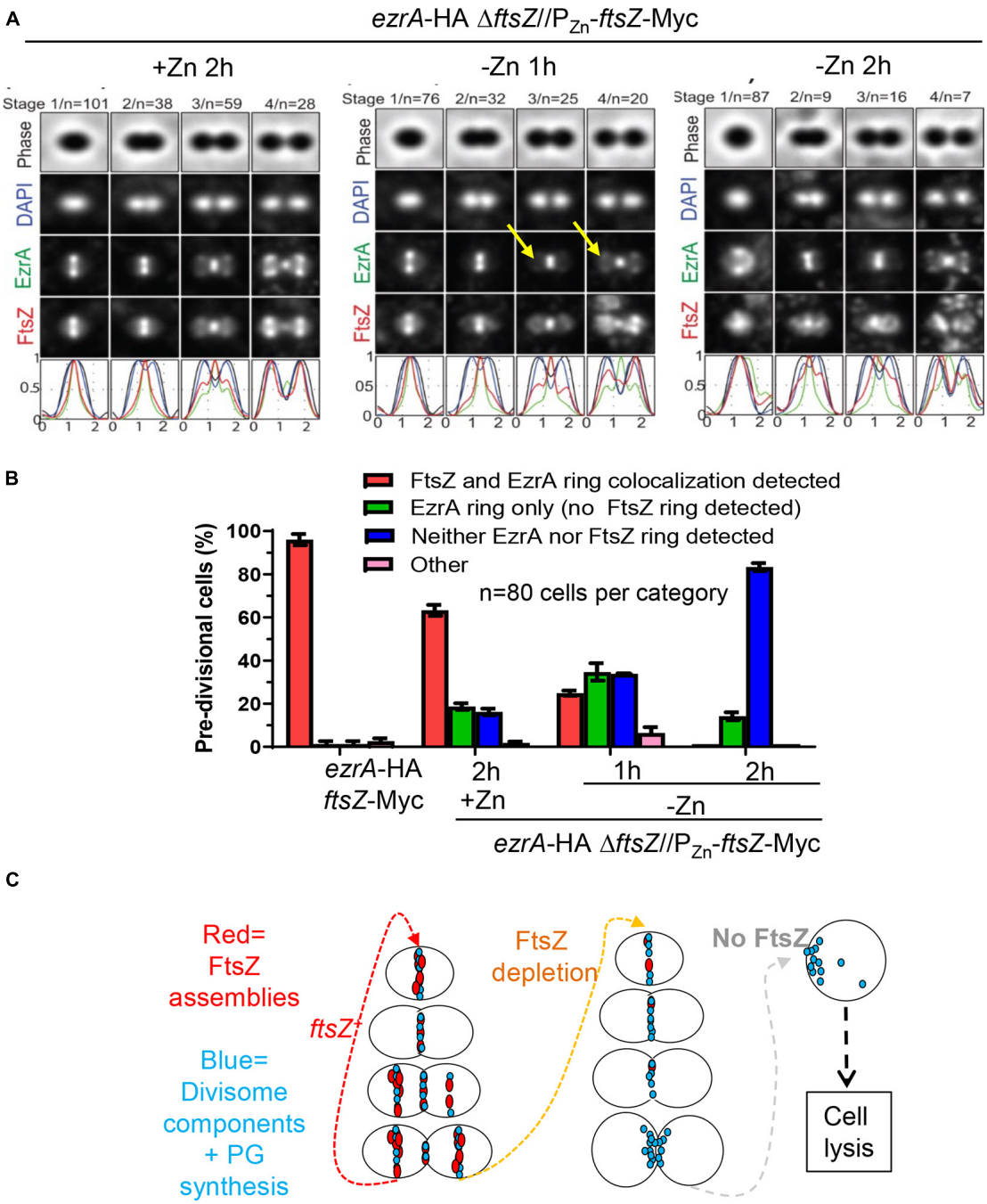

FIGURE 8 | Recruitment of EzrA-rings to equators of future dividing cells is dependent on FtsZ. Wild-type parent strain IU7223 (*ftsZ*-Myc *ezrA*-HA) and FtsZ depletion strain IU8237 (*ezrA*-HA Δ*ftsZ*//*bgaA*::P_{Zn}-*ftsZ*-Myc) were grown exponentially, and IU8237 was depleted of FtsZ-Myc by shifting cells to BHI broth not supplemented with additional $ZnCl_2$ and $MnSO_4$ as described in section "Materials and Methods." Cells were obtained at appropriate time intervals and prepared for IFM as described in *Materials and Methods*. Data are from two independent biological replicates. **(A)** Averaged images with fluorescence intensity traces showing FtsZ-Myc and EzrA-HA localization during FtsZ-Myc depletion in IU8237 (*ezrA*-HA Δ*ftsZ*//P_{Zn}-*ftsZ*-Myc). Cells were binned into division stages 1-4, and images from the indicated number of cells (*n*) from at least two independent biological replicates were averaged using IMA-GUI program as described in section "Materials and Methods." (i) Row 1, cell shapes determined from phase-contrast images; row 2, nucleoid locations from DAPI labeling; row 3, EzrA-HA locations from IFM; row 4, FtsZ-Myc locations from IFM; row 5, normalized mean fluorescence intensity distributions along the horizontal cell axis for each channel (black, phase image; blue, DNA; green, EzrA; red, FtsZ). Arrows indicate equatorial ring where EzrA is recruited in +Zn condition but less in -Zn conditions. **(B)** Bar graph quantifying FtsZ-Myc and EzrA-HA-ring co-occurrence during FtsZ-Myc depletion. Bars are the averages of two separate biological replicates while error bars are the SD. **(C)** Schematic for the orchestration of divisome components (turquoise) by FtsZ (red). FtsZ is required to assemble division sites. In the absence of FtsZ, pre-formed divisome rings can still exist but recruitment of the divisome to equators of future dividing daughter cells ceases to exist. Diffuse unorganized PG synthesis at old division sites still occurs, which leads to enlargement of cells, cell death, and eventual cell lysis.

TABLE 2 | Co-immunoprecipitation of complexes containing EzrA-FLAG[3] from cross-linked *Spn* cells[a].

Prey	Mean ratio[b]	Detected prey in complex?[c]	Strains used[d]
Z-ring regulators			
FtsZ	22.5 ± 10.9	Yes	IU6933/IU11602
FtsA	25.4 ± 9.5	Yes	IU6933/IU11602
ZapA-HA	1.2 ± 0.02	No	IU10267/IU11322
Penicillin-bindingproteins (PBPs)			
aPBP2a-HA[4]	1.04 ± 0.12	No	IU7797/IU11610
aPBP2b-HA	1.1 ± 0.04	No	IU6933/IU11602
Cell-cycle regulation			
MreC	1.0 ± 0.1	No	IU7797/IU11610

[a] *Co-IP experiments were performed as described in section "Materials and Methods." Prey proteins were detected with anti-HA, anti-FtsZ, Anti-FtsA, or anti-MreC.*

[b] *The mean ratio is determined by dividing Western blot ROI signals of epitope tagged prey in strain expressing ezrA$^+$ by the ROI signal of epitope tagged prey in strain expressing ezrA-FLAG[3] ([ROI prey-HA]$_{ezrA}{}^+$/[ROI prey-HA]$_{ezrA-FLAG}{}^3$). ROI values are determined as described previously in Materials and Methods. ± , SEM from two independent biological replicates.*

[c] *A positive interaction was determined based on the mean ratio value greater than two.*

[d] *Complete genotypes are listed in* ***Supplementary Table 1****. Strain numbers are listed in the following order; the strain listed first expresses the epitope-tagged prey and untagged EzrA (i.e., IU10302; ftsZ-Myc ezrA$^+$), while the second strain listed contains the epitope tagged prey and EzrA-FLAG[3] as the bait (i.e., IU11340; ftsZ-Myc ezrA-FLAG[3]).*

TABLE 3 | Co-immunoprecipitation of FLAG-tagged divisome proteins from cross-linked *Spn* cells[a].

Bait Used	Prey	Mean ratio[b]	Detected prey in complex?[c]	Strains used[d]
FLAG-FtsA	FtsZ-Myc	18.1 ± 10.8	Yes	IU9713/IU11476
	EzrA-HA	223 ± 49	Yes	
DivIVA-FLAG[3]	FtsZ-Myc	1.5 ± 0.5	Marginal	IU9713/IU11414
	EzrA-HA	1.8 ± 0.5	Marginal	
MapZ-FLAG[3]	FtsZ-Myc	1.6 ± 0.5	Marginal	IU9713/IU11430
	EzrA-HA	6.4 ± 0.5	Yes	
FtsK-FLAG[2]	FtsZ-Myc	1.5 ± 0.5	Marginal	IU9713/IU11664
	EzrA-HA	4.3 ± 0.7	Yes	
ZapA-FLAG	EzrA-HA	8.2 ± 1.5	Yes	IU11939/IU11840
	FtsZ	14.2 ± 3.4	Yes	
	FtsA	2.2 ± 0.1	Yes	
aPBP1a-FLAG[3]	EzrA-HA	3.6 ± 1.9	Yes	IU6810/IU12069
	FtsZ	1.3 ± 0.2	No	
	FtsA	1.2 ± 0.2	No	
	MreC	4.6 ± 2.5	Yes	
SepF-FLAG	EzrA-HA	15.9 ± 6.2	Yes	IU6810/IU12076
	FtsZ	1.1 ± 0.2	No	
	FtsA	13.3 ± 2	Yes	
StkP-FLAG[2]	EzrA-HA	13.9 ± 2.3	Yes	IU6810/IU12077
	FtsZ	1.2 ± 0.1	No	
	FtsA	1.7 ± 0.3	Marginal	
bPBP2x-FLAG[3]	EzrA-HA	1.8 ± 0.6	Marginal	IU6810/IU11880
	FtsZ	1.1 ± 0.0	No	
	FtsA	1.7 ± 0.2	Marginal	
FtsZ-FLAG	ZapA-HA	5.9 ± 3.4	Yes	IU10267/IU11322
	FtsA	5.7 ± 1.0	Yes	
	FtsZ	173 ± 79	Yes	

[a] *Co-IP experiments were performed as described in section "Materials and Methods."*

[b] *The mean ratio is determined by dividing Western blot ROI signals of epitope tagged prey in strain expressing bait$^+$ by the ROI signal of epitope tagged prey in strain expressing bait-FLAG[3] ([ROI prey-HA]$_{bait}{}^+$/[ROI prey-HA]$_{bait-FLAG}{}^3$). ROI values are determined as described in Materials and Methods. ± , SEM from two independent biological replicates.*

[c] *A positive association was determined based on the mean ratio value greater than 2.0. A mean value between 1.5 and 2.0 was labeled "marginally detected" association because prey proteins were indeed detected in the bait complex, although not "high" relative to prey protein in non-bait complex.*

[d] *Complete genotypes are listed in* ***Supplementary Table 1****. Strain numbers are listed in the following order: the strain listed first expresses the epitope-tagged prey and untagged/no bait FtsA (i.e., IU9713; ftsZ-Myc ezrA-HA ftsA$^+$), while the second strain listed contains the epitope tagged prey and a FLAG tagged bait protein (i.e., IU11476 ftsZ-Myc ezrA-HA FLAG-ftsA). All strains used here showed wild-type cell morphology and growth characteristics, with the exception of IU11430 that showed some slight cell size variability with rounder cells.*

We tested whether EzrA(*Spn*) can be detected in complexes at some stage of cell division with FtsZ-ring regulators, including FtsA, SepF, and ZapA, as was determined previously by co-IP for EzrA in *Bsu* (Ishikawa et al., 2006). We also tested if EzrA(*Spn*) is in a complex with MapZ, which guides formation of equatorial Z-rings (Fleurie et al., 2014a; Holeckova et al., 2015; Perez et al., 2019). Consistent with a role for EzrA in regulating Z-ring dynamics, EzrA(*Spn*) was detected in complexes with FtsZ and the other inferred Z-ring regulators, FtsA, SepF, ZapA, and MapZ (**Figure 9A** and **Tables 2**, **3**). Strong co-IP signals were detected for at least one bait:prey combination with EzrA and each of these proteins. For EzrA and ZapA, complex formation was detected for ZapA(bait):EzrA(prey) (**Table 3**), but not for EzrA(bait):ZapA(prey) (**Table 2**), perhaps indicating a detection limit of our co-IP assay. Interactions between EzrA and FtsZ, FtsA, SepF, and MapZ were corroborated by B2H assays (**Supplementary Figure 21**), indicating that EzrA directly interacts with these proteins at some stage of the cell cycle (**Figure 9B**). In contrast, we did not detect direct interactions in B2H assays between EzrA(*Spn*) and ZapA or its partner ZapJ, which is discussed below (**Supplementary Figure 21**). This negative result could reflect the inability of ZapA(*Spn*) and ZapJ to interact in the absence of each other in *Eco* or cross-binding of ZapA(*Spn*) to ZapAB(*Eco*) or FtsZ(*Eco*) in B2H assays.

We also probed for EzrA(*Spn*) interactions with PBPs and cell-cycle regulators. In *Bsu* and *Sau*, EzrA interacts with PBPs based on B2H assays (Claessen et al., 2008; Jorge et al., 2011; Steele et al., 2011). In *Spn*, we detected an unambiguous co-IP signal for complexes containing EzrA and aPBP1a (**Supplementary Figures 23A,B**; **Table 3**). In contrast, we detected a marginal co-IP signal for complexes containing EzrA and bPBP2x (**Supplementary Figure 22C**; **Table 3**) and no detectable complex between EzrA and aPBP2a or bPBP2b (**Supplementary Figure 22C**; **Table 2**). Consistent with the co-IP data, B2H assays detected interactions between EzrA and aPBP1a or bPBP2x and a lack of detection with bPBP2b, although an interaction with aPBP2a was detected using B2H (**Supplementary Figure 21**). We conclude that complexes containing EzrA(*Spn*) also contain certain PBPs (**Figure 9B**).

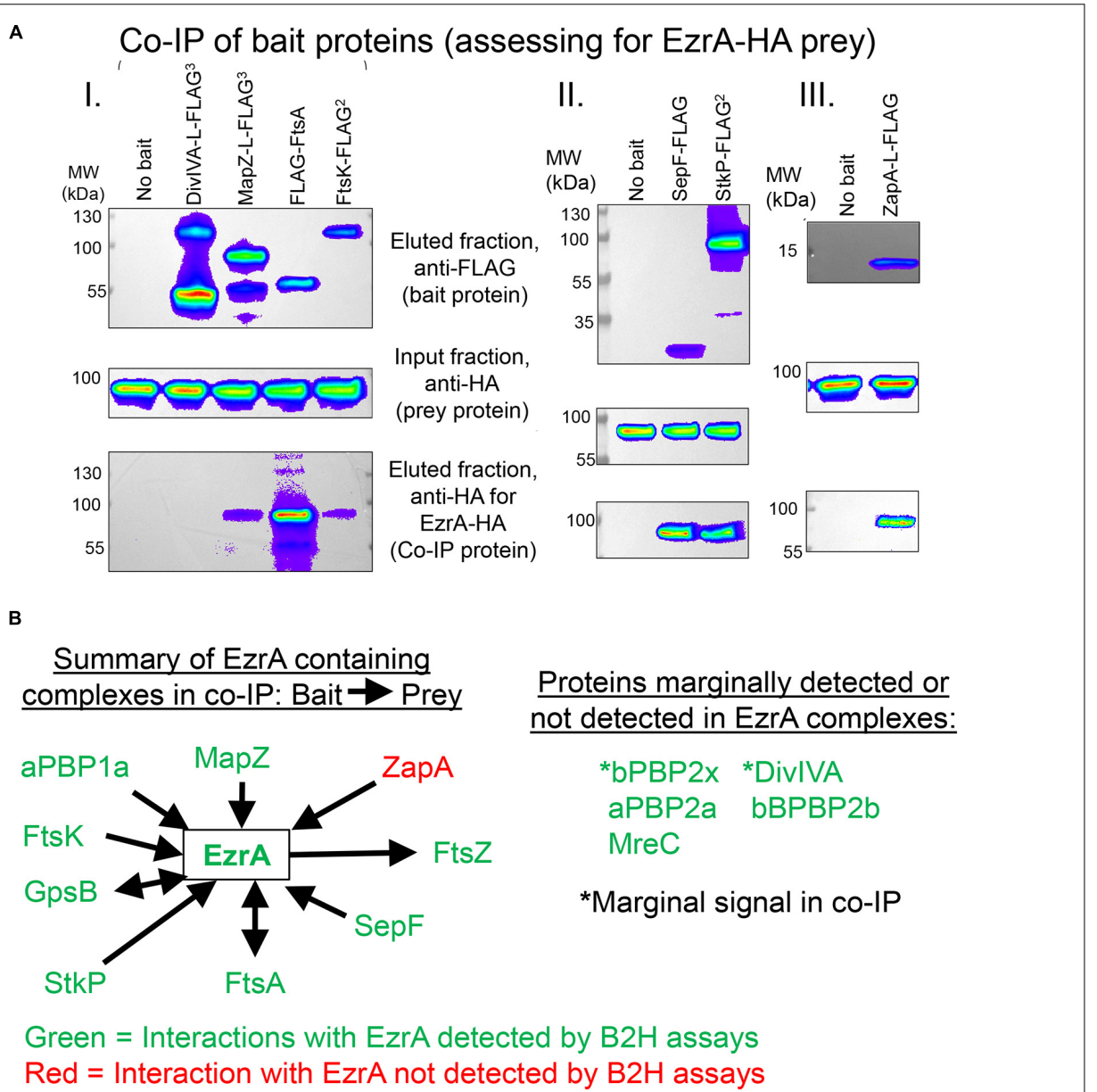

FIGURE 9 | EzrA is in complex with Z-ring regulators and cell-cycle regulators. Associations of EzrA with FtsZ-ring regulators (MapZ, FtsA, SepF, ZapA) and cell-cycle regulators (DivIVA, FtsK, StkP) in *Spn* were tested by co-IP in **(A)** and **(B)** or B2H in **(B)**. Experiments are representative from two independent biological replicates. **(A)** Top panels, labeling of transferred membranes with anti-FLAG in the eluted fractions shows the presence of FLAG-tagged bait protein. Middle panels, labeling with anti-HA in the input fraction shows the presence of EzrA-HA. Bottom panels, labeling with anti-HA in the eluted fraction shows if EzrA-HA was associated with the bait protein. Strains were subjected to Co-IP and Western blotting as described in section "Materials and Methods." Complete genotypes are listed in **Supplementary Table 1**. (I) "No bait" (IU9713), DivIVA-FLAG^3 (IU11414), MapZ-FLAG^3 (IU11430), FLAG-FtsA (IU11476), FtsK-FLAG^2 (IU11664. (II) "No bait" (IU6810), SepF-FLAG (IU12076), or StkP-FLAG^2 (IU12077). (III) "No bait" (IU11939) and ZapA-FLAG (IU11840). **(B)** Summary of EzrA co-IP results and pairwise B2H interaction assays. See **Tables 2**, **3** for quantitation and tabulation of co-IP results. See **Supplementary Figure 21** for B2H results.

We further tested whether EzrA can be detected in complexes with the cell cycle and PG-synthesis regulators DivIVA (morphogenetic determinant Fadda et al., 2007; Fleurie et al., 2014b), StkP (serine/threonine kinase Novakova et al., 2010; Beilharz et al., 2012; Fleurie et al., 2014b), GpsB (regulator of PBP activity Cleverley et al., 2016, 2019; Rued et al., 2017), and FtsK (chromosome partitioning and dimer resolution Le Bourgeois et al., 2007; Burton and Dubnau, 2010; Massidda et al., 2013; Pinho et al., 2013). Previous B2H and surface plasmon resonance assays suggested that EzrA(*Spn*) interacts with GpsB, StkP, and DivIVA (Fleurie et al., 2014b). Previously, we reported complexes containing EzrA and GpsB in *Spn* cells (Rued et al., 2017). We detected strong co-IP signals for complexes in *Spn* cells containing EzrA and StkP or FtsK (**Figure 9A** and

Table 3). In contrast, the signal for DivIVA(prey):EzrA(bait) complexes was marginal (**Figure 9A** and **Table 3**), as was the signal for DivIVA(bait):FtsZ(prey) complexes (**Supplementary Figure 24A**; **Table 3**), possibly indicating a detection limit of the co-IP assay. Interactions between EzrA and GpsB, StkP, or FtsK were corroborated by B2H assays (**Supplementary Figure 21**). We also tested for complex the formation between EzrA and MreC (PG elongasome/pPG synthesis regulator) by co-IP and B2H assays. We were unable to detect a complex containing EzrA and MreC in *Spn* by co-IP (**Table 2**), but we did detect an interaction by B2H assays (**Supplementary Figure 21**), possibly indicating a transient interaction in cells.

Finally, we used the B2H assay to test for interactions between EzrA(*Spn*) and several proteins not tested in co-IP assays. These assays indicate possible direct interactions between EzrA and MacP (positive regulator of PBP2a) (Fenton et al., 2018), RodA (SEDS GTase in pPG synthesis) (Meeske et al., 2016), MreD and RodZ (PG elongasome/pPG regulators) (Massidda et al., 2013; Briggs et al., 2021), MpgA (formerly MltG; glycosidase in pPG synthesis) (Taguchi et al., 2021), and FtsQ/L (divisome assembly proteins) (Noirclerc-Savoye et al., 2005; Briggs et al., 2021). Taken together, these results show that EzrA(*Spn*) forms complexes and interacts with many key proteins that mediate Z-ring regulation, cell division, and PG synthesis (**Figure 9B** and **Supplementary Figure 21**), consistent with its extended spectrin-like repeated structure (**Supplementary Figure 1D**) and the diverse interactions reported for EzrA in other bacteria. These multiple EzrA interactions support a model in which EzrA is not only required as a positive regulator of Z-ring assembly in *Spn* (above; **Figure 6**), but functions as a regulator that helps link FtsZ/FtsA filaments/bundles to PG synthesis and cell-cycle checkpoints.

ZapA Is a Late-Arriving Protein at the Equators of Daughter Cells in Contrast to EzrA

EzrA(*Spn*) is in complexes with several proteins that regulate FtsZ-ring formation, including FtsA, SepF, and ZapA (**Figure 9A** and **Tables 2**, **3**). FtsA and SepF have been characterized previously in *Spn* (Mura et al., 2016; Perez et al., 2019). FtsA is essential and always co-localizes with FtsZ in *Spn*, whereas Δ*sepF* deletion mutants form elongated, widened cells lacking septal constrictions, suggesting that SepF polymers mediate FtsZ-ring closure during septation, possibly by acting as a curved clamp at the leading edge of the closing septum (Wenzel et al., 2021). Despite these phenotypes, Δ*sepF* mutants grow, similarly, to WT in BHI broth, and the cell morphology defects of Δ*sepF* mutants are largely reversed by FtsA overexpression (Mura et al., 2016). In contrast to SepF, nothing has been reported about ZapA function in *Spn* or other ovococcal bacteria.

Co-immunoprecipitation experiments detected ZapA in complex with FtsZ, FtsA, and EzrA in *Spn* cells (**Supplementary Figure 25**; **Table 3**), so we compared the spatiotemporal location of ZapA with that of FtsZ. Δ*zapA* mutants did not show any overt growth or cell morphology defects compared to WT in BHI broth or C+Y media (**Supplementary Figure 27B**; data not shown). We constructed a strain expressing FtsZ-Myc and ZapA-L-FLAG from their chromosomal loci (strain IU10752) and compared their localization to FtsZ-Myc and EzrA-L-FLAG[3] (IU8681) by 2D EFm (**Figure 10B** and **Supplementary Figure 26A**). Unlike EzrA, which co-localizes with FtsZ and moves to the equatorial rings of daughter cells in stages 3 and 4 of the division cycle, ZapA remains at the midcell septal ring until late in cell division (**Figure 10B**). Moreover, quantitative comparisons of ring widths of C-terminal-tagged EzrA- EzrA-L-FLAG[3] or ZapA-L-FLAG with FtsZ-Myc indicated that EzrA-rings are slightly larger than FtsZ-rings (**Figure 10B** and **Supplementary Figure 26A**), as discussed above (**Supplementary Figure 2**). In contrast, ZapA-rings have a considerably smaller width than FtsZ widths (**Figure 10B** and **Supplementary Figure 26A**), indicative of separate sublocations of EzrA and ZapA in FtsZ-rings.

Late arrival of ZapA at equators compared to FtsZ was confirmed by 3D-SIM of the FtsZ-Myc and ZapA-L-FLAG epitope-tagged strains (**Supplementary Figure 26B**) and separately by demograph analysis of 2D-EFm images of live cells expressing ZapA-sfGFP (strain IU10065) or FtsZ-sfGFP (strain IU9985) (**Figure 10C**). These results indicate that ZapA is not present in the nascent MapZ/FtsZ/FtsA/EzrA-rings that move out from the septum to the equators during *Spn* division (Perez et al., 2019) or in early equatorial rings. Consistent with this conclusion, the velocity of FtsZ treadmilling in nascent and early equatorial rings was the same in a Δ*zapA* mutant as the WT *zapA*$^{+}$ strain (**Supplementary Figure 27A**). Similar to ZapA, 2D-EFm and 3D-SIM showed that SepF remains at septa throughout most of the division cycle and arrives late at the equators of daughter cells (**Supplementary Figures 28A,C**; Mura et al., 2016). However, unlike ZapA, the width of the SepF ring at the midcell is very similar to that of FtsZ (**Supplementary Figure 28B**). Together, these results are consistent with the idea that the pneumococcal FtsZ regulators EzrA, FtsA, SepF, and ZapA form a spatially ordered network, analogous to the one proposed for *Eco* (Buss et al., 2015).

ZapA Is Required for the Slow-Growth Phenotype of EzrA-Depleted *Spn* Cells

As shown above (**Figures 3**, **4**, **6**), EzrA acts as a positive regulator of FtsZ-ring formation in *Spn*. We wanted to examine whether ZapA and SepF contribute to this positive regulation. Δ*zapA* mutants do not exhibit growth or cell morphology defects under the culture conditions tested (**Supplementary Figure 27B**), so we determined the effects on growth when EzrA is depleted in a Δ*zapA* or Δ*sepF* mutant. As noted above, depletion of EzrA results in bacteriostatic spheroid cells for long periods of time (**Figure 2**; **Supplementary Table 3**). Lack of ZapA (**Figure 10A**) or SepF (**Supplementary Figure 28D**) prevents prolonged growth upon EzrA depletion, whereas lack of MapZ does not (**Supplementary Figure 28D**). Depletion of EzrA in the Δ*zapA* or in the Δ*sepF* mutant gave mostly viable, irregularly shaped spheroid cells, typical of EzrA depletion in the WT strain (**Figure 2B** and **Supplementary Figure 29**).

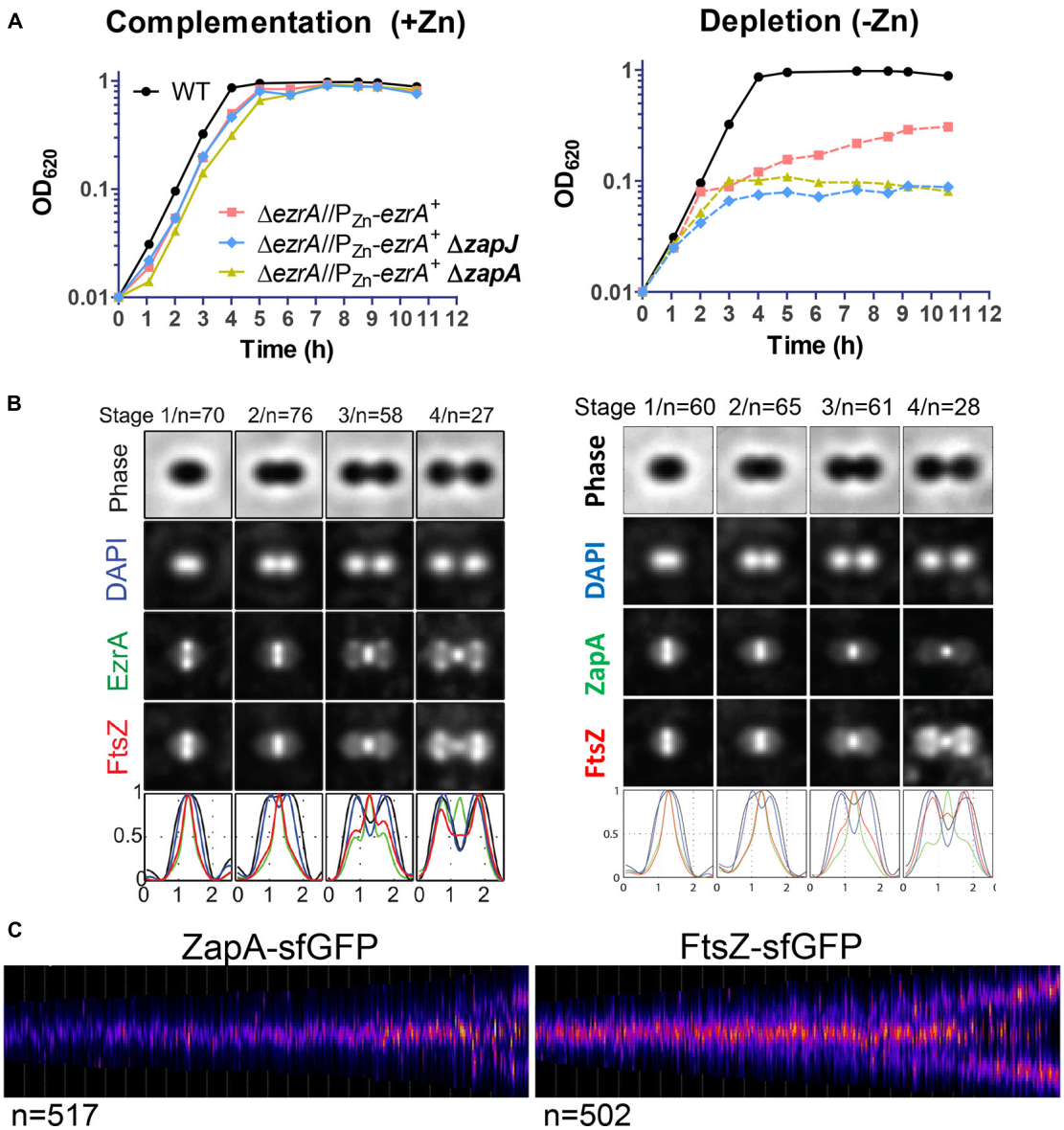

FIGURE 10 | Localization of ZapA relative to FtsZ and combined defects of Δ*zapA* or Δ*zapJ* with EzrA depletion in *Spn*. **(A)** Graph demonstrating the growth curve upon EzrA complementation (left graph) or EzrA depletion (right graph) in otherwise WT, Δ*zapA*, or Δ*zapJ* mutant backgrounds. Wild-type EzrA was induced by supplementation of 0.5 mM $ZnCl_2$ and 0.05 mM $MnSO_4$ or depleted by growth in the absence of supplemented Zn/Mn. Strains used were IU1945, IU8799, IU10839, and IU15029. **(B)** Averaged images with fluorescence intensity traces showing FtsZ and EzrA localization from IFM performed on IU8681 (left) or IU10752 (right). Cells were binned into division stages 1-4, and images from the indicated number of cells (*n*) from at least two independent biological replicates were averaged using the IMA-GUI program as described in section "Materials and Methods" and previously (Tsui et al., 2014). (i) Row 1, cell shapes determined from phase-contrast images; row 2, nucleoid locations from DAPI labeling; row 3, EzrA (left panel) or ZapA (right panel) locations from IFM; row 4, FtsZ locations from IFM; row 5, normalized mean fluorescence intensity distributions along the horizontal cell axis for each channel (black, phase image; blue, DNA; green, EzrA or ZapA; red, FtsZ). Cells from at least two independent biological replicates were collected at OD_{620} ≈0.1–0.2 and prepared for each set of cells as described in section "Materials and Methods." **(C)** Demographs of ZapA-sfGFP localization from strain IU10065 compared to FtsZ-sfGFP localization from strain IU9985 obtained using snapshot 2D-EFm of live cells. The indicated number of cells (*n*) from at least two independent biological replicates were analyzed using MicrobeJ and as described in section "Materials and Methods" and previously (Perez et al., 2019).

However, Δ*sepF* cells during depletion of EzrA appear larger than Δ*zapA* cells under EzrA depletion (**Supplementary Figure 29**), consistent with the increased length and width of Δ*sepF* mutants (Mura et al., 2016). By comparison, Δ*zapA* Δ*sepF* mutants grew, similarly, to Δ*sepF* single mutants, forming elongated and widened cells (data not shown; Mura et al., 2016). Finally, lack of ZapA did not alter the growth stoppage and lysis when FtsZ was depleted (**Supplementary Figure 27B**), but Δ*zapA* Δ*mapZ* mutants grew slightly slower than a Δ*mapZ* mutant (**Supplementary Figure 27C**). Together, these results are

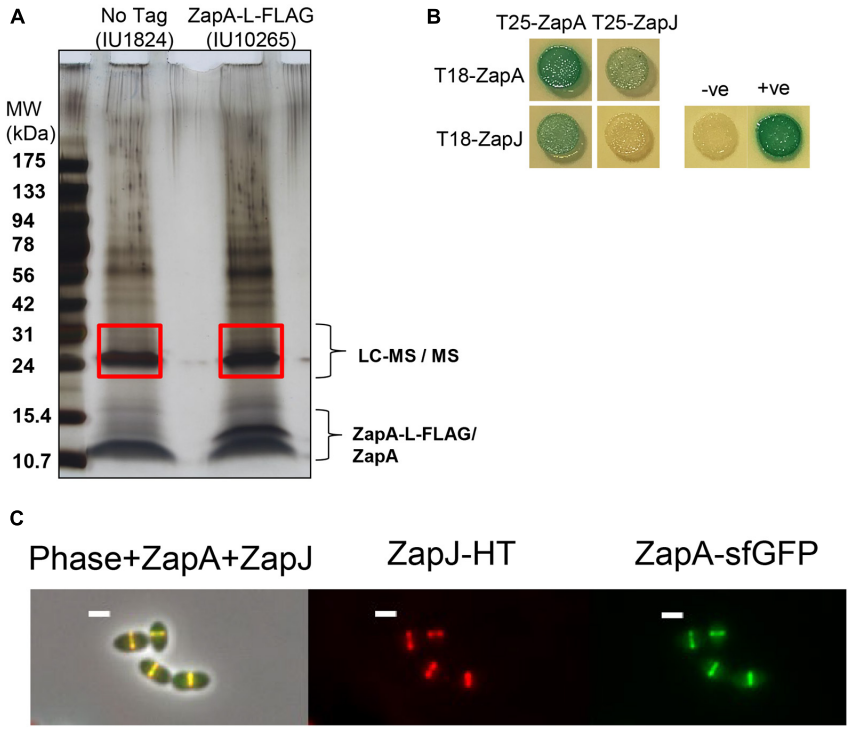

FIGURE 11 | ZapA can co-IP ZapJ (Spd_1350) and these proteins co-localize at midcell rings. Cells were cultured in BHI broth and harvested at OD_{620}≈0.1-0.25 for experiments. **(A)** Silver-stained SDS-PAGE gel from Co-IP experiments performed using WT (IU1824, lane 1 non-flagged control) and ZapA-FLAG (IU10265, lane 2) as bait. Red boxes indicate excised bands that were processed for LC-MS/MS (see section "Materials and Methods"). PAGE ruler pre-stained ladder and calibrated MW shown on the left. **(B)** ZapA and ZapJ from *Spn* interact directly, and ZapA self-interacts by B2H assays. T25 or T18 fusions are expressed from low-or high-copy plasmids, respectively. Plasmid pairs pKT25/pUT18C and pKT25-*zip*/pUT18C-*zip* were used as negative (–ve) and positive (+ve) controls. B2H assays were performed as described in *Materials and Methods*. Agar plates were photographed after 40 h at 30°C. B2H assays were performed at least twice with similar results. **(C)** Co-localization of ZapJ-HT and ZapA-sfGFP in the same cells of strain IU15116. Cells were labeled with 500 nM HT-TMR ligand and imaged using conventional microscopy as described previously (Perez et al., 2019). Representative images are shown.

consistent with ZapA and SepF, playing accessory roles to EzrA in positively regulating FtsZ-ring formation, separate from MapZ, in *Spn*.

ZapA Forms a Complex With ZapJ (Spd_1350), and Δ*zapJ* Phenocopies Δ*zapA*

In *Eco*, ZapA interacts with a partner protein, called ZapB (Ebersbach et al., 2008; Galli and Gerdes, 2012). *Spn* does not encode an obvious ZapB homolog. NCBI blast search of the gene (*spd_0370*) immediately downstream from *zapA* in the *Spn* D39 genome identified a colicin V superfamily protein as a homologue, but not *zapB*(*Eco*). *spd_0370* was annotated as *zapB* (Slager et al., 2018) in D39V, and as a colicin V superfamily protein (Lanie et al., 2007) in D39W, and is a homologue of *yshB*(*Bsu*), a gene downstream of *zapA*(*Bsu*) (BioCyc). To test experimentally whether Spd_0370 might be involved in Z-ring dynamics in *Spn*, we fused the N- and C-termini of Spd_0370 to GFP and to the FLAG epitope tag and determined its localization in *Spn* cells. 2D-EFm showed that Spd_0370 localized to the membrane but did not localize to the midcell divisome region, despite confirmed expression by Western blotting (data not shown). Given its lack of homology to *Eco* ZapB and its localization, we conclude that *spd_0370* does not encode an FtsZ-ring regulator, despite its co-transcription with *zapA* (Slager et al., 2018).

To identify a partner of ZapA(*Spn*), we turned to an unbiased co-IP/MS approach. We formaldehyde-cross-linked *Spn* cells expressing ZapA-FLAG, which was then enriched on magnetic beads, and potential interactors were resolved by SDS-PAGE followed by silver staining as described in section "Materials and Methods" (**Figure 11A**). A single faint band with a molecular mass of about 24 kDa was present in the extract from cells expressing ZapA-FLAG, but absent from control cells lacking any FLAG-tagged proteins. The region between ≈21 and 31 kDa was excised from both lanes and subjected to peptide analysis by mass spectroscopy. Comparison of peptides from the ZapA-FLAG sample with the untagged $ZapA^{+}$ control revealed that ZapA-FLAG pulled down the protein Spd_1350, which we renamed ZapJ (calculated molecular mass = 23,844 kDa and pI = 9.11). *zapJ* appears to be in a single-gene operon (Slager et al., 2018) and is located upstream of *murC* (**Supplementary Figure 30A**) that encodes UPD-N-acetylmuramate-alanine ligase, which catalyzes the third reaction in Lipid II precursor synthesis (**Supplementary Figure 30A**). ZapJ was putatively annotated as a cystathionine

γ-synthase (Slager et al., 2018), which is inconsistent with the genetic relationships of Δ*zapJ* mutants that we observed below. B2H assays confirmed a direct interaction between ZapA and ZapJ and a self-interaction of ZapA (**Figure 11B**).

For every phenotype examined, ZapJ completely phenocopied ZapA. Similar to Δ*zapA* mutants, Δ*zapJ* mutants grew like WT and did not show cell morphology defects under the culture conditions tested (**Figure 10A**; data not shown). ZapJ fused at its C-terminus to Halotag (HT) or sfGFP localized to the midcell (**Figure 11C** and **Supplementary Figure 30B**), and ZapJ co-localized with ZapA in cells at different division stages (**Figure 11C**). Like ZapA, demograph analysis showed that ZapJ is a late-arriving protein to the equators of daughter cells (**Figure 10C** and **Supplementary Figure 30C**). EzrA depletion in a Δ*zapA* or Δ*zapJ* mutant rapidly prevented continued growth (**Figure 10A**), and the impaired growth of Δ*zapA* or Δ*zapJ* in Δ*mapZ* mutant backgrounds was indistinguishable (**Supplementary Figure 27C**). Together, these results support the hypothesis that ZapA and ZapJ interact and act as accessory positive regulators of FtsZ-ring formation in *Spn*. Finally, ZapJ is confined to *Streptococci*, which appear to lack a ZapB homolog, and *zapJ* is genetically closely linked to *murC* across *Streptococcus* species (**Supplementary Figure 31**).

DISCUSSION

In this paper, we show that EzrA and FtsZ are both essential for the growth, division, ovoid shape, and normal size of pneumococcal cells (**Figures 2**, **7**). *Spn* EzrA and FtsZ always co-localize during the cell cycle, and their localization is interdependent (summarized in **Figure 12**). The importance of EzrA to the midcell presence and placement of the divisome was corroborated by the complementary approaches of FtsZ localization by IFM (**Figure 3**) and FtsZ-GFP in live cells by EFm (**Figure 4** and **Supplementary Figure 11**) and localization of regions of PG synthesis by FDAA pulse-chase labeling (**Figure 5**, and **Supplementary Figures 12, 13**). Moreover, EzrA depletion resulted in cells with non-medial placement of FtsZ-rings, including minicells lacking DNA (**Figures 3B**, **12B**, **Supplementary Figures 10, 11C**). Of particular note, overexpression of EzrA led to the formation of extra Z-rings (**Figures 6**, **12C** and **Supplementary Figure 14**). Finally, we show that a multicomponent network of Z-ring regulators, including EzrA (essential), SepF (non-essential), ZapA (non-essential), and newly identified ZapJ (non-essential), synergistically support cell division in *Spn* (**Figures 10**, **12E** and **Supplementary Figure 28**). Altogether, this work is consistent with positive roles for EzrA, SepF, ZapA, and ZapJ in promoting Z-ring assembly in *Spn*.

Biochemical and physiological evidence implicates that EzrA is a negative regulator of FtsZ-ring formation in *Bsu* and possibly other bacteria (Levin et al., 1999; Haeusser et al., 2004; Singh et al., 2007; Cleverley et al., 2014). In contrast, the data presented here show that EzrA positively regulates Z-ring formation in *Spn* in the midcell and elsewhere. Depletion of EzrA(*Spn*) leads to cells lacking Z-rings or containing misplaced Z-rings (**Figures 3**, **4**, and **Supplementary Figure 11**), in contrast to the formation of additional Z-rings in *Bsu* Δ*ezrA* mutants. Consistent with positive regulation, overexpression of EzrA leads to *Spn* cells with multiple extra Z-rings (**Figure 6** and **Supplementary Figure 14**). Other positive regulators of Z-ring formation, including SepF, ZapA, and newly discovered ZapJ, are required for the continued slow growth of cells upon depletion of EzrA(*Spn*) (**Figure 10A** and **Supplementary Figure 28D**). Previous work demonstrated that a nascent division ring containing EzrA moves away from the septal ring of WT cells with MapZ, FtsZ, and FtsA toward the equators of daughter cells, presumably driven by pPG synthesis (Perez et al., 2019). By contrast, both SepF and ZapA remain at the septum throughout most of the division cycle and only arrive late at equators (**Figures 10B,C** and **Supplementary Figure 28A**; Mura et al., 2016). These results are consistent with EzrA(*Spn*) acting as a positive regulator that corrals FtsZ/FtsA filaments/bundles into new and nascent Z-rings.

Depletion of EzrA(*Spn*) is bacteriostatic for a surprising long period of time (**Figure 2A** and **Supplementary Figure 29**), whereas depletion of FtsZ(*Spn*) is catastrophic and leads to drastic decrease in cell viability and the formation of large spherical cells that are rapidly autolysed by the stress-induced LytA PG amidase (**Figure 7A** and **Supplementary Figure 15A**; Mellroth et al., 2012; Flores-Kim et al., 2019). FtsZ depletion in *Spn* severely disorganizes the localization of EzrA, FtsA, and PG synthesis from their normal positions in septal and equatorial rings (**Figure 8** and **Supplementary Figures 16–20**). While we have previously shown that early-onset depletion of FtsA leads to more heterogeneous cell shapes (Mura et al., 2016) than FtsZ depletion shown here, later depletion timepoints of FtsA also show enlarged and completely sphere-shaped cells caused by diffuse and disorganized PG synthesis. This terminal FtsA depletion phenotype resembles FtsZ depletion reported here. This disorganization is consistent with the model that the FtsZ/FtsA-ring initially organizes both sPG and pPG synthesis at midcells of pre-divisional *Spn* cells and continues to organize sPG synthesis during septal constriction as division progresses (Briggs et al., 2021; Perez et al., 2021). It also underscores the absence of a separate mechanism for the organization of pPG synthesis, analogous to that mediated in rod-shaped bacteria by MreB, which maintains continued lateral synthesis when FtsZ is depleted, resulting in long, filamentous cells (Beall and Lutkenhaus, 1991; Dai and Lutkenhaus, 1991). Similar disorganization of PG synthesis caused by FtsZ depletion occurs in *Sau* (Pinho and Errington, 2003) and likely occurs in other coccal and ovococcal species that lack MreB.

In Δ*mapZ* mutants, EzrA still co-localizes and streams with FtsZ by a failsafe mechanism to form new Z-rings near the middles of daughter *Spn* cells (**Supplementary Figures 4, 12D**; Perez et al., 2019). Consequently, Δ*mapZ* mutants show relatively minor defects in Z-ring presence and placement, compared to the severe effects caused EzrA depletion (**Figure 3** and **Supplementary Figures 2A,B**). In this work, we further demonstrated co-localization of EzrA and FtsZ treadmilling dynamics in nascent and equatorial rings of WT cells (**Supplementary Figure 5**) and during streaming in Δ*mapZ*

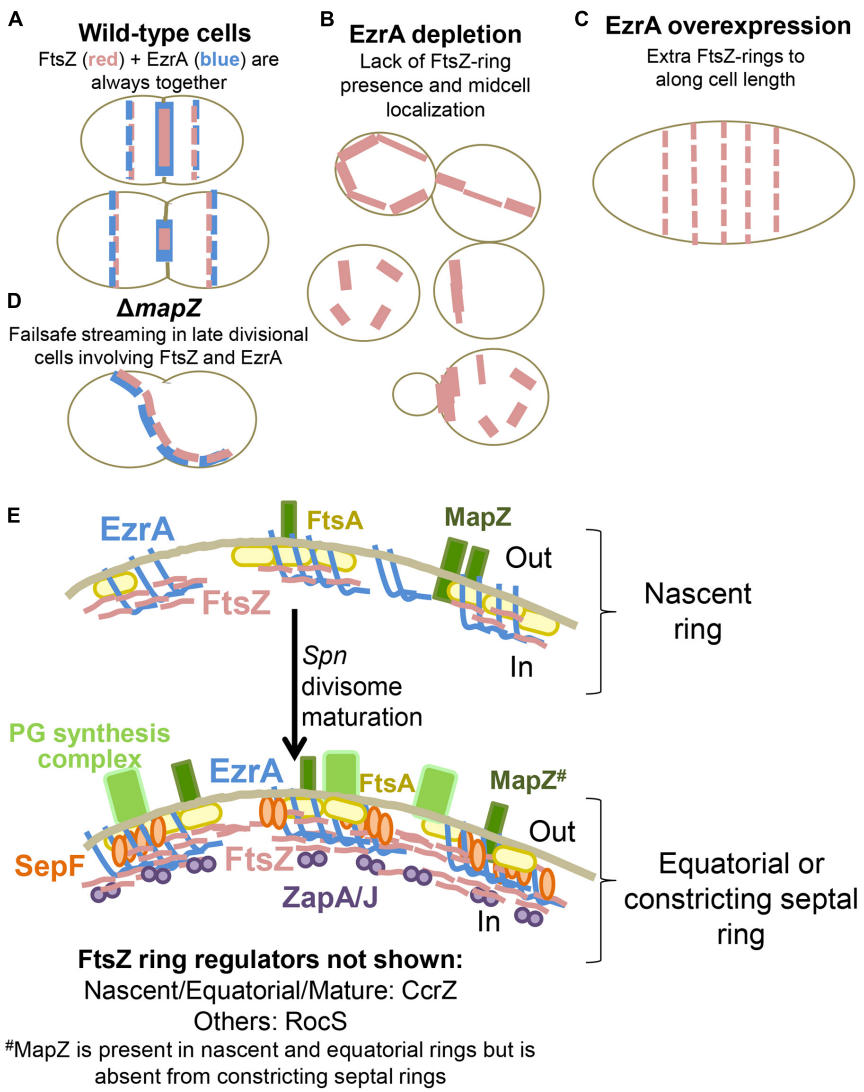

FIGURE 12 | Schematic drawings indicating EzrA as a positive Z-ring regulator in *Spn,* whereas EzrA, SepF, ZapA, and ZapJ form a multi-layered network of proteins that synergistically regulate the FtsZ-ring and cell division in *Spn* during divisome maturation. **(A–D)** Phenotypes of cell shape and FtsZ localizations observed in **(A)** WT, **(B)** EzrA depletion **(C)** EzrA overexpression and **(D)** Δ*mapZ*. **(E)** Summary diagram depicting the spatial localization patterns of FtsZ, EzrA, ZapA/J, SepF, and PG synthesis complexes during divisome maturation in *Spn.* EzrA/FtsZ/FtsA and MapZ form early arriving Z-ring regulators while ZapA/J and SepF are late arriving Z-ring regulators. RocS arrives early but is not divisome associated while CcrZ connects early Z-ring formation with DNA replication. EzrA and FtsA are membrane anchors for FtsZ filaments. SepF localizes with FtsZ, while ZapA, and by extension ZapJ, are on the inside of the Z-ring.

mutants (**Supplementary Figure 3**). The TM domain and the conserved C-terminal QNR motif of EzrA(*Spn*) are required for localization and function (**Supplementary Figure 9**), similar to what was reported previously for EzrA(*Bsu*) (Cleverley et al., 2014; Land et al., 2014). Other mutations near the C-terminal QNR motif of EzrA(*Spn*) result in a temperature-sensitive phenotype (Perez et al., 2021). Together, these results support a critical role for EzrA(*Spn*) in anchoring FtsZ filaments/bundles to membranes, whereas MapZ guides FtsZ/EzrA/FtsA bundles filaments/bundles from the nascent ring to the equators of daughter cells.

Ensemble labeling shows that EzrA(*Spn*) moves dynamically with FtsZ and FtsA in filaments/bundles at a velocity of ≈34 nm/s in nascent and equatorial rings of dividing *Spn* cells (**Supplementary Figure 5**; Perez et al., 2019). Likewise, EzrA-GFP expressed from the native *ezrA* promoter in *Sau* moves with a similar velocity to FtsZ filaments/bundles (Monteiro et al., 2018). At the same time, single molecules of FtsZ in filaments appear stationary, because of the treadmilling mechanism (Bisson-Filho et al., 2017; Yang et al., 2017; Perez et al., 2019). It was recently reported that single molecules of EzrA(*Bsu*) and other FtsZ-binding proteins appear to be immobile at division

sites in treadmilling FtsZ filaments/bundles (Squyres et al., 2021). Similarly, some single molecules of EzrA(*Spn*) appear to be immobile at the midcell of *Spn* cells (data not shown). In addition, we observed a population of EzrA that is not strongly associated with FtsZ or FtsA in equatorial and nascent rings (**Supplementary Figure 5**). These combined results suggest that there are two populations of EzrA at *Spn* division sites: (i) diffusing, FtsZ-unassociated EzrA molecules are not bound to treadmilling FtsZ/FtsA filaments/bundles, but are confined to the division ring plane and (ii) immobile, FtsZ-associated EzrA molecules are transiently bound to and released from treadmilling FtsZ/FtsA filaments/bundles, resulting in collective migration (Baranova et al., 2020). Finally, the processive ensemble motion of FtsZ/EzrA/FtsA filaments/bundles in *Spn* is distinct from the processive single-molecule motions of septal cell-wall synthase PBP2x:FtsW(*Spn*) complexes. Processive septal cell-wall synthase complexes are driven by PG synthesis independent of FtsZ treadmilling (Perez et al., 2019) or from the treadmilling-linked Brownian-ratchet mechanism that moves non-synthesizing bPBP(FtsI) in the septum of *Eco* cells (McCausland et al., 2021; Yang et al., 2021).

We show that EzrA(*Spn*) is in complexes with numerous proteins involved in FtsZ-ring placement (MapZ) and stabilization (FtsZ, FtsA, ZapA, and SepF), cell division and chromosomal segregation (FtsK and possibly DivIVA), PG synthesis (aPBP1a and possibly bPBP2x), and PG regulation (GpsB and StkP) (**Figure 9B**) at some stage in cell division. EzrA(*Spn*) has the capacity to bind directly to all of these proteins, with the possible exception of ZapA, based on B2H assays (**Supplementary Figure 21**). Moreover, a new paper reports that EzrA(*Spn*) interacts directly with the CcrZ cell-cycle regulator that also interacts with FtsZ, FtsA, and ZapA and couples cell division with DNA replication through control of DnaA activity (Gallay et al., 2021). Wide binding versatility of EzrA was previously noted in *Sau*, although where and when these diverse proteins bind to the spatially complex EzrA spectrin-like loop structure (**Supplementary Figure 1**) remains to be determined. The essentiality, different phenotypes caused by EzrA depletion compared to FtsZ depletion, including FDAA labeling efficiency (**Supplementary Figure 12**), and the inability to isolate stable suppressor mutations of Δ*ezrA* (see section "RESULTS") are consistent with EzrA orchestrating Z-ring regulation with cell division and PG synthesis in *Spn*.

EzrA remains associated with FtsZ in all locations throughout the cell cycle of *Spn* cells (**Figures 1**, **12**), including the following: in FtsZ/FtsA/EzrA nascent ring planes that move with MapZ outward to the equators of daughter cells (**Supplementary Figures 3, 5**; Perez et al., 2019); in constricting septa (**Figure 1** and **Supplementary Figure 2C**) until remaining FtsZ migrates to the equators of daughter cells before sPG synthesis is completed (**Supplementary Figure 6**); and in streaming FtsZ filaments in Δ*mapZ* mutants (**Supplementary Figure 4**). FtsA also shows very similar localizations and dynamics as FtsZ and EzrA (Mura et al., 2016; Perez et al., 2019). The other FtsZ-positive regulators in *Spn*, SepF, ZapA, and presumably its partner ZapJ arrive later to the FtsZ-rings that form at the equators of daughter cells (**Figure 10**, **Supplementary Figures 28, 30**) (Mura et al., 2016). This pattern contrasts sharply with the early arrival of ZapA with FtsZ and FtsA in rod-shaped bacteria (Aarsman et al., 2005; Gamba et al., 2015). Nevertheless, SepF, ZapA, and ZapJ are required to maintain the slow growth phenotype of EzrA-depleted *Spn* cells (**Figure 10A** and **Supplementary Figure 28D**), suggesting accessory roles of these proteins to EzrA in maintaining FtsZ-rings in mature equatorial and septal rings. FtsA was shown to be essential, and prolonged FtsA depletion resulted in cell lysis and severe mislocalization of FtsZ. Thus, FtsA is another essential positive Z-ring regulator while also playing a role in sPG and pPG synthesis (Mura et al., 2016). The association of EzrA and FtsZ in nascent rings that lack other accessory FtsZ-positive regulators may underlie why EzrA functions as a positive regulator in *Spn*, instead of a negative regulator as in *Bsu*.

The discovery of ZapJ as a partner for ZapA (**Figures 11A**, **12**) may account for the lack of ZapB homologues in *Streptococcus* species. Similar to ZapA(*Eco*) and ZapB(*Eco*), ZapA(*Spn*) and ZapJ(*Spn*) localize in the midcell and interact directly with each other (Galli and Gerdes, 2010, 2012). Additionally, similar to Δ*zapA*(*Eco*) and Δ*zapB*(*Eco*) (Buss et al., 2013), Δ*zapA*(*Spn*) phenocopied Δ*zapJ*(*Spn*) in every physiological assay shown in this study, further suggesting that ZapA:ZapJ function together as part of the same complex in *Spn* and potentially other *Streptococci*. While ZapJ is conserved in *Streptococci*, ZapB is absent from Gram-positive bacteria and, instead, restricted to the Gammaproteobacteria class (Adams and Errington, 2009; Huang et al., 2013). Within the resolution limits of IFM methods, EzrA, FtsA, and ZapA form rings with different diameters relative to FtsZ in *Spn* (**Supplementary Figures 2C, 26**; Mura et al., 2016), consistent with a multilayered network of FtsZ stabilizers (**Figure 12E**), analogous to the that proposed for *Eco* (Buss et al., 2015; Coltharp et al., 2016). Recently discovered CcrZ, which controls DNA replication and clearly interacts directly with FtsZ in *Spn* cells, couples the timing of DNA replication to Z-ring placement in this multicomponent network (Gallay et al., 2021), replacing *Eco* MatP, which is absent in *Streptococcus* species. Aberrant timing of DNA replication at the midcell FtsZ-ring in mutants lacking CcrZ leads to chromosome mis-segregation and anucleate cells (Gallay et al., 2021), similar to what occurs when the FtsZ-ring structure is disrupted by EzrA depletion in *Spn* (**Supplementary Figure 10**). Future studies are needed to understand the roles of EzrA, SepF, ZapA:ZapJ, and FtsA in mediating septal closure and chromosome segregation in *Spn.*

Finally, *Streptococcus* species are resistant to compound PC190723, which inhibits FtsZ polymerization in *Sau*, *Bsu*, *Eco*, *Bacillus anthracis*, and other bacteria (Haydon et al., 2008). The discovery of ZapJ and further characterization of FtsZ-ring regulation offer the potential for identifying new vulnerabilities for antibiotic discovery against *Spn* and other *Streptococci*, which are becoming increasingly antibiotic resistant (Centers for Disease Control and Prevention, 2019).

DATA AVAILABILITY STATEMENT

The original contributions presented in the study are included in the article/**Supplementary Material**, further inquiries can be directed to the corresponding author/s.

AUTHOR CONTRIBUTIONS

AP, H-CT, and MW contributed to the conception and design of this study. AP, JV, H-CT, MD, MB, and OM contributed to the acquisition, analysis, and interpretation of data. AP and MW contributed to the writing and editing of the manuscript with input from the other authors. All authors contributed to the article and approved the submitted version.

FUNDING

Funding for this work was provided by the National Institutes of Health grants R35GM131767 to MW, Predoctoral Quantitative and Chemical Biology Training Grant T32 GM109825 to AP, and Equipment Grant S10OD024988 to the Indiana University Bloomington Light Microscopy Imaging Center, by an Indiana University President's Diversity Dissertation Fellowship Grant to AP, and by Institutional Research Funds from the CIBIO Department of the University of Trento to OM.

ACKNOWLEDGMENTS

We thank Adrian Land and other members of the Winkler Lab for advice and discussions; Bhagyashree Sarda, Bob Kupeska, Dalia Denapaite, and Alessia Zanardi for strain/plasmid constructions, microscopy, and/or performing B2H assays; Dan Kearns, Sidney Shaw, and Kevin Bruce for the scientific input; Jonathan Trinidad for assistance with mass spectrometry; and Jim Powers for assistance with microscopy. We also thank Luke Lavis (Janelia Lab) for Fluor 549, Michael VanNieuwenhze (Indiana University) for FDAA dyes, and Karolina Buriánková and Pavel Branny (Czech Academy of Sciences) for MapZ/LocZ constructs.

SUPPLEMENTARY MATERIAL

The Supplementary Material for this article can be found online at: https://www.frontiersin.org/articles/10.3389/fmicb.2021.780864/full#supplementary-material

REFERENCES

Aarsman, M. E., Piette, A., Fraipont, C., Vinkenvleugel, T. M., Nguyen-Disteche, M., and den Blaauwen, T. (2005). Maturation of the *Escherichia coli* divisome occurs in two steps. *Mol. Microbiol.* 55, 1631–1645. doi: 10.1111/j.1365-2958.2005.04502.x

Adams, D. W., and Errington, J. (2009). Bacterial cell division: assembly, maintenance and disassembly of the Z ring. *Nat. Rev. Microbiol.* 7, 642–653. doi: 10.1038/nrmicro2198

Baranova, N., Radler, P., Hernández-Rocamora, V. M., Alfonso, C., López-Pelegrín, M., Rivas, G., et al. (2020). Diffusion and capture permits dynamic coupling between treadmilling FtsZ filaments and cell division proteins. *Nat. Mirobiol.* 5, 407–417. doi: 10.1038/s41564-019-0657-5

Beall, B., and Lutkenhaus, J. (1991). FtsZ in *Bacillus subtilis* is required for vegetative septation and for asymmetric septation during sporulation. *Genes Dev.* 5, 447–455.

Beilharz, K., Novakova, L., Fadda, D., Branny, P., Massidda, O., and Veening, J. W. (2012). Control of cell division in *Streptococcus pneumoniae* by the conserved Ser/Thr protein kinase StkP. *Proc. Natl. Acad. Sci. U.S.A.* 109, E905–E913. doi: 10.1073/pnas.1119172109

Bernhardt, T. G., and de Boer, P. A. (2005). SlmA, a nucleoid-associated, FtsZ binding protein required for blocking septal ring assembly over chromosomes in E. coli. *Mol. Cell.* 18, 555–564. doi: 10.1016/j.molcel.2005.04.012

Bi, E. F., and Lutkenhaus, J. (1991). FtsZ ring structure associated with division in *Escherichia coli*. *Nature* 354, 161–164. doi: 10.1038/354161a0

Bisson-Filho, A. W., Hsu, Y. P., Squyres, G. R., Kuru, E., Wu, F., Jukes, C., et al. (2017). Treadmilling by FtsZ filaments drives peptidoglycan synthesis and bacterial cell division. *Science* 355, 739–743.

Boersma, M. J., Kuru, E., Rittichier, J. T., VanNieuwenhze, M. S., Brun, Y. V., and Winkler, M. E. (2015). Minimal peptidoglycan (PG) turnover in Wild-type and PG hydrolase and cell division mutants of *Streptococcus pneumoniae* D39 growing planktonically and in host-relevant biofilms. *J. Bacteriol.* 197, 3472–3485. doi: 10.1128/jb.00541-15

Briggs, N., Bruce, K. E., Naskar, S., Winkler, M. E., and Roper, D. (2021). The pneumococcoccal divisome: dynamic control of *Streptococcus pneumoniae* cell division. *Front. Microbiol.* 12:737396. doi: 3389/fmicb.2021.737396

Burton, B., and Dubnau, D. (2010). Membrane-associated DNA transport machines. *Cold Spring Harb Perspect Biol.* 2:a000406. doi: 10.1101/cshperspect.a000406

Buss, J., Coltharp, C., Huang, T., Pohlmeyer, C., Wang, S. C., Hatem, C., et al. (2013). In vivo organization of the FtsZ-ring by ZapA and ZapB revealed by quantitative super-resolution microscopy. *Mol. Microbiol.* 89, 1099–1120. doi: 10.1111/mmi.12331

Buss, J., Coltharp, C., Shtengel, G., Yang, X., Hess, H., and Xiao, J. (2015). A multi-layered protein network stabilizes the *Escherichia coli* FtsZ-ring and modulates constriction dynamics. *PLoS Genet* 11:e1005128. doi: 10.1371/journal.pgen.1005128

Caldas, P., López-Pelegrín, M., Pearce, D., Budanur, N. B., Brugués, J., and Loose, M. (2019). Cooperative ordering of treadmilling filaments in cytoskeletal networks of FtsZ and its crosslinker ZapA. *Nat. Commun.* 10:5744.

Centers for Disease Control and Prevention (2019). Centers for Disease Control and Prevention; Available online at: https://www.cdc.gov/drugresistance/biggest-threats.html (accessed August 22, 2021).

Chung, K. M., Hsu, H. H., Yeh, H. Y., and Chang, B. Y. (2007). Mechanism of regulation of prokaryotic tubulin-like GTPase FtsZ by membrane protein EzrA. *J. Biol. Chem.* 282, 14891–14897. doi: 10.1074/jbc.M605177200

Claessen, D., Emmins, R., Hamoen, L. W., Daniel, R. A., Errington, J., and Edwards, D. H. (2008). Control of the cell elongation-division cycle by shuttling of PBP1 protein in *Bacillus subtilis*. *Mol. Microbiol.* 68, 1029–1046. doi: 10.1111/j.1365-2958.2008.06210.x

Cleverley, R. M., Barrett, J. R., Basle, A., Bui, N. K., Hewitt, L., Solovyova, A., et al. (2014). Structure and function of a spectrin-like regulator of bacterial cytokinesis. *Nat. Commun.* 5:5421. doi: 10.1038/ncomms6421

Cleverley, R. M., Rismondo, J., Lockhart-Cairns, M. P., Van Bentum, P. T., Egan, A. J., Vollmer, W., et al. (2016). Subunit arrangement in GpsB, a regulator of cell wall biosynthesis. *Microb. Drug Resist.* 22, 446–460. doi: 10.1089/mdr.2016.0050

Cleverley, R. M., Rutter, Z. J., Rismondo, J., Corona, F., Tsui, H. T., Alatawi, F. A., et al. (2019). The cell cycle regulator GpsB functions as cytosolic adaptor for multiple cell wall enzymes. *Nat. Commun.* 10:261. doi: 10.1038/s41467-018-08056-2

Coltharp, C., Buss, J., Plumer, T. M., and Xiao, J. (2016). Defining the rate-limiting processes of bacterial cytokinesis. *Proc. Natl. Acad. Sci. U.S.A.* 113, E1044–E1053.

Dai, K., and Lutkenhaus, J. (1991). ftsZ is an essential cell division gene in *Escherichia coli*. *J. Bacteriol.* 173, 3500–3506.

Den Blaauwen, T., Aarsman, M. E., Vischer, N. O., and Nanninga, N. (2003). Penicillin-binding protein PBP2 of *Escherichia coli* localizes preferentially in the lateral wall and at mid-cell in comparison with the old cell pole. *Mol. Microbiol.* 47, 539–547.

Ducret, A., Quardokus, E. M., and Brun, Y. V. (2016). MicrobeJ, a tool for high throughput bacterial cell detection and quantitative analysis. *Nat. Microbiol.* 1:16077. doi: 10.1038/nmicrobiol.2016.77

Duman, R., Ishikawa, S., Celik, I., Strahl, H., Ogasawara, N., Troc, P., et al. (2013). Structural and genetic analyses reveal the protein SepF as a new membrane anchor for the Z ring. *Proc. Natl. Acad. Sci. U.S.A.* 110, E4601–E4610. doi: 10.1073/pnas.1313978110

Ebersbach, G., Galli, E., Møller-Jensen, J., Löwe, J., and Gerdes, K. (2008). Novel coiled-coil cell division factor ZapB stimulates Z ring assembly and cell division. *Mol. Microbiol.* 68, 720–735. doi: 10.1111/j.1365-2958.2008.06190.x

Fadda, D., Santona, A., D'Ulisse, V., Ghelardini, P., Ennas, M. G., Whalen, M. B., et al. (2007). *Streptococcus pneumoniae* DivIVA: localization and interactions in a MinCD-free context. *J. Bacteriol.* 189, 1288–1298. doi: 10.1128/JB.01168-06

Fenton, A. K., Manuse, S., Flores-Kim, J., Garcia, P. S., Mercy, C., Grangeasse, C., et al. (2018). Phosphorylation-dependent activation of the cell wall synthase PBP2a in *Streptococcus pneumoniae* by MacP. *Proc. Natl. Acad. Sci. U.S.A.* 115, 2812–2817. doi: 10.1073/pnas.1715218115

Fleurie, A., Lesterlin, C., Manuse, S., Zhao, C., Cluzel, C., Lavergne, J. P., et al. (2014a). MapZ marks the division sites and positions FtsZ rings in *Streptococcus pneumoniae*. *Nature* 516, 259–262.

Fleurie, A., Manuse, S., Zhao, C., Campo, N., Cluzel, C., Lavergne, J. P., et al. (2014b). Interplay of the serine/threonine-kinase StkP and the paralogs DivIVA and GpsB in pneumococcal cell elongation and division. *PLoS Genet* 10:e1004275. doi: 10.1371/journal.pgen.1004275

Flores-Kim, J., Dobihal, G. S., Fenton, A., Rudner, D. Z., and Bernhardt, T. G. (2019). A switch in surface polymer biogenesis triggers growth-phase-dependent and antibiotic-induced bacteriolysis. *eLife* 8:e44912. doi: 10.7554/eLife.44912

Gallay, C., Sanselicio, S., Anderson, M. E., Soh, Y. M., Liu, X., Stamsås, G. A., et al. (2021). CcrZ is a pneumococcal spatiotemporal cell cycle regulator that interacts with FtsZ and controls DNA replication by modulating the activity of DnaA. *Nat. Microbiol.* 6:1175. doi: 10.1038/s41564-021-00949-1

Galli, E., and Gerdes, K. (2010). Spatial resolution of two bacterial cell division proteins: ZapA recruits ZapB to the inner face of the Z-ring. *Mol. Microbiol.* 76, 1514–1526. doi: 10.1111/j.1365-2958.2010.07183.x

Galli, E., and Gerdes, K. (2012). FtsZ-ZapA-ZapB interactome of *Escherichia coli*. *J. Bacteriol.* 194, 292–302. doi: 10.1128/JB.05821-11

Gamba, P., Rietkotter, E., Daniel, R. A., and Hamoen, L. W. (2015). *Tetracycline hypersensitivity* of an ezrA mutant links GalE and TseB (YpmB) to cell division. *Front. Microbiol.* 6:346. doi: 10.3389/fmicb.2015.00346

Gamba, P., Veening, J. W., Saunders, N. J., Hamoen, L. W., and Daniel, R. A. (2009). Two-step assembly dynamics of the *Bacillus subtilis* divisome. *J. Bacteriol.* 191, 4186–4194. doi: 10.1128/jb.01758-08

Grimm, J. B., English, B. P., Chen, J., Slaughter, J. P., Zhang, Z., Revyakin, A., et al. (2015). A general method to improve fluorophores for live-cell and single-molecule microscopy. *Nat. Methods* 12, 244–250.

Gueiros-Filho, F. J., and Losick, R. (2002). A widely conserved bacterial cell division protein that promotes assembly of the tubulin-like protein FtsZ. *Genes Dev.* 16, 2544–2556. doi: 10.1101/gad.1014102

Haeusser, D. P., Garza, A. C., Buscher, A. Z., and Levin, P. A. (2007). The division inhibitor EzrA contains a seven-residue patch required for maintaining the dynamic nature of the medial FtsZ ring. *J. Bacteriol.* 189, 9001–9010. doi: 10.1128/jb.01172-07

Haeusser, D. P., and Margolin, W. (2016). Splitsville: structural and functional insights into the dynamic bacterial Z ring. *Nat. Rev. Microbiol.* 14, 305–319. doi: 10.1038/nrmicro.2016.26

Haeusser, D. P., Schwartz, R. L., Smith, A. M., Oates, M. E., and Levin, P. A. (2004). EzrA prevents aberrant cell division by modulating assembly of the cytoskeletal protein FtsZ. *Mol. Microbiol.* 52, 801–814. doi: 10.1111/j.1365-2958.2004.04016

Haydon, D. J., Stokes, N. R., Ure, R., Galbraith, G., Bennett, J. M., Brown, D. R., et al. (2008). An inhibitor of FtsZ with potent and selective anti-staphylococcal activity. *Science* 321, 1673–1675. doi: 10.1126/science.1159961

Holeckova, N., Doubravova, L., Massidda, O., Molle, V., Buriankova, K., Benada, O., et al. (2015). LocZ is a new cell division protein involved in proper septum placement in *Streptococcus pneumoniae*. *mBio* 6, e01700–e01714. doi: 10.1128/mBio.01700-14

Huang, K. H., Durand-Heredia, J., and Janakiraman, A. (2013). FtsZ ring stability: of bundles, tubules, crosslinks, and curves. *J. Bacteriol.* 195, 1859–1868. doi: 10.1128/JB.02157-12

Ishikawa, S., Kawai, Y., Hiramatsu, K., Kuwano, M., and Ogasawara, N. (2006). A new FtsZ-interacting protein, YlmF, complements the activity of FtsA during progression of cell division in *Bacillus subtilis*. *Mol. Microbiol.* 60, 1364–1380. doi: 10.1111/j.1365-2958.2006.05184.x

Jacobsen, F. E., Kazmierczak, K. M., Lisher, J. P., Winkler, M. E., and Giedroc, D. P. (2011). Interplay between manganese and zinc homeostasis in the human pathogen *Streptococcus pneumoniae*. *Metallomics* 3, 38–41. doi: 10.1039/c0mt00050g

Jorge, A. M., Hoiczyk, E., Gomes, J. P., and Pinho, M. G. (2011). EzrA contributes to the regulation of cell size in *Staphylococcus aureus*. *PLoS One* 6:e27542. doi: 10.1371/journal.pone.0027542

Karimova, G., Dautin, N., and Ladant, D. (2005). Interaction network among *Escherichia coli* membrane proteins involved in cell division as revealed by bacterial two-hybrid analysis. *J. Bacteriol.* 187, 2233–2243. doi: 10.1128/JB.187.7.2233-2243.2005

Kelley, L. A., Mezulis, S., Yates, C. M., Wass, M. N., and Sternberg, M. J. E. (2015). The Phyre2 web portal for protein modeling, prediction and analysis [protocol]. *Nat. Protocols* 10, 845–858. doi: 10.1038/nprot.2015.053

Kuru, E., Hughes, H. V., Brown, P. J., Hall, E., Tekkam, S., Cava, F., et al. (2012). In Situ probing of newly synthesized peptidoglycan in live bacteria with fluorescent D-amino acids. *Angew Chem. Int. Ed. Engl.* 51, 12519–12523. doi: 10.1002/anie.201206749

Land, A. D., Luo, Q., and Levin, P. A. (2014). Functional domain analysis of the cell division inhibitor EzrA. *PLoS One* 9:e102616. doi: 10.1371/journal.pone.0102616

Land, A. D., Tsui, H. C., Kocaoglu, O., Vella, S. A., Shaw, S. L., Keen, S. K., et al. (2013). Requirement of essential Pbp2x and GpsB for septal ring closure in *Streptococcus pneumoniae* D39. *Mol. Microbiol.* 90, 939–955. doi: 10.1111/mmi.12408

Land, A. D., and Winkler, M. E. (2011). The requirement for pneumococcal MreC and MreD is relieved by inactivation of the gene encoding PBP1a. *J. Bacter.* 193, 4166–4179. doi: 10.1128/jb.05245-11

Lanie, J. A., Ng, W. L., Kazmierczak, K. M., Andrzejewski, T. M., Davidsen, T. M., Wayne, K. J., et al. (2007). Genome sequence of Avery's virulent serotype 2 strain D39 of *Streptococcus pneumoniae* and comparison with that of unencapsulated laboratory strain R6. *J. Bacter.* 189, 38–51. doi: 10.1128/jb.01148-06

Lara, B., Rico, A. I., Petruzzelli, S., Santona, A., Dumas, J., Biton, J., et al. (2005). Cell division in cocci: localization and properties of the *Streptococcus pneumoniae* FtsA protein. *Mol. Microbiol.* 55, 699–711. doi: 10.1111/j.1365-2958.2004.04432.x

Le Bourgeois, P., Bugarel, M., Campo, N., Daveran-Mingot, M.-L., Labonté, J., Lanfranchi, D., et al. (2007). The unconventional xer recombination machinery of streptococci/lactococci [article]. *PLoS Genet* 3:e117–e119. doi: 10.1371/journal.pgen.0030117

Levin, P. A., Kurtser, I. G., and Grossman, A. D. (1999). Identification and characterization of a negative regulator of FtsZ ring formation in *Bacillus subtilis*. *Proc. Natl. Acad. Sci. U.S.A.* 96, 9642–9647.

Li, Y., Shao, S., Xu, X., Su, X., Sun, Y., and Wei, S. (2018). MapZ forms a stable ring structure that acts as a nanotrack for FtsZ treadmilling in *Streptococcus mutans*. *ACS Nano* 12, 6137–6146.

Liu, X., Gallay, C., Kjos, M., Domenech, A., Slager, J., van Kessel, S. P., et al. (2017). High-throughput CRISPRi phenotyping identifies new essential genes in *Streptococcus pneumoniae*. *Mol. Syst. Biol.* 13:931.

Lutkenhaus, J., Pichoff, S., and Du, S. (2012). Bacterial cytokinesis: from Z ring to divisome. *Cytoskeleton (Hoboken)* 69, 778–790. doi: 10.1002/cm.21054

Massidda, O., Novakova, L., and Vollmer, W. (2013). From models to pathogens: how much have we learned about *Streptococcus pneumoniae* cell division? *Environ. Microbiol.* 15, 3133–3157. doi: 10.1111/1462-2920.12189

McCausland, J. W., Yang, X., Squyres, G. R., Lyu, Z., Bruce, K. E., Lamanna, M. M., et al. (2021). Treadmilling FtsZ polymers drive the directional movement of sPG-synthesis enzymes via a brownian ratchet mechanism. *Nat. Commun.* 12:609.

Meeske, A. J., Riley, E. P., Robins, W. P., Uehara, T., Mekalanos, J. J., Kahne, D., et al. (2016). SEDS proteins are a widespread family of bacterial cell wall polymerases. *Nature* 537, 634–638. doi: 10.1038/nature19331

Mellroth, P., Daniels, R., Eberhardt, A., Rönnlund, D., Blom, H., Widengren, J., et al. (2012). LytA, major autolysin of *Streptococcus pneumoniae*, requires access to nascent peptidoglycan. *J. Biol. Chem.* 287, 11018–11029. doi: 10.1074/jbc.M111.318584

Mercy, C., Ducret, A., Slager, J., Lavergne, J. P., Freton, C., Nagarajan, S. N., et al. (2019). RocS drives chromosome segregation and nucleoid protection in *Streptococcus pneumoniae*. *Nat. Microbiol.* 4, 1661–1670.

Monahan, L. G., Liew, A. T., Bottomley, A. L., and Harry, E. J. (2014). Division site positioning in bacteria: one size does not fit all. *Front. Microbiol.* 5:19.

Monteiro, J. M., Pereira, A. R., Reichmann, N. T., Saraiva, B. M., Fernandes, P. B., Veiga, H., et al. (2018). Peptidoglycan synthesis drives an FtsZ-treadmilling-independent step of cytokinesis. *Nature* 554, 528–532.

Mura, A., Fadda, D., Perez, A. J., Danforth, M. L., Musu, D., Rico, A. I., et al. (2016). Roles of the essential protein FtsA in cell growth and division in *Streptococcus pneumoniae*. *J. Bacteriol.* 199:e00608-16. doi: 10.1128/jb.00608-16

Noirclerc-Savoye, M., Le Gouëllec, A., Morlot, C., Dideberg, O., Vernet, T., and Zapun, A. (2005). In vitro reconstitution of a trimeric complex of DivIB, DivIC and FtsL, and their transient co-localization at the division site in *Streptococcus pneumoniae*. *Mol. Microbiol.* 55, 413–424. doi: 10.1111/j.1365-2958.2004.04408.x

Novakova, L., Bezousková, S., Pompach, P., Spidlová, P., Sasková, L., Weiser, J., et al. (2010). Identification of multiple substrates of the StkP Ser/Thr protein kinase in *Streptococcus pneumoniae*. *J. Bacter.* 192, 3629–3638. doi: 10.1128/JB.01564-09

Perez, A. J., Boersma, M. J., Bruce, K. E., Lamanna, M. M., Shaw, S. L., Tsui, H. T., et al. (2021). Organization of peptidoglycan synthesis in nodes and separate rings at different stages of cell division of *Streptococcus pneumoniae*. *Mol. Microbiol.* 115, 1152–1169. doi: 10.1111/mmi.14659

Perez, A. J., Cesbron, Y., Shaw, S. L., Bazan Villicana, J., Tsui, H. T., Boersma, M. J., et al. (2019). Movement dynamics of divisome proteins and PBP2x:FtsW in cells of *Streptococcus pneumoniae*. *Proc. Natl. Acad. Sci. U.S.A.* 116, 3211–3220. doi: 10.1073/pnas.1816018116

Pinho, M. G., and Errington, J. (2003). Dispersed mode of *Staphylococcus aureus* cell wall synthesis in the absence of the division machinery. *Mol. Microbiol.* 50, 871–881.

Pinho, M. G., Kjos, M., and Veening, J. W. (2013). How to get (a)round: mechanisms controlling growth and division of coccoid bacteria. *Nat. Rev. Microbiol.* 11, 601–614. doi: 10.1038/nrmicro3088

Pompeo, F., Foulquier, E., Serrano, B., Grangeasse, C., and Galinier, A. (2015). Phosphorylation of the cell division protein GpsB regulates PrkC kinase activity through a negative feedback loop in *Bacillus subtilis*. *Mol. Microbiol.* 97, 139–150. doi: 10.1111/mmi.13015

Richards, V. P., Palmer, S. R., Pavinski Bitar, P. D., Qin, X., Weinstock, G. M., Highlander, S. K., et al. (2014). Phylogenomics and the dynamic genome evolution of the genus *Streptococcus*. *Genome Biol. Evol.* 6, 741–753.

Rued, B. E., Zheng, J. J., Mura, A., Tsui, H. T., Boersma, M. J., Mazny, J. L., et al. (2017). Suppression and synthetic-lethal genetic relationships of ΔgpsB mutations indicate that GpsB mediates protein phosphorylation and penicillin-binding protein interactions in *Streptococcus pneumoniae* D39. *Mol. Microbiol.* 103, 931–957.

Sham, L. T., Barendt, S. M., Kopecky, K. E., and Winkler, M. E. (2011). Essential PcsB putative peptidoglycan hydrolase interacts with the essential FtsXSpn cell division protein in *Streptococcus pneumoniae* D39. *Proc. Natl. Acad. Sci. U.S.A.* 108, E1061–E1069. doi: 10.1073/pnas.1108323108

Sham, L. T., Jensen, K. R., Bruce, K. E., and Winkler, M. E. (2013). Involvement of FtsE ATPase and FtsX extracellular loops 1 and 2 in FtsEX-PcsB complex function in cell division of *Streptococcus pneumoniae* D39. *mBio* 4:e00431-13. doi: 10.1128/mBio.00431-13

Singh, J. K., Makde, R. D., Kumar, V., and Panda, D. (2007). A membrane protein, EzrA, regulates assembly dynamics of FtsZ by interacting with the C-terminal tail of FtsZ. *Biochemistry* 46, 11013–11022. doi: 10.1021/bi700710j

Slager, J., Aprianto, R., and Veening, J. W. (2018). Deep genome annotation of the opportunistic human pathogen *Streptococcus pneumoniae* D39. *Nucleic Acids Res.* 46, 9971–9989. doi: 10.1093/nar/gky725

Son, S. H., and Lee, H. H. (2013). The N-terminal domain of EzrA binds to the C terminus of FtsZ to inhibit *Staphylococcus aureus* FtsZ polymerization. *Biochem. Biophys. Res. Commun.* 433, 108–114. doi: 10.1016/j.bbrc.2013.02.055

Squyres, G. R., Holmes, M. J., Barger, S. R., Pennycook, B. R., Ryan, J., Yan, V. T., et al. (2021). Single-molecule imaging reveals that Z-ring condensation is essential for cell division in *Bacillus subtilis*. *Nat. Microbiol.* 6, 553–562.

Steele, V. R., Bottomley, A. L., Garcia-Lara, J., Kasturiarachchi, J., and Foster, S. J. (2011). Multiple essential roles for EzrA in cell division of *Staphylococcus aureus*. *Mol. Microbiol.* 80, 542–555. doi: 10.1111/j.1365-2958.2011.07591.x

Straume, D., Stamsås, G. A., Berg, K. H., Salehian, Z., and Håvarstein, L. S. (2017). Identification of pneumococcal proteins that are functionally linked to penicillin-binding protein 2b (PBP2b). *Mol. Microbiol.* 103, 99–116. doi: 10.1111/mmi.13543

Taguchi, A., Page, J. E., Tsui, H. T., Winkler, M. E., and Walker, S. (2021). Biochemical reconstitution defines new functions for membrane-bound glycosidases in assembly of the bacterial cell wall. *Proc. Natl. Acad. Sci. U.S.A.* 118, e2103740118. doi: 10.1073/pnas.2103740118

Thanassi, J. A., Hartman-Neumann, S. L., Dougherty, T. J., Dougherty, B. A., and Pucci, M. J. (2002). Identification of 113 conserved essential genes using a high-throughput gene disruption system in *Streptococcus pneumoniae*. *Nucleic Acids Res.* 30, 3152–3162.

Thanbichler, M., and Shapiro, L. (2006). MipZ, a spatial regulator coordinating chromosome segregation with cell division in caulobacter. *Cell* 126, 147–162. doi: 10.1016/j.cell.2006.05.038

Trip, E. N., and Scheffers, D. J. (2015). A 1 MDa protein complex containing critical components of the *Escherichia coli* divisome. *Sci. Rep.* 5:18190. doi: 10.1038/srep18190

Trouve, J., Zapun, A., Arthaud, C., Durmort, C., Di Guilmi, A. M., Söderström, B., et al. (2021). Nanoscale dynamics of peptidoglycan assembly during the cell cycle of *Streptococcus pneumoniae*. *Curr. Biol.* 31, 2844–2856.e6. doi: 10.1016/j.cub.2021.04.041

Tsui, H. C., Boersma, M. J., Vella, S. A., Kocaoglu, O., Kuru, E., Peceny, J. K., et al. (2014). Pbp2x localizes separately from Pbp2b and other peptidoglycan synthesis proteins during later stages of cell division of *Streptococcus pneumoniae* D39. *Mol. Microbiol.* 94, 21–40. doi: 10.1111/mmi.12745

Tsui, H. C., Mukherjee, D., Ray, V. A., Sham, L. T., Feig, A. L., and Winkler, M. E. (2010). Identification and characterization of noncoding small RNAs in *Streptococcus pneumoniae* serotype 2 strain D39. *J. Bacter.* 192, 264–279. doi: 10.1128/jb.01204-09

Tsui, H. T., Zheng, J. J., Magallon, A. N., Ryan, J. D., Yunck, R., Rued, B. E., et al. (2016). Suppression of a deletion mutation in the gene encoding essential PBP2b reveals a new lytic transglycosylase involved in peripheral peptidoglycan synthesis in *Streptococcus pneumoniae* D39. *Mol. Microbiol.* 100, 1039–1065. doi: 10.1111/mmi.13366

van Opijnen, T., Bodi, K. L., and Camilli, A. (2009). Tn-seq: high-throughput parallel sequencing for fitness and genetic interaction studies in microorganisms. *Nat. Methods* 6, 767–772. doi: 10.1038/nmeth.1377

van Raaphorst, R., Kjos, M., and Veening, J. W. (2017). Chromosome segregation drives division site selection in *Streptococcus pneumoniae*. *Proc. Natl. Acad. Sci. U.S.A.* 114, E5959–E5968. doi: 10.1073/pnas.1620608114

Vollmer, W., Massidda, O., and Tomasz, A. (2019). The cell wall of *Streptococcus pneumoniae*. *Microbiol. Spectr.* 7:2018. doi: 10.1128/microbiolspec.GPP3-0018-2018

Wayne, K. J., Li, S., Kazmierczak, K. M., Tsui, H. C., and Winkler, M. E. (2012). Involvement of WalK (VicK) phosphatase activity in setting WalR (VicR) response regulator phosphorylation level and limiting cross-talk in *Streptococcus pneumoniae* D39 cells. *Mol. Microbiol.* 86, 645–660. doi: 10.1111/mmi.12006

Wayne, K. J., Sham, L. T., Tsui, H. C., Gutu, A. D., Barendt, S. M., Keen, S. K., et al. (2010). Localization and cellular amounts of the WalRKJ (VicRKX) two-component regulatory system proteins in serotype 2 *Streptococcus pneumoniae*. *J. Bacteriol.* 192, 4388–4394. doi: 10.1128/jb.00578-10

Weiser, J. N., Ferreira, D. M., and Paton, J. C. (2018). *Streptococcus pneumoniae*: transmission, colonization and invasion. *Nat. Rev. Microbiol.* 16, 355–367.

Wenzel, M., Celik Gulsoy, I. N., Gao, Y., Teng, Z., Willemse, J., Middelkamp, M., et al. (2021). Control of septum thickness by the curvature of

SepF polymers. *Proc. Natl. Acad. Sci. U.S.A.* 118:e2002635118. doi: 10.1073/pnas.2002635118

Wheeler, R., Mesnage, S., Boneca, I. G., Hobbs, J. K., and Foster, S. J. (2011). Super-resolution microscopy reveals cell wall dynamics and peptidoglycan architecture in ovococcal bacteria. *Mol. Microbiol.* 82, 1096–1109. doi: 10.1111/j.1365-2958.2011.07871.x

Wu, L. J., and Errington, J. (2004). Coordination of cell division and chromosome segregation by a nucleoid occlusion protein in *Bacillus subtilis*. *Cell* 117, 915–925. doi: 10.1016/j.cell.2004.06.002

Xiang, Z., Li, Z., Ren, Z., Zeng, J., Peng, X., Li, Y., et al. (2019). EzrA, a cell shape regulator contributing to biofilm formation and competitiveness in *Streptococcus mutans*. *Mol. Oral. Microbiol.* 34, 194–208.

Yang, X., Lyu, Z., Miguel, A., McQuillen, R., Huang, K. C., and Xiao, J. (2017). GTPase activity-coupled treadmilling of the bacterial tubulin FtsZ organizes septal cell wall synthesis. *Science* 355, 744–747.

Yang, X., McQuillen, R., Lyu, Z., Phillips-Mason, P., De La Cruz, A., McCausland, J. W., et al. (2021). A two-track model for the spatiotemporal coordination of bacterial septal cell wall synthesis revealed by single-molecule imaging of FtsW. *Nat. Microbiol.* 6, 584–593. doi: 10.1038/s41564-020-00853-0

Yu, Y., Zhou, J., Gueiros-Filho, F. J., Kearns, D. B., and Jacobson, S. C. (2021). Noc corrals migration of FtsZ protofilaments during cytokinesis in *Bacillus subtilis*. *mBio* 12, e2964–e2920. doi: 10.1128/mBio.02964-20

Zheng, J. J., Perez, A. J., Tsui, H. T., Massidda, O., and Winkler, M. E. (2017). Absence of the KhpA and KhpB (JAG/EloR) RNA-binding proteins suppresses the requirement for PBP2b by overproduction of FtsA in *Streptococcus pneumoniae* D39. *Mol. Microbiol.* 106, 793–814. doi: 10.1111/mmi.13847

Conflict of Interest: The authors declare that the research was conducted in the absence of any commercial or financial relationships that could be construed as a potential conflict of interest.

Publisher's Note: All claims expressed in this article are solely those of the authors and do not necessarily represent those of their affiliated organizations, or those of the publisher, the editors and the reviewers. Any product that may be evaluated in this article, or claim that may be made by its manufacturer, is not guaranteed or endorsed by the publisher.

frontiers in Microbiology

ORIGINAL RESEARCH
published: 09 December 2021
doi: 10.3389/fmicb.2021.733850

Localized Peptidoglycan Biosynthesis in *Chlamydia trachomatis* Conforms to the Polarized Division and Cell Size Reduction Developmental Models

*George W. Liechti**

Department of Microbiology and Immunology, Uniformed Services University, Bethesda, MD, United States

OPEN ACCESS

Edited by:
Shishen Du,
Wuhan University, China

Reviewed by:
Nicolas Jacquier,
Centre Hospitalier Universitaire Vaudois (CHUV), Switzerland
Scott Hefty,
University of Kansas, United States

***Correspondence:**
George W. Liechti
george.liechti@usuhs.edu

Specialty section:
This article was submitted to Microbial Physiology and Metabolism, a section of the journal Frontiers in Microbiology

Received: *30 June 2021*
Accepted: *17 November 2021*
Published: *09 December 2021*

Citation:
Liechti GW (2021) Localized Peptidoglycan Biosynthesis in Chlamydia trachomatis Conforms to the Polarized Division and Cell Size Reduction Developmental Models. Front. Microbiol. 12:733850. doi: 10.3389/fmicb.2021.733850

Cell size regulation in bacteria is a function of two basic cellular processes: the expansion of the cell envelope and its constriction at spatially defined points at what will eventually become the division plane. In most bacterial species, both cell wall expansion and restriction are dependent on peptidoglycan (PG), a structural polymer comprised of sugars and amino acids that imparts strength and rigidity to bacterial membranes. Pathogenic *Chlamydia* species are unique in that their cell walls contain very little PG, which is restricted almost entirely to the apparent division plane of the microbe's replicative forms. Very little is known about the degree to which PG affects the size and shape of *C. trachomatis* during its division process, and recent studies suggest the process is initiated *via* a polarized mechanism. We conducted an imaging study to ascertain the dimensions, orientation, and relative density of chlamydial PG throughout the organism's developmental cycle. Our analysis indicates that PG in replicating *C. trachomatis* can be associated with four, broad structural forms; polar/septal disks, small/thick rings, large rings, and small/thin rings. We found that PG density appeared to be highest in septal disks and small/thick rings, indicating that these structures likely have high PG synthesis to degradation ratios. We also discovered that as *C. trachomatis* progresses through its developmental cycle PG structures, on average, decrease in total volume, indicating that the average cell volume of chlamydial RBs likely decreases over time. When cells infected with *C. trachomatis* are treated with inhibitors of critical components of the microbe's two distinct PG synthases, we observed drastic differences in the ratio of PG synthesis to degradation, as well as the volume and shape of PG-containing structures. Overall, our results suggest that *C. trachomatis* PG synthases differentially regulate the expansion and contraction of the PG ring during both the expansion and constriction of the microbe's cell membrane during cell growth and division, respectively.

Keywords: cell division, cell size regulation, *Chlamydia*, peptidoglycan, pathoadaptation

INTRODUCTION

All *Chlamydia* species share a biphasic developmental cycle (**Figure 1a**). These obligate intracellular pathogens alternate between a small (~0.3 μm) extracellular, infectious form (Elementary Body or EB) and a larger (~1 μm), intracellular, replicative form (Reticulate Body or RB; Elwell et al., 2016). EB membranes contain a number of highly cross-linked (disulfide bonded), cysteine-rich outer membrane proteins that provide the microbe with the structural rigidity needed for maintaining cell integrity in an extracellular environment. Upon coming into contact with a host cell, EBs are rapidly internalized into a vacuole (termed an "inclusion") and utilize a type III secretion system (T3SS) to secrete a wide assortment of effector proteins into the cell cytoplasm. Within ~8–12 h, EBs begin differentiating into RBs, during which time the outer membrane proteins begin to un-crosslink, the cells enlarge, and begin to replicate. Temporal gene expression largely determines when this transition occurs (Belland et al., 2003), and the expression of early, mid, and late genes roughly corresponds to different phases of the chlamydial developmental cycle (Belland et al., 2003). Sixteen to twenty-four hours after entering a host cell these RBs begin to asynchronously decrease in size (Lee et al., 2018), transition into intermediate forms (IBs), express cysteine-rich outer membrane proteins, and transition into EBs. EBs then exit the cell by one of two routes: (i) the inclusion expands enough to lyse the cell, expelling the newly formed EBs, or (ii) portions of the inclusion begin to "bleb off" into the extracellular environment in a process termed extrusion (Hybiske and Stephens, 2007). The disruption of either of these transition events (EB to RB or RB to EB) effectively halts the developmental cycle and prevents the bacterium from entering new host cells (Beatty et al., 1994).

Peptidoglycan (PG) is an essential structural element in the vast majority of bacterial species (Egan and Vollmer, 2013). This sugar/amino acid polymer encases the bacterium in a mesh-like layer (the sacculus) that provides strength, rigidity, and shape to bacterial cell walls. PG also acts to tether the inner and outer membranes together in Gram-negative bacteria (Egan and Vollmer, 2013) and thus aids in the constriction of the bacterial septum during division (Gray et al., 2015). Nascent PG synthesis is spatially and temporally restricted within bacterial cells *via* two known molecular complexes, each relying on a principle, filament-forming protein: the FtsZ complex ("divisome"), which is associated with septal PG synthesis required during cell division, and the MreB/Rod complex ("elongasome"), which is primarily associated with lateral cell wall synthesis. Members of the Chlamydiae do not encode FtsZ and originally were thought to completely lack PG (Tamura and Manire, 1967; Garrett et al., 1974; Barbour et al., 1982; Fox et al., 1990). Despite the apparent absence of PG, these microbes are still susceptible to PG-targeting antibiotics (Gogolak and Weiss, 1950; Weiss, 1950; Hurst et al., 1953; Moulder et al., 1963; Lin and Moulder, 1966) and this discrepancy was termed the "chlamydial anomaly" (Moulder, 1993). Unlike all other bacterial species described to date, members of the Chlamydiales do not synthesize a PG cell wall or "sacculus" but maintain their PG in a narrow band corresponding to the septal division plane (Liechti et al., 2014, 2016). This PG "ring" plays an active role in *Chlamydia* cell division (Liechti et al., 2016) and is synthesized by a rudimentary

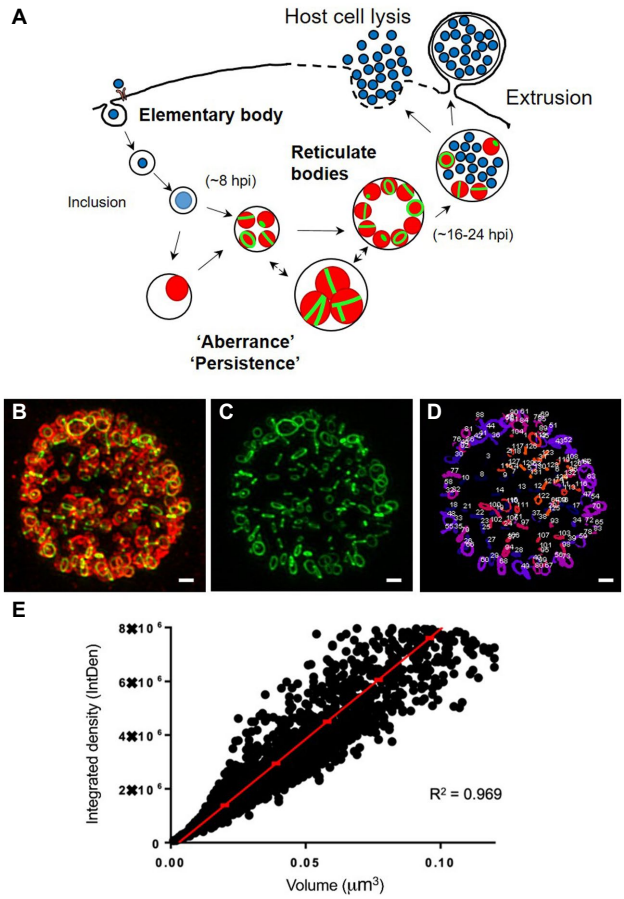

FIGURE 1 | Analysis of peptidoglycan conformation in intracellular *Chlamydia trachomatis*. **(a)** Diagram of the *C. trachomatis* biphasic developmental cycle. Infectious elementary bodies, replicating reticulate bodies, and non-replicating aberrant/persistent forms are shown. **(b–d)** Imaging and analysis workflow for comparing PG-containing structures within chlamydial inclusions. Cell monolayers were infected with *C. trachomatis* L2 434 Bu at an MOI of 1. Infected cells were initially placed on a rocker for 2 h and then incubated under static conditions for an additional 22 h. At 24 hpi, cells were fixed, permeabilized, and labeled. Z-stacks were collected by Structured Illumination Microscopy (SIM) from fixed cells labeled for PG (green) and the chlamydial Major Outer Membrane protein (MOMP, red; **b**). 3D objects were defined "pixel-by-pixel" from the PG-labeled channel **(c)** utilizing the ImageJ addon 3D Object Counter, enabling each object to be spatially defined. A colorimetric readout was used to compare objects' relative locations within an inclusion with objects occupying a similar Z plane sharing a common color **(d)**. Scale bars ~1 μm. A statistical analysis was subsequently conducted on each individual object within inclusions. Objects were compared by three distinct calculated features: volume, integrated density, and mean fluorescent intensity. **(e)** All PG-containing objects observed within a representative 15 chlamydial inclusions are shown. Object volume and integrated density have been plotted, and the data were observed to fit a linear regression ($R^2 = 0.969$). Object variance from this best-fit regression line corresponds to the relative differences in the mean fluorescent intensities of objects within this data set.

MreB/Rod complex. While some *Chlamydia*-like bacteria still utilize a PG sacculus (Pilhofer et al., 2013), evolution within an intracellular environment may have removed the selective pressure to maintain a sacculus for osmotic protection (Mercier et al., 2014; Kawai et al., 2018), thus allowing other members of the Chlamydiales to survive with only enough PG for carrying out the cell division process. As chlamydial PG is immunostimulatory and signals through cytoplasmic NOD receptors (Welter-Stahl et al., 2006), it has been proposed that some *Chlamydia* species have evolved to limit PG utilization, thereby decreasing the pathogen's immunogenic profile (Liechti et al., 2016; Singh et al., 2020; Brockett and Liechti, 2021).

It has long been held that *Chlamydia* species, like most other bacteria, divide by "classical" binary fission (Gaylord, 1954) in which a parent bacterial cell gives rise to two daughter cells of equal size and volume. However, the very first observations of *Chlamydia* species examined by EM noted that the two membrane-enclosed segments within each RB were either "equal or unequal" in size (Gaylord, 1954). Recent studies suggest that the beginning of the chlamydial division process resembles a polarized mechanism akin to budding, in which a daughter cell initially expands out from one pole of the RB (Abdelrahman et al., 2016; Liechti et al., 2016; Cox et al., 2020). During this initial, polarly restricted expansion of the bacterial membrane, PG localizes to the intermediate zone between the parent and newly expanding daughter cell (Liechti et al., 2016; Cox et al., 2020). A number of earlier studies have reported an initial asymmetry during the division process in a wide array of *Chlamydia* species (Gaylord, 1954; Tanami and Yamada, 1973; Falcieri et al., 1979; Phillips et al., 1984; Hackstadt et al., 1996; Wolf et al., 2000), including some from human endocervical samples (Swanson et al., 1975; Lewis et al., 2014). Despite this initial asymmetry, the chlamydial division process eventually results in two equally sized daughter cells, indicating the presence of an underlying, cell size regulatory mechanism. While "budding-like" division has been described in members of the Planctomycetes (Fuerst, 1995; Lee et al., 2009; Santarella-Mellwig et al., 2013), this process differs significantly from "polarized division" in that it gives rise to daughter cells of different sizes. Polarized division (or "polarized binary fission") has not been described outside members of the Chlamydiaceae to date, and it is unclear how the process is regulated and what benefit it might confer to pathogenic *Chlamydia* species.

Cell size maintenance in bacteria is principally a function of opposing cellular activities: (i) fatty acid biosynthesis and (ii) the competing processes of localized PG synthesis, remodeling, and degradation. Fatty acids are required for the generation of phospholipids and lipopolysaccharide that compose bacterial cell membranes, whereas PG remodeling is critical for maintaining bacterial cell shape, rigidity and enables the terminal step in the division process (septation). Because pathogenic *Chlamydia* species lack a PG sacculus (Liechti et al., 2014, 2016), but maintain septal PG for cell division and differentiation, the size of a given *Chlamydia* RB should therefore be dependent on the corresponding rates of PG and fatty acid biosynthesis. Most bacteria control cell size utilizing the second messenger (p)ppGpp, which regulates fatty acid biosynthesis (Vadia et al., 2017). Under nutrient starvation conditions, cell size is reduced close to three-fold in most bacterial species (Shi et al., 2021), resulting from the accumulation of ppGpp. By comparison, *Chlamydia* species do not encode the enzymes necessary for ppGpp synthesis (Stephens et al., 1998), and in response to nutrient starvation, RBs frequently increase in size (Harper et al., 2000; Panzetta et al., 2018). When fosfomycin is used to inhibit PG biosynthesis in the *Chlamydia*-related bacterium *Waddlia chondrophila*, bacterial cells similarly continue to increase in size (Jacquier et al., 2014). By comparison, cell division inhibitors that completely abolished PG synthesis in *C. trachomatis* effectively limit cell size expansion (Brockett and Liechti, 2021); however, this is likely due to their effect on global protein synthesis (Bonner et al., 2014; Brinkworth et al., 2018). Another study has reported that *C. trachomatis* RBs undergo cell size reduction prior to differentiating into their non-replicative, infectious forms (Lee et al., 2018), effectively linking the processes of cell size regulation, division, and differentiation. The processes of DNA replication and septation are decoupled in *C. trachomatis* (Lambden et al., 2006); however, the inhibition of replication has been shown to directly affect PG septal formation (Brothwell et al., 2021). The exact mechanism by which RBs regulate their division process and by proxy their cell size, remains unknown.

In this study, we set out to determine how PG synthesis influences the size and shape of chlamydial RBs throughout the pathogen's division process and developmental cycle. We conducted an analysis of the localization and relative synthesis activity of PG throughout *Chlamydia*'s developmental cycle and compared our data to predictions based on assumptions inherent to both the polarized division model and cell size reduction-preceding-differentiation model of chlamydial development.

MATERIALS AND METHODS

Bacterial Strains and Cell Lines

Chlamydia trachomatis serovar L2 strain 434/Bu was provided by Dr. Anthony Maurelli (University of Florida). Chlamydial infections were carried out in HeLa cells or L2 cells (also provided by Dr. Anthony Maurelli) unless otherwise noted. The L2 mouse fibroblast cells and HeLa cell lines were passaged in high glucose Dulbecco's modified Eagle medium (DMEM, Gibco) and 10% fetal bovine serum (FBS, HyClone). HEK-Blue-hNOD1 and -Null1 cells were purchased from InvivoGen and propagated according to the manufacturer's instructions.

Chlamydial Infections

HeLa cells were plated on glass coverslips in 24 well tissue culture treated plate (Costar) at a confluency of ~70–80%. Cells were infected with *C. trachomatis* L2 434/Bu in cold *Dulbecco's* modified Eagle medium (DMEM; Gibco; 250 µl per well) and placed on a rocker in the 37°C tissue culture incubator for 2 h. Subsequently, the DMEM was removed and replaced with DMEM supplemented with 10% FBS (HyClone) and 1x MEM Non-Essential Amino Acids Solution (Sigma; 250 µl per well). The following aberrance inducing conditions were tested

in this study and added at either the time of infection or at 22 hpi: 10 μM piperacillin, 10 μM mecillinam, 10 μM penicillin G, 125 μM MP265 (polymerization inhibitor of the bacterial cytoskeletal protein MreB), and 3 μM chloramphenicol.

Labeling of Chlamydial Peptidoglycan

HeLa cells were infected with *C. trachomatis* L2 434/Bu at an MOI of 1 unless otherwise stated. Cells and replicating intracellular *Chlamydia* were grown in the presence of the PG intercalating reagent ethynyl-D-alanyl-D-alanine (EDA-DA) at a concentration of 1 mM. At 24 hpi, cells were washed 3 times with 1X PBS, permeabilized with methanol and 0.5% Triton X (5 min each) prior to blocking with 3% Bovine Serum Albumin (BSA) for 1 h and antibody labeling. Click chemistry was carried out to link the PG-associated EDA-DA with conjugated fluorophore Azide-Alexa Fluor 488, as previously described (Liechti et al., 2014, 2016). The chlamydial Major Outer Membrane Protein (MOMP) was labeled with anti-MOMP primary antibody (goat) and secondary antibody (donkey anti-goat Alexa Fluor 594) at the dilutions 1:500 and 1:1,000, respectively. All coverslips were mounted on slides with ProLong Gold Antifade Mounting Media and stored in the dark at 4°C prior to imaging.

Imaging and Analysis of Peptidoglycan and MOMP-Labeled Objects

All imaging was conducted with a Zeiss ELYRA PS.1 in Structured Illumination (SIM) mode. Settings were fixed at the beginning of image acquisition, Z-stacks were collected for all images taken, and the same parameters were applied for collecting and post-processing all images taken within each experiment. All SIM processing was conducted in RAW fluorescent units (as opposed to averages or percentile standardizations), thus maintaining readouts well below maximum threshold and eliminating the potential for post-processing steps to approach pixel saturation. All post-image processing was conducted on Zen 2012 (Carl Zeiss) software. ImageJ was used for all subsequent image analysis utilizing the FIJI addon "3D Objects Counter" to identify the 3-dimensional spatial constraints of all PG-containing objects within individual *C. trachomatis* inclusions. Relative object volumes were estimated based off of pixel fluorescence data present throughout a Z-stack. Pixels were assigned a "1" or a "0" value based on a common threshold setting applied to all images examined. A composite of all connected "1" pixels through x, y, and z planes was thus constructed from that imaging data. Each PG-labeled object was assigned an estimated volume (in μm^3), fluorescence mean intensity (average pixel intensity), and integrated density (the sum of all pixel intensity measurements comprising an object). Object size thresholding was restricted to objects larger than 0.001 μm^3, the detection limit of this approach, corresponding to a single pixel. Statistical significance values were calculated utilizing a one-way ANOVA coupled with a multiple comparisons test with each condition compared with the untreated control group. Inclusion diameters were calculated using the average of the maximum diameter visible from all corresponding z planes and the diameter of a line perpendicular to this maximum diameter.

Infection of HEK-Blue hNOD1 and Null1 Cells With *Chlamydia trachomatis* and NF-κB Reporter Assay

HEK-Blue cells expressing the hNOD1 receptor and carrying the NF-kB SEAP (secreted embryonic alkaline phosphatase) reporter gene (InvivoGen) were used according to the manufacturer's instructions and adapted to assess NOD1-specific NF-κB activity during infection with *C. trachomatis*, as previously described (Brockett and Liechti, 2021). Briefly, 3×10^5 cells/mL of HEK-Blue hNOD1 or Null1 cells were plated in 96-well plates (total reaction volume of 200 μl per well, ~6.0×10^4 cells per well) and allowed to adhere for 6 h at 37°C. These cells were subsequently infected with *C. trachomatis* L2 434/Bu at a MOI of ~1. Plates were centrifuged for 1 h at 2,000 g to enhance the synchronization of infections and then incubated in a CO_2 incubator at 37°C. Supernatants were collected at the designated time points for subsequent analysis of SEAP activity. A colorimetric reporter assay was then utilized in order to quantify the abundance of SEAP in cell supernatants. Twenty microliter of supernatants collected from infected cells were added to 180 μl of the SEAP-detection solution (InvivoGen) followed by incubation at 37°C for ~8 h. SEAP enzymatic activity was then quantified using a plate reader set to 650 nm. Infected cells were compared to uninfected controls, as well as infected cells that had been treated with various PG-targeting antibiotics. Uninfected cells treated with the known NOD1 signaling ligand Tri-DAP (1 μg/ml) were used as a positive control. All experiments were carried out in parallel in the HEK-Blue Null1 cell line, which contains the empty expression vector but lacks hNOD1. HEK-Blue NOD1 SEAP and Null1 reporter assays were carried out independently in biological triplicate, statistical analysis was conducted by 2-way ANOVA, and significance values were analyzed utilizing Sidak's multiple comparisons test. Values plotted are means of the raw OD650 measurements.

RESULTS

Peptidoglycan Structures Differ in Their Volume and Labeling Intensity Within *Chlamydia trachomatis* Inclusions

To determine the extent to which PG labeling can be utilized to investigate the stages of the *Chlamydia* division process, we carried out a mapping study of all PG-containing objects within 100 chlamydial inclusions. Infected cells were incubated with the PG intercalating agent ethynyl-D-alanyl-D-alanine (EDA-DA; Liechti et al., 2014) and allowed to grow for 24 h, at which time the cells were fixed, permeabilized, incubated with cupric sulfate and an azide-conjugated fluorophore in a click chemistry reaction. Cells were subsequently immunolabeled with a monoclonal antibody specific for the pathogen's Major Outer Membrane Protein (MOMP). Labeled cells were then

imaged by structured illumination microscopy (SIM), Z-stacks of infected cell monolayers were collected, all EDA-DA labeled objects within each inclusion were counted and assigned corresponding spatial dimensions and labeling intensities (**Figures 1b–d**).

We have reported previously that septal ("ring") PG in *Chlamydia* species is not uniform and can differ in diameter between individual bacterial RBs (Liechti et al., 2016). We have also noted that peptidoglycan in *C. trachomatis* is transient and can dissociate rapidly when the cell division apparatus is inhibited (Liechti et al., 2016) or when "persistence" is induced utilizing various stressors (Brockett and Liechti, 2021). PG labeling intensity is a function of multiple cellular processes: (i) the uptake of the labeling reagent, (ii) the relative rates of its incorporation during peptidoglycan biosynthesis and dissociation during peptidoglycan degradation, and (iii) the relative density of the PG-containing structure. Having observed differences in PG labeling intensities when PG biosynthesis was directly interrupted, we questioned whether PG rings differed significantly in their labeling intensities throughout chlamydial development. We reasoned that if differences exist in either (1) the rates of PG synthesis and PG degradation or (2) the density of PG produced between bacteria at different stages of development, then we should be able to observe corresponding differences in PG labeling intensity. To investigate this question, we plotted PG-containing object volume against object fluorescence integrated density for all labeled objects within 15 chlamydial inclusions (**Figure 1e**). The overall data fit well within the linear range ($R^2 = 0.969$), and we found that as object volume increased, so too did the variance in mean fluorescent intensity labeling, as judged by the distance of each data point relative to the calculated linear regression line for the data set. As integrated density is a function of a labeled object's volume and mean fluorescent intensity, we reasoned that these differences in the labeling intensities of larger objects could signify differences in either object shape, the density of the labeled PG within objects, or the kinetics of PG assembly and degradation occurring in these structures.

PG Ring Volume and Labeling Intensities Vary Between RBs at Different Stages of the *Chlamydia* Division Process

To assess whether the divergence in PG labeling observed in the pooled inclusion data was representative of RB populations within individual inclusions, we repeated our examination for each inclusion from the previous analysis and plotted PG-labeled object volume and intensity measurements for every labeled object within each inclusion. We found similar levels of variance in object mean fluorescent intensity in all inclusions, and examining inclusions containing fewer bacteria allowed us to focus on individual PG-containing objects and compare their relative shapes and staining intensities. For both smaller (<5 μm diameter, **Figure 2A**) and larger (≥5 μm, **Figure 2B**) inclusions, "brighter" objects (high mean fluorescent intensity) appeared to orient as disks or smaller, compact rings (**Figures 2A,B**; red/yellow), whereas "dimmer" objects (low mean fluorescent intensity) varied in ring diameter and appeared thinner across the ring width (**Figures 2A,B**; blue/green). Striking differences in labeling intensity between objects of similar volume were found to be the result of relative differences in the apparent thickness of otherwise smaller rings (**Figure 2B**, lower left panel, objects 56 and 60). Based on these three defining features (shape, volume, and labeling intensity), we found that PG orientation within intracellular chlamydial RBs fit within four broad categories: (i) disks, (ii) small diameter/large volume (≥0.06 μm^3) rings, (iii) large diameter /large volume (≥0.06 μm^3) rings, and (iv) small diameter/small volume (< 0.06 μm^3) rings.

We hypothesized that objects with higher-than-average labeling intensities represented PG undergoing rapid synthesis, as would be predicted during septation, the terminal step in bacterial cell division (**Figure 2C**). However, because it has been reported that *Chlamydia* PG initially localizes to the interface between parent and daughter cell during the initial polar expansion of the cell membrane (Liechti et al., 2016; Cox et al., 2020), we wanted to know whether active PG synthesis was also occurring at this earlier stage of the division process (**Figure 3a**). We examined PG-labeled objects in 100 labeled inclusions and found that most inclusions larger than 5 μm in diameter contained between one to three examples of RBs in which PG was asymmetrically bisecting the bacterial cell, consistent with the "polar budding" phenotype (**Figures 3b–d**). PG-labeled objects in cells that appeared to be undergoing polar expansion had labeling intensities higher, on average, than all other objects within the inclusions (**Figures 3b–d**), similar to PG-labeled objects in cells undergoing septation (**Figure 3e**). Taken together, these data indicate that EDA-DA incorporated PG is maximally present during both the budding and septation phases of chlamydial division.

PG Ring Volume and Labeling Intensity Is Directly Affected by Protein Synthesis, MreB Polymerization, and Penicillin-Binding Protein Activity

Given the differences we observed in labeling intensities for individual PG structures within RB populations, we next wanted to examine how changes to basic molecular processes affected our PG-labeled objects. We hypothesized that object size and shape were dependent on *Chlamydia*'s division cycle and that object labeling intensity, as measured by our assay, is affected by two distinct processes: PG synthesis and degradation. While each of these activities requires protein synthesis, we reasoned that we could delineate which was the prevailing process by incubating cells with a short, sub-inhibitory dose of the protein synthesis inhibitor chloramphenicol (Cm) and measuring the resulting changes in mean object volume and labeling intensity. Cm treatment had no discernable effect on average object volume but did result in decreasing object labeling intensity (**Figures 4A–C**). By comparison, similar treatment with MP265, an MreB polymerization inhibitor that blocks MreB-dependent PG synthesis in *C. trachomatis* (Liechti et al., 2016), results in large reductions in both PG object volume and labeling

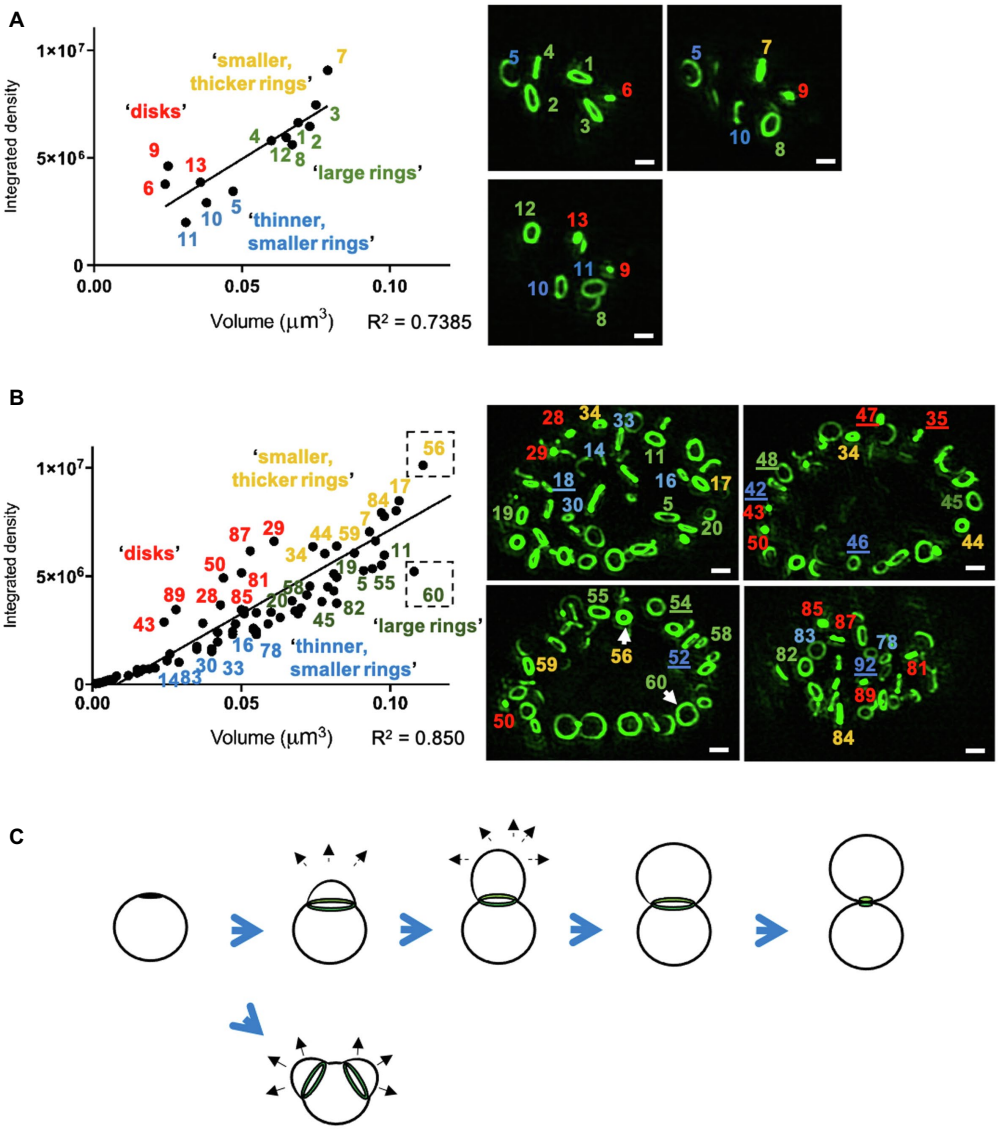

FIGURE 2 | PG ring volume and labeling intensities differ between RBs at distinct stages of the chlamydial division process. **(A,B)** Representative inclusion analysis of all PG-labeled objects within small (**A**, < 5 μm) and large (**B**, ≥ 5 μm) chlamydial inclusions. Picture panels (right panels, green) represent single imaging planes from two of the 100 independently imaged and analyzed *C. trachomatis* inclusions that were fixed and labeled at 24 h post-infection. Image brightness has been increased uniformly across all images so that dimmer objects are more visible. The calculated volumes of the corresponding labeled objects were plotted against each object's integrated density, which is a function of object volume and mean fluorescent intensity. Distance from the calculated linear regression indicates divergence from the average mean intensity calculated for all objects within an inclusion. PG-labeled objects are numbered, and number color corresponds to the defined group to which each object was assigned. Numerical designations of objects that could not be listed on the data plot are underlined in the image panels. Arrows indicate rings of similar volume but different diameters and labeling intensities. Scale bars ~1 μm. **(C)** Illustration of the polarized division model of chlamydial cell division, which is characterized by the heightened density of MOMP labeling and subsequent polar expansion of the cell membrane (black arrows) from one or two locations (as reported by Abdelrahman et al., 2016).

intensity (**Figures 4B,C**). The decrease in mean intensity during Cm treatment suggests that the balance between synthesis and degradation shifts toward turnover when protein synthesis is reduced, however, this degradation appears to be uniform across the entire PG ring as opposed to being localized to specific points on the ring. This may be a result of the timing and kinetics of the assay as previous reports investigating the effects of the inhibition of MreB polymerization on PG in *C. trachomatis* noted an initial reduction in PG ring labeling intensity that was subsequently followed by PG ring degradation (Liechti et al., 2016).

Previous studies investigating the effects of the ß-lactam antibiotic ampicillin on *Chlamydia* ring morphology have demonstrated that while EDA-DA incorporation continues to occur, PG-labeled objects exhibit an enlarged, irregular morphology (Liechti et al., 2014, 2016; Slade et al., 2019; Brockett and Liechti, 2021). This was originally thought to be due to the fact that transpeptidation is not required for the incorporation of EDA-DA,

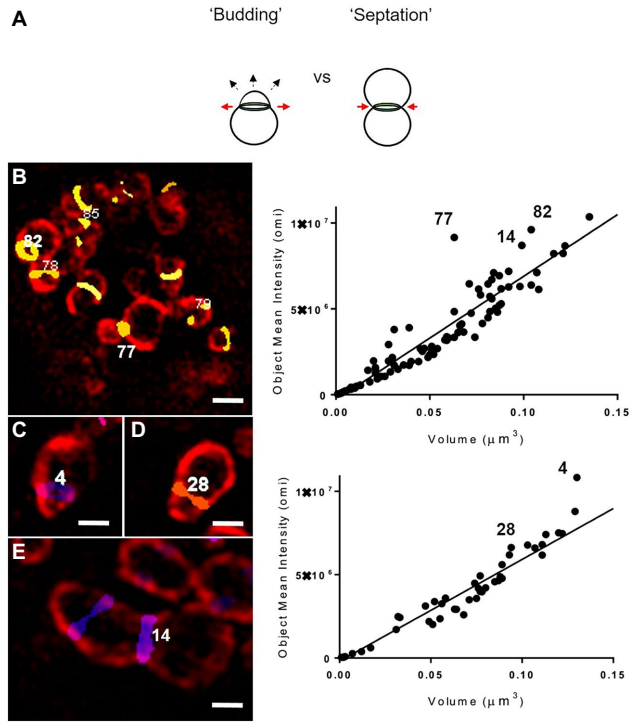

FIGURE 3 | Both "budding" and "septation" processes are associated with PG-labeled objects with higher mean fluorescent intensity values. **(a)** Illustration of the budding and septation stages of the chlamydial division process. The budding phenotype is defined by the polar expansion of the bacterial membrane (dashed arrows) and the expansion of the PG ring (red arrows), whereas septation is defined by the constriction of the PG ring (red arrows), resulting in two daughter cells of equal size. Representative images displaying *C. trachomatis* RBs undergoing either the initial "budding" **(b–d)** or the terminal septation **(e)** stage of their division cycle. RBs are labeled with a monoclonal antibody for MOMP (red) and PG-labeled objects are displayed utilizing a colorimetric "heatmap" corresponding to their relative Z plane positioning within an inclusion. Images are representative of observations made for 51 inclusions >5 µm **(b,e)** and 49 inclusions ≤5 um **(c,d)**. Scale bars ~1 µm **(b)** and ~0.5 µm **(c–e)**. Each PG-labeled object was assigned a numerical value that can be viewed as a function of its volume and mean intensity measurement (right panels). Variance from the linear regression line represents an object's relative divergence from the average integrated density for all objects within an inclusion.

as this process occurs in the cytoplasmic space during Lipid II biosynthesis (Kuru et al., 2019). We wanted to further examine this irregular PG phenotype and establish whether it is unique to the inhibition of specific PBPs in *Chlamydia*. We incubated *Chlamydia*-infected cells for 2 h in the presence of inhibitors specific for PBP2 (mecillinam; mec), PBP3 (piperacillin; pip), or both (penicillin G; penG) and compared the relative volume and intensities of PG-positive objects with an untreated control group. When PBP2 activity was inhibited alone, or in conjunction with PBP3, we saw a significant reduction in mean object volume (**Figures 4A,B**), however, object mean fluorescent intensity did not decrease (**Figure 4C**). Conversely, inhibition of PBP3 resulted in an increase in object volume (**Figure 4A**, bottom left panel). The effect was so robust that our subsequent imaging analysis could not distinguish a large number of individual objects, resulting in their removal from the analysis, and a subsequent "low confidence" score in our reported average volume for this treatment condition (**Figure 4B**). When both PBP2 and PBP3 are inhibited together, both object volume and object labeling intensity was significantly reduced. As an object's integrated density (IntDen) is a function of both its volume and its labeling intensity, these measurements largely tracked with our mean fluorescent intensity measurements (**Figures 4C,D**) with the notable exception of the Mecillinam-treated group. Given the relative expansion of the PG ring when PBP3 was inhibited and the relative disassembly of the PG ring when PBP2 was inhibited, our observations suggest that PG structure in *C. trachomatis* is a function of these two differential PG synthases.

We next wanted to ensure that the loss of PG labeling under our treatment with ß-lactam antibiotics was the result of defects in PG assembly, rather than resulting from the complete inhibition of PG biosynthesis. Gram-negative bacteria are known to continue to synthesize lipid II and attempt to assemble PG despite a block on transpeptidation (Cho et al., 2014). This has previously been demonstrated with D-cycloserine (Packiam et al., 2015) and ampicillin (Brockett and Liechti, 2021) in *C. trachomatis*, utilizing a NOD reporter assay. We examined each treatment condition in a NOD1-signaling reporter cell line that reacts to PG-derived muropeptides produced by *C. trachomatis* that contain meso-diaminopimelic acid (mDAP; Brockett and Liechti, 2021). Similar to ampicillin, we found that *C. trachomatis* continues to generate mDAP-containing muropeptides in the presence of all other ß-lactam antibiotics (**Figure 5**), indicating that the absence of labeling in our mec and penG treatment conditions is not the result of an absence of Lipid II production. Coupled with our imaging analysis, these data suggest that chlamydial PBP2 and PBP3 activities are associated with different stages of the bacterium's cell division process. Interestingly, we also found that only the complete interruption of PG assembly (*via* penicillin G) or PG biosynthesis (*via* D-cycloserine) significantly enhanced NOD1-ligand production and release. PG-derived muropeptide turnover was not significantly enhanced when PBP2 or PBP3 functions were selectively inhibited with mecillinam and piperacillin, respectively.

Average Peptidoglycan Ring Volume and Labeling Intensity Decreases as *Chlamydia trachomatis* Progresses Through Its Developmental Cycle

We next sought to examine PG-labeled objects in the context of the *C. trachomatis* developmental cycle. For this analysis, cell monolayers were infected *via* rocking, as opposed to centrifugation, and infection inoculates were left on the cell layers in order to achieve an asynchronous population of *C. trachomatis* infected cells all at different stages of the microbe's developmental cycle. Cells were fixed, stained, imaged, and processed as before, but inclusion size measurements were also collected as an indicator of the stage of development that individual inclusions had reached by the point of fixation. *Chlamydia* inclusions fuse and expand throughout the pathogen's

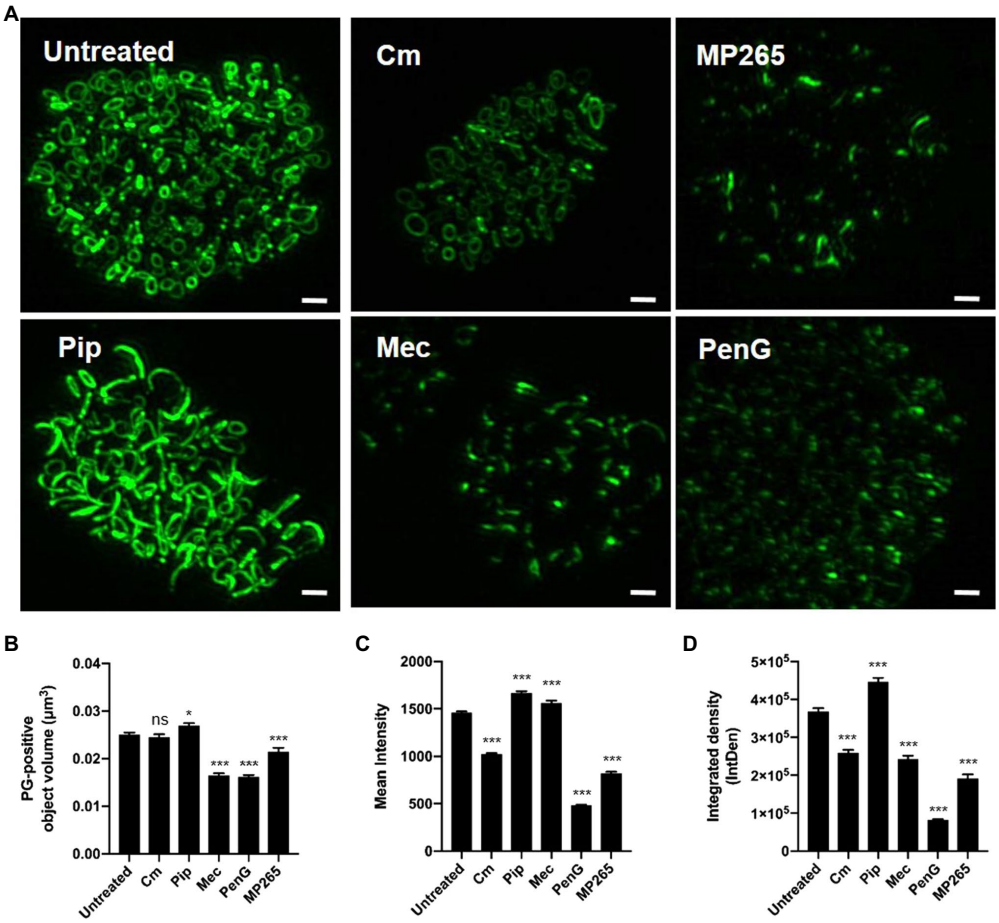

FIGURE 4 | PG ring volume and labeling intensity are directly influenced by protein synthesis, MreB polymerization, and penicillin-binding protein activity. **(A)** PG-labeled objects present within *C. trachomatis* inclusions 24 h post-infection that have either been left untreated, or have been treated for 2 h with the chemical inhibitors specified. Scale bars ~2 µm. Average object volume **(B)**, mean fluorescent intensity **(C)**, and integrated density **(D)** for each group were then compared to untreated controls. A statistical analysis was conducted utilizing one-way ANOVA with multiple comparisons testing. Values represent data acquired from 10 inclusions per experimental group collected over two independent biological replicates. Cm; Chloramphenicol, MP265; MreB polymerization inhibitor, Pip; Piperacillin, Mec; Mecillinam, PenG; Penicillin G. $^{*}p < 0.05$, $^{***}p < 0.001$, ns; not significant.

developmental cycle and larger inclusions result from longer incubation times.

An analysis of inclusion dimensions revealed a relatively good distribution of inclusion sizes present in our study population (**Figure 6A**), which exhibited a slight bimodal distribution (**Figure 6B**). As replicating *Chlamydia* RBs should increase logarithmically over time, we hypothesized that PG-labeled objects should similarly exhibit a logarithmic function when plotted against inclusion diameter. We observed this exact phenomenon (**Figure 6C**), strengthening our confidence that inclusion diameter could be used as a readout for the relative age of the bacterial population within. In examining PG-labeled objects from individual inclusions, we determined that object volumes ≤0.1 µm were of higher confidence than object volumes ≥0.1 µm, due to the vast majority of the larger objects resulting from multiple, overlapping smaller objects being mistakenly reported as single large objects. We examined the presence of these larger objects throughout the range of inclusion diameters present in our data set, expecting to find more per inclusion later in development, when the inclusions contain significantly more labeled objects. Surprisingly, we found the reverse to be true, with the ratio of smaller to larger objects increasing as inclusion diameter increased (**Figure 6D**).

Previous reports have indicated that as *Chlamydia* proceeds through its developmental cycle its replicative forms (on average) decrease in size with subsequent division events (Lee et al., 2018). According to this model, a gradual reduction in RB size eventually enables *C. trachomatis* to drop below a critical size threshold, enabling the pathogen's replicative form to convert to its infectious form (**Figure 7A**). This model has been difficult to test utilizing fluorescence microscopy, as delineating individual bacterial cell boundaries within densely packed, intracellular inclusions are challenging. However, given our success mapping PG-labeled objects associated with individual *Chlamydia* RBs, we sought to validate this model by conducting an analysis of the relative volume and density of PG-labeled structures throughout the course of *Chlamydia*'s developmental cycle.

Given the size-reduction-precedes-differentiation model's constraints, we hypothesized that PG object volume should significantly decrease over time, as a result of *Chlamydia* progressing through its development, while labeling intensity should increase, as it has been proposed that *C. trachomatis* maximizes its replication rate by the mid-stage in its development. We plotted average object volumes, integrated densities, and mean fluorescent intensity values against the diameters of each inclusion for both sets of objects collected ($< 0.1\,\mu m^3$ and $> 0.1\,\mu m^3$). For objects $\leq 0.1\,\mu m^3$ we found that average object mean fluorescent intensity (**Figure 7B**), object integrated density (**Figure 7C**), and object volume (**Figure 7D**) all decreased as inclusion diameters increased. For objects $>0.1\,\mu m^3$, no similar decrease in average object integrated density or volume was observed as inclusion diameter increased (**Figures 7C,D**). Interestingly, objects $>0.1\,\mu m^3$ did exhibit a similar trend as smaller objects in that their mean fluorescent intensities appeared to significantly decrease as inclusion diameter increased (**Figure 7B**). Overall, these observations appear to conform to the size-reduction-before-differentiation model in that average PG volume decreases over the span of a developmental cycle.

DISCUSSION

Cell size regulation is critical for bacterial species, enabling microbes to respond to favorable and detrimental changes in their respective environments. The mechanism(s) employed for regulating cell size are predominantly well-conserved in bacteria; however, the notable exception is members of the Chlamydiales that lack sacculi (Liechti et al., 2014, 2016). For these organisms, cell expansion is presumably limited only by fatty acid biosynthesis and the rate of PG-dependent cell division, rather than the remodeling of a PG-containing cell wall. When PG synthesis is inhibited in these organisms, cell size increases dramatically, indicating that cell size reduction in *Chlamydia* species is largely dependent on the rate of cell division. *C. trachomatis* is capable of halting its biphasic developmental cycle during unfavorable environmental conditions by simply inhibiting PG biosynthesis (Liechti et al., 2016; Slade et al., 2019; Brockett and Liechti, 2021). This prevents cell size-reduction, as well as completely inhibits PG synthesis, enabling the degradation of the PG ring when the pathogen is subjected to iron- and/or tryptophan depletion (Brockett and Liechti, 2021), two conditions utilized by the innate immune system to ward off intracellular bacteria (Feng and Taylor, 1989). These two cell stressors are generally associated with the induction of the pathogen's aberrant/persistent state (**Figure 1A**; Wyrick, 2010).

While members of the Chlamydiae encode a number of components involved in localized PG synthesis, they lack the central protein responsible for directing the septal division machinery in most other bacterial species; FtsZ (Ouellette et al., 2020). However, these organisms do possess the fundamental elements of the side wall (RodA (Meeske et al., 2016), PBP2) and septal (FtsW (Taguchi et al., 2019), PBP3) PG polymerases. The exact role(s) played by each of these two complexes in the context of i) the newly characterized stages of the *Chlamydia* division process (**Figure 8A**) and

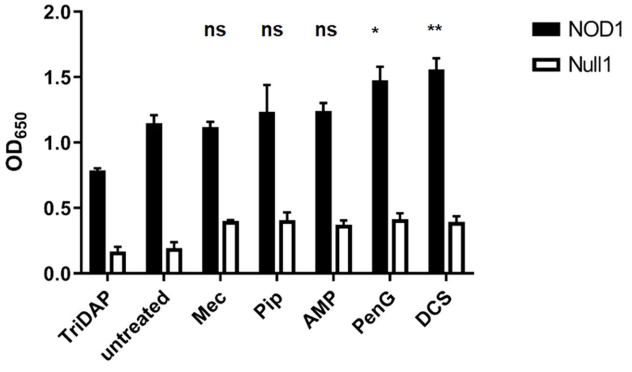

FIGURE 5 | PG synthesis and transpeptidase inhibitors fail to prevent the synthesis of PG precursors in *C. trachomatis*. HEK hNOD1 and HEK Null1 SEAP-reporter cell lines were utilized to quantify the relative abundance of PG-derived muropeptides shed by intracellular *C. trachomatis* in the presence of Mecillinam (Mec), Piperacillin (Pip), Ampicillin (AMP), Penicillin G (PenG), and D-cycloserine (DCS). TriDAP was used as a positive control for NOD1 signaling, and infections were carried out in parallel in a Null1 cell line as a negative control. Data presented are the mean of three independent, biological replicates and error bars represent standard deviation from the mean. A statistical analysis was carried out by 2-way ANOVA with multiple comparisons. Significance values displayed represent comparisons for each group against the untreated control. $^*p < 0.001$, $^{**}p < 0.0001$, ns; not significant. No significant difference was observed between all comparisons of the treatments carried out in the Null 1 cell line.

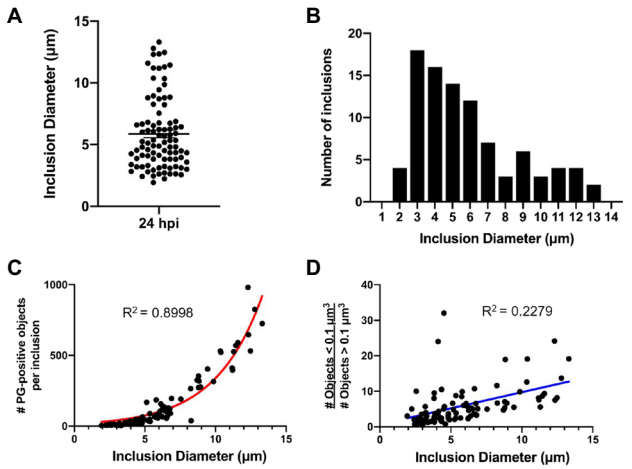

FIGURE 6 | *C. trachomatis* inclusion diameter is an indicator of the relative maturity of the bacterial population that resides within it. Cell monolayers were infected with *C. trachomatis* asynchronously, without centrifugation, as described in **Figure 1**. **(A,B)** Diameter measurements were taken for 96 chlamydial inclusions that were fixed and imaged 24 h post-infection. Data are presented as a point spread from the average inclusion diameter **(A)** as well as *via* histogram **(B)** to show the size distribution throughout the population. **(C)** Inclusion diameter was plotted against the number of PG-positive objects present within each individual inclusion. Data were consistent with a logarithmic growth function (red line). **(D)** The abundance of low confidence objects ($> 0.1\,\mu m^3$) to high confidence objects ($\leq 0.1\,\mu m^3$) was plotted as a function of inclusion diameter. Data were inconsistent with a linear regression (blue line).

ii) the microbe's biphasic developmental cycle is only now being actively investigated. Our analysis of the PG composition of 1,000 of chlamydial RBs has led us to conclude that the *Chlamydia* division process can be broken into four stages based on PG localization and intensity measurements: priming/initiation, budding, resting, and septation (**Figure 8A**). Our observations are consistent with previous reports describing an initial budding stage in the replication cycle of *C. trachomatis* (Abdelrahman et al., 2016; Liechti et al., 2016; Cox et al., 2020), and we found that both the budding and septation phases of the process appear to exhibit the highest rates of PG synthesis, as measured by active incorporation of our labeling probe. These observations suggest that a high degree of PG synthesis activity is characteristic of both the expansion and constriction stages of the PG ring at the initiation and termination of cell division, respectively.

Researchers have hypothesized that *Chlamydia* MreB is capable of directing septal PG biosynthesis in the absence of FtsZ (Ouellette et al., 2012; Liechti et al., 2016), and a recent study has demonstrated that *Chlamydia* MreB is capable of directing septal PG biosynthesis in an *Escherichia coli* strain lacking both MreB and FtsZ activity, effectively enabling this strain to divide in the absence of FtsZ (Ranjit et al., 2020). The ability of the *Chlamydia* MreB protein ($MreB^{CT}$) to effectively direct PG synthesis to the septum in *E. coli* was dependent on the co-expressing of the *Chlamydia* RodZ protein ($RodZ^{CT}$), indicating that these two *Chlamydia* proteins are sufficient to direct septal PG synthesis not only in *C. trachomatis*, but also in surrogate systems. Researchers have previously established that MreB and RodZ are important for directing PG biosynthesis in *C. trachomatis*, and it has been proposed that MreB directs both PG synthases in these organisms (Ouellette et al., 2014; Kemege et al., 2015; Liechti et al., 2016). We found it interesting that despite inhibiting MreB activity, we were still able to observe trace amounts of PG labeling. PG-labeled objects subsequent to MP265 treatment, on average, tended to have smaller volumes and lower mean fluorescent intensities then untreated controls. Previous work investigating the dissociation of the *C. trachomatis* PG ring complex noted that even after dissociation single PG-positive puncta were nearly always observable (Liechti et al., 2016). This suggests that while MreB polymerization is essential for the construction of the chlamydial PG septum, some PG synthesis still occurs in the absence of this process. Alternatively, PG in the vicinity of the divisome complex may simply be spatially protected from degradation by the bacterium's PG hydrolysis enzymes.

PG biosynthesis and degradation pathways are decoupled in *C. trachomatis*, and inhibition of new synthesis results in the rapid degradation of the PG ring (Liechti et al., 2016). In conducting our analysis of PG-containing structures, we had originally assumed that $MreB^{CT}$ was capable of directing both the RodA-PBP2 and FtsW-PBP3 PG polymerase complexes in *Chlamydia*. Interestingly, we found that when chlamydial PBP2 and PBP3 functions are inhibited separately, significant

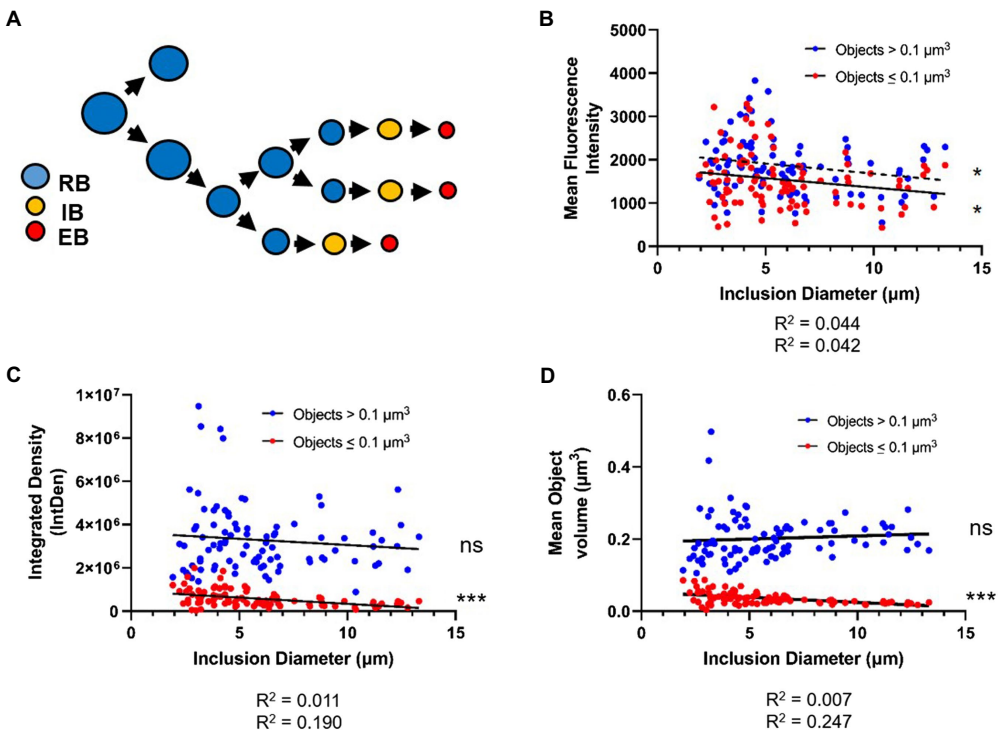

FIGURE 7 | PG-labeled object volume and mean fluorescent intensity decreases as inclusion diameter increases. **(A)** The cell size reduction-preceding-differentiation model, as proposed by Lee et al. The average values for PG-labeled object mean fluorescent intensity **(B)**, integrated density **(C)**, and object volume **(D)** were plotted against inclusion diameter. Objects in each inclusion were separated into those of "low confidence" (>0.1 µm³) and those of "high confidence" (≤0.1 µm³). Data for each object type were subjected to a linear regression analysis, and statistical analysis was performed to determine if the linear slope of the data diverged significantly from zero. ns; not significant, *$p < 0.5$, ***$p < 0.001$.

differences in PG probe incorporation occur (**Figure 4**). When either MreB or PBP2 function is selectively inhibited, the majority of the PG ring dissociates, however, some PG-labeled foci remain. When accounting for differences in volume (**Figure 4C**, mean intensity) these foci have comparable levels of PG synthesis activity to untreated and piperacillin-treated controls. These observations are consistent with localized, PG synthesis in the absence of PBP2 activity. By contrast, inhibition of PBP3 results in the accumulation of large PG-containing structures and an aberrant ring morphology similar to that observed upon treatment with ampicillin (Liechti et al., 2014, 2016; Brockett and Liechti, 2021). Interestingly, mean fluorescent intensities of PG-labeled objects in both mecillinam- and piperacillin-treated groups were slightly elevated compared to untreated controls.

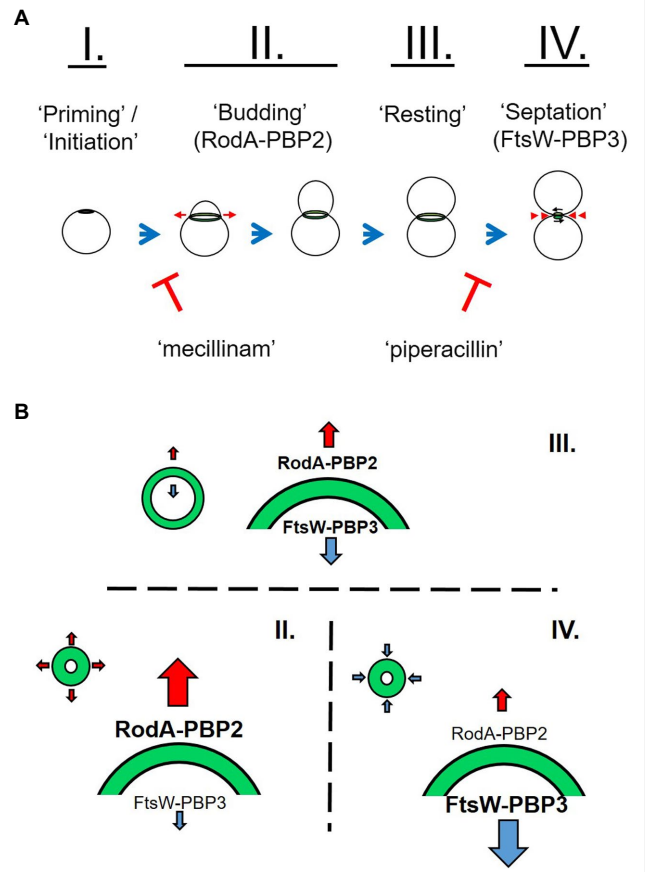

FIGURE 8 | Working model for the role of peptidoglycan in chlamydial polarized cell division. *C. trachomatis* appears to initiate PG synthesis at a single pole (I.). This polar disk expands outward (red arrows) as a result of MreB-dependent RodA-PBP2 PG polymerization on the disk periphery (**A,B**, II.). This coincides with the previously described process of asymmetrical membrane expansion. Due to the transient nature of chlamydial PG in the absence of new synthesis activity, the center of the PG-containing disk degrades, giving rise to a ring-like shape. The ring continues to expand from the outer edge to a point where the rate of PG synthase activity is roughly equivalent to that of PG degradation. This phase of lower intensity PG labeling is the predominant labeling pattern in RBs within *C. trachomatis* inclusions and is indicative of a resting state between the budding and septation stages of the division process (**A,B**, III.). Upon the initiation of septation, the FtsW-PBP3 PG polymerase acts to synthesize PG on the inner edge of the ring, effectively defining the septum as the ring constricts back into a disk, and ultimately dissociates (**A,B**, IV.).

When subjected to penicillin and D-cycloserine, bacterial cells often futilely attempt to overcome the perceived defect in their PG synthesis activity by enhancing the production of PG precursor molecules (Cho et al., 2014). As these PG precursors are highly detectable by our innate immune system, this effect can be observed by measuring signaling of NOD1 and NOD2 receptors (Packiam et al., 2015). Utilizing our NOD1 reporter assay, we found that treatment with PBP2- and PBP3-specific inhibitors did not significantly enhance the turnover and shedding of PG-derived muropeptides by *C. trachomatis* while treatment with penicillin G and D-cycloserine did (**Figure 5**). We took this as evidence that penicillin G is broadly affecting multiple PBPs in *C. trachomatis*, whereas piperacillin and mecillinam appear to be more targeted. D-cycloserine effectively prevents PG biosynthesis at a stage prior to transpeptidation, and therefore, it also significantly enhances NOD stimulation. As our ampicillin treatment group exhibits labeling and immunostimulatory profiles more similar to that of our piperacillin treatment condition, we reason that ampicillin (unlike penicillin G) preferentially inhibits PBP3 in *C. trachomatis*.

Given these differences, we propose that the two chlamydial PG synthases differ in their activities and likely determine PG ring dimensions during cell division (**Figure 8B**). A previous study found that PG synthesis *via* PBP2 was necessary to initiate polarized division in *C. trachomatis* (Cox et al., 2020), indicating that the PBP2-specific PG ring expansion we characterize in our study is likely essential to this initial division process. We postulate that RodA-PBP2 and FtsW-PBP3 complexes function independently during division and that the differences we observe in labeling localization represent either differences in the location of synthesized PG or that the stability of the PG each synthase generates is inherently different. Given the assumption that PG is a transient structure in *Chlamydia* species, differences in the relative activities of these two synthases would largely explain changes in PG ring dimensions throughout the division cycle (**Figure 8B**). When combined with our overall assessment of PG localization during the *Chlamydia* division process, we reason that the enhanced labeling we observe during the expansion and constriction of the PG ring is largely due to increased PBP2 and PBP3 activities, respectively.

Our observation that PG ring volume and labeling intensity decrease with time is consistent with the previously proposed cell size-precedes cell differentiation model of *C. trachomatis* development (Lee et al., 2018). Assuming a linear function, we calculate that the average PG-labeled object in an inclusion two microns in diameter (our smallest observed inclusion size) to have an average volume of ~0.047 um^3, whereas the average PG-labeled object present in an inclusion 13 µ in diameter (our largest observed inclusion size) would have an average volume of ~0.016 um^3. For comparison, Lee et al. found that compared to RB size at 12 h post-infection, average RB volume decreased by roughly half by 24 hpi and by roughly three quarters by 32 hpi (Lee et al., 2018).

Because *C. trachomatis* replicates more rapidly at later developmental stages, it is possible that our observation that

PG-labeled objects are smaller later in development is due to the presence of greater numbers of early (budding) and late (septation) division stages with the characteristic smaller PG rings. However, we posit that if there are greater numbers of smaller rings due to bacteria actively synthesizing PG and undergoing budding and septation, then we should have seen corresponding higher relative PG fluorescence mean intensity values, a readout of object density (**Figure 2**). Because this does not appear to be the case in larger, more mature inclusions (**Figure 7B**), we conclude that our data support cell size reduction of PG-containing *C. trachomatis* RBs over the span of the pathogen's developmental cycle. The underlying cause of this decrease in average PG mean intensity throughout the development of *C. trachomatis* is unknown, but may be a function of competing metabolic processes, the availability of some concentration-dependent nutrient, or simply the fact that the essential PG density required for budding/septation differs depending on cell size. Future studies will be needed to further elucidate how cell size affects basic metabolic processes such as PG synthesis and turnover in *Chlamydia* species.

DATA AVAILABILITY STATEMENT

The raw data supporting the conclusions of this article will be made available by the authors, without undue reservation.

AUTHOR CONTRIBUTIONS

GL: conceptualization and design, data curation, formal analysis, investigation, methodology, validation, visualization, writing, editing, funding acquisition, and project administration.

FUNDING

This work was supported by a MIRA ESI award (R35 GM138202) and a USU faculty start up award (HP73LIEC18) to GL. The funders had no role in study design, data collection, and interpretation or the decision to submit the work for publication. The opinions and assertions expressed herein are those of the author and do not necessarily reflect the official policy or position of the Uniformed Services University or the Department of Defense.

ACKNOWLEDGMENTS

I would like to thank my long-time collaborator Dr. Michael VanNieuwenhze (Indiana University) and his laboratory for providing us with the "clickable" D-alanine dipeptides (EDA-DA) used in our peptidoglycan-labeling experiments.

REFERENCES

Abdelrahman, Y., Ouellette, S. P., Belland, R. J., and Cox, J. V. (2016). Polarized cell division of *Chlamydia trachomatis*. *PLoS Pathog.* 12:e1005822. doi: 10.1371/journal.ppat.1005822

Barbour, A. G., Amano, K., Hackstadt, T., Perry, L., and Caldwell, H. D. (1982). *Chlamydia trachomatis* has penicillin-binding proteins but not detectable muramic acid. *J. Bacteriol.* 151, 420–428. doi: 10.1128/jb.151.1.420-428.1982

Beatty, W. L., Morrison, R. P., and Byrne, G. I. (1994). Persistent chlamydiae: from cell culture to a paradigm for chlamydial pathogenesis. *Microbiol. Rev.* 58, 686–699. doi: 10.1128/mr.58.4.686-699.1994

Belland, R. J., Nelson, D. E., Virok, D., Crane, D. D., Hogan, D., Sturdevant, D., et al. (2003). Transcriptome analysis of chlamydial growth during IFN-gamma-mediated persistence and reactivation. *Proc. Natl. Acad. Sci. U. S. A.* 100, 15971–15976. doi: 10.1073/pnas.2535394100

Bonner, C. A., Byrne, G. I., and Jensen, R. A. (2014). *Chlamydia* exploit the mammalian tryptophan-depletion defense strategy as a counter-defensive cue to trigger a survival state of persistence. *Front. Cell. Infect. Microbiol.* 4:17. doi: 10.3389/fcimb.2014.00017

Brinkworth, A. J., Wildung, M. R., and Carabeo, R. A. (2018). Genomewide transcriptional responses of iron-starved *Chlamydia trachomatis* reveal prioritization of metabolic precursor synthesis over protein translation. *mSystems*, 3, e00184–e001817. doi: 10.1128/mSystems.00184-17

Brockett, M. R., and Liechti, G. W. (2021). Persistence alters the interaction between *Chlamydia trachomatis* and its host cell. *Infect. Immun.* 89:e0068520. doi: 10.1128/IAI.00685-20

Brothwell, J. A., Brockett, M., Banerjee, A., Stein, B. D., Nelson, D. E., and Liechti, G. W. (2021). Genome copy number regulates inclusion expansion, septation, and infectious developmental form conversion in *Chlamydia trachomatis*. *J. Bacteriol.* 203, e00630–e006320. doi: 10.1128/JB.00630-20

Cho, H., Uehara, T., and Bernhardt, T. G. (2014). Beta-lactam antibiotics induce a lethal malfunctioning of the bacterial cell wall synthesis machinery. *Cell* 159, 1300–1311. doi: 10.1016/j.cell.2014.11.017

Cox, J. V., Abdelrahman, Y. M., and Ouellette, S. P. (2020). Penicillin-binding proteins regulate multiple steps in the polarized cell division process of *Chlamydia*. *Sci. Rep.* 10:12588. doi: 10.1038/s41598-020-69397-x

Egan, A. J., and Vollmer, W. (2013). The physiology of bacterial cell division. *Ann. N. Y. Acad. Sci.* 1277, 8–28. doi: 10.1111/j.1749-6632.2012.06818.x

Elwell, C., Mirrashidi, K., and Engel, J. (2016). *Chlamydia* cell biology and pathogenesis. *Nat. Rev. Microbiol.* 14, 385–400. doi: 10.1038/nrmicro.2016.30

Falcieri, E., Cevenini, R., Landini, M. P., and Donati, M. (1979). The replication cycle of *Chlamydia trachomatis* and *Chlamydia psittaci*: ultrastructural analysis. *Boll. Ist. Sieroter. Milan.* 58, 395–405.

Feng, G. S., and Taylor, M. W. (1989). Interferon gamma-resistant mutants are defective in the induction of indoleamine 2,3-dioxygenase. *Proc. Natl. Acad. Sci. U. S. A.* 86, 7144–7148. doi: 10.1073/pnas.86.18.7144

Fox, A., Rogers, J. C., Gilbart, J., Morgan, S., Davis, C. H., Knight, S., et al. (1990). Muramic acid is not detectable in *Chlamydia psittaci* or *Chlamydia trachomatis* by gas chromatography-mass spectrometry. *Infect. Immun.* 58, 835–837. doi: 10.1128/iai.58.3.835-837.1990

Fuerst, J. A. (1995). The planctomycetes: emerging models for microbial ecology, evolution and cell biology. *Microbiology* 141, 1493–1506. doi: 10.1099/13500872-141-7-1493

Garrett, A. J., Harrison, M. J., and Manire, G. P. (1974). A search for the bacterial mucopeptide component, muramic acid, in *Chlamydia*. *J. Gen. Microbiol.* 80, 315–318. doi: 10.1099/00221287-80-1-315

Gaylord, W. H. Jr. (1954). Intracellular forms of meningopneumonitis virus. *J. Exp. Med.* 100, 575–580. doi: 10.1084/jem.100.6.575

Gogolak, F. M., and Weiss, E. (1950). The effect of antibiotics on agents of the psittacosis-lymphogranuloma group. *J. Infect. Dis.* 87, 264–274. doi: 10.1093/infdis/87.3.264

Gray, A. N., Egan, A. J., Van't Veer, I. L., Verheul, J., Colavin, A., Koumoutsi, A., et al. (2015). Coordination of peptidoglycan synthesis and outer membrane constriction during *Escherichia coli* cell division. *elife* 4:e07118. doi: 10.7554/eLife.07118

Hackstadt, T., Rockey, D. D., Heinzen, R. A., and Scidmore, M. A. (1996). *Chlamydia trachomatis* interrupts an exocytic pathway to acquire endogenously synthesized sphingomyelin in transit from the Golgi apparatus to the plasma membrane. *EMBO J.* 15, 964–977. doi: 10.1002/j.1460-2075.1996.tb00433.x

Harper, A., Pogson, C. I., Jones, M. L., and Pearce, J. H. (2000). Chlamydial development is adversely affected by minor changes in amino acid supply, blood plasma amino acid levels, and glucose deprivation. *Infect. Immun.* 68, 1457–1464. doi: 10.1128/IAI.68.3.1457-1464.2000

Hurst, E. W., Landquist, J. K., Melvin, P., Peters, J. M., Senior, N., Silk, J. A., et al. (1953). The therapy of experimental psittacosis and lymphogranuloma venereum (inguinale) II. The activity of quinoxaline-1:4-dioxide and substituted and related compounds, with a note on the morphological changes induced in lymphogranuloma virus by these compounds and by antibiotics. *Br. J. Pharmacol. Chemother.* 8, 297–305. doi: 10.1111/j.1476-5381.1953.tb00798.x

Hybiske, K., and Stephens, R. S. (2007). Mechanisms of host cell exit by the intracellular bacterium *Chlamydia*. *Proc. Natl. Acad. Sci. U. S. A.* 104, 11430–11435. doi: 10.1073/pnas.0703218104

Jacquier, N., Frandi, A., Pillonel, T., Viollier, P. H., and Greub, G. (2014). Cell wall precursors are required to organize the chlamydial division septum. *Nat. Commun.* 5:3578. doi: 10.1038/ncomms4578

Kawai, Y., Mickiewicz, K., and Errington, J. (2018). Lysozyme counteracts beta-lactam antibiotics by promoting the emergence of L-form bacteria. *Cell* 172:e1010. doi: 10.1016/j.cell.2018.01.021

Kemege, K. E., Hickey, J. M., Barta, M. L., Wickstrum, J., Balwalli, N., Lovell, S., et al. (2015). *Chlamydia trachomatis* protein CT009 is a structural and functional homolog to the key morphogenesis component RodZ and interacts with division septal plane localized MreB. *Mol. Microbiol.* 95, 365–382. doi: 10.1111/mmi.12855

Kuru, E., Radkov, A., Meng, X., Egan, A., Alvarez, L., Dowson, A., et al. (2019). Mechanisms of incorporation for D-amino acid probes that target peptidoglycan biosynthesis. *ACS Chem. Biol.* 14, 2745–2756. doi: 10.1021/acschembio.9b00664

Lambden, P. R., Pickett, M. A., and Clarke, I. N. (2006). The effect of penicillin on *Chlamydia trachomatis* DNA replication. *Microbiology* 152, 2573–2578. doi: 10.1099/mic.0.29032-0

Lee, J. K., Enciso, G. A., Boassa, D., Chander, C. N., Lou, T. H., Pairawan, S. S., et al. (2018). Replication-dependent size reduction precedes differentiation in *Chlamydia trachomatis*. *Nat. Commun.* 9:45. doi: 10.1038/s41467-017-02432-0

Lee, K. C., Webb, R. I., and Fuerst, J. A. (2009). The cell cycle of the planctomycete Gemmata obscuriglobus with respect to cell compartmentalization. *BMC Cell Biol.* 10:4. doi: 10.1186/1471-2121-10-4

Lewis, M. E., Belland, R. J., AbdelRahman, Y. M., Beatty, W. L., Aiyar, A. A., Zea, A. H., et al. (2014). Morphologic and molecular evaluation of *Chlamydia trachomatis* growth in human endocervix reveals distinct growth patterns. *Front. Cell. Infect. Microbiol.* 4:71. doi: 10.3389/fcimb.2014.00071

Liechti, G. W., Kuru, E., Hall, E., Kalinda, A., Brun, Y. V., VanNieuwenhze, M., et al. (2014). A new metabolic cell-wall labelling method reveals peptidoglycan in *Chlamydia trachomatis*. *Nature* 506, 507–510. doi: 10.1038/nature12892

Liechti, G., Kuru, E., Packiam, M., Hsu, Y. P., Tekkam, S., Hall, E., et al. (2016). Pathogenic *Chlamydia* lack a classical Sacculus but synthesize a narrow, mid-cell peptidoglycan ring, regulated by MreB, for cell division. *PLoS Pathog.* 12:e1005590. doi: 10.1371/journal.ppat.1005590

Lin, H. S., and Moulder, J. W. (1966). Patterns of response to sulfadiazine, D-cycloserine and D-alanine in members of the psittacosis group. *J. Infect. Dis.* 116, 372–376. doi: 10.1093/infdis/116.3.372

Meeske, A. J., Riley, E. P., Robins, W. P., Uehara, T., Mekalanos, J. J., Kahne, D., et al. (2016). SEDS proteins are a widespread family of bacterial cell wall polymerases. *Nature* 537, 634–638. doi: 10.1038/nature19331

Mercier, R., Kawai, Y., and Errington, J. (2014). General principles for the formation and proliferation of a wall-free (L-form) state in bacteria. *elife* 3:e04629. doi: 10.7554/eLife.04629

Moulder, J. W. (1993). Why is *Chlamydia* sensitive to penicillin in the absence of peptidoglycan? *Infect. Agents Dis.* 2, 87–99.

Moulder, J. W., Novosel, D. L., and Officer, J. E. (1963). Inhibition of the growth of agents of the psittacosis group by D-Cycloserine and its specific reversal by D-alanine. *J. Bacteriol.* 85, 707–711. doi: 10.1128/jb.85.3.707-711.1963

Ouellette, S. P., Karimova, G., Subtil, A., and Ladant, D. (2012). *Chlamydia* co-opts the rod shape-determining proteins MreB and Pbp2 for cell division. *Mol. Microbiol.* 85, 164–178. doi: 10.1111/j.1365-2958.2012.08100.x

Ouellette, S. P., Lee, J., and Cox, J. V. (2020). Division without binary fission: cell division in the FtsZ-less *Chlamydia*. *J. Bacteriol.* 202, e00252–e002520. doi: 10.1128/JB.00252-20

Ouellette, S. P., Rueden, K. J., Gauliard, E., Persons, L., de Boer, P. A., and Ladant, D. (2014). Analysis of MreB interactors in *Chlamydia* reveals a RodZ homolog but fails to detect an interaction with MraY. *Front. Microbiol.* 5:279. doi: 10.3389/fmicb.2014.00279

Packiam, M., Weinrick, B., Jacobs, W. R. Jr., and Maurelli, A. T. (2015). Structural characterization of muropeptides from *Chlamydia trachomatis* peptidoglycan by mass spectrometry resolves "chlamydial anomaly", *Proc. Natl. Acad. Sci. U. S. A.* 112, 11660–11665. doi: 10.1073/pnas.1514026112

Panzetta, M. E., Valdivia, R. H., and Saka, H. A. (2018). *Chlamydia* persistence: a survival strategy to evade antimicrobial effects *in-vitro* and *in-vivo*. *Front. Microbiol.* 9:3101. doi: 10.3389/fmicb.2018.03101

Phillips, D. M., Swenson, C. E., and Schachter, J. (1984). Ultrastructure of *Chlamydia trachomatis* infection of the mouse oviduct. *J. Ultrastruct. Res.* 88, 244–256. doi: 10.1016/S0022-5320(84)90122-9

Pilhofer, M., Aistleitner, K., Biboy, J., Gray, J., Kuru, E., Hall, E., et al. (2013). Discovery of chlamydial peptidoglycan reveals bacteria with murein sacculi but without FtsZ. *Nat. Commun.* 4:2856. doi: 10.1038/ncomms3856

Ranjit, D. K., Liechti, G. W., and Maurelli, A. T. (2020). Chlamydial MreB directs cell division and peptidoglycan synthesis in *Escherichia coli* in the absence of FtsZ activity. *mBio* 11, e03222–e032219. doi: 10.1128/mBio.03222-19

Santarella-Mellwig, R., Pruggnaller, S., Roos, N., Mattaj, I. W., and Devos, D. P. (2013). Three-dimensional reconstruction of bacteria with a complex endomembrane system. *PLoS Biol.* 11:e1001565. doi: 10.1371/journal.pbio.1001565

Shi, H., Westfall, C. S., Kao, J., Odermatt, P. D., Anderson, S. E., Cesar, S., et al. (2021). Starvation induces shrinkage of the bacterial cytoplasm. *Proc. Natl. Acad. Sci. U. S. A.* 118:e2104686118. doi: 10.1073/pnas.2104686118

Singh, R., Liechti, G., Slade, J. A., and Maurelli, A. T. (2020). *Chlamydia trachomatis* oligopeptide transporter performs dual functions of oligopeptide transport and peptidoglycan recycling. *Infect. Immun.* 88, e00086–e000820. doi: 10.1128/IAI.00086-20

Slade, J. A., Brockett, M., Singh, R., Liechti, G. W., and Maurelli, A. T. (2019). Fosmidomycin, an inhibitor of isoprenoid synthesis, induces persistence in *Chlamydia* by inhibiting peptidoglycan assembly. *PLoS Pathog.* 15:e1008078. doi: 10.1371/journal.ppat.1008078

Stephens, R. S., Kalman, S., Lammel, C., Fan, J., Marathe, R., Aravind, L., et al. (1998). Genome sequence of an obligate intracellular pathogen of humans: *Chlamydia trachomatis*. *Science* 282, 754–759. doi: 10.1126/science.282.5389.754

Swanson, J., Eschenbach, D. A., Alexander, E. R., and Holmes, K. K. (1975). Light and electron microscopic study of *Chlamydia trachomatis* infection of the uterine cervix. *J. Infect. Dis.* 131, 678–687. doi: 10.1093/infdis/131.6.678

Taguchi, A., Welsh, M. A., Marmont, L. S., Lee, W., Sjodt, M., Kruse, A. C., et al. (2019). FtsW is a peptidoglycan polymerase that is functional only in complex with its cognate penicillin-binding protein. *Nat. Microbiol.* 4, 587–594. doi: 10.1038/s41564-018-0345-x

Tamura, A., and Manire, G. P. (1967). Preparation and chemical composition of the cell membranes of developmental reticulate forms of meningopneumonitis organisms. *J. Bacteriol.* 94, 1184–1188. doi: 10.1128/jb.94.4.1184-1188.1967

Tanami, Y., and Yamada, Y. (1973). Miniature cell formation in *Chlamydia psittaci*. *J. Bacteriol.* 114, 408–412. doi: 10.1128/jb.114.1.408-412.1973

Vadia, S., Tse, J. L., Lucena, R., Yang, Z., Kellogg, D. R., Wang, J. D., et al. (2017). Fatty acid availability sets cell envelope capacity and dictates microbial cell size. *Curr. Biol.* 27, 1757.e5–1767.e5. doi: 10.1016/j.cub.2017.05.076

Weiss, E. (1950). The effect of antibiotics on agents of the psittacosis-lymphogranuloma group. I. The effect of penicillin. *J. Infect. Dis.* 87, 249–263. doi: 10.1093/infdis/87.3.249

Welter-Stahl, L., Ojcius, D. M., Viala, J., Girardin, S., Liu, W., Delarbre, C., et al. (2006). Stimulation of the cytosolic receptor for peptidoglycan, Nod1, by infection with *Chlamydia trachomatis* or *Chlamydia muridarum*. *Cell. Microbiol.* 8, 1047–1057. doi: 10.1111/j.1462-5822.2006.00686.x

Wolf, K., Fischer, E., and Hackstadt, T. (2000). Ultrastructural analysis of developmental events in *Chlamydia* pneumoniae-infected cells. *Infect. Immun.* 68, 2379–2385. doi: 10.1128/IAI.68.4.2379-2385.2000

Wyrick, P. B. (2010). *Chlamydia trachomatis* persistence *in vitro*: an overview. *J. Infect. Dis.* 201, 88–95. doi: 10.1086/652394

Conflict of Interest: The author declares that the research was conducted in the absence of any commercial or financial relationships that could be construed as a potential conflict of interest.

Publisher's Note: All claims expressed in this article are solely those of the authors and do not necessarily represent those of their affiliated organizations, or those of the publisher, the editors and the reviewers. Any product that may be evaluated in this article, or claim that may be made by its manufacturer, is not guaranteed or endorsed by the publisher.

frontiers | Frontiers in Microbiology

HYPOTHESIS AND THEORY
published: 15 April 2022
doi: 10.3389/fmicb.2022.841171

How Do MinC-D Copolymers Act on Z-Ring Localization Regulation? A New Model of *Bacillus subtilis* Min System

*Na Wang[1], Tingting Zhang[2], Shuheng Du[1], Yao Zhou[1] and Yaodong Chen[1,2]**

[1] Key Laboratory of Resources Biology and Biotechnology in Western China, Ministry of Education, College of Life Sciences, Northwest University, Xi'an, China, [2] Provincial Key Laboratory of Biotechnology of Shaanxi Province, Northwest University, Xi'an, China

Division site selection in rod-shaped bacteria is strictly regulated spatially by the Min system. Although many sophisticated studies, including *in vitro* recombination, have tried to explain these regulations, the precise mechanisms are still unclear. A previous model suggested that the concentration gradient of MinC, an FtsZ inhibitor, regulates the position of the Z-ring in the cell. In *Escherichia coli,* the oscillation of MinCDE proteins leads to a gradient of Min proteins with the average concentration being lowest in the middle and highest near the poles. In contrast to the Min system of *E. coli*, the Min system of *Bacillus subtilis* lacks MinE and exhibits a stable concentration distribution, which is regulated by the binding of DivIVA to the negative curvature membrane. The Min proteins first accumulate at the poles of the cell and relocalize near the division site when the membrane invagination begins. It is inconsistent with the previous model of high concentrations of MinC inhibiting Z-ring formation. Our preliminary data here using electron microscopy and light scattering technology reported that *B. subtilis* MinC (BsMinC) and MinD (BsMinD) also assembled into large straight copolymers in the presence of ATP, similar to the Min proteins of *E. coli*. Their assembly is fast and dominated by MinD concentration. When BsMinD is 5 μM, a clear light scattering signal can be observed even at 0.3 μM BsMinC. Here, we propose a new model based on the MinC-D copolymers. In our hypothesis, it is not the concentration gradient of MinC, but the MinC-D copolymer assembled in the region of high concentration MinD that plays a key role in the regulation of Z-ring positioning. In *B. subtilis,* the regions with high MinD concentration are initially at both ends of the cell and then appear at midcell when cell division began. MinC-D copolymer will polymerize and form a complex with MinJ and DivIVA. These complexes capture FtsZ protofilaments to prevent their diffusion away from the midcell and narrow the Z-ring in the middle of the cell.

Keywords: bacterial cell division, MinC, MinD, MinC-D copolymers, Z-Ring, FtsZ

Abbreviations: EM, electron microscopy; BsMinC, MinC of *Bacillus subtilis*; BsMinD, MinD of *Bacillus subtilis*; PaMinC, MinC of *Pseudomonas aeruginosa*; PaMinD, MinD of *Pseudomonas aeruginosa.*

OPEN ACCESS

Edited by:
Hua Xiang,
Institute of Microbiology (CAS), China

Reviewed by:
Yan Liao,
University of Technology Sydney, Australia
Daniel Haeusser,
Canisius College, United States

***Correspondence:**
Yaodong Chen
ydchen@nwu.edu.cn

Specialty section:
This article was submitted to Microbial Physiology and Metabolism, a section of the journal Frontiers in Microbiology

Received: *22 December 2021*
Accepted: *14 March 2022*
Published: *15 April 2022*

Citation:
Wang N, Zhang T, Du S, Zhou Y and Chen Y (2022) How Do MinC-D Copolymers Act on Z-Ring Localization Regulation? A New Model of Bacillus subtilis Min System. Front. Microbiol. 13:841171. doi: 10.3389/fmicb.2022.841171

INTRODUCTION

Bacterial cell division is initiated by a dynamic Z-ring, which consists of the self-assembled FtsZ protofilaments and dozens of associate proteins (Haeusser and Margolin, 2016; Erickson and Osawa, 2017; McQuillen and Xiao, 2020). FtsZ, a bacterial tubulin homolog, is the key protein for bacterial division. In *Escherichia coli*, FtsZ and its membrane-tethering proteins ZipA and FtsA first form a proto-ring and then act as a scaffold to recruit dozens of downstream proteins to form a mature ring. FtsZ protofilament, as the most basic component of the Z-ring, exhibits very dynamic characteristics *in vitro* and *in vivo* (Stricker et al., 2002; Chen and Erickson, 2005, 2009). Recent studies revealed that FtsZ filaments or bundles exhibited treadmilling dynamics *in vivo*, traveling along the path of the Z-ring, selectively adding FtsZ subunits to one end, and releasing from another end (Bisson-Filho et al., 2017; Yang et al., 2017; Ramirez-Diaz et al., 2018; McCausland et al., 2021).

The bacterial division is strictly regulated spatially and temporally by a variety of regulatory proteins. The dynamic Z-ring in rod-shaped bacteria locates precisely in the center of the cell and is regulated by at least two negative regulation systems: the Min system and nucleoid occlusion (NO) system (Lutkenhaus and Du, 2017; Schumacher, 2017; Szwedziak and Ghosal, 2017). NO system, mediated by Noc in *Bacillus subtilis* or SlmA in *E. coli*, prevents bacteria from dividing over the chromosome. Meanwhile, the Min system prevents Z-ring assembly near the poles.

Current Model Suggests a Concentration Gradient of MinC in the Cell Regulates the Z-Ring Position. High Concentration of MinC Inhibits FtsZ Assembly to Prevent the Assembly of the Z Ring Near the Pole

Min systems are mainly summarized into two different types, MinCDE and MinCDJ, which have been well studied in Gram-negative bacteria *E. coli* and Gram-positive bacteria *B. subtilis*, respectively (Lutkenhaus and Du, 2017; Szwedziak and Ghosal, 2017). In general, the current inhibition model uses the uneven distribution of Min proteins and the inhibitory effect of MinC on FtsZ polymerization to explain why Z-ring is accurately located in the middle of the cell (**Figure 1**). This model is based on two important facts. First, MinD protein is unevenly distributed in cells. Second, MinC directly interacts with FtsZ and inhibits FtsZ polymerization.

Both MinC and MinD are the key proteins and exist in both systems. MinD is an ATPase with a deviant walker A motif (Lutkenhaus and Sundaramoorthy, 2003). ATP-bound MinD tends to form a dimer and prefers to bind to the membrane by its C-terminal amphipathic helices. MinC, as an FtsZ inhibitor, is the main component in the Min system to interact with FtsZ directly. The previous biochemical results showed that MinC inhibited the polymerization of FtsZ, but did not change the GTP hydrolysis activity of FtsZ (Hu et al., 1999). Subsequent results suggest that MinC may only shorten the length of FtsZ protofilaments, but does not affect the amount of FtsZ subunits in the filaments (Dajkovic et al., 2008; Shen and Lutkenhaus, 2010; Hernandez-Rocamora et al., 2013; Huang et al., 2018).

MinC has two distinct domains of similar size. Both domains are necessary for their physiological function to regulate the Z-ring position (Hu and Lutkenhaus, 2000). MinC C-terminal domain (MinCC) leads MinC to form a dimer and binds both MinD and C-terminal of FtsZ. However, MinC N-terminal domain (MinCN) binds to FtsZ and inhibits FtsZ assembly (Hu and Lutkenhaus, 2000; Cordell et al., 2001; Shiomi and Margolin, 2007; Shen and Lutkenhaus, 2009, 2010). It is proposed that MinCC is first connected to the C-tail of FtsZ, and then, MinCN attacks the H10 helix of FtsZ to break the FtsZ protofilament without affecting the GTPase significantly (Shen and Lutkenhaus, 2010).

MinCDE system mainly contains MinC, MinD, and MinE proteins. The previous studies showed that the MinCDE system in *E. coli* displayed an oscillating pattern; the proteins moved quickly from one end of the cell to the other, completing a cycle in ∼50 s (Hu and Lutkenhaus, 1999; Raskin and De Boer, 1999). The oscillation is mainly caused by a feedback loop of the ATPase MinD and its activator MinE (Loose et al., 2008; Park et al., 2011, 2017; Arumugam et al., 2014; Denk et al., 2018). The accumulation of MinE activates the ATPase activity of the MinD bound to the membrane, converting MinD from dimers to monomers and releasing them from the membrane. The oscillation of MinDE proteins leads to a gradient of MinD in the cell, with the average concentration being lowest in the middle of the cell and highest near the poles.

The previous results considered that only MinC of Min system directly interacted with FtsZ and inhibited the Z-ring formation (Hu et al., 1999). As a passenger, MinC combines with MinD and moves with MinD to form a concentration gradient. In the high concentration MinC region, FtsZ polymerization is inhibited, thereby preventing the assembly of Z-ring.

However, MinC is only a weak inhibitor of FtsZ. The previous biochemical results suggested that only a high concentration of MinC could shorten the length of FtsZ protofilaments (Scheffers, 2008; Huang et al., 2018) or reduce the FtsZ bundles (Dajkovic et al., 2008). Moreover, MinC concentration *in vivo* is pretty low. In *E. coli*, the previous reports revealed that the average MinC concentration was around 0.7 μM, which was 6–8 times less than that of FtsZ and MinD (Li et al., 2014; Erickson and Osawa, 2017). So, how does the small amount of MinC *in vivo* effectively regulate the Z-ring position? Although the existing inhibition models emphasize that MinC concentration *in vivo* varies with MinD concentration, it is still difficult to explain why MinC concentration is so low.

MinCDJ system includes at least four proteins, that is, MinC, MinD, MinJ, and DivIVA. In contrast to the oscillating MinCDE system, MinCDJ proteins are considered to exhibit a stationary bipolar gradient pattern, which is regulated by DivIVA (Cha and Stewart, 1997; Edwards and Errington, 1997). DivIVA favors attaching to the negative curvature membrane (Lenarcic et al., 2009) and accumulating at the pole region of the cell at the early stage. After recruiting the transmembrane protein MinJ as a

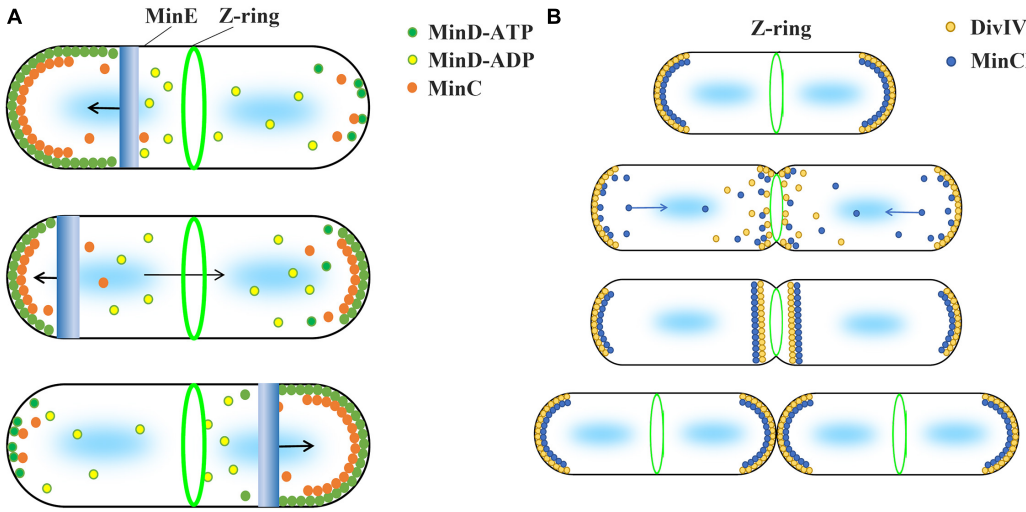

FIGURE 1 | Current model suggests that the concentration gradient of MinC in cell regulates the Z-ring position. The two types of Min system use different strategies to form protein concentration gradients. **(A)** The Min system of Gram-negative bacteria, such as *E. coli* and *P. aeruginosa*, consists of MinC, MinD, and MinE proteins and is known as the MinCDE system. The MinD-ATP dimer (green) preferentially binds to the membrane, while the MinD-ADP subunits (yellow) detach from the membrane. MinE (blue) can stimulate the ATPase activity of MinD and release MinD and MinE from the membrane. This makes MinE drive the oscillation of MinD from one end of the cell to the other, which leads to an apparent concentration gradient of MinD in the cell, with the average concentration being lowest in the middle of the cell and highest near the poles. MinC (orange), as an FtsZ inhibitor, binds to MinD and moves with the movement of MinD. High concentration of MinC inhibits FtsZ polymerization, which is used by current models to explain how the Min system regulates the positioning of Z-ring. **(B)** Gram-positive bacteria, such as *B. subtilis*, contain MinC, MinD, MinJ, and DivIVA proteins known as the MinCDJ system. Min proteins (blue) concentration gradient is regulated by DivIVA (orange), which favors attaching to the negative curvature membrane. When DivIVA is mainly bound at both ends of the cell, MinD exhibits a stationary bipolar gradient pattern. This is easily explained by current models. However, DivIVA proteins will relocalize at midcell as soon as the membrane invagination begins, and MinCDJ proteins localize to division sites and poles at the same time in dividing cells. It cannot be explained by the existing model that high concentration MinC inhibits the assembly of Z-ring. A revised model suggested that MinCDJ moved to the middle of the cell to prevent a new round of division and/or might act on some downstream proteins of Z-ring assembly.

bridge, the DivIVA/MinJ complex binds to MinD to regulate the position of MinD (Marston et al., 1998; Patrick and Kearns, 2008), which forms a rather stable concentration gradient with the highest at the poles and lowest in the middle to allow the Z-ring assembly at midcell. However, further studies discovered that part of the DivIVA protein would relocalize later near the division site as soon as the membrane invagination begins, and MinCDJ proteins preferentially localized to division sites and poles at the same time in dividing cells (Bramkamp et al., 2008; Gregory et al., 2008; van Baarle and Bramkamp, 2010; Eswaramoorthy et al., 2011; Bach et al., 2014). The accumulation of high concentrations of MinC at midcell in *B. subtilis* is still elusive, because it is inconsistent with the current model of high concentration of MinC inhibiting FtsZ assembly. The alternative model suggested that MinCDJ moved to the middle of the cell to prevent a new round of division and/or might act on downstream of Z-ring assembly (Bramkamp and van Baarle, 2009).

In summary, several experimental results contradict the model that high concentration of MinC near the poles inhibits FtsZ polymerization, so that Z-ring cannot assemble outside the middle of the cell. Specifically, in *B. subtilis*, MinC proteins gather not only at both ends of the cell, but also in the middle as soon as the beginning of cell division. The convergence of MinC protein in the middle of the cell is contradictory to the inhibition hypothesis. An alternative model attempts to explain this phenomenon, speculating that MinC might act on other unknown downstream proteins. But this explanation is not satisfactory. Also, the concentration of MinC in *E. coli*, as well as possibly in other bacteria, is much lower than that of FtsZ. It is difficult to explain with the existing assumptions about MinC concentration gradients.

MinC-D Copolymers in the MinCDE Systems Greatly Enhance the Binding Coefficient Between MinC and FtsZ

The formation of MinC-D copolymers can explain directly why MinC concentration is very low. The previous reports revealed that MinC and MinD from *E. coli* and *Pseudomonas aeruginosa* coassembled into long filaments with 1:1 stoichiometry and a $MinC_2$-$MinD_2$-$MinC_2$-$MinD_2$ pattern in the presence of ATP (Ghosal et al., 2014; Conti et al., 2015; Huang et al., 2018). These copolymers' assembly was mainly dominated by the concentration of MinD protein, and if MinD concentration was high enough (>4 μM for *P. aeruginosa*), a very low concentration of MinC could coassemble with MinD to form copolymers (Huang et al., 2018). It is consistent with the protein concentration *in vivo*, in which the MinC concentration is around 0.7 μM, only 1/6 of MinD (Erickson and Osawa, 2017). Due to the multi-sites binding between MinC-D copolymers and FtsZ protofilaments, this greatly enhances the binding coefficient between MinC and FtsZ, which can explain why the low

concentration of MinC *in vivo* can also function on FtsZ (Ghosal et al., 2014; Huang et al., 2018).

MinE not only removed MinD from the membrane but also disassembled MinC-D copolymers (Ghosal et al., 2014; Huang et al., 2018). Due to the rapid MinE oscillation in the cell, MinC and MinD in the MinCDE system may only polymerize into short copolymers *in vivo*. The assembly–disassembly cycle and the movement of the short MinC-D polymers are regulated by MinE and MinD oscillation. Since MinD concentration is 6–8 times higher than that of MinC and MinE disassemble the MinC-D polymer, the copolymerization of MinC-D is likely not to affect the oscillation of MinD. MinC *in vivo* will copolymerize with MinD in the region of high concentration of MinD, which is regulated by MinDE oscillation. MinC-D copolymers capture FtsZ filaments and prevent them from diffusing to the poles of the cell. After that, MinC promotes the depolymerization of FtsZ protofilaments and FtsZ monomers are released for the next round.

Our New Preliminary Results Show That MinC and MinD of *Bacillus subtilis* Can Also Coassemble to Form Similar Copolymers

There is no MinE in the MinCDJ system. MinD sequences among different bacterial species are well-conserved (**Supplementary Figure 1**), but MinC sequences are quite different (**Supplementary Figure 2**). The MinD sequence of *B. subtilis* and *P. aeruginosa* is 44% identical, whereas the MinC sequence is only about 20% identical. It is interesting to study whether or not MinC and MinD of the MinCDJ system can be copolymerized. If MinC-D of *B. subtilis* forms copolymer, they are likely to form large stable structures if BsMinC-D is difficult to depolymerize. During the division of *B. subtilis*, these structures will exist both at the poles and in the middle. To this end, we have purified *B. subtilis* MinC (BsMinC) and MinD (BsMinD) proteins and determined their assembly (the detailed methods are shown in **Supplementary Document**).

We first observed their assembly using the electron microscopy (EM)-negative stain technique. Incubating 8 μM BsMinD and 4 μM BsMinC with 2 mM ATP for 5 min, we observed long and large straight bundles composed of multiple filaments with a width of about 30–100 nm (**Figure 2A**), which were 5–8 times larger than the single- or double-strand MinC-D polymers of *P. aeruginosa* and *E. coli*. Sedimentation and SDS-PAGE analysis showed that the copolymer was composed of MinC and MinD in a ratio of 1:1 (**Figure 2B**). After centrifugation at 50,000 rpm, most copolymers were collected in the pellet. Although there are different initial concentrations of MinC and MinD, the ratio of MinC and MinD in the pellet is always approximately 1:1. As a control, only MinC or MinD alone (**Supplementary Figure 3**) and a mixture of MinC and MinD with ADP (**Figure 2B**) cannot form copolymers.

The electron microscope observation could not be well quantified, we next investigated the assembly properties of BsMinC-D copolymer with different protein concentrations and protein ratios using a light-scattering assay. An important conclusion of our previous studies on *P. aeruginosa* MinC-D assembly is that MinD protein dominated their polymerization, which is consistent with the concentration of these two proteins *in vivo* (Huang et al., 2018). We found similar results of BsMinC-D assembly. **Figure 3** shows the assembly dynamics at different concentrations of BsMinC and BsMinD in the presence of 2 mM ATP. We observed that 5 μM BsMinD gave a detectable light scattering signal even at 0.3 μM BsMinC. Also, the polymerization accelerated when BsMinC concentration increased (**Figure 3A**). Meanwhile, when there was 6 μM BsMinC in the solution, only a slight polymerization would be observed when BsMinD concentration was at 3 μM (**Figure 3B**). It is suggested that BsMinC-D assembly requires a high concentration of BsMinD, and the critical concentration of BsMinD is around 3 μM. If MinD concentration is high enough, a very low concentration of MinC would join in the copolymers. It implies that MinC-D copolymers may be assembled only in the high concentration region of MinD *in vivo*.

The Hypothesis That MinC-D Copolymer Is Involved in Z-Ring Position Regulation

Here, we reported that MinC and MinD of *B. subtilis* could also be copolymerized to form a large straight bundle. The previous reports of the copolymer formation of MinC-D from Gram-negative bacteria *E. coli*, *P. aeruginosa*, and *Aquifexaeolicus* (Ghosal et al., 2014; Huang et al., 2018), together with our results here, suggest that the polymerization of MinC-D copolymers may be widespread in both two types of bacterial Min systems. They have similar properties, and the MinD concentration dominates their polymerization. It suggests that MinC-D copolymers may be assembled only in the high concentration region of MinD *in vivo*.

We summarize two functions of MinC-D copolymers. The first is to increase the binding efficiency of MinC and FtsZ, so it greatly enhances the effect of MinC on FtsZ polymerization. Second, it can capture the diffused FtsZ protofilaments and prevent them from moving to both ends of the cell.

Based on the fact that in *B. subtilis*, MinC is also concentrated near the Z-ring in the middle of the cell, which is inconsistent with the model of MinC inhibiting the polymerization of FtsZ. Therefore, we propose a new model, which emphasizes that the capture of FtsZ protofilaments by MinC-D copolymer is the main regulation mode.

A New Model for Bacterial Division Site Selection by Min System of *Bacillus subtilis*

Here, we purpose a new model to explain the regulation of Z-ring by Min proteins. Compared with the previous model, we believe that MinC forms copolymers with MinD in the area of high concentration of MinD, which prevents the diffusion of FtsZ filaments and accelerates the depolymerization of FtsZ, which is the key to regulation.

Our model also believes that the uneven distribution of MinD is the first step in regulation. MinD gradient is regulated by MinE in the MinCDE system and by DivIVA/MinJ in the MinCDJ system. From our results, both the coassemblies of MinC-D of

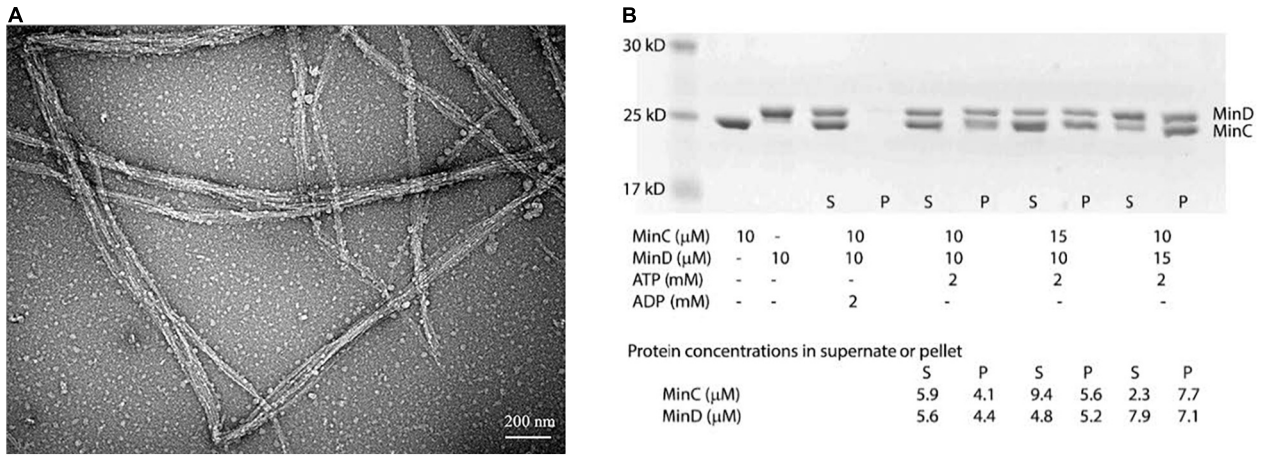

FIGURE 2 | BsMinC and BsMinD coassembled into a long and large bundle in the ratio of 1:1. **(A)** Negative stain EM showed that 8 μM BsMinD and 4 μM BsMinC coassembled into large bundles in the presence of 2 mM ATP. Bar represents 200 nm. **(B)** SDS-PAGE analysis of cosedimentation in different ratios of BsMinC and BsMinD showed that the ratio of BsMinC and BsMinD in the pellet is always approximately 1:1. The initial concentration of the mixture, the estimated MinC and MinD concentrations in the supernatant and pellet are presented at the bottom of the panel. S, supernatant; P, pellet.

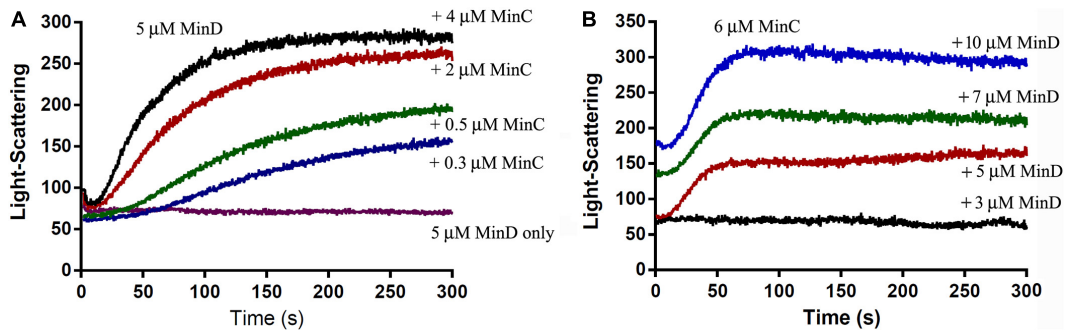

FIGURE 3 | The comparison of the assembly kinetics of BsMinC and BsMinD at different concentrations suggested that BsMinD concentration dominated the coassembly of BsMinC-D. **(A)** Assembly kinetics of 5 μM BsMinD and different concentrations of BsMinC from 0.3 to 4 μM. **(B)** Assembly kinetics of 6 μM BsMinC and different concentrations of BsMinD from 3 to 10 μM. ATP concentration is 2 mM.

P. aeruginosa and *B. subtilis* are dominated by the concentration of MinD protein. It is consistent with the concentration of Min proteins *in vivo* and it is suggested that MinC *in vivo* will coassemble with MinD in the area of high concentration of MinD.

Figure 4 shows our model of the inhibitory mechanism of Min system in *B. subtilis*, based on the role of MinC-D copolymers. Due to the multi-site binding between MinCD copolymer and FtsZ profilament, the binding efficiency of MinC and FtsZ is greatly enhanced, which can capture the diffused FtsZ profilament and strengthen the influence of MinC on FtsZ polymerization. This works on both MinCDE and MinCDJ systems (**Figure 4A**).

Figures 4B,C show the regulation of Z-Ring by *B. subtilis* Min protein. In the early stages of cell division of *B. subtilis*, DivIVA mainly binds to the curved membrane areas at both ends of the cell, and this makes MinD accumulate at the cell poles to form a bipolar gradient. MinC will coassemble with MinD at both ends of the cell, preventing the diffusion of FtsZ from leaving the middle of the cell. When membrane invagination begins, part of DivIVA will relocate to the curved membrane area at midcell next to the Z-ring and cause the DivIVA/MinJ/MinC-D complex to form on both sides of the Z-ring. MinC-D complex prevents FtsZ from diffusing and restricts the Z-ring to a narrow area in the middle. After the MinC-D copolymers and FtsZ protofilaments are tightly bound, MinC accelerates the depolymerization of FtsZ protofilaments. Then, the MinC-D copolymers will release FtsZ monomers and recapture the new diffusing FtsZ protofilaments.

The difference between **Figures 4B,C** is mainly to consider whether MinC/MinD/DivIVA/MinJ will form a stable large complex. Without MinE in the MinCDJ system, it seems that MinC and MinD will assemble into a stable large bundle and form a stable complex with MinJ and DivIVA *in vivo*. Eswaramoorthy et al. (2011) reported that two stable adjacent rings of *B. subtilis* Min proteins were assembled on both sides of the Z-ring during cytokinesis, which is an evidence that they form a stable structure. However, Feddersen et al. (2021) had recently observed using the FRAP technique that Min proteins in *B. subtilis* were also dynamic. It is reported that MinD, located in the middle of the

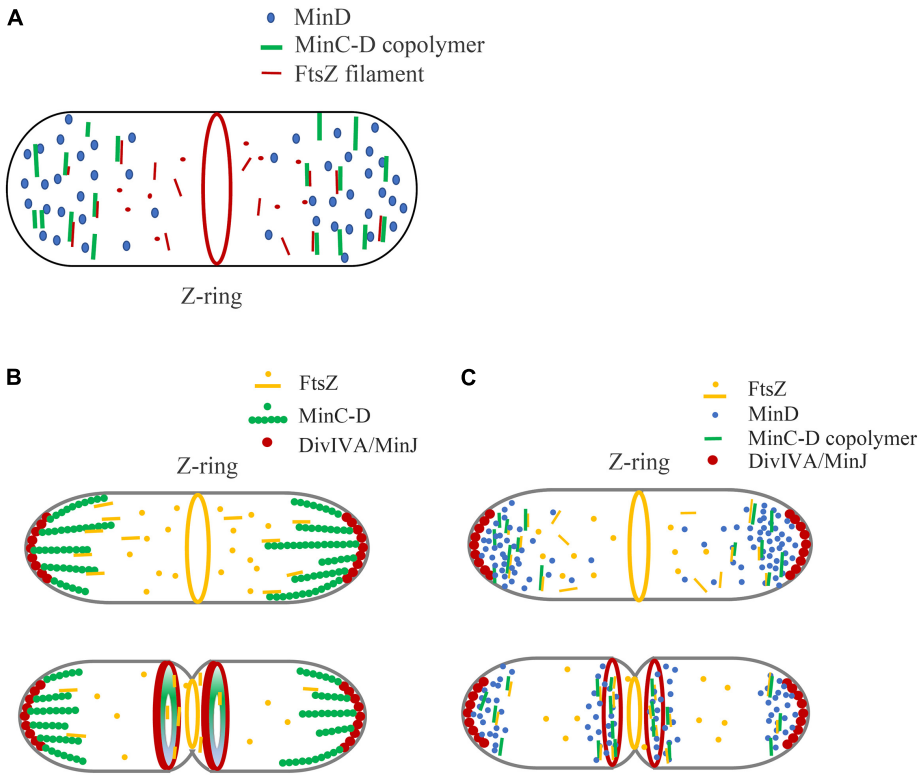

FIGURE 4 | A new model is proposed to explain the regulation of Min system on Z-ring assembly positioning, emphasizing the role of MinC-D copolymer. **(A)** In general, we think that the binding of MinC-D copolymer to FtsZ protofilament is the key to Z-ring localization regulation. MinC will coassemble with MinD in the area of high concentration of MinD. The tight binding between MinC-D copolymers and FtsZ filaments not only greatly enhances the binding coefficient between MinC and FtsZ subunits, but also can capture FtsZ protofilaments, and prevent their diffusion to the ends of the cell. This may occur in both MinCDE and MinCDJ systems. **(B,C)** Show our new model of how Min proteins regulate Z-ring position in *B. subtilis*, if Min proteins form stable structures **(B)** or dynamic structures **(C)**. Whether MinC/MinD/DivIVA/MinJ complex is stable or dynamic *in vivo* is controversial. The location of DivIVA determines the uneven distribution of MinD proteins: at the early stage of division, MinD is only located at both ends of the cell, and when membrane invagination begins, MinD accumulates both at the cell poles and midcell. MinC-D copolymers are formed in the area of high concentration of MinD, and form a relatively stable complex **(B)** or dynamic complex **(C)** with DivIVA and MinJ. If the complex is dynamic, MinC-D copolymers can be released from DivIVA and accumulated near DivIVA/MinJ complex. This protein complex, when located at the ends of the cell, prevents FtsZ from diffusing to the ends of the cell. And when it is in the middle, this complex can further restrict the Z-ring to a narrow area in the middle. After the MinC-D copolymers and FtsZ protofilaments are tightly combined, MinC accelerates the depolymerization of FtsZ protofilaments.

cell, as well as MinJ and DivIVA, also showed high dynamic characteristics. How is the dynamics of Min protein regulated? Is MinC-D complex also dynamic *in vivo*? Does this dynamic help the rapid depolymerization of MinC-D-FtsZ complex to quickly release the bound FtsZ subunits? Is their regulation related to DivIVA and MinJ, or to other unknown proteins? These are problems that need to be addressed.

SUMMARY

In conclusion, we propose a new model of Min protein regulation that emphasizes the role of MinC-D copolymers in this article. In our model, the key point is that we think that it is not the concentration gradient of MinC, but the MinC-D copolymer formed in the region of high concentration MinD that plays a key role in the regulation of Z-ring positioning. In general, the binding of MinC-D copolymer with FtsZ protofilament greatly enhances the binding efficiency of MinC and FtsZ, which not only accelerated the depolymerization of FtsZ but also prevented the diffusion of FtsZ filaments to the cell ends.

In the MinCDE system, our model is not significantly different from the existing models. Since MinC-D copolymer can be depolymerized by MinE protein, and the number of MinD *in vivo* is more than 6 times that of MinC, MinE-driven MinD oscillation may not be affected by the copolymerization of MinC-D. The role of MinC-D copolymer is to greatly increase the binding coefficient of MinC and FtsZ. The regulation of Z-Ring position can be interpreted as MinC inhibits the polymerization of FtsZ, or MinC-D copolymer prevents the diffusion of FtsZ filaments.

However, in the MinCDJ system, the existing inhibition model is inconsistent with the experimental results. MinC and MinD proteins in B. subtilis accumulate at both ends of cells, but also in the middle of cells when cell division begins. Thus, our new model can more directly explain its regulation. The MinC/MinD/DivIVA/MinJ complexes form near the Z-ring, preventing FtsZ from spreading out of the middle of the cell and narrowing the contraction ring.

DATA AVAILABILITY STATEMENT

The original contributions presented in the study are included in the article/**Supplementary Material**, further inquiries can be directed to the corresponding author/s.

AUTHOR CONTRIBUTIONS

NW, TZ, and YC did most of the experimental work and interpretation. SD and YZ contributed experimental work and interpretation. YC conceived the project and wrote the manuscript with contributions from all authors. All authors reviewed the results and approved the final version of the manuscript.

FUNDING

This research was funded by the National Natural Science Foundation of China (grant no. 31970050) to YC and Opening Foundation of Key Laboratory of Resource Biology and Biotechnology in Western China (Northwest University), Ministry of Education (grant no. ZSK2019004) to YC.

SUPPLEMENTARY MATERIAL

The Supplementary Material for this article can be found online at: https://www.frontiersin.org/articles/10.3389/fmicb.2022.841171/full#supplementary-material

REFERENCES

Arumugam, S., Petrasek, Z., and Schwille, P. (2014). MinCDE exploits the dynamic nature of FtsZ filaments for its spatial regulation. *Proc. Natl. Acad. Sci. U.S.A.* 111, E1192–E1200. doi: 10.1073/pnas.1317764111

Bach, J. N., Albrecht, N., and Bramkamp, M. (2014). Imaging DivIVA dynamics using photo-convertible and activatable fluorophores in Bacillus subtilis. *Front. Microbiol.* 5:59. doi: 10.3389/fmicb.2014.00059

Bisson-Filho, A. W., Hsu, Y. P., Squyres, G. R., Kuru, E., Wu, F., Jukes, C., et al. (2017). Treadmilling by FtsZ filaments drives peptidoglycan synthesis and bacterial cell division. *Science* 355, 739–743. doi: 10.1126/science.aak9973

Bramkamp, M., Emmins, R., Weston, L., Donovan, C., Daniel, R. A., and Errington, J. (2008). A novel component of the division-site selection system of Bacillus subtilis and a new mode of action for the division inhibitor MinCD. *Mol. Microbiol.* 70, 1556–1569. doi: 10.1111/j.1365-2958.2008.06501.x

Bramkamp, M., and van Baarle, S. (2009). Division site selection in rod-shaped bacteria. *Curr. Opin. Microbiol.* 12, 683–688. doi: 10.1016/j.mib.2009.10.002

Cha, J. H., and Stewart, G. C. (1997). The divIVA minicell locus of Bacillus subtilis. *J. Bacteriol.* 179, 1671–1683. doi: 10.1128/jb.179.5.1671-1683.1997

Chen, Y., and Erickson, H. P. (2005). Rapid *in vitro* assembly dynamics and subunit turnover of FtsZ demonstrated by fluorescence resonance energy transfer. *J. Biol. Chem.* 280, 22549–22554. doi: 10.1074/jbc.M500895200

Chen, Y., and Erickson, H. P. (2009). FtsZ filament dynamics at steady state: subunit exchange with and without nucleotide hydrolysis. *Biochemistry* 48, 6664–6673. doi: 10.1021/bi8022653

Conti, J., Viola, M. G., and Camberg, J. L. (2015). The bacterial cell division regulators MinD and MinC form polymers in the presence of nucleotide. *FEBS Lett.* 589, 201–206. doi: 10.1016/j.febslet.2014.11.047

Cordell, S. C., Anderson, R. E., and Löwe, J. (2001). Crystal structure of the bacterial cell division inhibitor MinC. *EMBO J.* 20, 2454–2461. doi: 10.1093/emboj/20.10.2454

Dajkovic, A., Lan, G., Sun, S. X., Wirtz, D., and Lutkenhaus, J. (2008). MinC spatially controls bacterial cytokinesis by antagonizing the scaffolding function of FtsZ. *Curr. Biol.* 18, 235–244. doi: 10.1016/j.cub.2008.01.042

Denk, J., Kretschmer, S., Halatek, J., Hartl, C., Schwille, P., and Frey, E. (2018). MinE conformational switching confers robustness on self-organized Min protein patterns. *Proc. Natl. Acad. Sci. U.S.A.* 115, 4553–4558. doi: 10.1073/pnas.1719801115

Edwards, D. H., and Errington, J. (1997). The Bacillus subtilis DivIVA protein targets to the division septum and controls the site specificity of cell division. *Mol. Microbiol.* 24, 905–915. doi: 10.1046/j.1365-2958.1997.3811764.x

Erickson, H. P., and Osawa, M. (2017). FtsZ constriction force - curved protofilaments bending membranes. *Subcell. Biochem.* 84, 139–160. doi: 10.1007/978-3-319-53047-5_5

Eswaramoorthy, P., Erb, M. L., Gregory, J. A., Silverman, J., Pogliano, K., Pogliano, J., et al. (2011). Cellular architecture mediates DivIVA ultrastructure and regulates min activity in Bacillus subtilis. *mBio* 2:e00257-11. doi: 10.1128/mBio.00257-11

Feddersen, H., Wurthner, L., Frey, E., and Bramkamp, M. (2021). Dynamics of the bacillus subtilis min system. *mBio* 12:e00296-21. doi: 10.1128/mBio.00296-21

Ghosal, D., Trambaiolo, D., Amos, L. A., and Lowe, J. (2014). MinCD cell division proteins form alternating copolymeric cytomotive filaments. *Nat. Commun.* 5:5341. doi: 10.1038/ncomms6341

Gregory, J. A., Becker, E. C., and Pogliano, K. (2008). Bacillus subtilis MinC destabilizes FtsZ-rings at new cell poles and contributes to the timing of cell division. *Genes Dev.* 22, 3475–3488. doi: 10.1101/gad.1732408

Haeusser, D. P., and Margolin, W. (2016). Splitsville: structural and functional insights into the dynamic bacterial Z ring. *Nat. Rev. Microbiol.* 14, 305–319. doi: 10.1038/nrmicro.2016.26

Hernandez-Rocamora, V. M., Garcia-Montanes, C., Reija, B., Monterroso, B., Margolin, W., Alfonso, C., et al. (2013). MinC protein shortens FtsZ protofilaments by preferentially interacting with GDP-bound subunits. *J. Biol. Chem.* 288, 24625–24635. doi: 10.1074/jbc.M113.483222

Hu, Z., and Lutkenhaus, J. (1999). Topological regulation of cell division in *Escherichia coli* involves rapid pole to pole oscillation of the division inhibitor MinC under the control of MinD and MinE. *Mol. Microbiol.* 34, 82–90. doi: 10.1046/j.1365-2958.1999.01575.x

Hu, Z., Mukherjee, A., Pichoff, S., and Lutkenhaus, J. (1999). The MinC component of the division site selection system in *Escherichia coli* interacts with FtsZ to prevent polymerization. *Proc. Natl. Acad. Sci. U.S.A.* 96, 14819–14824. doi: 10.1073/pnas.96.26.14819

Hu, Z. L., and Lutkenhaus, J. (2000). Analysis of MinC reveals two independent domains involved in interaction with MinD and FtsZ. *J. Bacteriol.* 182, 3965–3971. doi: 10.1128/JB.182.14.3965-3971.2000

Huang, H., Wang, P., Bian, L., Osawa, M., Erickson, H. P., and Chen, Y. (2018). The cell division protein MinD from *Pseudomonas aeruginosa* dominates the assembly of the MinC-MinD copolymers. *J. Biol. Chem.* 293, 7786–7795. doi: 10.1074/jbc.RA117.001513

Lenarcic, R., Halbedel, S., Visser, L., Shaw, M., Wu, L. J., Errington, J., et al. (2009). Localisation of DivIVA by targeting to negatively curved membranes. *EMBO J.* 28, 2272–2282. doi: 10.1038/emboj.2009.129

Li, G. W., Burkhardt, D., Gross, C., and Weissman, J. S. (2014). Quantifying absolute protein synthesis rates reveals principles underlying allocation of cellular resources. *Cell* 157, 624–635. doi: 10.1016/j.cell.2014.02.033

Loose, M., Fischer-Friedrich, E., Ries, J., Kruse, K., and Schwille, P. (2008). Spatial regulators for bacterial cell division self-organize into surface waves *in vitro*. *Science* 320, 789–792. doi: 10.1126/science.1154413

Lutkenhaus, J., and Du, S. (2017). E. coli cell cycle machinery. *Subcell. Biochem.* 84, 27–65. doi: 10.1007/978-3-319-53047-5_2

Lutkenhaus, J., and Sundaramoorthy, M. (2003). MinD and role of the deviant Walker A motif, dimerization and membrane binding in oscillation. *Mol. Microbiol.* 48, 295–303. doi: 10.1046/j.1365-2958.2003.03427.x

Marston, A. L., Thomaides, H. B., Edwards, D. H., Sharpe, M. E., and Errington, J. (1998). Polar localization of the MinD protein of Bacillus subtilis and its role in selection of the mid-cell division site. *Genes Dev.* 12, 3419–3430. doi: 10.1101/gad.12.21.3419

McCausland, J. W., Yang, X., Squyres, G. R., Lyu, Z., Bruce, K. E., Lamanna, M. M., et al. (2021). Treadmilling FtsZ polymers drive the directional movement of sPG-synthesis enzymes via a Brownian ratchet mechanism. *Nat. Commun.* 12:609. doi: 10.1038/s41467-020-20873-y

McQuillen, R., and Xiao, J. (2020). Insights into the structure, function, and dynamics of the bacterial cytokinetic FtsZ-ring. *Annu. Rev. Biophys.* 49, 309–341. doi: 10.1146/annurev-biophys-121219-081703

Park, K. T., Villar, M. T., Artigues, A., and Lutkenhaus, J. (2017). MinE conformational dynamics regulate membrane binding, MinD interaction, and Min oscillation. *Proc. Natl. Acad. Sci. U.S.A.* 114, 7497–7504. doi: 10.1073/pnas.1707385114

Park, K. T., Wu, W., Battaile, K. P., Lovell, S., Holyoak, T., and Lutkenhaus, J. (2011). The Min oscillator uses MinD-dependent conformational changes in MinE to spatially regulate cytokinesis. *Cell* 146, 396–407. doi: 10.1016/j.cell.2011.06.042

Patrick, J. E., and Kearns, D. B. (2008). MinJ (YvjD) is a topological determinant of cell division in Bacillus subtilis. *Mol. Microbiol.* 70, 1166–1179. doi: 10.1111/j.1365-2958.2008.06469.x

Ramirez-Diaz, D. A., Garcia-Soriano, D. A., Raso, A., Mucksch, J., Feingold, M., Rivas, G., et al. (2018). Treadmilling analysis reveals new insights into dynamic FtsZ ring architecture. *PLoS Biol.* 16:e2004845. doi: 10.1371/journal.pbio.2004845

Raskin, D. M., and De Boer, P. A. J. (1999). Rapid pole-to-pole oscillation of a protein required for directing division to the middle of *Escherichia coli*. *Proc. Natl. Acad. Sci. U.S.A.* 96, 4971–4976. doi: 10.1073/pnas.96.9.4971

Scheffers, D. J. (2008). The effect of MinC on FtsZ polymerization is pH dependent and can be counteracted by ZapA. *FEBS Lett.* 582, 2601–2608. doi: 10.1016/j.febslet.2008.06.038

Schumacher, M. A. (2017). Bacterial nucleoid occlusion: multiple mechanisms for preventing chromosome bisection during cell division. *Subcell. Biochem.* 84, 267–298. doi: 10.1007/978-3-319-53047-5_9

Shen, B., and Lutkenhaus, J. (2009). The conserved C-terminal tail of FtsZ is required for the septal localization and division inhibitory activity of MinC(C)/MinD. *Mol. Microbiol.* 72, 410–424. doi: 10.1111/j.1365-2958.2009.06651.x

Shen, B., and Lutkenhaus, J. (2010). Examination of the interaction between FtsZ and MinC in E. coli suggests how MinC disrupts Z rings. *Mol Microbiol.* 75, 1285–1298. doi: 10.1111/j.1365-2958.2010.07055.x

Shiomi, D., and Margolin, W. (2007). The C-terminal domain of MinC inhibits assembly of the Z ring in *Escherichia coli*. *J. Bacteriol.* 189, 236–243. doi: 10.1128/JB.00666-06

Stricker, J., Maddox, P., Salmon, E. D., and Erickson, H. P. (2002). Rapid assembly dynamics of the *Escherichia coli* FtsZ-ring demonstrated by fluorescence recovery after photobleaching. *Proc. Natl. Acad. Sci. U.S.A.* 99, 3171–3175. doi: 10.1073/pnas.052595099

Szwedziak, P., and Ghosal, D. (2017). FtsZ-ring architecture and its control by MinCD. *Subcell. Biochem.* 84, 213–244. doi: 10.1007/978-3-319-53047-5_7

van Baarle, S., and Bramkamp, M. (2010). The MinCDJ system in Bacillus subtilis prevents minicell formation by promoting divisome disassembly. *PLoS One* 5:e9850. doi: 10.1371/journal.pone.0009850

Yang, X., Lyu, Z., Miguel, A., McQuillen, R., Huang, K. C., and Xiao, J. (2017). GTPase activity-coupled treadmilling of the bacterial tubulin FtsZ organizes septal cell wall synthesis. *Science* 355, 744–747. doi: 10.1126/science.aak9995

Conflict of Interest: The authors declare that the research was conducted in the absence of any commercial or financial relationships that could be construed as a potential conflict of interest.

Publisher's Note: All claims expressed in this article are solely those of the authors and do not necessarily represent those of their affiliated organizations, or those of the publisher, the editors and the reviewers. Any product that may be evaluated in this article, or claim that may be made by its manufacturer, is not guaranteed or endorsed by the publisher.

frontiers | Frontiers in Microbiology

MINI REVIEW
published: 03 May 2022
doi: 10.3389/fmicb.2022.757711

How Does the Spatial Confinement of FtsZ to a Membrane Surface Affect Its Polymerization Properties and Function?

*Marisela Vélez**

Instituto de Catálisis y Petroleoquímica, Consejo Superior de Investigaciones Científicas, Madrid, Spain

FtsZ is the cytoskeletal protein that organizes the formation of the septal ring and orchestrates bacterial cell division. Its association to the membrane is essential for its function. In this mini-review I will address the question of how this association can interfere with the structure and dynamic properties of the filaments and argue that its dynamics could also remodel the underlying lipid membrane through its activity. Thus, lipid rearrangement might need to be considered when trying to understand FtsZ's function. This new element could help understand how FtsZ assembly coordinates positioning and recruitment of the proteins forming the septal ring inside the cell with the activity of the machinery involved in peptidoglycan synthesis located in the periplasmic space.

Keywords: bacterial division, bacterial cytoskeletal proteins, FtsZ, lipid membrane, polymerization

OPEN ACCESS

Edited by:
Cara C. Boutte,
University of Texas at Arlington,
United States

Reviewed by:
Ramanujam Srinivasan,
National Institute of Science Education and Research (NISER), India
Peter Sass,
University of Tübingen, Germany

***Correspondence:**
Marisela Vélez
marisela.velez@icp.csic.es

Specialty section:
This article was submitted to Microbial Physiology and Metabolism, a section of the journal Frontiers in Microbiology

Received: *12 August 2021*
Accepted: *27 January 2022*
Published: *03 May 2022*

Citation:
Vélez M (2022) How Does the Spatial Confinement of FtsZ to a Membrane Surface Affect Its Polymerization Properties and Function? Front. Microbiol. 13:757711. doi: 10.3389/fmicb.2022.757711

INTRODUCTION

Bacterial division requires a profound morphological change in the cell. It involves the concerted action in space and time of different cellular elements: chromosomes divide and distribute between the new cells as proteins forming the divisome localize in the center and promote active membrane deformation and peptidoglycan synthesis required to separate the cell into two new ones (Mahone and Goley, 2020).

The study of this fascinating field is considered to have started with the first description of the FtsZ ring in 1991 made by Bi and Lutkenhaus (1991). Since then, we have gained huge insight into how this complex process takes place. A combination of genetic and biochemical studies *in vitro* and *in vivo* have provided knowledge of the essential proteins participating and how they interact and assemble. There are several reviews summarizing our current knowledge of the formation of the septal ring (Adams and Errington, 2009; Mingorance et al., 2010; Den Blaauwen and Luirink, 2019; Du and Lutkenhaus, 2019; Mahone and Goley, 2020; McQuillen and Xiao, 2020; Barrows and Goley, 2021). Advances in single molecule fluorescence, applied both to reconstituted systems (Caldas et al., 2019; García-Soriano et al., 2020) and to whole cells (McCausland et al., 2021; Squyres et al., 2021; Yang et al., 2021), have allowed a more detailed analysis of the structural rearrangements occurring during this active energy-consuming process. These studies have revealed a highly dynamic and concerted interaction between septal ring and peptidoglycan synthesis proteins (Bisson-Filho et al., 2017; Yang et al., 2017; McCausland et al., 2021; Squyres et al., 2021).

FtsZ is the cytoskeletal protein that organizes the formation of the septal ring and orchestrates the division process (Margolin, 2005; Huang et al., 2013; Ortiz et al., 2015; Barrows and Goley, 2021). Since its first description (Dai and Lutkenhaus, 1991; Pla et al., 1991; de Boer et al., 1992; RayChaudhuri and Park, 1992), much work has focused in understanding how it behaves *in vitro* and how it interacts with other proteins. We know that membrane association is essential for its function and that, even when attached through an inserted transmembrane region, in the absence of any of the proteins present *in vivo*, it displays a dynamic rich behavior and deforms membranes (Osawa et al., 2009; Caldas et al., 2019; Ramirez-Diaz et al., 2021).

We have identified a large catalog of proteins participating in the formation of the septal ring, but we still have very few cues about how they communicate to coordinate cell division. Information is transferred between proteins located inside the membrane, that actively condense to form the septal ring, and proteins whose function involves communication and transfer of material across the membrane. Peptidoglycan building blocks are exported to the periplasmic space for the peptidoglycan synthetic machinery to work (Ruiz, 2016). Direct protein-protein interactions are frequently evoked as the main element guiding the concerted process, but it is difficult to imagine that the fluid membrane that hosts many of the proteins involved plays no role, as is frequently depicted in illustrations.

Membranes are not passive elements (Kalappurakkal et al., 2020), particularly when associated to active cytoskeletal proteins that form polymeric filamentous structures that reorganize by dissipating energy consumed from ATP or GTP hydrolysis (Litschel et al., 2021). The long-range order of cytoskeletal filaments is ideal for building sufficiently large structures responsive to multiple inputs that can generate mechanical forces. It is therefore not surprising that several bacterial cytoskeletal proteins play essential roles in cell division (Shih and Rothfield, 2006; Cabeen and Jacobs-Wagner, 2010; Ingerson-Mahar and Gitai, 2012; Pilhofer and Jensen, 2013; Busiek and Margolin, 2015; Siliakus et al., 2017). Some are involved in DNA segregation, ParM for example, and others, such as eukaryotic actin and tubulin homologues MreB, FtsA, and FtsZ, are associated to the membrane and play a major role in maintaining cell shape and remodeling the membrane.

Studies in eukaryotes have shown that active cytoskeletal proteins regulate lipid and protein distribution and membrane mechanical properties, originating non-equilibrium distributions and emerging properties (Gowrishankar et al., 2012; Longo, 2018; Steinkühler et al., 2019; Shaw et al., 2020). The actin cortex may influence plasma membrane organization either by direct interaction with lipids and proteins or through the flow of actin filaments generated by myosin-induced stresses. This activity can also drive actin-associated membrane components out of equilibrium inducing active processes such as persistent advection, clustering, and anomalous density fluctuations, even though measurable hydrodynamic flows in the plasma membrane of unconnected components are not present. The remodeling of the actomyosin layer also affects phase-segregation in the membrane bilayer. It has been experimentally shown that actin activity changes the size and dynamics of the formed domains and that, in addition, membrane domains influence the actin organization (Köster et al., 2016). Lipid domains, referred to as rafts, play an important role in regulating functions such as membrane trafficking (Redpath et al., 2020) and response of membrane receptors (Gowrishankar et al., 2012). Other membrane associated GTP self-aggregating proteins such as dynamins (Kalia and Frost, 2019) and septins (Lam and Calvo, 2019), also reshape the lipid membrane in eukaryotic cells by undergoing GTP-induced conformational changes, although the details of how this happens are still to be elucidated (Pannuzzo et al., 2018). Thus, the current picture of a cell membrane, based on experiments mostly carried out in eukaryotes, is that of a composite material in which lipids and proteins interact to transfer information across membrane components (Sezgin et al., 2017).

In this minireview I will focus on FtsZ polymerization on membranes, but I will first briefly update what we know about bacterial membranes to highlight the evidence that indicates that we should extrapolate what we have learned about cytoskeletal membrane associated proteins in eukaryotes to better understand what is happening in the bacterial membrane during cell division.

To what extent is the presence of the membrane surface and the confinement it imposes to the FtsZ filaments relevant to reveal the rich dynamic behavior observed? Can we also expect bacterial membranes to be responsive to the activity of membrane associated cytoskeletal proteins, as has been shown for eukaryotic cytoskeleton? Could protein modulated membrane properties participate in coordinating the complex interactions acting on the cell division machinery? These are the questions I will address. First, I will briefly summarize advances in our understanding of bacterial membrane organization. I will then briefly review what we know about the active and dynamic FtsZ filaments and their interaction with the membrane. In the discussion I will argue that it might be interesting to attend the role the lipid membrane could play in regulating the process in order to fully understand how bacterial cell division occurs.

THE BACTERIAL MEMBRANE

Bacterial membranes have been less subject to biophysical studies than eukaryotic membranes. Their small size and the complexity rendered by the presence of a peptidoglycan layer make their characterization difficult. However, spatial and temporal reorganization of lipids and proteins on bacterial surfaces take place during complex functions, just as happens in eukaryotes. High resolution optical fluorescence microscopy has confirmed that their inner membrane shares the lateral heterogeneity and complexity found in eukaryotic cells (Dempwolff et al., 2016; Raghunathan and Kenworthy, 2018). Domains and lipid rafts in bacterial membranes are highly organized with specific lipids and associated proteins forming specialized subcellular compartments. They have been referred to as functional membrane microdomains (FMM) to differentiate them from the eukaryotic lipids rafts containing cholesterol, not present in bacteria. The lateral segregation has been observed to be associated to the presence of anionic lipids, squalene,

phosphatidyl-ethanolamine, and proteins such as flotillins (Nishibori et al., 2005; Mileykovskaya and Dowhan, 2009; Bramkamp and Lopez, 2015; Lin and Weibel, 2016; Strahl and Errington, 2017; Yokoyama and Matsui, 2020).

Membrane structure and dynamics are interdependent. Structural heterogeneity has consequences in the heterogeneous dynamics of proteins on the membrane (Nenninger et al., 2014; Adhyapak et al., 2020; Pluhackova and Horner, 2021). Therefore, membrane composition also plays a regulatory role in cell physiology. Stress is known to trigger metabolic pathways that sense threats and mount a protective response involving modification of cell wall composition through the regulation of biosynthetic pathways of their components (Rowlett et al., 2017; Willdigg and Helmann, 2021). There is evidence that certain lipids are enriched in the division site (Mileykovskaya and Dowhan, 2005), indicating that the division process is no exception.

In summary, experimental results indicate that non-random distribution of proteins and lipids also play an important role in protein-protein interactions in bacteria (Raghunathan and Kenworthy, 2018; Zeno et al., 2020), as is well established for eukaryotic membranes.

FtsZ

Conformation and Dynamics in Solution

FtsZ is a soluble 40.3 kDa protein that binds and hydrolyzes GTP and shows a striking structural similarity to tubulins (Erickson, 1997). Its crystal structure was determined in 1998 (Löwe and Amos, 1998) and since then, much biochemical work on the isolated protein in solution has described its polymerization properties. Lateral interactions between individual filaments participate in bundling (Hörger et al., 2008a; Milam et al., 2012), affect their arrangement on surfaces (Márquez et al., 2017) and are strongly modulated by the presence of different ions or crowding agents (Erickson et al., 1996; Popp et al., 2009; **Figure 1**). The presence of curvature in the filaments has been controversial. In analogy to tubulin, it was first considered that the presence of GDP induced the curved conformation whereas the GTP loaded monomers formed straight filaments (Lu et al., 2000; Hsin et al., 2012). However, crystal structures of monomers containing GDP and GTP were not able to confirm this association of the nucleotide phosphorylation state with the degree of curvature (Oliva et al., 2004), and conditions in which the monomers contained essentially phosphorylated nucleotide were observed to be highly curved (Mateos-Gil et al., 2012b; Loose and Mitchison, 2013; Ramirez-Diaz García-Soriano et al., 2018). More recent structural characterizations, coming both from structural and molecular dynamics simulations, have depicted highly flexible monomer in which the relative orientation of the C-terminal and N-terminal domains, linked through a helix 7, can change up to nearly 30 degrees (Martín-Galiano et al., 2010; Matsui et al., 2012; Fujita et al., 2017; Wagstaff et al., 2017). Two monomer conformations have been described, open and close, also referred to as relaxed and tense, that appear to be associated to whether the monomer is isolated or polymerized (Schumacher et al., 2020; **Figure 1**). Molecular dynamics simulations have also revealed the presence of a significant angle between monomers that confers a twist to the filaments (Hsin et al., 2012; Gonzalez de Prado Salas et al., 2014; Lv et al., 2021). Experimental observations have confirmed that filaments on surfaces indeed manifest this twist (Arumugam et al., 2012; Gonzalez de Prado Salas et al., 2014; Ramirez-Diaz et al., 2021).

Early studies showed that FtsZ polymers are dynamic, both *in vivo* and *in vitro* (Stricker et al., 2002; Chen and Erickson, 2005, 2009; Chen et al., 2005), where filaments studied in solution revealed instability due to continuous monomer exchange associated to GTP hydrolysis (Romberg and Levin, 2003). Concentration dependent cooperative polymerization was detected quite early and opened questions regarding how individual filaments, the structures mainly observed at the time, could account for cooperativity, more compatible with the existence of double filaments (Chen et al., 2005; Erickson, 2017). Later cooperativity was attributed to a conformational switch (Huecas and Andreu, 2003) in the monomer that facilitates polymerization, in line with the increasing evidence that monomers are flexible (Martín-Galiano et al., 2010).

All together, the picture that emerged from biochemical and structural studies of filaments forming in solution was of soft, flexible, and polymorphic assemblies that can adopt a large range of shapes easily malleable through environmental conditions (**Figure 1**). A yet open challenge is to understand how such dynamic structures are responsible for coordinating and maintaining the formation of the septal ring when associated to the membrane.

Surface Confined Polymer Structure and Dynamics

The dynamic behavior of FtsZ showed unexpected complexity when filaments were observed associated to a surface. Although some biochemical studies in solution gave hints that polymer growth could be directional (Osawa and Erickson, 2005; Redick et al., 2005), it was not until single molecule fluorescence allowed visualizing polymers associated to membranes, both *in vivo* and *in vitro*, that dynamics of FtsZ filaments was clearly observed. Several groups confirmed that inside the cell FtsZ moves along the cell circumference in a treadmilling fashion along the cell-wall remodeling machinery (Bisson-Filho et al., 2017; Yang et al., 2017; Perez et al., 2019). Studies *in vitro*, also showed that FtsZ filaments on supported membranes manifested unexpected cooperative behavior based on treadmilling (Loose and Mitchison, 2013), forming vortices moving in opposite directions depending on the orientation of the monomers on the surface (Ramirez-Diaz García-Soriano et al., 2018). This behavior does not require any additional proteins, only a chimeric FtsZ containing a fluorescent protein and a membrane targeting sequence (MTS) incorporated at one end to allow for membrane attachment (Ramirez-Diaz García-Soriano et al., 2018; **Figure 1**). Addition of filament binding proteins such as ZapA modulate precision and robustness of the collective behavior (Caldas et al., 2019), but not the essential traits,

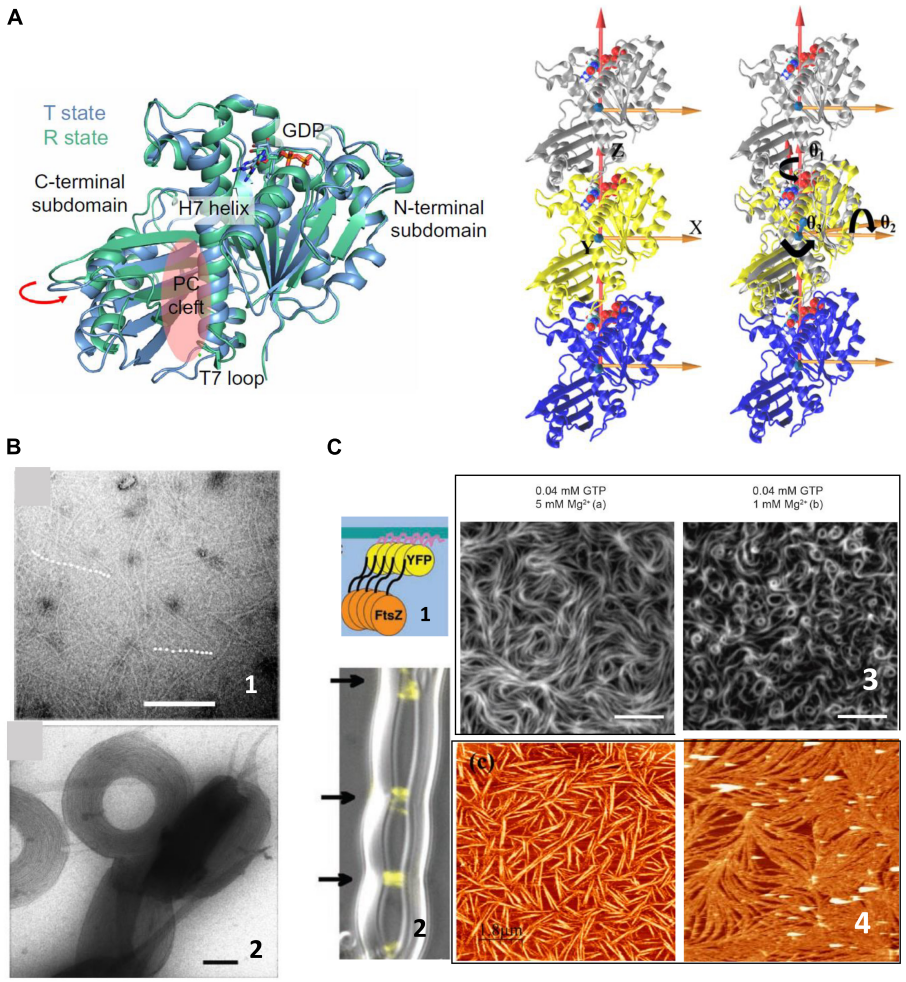

FIGURE 1 | FtsZ structure and polymerization in solution. **(A)** Left shows the two crystal structures of FtsZ from Staphylococcus aureus corresponding to the T and R state conformations in the same crystal, indicating the structural equilibrium of the two states (adapted from Fujita et al., 2017). The trimers on the right show the definitions of bending and twisting angles obtained from molecular dynamics simulations. The left trimer shows the coordinate system and the one on the right shows the bending angles, θ_1 (rotations around the Z axis), θ_2 (rotations around the X axis), and θ_3 (rotations around the Y axis), tracked by calculating the rotations of the top (silver) subunit to align the initial reference frame of the middle subunit (adapted from Lv et al., 2021). **(B)** Shows representative negative stained TEM images of FtsZ filaments in solution (1) and aggregates formed in the presence of crowding agents (2). Scale bar is 100 nm (adapted from Popp et al., 2009). **(C)** Shows surface confined FtsZ polymers. (1) Show a chimeric FtsZ containing a fluorescent protein and a membrane targeting sequence (MTS) on liposomes (2) (adapted from Osawa et al., 2008) and on planar supported membranes (3) (adapted from Ramirez-Diaz García-Soriano et al., 2018). Scale bars are 5 μm. (4) Shows Atomic Force Microscopy images of FtsZ filaments attached covalently to a lipid membrane (left) (adapted from Encinar et al., 2013) or bound through the protein ZipA (right) (adapted from Mateos-Gil et al., 2012a). Scale bars are 2 μm.

suggesting that FtsZ itself contains the required information to treadmill and rearrange on surfaces.

Experiments have shown that surface attachment regulates filament dynamics, as had been previously predicted from theoretical models (Mateos-Gil et al., 2019). Removing the C-terminal flexible linker abolishes treadmilling (García-Soriano et al., 2020). Filaments bind to several membrane associated regulatory proteins, such as FtsA, ZipA, or MinC, through the C-terminal constant region located at the end of a non-structured C-terminal linker (Buske and Levin, 2013; Gardner et al., 2013). This disordered region can vary in length between species but is required for proper cell division (Ohashi et al., 2002; Buske et al., 2015; Cohan et al., 2020). One interpretation is that regulating the distance and attachment strength through a flexible spacer is important for modulating the dynamic assembly. In some organisms, FtsZ binds to the membrane through ZipA, which provides an additional non-structured region that sits between the FtsZ monomer and the surface (Ohashi et al., 2002; Mateos-Gil et al., 2016). We can only speculate about why these flexible spacers and distance from the membrane are important for FtsZ function. We do not know if they affect the monomer conformational switch that has been proposed to regulate polymer dynamics. Another possibility is that attachment strength modulates filament twist and thus filament mechanical properties, as has been suggested by theory (Gonzalez de Prado Salas et al., 2014; Mateos-Gil et al., 2019).

Modulating the compactness of this variable region through the binding of regulatory proteins could be a way to affect filament dynamics and structure. Filaments grow from both ends, without treadmilling (Márquez et al., 2019), when they are firmly attached to a membrane with a defined orientation, confirming that surface attachment and orientation have a strong impact on their structure and dynamics on membranes.

Surface confinement and lipid type modulate both filament dynamics and shape (Mateos-Gil et al., 2012a; Encinar et al., 2013). Filament's preferential curvature, lateral interactions and twist (Hörger et al., 2008a,b; Paez A. et al., 2009; Paez P. et al., 2009; Mateos-Gil et al., 2019; Márquez et al., 2019) are revealed differently in solution and under confinement on a two dimensional surface. Theoretical models that include flexible monomer attachment and torsion provide testable hypothesis indicating that only these two elements are enough to induce an asymmetry in the filament ends accessibility to monomer addition that would generate different growth speed on each end, which manifests as treadmilling (Mateos-Gil et al., 2019). Asymmetric confinement to a surface is also likely to regulate the conformation of the flexible monomers and thus polymer dynamics.

Effect of the FtsZ Polymers Activity on the Lipid Membrane

Filaments on the surface play a GTP-dependent active role on membrane deformation, in spite of their continuous monomer exchange. The debate of whether the force needed to constrict the membrane during cell division comes exclusively from FtsZ filaments or from the peptidoglycan synthetic machinery is still open, although there is no question that at least some membrane deformation is provided by the protein activity (Xiao and Goley, 2016). Filaments create concave or convex deformations or inwards cone structures emerging from the membrane surface (Xiao and Goley, 2016), depending on whether they interact through the N-terminal or the C-terminal end of the protein, indicating drilling-like inward forces (Osawa et al., 2008, 2009). One available hypothesis to explain how flexible, dynamic filaments deform the membrane (Xiao and Goley, 2016) is that torsion provides partly the flexibility found in solution or on surfaces where the attachment is loose. Tight anchoring could stiffen the filaments (Gonzalez de Prado Salas et al., 2014), allowing them to readily deform the membrane and exert force (Mateos-Gil et al., 2019).

One question that is seldom addressed is how the activity of the filaments and the monomer exchange due to GTP hydrolysis affects the structure and integrity of the membrane. FtsZ has a GTP hydrolysis rate comparable to monomer turnover time, and releases the hydrolyzed nucleotide very fast (Romberg and Mitchison, 2004). This rapid release of products implies that the energy from GTP hydrolysis is quickly dissipated, in contrast to microtubules, where it is stored as strain in the polymer (Caplow et al., 1994) and released during microtubule disassembly to perform mechanical work.

How does this dissipated energy affect the membrane? There is experimental evidence that FtsZ filaments attached to a supported lipid bilayer affect the shape of lipid domains and that the segregated lipids also influence the distribution and shape of the filaments (González de Prado Salas et al., 2015). Modeling this behavior requires considering filament torsion, monomer exchange, lateral interactions, and preferential curvature (Gonzalez de Prado Salas et al., 2014), and the tendency of the lipids to segregate into domains (**Figure 2**). Given the complex composition of the lipids of the bacterial inner membrane, it is not difficult to imagine that this lipid-protein interplay will be relevant also in the living cell and that the membrane components will respond to the remodeling of the filaments on its surface. Experiments in model membranes provide evidence that this is indeed the case. Langmuir monolayers of *E. coli* lipids indicate that this lipid mixture is easily stretchable (López-Montero et al., 2008) and that the presence of active FtsZ filaments attached through ZipA further softened the membrane (López-Montero et al., 2012, 2013). The energy dissipated by GTP hydrolysis could be transmitted to the membrane affecting the distribution and size of lipid domains in the inner side of the *E. coli* membrane (Zerrouk et al., 2008). This domain reorganization could affect membrane plasticity and modulate its local mechanical properties (López-Montero et al., 2010). **Figure 2C** shows a cartoon of how the tension created by filament formation could affect lipid domain redistribution on the membrane.

DISCUSSION

Condensation of FtsZ filaments in the central position of the inner cell membrane orchestrates the complex process of cell division. This event transmits information along and across the membrane surface through its interaction with many other proteins located both in the membrane as well as protruding from either side, toward the periplasmic space or toward the intracellular space. The aim of this mini-review has been to try to stitch together information that has been gathered from different approaches to the study of FtsZ polymers. One of the important challenges that remains in the field is closing the gap between the information provided by various experimental approaches that access different spatial and temporal scales. Whereas molecular dynamics simulations describe a highly flexible monomer, it is difficult to associate these conformational switches to the cooperative polymerization and treadmilling assembly observed at surfaces. We do not know either how the functionally important C-terminal non-structured region is modulating monomer-monomer interactions or their association to membrane bound anchoring proteins. Individual monomer restructuring undergone during the nucleotide hydrolysis cycle could be affected by surface confinement on a charged lipid surface. However, it is experimentally difficult to associate monomeric conformations to the collective behavior of the filaments observed on the membrane. In order to reconcile all the information available we will most likely need to incorporate additional techniques such as solid state NMR or other spectroscopic techniques to look in more detail at the

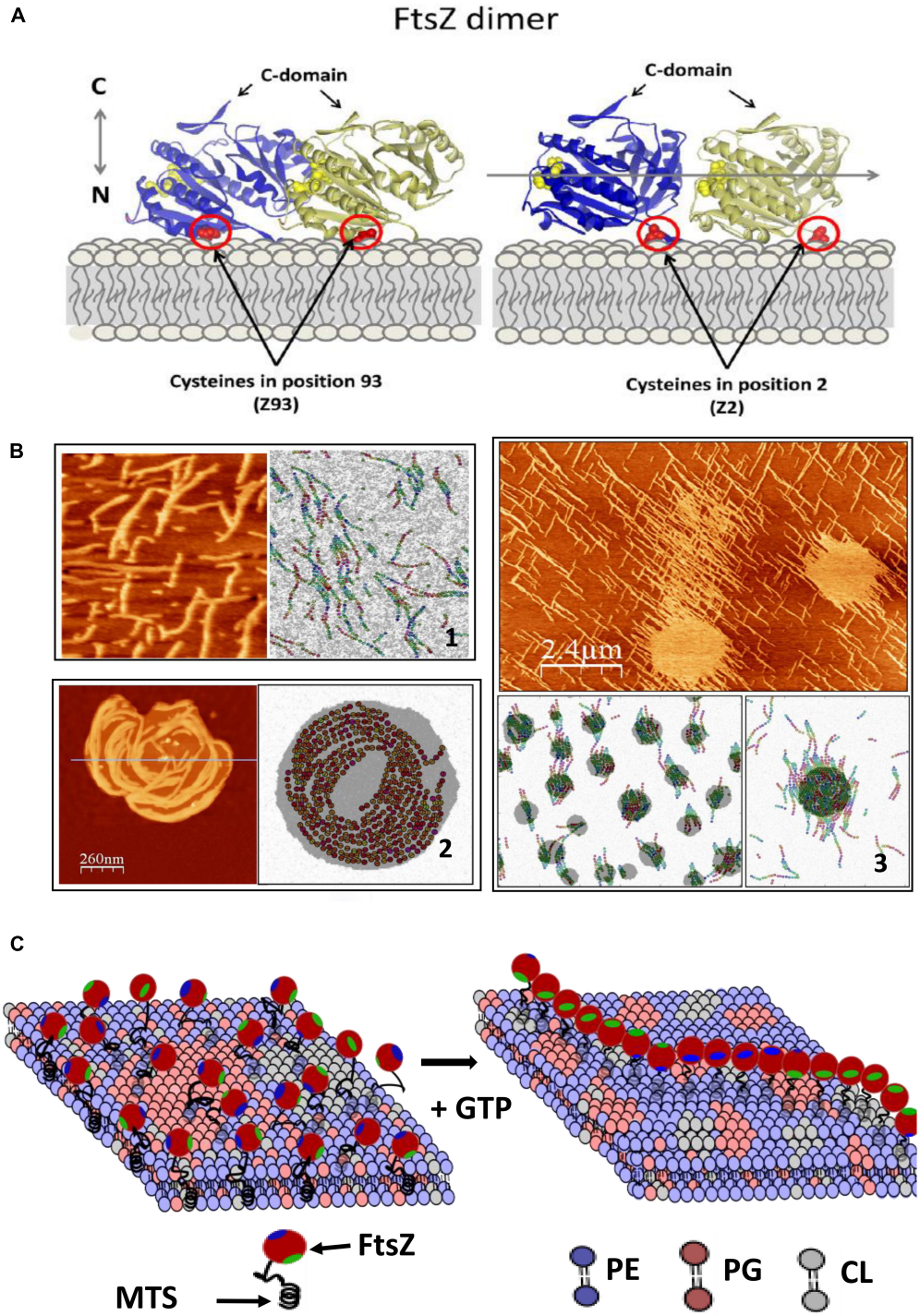

FIGURE 2 | FtsZ activity on the lipid membrane. **(A)** Shows how *E.coli* FtsZ monomers are oriented when attached covalently to a maleimide lipid (DSPE-MAL) in the bilayer through a cysteine placed in different positions. **(B)** Shows 3 examples of structures observed with AFM and snapshots of MC simulations of the model that describes the system including three terms: the dynamic interactions between protein monomers, the interactions between lipid components, and a mixed term considering protein–lipid interactions. Including torsion of the monomers within the filament in the model is necessary to account for the observed filament shapes. (1) Shows mutant E93C above lipid segregation temperature; (2) shows mutant F2C below lipid segregation temperature and (3) mutant E93C at higher DSPE-MAL concentration (adapted from González de Prado Salas et al., 2015). **(C)** Shows a schematic illustration of how polymerization of FtsZ could affect the membrane. The association is through a membrane targeting sequence (MTS) localized in the C-terminal region (green). The components are the main lipids present in the *E.coli* inner membrane (phosphatidylethanolamine, PE, phsophatidylglycerol, PG and cardiolipin, CL). Tension created by filament torsion and preferential curvature restrictions upon surface confinement could affect lipid reorganization.

structural rearrangement of the proteins and the lipids during the ring formation process.

Another issue that I have stressed is the potential importance of the lipid rearrangement due to the activity of FtsZ. There is another example of a membrane associated cytoskeletal protein participating in bacterial division for which there is evidence that its function is associated to membrane properties. MreB is a membrane associated actin homolog required in rod-shaped bacteria for cell shape maintenance and for peptidoglycan synthesis (Dempwolff et al., 2011; Nurse and Marians, 2013; Lee et al., 2020). Its direct interaction with FtsZ is required for septum synthesis and cell division in Escherichia coli (Varma and Young, 2009; Fenton and Gerdes, 2013). It has recently been shown that phospholipid composition and membrane fluidity affect the localization of MreB, which in turn affects peptidoglycan synthesis (Kurita et al., 2020). It has also been shown that MreB promotes membrane fluidity and affects membrane protein localization (Strahl et al., 2014; Oswald et al., 2016). This further illustrates that local modulation of membrane properties might be a strategy to convey information between different proteins involved in the various functions active during cell division.

CONCLUSION AND PERSPECTIVES

There is enough accumulated evidence indicating that proteins and lipids in membranes participate in a concerted fashion to generate complex functions. Active energy consuming proteins near a membrane invest part of this energy to transform membrane structure and properties. Although most of the experimental evidence of these interactions comes from studies done in eukaryotic cells, observations of FtsZ on lipid membranes indicate that in prokaryotic cells this two-way communication between protein activity and membrane properties also exists. Considering the mutual influence between the collective properties of active proteins and membrane lipids offers a wider conceptual framework to understand the intricate regulation of different protein activities during cell division. It is likely to provide additional elements to understand this complex yet fascinating process.

AUTHOR CONTRIBUTIONS

MV wrote the article.

ACKNOWLEDGMENTS

The author acknowledges Open Access funding provided thanks to the CRUE-CSIC agreement with Frontiers and financial support from Comunidad de Madrid/FEDER, EU through project SINOXPHOS-CM (S2018/BAA-4403) and MCIU/AEI/FEDER, EU, for funding project RTI2018-095090-B-I00. The author also thank Prof. Pedro Tarazona for fruitful discussions.

REFERENCES

Adams, D. W., and Errington, J. (2009). Bacterial cell division: assembly, maintenance and disassembly of the Z ring. *Nat. Rev. Microbiol.* 7, 642–653. doi: 10.1038/nrmicro2198

Adhyapak, P., Srivatsav, A. T., Mishra, M., Singh, A., Narayan, R., and Kapoor, S. (2020). Dynamical organization of compositionally distinct inner and outer membrane lipids of Mycobacteria. *Biophys. J.* 118, 1279–1291. doi: 10.1016/j.bpj.2020.01.027

Arumugam, S., Chwastek, G., Fischer-Friedrich, E., Ehrig, C. I, and Schwille, P. (2012). Surface topology engineering of membranes for the mechanical investigation of the tubulin homologue FtsZ. *Angew. Chem. Int. Ed.* 51, 11858–11862. doi: 10.1002/anie.201204332

Barrows, J. M., and Goley, E. D. (2021). FtsZ dynamics in bacterial division: what, how, and why? *Curr. Opin. Cell Biol.* 68, 163–172. doi: 10.1016/j.ceb.2020.10.013

Bi, E., and Lutkenhaus, J. (1991). FtsZ ring structure associated with division in *Escherichia coli*. *Nature* 354:161. doi: 10.1038/354161a0

Bisson-Filho, A. W., Hsu, Y. P., Squyres, G. R., Kuru, E., Wu, F., Jukes, C., et al. (2017). Treadmilling by FtsZ filaments drives peptidoglycan synthesis and bacterial cell division. *Science* 355:739. doi: 10.1126/science.aak9973

Bramkamp, M., and Lopez, D. (2015). Exploring the existence of lipid rafts in bacteria. *Microbiol. Mol. Biol. Rev.* 79, 81–100. doi: 10.1128/mmbr.00036-14

Busiek, K. K., and Margolin, W. (2015). Bacterial actin and tubulin homologs in cell growth and division. *Curr. Biol.* 25, R243–R254. doi: 10.1016/j.cub.2015.01.030

Buske, P. J., and Levin, P. A. (2013). A flexible C-terminal linker is required for proper FtsZ assembly *in vitro* and cytokinetic ring formation *in vivo*. *Mol. Microbiol.* 89, 249–263. doi: 10.1111/mmi.12272

Buske, P. J., Mittal, A., Pappu, R. V., and Levin, P. A. (2015). An intrinsically disordered linker plays a critical role in bacterial cell division. *Semin. Cell Dev. Biol.* 37, 3–10. doi: 10.1016/j.semcdb.2014.09.017

Cabeen, M. T., and Jacobs-Wagner, C. (2010). The bacterial cytoskeleton. *Annu. Rev. Genet.* 44, 365–392. doi: 10.1146/annurev-genet-102108-134845

Caldas, P., López-Pelegrín, M., Pearce, D. J. G., Budanur, N. B., Brugués, J., and Loose, M. (2019). Cooperative ordering of treadmilling filaments in cytoskeletal networks of FtsZ and its crosslinker ZapA. *Nat. Commun.* 10:5744. doi: 10.1038/s41467-019-13702-4

Caplow, M., Ruhlen, R. L., and Shanks, J. (1994). The free energy for hydrolysis of a microtubule-bound nucleotide triphosphate is near zero: all of the free energy for hydrolysis is stored in the microtubule lattice. *J. Cell Biol.* 127, 779–788. doi: 10.1083/JCB.127.3.779

Chen, Y., and Erickson, H. P. (2005). Rapid *in vitro* assembly dynamics and subunit turnover of FtsZ demonstrated by fluorescence resonance energy transfer. *J. Biol. Chem.* 280, 22549–22554. doi: 10.1074/JBC.M500895200

Chen, Y., and Erickson, H. P. (2009). FtsZ filament dynamics at steady state: subunit exchange with and without nucleotide hydrolysis. *Biochemistry* 48, 6664–6673. doi: 10.1021/bi8022653

Chen, Y., Bjornson, K., Redick, S. D., and Erickson, H. P. (2005). A rapid fluorescence assay for FtsZ assembly indicates cooperative assembly with a dimer nucleus. *Biophys. J.* 88, 505–514. doi: 10.1529/BIOPHYSJ.104.044149

Cohan, M. C., Eddelbuettel, A. M. P., Levin, P. A., and Pappu, R. V. (2020). Dissecting the functional contributions of the intrinsically disordered C-terminal tail of *Bacillus subtilis* FtsZ. *J. Mol. Biol.* 432, 3205–3221. doi: 10.1016/j.jmb.2020.03.008

Dai, K., and Lutkenhaus, J. (1991). FtsZ is an essential cell division gene in *Escherichia coli*. *J. Bacteriol.* 173, 3500–3506. doi: 10.1128/jb.173.11.3500-3506.1991

de Boer, P., Crossley, R., and Rothfield, L. (1992). The essential bacterial cell division protein FtsZ is a GTPase. *Nature* 359, 254–256. doi: 10.1038/359254a0

Dempwolff, F., Reimold, C., Reth, M., and Graumann, P. L. (2011). *Bacillus subtilis* MreB orthologs self-organize into filamentous structures underneath the cell

membrane in a heterologous cell system. *PLoS One* 6:e27035. doi: 10.1371/journal.pone.0027035

Dempwolff, F., Schmidt, F. K., Hervás, A. B., Stroh, A., Rösch, T. C., Riese, C. N., et al. (2016). Super resolution fluorescence microscopy and tracking of bacterial flotillin (Reggie) paralogs provide evidence for defined-sized protein microdomains within the bacterial membrane but absence of clusters containing detergent-resistant proteins. *PLoS Genet.* 12:e1006116. doi: 10.1371/journal.pgen.1006116

Den Blaauwen, T., and Luirink, J. (2019). Checks and balances in bacterial cell division. *mBio* 10:e00149-19. doi: 10.1128/mBio.00149-19

Du, S., and Lutkenhaus, J. (2019). At the heart of bacterial cytokinesis: the Z ring. *Trends Microbiol.* 27, 781–791. doi: 10.1016/j.tim.2019.04.011

Encinar, M., Kralicek, A. V., Martos, A., Krupka, M., Cid, S., Alonso, A., et al. (2013). Polymorphism of FtsZ filaments on lipid surfaces: role of monomer orientation. *Langmuir* 29, 9436–9446. doi: 10.1021/la401673z

Erickson, H. P. (1997). FtsZ, a tubulin homolog, in prokaryote cell division. *Trends Cell Biol.* 7, 362–367. doi: 10.1016/s0962-8924(97)01108-2

Erickson, H. P. (2017). The discovery of the prokaryotic cytoskeleton: 25th anniversary. *Mol. Biol. Cell* 28, 357–358. doi: 10.1091/mbc.E16-03-0183

Erickson, H. P., Taylor, D. W., Taylor, K. A., and Bramhill, D. (1996). Bacterial cell division protein FtsZ assembles into protofilament sheets and minirings, structural homologs of tubulin polymers. *Proc. Natl. Acad. Sci. U.S.A.* 93, 519–523. doi: 10.1073/pnas.93.1.519

Fenton, A. K., and Gerdes, K. (2013). Direct interaction of FtsZ and MreB is required for septum synthesis and cell division in *Escherichia coli*. *EMBO J.* 32, 1953–1965. doi: 10.1038/emboj.2013.129

Fujita, J., Harada, R., Maeda, Y., Saito, Y., Mizohata, E., Inoue, T., et al. (2017). Identification of the key interactions in structural transition pathway of FtsZ from *Staphylococcus aureus*. *J. Struct. Biol.* 198, 65–73. doi: 10.1016/j.jsb.2017.04.008

García-Soriano, D. A., Heermann, T., Raso, A., Rivas, G., and Schwille, P. (2020). The speed of FtsZ treadmilling is tightly regulated by membrane binding. *Sci. Rep.* 10:10447. doi: 10.1038/s41598-020-67224-x

Gardner, K. A. J. A., Moore, D. A., and Erickson, H. P. (2013). The C-terminal linker of *Escherichia coli* FtsZ functions as an intrinsically disordered peptide. *Mol. Microbiol.* 89, 264–275. doi: 10.1111/mmi.12279

González de Prado Salas, P., Encinar, M., Alonso, A., Vélez, M., and Tarazona, P. (2015). Modeling the interplay between protein and lipid aggregation in supported membranes. *Chem. Phys. Lipids* 185, 141–152. doi: 10.1016/j.chemphyslip.2014.06.006

Gonzalez de Prado Salas, P., Hörger, I., Martín-García, F., Mendieta, J., Alonso, Á, Encinar, M., et al. (2014). Torsion and curvature of FtsZ filaments. *Soft Matter* 10, 1977–1986. doi: 10.1039/C3SM52516C

Gowrishankar, K., Ghosh, S., Saha, S., Rumamol, C., Mayor, S., and Rao, M. (2012). Active remodeling of cortical actin regulates spatiotemporal organization of cell surface molecules. *Cell* 149, 1353–1367. doi: 10.1016/j.cell.2012.05.008

Hörger, I., Velasco, E., Mingorance, J., Rivas, G., Tarazona, P., and Vélez, M. (2008a). Langevin computer simulations of bacterial protein filaments and the force-generating mechanism during cell division. *Phys. Rev. E Stat. Nonlinear Soft Matter Phys.* 77:011902. doi: 10.1103/PhysRevE.77.011902

Hörger, I., Velasco, E., Rivas, G., Vélez, M., and Tarazona, P. (2008b). FtsZ bacterial cytoskeletal polymers on curved surfaces: the importance of lateral interactions. *Biophys. J.* 94, L81–L83. doi: 10.1529/biophysj.107.128363

Hsin, J., Gopinathan, A., and Huang, K. C. (2012). Nucleotide-dependent conformations of FtsZ dimers and force generation observed through molecular dynamics simulations. *Proc. Natl. Acad. Sci. U.S.A.* 109, 9432–9437. doi: 10.1073/pnas.1120761109

Huang, K.-H., Durand-Heredia, J., and Janakiraman, A. (2013). FtsZ ring stability: of bundles, tubules, crosslinks, and curves. *J. Bacteriol.* 195, 1859–1868. doi: 10.1128/JB.02157-12

Huecas, S., and Andreu, J. M. (2003). Energetics of the cooperative assembly of cell division protein FtsZ and the nucleotide hydrolysis switch. *J. Biol. Chem.* 278, 46146–46154. doi: 10.1074/jbc.M307128200

Ingerson-Mahar, M., and Gitai, Z. (2012). A growing family: the expanding universe of the bacterial cytoskeleton. *FEMS Microbiol. Rev.* 36, 256–267. doi: 10.1111/j.1574-6976.2011.00316.x

Kalappurakkal, J. M., Sil, P., and Mayor, S. (2020). Toward a new picture of the living plasma membrane. *Protein Sci.* 29, 1355–1365. doi: 10.1002/pro.3874

Kalia, R., and Frost, A. (2019). Open and cut: allosteric motion and membrane fission by dynamin superfamily proteins. *Mol. Biol. Cell* 30:2097. doi: 10.1091/MBC.E16-10-0709

Köster, D. V., Husain, K., Iljazi, E., and Mayor, S. (2016). Actomyosin dynamics drive local membrane component organization in an *in vitro* active composite layer. *Proc. Natl. Acad. Sci. U.S.A.* 113, E1645–E1654. doi: 10.1073/pnas.1514030113

Kurita, K., Kato, F., and Shiomi, D. (2020). Alteration of membrane fluidity or phospholipid composition perturbs rotation of MreB complexes in *Escherichia coli*. *Front. Mol. Biosci.* 7:582660. doi: 10.3389/fmolb.2020.582660

Lam, M., and Calvo, F. (2019). Regulation of mechanotransduction: emerging roles for septins. *Cytoskeleton (Hoboken)* 76, 115–122. doi: 10.1002/CM.21485

Lee, J., Cox, J. V., and Ouellette, S. P. (2020). Critical role for the extended N terminus of chlamydial MreB in directing its membrane association and potential interaction with divisome proteins. *J. Bacteriol.* 202:e00034-20. doi: 10.1128/JB.00034-20

Lin, T. Y., and Weibel, D. B. (2016). Organization and function of anionic phospholipids in bacteria. *Appl. Microbiol. Biotechnol.* 100, 4255–4267. doi: 10.1007/s00253-016-7468-x

Litschel, T., Kelley, C. F., Holz, D., Adeli Koudehi, M., Vogel, S. K., Burbaum, L., et al. (2021). Reconstitution of contractile actomyosin rings in vesicles. *Nat. Commun.* 12:2254. doi: 10.1038/s41467-021-22422-7

Longo, M. L. (2018). Preface to emergence of complex behavior in biomembranes. *Biochim. Biophys. Acta Biomembr.* 1860, 1955–1956. doi: 10.1016/j.bbamem.2018.08.015

Loose, M., and Mitchison, T. J. (2013). The bacterial cell division proteins FtsA and FtsZ self-organize into dynamic cytoskeletal patterns. *Nat. Cell Biol.* 16, 38–46. doi: 10.1038/ncb2885

López-Montero, I., Arriaga, L. R., Monroy, F., Rivas, G., Tarazona, P., and Vélez, M. (2008). High fluidity and soft elasticity of the inner membrane of *Escherichia coli* revealed by the surface rheology of model langmuir monolayers. *Langmuir* 24, 4065–4076. doi: 10.1021/la703350s

López-Montero, I., Arriaga, L. R., Rivas, G., Vélez, M., and Monroy, F. (2010). Lipid domains and mechanical plasticity of *Escherichia coli* lipid monolayers. *Chem. Phys. Lipids* 163, 56–63. doi: 10.1016/J.CHEMPHYSLIP.2009.10.002

López-Montero, I., López-Navajas, P., Mingorance, J., Vélez, M., Vicente, M., and Monroy, F. (2013). Membrane reconstitution of FtsZ-ZipA complex inside giant spherical vesicles made of *E. coli* lipids: large membrane dilation and analysis of membrane plasticity. *Biochim. Biophys. Acta Biomembr.* 1828, 687–698. doi: 10.1016/j.bbamem.2012.11.003

López-Montero, I., Mateos-Gil, P., Sferrazza, M., Navajas, P. L., Rivas, G., Vélez, M., et al. (2012). Active membrane viscoelasticity by the bacterial FtsZ-division protein. *Langmuir* 28, 4744–4753. doi: 10.1021/la204742b

Löwe, J., and Amos, L. C. (1998). Crystal structure of the bacterial cell-division protein FtsZ. *Nature* 391, 203–206. doi: 10.1038/34472

Lu, C. L., Reedy, M., and Erickson, H. P. (2000). Straight and curved conformations of FtsZ are regulated by GTP hydrolysis. *J. Bacteriol.* 182, 164–170. doi: 10.1128/jb.182.1.164-170.2000

Lv, D., Li, J., and Ye, S. (2021). The assembly switch mechanism of FtsZ filament revealed by all-atom molecular dynamics simulations and coarse-grained models. *Front. Microbiol.* 12:639883. doi: 10.3389/fmicb.2021.639883

Mahone, C. R., and Goley, E. D. (2020). Bacterial cell division at a glance. *J. Cell Sci.* 133:jcs237057. doi: 10.1242/jcs.237057

Margolin, W. (2005). FtsZ and the division of prokaryotic cells and organelles. *Nat. Rev. Mol. Cell Biol.* 6, 862–871. doi: 10.1038/nrm1745

Márquez, I. F., Mateos-Gil, P., Shin, J. Y., Lagos, R., Monasterio, O., and Vélez, M. (2017). Mutations on FtsZ lateral helix H3 that disrupt cell viability hamper reorganization of polymers on lipid surfaces. *Biochim. Biophys. Acta Biomembr.* 1859, 1815–1827. doi: 10.1016/j.bbamem.2017.06.009

Márquez, I., Díaz-Haro, G., and Vélez, M. (2019). Surface orientation and binding strength modulate shape of FtsZ on lipid surfaces. *Int. J. Mol. Sci.* 20:2545. doi: 10.3390/ijms20102545

Martín-Galiano, A. J., Buey, R. M., Cabezas, M., and Andreu, J. M. (2010). Mapping flexibility and the assembly switch of cell division protein FtsZ by computational and mutational approaches. *J. Biol. Chem.* 285, 22554–22565. doi: 10.1074/jbc.M110.117127

Mateos-Gil, P., Márquez, I., López-Navajas, P., Jiménez, M., Vicente, M., Mingorance, J., et al. (2012a). FtsZ polymers bound to lipid bilayers through

ZipA form dynamic two dimensional networks. *Biochim. Biophys. Acta Biomembr.* 1818, 806–813. doi: 10.1016/j.bbamem.2011.12.012

Mateos-Gil, P., Paez, A., Hörger, I., Rivas, G., Vicente, M., Tarazona, P., et al. (2012b). Depolymerization dynamics of individual filaments of bacterial cytoskeletal protein FtsZ. *Proc. Natl. Acad. Sci. U.S.A.* 109, 8133–8138. doi: 10.1073/pnas.1204844109

Mateos-Gil, P., Tarazona, P., and Vélez, M. (2019). Bacterial cell division: modeling FtsZ assembly and force generation from single filament experimental data. *FEMS Microbiol. Rev.* 039, 73–87. doi: 10.1093/femsre/fuy039

Mateos-Gil, P., Tsortos, A., Velez, M., and Gizeli, E. (2016). Monitoring structural changes in intrinsically disordered proteins using QCM-D: application to the bacterial cell division protein ZipA. *Chem. Commun.* 52, 6541–6544. doi: 10.1039/C6CC02127A

Matsui, T., Yamane, J., Mogi, N., Yamaguchi, H., Takemoto, H., Yao, M., et al. (2012). Structural reorganization of the bacterial cell-division protein FtsZ from *Staphylococcus aureus*. *Acta Crystallogr. Sect. D* 68, 1175–1188. doi: 10.1107/S0907444912022640

McCausland, J. W., Yang, X., Squyres, G. R., Lyu, Z., Bruce, K. E., Lamanna, M. M., et al. (2021). Treadmilling FtsZ polymers drive the directional movement of sPG-synthesis enzymes *via* a Brownian ratchet mechanism. *Nat. Commun.* 12:609. doi: 10.1038/s41467-020-20873-y

McQuillen, R., and Xiao, J. (2020). Insights into the structure, function, and dynamics of the bacterial cytokinetic FtsZ-ring. *Annu. Rev. Biophys.* 49, 309–341. doi: 10.1146/annurev-biophys-121219-081703

Milam, E., Osawa, M., and Erickson, H. P. (2012). Negative-stain electron microscopy of inside-out FtsZ rings reconstituted on artificial membrane tubules show ribbons of protofilaments. *Biophys. J.* 103, 59–68. doi: 10.1016/j.bpj.2012.05.035

Mileykovskaya, E., and Dowhan, W. (2005). Role of membrane lipids in bacterial division-site selection. *Curr. Opin. Microbiol.* 8, 135–142. doi: 10.1016/j.mib.2005.02.012

Mileykovskaya, E., and Dowhan, W. (2009). Cardiolipin membrane domains in prokaryotes and eukaryotes. *Biochim. Biophys. Acta Biomembr.* 1788, 2084–2091. doi: 10.1016/j.bbamem.2009.04.003

Mingorance, J., Rivas, G., Vélez, M., Gómez-Puertas, P., and Vicente, M. (2010). Strong FtsZ is with the force: mechanisms to constrict bacteria. *Trends Microbiol.* 18, 348–356. doi: 10.1016/j.tim.2010.06.001

Nenninger, A., Mastroianni, G., Robson, A., Lenn, T., Xue, Q., Leake, M. C., et al. (2014). Independent mobility of proteins and lipids in the plasma membrane of *Escherichia coli*. *Mol. Microbiol.* 92, 1142–1153. doi: 10.1111/mmi.12619

Nishibori, A., Kusaka, J., Hara, H., Umeda, M., and Matsumoto, K. (2005). Phosphatidylethanolamine domains and localization of phospholipid synthases in Bacillus subtilis membranes. *J. Bacteriol.* 187, 2163–2174. doi: 10.1128/JB.187.6.2163-2174.2005

Nurse, P., and Marians, K. J. (2013). Purification and characterization of *Escherichia coli* MreB protein. *J. Biol. Chem* 288, 3469–3475. doi: 10.1074/jbc.M112.413708

Ohashi, T., Hale, C. A., de Boer, P. A. J., and Erickson, H. P. (2002). Structural evidence that the P/Q Domain of ZipA is an unstructured, flexible tether between the membrane and the C-Terminal FtsZ-binding domain. *J. Bacteriol.* 184, 4313–4315. doi: 10.1128/jb.184.15.4313-4315.2002

Oliva, M. A., Cordell, S. C., and Lowe, J. (2004). Structural insights into FtsZ protofilament formation. *Nat. Struct. Mol. Biol.* 11, 1243–1250. doi: 10.1038/nsmb855

Ortiz, C., Natale, P., Cueto, L., and Vicente, M. (2015). The keepers of the ring: regulators of FtsZ assembly. *FEMS Microbiol. Rev.* 40, 57–67. doi: 10.1093/femsre/fuv040

Osawa, M., and Erickson, H. P. (2005). Probing the domain structure of FtsZ by random truncation and insertion of GFP. *Microbiology* 151, 4033–4043. doi: 10.1099/mic.0.28219-0

Osawa, M., Anderson, D. E., and Erickson, H. P. (2008). Reconstitution of contractile FtsZ Rings in liposomes. *Science* 320, 792–794. doi: 10.1126/science.1154520

Osawa, M., Anderson, D. E., and Erickson, H. P. (2009). Curved FtsZ protofilaments generate bending forces on liposome membranes. *EMBO J.* 28, 3476–3484. doi: 10.1038/emboj.2009.277

Oswald, F., Varadarajan, A., Lill, H., Peterman, E. J. G., and Bollen, Y. J. M. (2016). MreB-dependent organization of the *E. coli* cytoplasmic membrane controls membrane protein diffusion. *Biophys. J.* 110, 1139–1149. doi: 10.1016/j.bpj.2016.01.010

Paez, A., Tarazona, P., Mateos-Gil, P., and Vélez, M. (2009). Self-organization of curved living polymers: FtsZ protein filaments. *Soft Matter* 5, 2625–2637. doi: 10.1039/b902935d

Paez, P., Mateos-Gil Hörger, I., Mingorance, J., Rivas, G., Vicente, M., Vélez, M., et al. (2009). Simple modeling of FtsZ polymers on flat and curved surfaces: correlation with experimental *in vitro* observations. *PMC Biophys.* 2:8. doi: 10.1186/1757-5036-2-8

Pannuzzo, M., McDargh, Z. A., and Deserno, M. (2018). The role of scaffold reshaping and disassembly in dynamin driven membrane fission. *Elife* 7:e39441. doi: 10.7554/ELIFE.39441

Perez, A. J., Cesbron, Y., Shaw, S. L., Bazan Villicana, J., Tsui, H. T., Boersma, M. J., et al. (2019). Movement dynamics of divisome proteins and PBP2x: FtsW in cells of *Streptococcus pneumoniae*. *Proc. Natl. Acad. Sci. U.S.A.* 116, 3211–3220. doi: 10.1073/pnas.1816018116

Pilhofer, M., and Jensen, G. J. (2013). The bacterial cytoskeleton: more than twisted filaments. *Curr. Opin. Cell Biol.* 25, 125–133. doi: 10.1016/j.ceb.2012.10.019

Pla, J., Sanchez, M., Palacios, P., Vicente, M., and Aldea, M. (1991). Preferential cytoplasmic location of FtsZ, a protein essential for *Escherichia coli* septation. *Mol. Microbiol.* 5, 1681–1686. doi: 10.1111/j.1365-2958.1991.tb01915.x

Pluhackova, K., and Horner, A. (2021). Native-like membrane models of *E. coli* polar lipid extract shed light on the importance of lipid composition complexity. *BMC Biol.* 19:4. doi: 10.1186/s12915-020-00936-8

Popp, D., Iwasa, M., Narita, A., Erickson, H. P., and Maéda, Y. (2009). FtsZ condensates: an *in vitro* electron microscopy study. *Biopolymers* 91, 340–350. doi: 10.1002/BIP.21136

Raghunathan, K., and Kenworthy, A. K. (2018). Dynamic pattern generation in cell membranes: Current insights into membrane organization. *Biochim. Biophys. Acta Biomembr.* 1860, 2018–2031. doi: 10.1016/j.bbamem.2018.05.002

Ramirez-Diaz García-Soriano, D. A., Raso, A., Mücksch, J., Feingold, M., Rivas, G., and Schwille, P. (2018). Treadmilling analysis reveals new insights into dynamic FtsZ ring architecture. *PLoS Biol.* 16:e2004845. doi: 10.1371/journal.pbio.2004845

Ramirez-Diaz, D. A., Merino-Salomón, A., Meyer, F., Heymann, M., Rivas, G., Bramkamp, M., et al. (2021). FtsZ induces membrane deformations *via* torsional stress upon GTP hydrolysis. *Nat. Commun.* 12:3310. doi: 10.1038/s41467-021-23387-3

RayChaudhuri, D., and Park, J. T. (1992). *Escherichia coli* cell-division gene ftsZ encodes a novel GTP-binding protein. *Nature* 359, 251–254. doi: 10.1038/359251a0

Redick, S. D., Stricker, J., Briscoe, G., and Erickson, H. P. (2005). Mutants of FtsZ targeting the protofilament interface: effects on cell division and GTPase activity. *J. Bacteriol.* 187, 2727–2736. doi: 10.1128/JB.187.8.2727-2736.2005

Redpath, G. M. I., Betzler, V. M., Rossatti, P., and Rossy, J. (2020). Membrane heterogeneity controls cellular endocytic trafficking. *Front. Cell Dev. Biol.* 8:757. doi: 10.3389/fcell.2020.00757

Romberg, L., and Levin, P. A. (2003). Assembly dynamics of the bacterial cell division protein FtsZ: poised at the edge of stability. *Annu. Rev. Microbiol.* 57, 125–154. doi: 10.1146/annurev.micro.57.012903.074300

Romberg, L., and Mitchison, T. J. (2004). Rate-limiting guanosine 5′-triphosphate hydrolysis during nucleotide turnover by FtsZ, a prokaryotic tubulin homologue involved in bacterial cell division. *Biochemistry* 43, 282–288. doi: 10.1021/bi035465r

Rowlett, V. W., Mallampalli, V. K. P. S., Karlstaedt, A., Dowhan, W., Taegtmeyer, H., Margolin, W., et al. (2017). Impact of membrane phospholipid alterations in *Escherichia coli* on cellular function and bacterial stress adaptation. *J. Bacteriol.* 199:e00849-16. doi: 10.1128/JB.00849-16

Ruiz, N. (2016). Filling holes in peptidoglycan biogenesis of *Escherichia coli*. *Curr. Opin. Microbiol.* 34, 1–6. doi: 10.1016/j.mib.2016.07.010

Schumacher, M. A., Ohashi, T., Corbin, L., and Erickson, H. P. (2020). High-resolution crystal structures of *Escherichia coli* FtsZ bound to GDP and GTP. *Acta Crystallogr. Sect. F Struct. Biol. Commun.* 76, 94–102. doi: 10.1107/S2053230X20001132

Sezgin, E. I, Mayor, S., and Eggeling, C. (2017). The mystery of membrane organization: composition, regulation and roles of lipid rafts. *Nat. Rev. Mol. Cell Biol.* 18, 361–374. doi: 10.1038/nrm.2017.16

Shaw, T. R., Ghosh, S., and Veatch, S. L. (2020). Critical phenomena in plasma membrane organization and function. *Annu. Rev. Phys. Chem.* 72, 541–564. doi: 10.1146/annurev-physchem-090419

Shih, Y.-L., and Rothfield, L. (2006). The bacterial cytoskeleton. *Microbiol. Mol. Biol. Rev.* 70, 729–754. doi: 10.1128/mmbr.00017-06

Siliakus, M. F., van der Oost, J., and Kengen, S. W. M. (2017). Adaptations of archaeal and bacterial membranes to variations in temperature, pH and pressure. *Extremophiles* 21, 651–670. doi: 10.1007/s00792-017-0939-x

Squyres, G. R., Holmes, M. J., Barger, S. R., Pennycook, B. R., Ryan, J., Yan, V. T., et al. (2021). Single-molecule imaging reveals that Z-ring condensation is essential for cell division in *Bacillus subtilis*. *Nat. Microbiol.* 6, 553–562. doi: 10.1038/s41564-021-00878-z

Steinkühler, J., Sezgin, E., Urbančič, I., Eggeling, C., and Dimova, R. (2019). Mechanical properties of plasma membrane vesicles correlate with lipid order, viscosity and cell density. *Commun. Biol.* 2:337. doi: 10.1038/s42003-019-0583-3

Strahl, H., and Errington, J. (2017). bacterial membranes: structure, domains, and function. *Annu. Rev. Microbiol.* 71, 519–538. doi: 10.1146/annurev-micro-102215

Strahl, H., Bürmann, F., and Hamoen, L. W. (2014). The actin homologue MreB organizes the bacterial cell membrane. *Nat. Commun.* 5:3442. doi: 10.1038/ncomms4442

Stricker, J., Maddox, P., Salmon, E. D., and Erickson, H. P. (2002). Rapid assembly dynamics of the *Escherichia coli* FtsZ-ring demonstrated by fluorescence recovery after photobleaching. *Proc. Natl. Acad. Sci. U.S.A.* 99, 3171–3175. doi: 10.1073/pnas.052595099

Varma, A., and Young, K. D. (2009). In *Escherichia coli*, MreB and FtsZ direct the synthesis of lateral cell wall *via* independent pathways that require PBP 2. *J. Bacteriol.* 191, 3526–3533. doi: 10.1128/JB.01812-08

Wagstaff, M., Tsim, M., Oliva, M. A., García-Sanchez, A., Kureisaite-Ciziene, D., Andreu, J. M., et al. (2017). A polymerization-associated structural switch in ftsz that enables treadmilling of model filaments. *mBio* 8:e00254-17. doi: 10.1128/mBio.00254-17

Willdigg, J. R., and Helmann, J. D. (2021). Mini review: bacterial membrane composition and its modulation in response to stress. *Front. Mol. Biosci.* 8:634438. doi: 10.3389/fmolb.2021.634438

Xiao, J., and Goley, E. D. (2016). Redefining the roles of the FtsZ-ring in bacterial cytokinesis. *Curr. Opin. Microbiol.* 34, 90–96. doi: 10.1016/j.mib.2016.08.008

Yang, X., Lyu, Z., Miguel, A., McQuillen, R., Huang, K. C., and Xiao, J. (2017). GTPase activity–coupled treadmilling of the bacterial tubulin FtsZ organizes septal cell wall synthesis. *Science* 355:744. doi: 10.1126/science.aak9995

Yang, X., McQuillen, R., Lyu, Z., Phillips-Mason, P., De La Cruz, A., McCausland, J. W., et al. (2021). A two-track model for the spatiotemporal coordination of bacterial septal cell wall synthesis revealed by single-molecule imaging of FtsW. *Nat. Microbiol.* 6, 584–593. doi: 10.1038/s41564-020-00853-0

Yokoyama, H., and Matsui, I. (2020). The lipid raft markers stomatin, prohibitin, flotillin, and HflK/C (SPFH)-domain proteins form an operon with NfeD proteins and function with apolar polyisoprenoid lipids. *Crit. Rev. Microbiol.* 46, 38–48. doi: 10.1080/1040841X.2020.1716682

Zeno, W. F., Day, K. J., Gordon, V. D., and Stachowiak, J. C. (2020). Principles and applications of biological membrane organization. *Annu. Rev. Biophys.* 49, 19–39. doi: 10.1146/annurev-biophys-121219-081637

Zerrouk, Z., Alexandre, S., Lafontaine, C., Norris, V., and Valleton, J. M. (2008). Inner membrane lipids of *Escherichia coli* form domains. *Colloids Surf. B Biointerfaces* 63, 306–310. doi: 10.1016/J.COLSURFB.2007.12.016

Conflict of Interest: The author declares that the research was conducted in the absence of any commercial or financial relationships that could be construed as a potential conflict of interest.

Publisher's Note: All claims expressed in this article are solely those of the authors and do not necessarily represent those of their affiliated organizations, or those of the publisher, the editors and the reviewers. Any product that may be evaluated in this article, or claim that may be made by its manufacturer, is not guaranteed or endorsed by the publisher.

frontiers | Frontiers in Microbiology

ORIGINAL RESEARCH
published: 14 June 2022
doi: 10.3389/fmicb.2022.913949

A LytM-Domain Factor, ActS, Functions in Two Distinctive Peptidoglycan Hydrolytic Pathways in *E. coli*

*Pavan Kumar Chodisetti, Raj Bahadur, R. N. Amrutha and Manjula Reddy**

Council of Scientific and Industrial Research-Centre for Cellular and Molecular Biology, Hyderabad, India

Bacterial cell wall contains peptidoglycan (PG) to protect the cells from turgor and environmental stress. PG consists of polymeric glycans cross-linked with each other by short peptide chains and forms an elastic mesh-like sacculus around the cytoplasmic membrane. Bacteria encode a plethora of PG hydrolytic enzymes of diverse specificity playing crucial roles in growth, division, or turnover of PG. In *Escherichia coli*, the cross-link-specific endopeptidases, MepS, -M, and -H, facilitate the enlargement of PG sacculus during cell elongation, whereas LytM-domain factors, EnvC and NlpD activate the division-specific amidases, AmiA, -B, and -C to facilitate the cell separation. In a screen to isolate additional factors involved in PG enlargement, we identified *actS* (encoding a LytM paralog, formerly *ygeR*) as its overexpression compensated the loss of elongation-specific endopeptidase, MepS. The overexpression of ActS resulted in the generation of partly denuded glycan strands in PG sacculi, indicating that ActS is either an amidase or an activator of amidase(s). The detailed genetic and biochemical analyses established that ActS is not a PG hydrolase, but an activator of the division-specific amidase, AmiC. However, interestingly, the suppression of the *mepS* growth defects by *actS* is not mediated through AmiC. The domain-deletion experiments confirmed the requirement of the N-terminal LysM domain of ActS for the activation of AmiC, but not for the alleviation of growth defects in *mepS* mutants, indicating that ActS performs two distinctive PG metabolic functions. Altogether our results suggest that in addition to activating the division-specific amidase, AmiC, ActS modulates yet another pathway that remains to be identified.

Keywords: bacteria, peptidoglycan, cell division, YgeR, MepS, ActS, AmiC

Edited by:
Shishen Du,
Wuhan University, China

Reviewed by:
Tobias Dörr,
Cornell University, United States
Matthew Jorgenson,
University of Arkansas for Medical Sciences, United States

***Correspondence:**
Manjula Reddy
manjula@ccmb.res.in;
mreddy65@gmail.com

Specialty section:
This article was submitted to Microbial Physiology and Metabolism, a section of the journal Frontiers in Microbiology

Received: *06 April 2022*
Accepted: *03 May 2022*
Published: *14 June 2022*

Citation:
Chodisetti PK, Bahadur R, Amrutha RN and Reddy M (2022) A LytM-Domain Factor, ActS, Functions in Two Distinctive Peptidoglycan Hydrolytic Pathways in E. coli. Front. Microbiol. 13:913949. doi: 10.3389/fmicb.2022.913949

INTRODUCTION

Bacterial cell wall contains a unique protective exoskeleton called peptidoglycan (PG) or murein. PG confers shape, provides structural integrity, and prevents osmotic lysis of bacteria. In Gram-negative bacteria, such as *Escherichia coli*, PG is located in the periplasmic space between the outer membrane (OM) and the inner membrane (IM). It is a single large molecule that forms a mesh-like sacculus around the cytoplasmic membrane. Structurally, it is made up of multiple linear

glycan polymers interconnected by short cross-linked peptides (Höltje, 1998; Vollmer et al., 2008). Glycan chains consist of alternating disaccharide units of *N*-acetylglucosamine (GlcNAc) and *N*-acetylmuramic acid (MurNAc) residues linked together by a β-1,4-glycosidic bond. The lactoyl moiety of each MurNAc residue is covalently linked *via* an amide bond to a tetrapeptide chain, which typically comprises L-alanine (L-Ala)-γ-D-glutamic acid (D-Glu)-mesodiaminopimelic acid (mDAP)-D-Ala. In *E. coli*, approximately 30–40% of the peptide chains are cross-linked with each other either *via* D-Ala and mDAP residues (D-Ala^4-mDAP^3 or 4-3 cross-links) or two mDAP residues (mDAP^3–mDAP^3 or 3–3 cross-links). Of the total peptide cross-links, around 90–95% are of the 4-3 type, whereas 5–10% are of the 3-3 type (Vollmer et al., 2008).

Peptidoglycan precursor synthesis is initiated in the cytoplasm by the step-wise addition of amino acids to the nucleotide-activated sugar, UDP-MurNAc, to form UDP-MurNAc-pentapeptide (Bouhss et al., 2008). This is subsequently attached to the IM-bound lipid carrier, lipid-II. The monomeric lipid-II moieties are flipped across the IM to the periplasmic space, and subsequently polymerized to synthesize PG either for sidewall synthesis (during cell elongation) or septal wall synthesis at the mid-cell (during cell division). Two distinct multiprotein complexes, namely, elongasome and divisome, execute the side and septal wall syntheses, respectively (reviewed in Garde et al., 2021).

During bacterial cell elongation, the elongasomal complex synthesizes the side wall to facilitate PG expansion concomitantly with the growing cell volume. PG elongation requires cleavage of the cross-links in order to make space for the insertion of incoming nascent PG material and three cross-link specific *D,D*-endopeptidases- MepS, -M, and -H, are crucial for the growth of PG sacculus in *E. coli* (Singh et al., 2012). Among the elongation-specific PG hydrolases, MepS is highly expressed and stringently regulated at the level of post-translational stability (Singh et al., 2015). MepS and -H belong to the NlpC/P60 peptidase superfamily (Anantharaman and Aravind, 2003), whereas MepM belongs to the LytM or lysostaphin family of proteins (or M23 class of metallopeptidases). The other members of the LytM family are: EnvC, NlpD, and ActS (formerly known as YgeR; **Figure 1**). Unlike MepM, which is a cross-link specific endopeptidase, EnvC and NlpD do not have any enzymatic activity and are localized to the division site to facilitate cell–cell separation during cell division (Uehara et al., 2009).

The process of cell division is initiated by an essential cytoskeletal protein, FtsZ, which recruits several other divisomal proteins in a step-wise manner for the synthesis of septal PG in the mid cell (Levin and Janakiraman, 2021). Subsequently, EnvC and NlpD activate the division-specific amidases that specifically cleave the amide bonds between the MurNAc and L-Ala residues of the septal PG strands to enable the separation of the daughter cells. *E. coli* encodes three division-specific LytC-type *N*-acetylmuramyl-L-alanine amidases, AmiA, -B, and -C (Heidrich et al., 2001). EnvC stimulates the activity of AmiA and AmiB, whereas NlpD stimulates the activity of AmiC (Uehara et al., 2009; Peters et al., 2013). However, the function of ActS, an OM lipoprotein, has not been known until recently. While this work was in progress, two independent studies reported that ActS preferentially activates AmiC in OM stress (Gurnani Serrano et al., 2021) and AmiB in low pH conditions (Mueller et al., 2021).

Here, we identified *actS* as a multicopy suppressor of a mutant lacking *mepS*, the gene that encodes a major elongation-specific *D,D*-endopeptidase. Moreover, multiple copies of ActS in a WT strain led to the generation of partly denuded glycan strands in the PG sacculi suggesting that ActS is an amidase or an activator of amidase(s). However, ActS did not exhibit any detectable PG hydrolytic activity. Extensive PG analysis and microscopy of amidase mutants overexpressing *actS* indicated that ActS activates the division-specific amidase, AmiC, under physiological growth conditions. Interestingly, ActS suppression of *mepS* phenotype was not mediated through AmiC. Domain-deletion experiments further confirmed that the septal localization of ActS is crucial for AmiC activation but not for the alleviation of growth defects of *mepS* mutant, suggesting ActS directly or indirectly activates an alternate PG hydrolase that compensates the loss of MepS. We extensively tested the role of all known PG hydrolases in the suppression of the *mepS* phenotypes by ActS overexpression; however, none of these factors were found to be the candidates suggesting that ActS may either activate a yet unknown PG hydrolase or performs an alternate function independent of cell-wall hydrolysis.

MATERIALS AND METHODS

Media, Bacterial Strains, and Plasmids

The LB medium has 0.5% yeast extract, 1% tryptone, and 1% NaCl (Miller, 1992). LBON is LB without NaCl. Nutrient Agar (NA) has 0.5% peptone and 0.3% beef extract. Minimal A media (Miller, 1992) was supplemented with 0.2% glucose and 0.4% casamino acids. Unless otherwise indicated, antibiotics were used in the following concentrations (μg/mL): ampicillin (Amp)—50, chloramphenicol (Cm)—30, and kanamycin (Kan)—50. The growth temperature was 37°C unless otherwise indicated. The bacterial strains and plasmids are listed in **Supplementary Tables 2**, **3**.

Molecular and Genetic Techniques

The experiments involving recombinant DNA and plasmid constructions were performed as per the standard methods. MG1655 genomic DNA was used as a template, and Phusion HF DNA polymerase (NEB) was used for PCR amplifications. Plasmid clones were always confirmed by sequence analysis. P1-phage-mediated transductions and transformations were performed using the standard methods (Miller, 1992). All strains are derivatives of MG1655 (Coli Genetic Stock Centre, Yale University) unless otherwise indicated. Deletion mutations are from the Keio mutant collection (NBRP, Japan) (Baba et al., 2006). Whenever required, the antibiotic resistance marker (Kan^R) was flipped out using pCP20 plasmid encoding an Flp recombinase (Datsenko and Wanner, 2000).

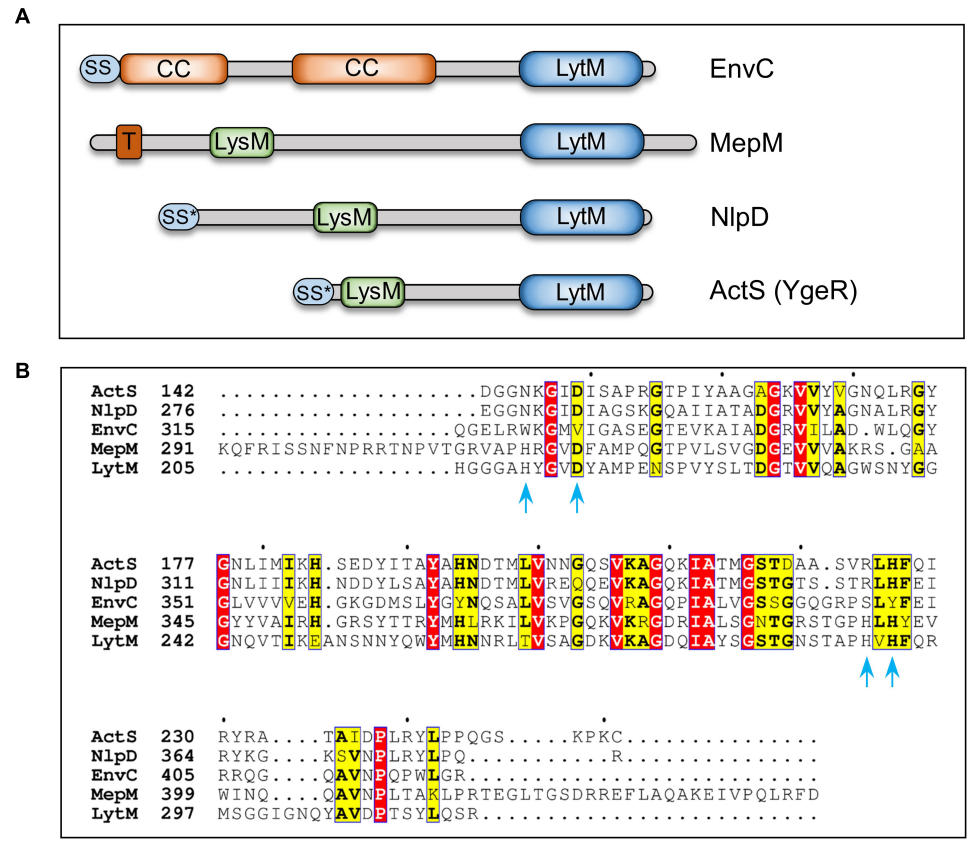

FIGURE 1 | Domain organization and sequence alignment of LytM-domain factors. **(A)** Domain architecture of LytM factors (EnvC, MepM, NlpD, and ActS) of *Escherichia coli*. **(B)** Sequence alignment of C-terminal domains of LytM, EnvC, NlpD, MepM, and ActS using T-Coffee and ESPript programs (Di Tommaso et al., 2011, http://espript.ibcp.fr). LytM is a glycyl-glycine endopeptidase that cleaves peptidoglycan of *Staphylococcus aureus*. Amino acid residues of LytM involved in Zinc binding and catalysis (Firczuk et al., 2005) are indicated with blue arrows. Red and yellow boxes highlight the identities and similarities, respectively. LytM, lysostaphin/peptidase M23 domain; LysM, PG-binding domain; CC, coiled-coil domain; T, transmembrane domain; SS, signal sequence; SS*, lipoprotein signal sequence.

Screen for Identification of Multicopy Suppressors

A genetic screening was performed to identify the multicopy suppressors of Δ*mepS* mutant. A pool of ASKA plasmid library (a complete collection of plasmids carrying individual *E. coli* genes cloned downstream to an IPTG-inducible promoter) (Kitagawa et al., 2005) was transformed into a Δ*mepS* mutant strain, and the transformants were plated on NA plates supplemented with 10 μM IPTG. Δ*mepS* mutants do not grow at all on NA at 42°C, but grow poorly at 37°C. The selection for the suppressors was done at 37°C to allow the identification of weak suppressors. The plasmids that conferred moderate growth to Δ*mepS* strain were isolated and the ORFs conferring suppression were identified by sequencing.

Viability Assays and Microscopy

The viability of the strains was checked by growing the strains overnight in permissive conditions, serially diluting (10^{-2}, 10^{-4}, 10^{-5}, and 10^{-6}) the strains, and placing 5 μL aliquots of each dilution onto the required plates followed by incubation at 37°C for 18–24 h. For microscopy, the cultures were immobilized on a thin 1% agarose pad and visualized using Axioimager microscope by DIC (Nomarski Optics).

Preparation of Peptidoglycan Sacculi

The isolation of PG was done as described earlier (Glauner et al., 1988). The cells (from 1,000 ml culture) grown to OD_{600} of 1.0 were harvested by centrifugation at 10,000 × *g* for 10 min at 4°C. Cell pellet was resuspended in 6 ml of ice-cold deionized water and added drop wise into 6 ml of boiling 8% SDS with vigorous stirring followed by boiling for another 45 min. The mixture was incubated overnight at room temperature. The PG pellet was washed thoroughly with deionized water to remove SDS by high-speed centrifugation (2,00,000 × *g* for 60 min). High-molecular weight glycogen and covalently bound lipoprotein, Lpp, were removed by treating with α-amylase (100 μg/ml in 10 mM Tris–HCl, pH 7.0, 2 h at 37°C) and pre-digested pronase (200 μg/ml, 90 min at 60°C). Enzymes were inactivated by boiling with an equal volume of 8% SDS for 15 min. Pure PG sacculi were obtained by ultracentrifugation and washed several times

with water till SDS was completely removed. The final pellet was resuspended in 0.5 ml of 25 mM Tris–HCl (pH 8.0) and stored at −30°C.

Analysis of Peptidoglycan Sacculi

Peptidoglycan analysis was done as described earlier (Glauner et al., 1988). Essentially, the sacculi were digested with 10 U mutanolysin (Sigma-Aldrich, St. Louis, MO, United States) at 37°C in 25 mM Tris–HCl (pH 8.0) for 16 h. Mutanolysin hydrolyzes β-1→4 glycosidic bond between MurNAc and GlcNAc residues in PG to form soluble muropeptide fragments. After centrifugation at 30,000 × *g* for 15 min, soluble muropeptide fragments in supernatant fraction were collected and reduced with 1 mg of sodium borohydride in 50 mM sodium borate buffer (pH 9.0) for 30 min and excess borohydride was destroyed by adding 20% phosphoric acid. pH was adjusted to 3–4 and the samples were loaded onto a reverse-phase C18 column (Zorbax 300 SB; 250 mm × 4.6 mm, 5 mm) connected to Agilent technologies RRLC 1200 system. Column temperature was 55°C and binding was done at a flow rate of 0.5 ml/min with 1% acetonitrile in water containing 0.1% trifluoroacetic acid (TFA) for 10 min. Muropeptides were eluted in a gradient of 1–10% acetonitrile containing 0.1% TFA at a flow rate of 0.5 ml/min for the next 60 min (using RRLC online software called Chemstation). The absorbance of muropeptides was detected at 205 nm.

Mass Spectrometry Analysis of Muropeptides

The muropeptide fractions collected during high-pressure liquid chromatography (HPLC) were dried and reconstituted in 5% acetonitrile with 0.1% formic acid and loaded onto a reverse-phase PepMap^{TM} RSLC – C18 column (3 μm, 100 Å,75 μm × 15 cm) connected to Q-Exactive^{TM} HF Hybrid Quadrupole-Orbitrap^{TM} Mass Spectrometer (Thermo Fisher Scientific, Waltham, MA, United States). The peaks were analyzed using mass spectrometry (MS) and the structures were decoded based on molecular mass of the fragments.

Protein Purification

ActS-encoding plasmid, pET21b-ActS$^{27-251}$, was transformed into BL21 λDE3 strain and a single transformant was inoculated into 10 ml LB broth with ampicillin and grown overnight. The culture was diluted 1:100 into a fresh pre-warmed LB broth with Amp, and was allowed to grow until OD_{600} of ∼0.6 was reached before being induced by the addition of 50 μM IPTG and grown further for 2 h at 37°C. The cells were recovered by centrifugation and the pellet was stored at −80°C until further use. The cell pellet was resuspended in 20 ml lysis buffer (50 mM Tris, 300 mM NaCl, 10 mM imidazole, pH 8.0) and was lysed by sonication (20% Amplitude; 10 s on–off). The cell debris was removed by centrifugation at 30,000 × *g* for 30 min at 4°C. The supernatant was mixed with 1 ml Ni^{2+}-NTA agarose (Qiagen, Hilden, Germany) and mixed at 4°C for 1 h. This mixture was loaded into empty plastic column (Bio-Rad, Hercules, CA, United States) and washed with 30 ml wash buffer-I (50 mM Tris, 300 mM NaCl, 20 mM imidazole, pH 8.0), 10 ml of wash buffer-II (50 mM Tris, 300 mM NaCl, 50 mM imidazole, pH 8.0), 10 ml of elution buffer-I (50 mM Tris, 300 mM NaCl, 100 mM imidazole pH 8.0), and 5 ml of elution buffer-II (50 mM Tris, 300 mM NaCl, 200 mM imidazole pH 8.0). Purified protein was pooled and concentrated to 2.5 ml using a 3 kDa cut-off centrifugal membrane filter (Millipore). This eluate was loaded onto a buffer exchange PD10 column (Amersham) and retained proteins were eluted in 3.5 ml storage buffer (100 mM Tris, 200 mM NaCl, and 2 mM DTT). The protein was concentrated to 250 μL by a 3 kDa cut-off centrifugal membrane filter before being mixed with an equal volume of 100% glycerol and stored at −30°C.

ActS$^{130-251}$ protein was purified using the plasmid pET21b-ActS$^{130-251}$, as described earlier, except that the induction for protein overexpression was for 2.5 h at 30°C.

Purification of CwlO

The C-terminal region of CwlO of *Bacillus subtilis* was overexpressed and purified to homogeneity using the plasmid, pET21b-CwlO$^{340-473}$, as described earlier, except that the induction for protein overexpression was done with 0.1 mM IPTG for 2 h at 30°C.

Zymogram Assay

Zymography of the proteins was performed as described earlier (Bernhardt and de Boer, 2004). Purified proteins were electrophoresed on two 12% SDS-gels, in which one gel was impregnated with *Micrococcus lysodeikticus* cells. After electrophoresis, this gel was incubated overnight in a renaturation buffer (25 mM Tris–Cl, pH 8.0, and 1% Triton X-100) for refolding the proteins. The gel was stained with methylene blue (0.1% methylene blue in 0.01% KOH) to visualize the cleared hydrolytic zones in blue background. The other gel stained with Coomassie brilliant blue was used as control.

Determination of Enzyme Activity

The total soluble muropeptides or intact PG sacculi were incubated with purified proteins, ActS^{FL}, ActS^{LytM}, or CwlO, at 30°C for 20 h. The samples were heat-inactivated (100°C, 5 min) and analyzed by reverse-phase-HPLC (RP-HPLC), as described earlier.

Western Blot Analysis

The samples were boiled with Laemmli loading dye and the proteins were separated by SDS-PAGE. Primary α-His antibodies were used at 1:3,000 dilution. Secondary anti-mouse-HRP conjugate antibodies were used at a dilution of 1:10,000 and blots were developed with ECL chemiluminescent detection kit (GE Biosciences, Chicago, IL, United States).

RESULTS

Identification of ActS as a Multicopy Suppressor of *mepS*

MepS is a major elongation-specific PG hydrolase that exhibits D,D-endopeptidase activity on 4-3 (D-ala^4-mDAP^3) cross-links to make space for the insertion of new material during the

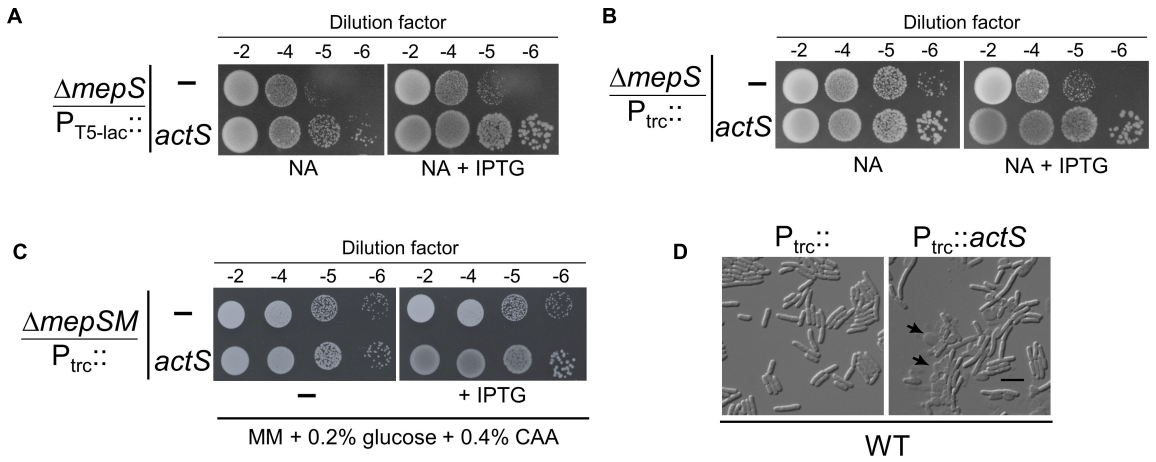

FIGURE 2 | Phenotypes caused by ActS overexpression. **(A)** Growth of Δ*mepS* mutant carrying the ASKA vector (P_{T5-lac}::) or vector encoding *actS* (P_{T5-lac}::*actS*) on NA plates supplemented with 10 μM isopropyl-thiogalactopyranoside (IPTG) at 37°C. **(B)** Growth of Δ*mepS* mutant carrying the empty vector (P_{trc}::) or vector encoding *actS* (P_{trc}::*actS*) on NA plates supplemented with 20 μM IPTG at 37°C. **(C)** Δ*mepS* Δ*mepM* double mutant harboring either pTRC99a (vector) or vector encoding *actS* (P_{trc}::*actS*) were grown in minimal media (MM) and tested for viability on MM plates supplemented with 0.2% glucose, 0.4% casamino acids (CAA), and 20 μM IPTG at 37°C. **(D)** WT cells carrying the vector (P_{trc}::) or vector encoding *actS* (P_{trc}::*actS*) were grown in LB supplemented with 50 μM IPTG at 37°C, harvested at 0.5 OD, and subjected to microscopy (DIC) as described in the "Materials and Methods" section. Arrows indicate cell lysis, and the scale bar represents 5 μm.

expansion of PG (Singh et al., 2012). A mutant of *E. coli* lacking *mepS* does not grow on low-osmolar media such as NA at high temperatures (Hara et al., 1996). To identify the additional factors involved in PG enlargement, we took advantage of the NA-sensitivity phenotype of the *mepS* deletion mutant and screened the ASKA plasmid library [a complete collection of plasmids carrying individual *E. coli* genes cloned downstream to an IPTG inducible promoter (P_{T5-lac}::)] (Kitagawa et al., 2005). This plasmid library was pooled and transformed into Δ*mepS* cells to obtain suppressors on NA plates (as described in the "Materials and Methods" section). Of the several suppressors obtained, we observed that a plasmid harboring an ORF, *ygeR* (*actS*) [pCA24N-*actS*] conferred moderate growth advantage to Δ*mepS* mutant (**Figure 2A**).

To further confirm the above observation, full-length *actS* was cloned under IPTG-inducible *trc* promoter (P_{trc}::) in a pTRC99a vector and introduced into Δ*mepS* mutant. Viability assays indicated that overexpression of *actS* conferred moderate growth to Δ*mepS* mutant on NA similar to that of pCA24N-*actS* (**Figure 2B**). Next, to check whether overexpression of *actS* can compensate for the loss of both *mepS* and *mepM*, we introduced pTRC99a-*actS* into a Δ*mepS* Δ*mepM* double mutant. It is known earlier that Δ*mepS* Δ*mepM* double mutants do not grow on rich media but grow on defined media (Minimal medium, MM) (Singh et al., 2012). **Figure 2C** shows that overexpression of *actS* weakly suppresses the growth defects of Δ*mepSM* double mutant. However, *actS* deletion did not confer any noticeable growth defect singly or when introduced into either Δ*mepS* or Δ*mepSM* mutants (data not shown). Interestingly, overexpression of *actS* in WT caused extensive cell lysis and microscopic (DIC) examination revealed misshapen cells with cellular contents oozing out into the medium (**Figure 2D** and **Supplementary Figures 1A,B**). All these observations collectively implied that ActS is either a PG hydrolase or activates an alternate hydrolase.

ActS Overexpression Generates Glycan Chains Lacking Stem Peptides

To further investigate the role of ActS, we examined the PG composition of cells lacking *actS*. PG sacculi from both WT and Δ*actS* strains were purified and subjected to muramidase (mutanolysin) digestion to obtain soluble muropeptides. These muropeptide fragments were fractionated by RP-HPLC. **Figure 3A** shows that the PG sacculi isolated from Δ*actS* cells did not have any noticeable changes compared to that of WT cells. Next, we examined the PG composition of WT cells overexpressing *actS*. Interestingly, HPLC chromatograms revealed the presence of two additional peaks with retention times of 43 min (peak A) and 54 min (peak B) (**Figure 3B**). MS analysis indicated peak A to be a monomer of tetrasaccharide tetrapeptide (abbreviated TS-tetra) and peak B as a heterodimer of tetrasaccharide tetrapeptide cross-linked to a disaccharide tetrapeptide (abbreviated TS-tetra-DS-tetra) with a molecular mass of 1,420 and 2,346 Da, respectively (**Figure 3C**).

The molecular identities of peak A (TS-tetra) and peak B (TS-tetra-DS-tetra) were verified after subjecting them to enzymatic digestion and further analysis of the resultant fragments. For this purpose, a *D,L*-endopeptidase, CwlO, from *Bacillus subtilis* that cleaves between D-Glu and mDAP within the stem peptide of PG was used (Yamaguchi et al., 2004). A hexahistidine-tagged truncated version of CwlO ($cwlO^{340-473}$-His_6) was cloned, purified, and shown to be active against the purified fraction of TS-tetra and TS-tetra-DS-tetra (**Figure 3D**). The molecular mass

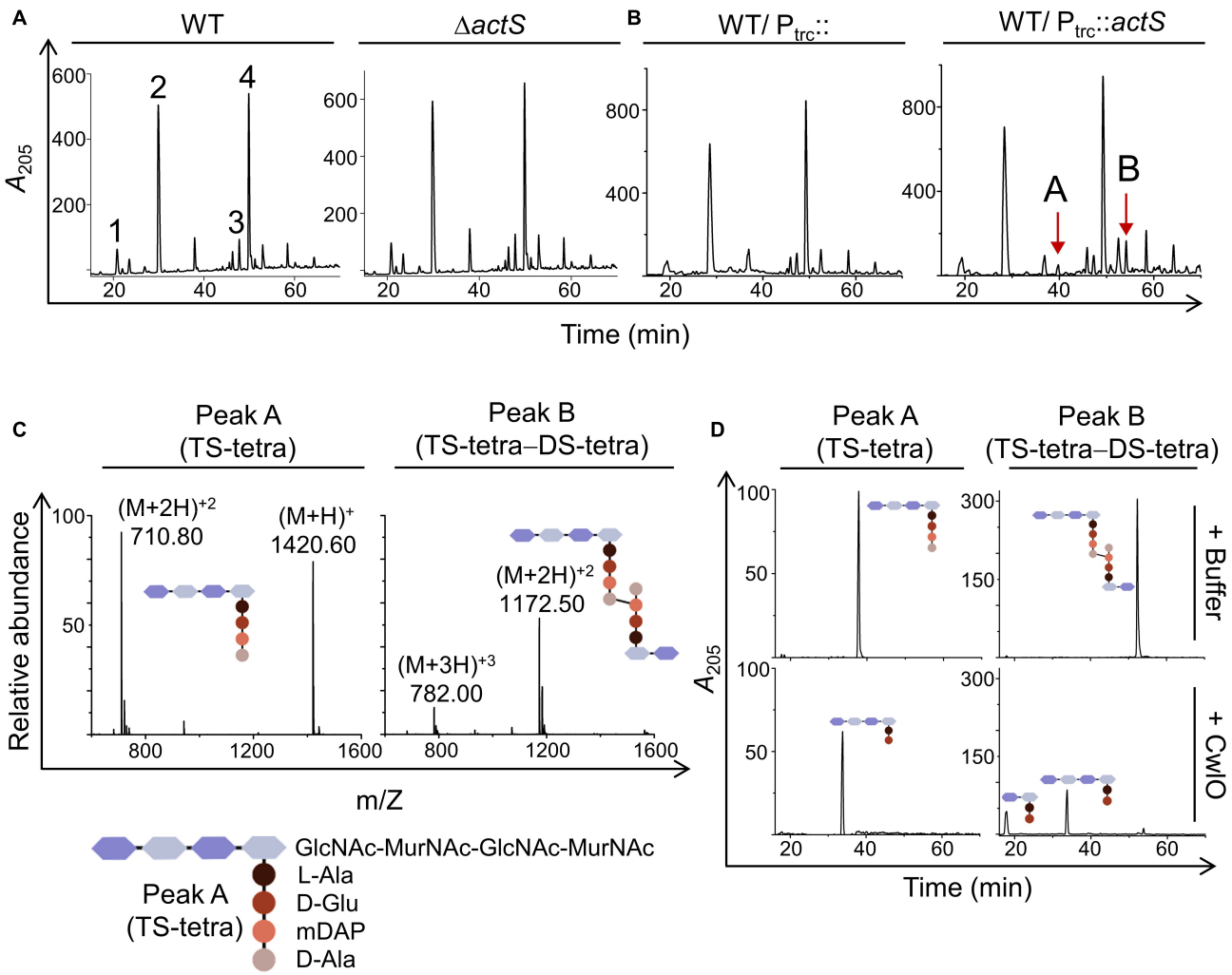

FIGURE 3 | Effect of *actS* on the composition of PG. **(A)** HPLC chromatograms depicting the PG composition of WT and Δ*actS* mutant. Peak 1: disaccharide tripeptide (tri), peak 2: disaccharide tetrapeptide (tetra), peak 3: tri-tetra (3-3), peak 4 - tetra-tetra (4-3). **(B)** HPLC chromatograms depicting the PG composition of cells overexpressing ActS. The additional muropeptide peaks are represented as peaks A and B. **(C)** Mass spectra of peaks A and B with molecular mass of 1,420 Da [$(M + 2H)^{+2}$ of 710.80 Da] and 2,346 Da [$(M + 2H)^{+2}$ of 1,172.50 Da], respectively. Peak A is tetrasaccharide tetrapeptide (TS-tetra), whereas peak B is tetrasaccharide tetrapeptide cross-linked to disaccharide tetrapeptide (TS-tetra-DS-tetra). Structures are depicted in the inset. **(D)** Purified TS-tetra and TS-tetra-DS-tetra were incubated either with buffer or purified CwlO (5 μM) for 20 h at 30°C and separated by RP-HPLC.

of the resultant peaks after CwlO cleavage was determined by MS analysis, which further validated the identity of peaks A and B to be TS-tetra and TS-tetra-DS-tetra, respectively. The presence of these non-canonical muropeptides allowed us to infer that the PG sacculi of *actS*-overexpressed cells contain partly denuded glycan chains which can only be produced by the activity of amidases. The above results suggested that ActS either can be an amidase or may activate other amidase(s).

ActS Has No Detectable Peptidoglycan Hydrolytic Activity

To examine whether ActS has any activity on PG sacculi or soluble muropeptides, we cloned, overexpressed, and purified signal-less, hexahistidine-tagged ActS derivative [$ActS^{27-251}$-His_6] by Ni-NTA affinity chromatography. ActS was subjected to zymogram analysis in which a zone of clearance was observed indicating that ActS may either possess PG binding or cleavage activity (**Figure 4**). However, incubation of soluble muropeptides or intact PG sacculi with ActS did not show any cleavage activity under several reaction conditions (data not shown). To test whether the LysM domain is interfering with the biochemical activity, we made a construct overexpressing only the LytM domain of ActS and purified the truncated variant of ActS, $ActS^{130-251}$-His_6 ($ActS^{LytM}$). $ActS^{LytM}$ also displayed a zone of clearance in the zymogram assay (**Figure 4**) but did not exhibit any cleavage activity on soluble muropeptides or intact PG sacculi (data not shown). These results are consistent with

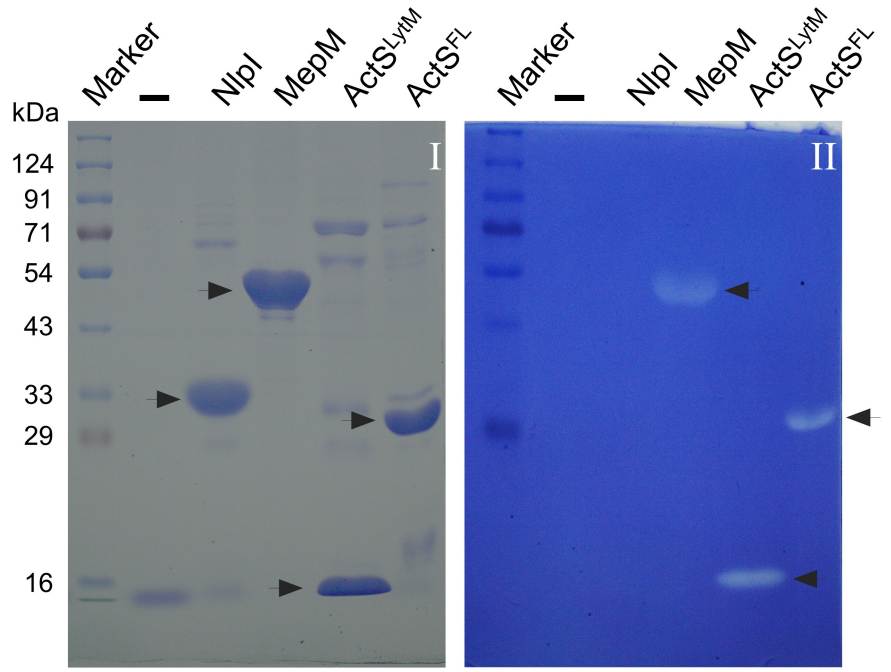

FIGURE 4 | Zymogram assay showing the activity of ActS. Indicated proteins were electrophoresed and the zymogram assay was done as described in the "Materials and Methods" section. Gel-I is stained with Coomassie blue and gel-II containing the *M. lysodeikticus* cells is stained with methylene blue. Purified ActS^{FL} (lane 6) and ActS^{LytM} (lane 5) exhibit zone of clearance. NlpI (lane 3), a lipoprotein serves as a negative control whereas MepM (lane 4) is a positive control.

the observation of ActS lacking two of the essential catalytic residues in the LytM domain (**Figure 1**; Uehara et al., 2010) and allowed us to conclude that ActS does not possess any PG hydrolytic activity.

ActS Activates the Division-Specific Amidase, AmiC

As ActS did not show amidase activity, we presumed that it may activate any of the division-specific amidases (AmiA, -B, and -C). To examine this possibility, we introduced pTRC99a-*actS* plasmid into single amidase deletion mutants lacking either *amiA*, *-B*, or *-C* and analyzed the composition of PG sacculi of these strains. The HPLC chromatograms clearly showed that the peaks corresponding to TS-tetra and TS-tetra-DS-tetra muropeptides were significantly lower in Δ*amiC* mutant compared to that of Δ*amiA* or Δ*amiB* mutants (**Figure 5A** and **Supplementary Table 1**). Additionally, these non-canonical muropeptides were completely absent in a Δ*amiABC* triple mutant overexpressing *actS* (**Figure 5A**). As the overproduction of ActS elicited lysis in WT cells (**Figure 2D**), we examined whether the lysis is mediated through any of these amidases. The viability assays indicated that the overexpression of *actS* confers sickness to AmiA and AmiB deletion mutants but not to AmiC deletion mutants (**Supplementary Figure 1A**). Accordingly, microscopic observations confirmed the lysis of WT, AmiA, and AmiB mutants but not that of AmiC mutant upon ActS overexpression (**Figure 5B**). Furthermore, cell morphology of various double amidase mutants (Δ*amiAB*, Δ*amiBC*, or Δ*amiAC*) overexpressing *actS* confirmed that the lysis is mostly mediated by AmiC (**Supplementary Figure 1B**). Altogether, these observations suggest that ActS predominantly activates the amidase, AmiC.

Since AmiC is a part of the divisomal complex that is recruited to the septum to facilitate cell–cell separation, ActS is also likely to be localized to the cell septa. Therefore, to examine the localization of ActS, we cloned it in the pBAD18-sfGFP vector under an arabinose-inducible promoter (P$_{ara}$::*actS-sfgfp*). **Figure 5C** shows septal localization of ActS-sfGFP mostly in cells having a deep and visible constriction at the mid-cell indicating ActS is a late-division protein. It has also been shown earlier that ActS (YgeR)–mCherry fusion exhibits weak septal localization (Uehara et al., 2009).

Activation of AmiC by ActS Is Not the Basis for Suppression of Δ*mepS* Growth Defect

As the above results indicated the activation of AmiC by ActS, next, we examined whether suppression of Δ*mepS* growth defects by overexpression of ActS is mediated through AmiC. For this purpose, we introduced *amiA*, *-B*, or *-C* single gene deletions into the Δ*mepS* mutant (to construct Δ*mepS* Δ*amiA*, Δ*mepS* Δ*amiB*, and Δ*mepS* Δ*amiC* double mutants) and examined the effect of *actS* overexpression on their growth. Interestingly, multiple copies of *actS* were able to suppress the NA-sensitivity of *mepS* deletion mutant lacking any of the amidase genes similar to that of *mepS* single mutant demonstrating that the suppression is not

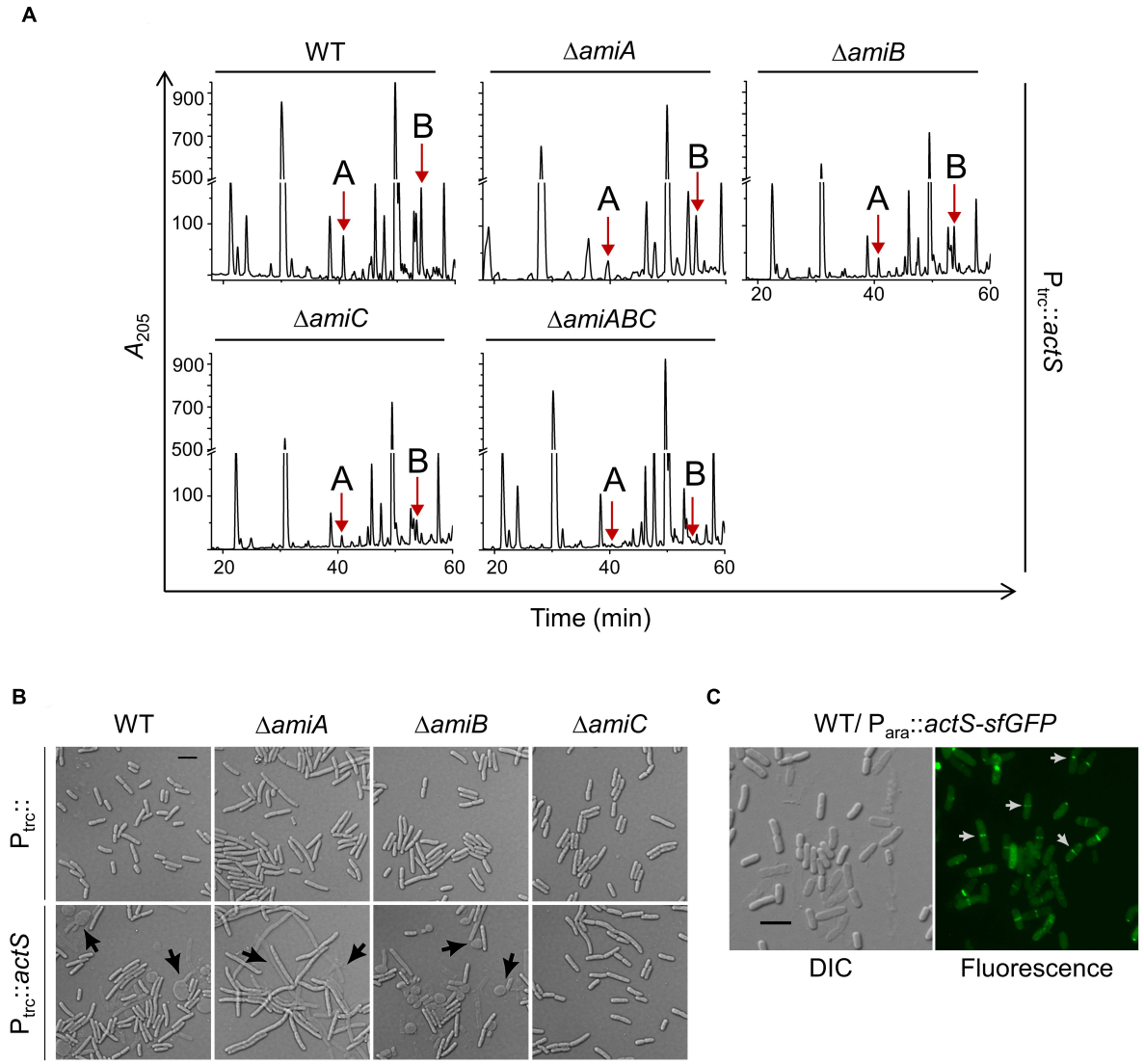

FIGURE 5 | Effect of ActS overexpression on WT and division-specific amidase mutants. **(A)** HPLC chromatograms depicting the PG composition of WT, Δ*amiA*, Δ*amiB*, Δ*amiC*, or Δ*amiABC* mutants with overexpressed *actS* (P_{trc}::*actS*). Strains were grown to an OD_{600} of ∼1 in LB containing 50 μM IPTG followed by isolation and analysis of PG sacculi. **(B)** The strains were grown overnight and diluted 1:100 into fresh LB broth supplemented with 50 μM IPTG and grown till OD_{600} of 0.5. Cells were collected and subjected to microscopy as described the "Materials and Methods" section. Arrows indicate cell lysis, and the scale bar represents 5 μm. **(C)** Localization of ActS-sfGFP was done in WT cells carrying pBAD18*actS*-sfGFP. Cells were grown with 0.2% arabinose and harvested at ∼0.4 OD and visualized by microscopy as described in the Materials and Methods. Arrows (in white) indicate ActS localization in cells with deep constriction. The scale bar represents 5 μm.

mediated through activation of any of these amidases (**Figure 6**). Moreover, plasmids overexpressing AmiA, -B, or -C did not rescue the Δ*mepS* mutant growth phenotypes corroborating the above observations (**Supplementary Figure 2**). These results ruled out the role of AmiA, -B, and -C in the suppression of Δ*mepS* mutant, implicating the existence of an alternative pathway as the basis of its growth rescue.

To examine whether the septal localization of ActS is important for the suppression of Δ*mepS* phenotype, we deleted the LysM domain of ActS, which is responsible for the septal recruitment (Poggio et al., 2010; Tsang et al., 2017) to construct a truncated version containing only the LytM domain (P_{trc}::$actS^{\Delta lysM}$ or $actS^{lytM}$). Multiple copies of $actS^{lytM}$ also suppressed Δ*mepS* growth defects like that of the WT *actS* allele (**Figure 7A**) and this suppression was independent of AmiA, -B, or -C (**Supplementary Figure 3**). Furthermore, PG analysis indicated that AmiC-derived non-canonical muropeptides (TS-tetra and TS-tetra-DS-tetra) were completely absent in cells overexpressing $actS^{lytM}$ (**Figure 7C**). In addition, overexpression of $actS^{lytM}$ did not elicit lysis in WT cells.

Next, to examine whether any active site residues of ActS are required for the suppression of Δ*mepS* phenotype, we

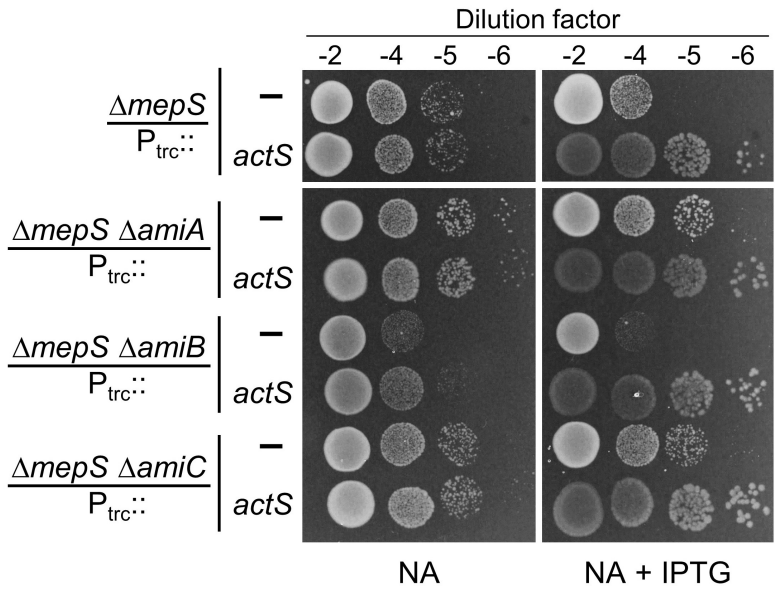

FIGURE 6 | Alleviation of Δ*mepS* growth defects by ActS is not mediated by AmiC. Indicated strains carrying empty vector (P_{trc}::) or vector encoding *actS* (P_{trc}::*actS*) were subjected to viability assay on NA plates with (20 μM) or without IPTG. For reasons not clear, loss of AmiA or AmiC conferred a subtle growth advantage to Δ*mepS* mutant.

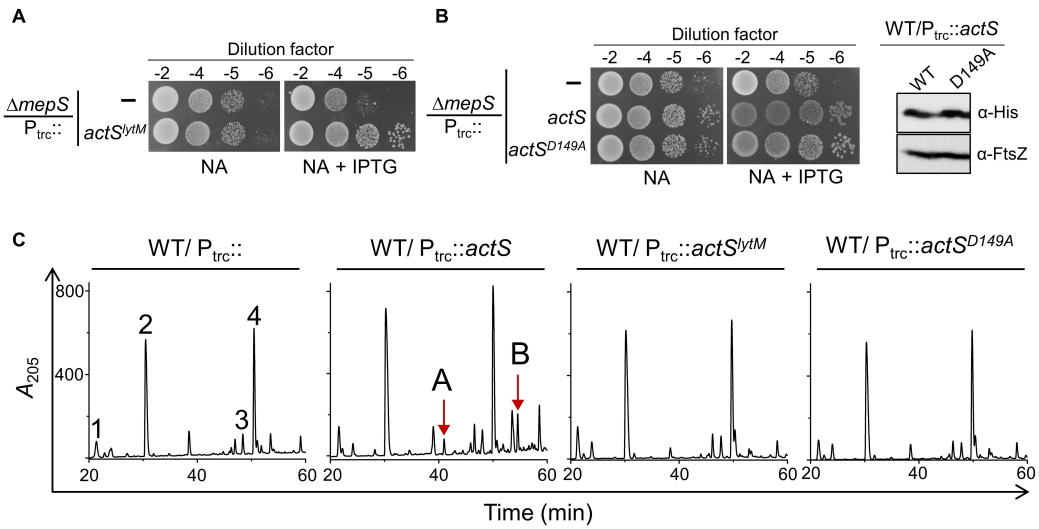

FIGURE 7 | Overexpression phenotypes of ActS variants. **(A)** Viability assay indicating the suppression of Δ*mepS* phenotype by $ActS^{LytM}$. **(B)** Viability assay indicating the suppression of Δ*mepS* phenotype by $ActS^{FL}$-His and $ActS^{D149A}$-His (B.1). Western blot showing the expression of $ActS^{WT}$-His and $ActS^{D149A}$-His induced with 20 μM IPTG (B.2). **(C)** HPLC chromatograms depicting the composition of PG of cells carrying either *actS* (P_{trc}::*actS*), $actS^{LytM}$ (P_{trc}::$actS^{LytM}$) or $actS^{D149A}$ (P_{trc}::$actS^{D149A}$). Strains were grown to an OD_{600} of ∼1 in LB containing 500 μM IPTG followed by isolation and analysis of PG sacculi.

constructed a variant of *actS* with an Aspartate149 residue substituted by alanine (pTRC99a-$actS^{D149A}$). In the LytM homolog of *Staphylococcus aureus*, the corresponding Asp214 residue is shown to be crucial for chelating a Zn^{2+} ion for its activity (Firczuk et al., 2005; Sabala et al., 2012). Similar to $actS^{lytM}$, overexpression of full-length *actS* containing D149A mutation compensated the loss of *mepS*, was unable to confer cell lysis, and failed to produce AmiC-derived muropeptides (**Figures 7B,C**). These observations showed that Asp149 residue and the septal localization are crucial to activate AmiC but not to rescue the growth defect of Δ*mepS* mutant.

The above results established that in addition to activating AmiC, ActS is capable of performing an alternate function that facilitates the growth of Δ*mepS* mutant. To examine whether ActS is functioning to activate any other known PG hydrolase of *E. coli*, we introduced single-gene deletions lacking either

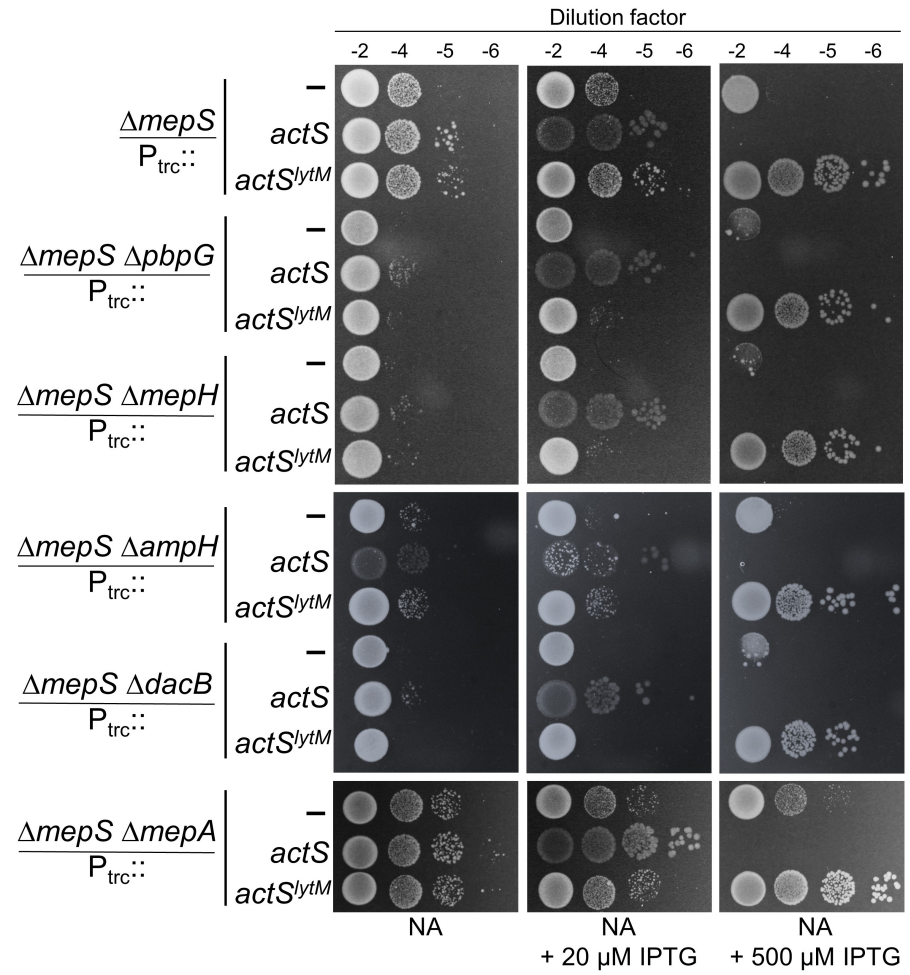

FIGURE 8 | Growth advantage to Δ*mepS* mutant by ActS is not mediated by *D,D*-endopeptidases. Δ*mepS* mutant and its derivatives carrying pTRC99a vector (P_{trc}::empty), vector encoding *actS* (P_{trc}::*actS*), or $actS^{lytM}$ (P_{trc}::$actS^{lytM}$) were grown in LB and tested for viability on NA plates supplemented with and without IPTG at 37°C.

D,D-endopeptidases (MepA, MepH, NlpC, YafL, AmpH, DacB, and PbpG), *L,D*-endopeptidases (MepK, LdtF), glycosylases (Slt, MltA, -B, -C, -D, -E, -F, -G, and DigH), or PG-recycling factors (AmpG, AmiD) into the Δ*mepS* mutant. However, the overexpression of *actS* or $actS^{lytM}$ alleviated the growth defects of all the double mutants like that of a single *mepS* deletion mutant (**Figure 8** and **Supplementary Figures 4–6**) showing that ActS does not function *via* any of these known PG hydrolases. These observations raise the possibility of ActS performing an alternate function that is independent of cell wall hydrolysis.

DISCUSSION

Escherichia coli contains a class of LytM factors encoded by *envC*, *nlpD*, *mepM*, and *actS* (formerly, *ygeR*). Of these, EnvC and NlpD facilitate cytokinesis by activating division-specific amidases, AmiA, AmiB, and AmiC, respectively (Uehara et al., 2010). In contrast, MepM is a 4-3 cross-link specific D,D-endopeptidase involved in PG enlargement (Singh et al., 2012). In this study, we show that ActS is an activator of the amidase, AmiC. In addition, we find that ActS is able to suppress the defects of an elongation-specific endopeptidase, MepS. Interestingly, these two activities of ActS are distinctive. ActS function has been recently elaborated by two other studies, where it has been shown to activate the amidases, AmiB and AmiC (Gurnani Serrano et al., 2021; Mueller et al., 2021).

We identified *actS* as its overexpression modestly suppressed the growth defects of a mutant lacking a major elongation-specific *D,D*-endopeptidase, MepS. Extensive genetic, molecular, and microscopic analyses revealed that ActS activates the division-specific amidase, AmiC. However, interestingly, the rescue of growth defects of Δ*mepS* mutant by ActS was not mediated by AmiC, but by a yet unknown mechanism. Domain-deletion experiments confirmed the requirement of the LysM domain of ActS for activation of AmiC, but not for alleviation of growth defects of

mepS mutant, clearly suggesting two distinct roles for ActS in PG metabolism.

Role of ActS in Septal Peptidoglycan Hydrolysis

ActS was earlier implicated to have a minor role in cell separation as deletion of *actS* somewhat exacerbated the chaining effect caused by the absence of the LytM domain factors, EnvC, NlpD, and MepM (Uehara et al., 2009). A recent study (Mueller et al., 2021) showed that ActS preferentially stimulates AmiB and to a lesser extent AmiC in cells grown under acidic pH conditions, and an accompanying study (Gurnani Serrano et al., 2021) demonstrated that ActS activates AmiC during envelope stress. In our study, we observed that the overexpression of ActS resulted in the formation of glycan strands lacking the peptide stems (**Figures 3B,C**). In addition, overexpression of ActS led to rapid cell lysis in the WT cells (**Figure 2D**). Both these overexpression phenotypes were significantly abolished in the absence of AmiC, thereby allowing us to conclude that ActS predominantly works *via* activation of AmiC (**Figures 5A,B**). All these studies collectively established that similar to other LytM-domain factors, EnvC and NlpD, ActS also functions to activate a sub-set of division-specific amidases.

It is known that AmiC is recruited to the midcell during division, and NlpD stimulates AmiC by displacing its alpha-helix, exposing the occluded active site of AmiC (Bernhardt and de Boer, 2003; Peters et al., 2013). However, the mechanism of stimulation of AmiC by ActS is not yet clear. Being a paralog of NlpD, ActS may also likely operate *via* an analogous mechanism. Similar to that of EnvC and NlpD, ActS is also a late-recruiter to the cell septum as ActS-GFP localizes exclusively to the deeply constricting cells (**Figure 5C**; Uehara et al., 2009). The requirement of the LysM domain of ActS for the activation of AmiC (**Figure 7C**; Tsang et al., 2017) suggests that septal localization is a prerequisite for its function. The essentiality of the aspartate-149 residue also indicates that coordination with a zinc residue is important for the activation of AmiC (**Figure 7C**).

An Alternate Role of ActS in Peptidoglycan Metabolism

The overexpression of ActS modestly rescued the growth defect of *mepS* deletion mutant on NA (**Figure 2B**); in addition, it weakly suppressed the growth defect of a mutant lacking both *mepS* and *mepM* indicating that ActS does not work through MepM (**Figure 2C**). However, *actS* deletion did not confer any discernible growth defect to Δ*mepS* or Δ*mepSM* deletion mutants under laboratory conditions. These results suggest that under normal physiological conditions, *actS* may not contribute significantly to PG expansion. Unlike ActS, overexpression of other division-specific LytM domain factors, EnvC and NlpD did not compensate for the loss of MepS, suggesting that the effect is specific only to ActS (**Supplementary Figure 7**). As we and others have clearly shown that ActS does not possess any biochemical activity (Gurnani Serrano et al., 2021; Mueller et al., 2021), and also that the LysM domain is not important for the rescue of MepS mutant, we presumed that overexpression of ActS may activate another PG hydrolase either directly, or indirectly *via* induction of a stress response pathway. We extensively tested the role of all known PG hydrolases in the suppression of *mepS* phenotypes by ActS overexpression (**Figure 8** and **Supplementary Figures 4–6**); however, none of these were found to be the candidates suggesting ActS may modulate yet another effector in *E. coli*. In this context, a previous study showed that ActS-mCherry displays a patchy peripheral localization in addition to a weak septal localization in cells with a deep constriction (Uehara et al., 2009). This pattern of peripheral localization correlates well with our observations of ActS having a dual role, one to activate AmiC at the septum and an alternate activity that is independent of its septal localization. Further efforts are required to uncover the basis of suppression of Δ*mepS* growth defects by ActS.

DATA AVAILABILITY STATEMENT

The original contributions presented in this study are included in the article/**Supplementary Material**, further inquiries can be directed to the corresponding author.

AUTHOR CONTRIBUTIONS

PC, RA, and MR conceived to the study. PC, RB, and RA performed the experiments. PC and MR analyzed the data and wrote the manuscript. All authors contributed to the article and approved the submitted version.

FUNDING

This work was supported by the funds from the Council of Scientific and Industrial Research (MLP0141) and the Department of Biotechnology, Ministry of Science and Technology (BT/PR33064/BRB/10/1819/2019), Government of India (to MR). We also acknowledge financial support from the University Grants Commission of India (to PC) and the Department of Biotechnology (to RB).

ACKNOWLEDGMENTS

We thank NBRP: *E. coli* for Keio collection and ASKA plasmid library, V. Krishna Kumari for HPLC, B. Raman and Y. Kameshwari for mass spectrometry analysis, and Asmita Sarowgi for helping with the plasmid constructions.

SUPPLEMENTARY MATERIAL

The Supplementary Material for this article can be found online at: https://www.frontiersin.org/articles/10.3389/fmicb.2022.913949/full#supplementary-material

REFERENCES

Anantharaman, V., and Aravind, L. (2003). Evolutionary history, structural features and biochemical diversity of the NlpC/P60 superfamily of enzymes. *Genome Biol.* 4:R11. doi: 10.1186/gb-2003-4-5-p3

Baba, T., Ara, T., Hasegawa, M., Takai, Y., Okumura, Y., Baba, M., et al. (2006). Construction of *Escherichia coli* K-12 in-frame, single-gene knockout mutants: the Keio collection. *Mol. Syst. Biol.* 2:2006.0008. doi: 10.1038/msb4100050

Bernhardt, T. G., and de Boer, P. A. (2003). The *Escherichia coli* amidase AmiC is a periplasmic septal ring component exported *via* the twin-arginine transport pathway. *Mol. Microbiol.* 48, 1171–1182. doi: 10.1046/j.1365-2958.2003.03511.x

Bernhardt, T. G., and de Boer, P. A. (2004). Screening for synthetic lethal mutants in *Escherichia coli* and identification of EnvC (YibP) as a periplasmic septal ring factor with murein hydrolase activity. *Mol. Microbiol.* 52, 1255–1269. doi: 10.1111/j.1365-2958.2004.04063.x

Bouhss, A., Trunkfield, A. E., Bugg, T. D., and Mengin-Lecreulx, D. (2008). The biosynthesis of peptidoglycan lipid-linked intermediates. *FEMS Microbiol. Rev.* 32, 208–233. doi: 10.1111/j.1574-6976.2007.00089.x

Datsenko, K. A., and Wanner, B. L. (2000). One-step inactivation of chromosomal genes in *Escherichia coli* K-12 using PCR products. *Proc. Natl. Acad. Sci. U.S.A.* 97, 6640–6645. doi: 10.1073/pnas.120163297

Di Tommaso, P., Moretti, S., Xenarios, I., Orobitg, M., Montanyola, A., Chang, J. M., et al. (2011). T-Coffee: a web server for the multiple sequence alignment of protein and RNA sequences using structural information and homology extension. *Nucleic Acids Res.* 39, W13–W17. doi: 10.1093/nar/gkr245

Firczuk, M., Mucha, A., and Bochtler, M. (2005). Crystal structures of active LytM. *J. Mol. Biol.* 354, 578–590. doi: 10.1016/j.jmb.2005.09.082

Garde, S., Chodisetti, P. K., and Reddy, M. (2021). Peptidoglycan: structure, synthesis, and regulation. *EcoSal Plus* 9. doi: 10.1128/ecosalplus.ESP-0010-2020

Glauner, B., Höltje, J. V., and Schwarz, U. (1988). The composition of the murein of *Escherichia coli*. *J. Biol. Chem.* 263, 10088–10095.

Gurnani Serrano, C. K., Winkle, M., Martorana, A. M., Biboy, J., Morè, N., Moynihan, P., et al. (2021). ActS activates peptidoglycan amidases during outer membrane stress in *Escherichia coli*. *Mol. Microbiol.* 116, 329–342. doi: 10.1111/mmi.14712

Hara, H., Abe, N., Nakakouji, M., Nishimura, Y., and Horiuchi, K. (1996). Overproduction of penicillin-binding protein 7 suppresses thermosensitive growth defect at low osmolarity due to an *spr* mutation of *Escherichia coli*. *Microb. Drug Resist.* 2, 63–72. doi: 10.1089/mdr.1996.2.63

Heidrich, C., Templin, M. F., Ursinus, A., Merdanovic, M., Berger, J., Schwarz, H., et al. (2001). Involvement of N-acetylmuramyl-L-alanine amidases in cell separation and antibiotic-induced autolysis of *Escherichia coli*. *Mol. Microbiol.* 41, 167–178. doi: 10.1046/j.1365-2958.2001.02499.x

Höltje, J. V. (1998). Growth of the stress-bearing and shape-maintaining murein sacculus of *Escherichia coli*. *Microbiol. Mol. Biol. Rev.* 62, 181–203. doi: 10.1128/MMBR.62.1.181-203.1998

Kitagawa, M., Ara, T., Arifuzzaman, M., Ioka-Nakamichi, T., Inamoto, E., Toyonaga, H., et al. (2005). Complete set of ORF clones of *Escherichia coli* ASKA library (a complete set of *E. coli* K-12 ORF archive): unique resources for biological research. *DNA Res.* 12, 291–299. doi: 10.1093/dnares/dsi012

Levin, P. A., and Janakiraman, A. (2021). Localization, assembly, and activation of the *Escherichia coli* cell division machinery. *EcoSal Plus* 9:eES00222021. doi: 10.1128/ecosalplus.ESP-0022-2021

Miller, J. H. (1992). *A Short Course in Bacterial Genetics: A Laboratory Manual and Handbook for Escherichia coli and Related Bacteria*. Cold Spring Harbor, NY: Cold Spring Harbor Laboratory.

Mueller, E. A., Iken, A. G., Öztürk, M. A., Winkle, M., Schmitz, M., Vollmer, W., et al. (2021). The active repertoire of *Escherichia coli* peptidoglycan amidases varies with physiochemical environment. *Mol. Microbiol.* 116, 311–328. doi: 10.1111/mmi.14711

Peters, N. T., Morlot, C., Yang, D. C., Uehara, T., Vernet, T., and Bernhardt, T. G. (2013). Structure-function analysis of the LytM domain of EnvC, an activator of cell wall remodelling at the *Escherichia coli* division site. *Mol. Microbiol.* 89, 690–701. doi: 10.1111/mmi.12304

Poggio, S., Takacs, C. N., Vollmer, W., and Jacobs-Wagner, C. (2010). A protein critical for cell constriction in the Gram-negative bacterium *Caulobacter crescentus* localizes at the division site through its peptidoglycan-binding LysM domains. *Mol. Microbiol.* 77, 74–89. doi: 10.1111/j.1365-2958.2010.07223

Sabala, I., Jonsson, I. M., Tarkowski, A., and Bochtler, M. (2012). Anti-staphylococcal activities of lysostaphin and LytM catalytic domain. *BMC Microbiol.* 12:97. doi: 10.1186/1471-2180-12-97

Singh, S. K., Parveen, S., SaiSree, L., and Reddy, M. (2015). Regulated proteolysis of a cross-link–specific peptidoglycan hydrolase contributes to bacterial morphogenesis. *Proc. Natl. Acad. Sci. U.S.A.* 112, 10956–10961. doi: 10.1073/pnas.1507760112

Singh, S. K., SaiSree, L., Amrutha, R. N., and Reddy, M. (2012). Three redundant murein endopeptidases catalyse an essential cleavage step in peptidoglycan synthesis of *Escherichia coli* K12. *Mol. Microbiol.* 86, 1036–1051. doi: 10.1111/mmi.12058

Tsang, M. J., Yakhnina, A. A., and Bernhardt, T. G. (2017). NlpD links cell wall remodeling and outer membrane invagination during cytokinesis in *Escherichia coli*. *PLoS Genet.* 13:e1006888. doi: 10.1371/journal.pgen.1006888

Uehara, T., Dinh, T., and Bernhardt, T. G. (2009). LytM-domain factors are required for daughter cell separation and rapid ampicillin-induced lysis in *Escherichia coli*. *J. Bacteriol.* 191, 5094–5107. doi: 10.1128/JB.00505-09

Uehara, T., Parzych, K. R., Dinh, T., and Bernhardt, T. G. (2010). Daughter cell separation is controlled by cytokinetic ring-activated cell wall hydrolysis. *EMBO J.* 29, 1412–1422. doi: 10.1038/emboj.2010.36

Vollmer, W., Blanot, D., and de Pedro, M. A. (2008). Peptidoglycan structure and architecture. *FEMS Microbiol. Rev.* 32, 149–167. doi: 10.1111/j.1574-6976.2007.00094.x

Yamaguchi, H., Furuhata, K., Fukushima, T., Yamamoto, H., and Sekiguchi, J. (2004). Characterization of a new *Bacillus subtilis* peptidoglycan hydrolase gene, *yvcE* (named *cwlO*), and the enzymatic properties of its encoded protein. *J. Biosci. Bioeng.* 98, 174–181. doi: 10.1016/S1389-1723(04)00262-2

Conflict of Interest: The authors declare that the research was conducted in the absence of any commercial or financial relationships that could be construed as a potential conflict of interest.

frontiers | Frontiers in Microbiology

TYPE Original Research
PUBLISHED 19 October 2022
DOI 10.3389/fmicb.2022.920117

OPEN ACCESS

EDITED BY
Iain G. Duggin,
University of Technology Sydney, Australia

REVIEWED BY
Paolo Natale,
Complutense University of Madrid, Spain
George Liechti,
Uniformed Services University of the Health Sciences, United States

*CORRESPONDENCE
Deepak Anand
deepak.anand@biol.lu.se

†These authors have contributed equally to this work

SPECIALTY SECTION
This article was submitted to Microbial Physiology and Metabolism, a section of the journal Frontiers in Microbiology

RECEIVED 14 April 2022
ACCEPTED 26 September 2022
PUBLISHED 19 October 2022

CITATION
Anand D, Jakkala K, Nair RR, Sharan D, Pradhan A, Mukkayyan N and Ajitkumar P (2022) Complete identity and expression of StfZ, the *cis*-antisense RNA to the mRNA of the cell division gene *ftsZ*, in *Escherichia coli*. *Front. Microbiol.* 13:920117. doi: 10.3389/fmicb.2022.920117

Complete identity and expression of StfZ, the *cis*-antisense RNA to the mRNA of the cell division gene *ftsZ*, in *Escherichia coli*

Deepak Anand[1,2]*, Kishor Jakkala[1,3†], Rashmi Ravindran Nair[1,4†], Deepti Sharan[1,5†], Atul Pradhan[1,6†], Nagaraja Mukkayyan[1,7†] and Parthasarathi Ajitkumar[1]

[1]Department of Microbiology and Cell Biology, Indian Institute of Science, Bengaluru, India, [2]Department of Biology, Lund University, Lund, Sweden, [3]Department of Microbiology and Immunology, Emory University School of Medicine, Atlanta, GA, United States, [4]Department of Microbiology, University of Alabama at Birmingham, Birmingham, AL, United States, [5]Department of Microbiology, The University of Chicago, Chicago, IL, United States, [6]Department of Medicine, Renaissance School of Medicine, Stony Brook University, Stony Brook, NY, United States, [7]Department of Microbial Pathogenesis, University of Maryland, Baltimore, MD, United States

Bacteria regulate FtsZ protein levels through transcriptional and translational mechanisms for proper cell division. A *cis*-antisense RNA, StfZ, produced from the *ftsA-ftsZ* intergenic region, was proposed to regulate FtsZ level in *Escherichia coli*. However, its structural identity remained unknown. In this study, we determined the complete sequence of StfZ and identified the isoforms and its promoters. We find that under native physiological conditions, StfZ is expressed at a 1:6 ratio of StfZ:*ftsZ* mRNA at all growth phases from three promoters as three isoforms of 366, 474, and 552 nt RNAs. Overexpression of StfZ reduces FtsZ protein level, increases cell length, and blocks cell division without affecting the *ftsZ* mRNA stability. We did not find differential expression of StfZ under the stress conditions of heat shock, cold shock, or oxidative stress, or at any growth phase. These data indicated that the *cis*-encoded StfZ antisense RNA to *ftsZ* mRNA may be involved in the fine tuning of *ftsZ* mRNA levels available for translation as per the growth-phase-specific requirement at all phases of growth and cell division.

KEYWORDS

***Escherichia coli*, StfZ *cis*-antisense RNA, *ftsZ* mRNA, FtsZ level, cell division**

Introduction

FtsZ is an essential protein for cell division and cytoskeletal integrity in most bacteria (Dai and Lutkenhaus, 1991; Pla et al., 1991; Löwe et al., 2004; Shih and Rothfield, 2006). In *Escherichia coli*, the ratio between FtsZ and FtsA molecules (5:1) (Rueda et al., 2003) is important for proper cell division (Ward and Lutkenhaus, 1985; Dai and Lutkenhaus, 1992; Dewar et al., 1992). It was shown that a 2- to 7-fold increase in FtsZ level results

in mini-cell formation, due to additional division events, whereas further higher levels or lower than normal levels cause filamentation due to imbalance in the FtsZ: FtsA stoichiometry (Bi and Lutkenhaus, 1990; Wang and Gayda, 1990). Thus, regulation of FtsZ level is crucial for proper cell division. The regulation of *ftsZ* occurs at the transcriptional and translational levels (Aldea et al., 1990; Cam et al., 1996; Flärdh et al., 1997; Flynn et al., 2003; Tamura et al., 2006; Camberg et al., 2009).

Trans-acting small non-coding antisense RNAs (asRNAs), which are usually encoded in the intergenic regions on the chromosome, control translation, or degradation of their target mRNAs. Generally, each trans-acting non-coding asRNA has multiple target mRNAs and binds near their ribosomal binding site (Saberi et al., 2016). A structural change in the non-coding RNA occurs through binding to small metabolites (riboswitches) or through a change of temperature (thermoregulators) or pH (pH sensors) (Saberi et al., 2016). In both cases, elevated temperature caused the phenotypic effects of asRNAs. One such asRNA, DicF, against *ftsZ* has been found to influence FtsZ protein level in certain strains of *Escherichia coli* (Tétart and Bouché, 1992). Besides DicF, Dewar and Donachie had proposed the expression of StfZ *cis*-asRNA, from the 60-bp spacer sequence and extending into the 5′ portion of *ftsZ*, which blocks cell division when placed in a high copy number plasmid at 42°C (Dewar and Donachie, 1993). However, StfZ was not studied further for its expression levels or promoters controlling its expression. Since regulation of the principal cell division gene *ftsZ* is crucial for cell division control, it is important to elucidate the mode of action and physiological role of StfZ *cis*-asRNA in *E. coli* cell division.

This study establishes the complete sequence of StfZ, its growth-phase-dependent expression, the stoichiometry of its expression with *ftsZ* mRNA, and its role in cell division. We showed that StfZ RNA has three isoforms transcribed from three promoters. The three isoforms are expressed at relatively similar levels. Further, we investigated its influence on FtsZ level and thereby on cell division. The generation of a knockout or deletion mutant of the *stfZ* was not possible as the StfZ sequence is overlapping with the sequence of the essential cell division gene, *ftsZ*. Nevertheless, the observations reported in this study show the expression of natural antisense RNA isoforms of StfZ as a novel factor that affects *ftsZ* mRNA level and thereby FtsZ protein level, as per the demand for growth and cell division in *E. coli*.

Materials and methods

Bacterial strains, plasmids, and growth

Bacterial strains and plasmids are listed in **Supplementary Tables 1**, **2**, respectively. All the strains were cultured in Luria-Bertani broth or agar for growth. Strains with plasmids were selected on ampicillin (100 μg/ml) or kanamycin (25 μg/ml). For StfZ, induction cultures were grown at 30°C and shifted to 37 or 42°C as per the experiment. All the cultures were balanced for OD and volume for the induction and stress experiments.

cDNA preparation

RNA was isolated using hot phenol method (Wecker, 1959; Roy et al., 2004). In brief, cells were lysed in lysis buffer (**Supplementary Table 3**). The aqueous phase of RNA was extracted with hot phenol (65°C, pH 5.2) followed by phenol: chloroform and chloroform extractions. RNA was precipitated and dissolved in RNase-free water. RNA preparations were treated with DNase-I which was verified using PCR for a 16S rRNA gene (Condon et al., 1995). RNA samples were loaded on 1% formaldehyde agarose gel to check the quality of RNA. cDNA was prepared using 5 μg total RNA with RevertAid-Premium Reverse Transcriptase kit (Fermentas). For each reaction, 20 pmoles of gene-specific reverse primer were added and annealed at 55°C for 10 min, followed by the addition of reverse transcriptase for extension at 55°C for 60 min. The reaction was stopped by incubating at 85°C for 10 min. The cDNA preparation was used for RT-PCR and quantitative PCR.

RT-PCR and real-time polymerase chain reaction

RevertAid-Premium Reverse-Transcriptase kit and Evagreen real-time PCR master mix (GBiosciences) were used for RT-PCR and real-time PCR, respectively (Wang et al., 2006). Primers ODA-01 and ODA-02 for StfZ, ODA-03 and ODA–04 for 16S rRNA, ODA–05 and ODA–06 for *ftsZ*, ODA–09 and ODA–10 for *mutgfp*, ODA–11 with ODA–12 for *ftsA*, ODA–40 and ODA–41 for *csp*A, ODA–42 and ODA–43 for *rpo*H, and ODA–44 and ODA–45 for *kat*G (**Supplementary Table 4**) were used. StfZ ODA–46 and ODA–47 for region "a," ODA–48- and ODA–49 for region "b," and ODA–50 and ODA–51 for region "c" were used for real-time PCR for the differential amounts of the three isoforms of StfZ RNA (**Supplementary Table 4**). Reactions were performed as per the described protocols. The cDNA of 16S rRNA was used as the normalisation control (Condon et al., 1995). Real-time PCR was performed in Applied Biosystems-ViiA7. The $2^{-\Delta\Delta Ct}$ method was used for quantitation (Livak and Schmittgen, 2001; Giangrossi et al., 2010). The fold changes of expression were presented as expressions relative to the control sample.

Stress induction

We tested heat-shock (46°C) (Grossman et al., 1984), cold-shock (16°C) (Etchegaray et al., 1996), and oxidative stress

(5 mM H_2O_2) (Schellhorn, 1995) conditions in WT cells from mid-log (OD 0.6). Cells were grown at 30°C to mid-log (OD 0.6) and then split into four sets. Each set was then exposed to 30 min of stress condition or untreated condition. Real-time PCR was performed for StfZ and *fts*Z mRNA. Corresponding known gene expression was also included for confirmation of the occurrence of stress responses. For heat shock response, *rpo*H expression; for cold shock, *csp*A expression and oxidative stress *kat*G expression were measured by real-time PCR (Grossman et al., 1984; Schellhorn, 1995; Etchegaray et al., 1996). For the gene expression control, expression level from the uninduced culture was used.

Primer extension assay

Primer extension assay was performed using 30 μg of total RNA isolated from *E. coli* K12 cells (Blattner et al., 1997) of 0.3 OD_{600nm} (OD). Primers, ODA-07 and ODA-08, were radiolabelled with [γ-^{32}P]-ATP using T4-polynucleotide kinase kit (Fermentas). Labelled primers were purified with Sephadex G-50 column, annealed to RNA, and extended at 55°C with 200 U of RevertAid-Premium Reverse-transcriptase for 60 min. Primer extension products were denatured at 95°C and fractionated on 8% polyacrylamide gel containing 7 M urea. A parallel manual sequencing reaction was performed using CycleReader^{TM} DNA Sequencing Kit (Fermentas) and loaded in the lane next to the PE reaction. The PCR product template for sequencing was generated using primer ODA-13 in combination with ODA-08 or ODA-07 (**Supplementary Table 4**). Autoradiography was performed using a phosphorimager after 24 h of exposure to the sample.

Molecular cloning

The oligonucleotide primers used in cloning are listed in **Supplementary Table 4** and the plasmids are listed in **Supplementary Table 2**.

pDA1

Linear 3′ RACE product was treated with T4 polynucleotide kinase and then ligated to *Eco*RV site in pBS(KS) (Alting-Mees and Short, 1989).

pDA2, pDA3, pDA4, pDA5, pDA6, and pDA7

StfZ promoters were cloned using oligonucleotide annealing method (Arumugam et al., 2012). For pDA2, ODA-16 and ODA–17, for pDA4, ODA-18 and ODA-19, and for pDA6, ODA–20 and ODA–21 oligos were annealed and cloned at *Kpn*I and *Bam*HI site in pFPV27 (Valdivia and Falkow, 1996). Similarly in case of −10 element deletion, for pDA3, ODA–22 and ODA–23, for pDA5, ODA–24 and ODA–25 for pDA7 ODA–26 and ODA–27 oligos were used.

pDA8

The entire region spanning the promoters P1 to P3 (including the −10 and −35 elements of the respective promoters) was amplified using ODA–28 and ODA–29 (**Supplementary Table 4**) and cloned between the *Kpn*I and *Bam*HI sites in the promoter probe vector, pFPV27.

pDA9

Region of *stfZ* was amplified from *E. coli* genomic DNA using primer ODA–14 and ODA–15. PCR product was digested with *Kpn*I and *Xba*I and ligated to pBS(KS) vector at the same sites.

pDA10

Cloning was performed by a reverse PCR on pDA9 using primer ODA–32 and ODA–33. The linear product was self-ligated after polynucleotide kinase treatment.

pDA11, pDA12, and pDA13

For substitution mutations of promoters, pDA11, ODA–34, and ODA–35; for pDA12, ODA–36, and ODA–37; and for pDA13, ODA–38, and ODA–39 were annealed and cloned at *Kpn*I and *Bam*HI site in pFPV27.

Promoter assay

Putative StfZ promoters and its entire-10 region deletion mutation or substitution mutation constructs (**Supplementary Table 2**) were expressed from JM109 strain (Yanisch-Perron et al., 1985) (**Supplementary Table 1**). cDNAs for *mutgfp* were synthesised using primer ODA–10 from total RNA isolated from the promoter construct transformants grown to the mid-log phase (0.6 OD). Promoter activity was quantitated using real-time PCR for *mutgfp* mRNA. cDNA was synthesised with ODA–10 oligo, and PCR was performed using the combination of ODA–09 and ODA–10 (**Supplementary Table 4**).

3′ rapid amplification of cDNA ends

Twenty micrograms of total RNA from 0.5 $OD_{600\ nm}$ culture was enriched for total mRNA using Ribominus^{TM} Transcriptome Isolation kit (Invitrogen K1550–03). The 5′ phosphorylated ODA–30 oligo (**Supplementary Table 4**) was ligated to the 3′ ends of ribominus RNA using T4 RNA ligase. The cDNA was synthesised with the complementary oligo ODA–31 (**Supplementary Table 4**). StfZ-specific cDNA was PCR amplified using ODA–01 and ODA–31 primers, using standard conditions. The PCR product was gel eluted and cloned in pBS(KS). The insert was sequenced.

Northern hybridisation

RNA probe was generated against the *stfZ* region by *in vitro* transcription from *Kpn*I digested pDA9 plasmid. HiScribe™ T7 High Yield RNA synthesis kit (NEB, Gothenburg, Sweden) was used as per the manufacturer's protocol with Biotin Labelling RNA Mix (Roche, Solna, Sweden) to obtain the *stfZ* complementary probe. About 100 μg total RNA from PAK02 and PAK12 strains (0.2 OD) were fractionated on 10% polyacrylamide denaturing gel with 7 M urea. RNA was blotted to a positively charged nylon membrane (BrightStar-™Plus, ThermoFischer Scientific, Gothenburg, Sweden). The membrane was subjected to UV cross-linking (1200 μJ/cm^2 for 20 min). The membrane was blocked in a pre-hybridisation buffer (**Supplementary Table 3**) at 60°C for 3 h. Pre-hybridisation buffer was replaced with hybridisation buffer containing 5 μg biotin-labelled RNA probe (denatured at 65°C for 5 min and snap-chilled on ice) and incubated overnight at 60°C. The nylon membrane was washed thrice with wash buffer (1x SSC containing 0.1% SDS) for 15 min each, at room temperature. The membrane was then blocked for 15 min and incubated with streptavidin-HRP conjugate (Invitrogen) (1:10,000 dilution) for 15 min. The membrane was washed and developed using Clarity Western ECL Substrate (Bio-Rad, Solna, Sweden).

Measurement of YFP fluorescence

The culture PAK13 was grown at 30°C and induced at 0.6 OD with either 0.1% arabinose (for *ftsZ-yfp* mRNA) or with 0.1% arabinose and 1 mM IPTG (for StfZ RNA) simultaneously. At 120 min of induction, the cells were placed on a glass slide and imaged for YFP fluorescence. Expression of FtsZ-YFP was measured from the cells and normalised to the area of the cell.

Immunofluorescence microscopy

Immunofluorescence microscopy was performed as described (Addinall et al., 1996), with a few modifications. The harvested cells were fixed with 0.4% paraformaldehyde and 0.25% glutaraldehyde solution for 10 min at room temperature and 50 min on ice. The cells were washed with 1x PBS (pH 7.4) (**Supplementary Table 3**), layered over poly-L-lysine (0.1%, w/v) coated multi-well slide, permeabilised with 2 mg/ml of lysozyme (Sigma), blocked with BSA (2% w/v in PBS), followed by incubation with 1:500 dilution of affinity-purified rabbit polyclonal anti-FtsZ antibody overnight at 4°C in a humid chamber. The cells were washed five times with 1x PBS, followed by 60 min incubation with 1:1000 dilution of Cy3 anti-rabbit IgG antibody (0.1 μg/ml; Sigma, Bengaluru, India). The cells were washed again with 1x PBST (**Supplementary Table 3**) and incubated with 0.5 μg/ml DAPI for 5 min. DAPI was washed off with 1x PBST solution and cells were mounted with 80% glycerol. Images were taken under the Zeiss AxioImager M1 fluorescence microscope. AxioVision software was used for size measurements and image processing.

Western blotting

Total protein (30 μg) was fractionated on 10% polyacrylamide gel and blotted onto a methanol-activated PVDF membrane. PVDF membrane was blocked overnight in blocking buffer (**Supplementary Table 3**) at 4°C. The blocking buffer was replaced with rabbit anti-FtsZ primary antibody (1:10000) solution for FtsZ or rabbit anti-RRF primary antibody (1:20000) solution for RRF. The membrane blots were washed and incubated with 1:10000 diluted anti-rabbit goat IgG (Sigma, Solna, Sweden) (Srivastava et al., 2016). The blots were washed and developed with X-ray film (Kodak) or chemiluminescence imager (ImageQuant LAS 4000) using Clarity Western ECL Substrate (Bio-Rad, Solna, Sweden).

SYTO9/PI staining

SYTO9 and propidium iodide (PI) were prepared according to the manufacturer's instructions [Live/Dead Bacterial Kit, Molecular Probes, Gothenburg, Sweden (Brantl, 2007)]. Cells in 50 μl of culture were stained with 0.1 mM SYTO9/PI mix for 15 min in dark at 25°C, washed with PBS solution, and images were taken with excitation and emission of 483/503 nm for SYTO9 and 485/630 nm for PI.

Statistical analysis for significance

Statistical analysis of significance was performed between two data sets in a two-tailed *t*-test. The *p*-values range were indicated with asterisks ($^*p < 0.05$, $^{**}p < 0.01$, $^{***}p < 0.001$).

Results

StfZ RNA is expressed at all growth phases

We determined the presence of StfZ transcript in *E. coli* K12 cells from 0.2 (early log phase) to 2.5 (late stationary phase) $OD_{600\ nm}$ (hereinafter called OD) cultures. RT-PCR analysis, performed using ODA-01 and ODA-02 primers located across the intergenic region of *ftsA* and *ftsZ*, showed the presence of 177 bp RT-PCR product from all the growth phases (**Figure 1A**). Cloning and sequencing of the StfZ RT-PCR product confirmed that StfZ is transcribed at all growth phases in a pattern of intensity that is growth phase dependent.

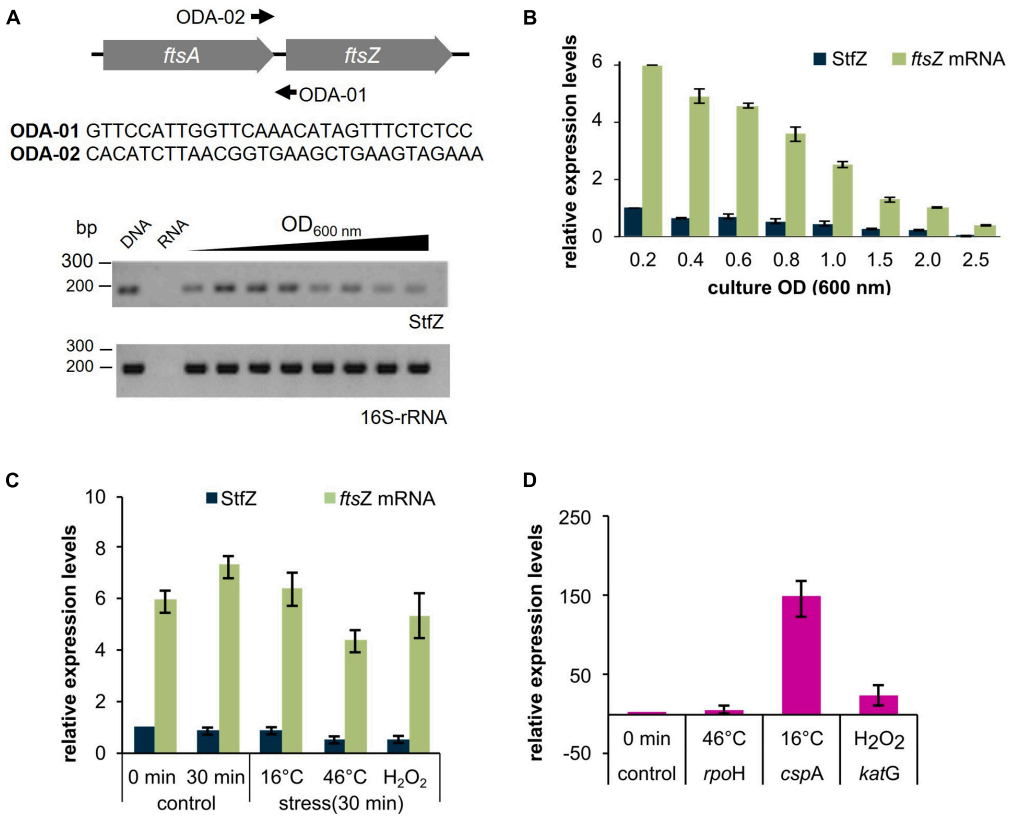

FIGURE 1
Detection and expression of StfZ RNA in stress conditions. RT-PCR for the detection of StfZ transcript. **(A)** The upper panel shows the location of the primers ODA-01 and ODA-02 used for StfZ RT-PCR and the sequence of the primers. Oligo ODA-02 was used for StfZ cDNA synthesis. The lower panel shows the RT-PCR products of StfZ and 16S rRNA after 30 cycles of amplification. G-DNA, genomic DNA as the positive control; RNA, RNA sample from 0.6 OD as the negative control; and cDNA from 0.2 to 2.5 OD cultures. The RT-PCR products were of 177 bp (StfZ) and 218 bp (16S-rRNA). **(B)** Bar-graph for the relative levels of the *ftsZ* and StfZ transcripts. Real-time PCR of *ftsZ* mRNA (green) and StfZ transcript (dark blue) from *E. coli* K12 cells from 0.2 to 2.5 OD cultures were performed on cDNA synthesised with ODA-06 oligo (for *ftsZ*) and ODA-02 oligo (for StfZ). Relative levels of *ftsZ* mRNA and StfZ are normalised to StfZ level from 0.2 OD. **(C)** Real-time PCR of *ftsZ* mRNA (green) and StfZ (dark blue) from K12 cells. Cells were stressed for 30 min at 16°C, 46°C, and 5 mM of H_2O_2 exposure. The bar graph represents the levels of the transcripts to StfZ at 0 min. **(D)** Real-time PCR of *rpoH*, *cspA*, and *katG* mRNA levels (markers for stress response) after 30 min of heat shock (Grossman et al., 1984), cold shock (Etchegaray et al., 1996), and oxidative stress (Erickson et al., 1987) response, respectively. Expression level from the uninduced culture was used as the expression control.

Stoichiometric expression of StfZ RNA to *ftsZ* mRNA

To find the stoichiometry between the antisense StfZ RNA and its target sense *ftsZ* mRNA at different growth phases, their levels were determined using quantitative real-time PCR. The StfZ RNA level was highest at the early log phase (0.2 OD) and was maintained at a relatively high level till the mid-log phase (0.6 OD) (**Figure 1B**). Subsequently, its levels progressively decreased as the culture approached stationary phase (1.5 OD), where the level was about 5-fold lower compared to those in the 0.2 OD cultures. The StfZ level was further reduced at 2.5 OD (**Figure 1B**). The decrease in the StfZ RNA level was thus found to be growth phase dependent. This decrease in StfZ RNA correlated with the steady decrease in the level of its target, *ftsZ* mRNA (**Figure 1B**). Consistent with this correlation, the ratio between StfZ RNA to *ftsZ* mRNA was found to be always ~1:6, irrespective of the growth phase. This indicated a coordinated expression of the sense and the antisense RNAs in a growth-phase-dependent manner.

StfZ expression in stress conditions

Bacteria respond to stress conditions by expressing genes that provide a defensive mechanism to counter and/or survive under the stress. During heat shock, a set of proteins called, heat-shock proteins (HSPs) are expressed (Grossman et al., 1984), in cold, cold shock proteins (CSPs) are expressed (Etchegaray et al., 1996) and in oxidative stress, catalases/hydroperoxidases are expressed (Schellhorn, 1995). In *E. coli*, small RNAs like OxyS are expressed to protect against oxidative damage. It induces cell

cycle arrest to allow DNA damage repair (Altuvia et al., 1997). We wanted to find out a stress condition that can influence the expression of StfZ and eventually cell division. We analysed the expression pattern of StfZ and *ftsZ* mRNA after 30 min of heat-shock, cold-shock, and oxidative stress. Levels of StfZ did not show any significant difference under any of the conditions tested as compared to the unstressed samples (**Figures 1C,D**). There was about a 40% decrease in StfZ after 30 min of heat shock and H_2O_2 treatment. However, both the changes were not statistically different from the 0 min sample. Therefore, we conclude that heat shock and oxidative stress have only a minor effect on StfZ levels.

Multiple transcripts of StfZ

For determining the 5′ and 3′ ends and thereby the length of StfZ RNA, primer extension assay (PEA), 3′ rapid amplification of cDNA ends (3′ RACE), and northern hybridisation were performed. PEA was performed using ODA-07 and ODA–08 primers (**Supplementary Table 4**) located in the intergenic region of *ftsA* and *ftsZ* (**Figure 2A**; **Supplementary Figure 1A**). We obtained three products from the extension of the ODA–07 primer. The first product was located at 9th, second at 117th, and third at 195th positions 3′ to *ftsZ* ATG start codon (**Supplementary Figure 1B**). Primer ODA–08 positioned downstream to ODA–07 binding site, gave two products, the one at the 117th and the other at the 195th positions 3′ to *ftsZ* ATG start codon (**Supplementary Figure 1C**). These products were overlapping with the products obtained from ODA–07, thereby confirming the authenticity of the PEA products. These three PE products were named TSS–9, TSS–117, and TSS–195, according to the distance from *ftsZ* 5′ end (**Figure 2A**). Subsequently, we compared the consensus sequences of −10 and −35 regions of *E. coli* promoters (Hawley and Mcclure, 1983; Lisser and Margalit, 1993; Mitchell et al., 2003) with the sequence in the region upstream of the respective 5′ end nt of the three respective PE products. Thus, the predicted promoter sequences for TSS–9, TSS–117, and TSS–195 were named P1, P2, and P3, respectively (**Figure 2B**). P1 and P2 showed −10 consensus with TATAAT and −35 consensus with TTGACA of the experimentally identified promoters of *E. coli* (Hawley and Mcclure, 1983; Lisser and Margalit, 1993; Hershberg et al., 2001; Mitchell et al., 2003). The predicted −10 and −35 sequences for the putative P3 promoter showed divergence (**Figure 2B**).

The predicted promoters of StfZ RNA drive reporter gene expression

The −10 regions of bacterial promoters are crucial for the initial stages of sigma factor interaction. Transcription initiation drastically fails in the absence of the −10 element (Ruff et al., 2015; Browning and Busby, 2016). This characteristic feature has been used to validate and map bacterial promoters. Taking the same approach to validate the predicted promoters, we constructed Δ-10 promoter constructs (pDA3, pDA5, and pDA7) (**Supplementary Table 2**), with *mutgfp* as the reporter gene, and compared its expression from the respective native promoter constructs (pDA2, pDA4, and pDA6) (**Supplementary Table 2**).

Deletion of predicted −10 elements of the three putative promoters showed about a 20–fold reduced expression of *mutgfp* (**Figure 2C**). The transcriptional activity of the three predicted promoters and its abrogation in the −10 deletion mutants validated the authenticity of the promoters. Individual activity of the putative promoters showed different significant levels of expression. Whereas a significant level of cumulative expression was observed from the combined P1-P2-P3 promoter construct, pDA8 (**Supplementary Table 2**; **Figure 2D**). These observations implied transcription of *stfZ* from three independent promoters producing three isoforms of StfZ. It was of interest to note that the P1 promoter region corresponded to the previously predicted promoter for StfZ (Dewar and Donachie, 1993).

To specifically study the activity of the promoters, we created mutant versions of the −10 elements of the three promoters and compared their activity. The selected mutations were substitution mutations in the FtsZ protein-coding sequence (**Supplementary Figure 2A**). Promoter activity was analysed using *mutgfp* reporter assay. We found that the sequences of the −10 mutant promoters did not show any significant difference in *mutgfp* expression as compared to the respective WT promoter sequence (**Supplementary Figure 2B**). This result shows that the promoter sequences are capable of initiating transcription even when minor changes are introduced in their −10 elements, as reported (Raghavan et al., 2012).

Northern blotting shows three isoforms

Northern blotting against StfZ RNA, which was performed using total RNA from *E. coli* K12 (wt) and PAK12 transformant carrying the cloned *stfZ* gene spanning all the three isoforms (**Supplementary Table 1**), showed bands in the range of ∼350, ∼450, and ∼500 nts (**Figure 2E**). The consistent presence of the expected three bands despite high stringency washes with 0.1x SCC and 0.1% SDS at 55°C indicated their authenticity. The low intensity of the bands suggested a low level of StfZ expression, which could be observed by RT-PCR (see **Figure 1A**).

Based on our experimental analysis, we examined the existing RNA-Seq data to know whether three StfZ transcripts were detected before this study. RNA-Seq data were extracted from the NCBI SRA database (accession number–SRX3413960)

10.3389/fmicb.2022.920117

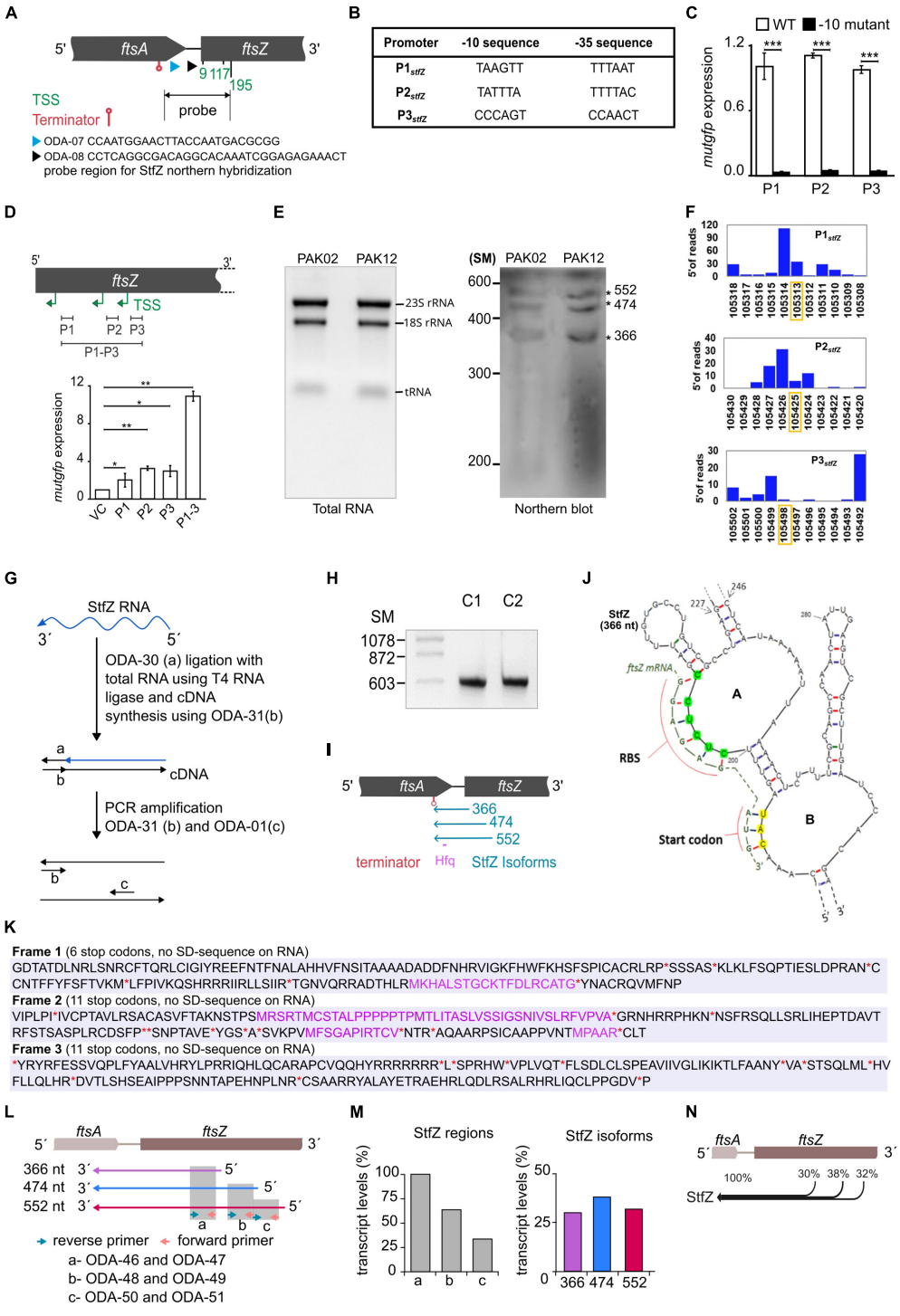

FIGURE 2

Identification of the 5′ end, the promoters, and the 3′ end of StfZ. **(A)** Schematic representation of the positions of the oligonucleotides used for primer extension analysis (PEA), which identified TSS sites and terminator. ODA–07 (blue), ODA–08 (black), TSS (green), and terminator (red). The double arrow line indicates the location of the probe used for northern blotting in 2E. **(B)** Putative promoters of the *stfZ* with their respective −10 and −35 sequences predicted from the PEA products. **(C)** Promoter assay using *mutgfp* as a reporter in pFPV27 vector. P1, P2, and P3 predicted promoters with native sequence (WT) (white bars) and respective −10 deletion mutant −10 mutant (black bars) were cloned upstream to *mutgfp*. Strain PAK05 (P1 wt), PAK07 (P2 wt), PAK09 (P3 wt), PAK06 (P1Δ-10), PAK08 (P2Δ-10), and PAK10 (P3Δ-10) were used. Y-axis indicates the relative expression. **(D)** Relative activity of *stfZ* promoters, P1, P2, and P3, individually and cumulative were analysed in PAK05, PAK07, PAK09, and PAK11 (P1 + P2 + P3) strains, respectively. The illustration (top) shows the cloned promoter regions (black horizontal lines). pFPV27 was used as the vector control. Bar graphs show the relative expression of *mutgfp* (y-axis) from different promoters (x-axis).

(Continued)

FIGURE 2 (Continued)
The *p*-values range were indicated with asterisks (***$p < 0.001$). **(E)** Northern blot for PAK02 and PAK12 RNA samples. PAK02 and PAK12 were probed with a single-stranded RNA probe. RNA ladder was used as a size marker. The asterisks indicate three bands of expected sizes, 366, 474, and 552 nt, approximately. **(F)** Transcription start site (TSS) frequency bar-plot from the existing RNA seq data represents the surrounding region of the StfZ 5′ end identified by primer extension. *stfZ*-P1, *stfZ*-P2, and *stfZ*-P3 in this graph represent the promoters of TSS−9, TSS−117, and TSS−195. The Y-axis on each graph represents the number of reads starting on each position and the X-axis represents the genomic positions. RNA-Seq data was extracted from NCBI-SRA (accession number- SRX3413960). The orange box shows the TSS determined from PEA in this study. **(G)** Strategy for 3′ RACE to identify the 3′ end of StfZ RNA. **(H)** The approximate size of the 3′ RACE product is 600 bp. C1 and C2 are two biological replicates of 3′ RACE. SM, size marker in nucleotides. **(I)** Concise diagram indicating the location of StfZ isoforms at *fts*A-*ftsZ* locus. Identified terminator position from 3′ RACE (red) predicted Hfq binding site (magenta), and different isoforms with their respective sizes (blue). **(J)** 5′ region of the predicted secondary structure of StfZ RNA (366 nt) from the Mfold web server. The *ftsZ* (yellow) ribosomal binding site (RBS) and of the AUG start codon complementary to the StfZ structure are shown next to the open loops, A and B, respectively. **(K)** *In silico* analysis of StfZ sequence for peptide reading frame. In black, peptides start without methionine; in violet, peptides start with methionine; and in red asterisk '*' and '**', stop codons. Ribosome binding sites are not present in the entire StfZ RNA sequence. **(L)** Primer map for real-time PCR to estimate the levels of individual StfZ isoforms. Isoforms 366, 474, and 552 are indicated as arrows below the gene locus of *ftsA-ftsZ* in violet, blue, and red, respectively. Green and orange arrows indicate the reverse and forward primers. Grey boxes, "a," "b," and "c," show the coverage from the primers as mentioned in the lower panel. **(M)** Bar graphs for the transcript levels of StfZ regions and isoforms. The bar graph in the left panel shows the transcript levels detected from regions "a," "b," and "c" (grey bars). The relative amount was calculated with respect to the region "a" taken as 100%. The bar graph in the right panel shows the relative levels of three StfZ isoforms as percent transcript. Violet- StfZ 366, blue- StfZ 474, and red- StfZ 552. Y-axis, percent transcript levels. **(N)** Map of StfZ isoforms and their contribution to StfZ RNA pool. Black merging horizontal lines with reference to *ftsA-ftsZ* genomic locus (top) show isoforms with relative amounts of their transcripts.

(Livingstone et al., 2018) and analysed for the genomic positions of TSSs (Transcription Start Sites) in the *stfZ* region. TSSs were plotted as bar graphs along the DNA sequence. The TSSs of StfZ were detected wherefrom TSS-9, TSS-117, and TSS-195 RNAs were transcribed (**Figure 2F**). However, the genomic positions did not match precisely with the RNA-Seq + 1 TSS from PEA. Thus, the slight variation in the RNA-Seq TSS sites suggested only a close possibility of TSS but not the exact position of TSS. Therefore, we relied on PEA data more than the RNA-Seq data.

Additionally, to verify the exact ends of the isomers and to find out whether it is a processed RNA product, we performed circular RACE with and without Tobacco Acid Pyrophosphatase (TAP) treatment of RNA (McGrath, 2011). TAP removes 5′ cap of RNA therefore processed RNA can be detected in circular RACE without TAP treatment but not a capped RNA. Using this method, we did not find any amplification from the StfZ region under any condition, which indicated that StfZ RNA was not a processed product of any primary RNA.

StfZ RNA 3′ end extends to upstream of *ftsZ*

Antisense RNA function depends on their coverage and location on the target RNA. Therefore, after determining the 5′ ends of StfZ transcripts, we performed 3′ RACE to find out the 3′ end(s) of the transcripts. For this, the ribominus RNA fraction (devoid of ribosomal RNAs) was ligated to an adaptor oligo, ODA-30, and the cDNAs were synthesised using complementary oligo ODA–31, as indicated in the cartoon (**Figure 2G**; **Supplementary Table 4**). The cDNA product was amplified with ODA–31 and ODA–01 primers to get the PCR product of ∼600 bp (**Figure 2H**). Biological replicates C1 and C2 of PCR amplified products were cloned in plasmid pDA1 and sequenced (**Figure 2H**; **Supplementary Table 2**). Sequencing the replicates from both ends showed 357th nt 5′ upstream of *ftsZ* as the common 3′ ends of all the three isoforms. The entire sequence of the three isoforms encompassed the ribosome binding sequence (RBS) of *ftsZ*, the entire *ftsA-ftsZ* intergenic region, and 297 nts on the 3′ end of *ftsA* gene located 5′ upstream of *ftsZ* (**Figure 2I**). From the three different transcription initiation sites, StfZ isoforms are produced as 366, 474, and 552 nt long RNAs (**Figure 2I**). These sizes corresponded to the sizes of the three PEA products and of the three bands in the northern blot (**Supplementary Figure 1**; **Figure 2E**). The sequences were deposited in Bankit database with accession numbers; stfZ_366 KX852304, stfZ_474 KX852303, and stfZ_552 KX852302.

Features of StfZ RNA

Interaction of antisense RNA with its target RNA involves the formation of a "kissing complex" which eventually makes a stable RNA–RNA complex (Gerhart et al., 1994; Lease and Woodson, 2004; Brantl, 2007). Therefore, we predicted a secondary structure of the 366-nt long StfZ isoform using Mfold (Zuker, 2003). The structure showed the presence of two successive loops A and B with 5′ CUCUCC 3′ (complementary region of *ftsZ* mRNA RBS, 5′ GGAGAG 3′) and 5′ CAU 3′ (complementary to *ftsZ* initiation codon 5′ AUG 3′) (**Figure 2J**). The StfZ sequence also has 5′ AATAATA 3′ sequence, which resembled the potential consensus sequence for the binding of Hfq (5′ AAYAAYAA 3′) (Lorenz et al., 2010). It is located at 156 nt upstream from the 3′ end of the StfZ transcript and it shares a complementary region of *ftsA* (**Figure 2I**). StfZ RNA

sequence has multiple stop codons (6 in reading frames 1, and 11 each in reading frames 2 and 3) and no ribosomal binding sites (RBS). There are small peptide open reading frames but no RBS for translation (**Figure 2K**).

StfZ isoforms are transcribed in comparable levels

After estimating the size of all the isoforms, we investigated the contribution of expression from individual isoforms. To do so, we used three sets of primers in such a way that it covers different regions of StfZ isoforms (**Figure 2L**, top panel). Real-time PCR was performed on these regions using the cDNAs prepared from the reverse primers, ODA-47, ODA-49, and ODA–51, for the 366 nt, 474 nt, and 552 nt isoforms, respectively. The level of the transcripts was calculated from three regions. Region "a" covers all three isoforms thus it was used as the 100% level. Region "b" covers two isoforms, 474 and 552. Region "c" covers only isoform 552. The relative level of region "a" was the highest, and region "c" was the lowest (**Figure 2M**, left panel). Using the maps from **Figure 2K**, we calculated the contributions of each isoform and found that the relative level of isoform 366 is 30%, isoform 474 is 38%, and isoform 552 is 32% (**Figure 2M**, right panel). Therefore, different isoforms contribute equally to StfZ RNA pool (**Figure 2N**).

StfZ RNA target is *ftsZ* mRNA

The sequence features of StfZ RNA and its location on the strand complementary to *ftsZ* mRNA reading frame revealed that it can function as an antisense RNA specific to *ftsZ* mRNA. Therefore, the effect of StfZ RNA overexpression on *ftsZ-yfp* translation was tested to verify its target specificity and to document the physiological changes brought about by StfZ overexpression. This method allowed measurement of the effect of the antisense RNA against its target *ftsZ* mRNA by fluorescence microscopy or directly by YFP fluorescence from bacterial cells. In principle, binding of StfZ RNA to *ftsZ-yfp* should rescue FtsZ-YFP overexpression phenotype (cell elongation/filamentation) and reduce YFP fluorescence in the PAK13 strain (**Figure 3A**). PAK13 contains, pDA9 (423 bp region of *stfZ*, spanning all the three isoforms, cloned under P_{lac}) and pBAD33-*ftsZ-yfp* (a gift from W. Margolin, *ftsZ-yfp* cloned under P_{BAD} promoter). The culture was induced at 0.6 OD with either 0.1% arabinose (for *ftsZ-yfp* mRNA) or 1 mM IPTG (for StfZ RNA) or with both the inducers simultaneously. Expression of FtsZ-YFP was measured at the fluorescence level in the culture and single-cell level by microscopy. Multiple FtsZ-YFP rings and a high level of YFP fluorescence were observed in the arabinose-induced cells due to overexpression of FtsZ-YFP (**Figure 3B**, c, d and **Figure 3C**, third bar). A high level of FtsZ-YFP interfered with the division process and induced cell elongation/filamentation (**Figure 3D**). The co-induction of StfZ RNA along with *ftsZ* mRNA rescued the cells from elongation/filamentation with a significant reduction in the cell length (**Figure 3D**). Inhibition of *ftsZ-yfp* translation could be inferred from the reduction in the YFP fluorescence level in the FtsZ-YFP induced cells (**Figure 3C**, second bar). This effect was also visible in the cells that were induced only with IPTG, which showed induction of low levels of FtsZ-YFP (**Figure 3C**, first bar). These cells did not filament as the overexpressed StfZ might have been engaged in the interaction mostly with *ftsZ-yfp* mRNA and probably to a low extent with the native *fts*Z mRNA. Thus, the sequestration of StfZ by the *ftsZ-yfp* mRNA might have effectively prevented its interaction with *ftsZ* mRNA and the consequential division inhibition and elongation/filamentation. The reduction in the YFP fluorescence in these cells supported this possibility (**Figure 3C**, second bar). These results suggested that StfZ interacts with *ftsZ* mRNA. There is a functional overlap between DicF and StfZ RNAs as they share the target region near the *ftsZ* RBS sequence (**Figure 3E**). However, *E. coli* K12 and JM109 strains did not contain DicF RNA as found using RT-PCR (data not shown), ruling out any interference by DicF RNA in these experiments.

StfZ RNA influences FtsZ level and thereby cell division

Unlike a large number of *trans*-antisense RNAs that are encoded at loci far away from the loci coding for their target RNAs (Majdalani et al., 2004; Papenfort et al., 2009; Guo et al., 2014), the sequence of StfZ RNA is complementary to the reading frame of its target RNA, *ftsZ*, which is essential for cell division. Therefore, the generation of *stfZ* knockout mutant and/or its promoter mutations, which would fall on *ftsZ* reading frame, could not be taken up to determine the physiological effect of the lack of expression of StfZ from the native locus. Therefore, we overexpressed StfZ to study its influence on FtsZ protein level, cell division, and growth. A 423 bp region of *stfZ*, which spans across the promoters and reading frames of all the three isoforms, was cloned and expressed from PAK12 (P_{lac}–*stfZ*) strain. The strains PAK02 (vector control) and PAK12 (**Supplementary Table 1**) were induced with 1 mM IPTG for 2 h at 30 and 42°C. A higher induction temperature of 42°C was used as per DicF *trans*-antisense RNA experiment, where the translation of FtsZ was blocked only at 42°C but not at lower temperatures probably due to its strong secondary structures (Tétart and Bouché, 1992). Upon induction of *stfZ* in the PAK12 cells, the levels of StfZ RNA increased 180-fold and 600-fold, at 30 and 42°C at 120 min, respectively, as compared to the levels of the endogenous StfZ RNA in the PAK02 cells (**Figure 4A**). Quantitation of the levels

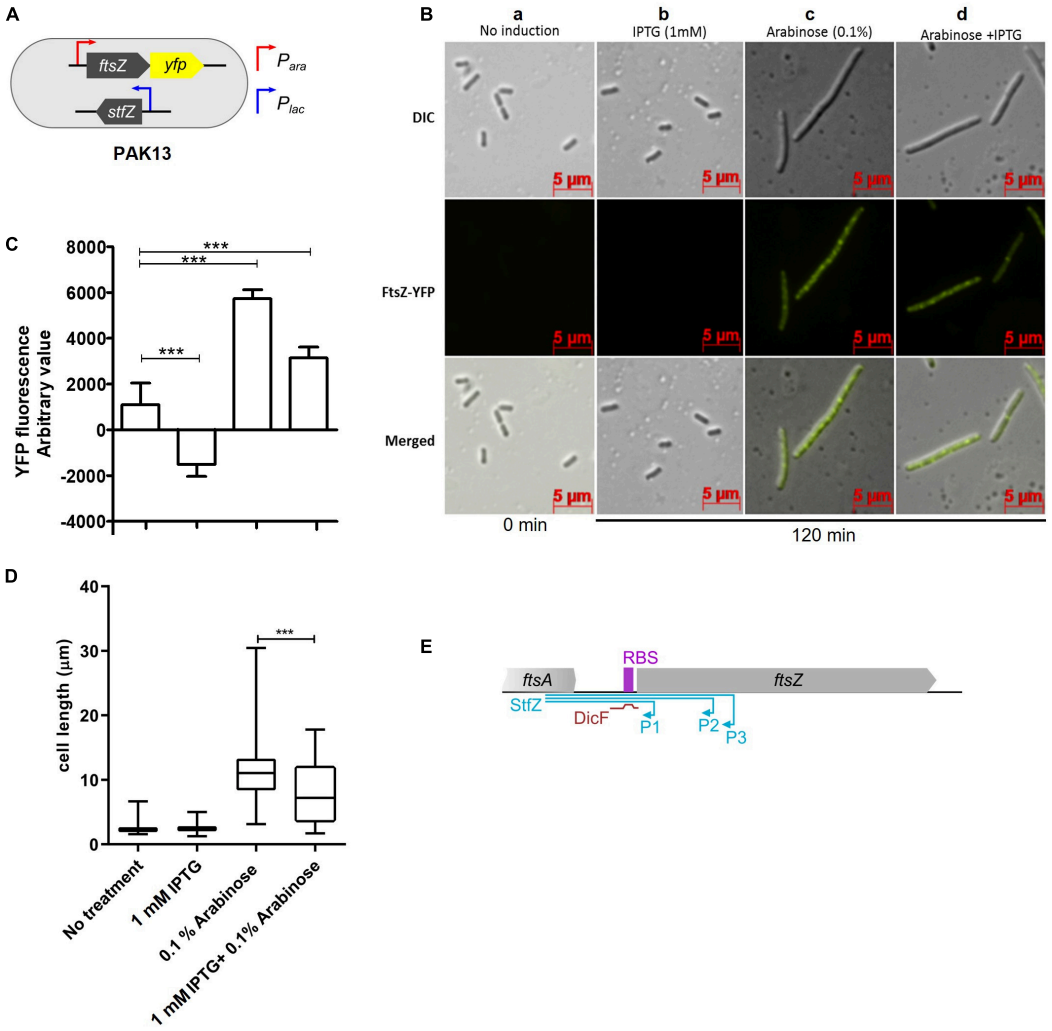

FIGURE 3
Inhibition of *ftsZ-yfp* mRNA translation by StfZ. PAK13 cells were induced with either 1 mM IPTG or/and 0.1% arabinose at 37°C for 120 min. **(A)** Schematic presentation of PAK13 strain with P_{ara}-*ftsZ-yfp* and P_{lac}-*stfZ* constructs. **(B)** Cells were imaged before induction (0 min) and after induction for 120 min. Columns: (a) negative control without induction of the culture; (b) positive control for StfZ RNA expression, induced with IPTG; (c) positive control for FtsZ-YFP expression, induced with arabinose; (d) experimental sample, induced for the co-expression of StfZ RNA and *ftsZ-yfp* fusion mRNA. Top row: DIC images; middle row: FtsZ-YFP images; and lower row: merged images. **(C)** Quantitation of the YFP fluorescence as arbitrary values for 0 min and 120 min post-induction from 200 µl culture. **(D)** Box chart for cell size at 0 min and 120 min of induction (n > 300). **(E)** Diagram representing the span of StfZ and DicF antisense RNA on *ftsZ* sequence. The *stfZ* (blue line) covers the complete intergenic region and a significant portion of ftsZ while DicF (brown line) partially covers the intergenic region. Statistical significance is indicated with asterisks (***$p < 0.001$).

of *ftsZ* and *ftsA* mRNAs from the PAK02 and PAK12 cells did not show any significant difference upon *stfZ* induction at either temperature even for 120 min indicating that *stfZ* induction did not degrade *ftsZ* mRNA (Figure 4A). However, at 120 min post-induction of *stfZ* at 42°C, the levels of FtsZ protein were only 17% in the PAK12 cells (Figure 4B, upper panel and Figure 4C). The change in the FtsZ levels at 30°C was not significant (Figure 4C). The loading control is shown for RRF (Figure 4B, lower panel). Thus, the target sense RNA did not get degraded in the case of StfZ RNA-*ftsZ* mRNA interaction, unlike in many cases (Dühring et al., 2006; Giangrossi et al., 2010; Lee and Groisman, 2010; Bordoy and Chatterjee, 2015).

The influence of reduced FtsZ level on cell division was examined by determining the ratio of FtsZ-rings per micrometre length of the cells by counting the number of cells with immunostained FtsZ rings. A higher number of FtsZ-rings per micron would show a higher rate of division while a lesser number would show a reduced frequency of division. In PAK02, the cell division ratio was comparable at 30 and 42°C. On the contrary, in the PAK12 cells, the ratio was significantly reduced at 30°C and even more so at 42°C, indicating a reduction in the

10.3389/fmicb.2022.920117

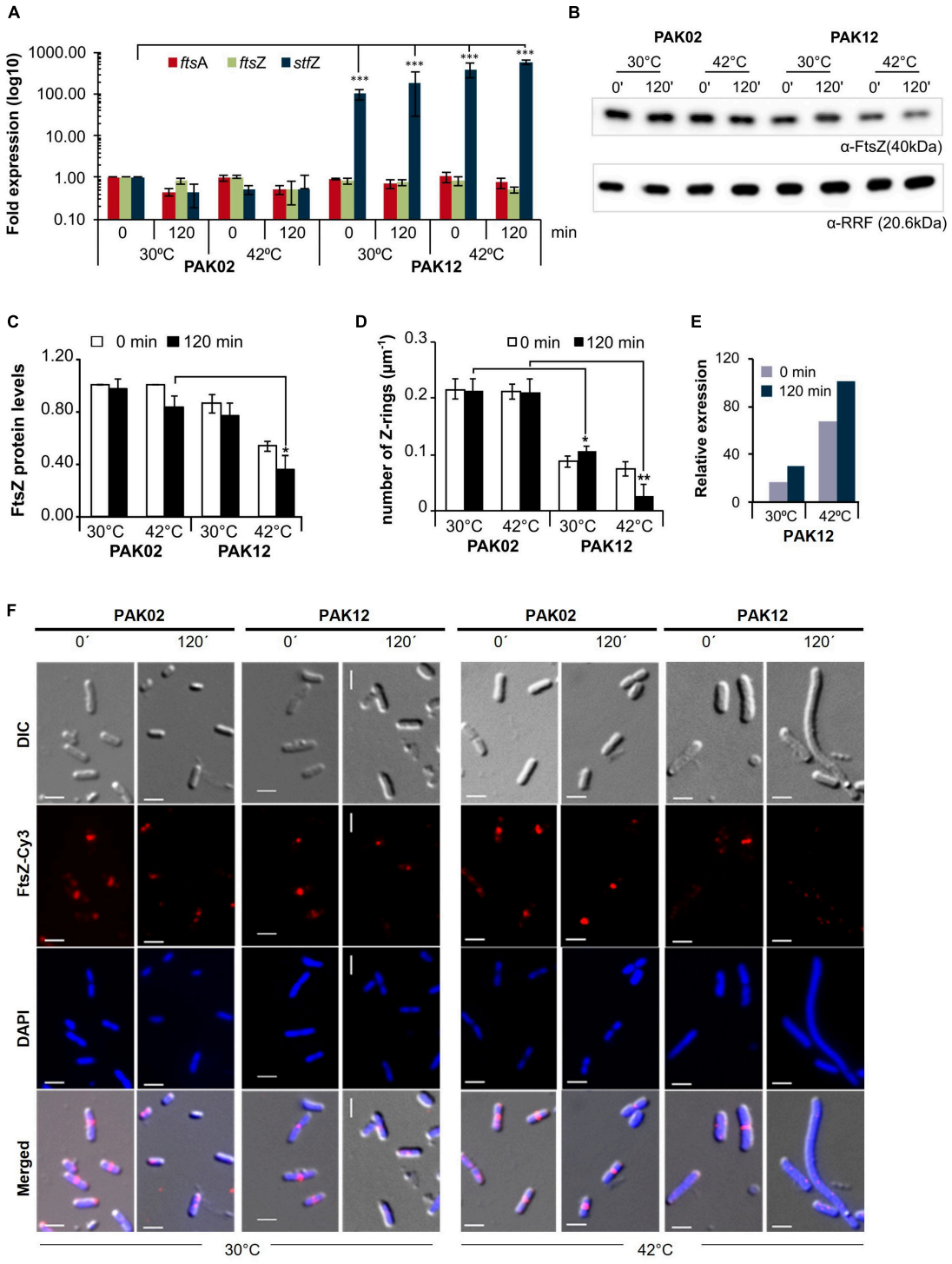

FIGURE 4

StfZ over induction decreases FtsZ level and blocks cell division. **(A)** Real-time PCR for StfZ, *ftsZ*, and *fts*A mRNA at 30 and 42°C in PAK02 (vector control) and PAK12 (StfZ expression) strains. **(B)** Western blot analysis for FtsZ level and equal loading profile of RRF protein (Ribosome-recycling factor). **(C)** Bar-graph for the quantitation of FtsZ from western blot. FtsZ level was calculated to PAK02 sample from 0 min at 30°C. **(D)** Bar-graph showing ratio of FtsZ rings per micron of cell length (n > 100). Cells were fixed after 0 min and 120 min of induction and immunostained for FtsZ. The total number of Z-ring was divided by the cumulative cell length of the population. **(E)** Estimation of relative RNA expression of StfZ compared to *ftsZ* mRNA at 30 and 42°C. Bar-graph showing RNA levels of StfZ RNA from real-time PCR data [data from panel **(A)**] normalised with *ftsZ* level by 6-fold. **(F)** Immunostaining for FtsZ in PAK02 and PAK12 cells from 30 and 42°C cultures. For each temperature (bottom), left panel PAK02 (vector control) and right panel PAK12 (StfZ expression) at 0 min and 120 min are shown. FtsZ-Cy3 (red) and DAPI (blue). Scale bar, 5 μm. Statistical significance is indicated with asterisks (*$p < 0.05$, **$p < 0.01$, ***$p < 0.001$).

number of cells undergoing division (Figure 4D). To calculate the amount of StfZ RNA needed to influence cell division significantly, we extrapolated the data from Figure 4A. We calculated the relative levels of StfZ RNA under overexpressed conditions with respect to native *ftsZ* mRNA levels. We found that 30- to 100-fold higher StfZ RNA expression at 30 and 42°C, respectively, as compared to *ftsZ* mRNA, caused cell division defects (Figure 4E). This data is reflected in the images of FtsZ-immunostained PAK02 and PAK12 cells at 30 and 42°C at 0 min and 120 min (Figure 4F). At 30°C, higher expression of StfZ did not cause any filamentation while resulting in cell elongation after 120 min at 42°C in PAK12 cells. Cells with vector control did not show any effect at both temperatures (Figure 4F).

At 37°C also, induced expression of StfZ for 120 min showed about a 1.75-fold reduction in the FtsZ level as compared to the 0 min sample (Supplementary Figure 3A). Commensurate with this reduction, the proportion of the cells with FtsZ-ring also decreased significantly from ∼60 to ∼40% in 120 min (Supplementary Figure 3B).

Measurement of optical density of the cells carrying uninduced and induced StfZ RNA at 42°C showed a significant increase in PAK02 and PAK12 mass (Supplementary Figure 3C). However, PAK12 mass was significantly low at 120 min compared to PAK02 indicating inhibition of cell division and the consequential lack of increase in the cell number. The higher OD of PAK02 at 120 min might be from the cell number increase due to cell division. Colony-forming unit (CFU) at 120 min showed a significant increase in the PAK02 population while the PAK12 cells did not show a significant increase between 0 and 120 min (Supplementary Figure 3D). The CFU data corroborated with the cell mass data that the lack of increase in cell mass in PAK12 was a result of cell division inhibition and that the increase in cell mass in PAK02 was due to an increase in the cell number by cell division. SYTO9/PI staining confirmed that 120 min of StfZ induction did not affect the cell viability (Supplementary Figure 3E).

To understand the effect of the interaction between StfZ RNA and *ftsZ* mRNA, we designed an StfZ variant without its *ftsZ*-RBS complementary sequence (StfZ-ΔRBSc; PAK14; Supplementary Table 1). It was overexpressed by induction identical to StfZ overexpression at 30 and 42°C. Like the overexpressed StfZ RNA, the overexpressed StfZ-ΔRBSc RNA did not affect *ftsZ* mRNA stability as it did not decrease the levels of the target RNA (Supplementary Figure 4A), which meant that it did not degrade *ftsZ* mRNA. Further, like the StfZ RNA, StfZ-ΔRBSc RNA also affected the levels of FtsZ protein (Supplementary Figures 4B,C). The reduction in the levels of FtsZ reduced the number of cells undergoing cell division (i.e., the number of cells with FtsZ-rings) after 120 min of induction at 42°C thereby affecting cell division (Supplementary Figures 4D,E). However, the number of Z-rings per micrometre of PAK14 cells did not show a statistically significant difference compared to that of the PAK12 cells (Supplementary Figure 4E). Thus, the effect of StfZ-ΔRBSc RNA on FtsZ and cell division was relatively similar to StfZ.

Thus, taken together, the *cis*-encoded StfZ RNA emerges as a novel factor involved in the maintenance of *ftsZ* mRNA levels available for translation, and hence of FtsZ protein levels, at all phases of growth and cell division in *E. coli*.

Discussion

Features of structure and expression of StfZ RNA

This study showed for the first time the complete sequence identity of StfZ RNA, with its 5′ and 3′ ends, three promoters transcribing them, stoichiometric expression with respect to *ftsZ* mRNA, and its ability to reduce FtsZ levels when overexpressed (Figures 2, 4). Overexpressed levels of StfZ imposed cell division block, resulting in cell elongation and filamentation. The predicted StfZ structure showed its possible initial interaction with *ftsZ* mRNA at the RBS site to form a "kissing complex" followed by a complete stable duplex (Figure 2J; Gerhart et al., 1994; Lease and Woodson, 2004; Brantl, 2007). However, the deletion of the RBS interacting region from StfZ showed a possibility of another open loop interaction that also reduced FtsZ levels (Supplementary Figure 4). Also, FtsZ protein reduction was not due to a decrease in the *ftsZ* mRNA levels unlike in the case of many sense-antisense RNA interactions (Figure 4A; Dühring et al., 2006; Giangrossi et al., 2010; Lee and Groisman, 2010; Bordoy and Chatterjee, 2015). StfZ RNA lacks the ribosome binding site (RBS) consensus sequence to translate any possible small ORF. From the existing proteomics data, we did not find any evidence of peptide that matches the StfZ region. This ruled out the possibility of StfZ coding for any short peptide, unlike the possibility predicted in the earlier study (Dewar and Donachie, 1993). The expression of StfZ throughout the entire growth phase showed growth-phase-dependent expression. Its levels at 1/6th of the proportion of *ftsZ* mRNA indicated that it may be involved in the fine regulation of *ftsZ* mRNA levels available for translation during different stages of growth, as per the growth-phase-specific demand in the bacteria. The higher levels of both *ftsZ* mRNA and StfZ RNA during early phases of active growth and their proportionate decrease during phases of reduced growth are indicative of the "synthesis-as-per-demand" mode of expression of FtsZ. However, the StfZ levels did not change during the 30 min of heat shock, cold shock, or oxidative stress (Figures 1C,D). This does not rule out the possibility of some other stress conditions under which a significant change may occur in the StfZ expression or the 1:6 ratio of StfZ to *ftsZ* mRNA. From the real-time PCR data, we extrapolated the stoichiometry between StfZ and *ftsZ* mRNA (Figure 4E) and found that StfZ could influence FtsZ levels at 30-fold higher expression compared to *ftsZ* mRNA, at 30°C in 120 min. A further increase to 100-fold

(at 42°C, 120 min) caused more severe division inhibition. Such levels of StfZ RNA may be unnatural and we did not find such levels of StfZ at any phase of growth. Nevertheless, it indicated that the effects of StfZ RNA on *ftsZ* mRNA levels, and hence on FtsZ protein levels, are concentration dependent, which may mean a smaller increase affects cell size while a higher amount inhibits cell division. Therefore, it was imperative on the part of the cell to maintain the StfZ:*ftsZ* ratio at 1:6 at all phases of growth and cell division, which was what we observed.

The effect of StfZ RNA on *ftsZ* mRNA was higher at higher temperature (42°C) as in the case of DicF RNA (Bouché and Bouché, 1989). We speculated that higher temperature might have helped to melt the secondary structure which was essential for its interaction with the target RNA to form the "kissing complex."

Isoforms of StfZ RNA

Many *trans*-antisense RNAs have isoforms that are most often the processed forms of a primary transcript expressed from a single promoter. Some of such *trans*-antisense RNAs are the DicF (Bouché and Bouché, 1989), ArcZ (Papenfort et al., 2009; Soper et al., 2010), RprA (Majdalani et al., 2004), and MicL (Guo et al., 2014) RNAs of *E. coli*. On the contrary, in the case of StfZ RNA, the loss of activity of the −10 deletion mutants of the three promoters, predicted based on the 5′ end identification using PEA, validated the authenticity of the predicted promoters and the existence of three isoforms (**Figure 2C**). The transcriptional activity of the three predicted promoters and its abrogation in the respective Δ-10 constructs indicated that the predicted promoter sequences were capable of initiating transcription and therefore the primer extension products were not a result of a processed product. The −35 sequence (CCAACTT) of P3 promoter was interesting as it showed consensus with the −35 sequence (GGAACTT) of *rpoEp*3 gene of *Salmonella enterica serovar Typhimurium* (Skovierova et al., 2006; see **Figure 2B**). Many antisense RNA promoters of enteric bacteria do not show conservation in the −10 and −35 sequences (Raghavan et al., 2012). However, it was interesting to see the StfZ promoters also fall into the same category. We found that the P3 promoter would be one such promoter. It was also interesting to see all three promoters in the cloned format having similar strength in the plasmid context (**Figure 2D**). Additionally, real-time PCR from different regions of StfZ showed that the individual isoforms are expressed at similar levels (**Figures 2M,N**). This similarity did not correlate with the differences in the intensities of the three PEA products (see **Supplementary Figure 1**). This incongruity between the PEA data and the promoter assay data is not surprising as bacterial promoters showing different activities at different locations, such as in the genomic context or as individual clones in a plasmid, have been reported in many instances (Cases and de Lorenzo, 2005; Davis et al., 2011; Hocine et al., 2015; Srivastava et al., 2016). Further, the presence of three potential primer extension products or three bands in the northern blot could not alone conclude the existence of three promoters for StfZ RNA. Further, the *cis*-encoded nature of StfZ RNA to the essential gene *ftsZ* also did not permit their conclusive verification by mutating the promoters one at a time in the genome and checking for the decrease in the levels of StfZ RNA and consequential increase in FtsZ levels as it would have adversely affected the expression of the sense RNA causing lethality. Thus, studies of *cis*-encoded antisense RNAs have been possible only through overexpression, such as in the case of *ureB cis*-encoded antisense RNA against *ureAB* mRNA (Wen et al., 2011). Another example of a *cis*-encoded antisense RNA that exists in three isoforms is the *cis*-encoded GadY RNA, which regulates acid response genes in *E. coli* (Opdyke et al., 2004). Like in the case of StfZ RNA, all three isoforms of GadY RNA were detected at all growth phases in a growth-phase-dependent manner (Opdyke et al., 2004).

The probable role of StfZ

It may be stated that differential expression of StfZ RNA from multiple promoters may help fine-tune the levels of *ftsZ* mRNA available for translation. It helps by controlling fluctuations in the FtsZ protein levels which is essential for proper cell division (Ward and Lutkenhaus, 1985; Bi and Lutkenhaus, 1990). Fine-tuning by StfZ seems to be a logical necessity for the cells to maintain a critical level of FtsZ, expressed from multiple promoters and through various other mechanisms (Vicente et al., 1998; Dewar and Dorazi, 2000). Differential expression of StfZ may also be important under certain stress conditions, which would be other than those that we tested. However, it is also possible that only under normal growth conditions, StfZ may be involved in the fine tuning of *ftsZ* mRNA levels and may not be under any stress conditions. Nevertheless, from the level of its expression being commensurate with the level of *ftsZ* mRNA at 1:6 ratio, it is tempting to speculate that the level of StfZ RNA would change in concert with *ftsZ* mRNA levels to keep the translatable *ftsZ* mRNA available at the required level at every phase of growth and cell division. This brings up the exciting proposition of the co-ordinated regulated expression of StfZ RNA and *ftsZ* mRNA genes. Future research in this direction would reveal the mechanisms behind StfZ RNA-mediated maintenance of the levels of *ftsZ* mRNA available for translation and hence of the levels of the essential cytokinetic protein, FtsZ, at all phases of growth and cell division. This will also open up questions on what other sense and *cis*-antisense genes are regulated similarly.

Data availability statement

The datasets presented in this study can be found in online repositories. The names of the repository/repositories and

accession number(s) can be found in the article/**Supplementary material**.

Author contributions

PA, DA, DS, RN, and KJ conceived and designed the experiments. DA, DS, RN, and KJ performed experiments. PA, DA, DS, RN, KJ, and NM analysed the data and contributed reagents, materials, and analysis tools. PA, DA, DS, and RN wrote the manuscript. All authors contributed to the article and approved the submitted version.

Funding

This work was supported by the Department of Biotechnology, Government of India (grant number BT-PR7695-AGR-36-737-2013 to PA).

Acknowledgments

The authors thank Raphael Valdivia for pFPV27 vector and William Margolin for pBAD33/*ftsZ-yfp*. The authors acknowledge technical help from H. S. Rajeswari in immunostaining and western blotting and José Vicente Gomes for RNA-Seq data analysis.

Conflict of interest

The authors declare that the research was conducted in the absence of any commercial or financial relationships that could be construed as a potential conflict of interest.

Publisher's note

Supplementary material

The Supplementary Material for this article can be found online at: https://www.frontiersin.org/articles/10.3389/fmicb.2022.920117/full#supplementary-material

References

Addinall, S. G., Erfei, B., and Lutkenhaus, J. (1996). FtsZ ring formation in fts mutants. *J. Bacteriol.* 178, 3877–3884. doi: 10.1128/jb.178.13.3877-3884.1996

Aldea, M., Garrido, T., Pla, J., and Vicente, M. (1990). Division genes in *Escherichia coli* are expressed coordinately to cell septum requirements by gearbox promoters. *EMBO J.* 9, 3787–3794. doi: 10.1002/j.1460-2075.1990.tb07592.x

Alting-Mees, M. A., and Short, J. M. (1989). pBluescript II: Gene mapping vectors. *Nucleic Acids Res.* 17:9494. doi: 10.1093/nar/17.22.9494

Altuvia, S., Weinstein-Fischer, D., Zhang, A., Postow, L., and Storz, G. (1997). A small, stable RNA induced by oxidative stress: Role as a pleiotropic regulator and antimutator. *Cell* 90, 43–53. doi: 10.1016/s0092-8674(00)80312-8

Arumugam, M., Anand, D., Vijayarangan, N., Anbukayalvizhi, C., Rao, M., Vijay, S., et al. (2012). Nucleoside diphosphate kinase gene is expressed through multiple iranscripts in *Mycobacterium smegmatis*. *Int. J. Microbiol. Res.* 4, 201–210. doi: 10.9735/0975-5276.4.4.201-210

Bi, E., and Lutkenhaus, J. (1990). FtsZ regulates frequency of cell division in *Escherichia coli*. *J. Bacteriol.* 172, 2765–2768. doi: 10.1128/jb.172.5.2765-2768.1990

Blattner, F. R., Plunkett, G. III, Bloch, C. A., Perna, N. T., Burland, V., Riley, M., et al. (1997).

The complete genome sequence of *Escherichia coli* K-12. *Science* 277, 1453–1462. doi: 10.1126/science.277.5331.1453

Bordoy, A. E., and Chatterjee, A. (2015). Cis-Antisense transcription gives rise to tunable genetic switch behavior: A mathematical modeling approach. *PLoS One* 10:e0133873. doi: 10.1371/journal.pone.0133873

Bouché, F., and Bouché, J. P. (1989). Genetic evidence that DicF, a second division inhibitor encoded by the *Escherichia coli* dicB operon, is probably RNA. *Mol. Microbiol.* 3, 991–994. doi: 10.1111/j.1365-2958.1989.tb00249.x

Brantl, S. (2007). Regulatory mechanisms employed by cis-encoded antisense RNAs. *Curr. Opin. Microbiol.* 10, 102–109. doi: 10.1016/j.mib.2007.03.012

Browning, D. F., and Busby, S. J. W. (2016). Local and global regulation of transcription initiation in bacteria. *Nat. Rev. Microbiol.* 14, 638–650. doi: 10.1038/nrmicro.2016.103

Cam, K., Rome, G., Krisch, H. M., and Bouché, J. P. (1996). RNase E processing of essential cell division genes mRNA in *Escherichia coli*. *Nucleic Acids Res.* 24, 3065–3070. doi: 10.1093/nar/24.15.3065

Camberg, J. L., Hoskins, J. R., and Wickner, S. (2009). ClpXP protease degrades the cytoskeletal protein, FtsZ, and modulates FtsZ polymer dynamics. *Proc. Natl. Acad. Sci. U. S. A.* 106, 10614–10619. doi: 10.1073/pnas.0904886106

Cases, I., and de Lorenzo, V. (2005). Promoters in the environment: Transcriptional regulation in its natural context. *Nat. Rev. Microbiol.* 3, 105–118. doi: 10.1038/nrmicro1084

Condon, C., Squires, C., and Squires, C. L. (1995). Control of rRNA transcription in *Escherichia coli*. *Microbiol. Rev.* 59, 623–645. doi: 10.1128/mr.59.4.623-645.1995

Dai, K., and Lutkenhaus, J. (1991). ftsZ Is an essential cell division gene in *Escherichia coli*. *J. Bacteriol.* 173, 3500–3506. doi: 10.1128/jb.173.11.3500-3506.1991

Dai, K., and Lutkenhaus, J. (1992). The proper ratio of FtsZ to FtsA is required for cell division to occur in *Escherichia coli*. *J. Bacteriol.* 174, 6145–6151. doi: 10.1128/jb.174.19.6145-6151.1992

Davis, J. H., Rubin, A. J., and Sauer, R. T. (2011). Design, construction and characterization of a set of insulated bacterial promoters. *Nucleic Acids Res.* 39, 1131–1141. doi: 10.1093/nar/gkq810

Dewar, S. J., and Donachie, W. D. (1993). Antisense transcription of the ftsZ-ftsA gene junction inhibits cell division in *Escherichia coli*. *J. Bacteriol.* 175, 7097–7101. doi: 10.1128/jb.175.21.7097-7101.1993

Dewar, S. J., and Dorazi, R. (2000). Control of division gene expression in *Escherichia coli*. *FEMS Microbiol. Lett.* 187, 1–7. doi: 10.1111/j.1574-6968.2000.tb09127.x

Dewar, S. J., Begg, K. J., and Donachie, W. D. (1992). Inhibition of cell division initiation by an imbalance in the ratio of FtsA to FtsZ. *J. Bacteriol.* 174, 6314–6316. doi: 10.1128/jb.174.19.6314-6316.1992

Dühring, U., Axmann, I. M., Hess, W. R., and Wilde, A. (2006). An internal antisense RNA regulates expression of the photosynthesis gene isiA. *Proc. Natl. Acad. Sci. U. S. A.* 103, 7054–7058. doi: 10.1073/pnas.0600927103

Erickson, J., Vaughn, V., Walter, W., Neidhardt, F., and Gross, C. (1987). Regulation of the promoters and transcripts of rpoH, the Escherichia coli heat shock regulatory gene. *Gene Dev.* 1, 149–432. doi: 10.1101/gad.1.5.419

Etchegaray, J. P., Jones, P. G., and Inouye, M. (1996). Differential thermoregulation of two highly homologous cold-shock genes, cspA and cspB, of *Escherichia coli*. *Genes Cells* 1, 171–178. doi: 10.1046/j.1365-2443.1996.d01-231.x

Flärdh, K., Garrido, T., and Vicente, M. (1997). Contribution of individual promoters in the ddlB-ftsZ region to the transcription of the essential cell-division gene ftsZ in *Escherichia coli*. *Mol. Microbiol.* 24, 927–936. doi: 10.1046/j.1365-2958.1997.4001762.x

Flynn, J. M., Neher, S. B., Kim, Y. I., Sauer, R. T., and Baker, T. A. (2003). Proteomic discovery of cellular substrates of the ClpXP protease reveals five classes of ClpX-recognition signals. *Mol. Cell* 11, 671–683. doi: 10.1016/S1097-2765(03)00060-1

Gerhart, E., Wagner, H., and Simons, R. W. (1994). Antisense RNA control in bacteria, phages, and plasmids. *Annu. Rev. Microbiol.* 48, 713–742. doi: 10.1146/annurev.mi.48.100194.003433

Giangrossi, M., Prosseda, G., Tran, C. N., Brandi, A., Colonna, B., and Falconi, M. (2010). A novel antisense RNA regulates at transcriptional level the virulence gene icsA of *Shigella flexneri*. *Nucleic Acids Res.* 38, 3362–3375. doi: 10.1093/nar/gkq025

Grossman, A., Erickson, J., and Gross, C. (1984). The htpR gene product of *E. coli* is a sigma factor for heat-shock promoters. *Cell* 38, 383–390. doi: 10.1016/0092-8674(84)90493-8

Guo, M. S., Updegrove, T. B., Gogol, E. B., Shabalina, S. A., Gross, C. A., and Storz, G. (2014). MicL, a new σE-dependent sRNA, combats envelope stress by repressing synthesis of Lpp, the major outer membrane lipoprotein. *Genes Dev.* 28, 1620–1634. doi: 10.1101/gad.243485.114

Hawley, D. K., and Mcclure, W. R. (1983). Compilation and analysis of *Escherichia coli* promoter DNA sequences. *Nucleic Acids Res.* 11, 2237–2255. doi: 10.1093/nar/11.8.2237

Hershberg, R., Bejerano, G., Santos-Zavaleta, A., and Margalit, H. (2001). PromEC: An updated database of *Escherichia coli* mRNA promoters with experimentally identified transcriptional start sites. *Nucleic Acids Res.* 29:277.

Hocine, S., Vera, M., Zenklusen, D., and Singer, R. H. (2015). Promoter-autonomous functioning in a controlled environment using single molecule FISH. *Sci. Rep.* 5, 1–11. doi: 10.1038/srep09934

Lease, R. A., and Woodson, S. A. (2004). Cycling of the Sm-like protein Hfq on the DsrA small regulatory RNA. *J. Mol. Biol.* 344, 1211–1223. doi: 10.1016/j.jmb.2004.10.006

Lee, E. J., and Groisman, E. A. (2010). An antisense RNA that governs the expression kinetics of a multifunctional virulence gene. *Mol. Microbiol.* 76, 1020–1033. doi: 10.1111/j.1365-2958.2010.07161.x

Lisser, S., and Margalit, H. (1993). Compilation of *E. coli* mRNA promoter sequences. *Nucleic Acids Res.* 21, 1507–1516. doi: 10.1093/nar/21.7.1507

Livak, K. J., and Schmittgen, T. D. (2001). Analysis of relative gene expression data using real-time quantitative PCR and the $2^{-\Delta\Delta CT}$ method. *Methods* 25, 402–408. doi: 10.1006/meth.2001.1262

Livingstone, P. G., Millard, A. D., Swain, M. T., and Whitworth, D. E. (2018). Transcriptional changes when Myxococcus xanthus preys on *Escherichia coli* suggest myxobacterial predators are constitutively toxic but regulate their feeding. *Microb. Genom.* 4:e000152. doi: 10.1099/mgen.0.000152

Lorenz, C., Gesell, T., Zimmermann, B., Schoeberl, U., Bilusic, I., Rajkowitsch, L., et al. (2010). Genomic SELEX for Hfq-binding RNAs identifies genomic aptamers predominantly in antisense transcripts. *Nucleic Acids Res.* 38, 3794–3808. doi: 10.1093/nar/gkq032

Löwe, J., Van Den Ent, F., and Amos, L. A. (2004). Molecules of the bacterial cytoskeleton. *Annu. Rev. Biophys. Biomol. Struct.* 33, 177–198. doi: 10.1146/annurev.biophys.33.110502.132647

Majdalani, N., Chen, S., Murrow, J., St John, K., and Gottesman, S. (2004). Regulation of RpoS by a novel small RNA: The characterization of RprA. *Mol. Microbiol.* 39, 1382–1394. doi: 10.1111/j.1365-2958.2001.02329.x

McGrath, P. T. (2011). Characterizing cDNA ends by circular RACE. *Methods Mol. Biol.* 772, 257–265. doi: 10.1007/978-1-61779-228-1_15

Mitchell, J. E., Zheng, D., Busby, S. J. W., and Minchin, S. D. (2003). Identification and analysis of "extended -10" promoters in *Escherichia coli*. *Nucleic Acids Res.* 31, 4689–4695. doi: 10.1093/nar/gkg694

Opdyke, J. A., Kang, J. G., and Storz, G. (2004). GadY, a small-RNA regulator of acid response genes in *Escherichia coli*. *J. Bacteriol.* 186, 6698–6705. doi: 10.1128/JB.186.20.6698-6705.2004

Papenfort, K., Said, N., Welsink, T., Lucchini, S., Hinton, J. C. D., and Vogel, J. (2009). Specific and pleiotropic patterns of mRNA regulation by ArcZ, a conserved, Hfq-aependent small RNA. *Mol. Microbiol.* 74, 139–158. doi: 10.1111/j.1365-2958.2009.06857.x

Pla, J., Sanchez, M., Patacios, P., Vicente, M., and Aldea, M. (1991). Preferential cytoplasmic location of FtsZ, a protein essential for *Escherichia coli* septation. *Mol. Microbiol.* 5, 1681–1686. doi: 10.1111/j.1365-2958.1991.tb01915.x

Raghavan, R., Sloan, D. B., and Ochman, H. (2012). Antisense transcription is pervasive but rarely conserved in enteric bacteria. *Mbio* 3, e00156–12. doi: 10.1128/mBio.00156-12

Roy, S., Mir, M. A., Anand, S. P., Niederweis, M., and Ajitkumar, P. (2004). Identification and semi-quantitative analysis of *Mycobacterium tuberculosis* $H_{37}R_v$ ftsZ gene-specific promoter activity-containing regions. *Res. Microbiol.* 155, 817–826. doi: 10.1016/j.resmic.2004.06.004

Rueda, S., Vicente, M., and Mingorance, J. (2003). Concentration and assembly of the division ring proteins FtsZ, FtsA, and ZipA during the *Escherichia coli* cell cycle. *J. Bacteriol.* 185, 3344–3351. doi: 10.1128/JB.185.11.3344-3351.2003

Ruff, E. F., Thomas Record, M., and Artsimovitch, I. (2015). Initial events in bacterial transcription initiation. *Biomolecules* 5, 1035–1062. doi: 10.3390/biom5021035

Saberi, F., Kamali, M., Najafi, A., Yazdanparast, A., and Moghaddam, M. M. (2016). Natural antisense RNAs as mRNA regulatory elements in bacteria: A review on function and applications. *Cell. Mol. Biol. Lett.* 21:17. doi: 10.1186/s11658-016-0007-z

Schellhorn, H. E. (1995). Regulation of hydroperoxidase (catalase) expression in *Escherichia coli*. *FEMS Microbiol. Lett.* 131, 113–119. doi: 10.1111/J.1574-6968.1995.TB07764.X

Shih, Y.-L., and Rothfield, L. (2006). The Bacterial Cytoskeleton. *Microbiol. Mol. Biol. Rev.* 70, 729–754. doi: 10.1128/mmbr.00017-06

Skovierova, H., Rezuchova, B., Homerova, D., Roberts, M., and Kormanec, J. (2006). Characterization of the σE-dependent rpoEp3 promoter of *Salmonella enterica* serovar Typhimurium. *FEMS Microbiol. Lett.* 261, 53–59. doi: 10.1111/j.1574-6968.2006.00325.x

Soper, T., Mandin, P., Majdalani, N., Gottesman, S., and Woodson, S. A. (2010). Positive regulation by small RNAs and the role of Hfq. *Proc. Natl. Acad. Sci. U. S. A.* 107, 9602–9607. doi: 10.1073/pnas.1004435107

Srivastava, S. K., Iyer, V. R., Ghosh, T., Lambadi, P. R., Pathania, R., and Navani, N. K. (2016). Isolation of a non-genomic origin fluoroquinolone responsive regulatory element using a combinatorial bioengineering approach. *Nucleic Acids Res.* 44, 2451–2461. doi: 10.1093/nar/gkw029

Tamura, M., Lee, K., Miller, C. A., Moore, C. J., Shirako, Y., Kobayashi, M., et al. (2006). RNase E maintenance of proper FtsZ/FtsA ratio required for nonfilamentous growth of *Escherichia coli* cells but not for colony-forming ability. *J. Bacteriol.* 188, 5145–5152. doi: 10.1128/JB.00367-06

Tétart, F., and Bouché, J. P. (1992). Regulation of the expression of the cell-cycle gene ftsZ by DicF antisense RNA. Division does not require a fixed number of FtsZ molecules. *Mol. Microbiol.* 6, 615–620. doi: 10.1111/j.1365-2958.1992.tb01508.x

Valdivia, R. H., and Falkow, S. (1996). Bacterial genetics by flow cytometry: Rapid isolation of *Salmonella typhimurium* acid-inducible promoters by differential fluorescence induction. *Mol. Microbiol.* 22, 367–378. doi: 10.1046/j.1365-2958.1996.00120.x

Vicente, M., Gomez, M. J., and Ayala, J. A. (1998). Regulation of transcription of cell division genes in the *Escherichia coli* dcw cluster. *Cell. Mol. Life Sci.* 54, 317–324. doi: 10.1007/s000180050158

Wang, H., and Gayda, R. C. (1990). High-level expression of the FtsA protein inhibits cell septation in *Escherichia coli* K-12. *J. Bacteriol.* 172, 4736–4740. doi: 10.1128/jb.172.8.4736-4740.1990

Wang, W., Chen, K., and Xu, C. (2006). DNA quantification using EvaGreen and a real-time PCR instrument. *Anal. Biochem.* 356, 303–305.

Ward, J. E., and Lutkenhaus, J. (1985). Overproduction of FtsZ induces minicell formation in *E. coli*. *Cell* 42, 941–949. doi: 10.1016/0092-8674(85)90290-9

Wecker, E. (1959). The extraction of infectious virus nucleic acid with hot phenol. *Virology* 7, 241–243. doi: 10.1016/0042-6822(59)90191-6

Wen, Y., Feng, J., Scott, D. R., Marcus, E. A., and Sachs, G. (2011). A cis-encoded antisense small RNA regulated by the HP0165-HP0166 two-component system controls expression of ureB in *Helicobacter pylori*. *J. Bacteriol.* 193, 40–51. doi:10.1128/JB.00800-10

Yanisch-Perron, C., Vieira, J., and Messing, J. (1985). Improved M13 phage cloning vectors and host strains: Nucleotide sequences of the M13mp18 and pUC19 vectors. *Gene* 33, 103–119. doi: 10.1016/0378-1119(85)90120-9

Zuker, M. (2003). Mfold web server for nucleic acid folding and hybridization prediction. *Nucleic Acids Res.* 31, 3406–3415. doi: 10.1093/nar/gkg595

Frontiers in Microbiology

Explores the habitable world and the potential of microbial life

The largest and most cited microbiology journal which advances our understanding of the role microbes play in addressing global challenges such as healthcare, food security, and climate change.

Discover the latest Research Topics

See more →

Frontiers

Avenue du Tribunal-Fédéral 34
1005 Lausanne, Switzerland
frontiersin.org

Contact us

+41 (0)21 510 17 00
frontiersin.org/about/contact